Deformation of Gabbros Accreted at Slow-Spreading Ridges within Oceanic Core Complexes

Maël Allard

THÈSE POUR OBTENIR LE GRADE DE DOCTEUR DE L'UNIVERSITÉ DE MONTPELLIER

En Géosciences

École doctorale GAIA : Biodiversité, Agriculture, Alimentation, Environnement, Terre, Eau

Unité de recherche Géosciences Montpellier – UMR 5243

Deformation of Gabbros Accreted at Slow-Spreading Ridges within Oceanic Core Complexes

Présentée par Maël ALLARD
Le 10 décembre 2021

Sous la direction de Benoît ILDEFONSE et Émilien OLIOT

Devant le jury composé de

Sandra PIAZOLO, Professeure des Universités – University of Leeds (UK)	Rapporteure
Mathilde CANNAT, Directrice de Recherche CNRS – Institut de Physique du Globe de Paris	Rapporteure
Andréa TOMMASI, Directrice de Recherche CNRS – Université de Montpellier	Examinatrice (Présidente)
Alessio SANFILIPPO, Maître de Conférences – Università degli studi di Pavia (Italie)	Examinateur
Holger STÜNITZ, Professeur des Universités – The Arctic University of Norway	Examinateur
Benoît ILDEFONSE, Directeur de Recherche CNRS – Université de Montpellier	Directeur de thèse
Émilien OLIOT, Maître de Conférences – Université de Montpellier	Co-encadrant de thèse

UNIVERSITÉ DE MONTPELLIER

“{Insérer une citation ici}”

Maël Allard

TABLE DES MATIÈRES

REMERCIEMENTS

En guises de préambule, je tiens tout d'abord à adresser un grand merci à Larry Tesler et Warren Teitelman pour l'invention des trois éléments essentiels à toute vie sur Terre, à savoir Ctrl+c, Ctrl+v, et Ctrl+z.

This being established, I wish to thank the members of my jury: Sandra Piazolo, Mathilde Cannat, Andréa Tommasi, Alessio Sanfilippo, and Holger Stünitz for the time you are about to spent reviewing my manuscript and for your interest in the subject.

Pour son accueil, je remercie le laboratoire Géosciences Montpellier dans son ensemble ainsi que tous les permanents avec qui j'ai interagi au cours de ces années de thèse. Un merci particulier aux membres de l'équipe manteau, pour les discussions constructives que nous avons pu avoir.

Benoît et Émilien, c'est avec un grand plaisir que j'ai travaillé avec vous durant ces 3 années ! De par votre passion, vos connaissances, et votre sympathie vous avez su me guider et m'encourager tout au long de cette thèse, et ce toujours dans la bonne humeur.
Merci aussi pour les différents voyages qui ont accompagné cette thèse, Benoît pour le Japon, qui était une expérience très enrichissante, tant d'un point de vue scientifique que culturel mais aussi (surtout ?) culinaire ; et Émilien, pour l'Italie, même si je persiste à croire que fin Juillet à proximité des cinq Terres c'est idéal pour les paysages et les spécialités locales (la nourriture à toujours son importance), mais pour des journées de terrains sans un arbre pour nous faire de l'ombre, ça n'était peut-être pas la meilleure période qui soit !

Merci également aux différentes personnes avec qui j'ai travaillé durant cette thèse hors des murs de GM. À Pierre Lanari, de l'Institut des Sciences Géologiques de Berne, pour ton aide et tes conseils quant à la valorisation des belles données pétro-géochimiques que nous avons acquises. Merci aussi pour avoir rendu possible la tenue de l'ensemble des analyses souhaitées malgré un contexte plutôt chargé en matière de demandes. Merci à Holger Stünitz, de l'Université Arctique de Norvège, pour avoir suivi cette thèse depuis le début et pour tes conseils et ton expertise. Merci enfin au laboratoire Chrono-Environnement de Besançon pour son accueil.

Aux doctorants (et affiliés : post-doc, Ater…), merci à vous pour les bons moments passés au labo et pour la bonne ambiance générale qui était facile à dénicher au détour d'un muret, d'un couloir ou d'un café. À Adeline, qui, tel un bouquetin, était toujours prête à bondir de rocher en rocher. À Julia, toujours la banane, la pêche, bref un cocktail pétillant, et toujours pleine de bons conseils. À Matthieu, même si parfois un peu satellisés, que je remercie pour ses nombreux conseils « oui c'est bien comme ça. Quoi que… non peut-être un peu plus penché sur la gauche… oui voilà, là c'est mieux ! », rien ne vaut un bon plasman et que tout le monde se tienne à Caro ! En parlant de placement, Herr Decrausatz je te remercie également pour

bons moments au labo ou encore la raquette (ou raclette ?) à la main. Thomas, je te remercie avant tout pour avoir su occuper l'espace dans notre bureau et le tenir bien rangé. Remarque le « notre », après tout ton nom était aussi sur la porte ! (grâce à qui ?...). Mossieur Cyp, difficile de ne faire apparaitre qu'une jambe ou un pied par l'entrebâillement d'une porte au travers de quelques lignes, mais sache que l'intention est là, et merci pour ces soirées à jouer, que ça soit en lançant des dés ou bien la manette… Tient en parlant des jeunes, merci aussi à toi Oswlad, qui a toujours le bon mot, la bonne réplique pour paraître agréable envers tes (très-) congénères. Merci aussi à toi Rémi, pour ta bonne humeur, et surtout pour tes belles interprétations de vieux sénile à nos séances de jdr ! Enfin, Dominik c'était un plaisir d'avoir partagé ce bureau avec toi, Ich wünsche Ihnen viel Glück und hoffe, Sie irgendwann wiederzusehen.

Enfin un grand merci à toi, elle se reconnaitra… Bon, trêve de niaiserie, merci Agathe pour ton soutien et ton expérience (comme quoi ça a du bon de passer en deuxième des fois), et pour le fait de m'avoir amené au pays du comté pour finir cette thèse au calme, c'était délicieux. Il serait peut-être exagéré de dire que je n'y serais pas arrivé sans toi (ça commence bien non ?), mais sache que tu y as beaucoup contribué et je t'en remercie sincèrement ! Enfin, dans ma grande bonté, je considère ton serment accompli, comme le disait Aragorn.

ABSTRACT

Slow-spreading ridges are characterized by heterogeneous architecture and seafloor geology. The association of serpentinized mantle rocks and lower crustal gabbros with basalts and marine sediments is common at the seafloor in the vicinity of slow- and ultraslow-spreading ridges. These rocks are exhumed through low-angle normal faults, referred to as detachment faults, which develop in response to the weak magmatic activity at the ridge axis. A significant part of the ridge spreading is accommodated by detachment faulting that progressively evolves into a domed edifice, known as an oceanic core complex, hosting the exhumed lithologies. These core complexes are key localities for investigating tectono-magmatic processes operating at slow-spreading ridges axes. To examine the characteristics of plastic deformation occurring at slow-spreading ridges, I studied a gabbroic sequence drilled on the Atlantis Bank (57°E, Southwest Indian Ridge), and gabbros sampled in a fossil oceanic core complex, the Bracco-Gabbro Complex (Internal Ligurides, Northern Apennines, Italy).

I performed microstructural and petro-geochemical studies of gabbros from the Atlantis Bank and the Bracco-Gabbro Complex and complemented them by thermodynamic modeling (Atlantis Bank gabbros). My thesis focusses on IODP Hole U1473A drilled to ~800 m below seafloor in 2016 on the Atlantis bank. The widespread plastic deformation observed in gabbros throughout the core was essentially achieved by dislocation creep, inducing significant dynamic recrystallization of plagioclase, olivine, and clinopyroxene. This deformation is related to emplacement and cooling of the gabbros in the lithosphere and to their subsequent exhumation by detachment faulting. The four main successive episodes of deformation are : (I) hypersolidus crystal-plastic deformation (> 1050 °C, 200-300 MPa) resulting from spreading-related forces at the ridge; (II) solid-state plastic deformation associated to detachment faulting, locally accompanied by melt channeling (1000-1050 °C, 200-300 MPa). Where present, the melt induces melt-rock reactions and enhances strain localization associated with melt-assisted grain boundary sliding; (III) solid-state mylonitization and intracrystalline hardening during strain localization (800-860 °C, 130-150 MPa); (IV) solid-state to semi-brittle strain localization associated to hydrothermal fluid circulation (700 °C, 100 MPa). A change to fluid-assisted grain boundary sliding occurs in highly localized shear zones.
This continuum of deformation was essentially achieved by dislocation creep from hypersolidus to amphibolitic conditions, and is associated with the dominant activity of the [100](010) slip system in plagioclase grains. Decreasing temperature during exhumation and synchronous ductile deformation results in the activation of different slip systems from granulitic to amphibolitic conditions.

The Bracco-Gabbro Complex is an Alpine Tethys fossil oceanic core complex exposed in the Internal Ligurides. In contrast to the Atlantis Bank, high-grade plastic deformation is poorly

developed in the exhumed gabbro pluton. Deformation episodes are documented to occur under granulitic (> 850 °C) to greenschist and sub-greenschist conditions (< 550 °C) and are assumed in previous studies to represent a continuous evolution path during detachment faulting. Dislocation creep is dominant at HT conditions, leading to the dynamic recrystallization of constitutive minerals, assisted by the dominant activation of the [100](010) slip system in plagioclase, and the development of a granulitic foliation. I propose that the Bracco-Gabbro Complex corresponds to a "late-capture OCC", with higher shear stresses associated to the development of high-grade shear zones, in opposition to the "early-capture OCC" such as the Atlantis Bank. The gabbro pluton was then almost fully crystallized before the detachment faulting initiation.

RÉSUMÉ

L'association de roches serpentinisées du manteau et de gabbros de la croûte inférieure avec des basaltes et des sédiments marins est fréquente sur le plancher océanique à proximité des dorsales lentes et ultra-lentes. Ces roches sont exhumées par des failles normales à faible pendage, les failles de détachement, qui se développent en réponse à la faible activité magmatique à l'axe de la dorsale. Une part importante de l'extension à la dorsale est accommodée par ces failles qui mènent à la formation d'un édifice en dôme, un core complexe océanique, qui abrite les lithologies exhumées. Ces core complexes sont des lieux clés pour l'étude des processus tectono-magmatiques opérant aux dorsales lentes. Pour examiner les caractéristiques de la déformation plastique qui se produit au niveau des dorsales lentes, j'ai étudié une séquence gabbroïque forée à l'Atlantis Bank (57°E, dorsale sud-ouest Indienne), et des gabbros échantillonnés dans un core complexe océanique fossile, le complexe gabbroïque de Bracco (Ligurides internes, Apennins du Nord, Italie).

J'ai réalisé des études microstructurales et pétro-géochimiques dans les gabbros de l'Atlantis Bank et du complexe gabbroïque de Bracco et les ai complétées par une modélisation thermodynamique (Atlantis Bank). Ma thèse se concentre sur le puits IODP U1473A foré jusqu'à ~800 m de profondeur à l'Atlantis Bank en 2016. La déformation plastique omniprésente observée dans les gabbros tout au long de la carotte s'est essentiellement produite par fluage des dislocations, induisant une recristallisation dynamique importante du plagioclase, de l'olivine et du clinopyroxène. Cette déformation est liée à la mise en place et l'exhumation des gabbros par le biais de la faille de détachement. Les quatre principaux épisodes successifs de déformation sont : (I) déformation plastique hypersolidus (> 1050 °C, 200-300 MPa) résultant d'un forcage externe lié à l'extension à la dorsale ; (II) déformation plastique à l'état solide associée à la formation de la faille de détachement (1000-1050 °C, 200-300 MPa). Localement, la circulation de liquide magmatique induit des interactions magma-roche et favorise la localisation de la déformation ; (III) mylonitisation à l'état solide et durcissement intra-cristallin associés à la localisation de la déformation (800-860 °C, 130-150 MPa) ; (IV) localisation de la déformation à l'état solide à semi-fragile associée à la circulation de fluides hydrothermaux (700 °C, 100 MPa).

Ce continuum de déformation s'est essentiellement produit par fluage des dislocations depuis des conditions hyper-solidus jusqu'à des conditions amphibolitiques, et est associé à l'activité dominante du système de glissement [100](010) dans le plagioclase. Différents systèmes de glissement sont activés lors de la déformation plastique accompagnant le métamorphisme rétrograde.

Le complexe gabbroïque de Bracco est un core complexe océanique fossile formé dans la Téthys alpine et aujourd'hui exposé dans les Ligurides internes. Contrairement l'Atlantis Bank, la déformation plastique HT est peu développée dans le pluton exhumé. Les épisodes de déformation sont documentés depuis des conditions granulitiques (> 850 °C) jusqu'aux schistes verts et inférieur (< 550 °C) et sont supposés, dans la littérature, représenter un

chemin d'évolution continu pendant la formation de la faille de détachement. Le fluage des dislocations est dominant dans les conditions HT, conduisant à la recristallisation dynamique des minéraux constitutifs, assistée par l'activation dominante du système de glissement [100](010) dans le plagioclase. Je propose que le complexe de Bracco corresponde à un OCC de type « capture tardive », avec des contraintes différentielles plus élevées associées au développement de zones de cisaillement HT, à l'inverse des OCC de type « capture précoce » tels que l'Atlantis Bank. Le pluton de Bracco était ainsi presque entièrement cristallisé avant l'initiation du détachement.

RÉSUMÉ ÉTENDU

La croûte océanique est la couche rigide supérieure qui couvre jusqu'à 55 % de la surface terrestre. Elle est formée en permanence par l'ascension et l'accrétion de roches fondues d'origine mantelliques au niveau des dorsales médio-océaniques qui constituent des frontières de plaques tectoniques divergentes. Plusieurs classes de dorsales médio-océaniques sont reconnues, en fonction de leur activité magmatique, de leur taux d'expansion et de la morphologie de leurs fonds marins (Ildefonse, 2014, et références y figurant ; Dunn, 2015). Au niveau des dorsales médio-océaniques caractérisées par des taux d'expansion lents, comme la dorsale sud-ouest Indienne ou la dorsale médio-Atlantique, la croûte ignée inférieure et les lithologies du manteau sont exposées sur le plancher océanique le long de certains segments de dorsale. Ce phénomène est interprété comme le résultat d'une activité magmatique faible ou absente pendant l'extension à la dorsale, en lien avec la tectonique (Karson & Dick, 1983; Cannat, 1993). Cette activité tectonique correspond au développement de failles normales à faible pendage et à longue durée d'activité (Escartín et al., 2008) qui accommodent une part importante de l'extension de la dorsale. Ces failles sont appelées failles de détachement et conduisent à l'exhumation des roches de la croûte profonde et du manteau supérieur, formant *in fine* des structures en dôme appelées "core complexes océaniques" (OCC ; Cann et al., 1997; Escartín & Canales, 2011). Les OCC sont caractérisés par des interactions complexes entre les processus de déformation et les processus magmatiques opérant pendant l'accrétion crustale. La profondeur de pénétration et le moment ou survient la déformation associée aux failles de détachement, ainsi que l'accrétion magmatique à l'axe de la dorsale, ont un impact important sur l'architecture de la croûte.

L'exploration des OCC offre une opportunité unique d'accéder à la croûte inférieure et de comprendre les processus impliqués dans son accrétion. L'étude de la croûte océanique formée aux dorsales lentes était principalement axée sur les ophiolites (Lagabrielle & Cannat, 1990; Lagabrielle, 2009) avant les progrès réalisés en géologie marine au cours des ~50 dernières années. Les premiers modèles de structure de la croute au niveau des dorsales lentes ont été construits progressivement grâce à des travaux détaillés réalisés dans la ceinture orogénique Alpine-Apennine en parallèle du dragage des fonds marins (Lagabrielle, 2009, et références y figurant). Aujourd'hui, nous possédons une plus grande connaissance sur la nature des magmas accrétés et sur leur mise en place dans la croûte inférieure, ainsi que sur les modes de déformation et la localisation des déformations. Une analyse détaillée de la déformation, en interaction avec les liquides magmatiques et les fluides en circulation, est importante car elle reflète le comportement rhéologique des croûtes océaniques lentes. Dans ce contexte, cette thèse vise à caractériser davantage et à quantifier précisément la déformation ductile en termes de mécanismes et de conditions de température. La déformation des plagioclases a été particulièrement explorée en raison de leur rôle primordial lors de la déformation des roches gabbroïques.

Ce projet de thèse est principalement basé sur l'étude des gabbros échantillonnés dans le puits IODP U1473A foré à l'Atlantis Bank (57°E) à de la dorsale sud-ouest Indienne lors de l'expédition IODP 360 (Dick et al., 2019b). Une collection de gabbros échantillonnés dans l'ophiolite de Bracco dans les Apennins du Nord a également été étudiée à des fins de comparaison. Tous les gabbros étudiés se sont formés à l'axe d'une dorsale lente et ont été exhumés sur le plancher océanique au sein d'un core complexe océanique.

La question générale abordée dans cette thèse est : quelles sont les caractéristiques de la déformation plastique qui se produit dans les gabbros pendant leur accrétion ainsi que leur exhumation au sein d'un core complexe océanique ?

Les aspects suivants ont été explorés pour répondre à cette question centrale :

(1) Quels sont les principaux mécanismes de déformation actifs, et quel est le rôle les principaux minéraux (en particulier le plagioclase) des gabbros dans l'accommodation de cette déformation ?

(2) Dans quelles conditions (pression-température-fluide), la déformation plastique se produit-elle ?

(3) Comment les structures de déformation sont-elles distribuées et organisées à l'échelle d'un pluton gabbro ?

Les principales approches utilisées dans cette thèse pour répondre à ces questions sont l'analyse microstructurale et l'analyse pétro-géochimique. L'analyse microstructurale s'appuie sur les observations pétrographiques classiques en lames minces et sur la micro-cartographie par diffraction d'électrons rétrodiffusés (EBSD). Elle vise à quantifier la déformation plastique et à identifier les mécanismes de déformation activés dans les principaux minéraux des gabbros. Ces aspects sont caractérisés par l'analyse des orientations cristallographiques préférentielles (CPO) au sein des agrégats de grains recristallisés, ainsi que par l'analyse des désorientations internes mesurées dans ces grains avec l'outil MTEX (Mainprice et al., 2015). Des analyses pétro-géochimiques ont été réalisées sur une sélection d'échantillons provenant des deux plutons gabbroïques étudiés, par le biais d'analyses in situ à la microsonde électronique (EPMA) et de cartographie chimique quantitative. D'autres caractérisations par modélisation thermodynamique avec le logiciel Perple_X (Connolly, 2005) ont été effectuées dans le system $NCKFe^{2+}Fe^{3+}MASHT$ sur les échantillons sélectionnés à l'Atlantis Bank. Elles servent à quantifier les changements chimiques associés aux déformations et à définir les conditions auxquelles se produisent les déformations.

La dorsale sud-ouest Indienne (SWIR) est une dorsale de type ultra-lent dont le taux d'expansion total est de ~14 mm.an^{-1} (expansion asymétrique de 8,5 mm.an^{-1} au sud et de 5,5 mm.an-^{1} au nord ; Hosford et al., 2003). Situé à 73-116 km au sud de l'axe de la dorsale, le l'Atlantis Bank est un pluton gabbroïque plurikilométrique bordé sur son flanc ouest par la faille transformante nord-sud Atlantis II (Figure 1a). Ce massif sous-marin est un OCC récent, formé il y a 11-13 Ma, qui émerge de ~3000 m à ~700 m du plancher océanique. Son sommet est une surface plane correspondant à une plate-forme érodée par les vagues il y a ~9,5 Ma (Figure 1a ; Dick et al., 1991). Bien que la surface de l'Atlantis Bank ne soit pas une surface de détachement classique, la présence de schistes à talc-serpentine autour du massif est documentée (Baines et al., 2003; Dick et al., 2019a) ainsi que des zones de cisaillement ductiles à faible pendage situées dans les parties supérieures du puits ODP 735B et du puits IODP U1473A (Dick et al., 2000, 2019b). Ces zones de cisaillement présentent principalement un sens de cisaillement normal dans les 50 m supérieurs et ~450 m des puits U1473A et 735B, respectivement, avant de devenir inverses à des profondeurs plus importantes (Dick et al., 2019b). Le puits IODP U1473A a été foré depuis le sommet de l'Atlantis Bank jusqu'à 809,4 m en dessous du fond marin (mbsf : « meters below seafloor ») au cours des expéditions IODP 360 et 362T (Blum et al., 2017; Dick et al., 2019b). Deux autres puits avaient été forés entre 1987 et 1998 et sont situés à 1-2 km du puits U1473A : le puits ODP 735B (1508 mbsf ; Dick et al., 2000) et le puits ODP 1105A (158 mbsf ; Pettigrew et al., 1999). Les sections de carotte récupérées dans ces trois puits sont constituées de gabbros à olivine ainsi que de gabbros à oxydes, de gabbros *sensu stricto* et de troctolites (Figure 1b ; Pettigrew et al., 1999; Dick et al., 2000, 2019b). Les lithologies gabbroïques du puits U1473A sont fréquemment affectées par une déformation ductile, en particulier dans les 500 mbsf supérieurs où les textures porphyroclastiques à protomylonitiques évoluant en ultramylonites à l'échelle du mètre sont courantes (Figure 1c). Deux larges zones quasi-continues associées à une intense déformation plastique sont situées dans les intervalles ~150-250 mbsf et ~300-400 mbsf du puits (Figure 1c ; MacLeod et al., 2017). La partie plus profonde du puits U1473A (de 500-600 à ~800 mbsf, Figure 1c) est affectée par une déformation ductile plus localisée. Elle est caractérisée par d'étroites zones de forte déformation réparties de manière hétérogène au sein de lithologies gabbroïques principalement non déformées à porphyroclastiques. Ces zones de cisaillement correspondent à des ultramylonites d'échelle centimétrique à de rares mylonites d'échelle métrique. Les observations faites à bord du navire lors de la campagne de forage révèlent des textures magmatiques préservées dans 42 % des sections de carottes. La catégorisation qualitative des textures associées à la déformation plastique par leur intensité de déformation (indice CPF, pour « Crystal Plastic Fabric »), allant de 0 à 5 (indice CPF : 0 = non déformé, 1 = folié, 2 = porphyroclastique, 3 = protomylonique, 4 = mylonitique, 5 = ultramylonique), montre que les zones déformées sont caractérisées à 32 % par de textures

porphyroclastiques à protomylonitiques, et à 13 % par des textures mylonitiques à ultramylonitiques (Figure 1c ; MacLeod et al., 2017).

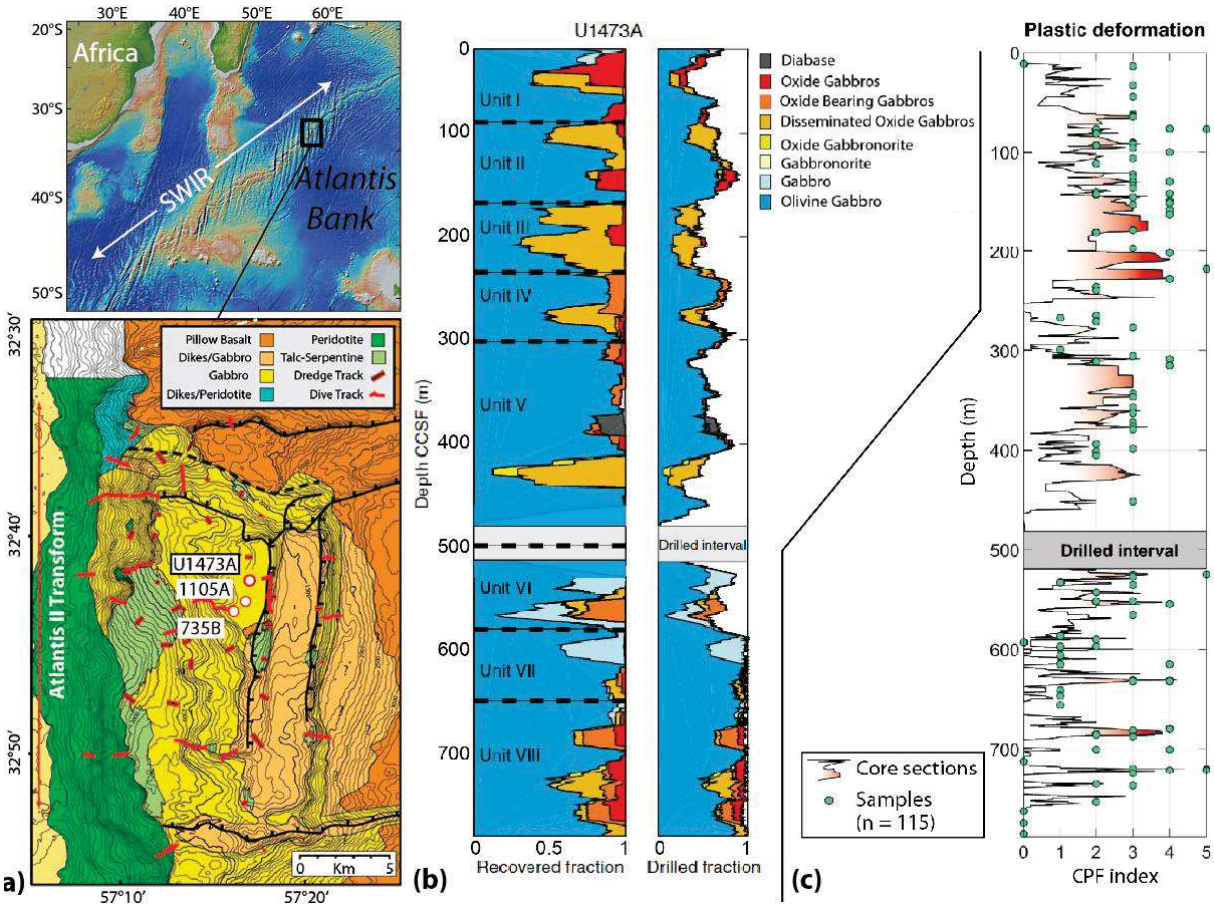

Figure 1 *- Localisation et caractéristiques du Puits IODP U1473A. (a) Localisation de l'Atlantis Bank à la dorsale sud-ouest Indienne (SWIR ; carte bathymétrique d'après Ryan et al. (2009), et carte géologique de l'Atlantis Bank, modifiée d'après Dick et al. (2019a). (b) Lithologies dans le puits U1473A, d'après MacLeod et al. (2017). (c) Moyenne mobile de l'intensité de la déformation plastique apparente, c'est-à-dire les indices de texture (indice CPF) déduits des observations macroscopiques des carottes (moyenne mobile sur cinq intervalles de profondeur, d'après MacLeod et al. (2017b). Indice CPF : 0 = non déformé, 1 = folié, 2 = porphyroclastique, 3 = protomylonitique, 4 = mylonitique, 5 = ultramylonitique. Les cercles verts dans (c) indiquent la position des échantillons étudiés.*

L'ensemble de l'histoire de la déformation ductile au sein de l'Atlantis Bank semble s'être déroulée de manière continue, depuis des conditions hyper-solidus jusqu'à de plus basses températures, tandis que des intrusions gabbroïques successives se sont mises en place dans la

lithosphère. Ce processus est décrit comme un processus d'accrétion dynamique, caractéristique des dorsales lentes avec un magmatisme faible à intermédiaire (Dick et al., 2019b).
Les conditions de la déformation ductile au niveau de l'Atlantis Bank correspondent à une succession de différents épisodes. Deux types dominants de déformation sont identifiés : une déformation à l'état solide par fluage des dislocations, et une déformation en présence de liquide magmatique, à la fois par des interactions magma-roche et par le fluage des dislocations. Une première étape de déformation à l'état solide (étape 1) a conduit à la recristallisation des grains primaires de plagioclase, de clinopyroxènes et d'olivine. Elle est documentée à 907-1093°C (médiane = 1026°C ; Gardner et al., 2020) et ~860-940°C (Mehl & Hirth, 2008) dans le puits 735B, à 862-910°C dans les échantillons récupérés lors de plongée en submersibles de la surface de l'Atlantis Bank (Miranda & John, 2010). Après cette étape initiale de déformation à l'état solide, deux épisodes de déformation en présence de liquides magmatiques sont mis en évidence (regroupés dans le stade 2). Le premier épisode (Stade 2a) s'est produit à 846-969°C (médiane à 949°C et 906°C ; Gardner et al., 2020), et le second (Stade 2b) à 817-1000°C, principalement de ~800 à 900°C (Gardner et al., 2020; Taufner et al., 2021). Un épisode de déformation à l'état solide de plus basse température (Stade 3) est documenté dans les mylonites à 740-840°C (médiane à 780°C dans Miranda et al., 2016, et 795°C dans Miranda & John, 2010). Un stade ultime de déformation à l'état solide - semi-fragile (stade 4) est enregistré principalement dans les mylonites/ultramylonites à plagioclase-amphibole à 665 ± 40°C (Miranda & John, 2010).

Suite aux analyses microstructurales, pétro-géochimiques et les modélisations thermodynamiques réalisées dans le cadre de ce projet, les quatre stades de déformation identifiés à l'Atlantis Bank sont réévalués. Il est proposé qu'un épisode de recristallisation primaire se produise à des températures > 1030 °C sous l'effet de forçages externes (Figure 2a). Puis la recristallisation s'intensifie fortement pour former des microstructures porphyroclastiques à protomylonitiques à ~1000-1050 °C et 200-300 MPa lorsque la faille de détachement pénètre dans la zone d'intrusion active, comme attesté par les observations pétrographiques et la modélisation thermodynamique (Figure 2b). Dans des conditions similaires, certains intervalles du puits étudié présentent des microstructures témoignant d'une circulation de liquides magmatiques associée à une localisation de la déformation. Les interactions magma-roche induites ont conduit à la formation d'une nouvelle génération de grains de plagioclase, d'olivine, d'orthopyroxène et d'amphibole caractérisés par une croissance épitaxiale ainsi qu'à un fort affaiblissement de la CPO dans tous les minéraux lié à du glissement aux joints de grains assisté par la présence locale de magma (Figure 2b). Dans d'autres intervalles de profondeur, la déformation plastique s'est poursuivie dans un régime purement solide, entraînant une recristallisation intense et une réduction importante de la taille des grains accompagnée d'un durcissement intra-cristallin dans les plagioclases (Figure 2c). Des CPO d'intensité moyenne sont mesurées dans les grains recristallisés de plagioclase, tandis que les CPO des grains de clinopyroxènes sont fortement

contrôlées par la bande monominérale dans laquelle elles sont mesurées. La modélisation de l'équilibre des phases et les modèles de déformation des produits de réaction de la roche fondue, orthopyroxène et d'amphibole, indiquent des conditions granulitiques pour la déformation à 867 °C et 155 MPa (Figure 2c). Un ultime épisode de déformation fragile-ductile en présence de fluides hydrothermaux a conduit à la formation d'étroites zones de cisaillement à plagioclase-amphibole (Figure 2d). Cette circulation intense de fluides pendant la localisation de la déformation a conduit à l'altération rétrograde du clinopyroxène en amphibole édénitique, et à la nucléation de grains d'édénite aux joints de grains de plagioclase. Les CPO mesurées dans le plagioclase sont aléatoires ou extrêmement faibles, ce qui indique du glissement aux joints de grains accompagnant la circulation de fluides. La localisation de la déformation en présence de fluides hydratés est prédite stable à ~700 °C et 100 MPa par la modélisation thermodynamique (Figure 2d). Les quatre épisodes de déformation identifiés dans cette étude représentent les principaux épisodes de déformation de haute-température qui se sont produits à l'Atlantis Bank dans le puits U1473A comme un continuum depuis des conditions hyper-solidus résultant de l'extension à la dorsale, jusqu'à des conditions de plus faible degré métamorphique en conditions granulitiques à amphibolitiques.

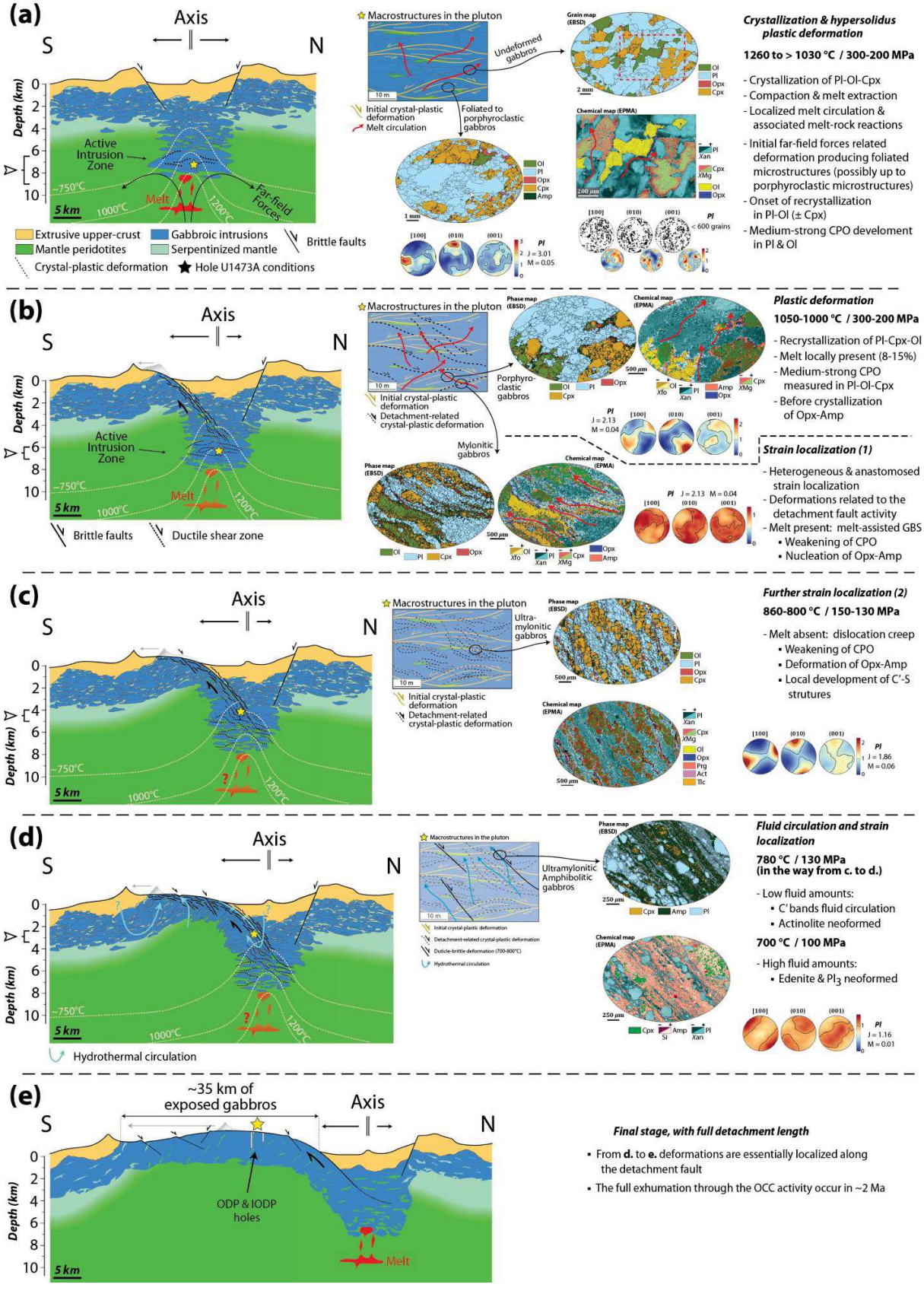
(a)
Axis
S
N
Depth (km)
Active Intrusion Zone
~750°C
Melt
1000°C
1200°C
Far-field Forces
5 km
Extrusive upper-crust
Gabbroic intrusions
Brittle faults
Mantle peridotites
Serpentinized mantle
Crystal-plastic deformation
Hole U1473A conditions
Macrostructures in the pluton
Undeformed gabbros
Foliated to porphyroclastic gabbros
Initial crystal-plastic deformation
Melt circulation
Grain map (EBSD)
Chemical map (EPMA)
Crystallization & hypersolidus plastic deformation
1260 to > 1030 °C / 300-200 MPa
- Crystallization of Pl-Ol-Cpx
- Compaction & melt extraction
- Localized melt circulation & associated melt-rock reactions
- Initial far-field forces related deformation producing foliated microstructures (possibly up to porphyroclastic microstructures)
- Onset of recrystallization in Pl-Ol (± Cpx)
- Medium-strong CPO develoment in Pl & Ol
(b)
Axis
S
N
Active Intrusion Zone
~750°C
Melt
1000°C
1200°C
5 km
Brittle faults
Ductile shear zone
Macrostructures in the pluton
Porphyro-clastic gabbros
Initial crystal-plastic deformation
Detachment-related crystal-plastic deformation
Mylonitic gabbros
Phase map (EBSD)
Chemical map (EPMA)
Plastic deformation
1050-1000 °C / 300-200 MPa
- Recrystallization of Pl-Cpx-Ol
- Melt locally present (8-15%)
- Medium-strong CPO measured in Pl-Ol-Cpx
- Before crystallization of Opx-Amp
Strain localization (1)
- Heterogeneous & anastomosed strain localization
- Deformations related to the detachment fault activity
- Melt present: melt-assisted GBS
▪ Weakening of CPO
▪ Nucleation of Opx-Amp
(c)
Axis
S
N
Depth (km)
~750°C
1000°C
1200°C
5 km
Macrostructures in the pluton
Ultra-mylonitic gabbros
Initial crystal-plastic deformation
Detachment-related crystal-plastic deformation
Phase map (EBSD)
Chemical map (EPMA)
Further strain localization (2)
860-800 °C / 150-130 MPa
- Melt absent: dislocation creep
▪ Weakening of CPO
▪ Deformation of Opx-Amp
▪ Local development of C'-S strutures
(d)
Axis
S
N
Depth (km)
~750°C
1000°C
1200°C
5 km
Hydrothermal circulation
Macrostructures in the pluton
Ultramylonitic Amphibolitic gabbros
Initial crystal-plastic deformation
Detachment-related crystal-plastic deformation
Ductile-brittle deformation (700-800°C)
Hydrothermal circulation
Phase map (EBSD)
Chemical map (EPMA)
Fluid circulation and strain localization
780 °C / 130 MPa
(in the way from c. to d.)
- Low fluid amounts:
▪ C' bands fluid circulation
▪ Actinolite neoformed
700 °C / 100 MPa
- High fluid amounts:
▪ Edenite & Pl3 neoformed
(e)
~35 km of exposed gabbros
Axis
S
N
Depth (km)
ODP & IODP holes
Melt
5 km
Final stage, with full detachment length
▪ From d. to e. deformations are essentially localized along the detachment fault
▪ The full exhumation through the OCC activity occur in ~2 Ma

Figure 2 *- Synthèse de l'histoire de la déformation observée à l'Atlantis Bank au travers de l'analyse des sections de carottes du puits IODP U1473A. A chaque étape, depuis la cristallisation (a), aux conditions d'hydratation rétrograde (d), nous proposons une coupe schématique à l'axe de la dorsale montrant le développement progressif du OCC, un croquis synthétique montrant les relations entre les épisodes de déformation et les circulations de liquides magmatiques et/ou de fluides, un exemple de microstructure (carte de grains EBSD) et de figures de pôles de plagioclase, et la carte chimique quantitative associée (carte des variations chimiques des phases combinées EPMA). L'intervalle de profondeur auquel les structures de déformation sont observées dans le puits est indiqué par l'étoile orange et par la flèche et les crochets le long de l'échelle de profondeur. Structure générale de la dorsale d'après Dick et al. (2019a) et stade final d'après Baines et al. (2008). Voir le texte pour plus de détails.*

Globalement, la déformation plastique des grains de plagioclase produit des fabriques cristallographiques faibles à moyens, qui sont progressivement acquises au fur et à mesure que la recristallisation augmente dans la roche (Figure 3). La recristallisation dynamique est principalement accomplie par la rotation des sous-grains, et le fluage des dislocations se produit avec l'activation dominante du système de glissement [100](010) dans le plagioclase, qui induit une orientation cristallographique préférée (Figure 3). L'affaiblissement de la CPO du plagioclase dans les ultramylonites où l'on observe que le fluage des dislocations est dominant s'explique par la dispersion progressive des orientations des grains suite à la recristallisation par rotation de sous-grains (Figure 3e). En plus de la recristallisation dynamique, des changements dans l'activité du système de glissement avec la diminution de la température de déformation sont documentés. Quatre systèmes de glissement différents sont identifiés par l'analyse des désorientations intra-granulaire : [001](010), [100](001), et deux de la famille ⟨100⟩ (001). Dans les mylonites/ultramylonites à grains fins où la circulation de liquides magmatique ou de fluides est documentée, le mécanisme de glissement aux joints grains est proposé de produire l'affaiblissement observé de la CPO. Enfin, la taille moyenne des grains recristallisés est plus élevée dans la partie supérieure du puits U1473A (> 500 mbsf), où la déformation est omniprésente et distribuée, que dans la partie inférieure du puits (500-800 mbsf) où la déformation est plus éparse et localisée. Dans cette partie inférieure, le passage d'une recristallisation par migration des limites des grains à une recristallisation par rotation des sous-grains semble lié aux variations des contraintes différentielles pendant la déformation plutôt qu'aux variations de température.

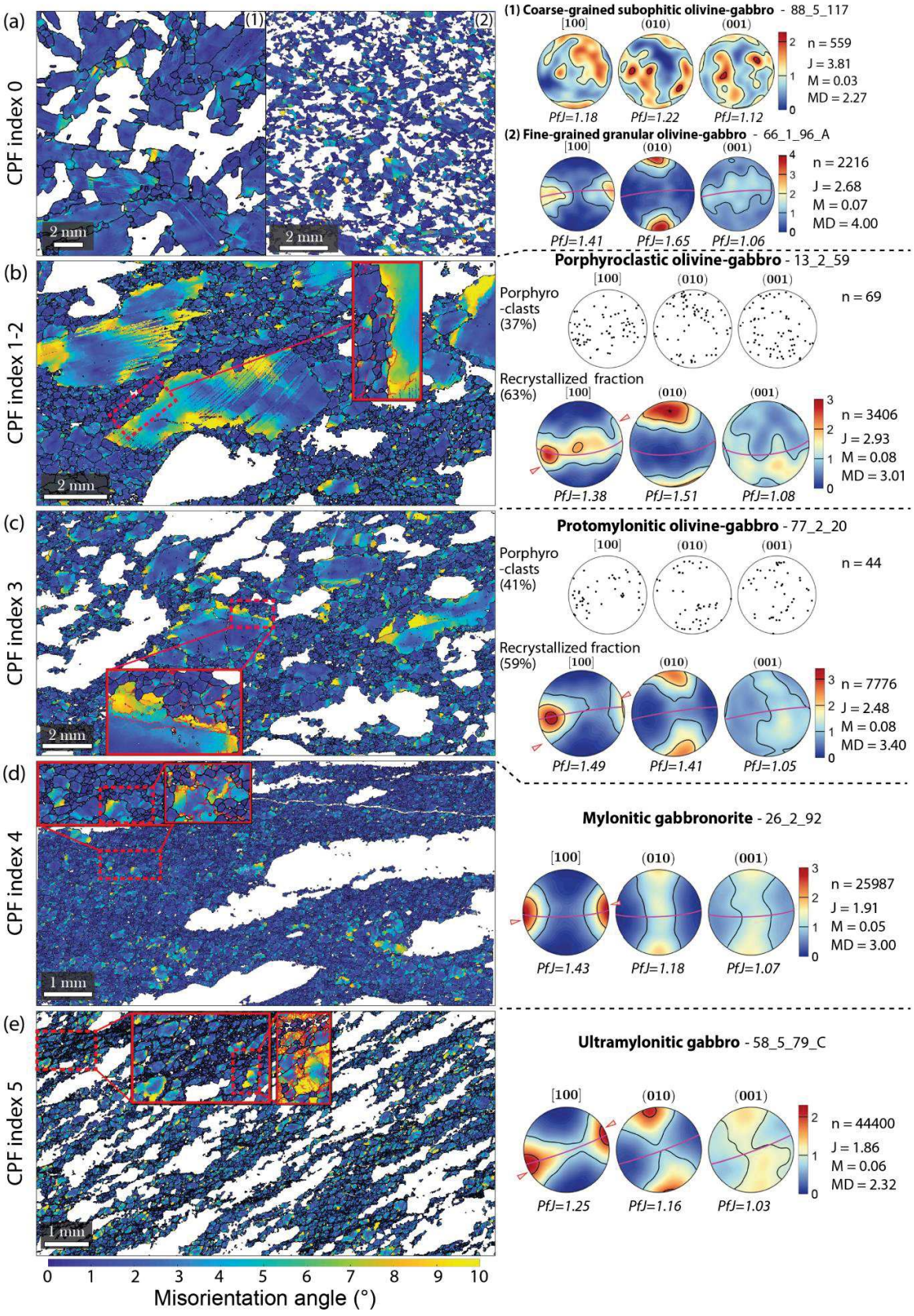
(a)
CPF index 0
(1)
(2)
2 mm
2 mm
(1) Coarse-grained subophitic olivine-gabbro - 88_5_117
[100] (010) (001)
PfJ=1.18 PfJ=1.22 PfJ=1.12
n = 559
J = 3.81
M = 0.03
MD = 2.27
(2) Fine-grained granular olivine-gabbro - 66_1_96_A
[100] (010) (001)
PfJ=1.41 PfJ=1.65 PfJ=1.06
n = 2216
J = 2.68
M = 0.07
MD = 4.00
(b)
CPF index 1-2
2 mm
Porphyroclastic olivine-gabbro - 13_2_59
Porphyro -clasts (37%)
[100] (010) (001)
n = 69
Recrystallized fraction (63%)
[100] (010) (001)
PfJ=1.38 PfJ=1.51 PfJ=1.08
n = 3406
J = 2.93
M = 0.08
MD = 3.01
(c)
CPF index 3
2 mm
Protomylonitic olivine-gabbro - 77_2_20
Porphyro -clasts (41%)
[100] (010) (001)
n = 44
Recrystallized fraction (59%)
[100] (010) (001)
PfJ=1.49 PfJ=1.41 PfJ=1.05
n = 7776
J = 2.48
M = 0.08
MD = 3.40
(d)
CPF index 4
1 mm
Mylonitic gabbronorite - 26_2_92
[100] (010) (001)
PfJ=1.43 PfJ=1.18 PfJ=1.07
n = 25987
J = 1.91
M = 0.05
MD = 3.00
(e)
CPF index 5
1 mm
Ultramylonitic gabbro - 58_5_79_C
[100] (010) (001)
PfJ=1.25 PfJ=1.16 PfJ=1.03
n = 44400
J = 1.86
M = 0.06
MD = 2.32
0 1 2 3 4 5 6 7 8 9 10
Misorientation angle (°)

Figure 3 *- Cartes des désorientations par rapport à l'orientation moyenne des grains dans le plagioclase, et figures de pole associées (données d'orientation moyenne des grains, hémisphère inférieur, projection à aire égale) mesurées dans des domaines représentatifs des indices CPF 0 à 5. La trace du plan (010) dans le plagioclase (définie par le vecteur propre principal du tenseur d'orientation) est représentée par les grands cercles roses, et l'orientation de la trace de la foliation mesurée dans les échantillons, lorsqu'elle est observée avec confiance, est indiquée par les flèches rouges à la périphérie des figures de pole [100]. La couleur blanche dans les cartes correspond aux autres phases, et les limites rouges dans les encarts sont les limites de sous-grains. Les intervalles des contours sont des multiples d'une distribution uniforme, et la densité minimale est fixée à zéro pour permettre la comparaison directe entre les domaines analysés. Les cartes et les figures de pôle sont présentées respectivement avec la profondeur augmentant de haut en bas et du pôle nord vers le pôle sud dans les figures de pole. "n" est le nombre de grains, "J" est l'indice de texture J, "M" est l'indice misorientation M, "MD" est la densité maximale, et "PfJ" sont les densités polaires de chaque figure de pole. Les pourcentages indiqués dans (c) et (d) sont les fractions mesurées de porphyroclastes et des grains recristallisés.*

Le complexe gabbroïque de Bracco (BGC) appartient aux Ligurides internes, et consiste en un pluton gabbroïque stratifié d'échelle kilométrique (5 par 6 km de large). Il intrude dans des péridotites mantelliques serpentinisées d'âge jurassique, et est associé en quantités limitées à des harzburgites et des dunites (Figure 4 ; Baumgartner et al., 2013; Tribuzio et al., 2016, et références y figurant). Des laves en coussins, des brèches ophiolitiques et des sédiments se trouvent au-dessus des gabbros et des péridotites. L'ensemble du complexe a été soumis, à des degrés variables, à un métamorphisme de basse température conduisant principalement à la formation de serpentine rétrograde, de chlorite, de prehnite et d'oxydes. Au SE du BGC (vers Levanto, Figure 4b), des proportions dominantes de roches du manteau sont exposées et sont interprétées comme représentant la base de la chambre magmatique (Cortesogno et al., 1987; Schwarzenbach et al., 2021). Le gabbro *sensu stricto* est la lithologie la plus courante, et les gabbros à olivines, les troctolites et les peridotites à plagioclases sont également documentées en quantités moindres dans le complexe. Dans les gabbros ignés, le plagioclase est de composition labradorite (~An60), le clinopyroxène se présente sous forme de diopside, et généralement l'olivine est fortement serpentinisée lorsqu'elle est présente dans ces roches. Le litage magmatique est fréquent dans les lithologies gabbroïques, et marqué par des variations de taille des grains ou de lithologie, parfois organisées en lentilles au sein du gabbro isotrope (Menna, 2009). Ce litage est généralement orientée NE-SW dans les domaines sud et ouest de la BGC, et change pour une orientation NW-SE dans la région centrale et nord (Figure 4c).

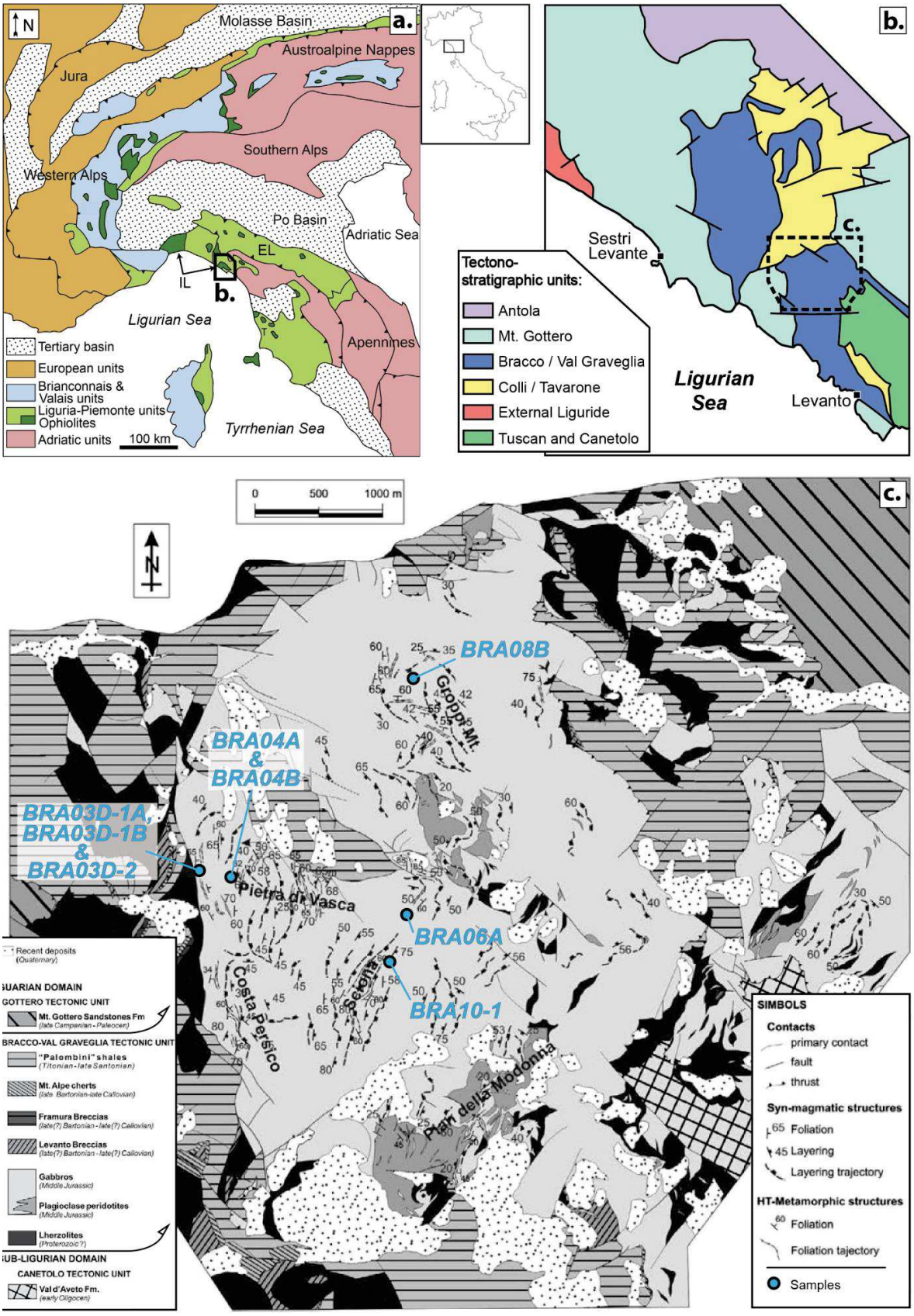
a.
N
Molasse Basin
Austroalpine Nappes
Jura
Southern Alps
Western Alps
Po Basin
Adriatic Sea
EL
IL
b.
Ligurian Sea
Apennines
Tyrrhenian Sea
Tertiary basin
European units
Brianconnais & Valais units
Liguria-Piemonte units Ophiolites
Adriatic units
100 km
b.
c.
Sestri Levante
Levante
Ligurian Sea
Tectono-stratigraphic units:
Antola
Mt. Gottero
Bracco / Val Graveglia
Colli / Tavarone
External Liguride
Tuscan and Canetolo
c.
0 500 1000 m
N
BRA08B
Groppo Mt.
BRA04A & BRA04B
BRA03D-1A, BRA03D-1B & BRA03D-2
Pietra di Vasca
BRA06A
BRA10-1
Costa Persico
Piana
Piani della Madonna
Recent deposits (Quaternary)
LIGURIAN DOMAIN
GOTTERO TECTONIC UNIT
Mt. Gottero Sandstones Fm (late Campanian - Paleocen)
BRACCO-VAL GRAVEGLIA TECTONIC UNIT
"Palombini" shales (Tithonian - late Santonian)
Mt. Alpe cherts (late Bartonian-late Callovian)
Framura Breccias (late(?) Bartonian - late(?) Callovian)
Levanto Breccias (late(?) Bartonian - late(?) Callovian)
Gabbros (Middle Jurassic)
Plagioclase peridotites (Middle Jurassic)
Lherzolites (Proterozoic?)
SUB-LIGURIAN DOMAIN
CANETOLO TECTONIC UNIT
Val d'Aveto Fm. (early Oligocen)
SIMBOLS
Contacts
primary contact
fault
thrust
Syn-magmatic structures
65 Foliation
45 Layering
Layering trajectory
HT-Metamorphic structures
60 Foliation
Foliation tajectory
Samples

Figure 4 *- Géologie de la région Alpe-Apennin et Bracco. (a) Carte géologique simplifiée des Alpes Liguries Centre-Ouest et des Apennins du Nord (d'après Rampone et al., 2020). IL : Ligurides internes, EL : Ligurides externes. (b) Carte géologique simplifiée de l'unité des Ligurides internes (modifiée d'après Marroni & Pandolfi, 1996). (c) Carte structurale de la zone de Bracco avec la localisation des échantillons étudiés (modifié d'après Menna, 2009).*

En plus de ce litage, une foliation magmatique est documentée avec une orientation similaire. Les zones de cisaillement mylonitiques documentées se sont généralement formées parallèlement aux structures magmatiques au cours de conditions métamorphiques rétrogrades, associées principalement à la recristallisation du plagioclase et du clinopyroxène. La variation de la composition du clinopyroxène pendant la recristallisation indique des conditions sub-solidus, estimées entre 850°C et 950°C sur la base de la teneur en TiO_2 des amphiboles présentes dans les agrégats de clinopyroxène recristallisé (Tribuzio et al., 2000; Montanini et al., 2008). Les zones de cisaillement formées pendant cette première phase de déformation plastique D_1 sont d'épaisseur variable, de quelques dizaines de centimètres à quelques dizaines de mètres, avec une intensité de déformation croissante vers le cœur de la zone (Molli, 1996; Menna, 2009). Quatre types de microstructures déformées sont identifiés associés à cette phase D_1. Elles correspondent à une évolution de l'intensité de la déformation depuis de faibles intensités, Fabriques I (idem aux indices de CPF 2), associées à la recristallisation progressive des grains amenant au développement d'une texture porphyroclastique, à de très fortes intensités, Fabriques IV (idem aux indices de CPF 5 mais avec une plus faible taille de grain), associées à une recristallisation complète de tous les grains en agrégats très fins formant des bandes riches en plagioclase et d'autres riches en clinopyroxene en alternance.
Des transitions à la fois progressives et discontinues entre les quatre types de fabriques peuvent être observées dans les roches, et correspondent à une intensité de déformation croissante (Molli, 1994; Menna, 2009).

La recristallisation statique des phases métamorphiques rétrogrades (principalement des amphiboles) est un trait caractéristique de la phase de déformation D2. Contrairement aux zones de cisaillement de la phase D1, celles formées pendant la phase D2 sont rares. La foliation résultante consiste en une alternance de bandes de plagioclase et d'amphiboles, et est souvent discontinue (Menna, 2009). Les zones de cisaillement s'étendent généralement jusqu'à une dizaine de mètres au maximum avec une épaisseur variable (< 4 m), se superposant parfois aux zones de cisaillement D_1. Les grains de plagioclase sont soumis à une cataclase et à un maclage mécanique, ainsi qu'à une réduction de la taille des grains. Les amphiboles croissent aux dépens du clinopyroxène durant cette phase, plus ou moins de manière statique, ce qui conduit à leur parallélisme avec l'orientation D_1. Les veines coupant les zones de cisaillement D_2 sont constituées de hornblende magnésiennes seule ou en association avec de la trémolite-actinolite (±

plagioclase, épidote et prehnite-pumpellyite). La serpentinisation est attribuée à la fin de cette phase de déformation, qui est proposée de se produire à ~550°C et 2 kbar et de se poursuivre en dessous de 500°C (c'est-à-dire jusqu'au début de la serpentinisation ; Menna, 2009).

Le troisième et dernier épisode de déformation D_3 consiste en un remplacement des anciennes phases mafiques par des amphiboles (tremolite-actinolite). On attribue souvent à cette phase des zones de cisaillement étroites et une crénulation de clivage, que l'on retrouve généralement le long des zones de cisaillement D_2. Accompagnant le développement des cataclasites, la phase D_3 s'est probablement produite à des températures inférieures à 500°C.

Les différents stades de déformation sont proposés de se produire en un continuum allant de conditions syn-magmatiques, granulitiques à des conditions amphibolitiques et enfin à des conditions de faciès schistes-verts (Menna, 2009). Bien qu'une transition des conditions granulitiques aux conditions amphibolitiques soit observée, elle peut simplement refléter la circulation des fluides (par exemple, l'eau de mer) plutôt que des changements dans les conditions de pression et de température.

Le complexe gabbroïque de Bracco présente de nombreuses caractéristiques structurales et compositionnelles similaires à celles des dorsales océaniques modernes à étalement lent, également reconnues dans d'autres ophiolites des Apennins du Nord. Le pluton gabbro exposé dans le Bracco conserve des zones de cisaillement de haut degré qui se sont développées à l'axe de la dorsale dans des conditions granulitiques. Les grains de plagioclase et de clinopyroxène à l'intérieur de ces zones de cisaillement se sont fortement recristallisés sous le régime de fluage des dislocations, produisant un CPO moyen à faible (Figure 5). On observe que l'intensité des CPO reste faible bien que l'intensité de la déformation augmente dans les échantillons. Ces CPO suggèrent l'activation dominante du système de glissement [100](010) dans les grains de plagioclase, et du système jumeau [100](001) dans les grains de clinopyroxène (Figure 5). Il est proposé que l'évolution tectonique du pluton au niveau de la dorsale corresponde à un OCC de type "capture tardive" tel que reconnu dans l'OCC de la dorsale médio-atlantique. Cela implique que les zones de cisaillement granulitiques ne sont peut-être pas directement liées à la faille de détachement (Figure 6). Les contraintes différentielles estimées indiquent des valeurs plus élevées dans ces structures lorsqu'elles sont formées dans un OCC de type "capture tardive" plutôt que dans un OCC de type "capture précoce".

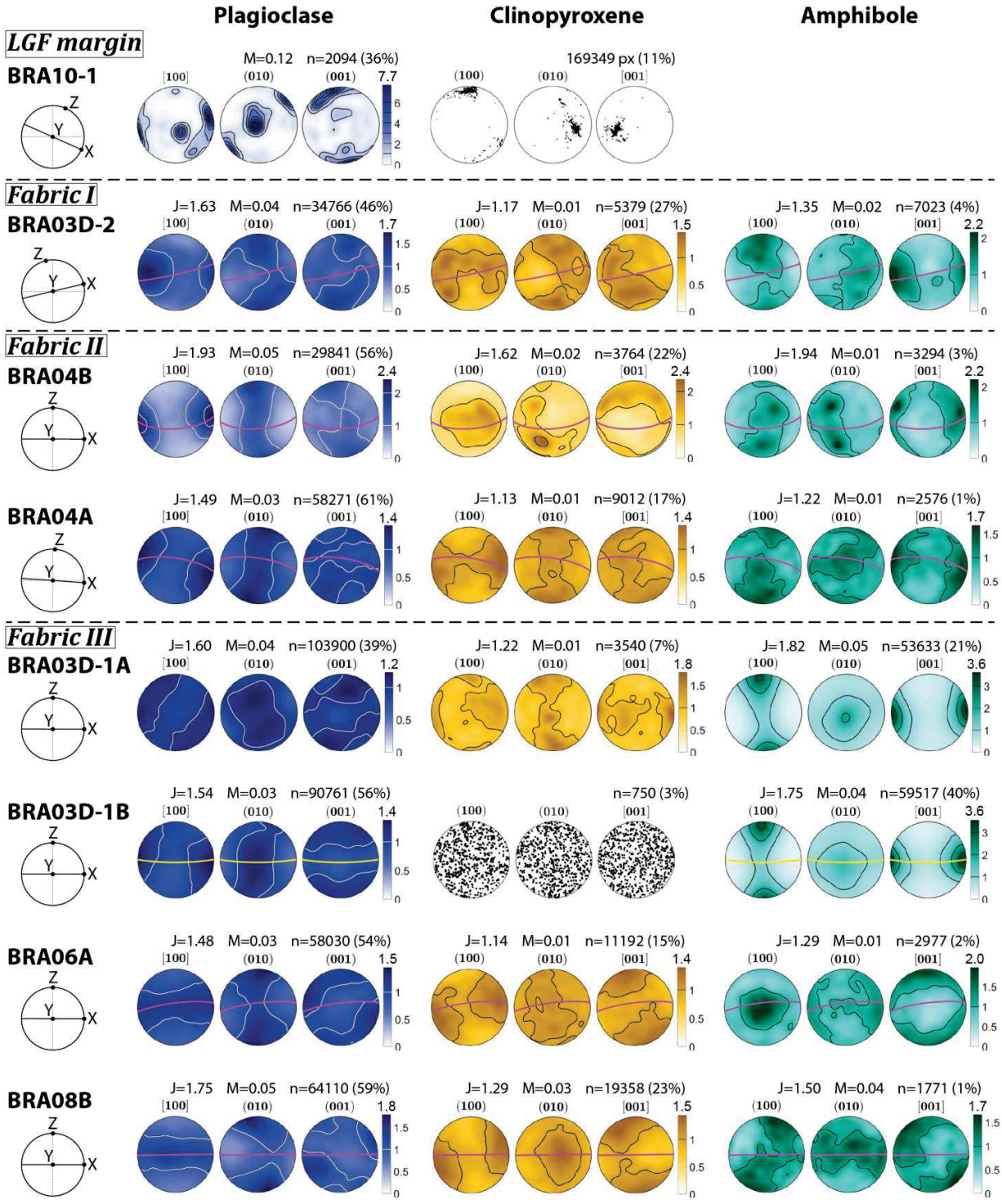

Figure 5 - *Figures de pôles dans les grains de plagioclase (à gauche, bleu), de clinopyroxène (au milieu, brun) et d'amphibole (à droite, vert) dans les échantillons étudiés (données d'orientation moyenne des grains, hémisphère inférieur, projection à aire égale). Les intervalles des contours sont des multiples de la distribution uniforme, et la densité minimale est fixée à zéro pour la*

comparaison entre les domaines analysés. La trace du plan (010) dans le plagioclase (défini par le vecteur propre principal du tenseur d'orientation) est représentée par les grands cercles roses, et les jaunes correspondent au plan (001). Les directions cinématiques de la déformation dans les échantillons (X, Y, et Z) sont représentées dans le stéréogramme de gauche. La densité maximale dans les figures de pôle est indiquée au-dessus de la barre de couleur. Les autres paramètres sont détaillés dans la légende de la figure 3.

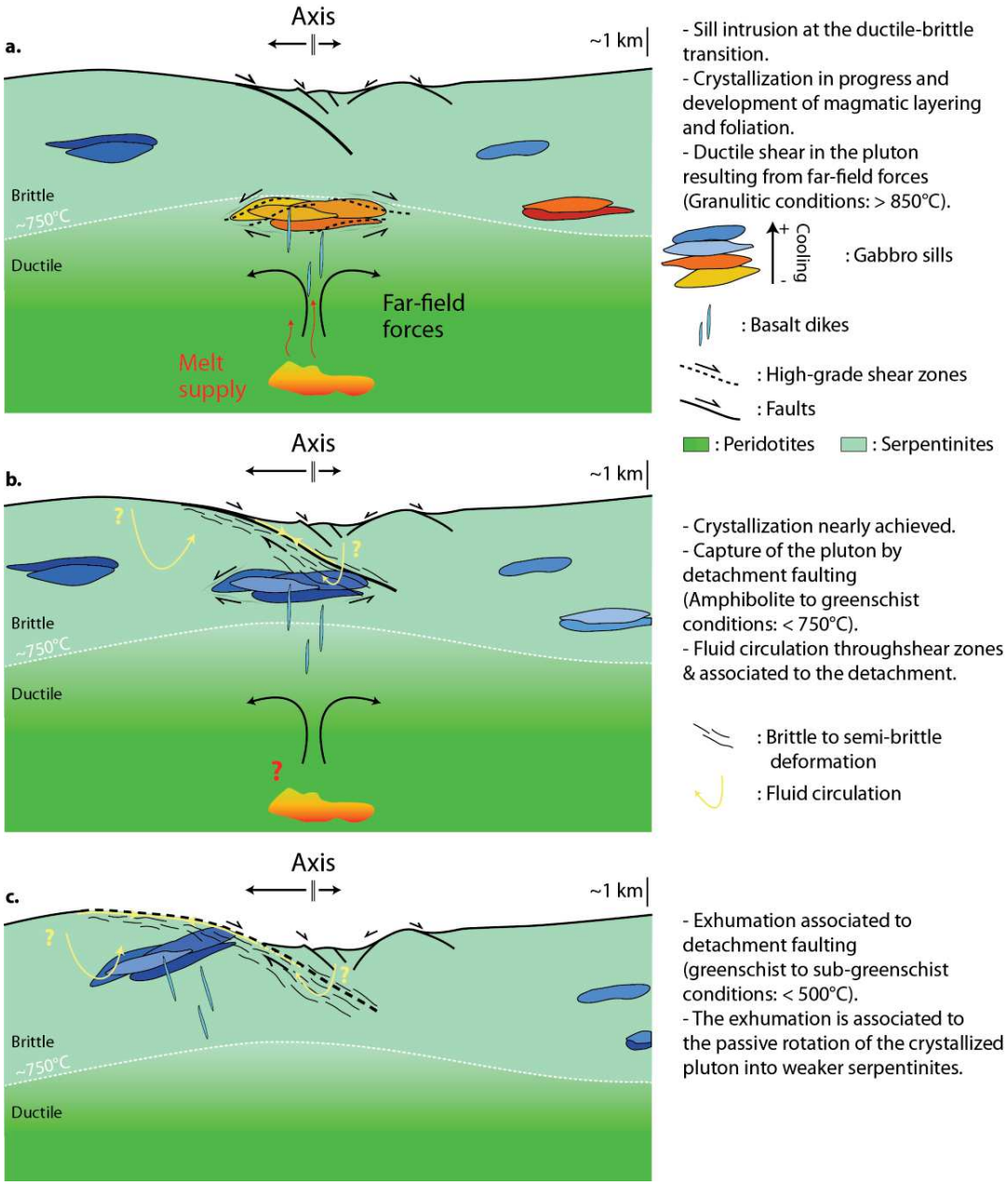

Figure 6 *- Modèle schématique d'un OCC de type "capture tardive" comme proposé pour le complexe gabbroïque de Bracco (adapté d'après Sanfilippo & Tribuzio, 2011).*

REFERENCES

Baines, A.G., Cheadle, M.J., Dick, H.J.B., Hosford Scheirer, A., John, B.E., Kusznir, N.J., Matsumoto, T., 2003. Mechanism for generating the anomalous uplift of oceanic core complexes: Atlantis Bank, southwest Indian Ridge. Geology 31, 1105. https://doi.org/10.1130/G19829.1

Baines, A.G., Cheadle, M.J., John, B.E., Schwartz, J.J., 2008. The rate of oceanic detachment faulting at Atlantis Bank, SW Indian Ridge. Earth and Planetary Science Letters 273, 105–114. https://doi.org/10.1016/j.epsl.2008.06.013

Baumgartner, R.J., Zaccarini, F., Garuti, G., Thalhammer, O.A.R., 2013. Mineralogical and geochemical investigation of layered chromitites from the Bracco–Gabbro complex, Ligurian ophiolite, Italy. Contributions to Mineralogy and Petrology 165, 477–493. https://doi.org/10.1007/s00410-012-0818-5

Blum, P., Dick, H.J.B., MacLeod, C.J., Expedition 360 Scientists, 2017. Hole U1473A remediation operations, Expedition 362T, Proceedings of the International Ocean Discovery Program. International Ocean Discovery Program. https://doi.org/10.14379/iodp.proc.360.2017

Cann, J.R., Blackman, D.K., Smith, D.K., McAllister, E., Janssen, B., Mello, S., Avgerinos, E., Pascoe, A.R., Escartín, J., 1997. Corrugated slip surfaces formed at ridge–transform intersections on the Mid-Atlantic Ridge. Nature 385, 329–332. https://doi.org/10.1038/385329a0

Cannat, M., 1993. Emplacement of mantle rocks in the seafloor at mid-ocean ridges. Journal of Geophysical Research: Solid Earth 98, 4163–4172. https://doi.org/10.1029/92JB02221

Connolly, J.A.D., 2005. Computation of phase equilibria by linear programming: A tool for geodynamic modeling and its application to subduction zone decarbonation. Earth and Planetary Science Letters 236, 524–541. https://doi.org/10.1016/j.epsl.2005.04.033

Cortesogno, L., Galbiati, B., Principi, G., 1987. Note alla '"Carta geologica delle ofioliti del Bracco"' e ricostruzione della paleogeografia Giurassico, Cretacica. Edizioni ETS.

Dick, H.J.B., Kvassnes, A.J.S., Robinson, P.T., MacLeod, C.J., Kinoshita, H., 2019a. The Atlantis Bank Gabbro Massif, Southwest Indian Ridge. Progress in Earth and Planetary Science 6, 64. https://doi.org/10.1186/s40645-019-0307-9

Dick, H.J.B., MacLeod, C.J., Blum, P., Abe, N., Blackman, D.K., Bowles, J.A., Cheadle, M.J., Cho, K., Ciążela, J., Deans, J.R., Edgcomb, V.P., Ferrando, C., France, L., Ghosh, B., Ildefonse, B., John, B., Kendrick, M.A., Koepke, J., Leong, J.A.M., Liu, C., Ma, Q., Morishita, T., Morris, A., Natland, J.H., Nozaka, T., Pluemper, O., Sanfilippo, A., Sylvan, J.B., Tivey, M.A., Tribuzio, R., Viegas, G., 2019b. Dynamic Accretion Beneath a Slow-Spreading Ridge Segment: IODP Hole 1473A and the Atlantis Bank Oceanic Core

Complex. Journal of Geophysical Research 124, 12631–12659. https://doi.org/10.1029/2018JB016858

Dick, H.J.B., Meyer, P.S., Bloomer, S., Kirby, S., Stakes, D., Mawer, C., 1991. Proceedings of the Ocean Drilling Program, 118 Scientific Results, Proceedings of the Ocean Drilling Program. Ocean Drilling Program. https://doi.org/10.2973/odp.proc.sr.118.1991

Dick, H.J.B., Natland, J.H., Alt, J.C., Bach, W., Bideau, D., Gee, J.S., Haggas, S., Hertogen, J.G.H., Hirth, G., Holm, P.M., Ildefonse, B., Iturrino, G.J., John, B.E., Kelley, D.S., Kikawa, E., Kingdon, A., LeRoux, P.J., Maeda, J., Meyer, P.S., Miller, D.J., Naslund, H.R., Niu, Y.-L., Robinson, P.T., Snow, J., Stephen, R.A., Trimby, P.W., Worm, H.-U., Yoshinobu, A., 2000. A long in situ section of the lower ocean crust: results of ODP Leg 176 drilling at the Southwest Indian Ridge. Earth and Planetary Science Letters 179, 31–51. https://doi.org/10.1016/S0012-821X(00)00102-3

Dunn, R.A., 2015. Crust and Lithospheric Structure - Seismic Structure of Mid-Ocean Ridges. Treatise on Geophysics. Elsevier, 419–451. https://doi.org/10.1016/B978-0-444-53802-4.00011-7

Escartín, J., Canales, J.P., 2011. Detachments in Oceanic Lithosphere: Deformation, Magmatism, Fluid Flow, and Ecosystems. Eos, Transactions American Geophysical Union 92, 31–31. https://doi.org/10.1029/2011EO040003

Escartín, J., Smith, D.K., Cann, J., Schouten, H., Langmuir, C.H., Escrig, S., 2008. Central role of detachment faults in accretion of slow-spreading oceanic lithosphere. Nature 455, 790–794. https://doi.org/10.1038/nature07333

Gardner, R.L., Piazolo, S., Daczko, N.R., Trimby, P., 2020. Microstructures reveal multistage melt present strain localisation in mid-ocean gabbros. Lithos 366–367, 105572. https://doi.org/10.1016/j.lithos.2020.105572

Hosford, A., Tivey, M., Matsumoto, T., Dick, H., Schouten, H., Kinoshita, H., 2003. Crustal magnetization and accretion at the Southwest Indian Ridge near the Atlantis II fracture zone, 0-25 Ma. Journal of Geophysical Research: Solid Earth 108. https://doi.org/10.1029/2001JB000604

Ildefonse, B., 2014. Crustal Accretion. Earth Sciences Series. Encyclopedia of Marine Geosciences, Springer 1–7. https://doi.org/10.1007/SpringerReference_350453

Karson, J.A., Dick, H.J.B., 1983. Tectonics of ridge-transform intersections at the Kane fracture zone. Marine Geophysical Researches 6, 51–98. https://doi.org/10.1007/BF00300398

Lagabrielle, Y., 2009. Mantle exhumation and lithospheric spreading: An historical perspective from investigations in the Oceans and in the Alps-Apennines ophiolites. Italian Journal of Geosciences 279–293. https://doi.org/10.3301/IJG.2009.128.2.279

Lagabrielle, Y., Cannat, M., 1990. Alpine Jurassic ophiolites resemble the modern central Atlantic basement. Geology 18, 319–322. https://doi.org/10.1130/0091-7613(1990)018<0319:AJORTM>2.3.CO;2

MacLeod, C.J., Dick, H.J.B., Blum, P., Expedition 360 Scientists, 2017a. Site U1473A, Proceedings of the International Ocean Discovery Program. International Ocean Discovery Program. https://doi.org/10.14379/iodp.proc.360.2017

MacLeod, C.J., Dick, H.J.B., Blum, P., Expedition 360 Scientists, 2017b. Expedition 360 methods, Proceedings of the International Ocean Discovery Program. International Ocean Discovery Program. https://doi.org/10.14379/iodp.proc.360.2017

Mainprice, D., Bachmann, F., Hielscher, R., Schaeben, H., 2015. Descriptive tools for the analysis of texture projects with large datasets using MTEX : strength, symmetry and components. Geological Society, London, Special Publications 409, 251–271. https://doi.org/10.1144/SP409.8

Marroni, M., Pandolfi, L., 1996. The deformation history of an accreted ophiolite sequence: the Internal Liguride units (Northern apennines, Italy). Geodinamica Acta 9, 13–29. https://doi.org/10.1080/09853111.1996.11417260

Mehl, L., Hirth, G., 2008. Plagioclase preferred orientation in layered mylonites: Evaluation of flow laws for the lower crust. Journal of Geophysical Research 113, B05202. https://doi.org/10.1029/2007JB005075

Menna, F., 2009. From magmatic to metamorphic deformations in a jurassic ophiolitic complex: the bracco gabbroic massif, eastern liguria (italy). Ofioliti 34, 109–130. https://doi.org/10.4454/ofioliti.v34i2.382

Miranda, E.A., Hirth, G., John, B.E., 2016. Microstructural evidence for the transition from dislocation creep to dislocation-accommodated grain boundary sliding in naturally deformed plagioclase. Journal of Structural Geology 92, 30–45. https://doi.org/10.1016/j.jsg.2016.09.002

Miranda, E.A., John, B.E., 2010. Strain localization along the Atlantis Bank oceanic detachment fault system, Southwest Indian Ridge. Geochemistry, Geophysics, Geosystems 11, 34. https://doi.org/10.1029/2009GC002646

Molli, G., 1996. Pre-orogenic tectonic framework of the northern Apennine ophiolites. Eclogae Geologicae Helvetiae 89, 163–180. https://doi.org/10.5169/seals-167898

Molli, G., 1994. Microstructural features of high temperature shear zones in gabbros of the Northern Apennine Ophiolites. Journal of Structural Geology 16, 1535–1541. https://doi.org/10.1016/0191-8141(94)90031-0

Montanini, A., Tribuzio, R., Vernia, L., 2008. Petrogenesis of basalts and gabbros from an ancient continent–ocean transition (External Liguride ophiolites, Northern Italy). Lithos 101, 453–479. https://doi.org/10.1016/j.lithos.2007.09.007

Pettigrew, T., Casey, J., Miller, D., Araki, E., Boissonnas, R., Busby, R., Einaudi, F., Gerdom, M., Guo, Z., Hopkins, H., 1999. Leg 179 summary. ODP, Texas A and M Univ., USA.

Rampone, E., Borghini, G., Basch, V., 2020. Melt migration and melt-rock reaction in the Alpine-Apennine peridotites: Insights on mantle dynamics in extending lithosphere. Geoscience Frontiers 11, 151–166. https://doi.org/10.1016/j.gsf.2018.11.001

Ryan, W.B.F., Carbotte, S.M., Coplan, J.O., O'Hara, S., Melkonian, A., Arko, R., Weissel, R.A., Ferrini, V., Goodwillie, A., Nitsche, F., Bonczkowski, J., Zemsky, R., 2009. Global Multi-Resolution Topography synthesis: global multi-resolution topography synthesis. Geochemistry, Geophysics, Geosystems 10, n/a-n/a. https://doi.org/10.1029/2008GC002332

Sanfilippo, A., Tribuzio, R., 2011. Melt transport and deformation history in a nonvolcanic ophiolitic section, northern Apennines, Italy: Implications for crustal accretion at slow spreading settings. Geochemistry, Geophysics, Geosystems 12, n/a-n/a. https://doi.org/10.1029/2010GC003429

Schwarzenbach, E.M., Vogel, M., Früh-Green, G.L., Boschi, C., 2021. Serpentinization, Carbonation, and Metasomatism of Ultramafic Sequences in the Northern Apennine Ophiolite (NW Italy). Journal of Geophysical Research: Solid Earth 126. https://doi.org/10.1029/2020JB020619

Taufner, R., Viegas, G., Faleiros, F.M., Castellan, P., Silva, R., 2021. Deformation mechanisms of granulite-facies mafic shear zones from hole U1473A, Atlantis Bank, Southwest Indian Ridge (IODP Expedition 360). Journal of Structural Geology 149, 104380. https://doi.org/10.1016/j.jsg.2021.104380

Tribuzio, R., Garzetti, F., Corfu, F., Tiepolo, M., Renna, M.R., 2016. U–Pb zircon geochronology of the Ligurian ophiolites (Northern Apennine, Italy): Implications for continental breakup to slow seafloor spreading. Tectonophysics 666, 220–243. https://doi.org/10.1016/j.tecto.2015.10.024

Tribuzio, R., Tiepolo, M., Vannucci, R., 2000. Evolution of gabbroic rocks of the Northern Apennine ophiolites (Italy): Comparison with the lower oceanic crust from modern slow-spreading ridges. Special Paper 349: Ophiolites and Oceanic Crust: New Insights from Field Studies and the Ocean Drilling Program. Geological Society of America, 129–138. https://doi.org/10.1130/0-8137-2349-3.129

INTRODUCTION

The oceanic crust is the uppermost rigid layer covering up to 55% of Earth's surface. It is formed continuously by the ascension and accretion of molten mantle rocks at mid-oceanic ridges that constitute divergent tectonic plate boundaries. Several classes of mid-oceanic ridges are recognized, depending on their magmatic activity, expansion rate, and associated seafloor morphology (e.g., Ildefonse, 2014, and references therein; Dunn, 2015). At mid-ocean ridges characterized by slow-spreading rates such as the Southwest Indian Ridge or the Mid-Atlantic Ridge, lower igneous crust and mantle lithologies are exposed on the seafloor along parts of the ridge segments. This is interpreted to result from a weak or absent magmatic activity during extension at the ridge in conjunction with tectonics (e.g., Karson & Dick, 1983; Cannat, 1993). This tectonic activity corresponds to the development of long-lived low-angle normal faults (e.g., Escartín et al., 2008) that accommodate a substantial part of the ridge spreading. These are referred to as detachment faults and lead to the exhumation of the deep-crustal and upper-mantle rocks, ultimately forming domal structures called "oceanic core complexes" (OCC; e.g., Cann et al., 1997; Escartín & Canales, 2011). OCC are characterized by complex interactions between deformation and magmatic processes operating during crustal accretion. The timing of the onset and the depth of penetration of deformation associated with detachment faulting, together with magmatic accretion at the ridge axis, strongly impact the architecture of the crust.

Exploring OCC provides a unique opportunity to access the lower crust and to understand the processes involved in its accretion. The study of slow-spread oceanic crust was focused mainly on ophiolites (e.g., Lagabrielle & Cannat, 1990; Lagabrielle, 2009) before advances made in marine geology over the last ~50 years. The first models of slow-spreading ridge architecture were built progressively by detailed works extensively performed in the Alpine-Apennine belt in conjunction with seafloor dredging (e.g., Lagabrielle, 2009, and references therein). Nowadays, more is known regarding the nature of accreted magmas and their emplacement within the lower crust, as well as the modes of deformation and strain localization. A detailed analysis of deformation, which interacts with circulating melts and fluids, is important as it reflects the rheological behavior of slow-spreading oceanic crusts. In that context, this thesis aims at further characterizing and precisely quantifying the ductile deformation in terms of mechanisms and temperature conditions. The deformation of plagioclase minerals has been especially explored because of their primary role during the deformation of gabbroic rocks.

This thesis project was mainly based on studying gabbros recovered in IODP Hole U1473A drilled at the Atlantis Bank (57°E) at the Southwest Indian Ridge during IODP Expedition 360 (Dick et al., 2019). A collection of gabbros sampled in the Bracco ophiolite in the Northern Apennines was also studied for comparative purposes. All studied gabbros formed at the axis of a slow-spreading ridge and were exhumed on the seafloor within an oceanic core complex.

The general question addressed in this thesis is: what are the characteristics of the plastic deformation occurring in gabbros during their accretion and subsequent exhumation in an oceanic core complex?
The following aspects were explored to answer this central question:

(1) What are the dominant active deformation mechanisms, and which role do the main minerals (particularly plagioclase) in gabbros play in the accommodation of this deformation?

(2) Under which conditions (pressure-temperature-fluid), does plastic deformation occurs?

(3) How are the deformation structures distributed and organized at the scale of a gabbro pluton?

The main approaches used herein to answer these questions are microstructural and petro-geochemical investigation. Microstructural analysis elaborates on classical petrographic observations in thin sections and Electron Back-Scattered Diffraction (EBSD) mapping. It aims at quantifying plastic deformation and identifying the activated deformation mechanisms in the principal minerals of gabbros. Petro-geochemical analyses were performed on a selection of samples from the two studied gabbro plutons through *in situ* Electron Probe Micro-Analyses (EPMA) and quantitative chemical mapping. Further characterizations through thermodynamic forward modeling were conducted in the selected samples from the Atlantis Bank. These serve at quantifying chemical changes associated to deformations and at defining the conditions under which deformations occur.

This manuscript is composed of six chapters and four annexes, as outlined below.

The first chapter details the current knowledge on mid-oceanic ridges, the different classes of ridges recognized and the processes operating during accretion and expansion at the ridge axis. It also provides an extended summary of the state of the art in the two studied areas. Finally, it presents the concepts relating to plastic deformation.

The second chapter presents the analytical methods used in the different chapters of the manuscript and details the parameters I used.

The third chapter is divided in two parts. The first part documents the different petrographic observations made in the large collection of studied samples from IODP Hole U1473A. The second part is an article recently published in *Journal of Geophysical Research: Solid Earth*. It is

entitled "*Plastic Deformation of Plagioclase in Oceanic Gabbro Accreted at a Slow-Spreading Ridge (Hole U1473A, Atlantis Bank, Southwest Indian Ridge)*" and focusses on the active deformation mechanisms and slip systems in plagioclase.

The fourth chapter presents an article in preparation, to be submitted to *Journal of Metamorphic Geology*. It is entitled *"High-Temperature Deformation and Retrograde Strain Localization during Cooling and Exhumation of a Gabbroic Pluton in an Oceanic Core Complex (Hole U1473A, Atlantis Bank, Southwest Indian Ridge)*" and explores the deformation conditions in the studied gabbros and associated deformation mechanisms.

The fifth chapter is the preliminary version of an article in preparation, based on the sampling performed in the Bracco gabbro complex, which evaluates the general distribution of high-grade deformation, and identifies the deformation mechanisms that occurred in the studied gabbros. This study is used to draw comparisons with the results I present for the Southwest Indian Ridge gabbros, and more generally with present-day OCC.

The sixth and last chapter provides a short synthesis of the principal results presented in the manuscript and proposes integrated points of conclusions.

The different annex sections are presented at the end of the concerned chapters, except for the two additional annexes providing a detailed presentation of samples focused on the EBSD analyses performed that are given for chapters IV and V at the end of the manuscript.

REFERENCES

Cann, J.R., Blackman, D.K., Smith, D.K., McAllister, E., Janssen, B., Mello, S., Avgerinos, E., Pascoe, A.R., Escartín, J., 1997. Corrugated slip surfaces formed at ridge–transform intersections on the Mid-Atlantic Ridge. Nature 385, 329–332. https://doi.org/10.1038/385329a0

Cannat, M., 1993. Emplacement of mantle rocks in the seafloor at mid-ocean ridges. Journal of Geophysical Research: Solid Earth 98, 4163–4172. https://doi.org/10.1029/92JB02221

Dick, H.J.B., MacLeod, C.J., Blum, P., Abe, N., Blackman, D.K., Bowles, J.A., Cheadle, M.J., Cho, K., Ciążela, J., Deans, J.R., Edgcomb, V.P., Ferrando, C., France, L., Ghosh, B., Ildefonse, B., John, B., Kendrick, M.A., Koepke, J., Leong, J.A.M., Liu, C., Ma, Q., Morishita, T., Morris, A., Natland, J.H., Nozaka, T., Pluemper, O., Sanfilippo, A., Sylvan, J.B., Tivey, M.A., Tribuzio, R., Viegas, G., 2019. Dynamic Accretion Beneath a Slow-Spreading Ridge Segment: IODP Hole 1473A and the Atlantis Bank Oceanic Core Complex. Journal of Geophysical Research 124, 12631–12659. https://doi.org/10.1029/2018JB016858

Dunn, R.A., 2015. Crust and Lithospheric Structure - Seismic Structure of Mid-Ocean Ridges. Treatise on Geophysics. Elsevier, 419–451. https://doi.org/10.1016/B978-0-444-53802-4.00011-7

Escartín, J., Canales, J.P., 2011. Detachments in Oceanic Lithosphere: Deformation, Magmatism, Fluid Flow, and Ecosystems. Eos, Transactions American Geophysical Union 92, 31–31. https://doi.org/10.1029/2011EO040003

Escartín, J., Smith, D.K., Cann, J., Schouten, H., Langmuir, C.H., Escrig, S., 2008. Central role of detachment faults in accretion of slow-spreading oceanic lithosphere. Nature 455, 790–794. https://doi.org/10.1038/nature07333

Ildefonse, B., 2014. Crustal Accretion. Earth Sciences Series. Encyclopedia of Marine Geosciences, Springer 1–7. https://doi.org/10.1007/SpringerReference_350453

Karson, J.A., Dick, H.J.B., 1983. Tectonics of ridge-transform intersections at the Kane fracture zone. Marine Geophysical Researches 6, 51–98. https://doi.org/10.1007/BF00300398

Lagabrielle, Y., 2009. Mantle exhumation and lithospheric spreading: An historical perspective from investigations in the Oceans and in the Alps-Apennines ophiolites. Italian Journal of Geosciences 279–293. https://doi.org/10.3301/IJG.2009.128.2.279

Lagabrielle, Y., Cannat, M., 1990. Alpine Jurassic ophiolites resemble the modern central Atlantic basement. Geology 18, 319–322. https://doi.org/10.1130/0091-7613(1990)018<0319:AJORTM>2.3.CO;2

CHAPTER I

STATE OF THE ART

1. Accretion of the Lower Oceanic crust at Mid-Ocean Ridges

Since the 60's, a burgeoning series of publications building on the "continental drift" theory, earlier formulated by (Wegener, 1912), emerged in the scientific community leading to the universally accepted concept of plate tectonics (e.g., Dietz, 1961; Hess, 1962; Vine & Matthews, 1963; Bullard et al., 1965; Heezen & Tharp, 1965; Holmes, 1965; Heirtzler et al., 1968; Le Pichon, 1968). In this concept, tectonic plates represent rigid blocs corresponding to the lithosphere (composed of the crust and a portion of the upper mantle) that moves past to each other thanks to mantle convection in the underlying asthenosphere (e.g., Heezen & Tharp, 1964; Bullard et al., 1965; Holmes, 1965). The first observations of mid-ocean ridges were introduces by oceanographic explorations (e.g., Hess, 1962 and references therein), and mapped at the global scale by Heezen & Tharp (1964). It provided an image of submarine mountain chains separating oceanic basins: the mid-ocean ridges (Figure 1.1).

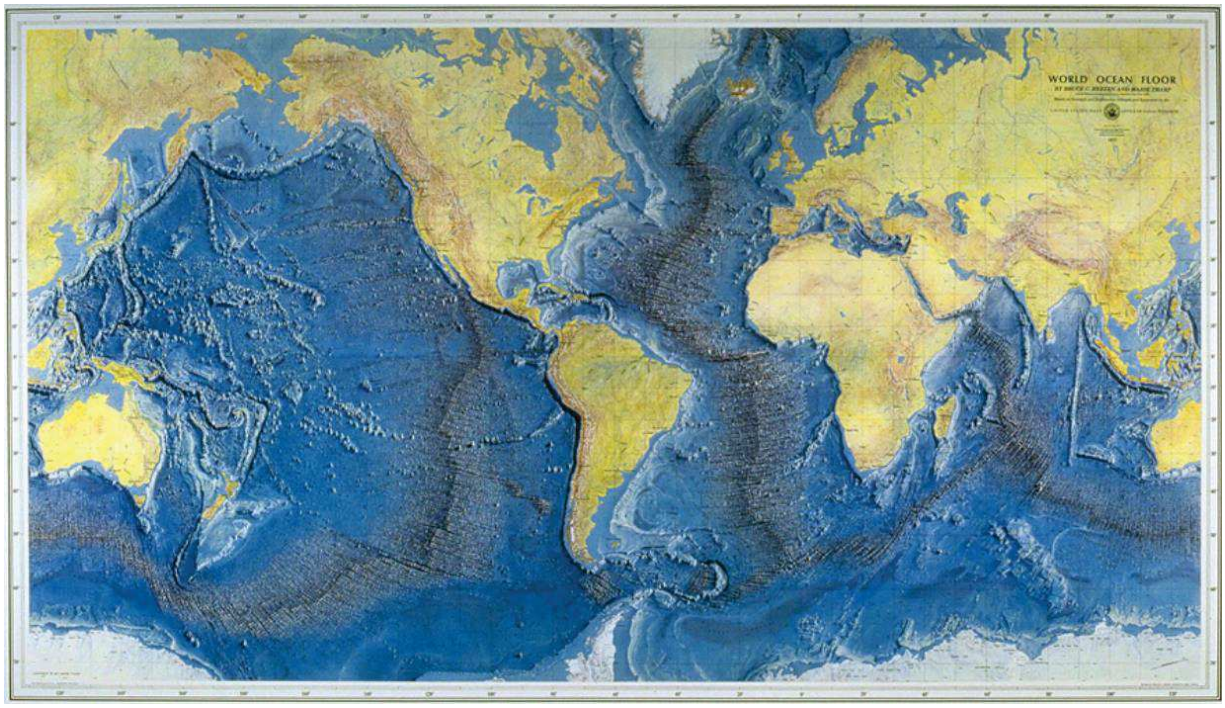

Figure 1.1 *- World ocean floor (after Heezen & Tharp, 1977; colorized by Berann).*

A key to the understanding of "seafloor spreading" (Dietz, 1961) and divergent tectonic plate boundaries is the rise of magnetic anomaly studies in the same period of time (e.g., Vine & Matthews, 1963; Heirtzler et al., 1968). These studies demonstrated a record of geomagnetic field polarity inversion in seafloor rocks around oceanic ridges. The Vine-Matthews-Morley hypothesis theorizes that a solidifying basaltic lava erupted at the ridge will rapidly cool down to Curie temperature of constituting minerals, then fossilizing the current geomagnetic field

orientation (Figure 1.2; e.g., Lowrie, 2007). The continued spreading and basalt emplacement over time results in the formation of a symmetrical distribution of magnetic anomalies on each sides of the ridge axis. Then, by measuring the distance between each magnetized band edges, and comparing it with the known period of time to which it corresponds (e.g., from onshore erupted lavas) the spreading rate of the ridge can be deduced (Vine, 1966). Calculated spreading rates across a wide variety of mid-ocean ridges indicated different spreading rates, historically classified in three main groups (e.g., Dunn, 2015): fast-spreading (e.g., East-Pacific Rise), intermediate-spreading (e.g., SouthEast Indian Ridge), and slow-spreading ridges (e.g., Mid-Atlantic Ridge). For the sake of simplicity, I will focus herein on slow- and fast-spreading ridges. The formation of oceanic crust at ridge axes is the principal mass redistribution within the Earth and is responsible for the production of ~88% of its surface over time (Bird, 2003).

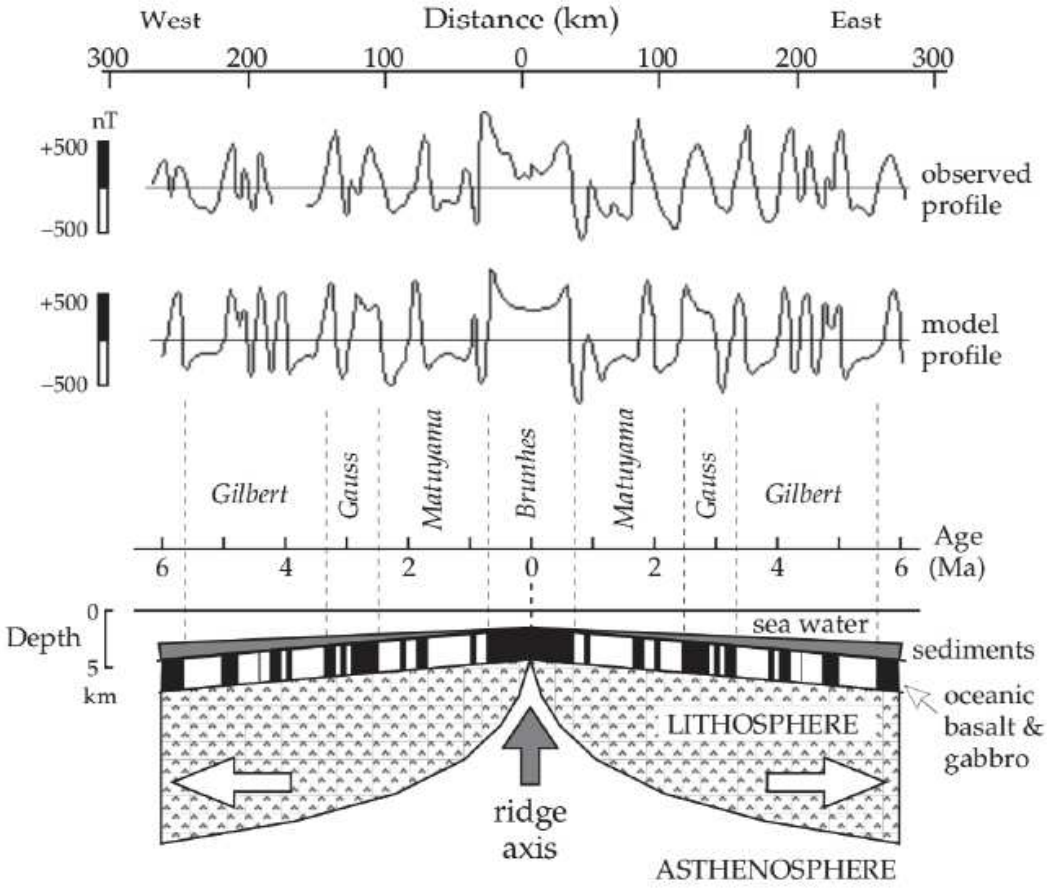

Figure 1.2 *- Magnetic field variations recorded in the oceanic crust with time during seafloor spreading (Lowrie, 2007). The alternation of black (positive) and white (negative) bands in the oceanic crust represents the polarity of the recorded magnetic field at the time of emplacement at the seafloor.*

Historically, the research on oceanic lithosphere initially focused on ophiolitic complexes that were exhumed and emplaced on continental emerged lands. Numerous observations and three-dimensional characterizations of structures and lithologies in these complexes permit to establish the different concepts nowadays accepted on the building of the oceanic crust and its architecture. Although ophiolites represent great analogues for studying actual oceanic ridge systems and lithospheres, they are often imprinted by various processes that occurred during their tectonic emplacement on land, during their obduction and incases during subduction (e.g., Boudier et al., 1985; Milnes et al., 1997; Manatschal et al., 2011; Angiboust et al., 2014; Lagabrielle et al., 2015). Since the advancement in piston coring in the 1940s, and of dynamic positioning in the 1960s, the scientific community started *in situ* investigation of sub-seafloor rocks and sediments through oceanographic campaigns. In 1957, the American geophysicist Walter Munk proposed the first project, Project MoHole, aiming at drilling the Earth's crust down to the Mohorovicic discontinuity (i.e., the Moho) that marks the physical boundary between the crust and the mantle (Lill, 1961). Although this project stopped way before reaching its highly ambitious objective, it paved the way to future scientific drilling of the oceanic crust. In the following decades, several projects led to fundamental discoveries to further understand the architecture of the ocean crust and related accretion processes. These projects were implemented in 1966-1983 with the Deep Sea Drilling Project (DSDP), the first international Ocean Drilling Program (ODP) in 1983-2003, the International Ocean Drilling Program (IODP) in 2003-2013, and finally the International Ocean Discovery Program (IODP) since 2013. These different programs permit to drill and recover over 6 km of oceanic crust worldwide, but a complete continuous section of a pristine oceanic crust down to the Moho is still to be drilled (e.g., Dick et al., 2006; Ildefonse et al., 2007a, 2007b).

1.1. Fast-spreading ridges

Fast-spread oceanic crust represents the major part of the oceanic crust formed on Earth (~45%) although it formed at < 20% of actual spreading centres (Expedition 335 Scientists, 2012; Dunn, 2015). This class of mid-ocean ridges, with an average spreading rate > 80 mm.yr^{-1} (Figure 1.3), is characterized by a rather homogeneously layered internal structure, and a relatively smooth topography. This result from the continuous magmatic supply arising from the melt lens that runs all along the ridge axis. The magmatic activity is crucial in the building of their structure by crustal accretion, and responsible for the formation of an elevated crest at the ridge axis referred to as a "rise", in contrast to "rifts" that develop at slower expansion rates (Figure 1.3). This axial relief is observed to be of ~400m on average (Heezen, 1960).

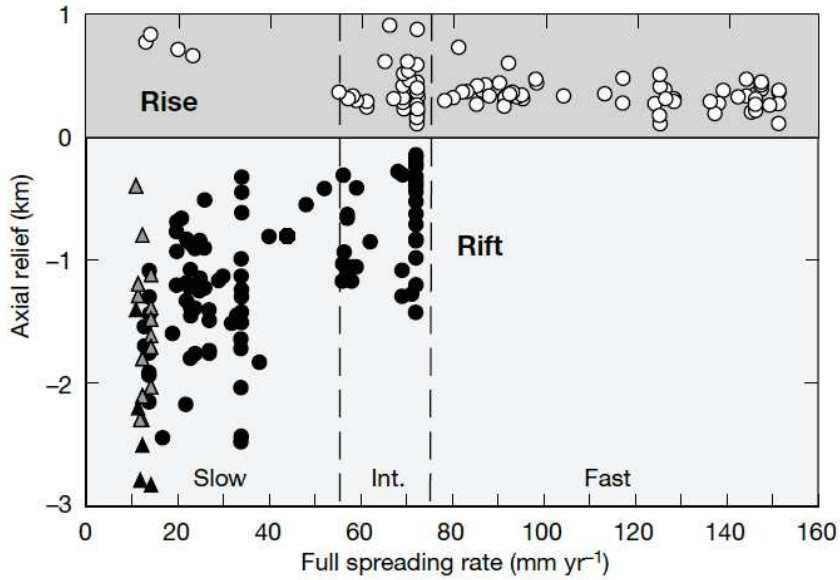

Figure 1.3 *- Relation between the spreading rate and the axial topography of the ridge (after Dick et al., 2003). White circles indicate an axial rise, while black and dark-grey markers indicate rift morphology.*

The magma chamber has been imaged by seismic reflection at a high level in the crust (2-3 km of depth), near the base of the sheeted-dike complex (e.g., Figure 1.4a), in the form of a thin magmatic lens on top of a crystal mush zone (e.g., Morton & Sleep, 1985; Detrick et al., 1987; Sinton & Detrick, 1992). The lithostratigraphy of fast-spread crust is composed of, from the sea-floor downwards: pillow-basalts, a sheeted-dike complex, and gabbros (upper and lower) that are underlaied by peridotites (Figure 1.4a). This rock sequence is continuous and forms a layered crust with a thickness of about 6 to 7 km (White et al., 1992). Seafloor explorations and ophiolites studies confirm these characteristics that are corroborated by the variation measured of seismic wave velocities (Figure 1.4a).

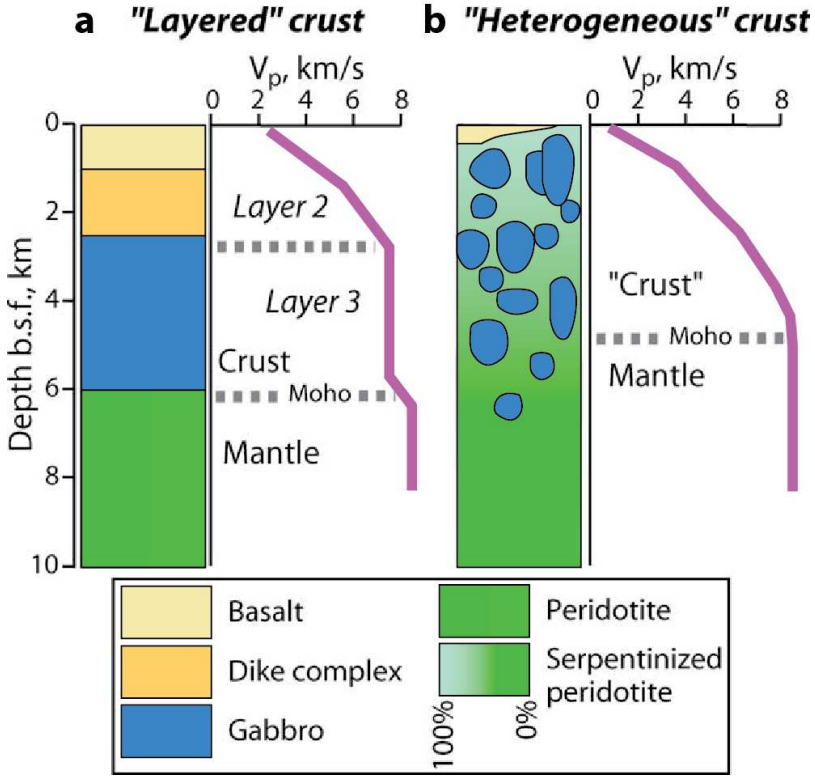

Figure 1.4 *- Endmember profiles for the two type of oceanic crust interpreted from seismic wave velocities (after Mével, 2003). (a) Penrose model for a layered oceanic crust build up by magmatic rocks. (b) Heterogenous oceanic crust as formed in slow-spreading environments with gabbroic plutons intruding into the serpentinized mantle. V_P: P-waves velocity; b.s.f.: below sea-floor.*

The analysis of heat flux at the ridge axis revealed the important contribution of seawater circulation through the crust upon cooling, circulation that is restituted back to the seafloor through black smokers. These edifices are hot springs chimneys constructed by the progressive deposit of metal-rich particles brought by the erupting water at a temperature of ~350°C. This results from seawater infiltration through fractures in the spreading crust, progressively heated to 400-450°C as it penetrates down to the base of the dike complex (2-3 km). Seawater circulation within crustal rocks causes their alteration, and in particular dissolves metals. Finally, this fluid heating episode at depth induces it ascend, and when restituted back to the ocean floor the contact of ascending hot water and cold seawater causes the precipitation of dissolved sulphides (e.g., Nicolas, 1995; Tivey, 2007). The extent of hydrothermal circulation at depth is not entirely understood to date (e.g., Hasenclever et al., 2014); hence various models are proposed for the architecture of the lower gabbroic crust. One endmember is the “gabbro glacier” model, where the lower gabbroic crust is formed by the crystallization of cumulates in the magmatic lens before

being transported downward and outward of the ridge axis within the crystal mush zone (Figure 1.5a; e.g., Detrick et al., 1987; Dewey & Kidd, 1977; Quick & Denlinger, 1993; Sinton & Detrick, 1992; Sleep, 1975). This downward flow movement in the mush zone during crustal extension is proposed by Dewey & Kidd (1977) to account for the layering of lower gabbros. A second endmember proposes a "sheeted-sill" architecture of the lower oceanic crust (Figure 1.5b). It corresponds to the feeding of the lower crustal section by successive *in situ* sill emplacement (e.g., Bédard et al., 1988; Kelemen, 1990; Bédard, 1991, 1993; Boudier et al., 1996; Korenaga & Kelemen, 1997). The cooling of such a system requires a deep hydrothermal penetration in the vicinity of the ridge axis, down to the Moho (Maclennan et al., 2004, 2005). Other authors propose a hybrid model through the observation of distinct microstructures and crystallographic fabrics between the upper and lower gabbros in the layer 3 (Boudier et al., 1996; Mock et al., 2021). In this model the upper gabbroic crust forms by shallow crystallization and subsequent subsidence or deeper crystallization and upward migration, while the lower crust is built up by multiple sill intrusions (Mock et al., 2021).

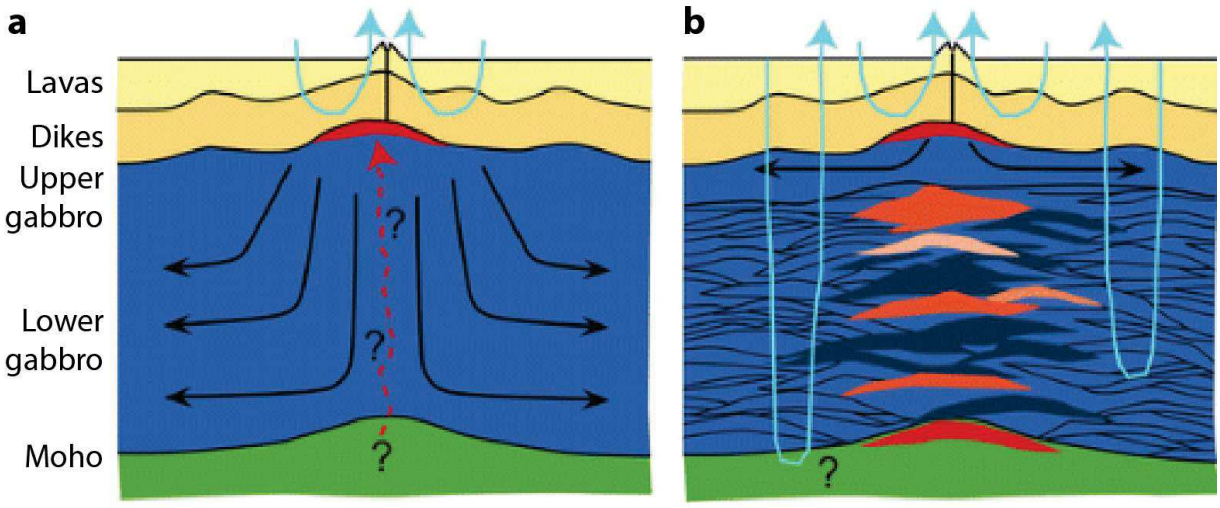

Figure 1.5 *- Schematic crustal accretion model endmembers (after Ildefonse (2014), modified from Kelemen et al., 1997. (a) "Gabbro glacier" model. (b) "Sheeted sill" (see text for details).*

1.2. Slow-spreading ridges

The majority of present-day oceanic crust has been accreted at slow spreading ridges (~55%; Expedition 335 Scientists, 2012; Dunn, 2015) with an average full spreading rate of < 40 mm.yr^{-1}. In comparison to fast-spreading endmembers, the seafloor topography is rugged and results from the importance of brittle and ductile deformation upon magmatism at the ridge axis. The axial valley of the ridge displays a negative topography with highly variable relief between ~400 m to 2500 m (Figure 1.3; Small, 1998). Being cooler, the lower slow-spread oceanic crust can

experience shear strain to accommodate extension at the spreading centres (e.g., Dick et al., 2017). In addition, the occurrence of deep crustal and mantle rocks along certain segments of slow-spreading ridges is interpreted to arise from magma-poor or amagmatic spreading in conjunction with tectonics (e.g., Karson & Dick, 1983; Karson et al., 1987; Brown & Karson, 1988; Karson, 1991; Mével et al., 1991; Cannat, 1993). Although the presence of an axial magmatic lens is locally imaged by seismic reflection at the Mid-Atlantic Ridge, its extent is limited in length (Singh et al., 2006). The resulting oceanic crust is then largely heterogeneous, and the rock sequence encountered in slow-spread crust is in place uncomplete compared to the fast-spreading reference (Figure 1.4b). The disrupted nature of magmatic lenses underneath the ridge axis produces variable amounts of basalt and sheeted-dikes at the top of the crustal section, and in some areas no dikes are observed (e.g., Cannat, 1993).

Heterogeneity results from the variability of magma input along ridge segments. These segments are bounded by transform faults oriented parallel to the spreading direction, as well as non-transformed boundaries. At the mid-Atlantic Ridge, Cannat et al. (1995) indicates a correlation between ultramafic rock exposure and a thinning of the crust measured by residual, positive, gravity anomalies. These domains also comprise igneous rocks (gabbros, basalts, and, in lower amounts, dikes) pointing to the presence of a magmatic crust even in regions where the crust is thinned, down to 3-4 km width, the thinning essentially occurring in the layer 3 of the "Penrose-type" crust (Figure 1.4a; Kuo & Forsyth, 1988; Lin et al., 1990; Tolstoy et al., 1993; Cannat et al., 1995). It is also reported that domains of thin crust frequently coincides with pervasive fracturing, consisting of ridge-perpendicular strike-slip faults and ridge-oblique oblique-slip faults. The width of these tectonic domains corresponds to that of crust-thinning (Figure 1.6, and their activation may result from external constraints like an offset of the ridge axis between two segments or different tectonic regimes (e.g., Karson, 1991; Cannat et al., 1995).

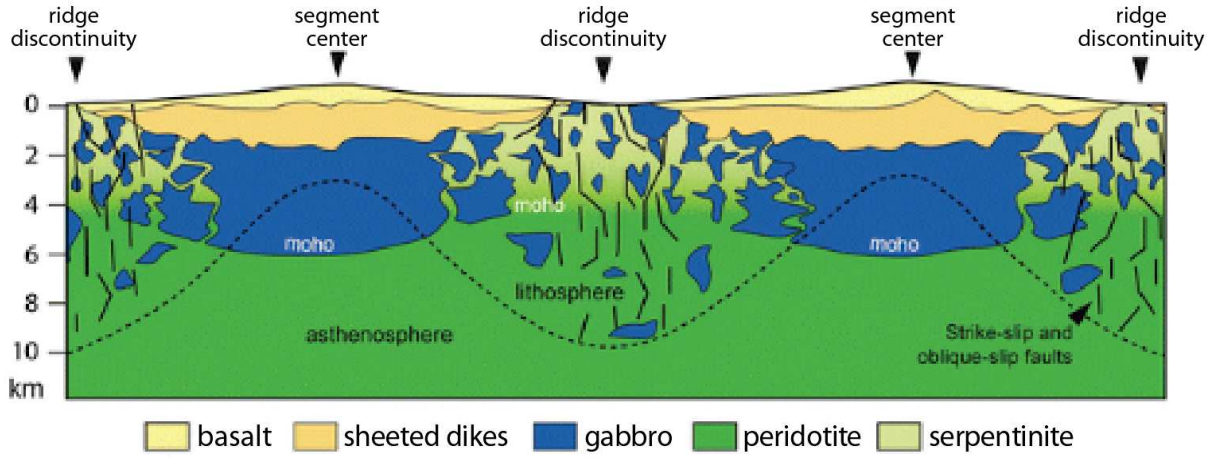

Figure 1.6 *- Along-axis schematic section of a slow-spread oceanic crust (Ildefonse, 2014; modified from Cannat et al., 1995).*

The formation, of both thinner and thicker crust domains in ridge segments arise from heterogeneous magmatic supply, that preferentially focusses to the segment centres (Lin et al., 1990). This focused magmatic accretion would be maintained over time by the feedback created between mantle melting and upwelling which increases locally the mantle buoyancy and reduces its viscosity.

The role of tectonics in the construction of the oceanic crust at slow (and ultraslow) spreading ridges is demonstrated by the formation of detachment faults (Figure 1.7). For example, at the Mid-Atlantic Ridge, detachment faulting dominates the accommodation of axis spreading over ~50% (> 1200 km) of the ridge length between 12.5°N and 35°N (Escartín et al., 2008). Asymmetrical accretion through detachment faulting is in close association with hydrothermal circulation, and displays an important seismicity. Generally the hydrothermal field is located off-axis, on the detachment surface, implying a fluid circulation in the footwall of the detachment (Escartín et al., 2017). When the activity of a detachment fault is protracted over hundreds of thousand years or million years (~1-2 Ma), a domed edifice develop by the evolution from steep to low angle normal geometry of the detachment fault, together with its shallowing, and the rotation of the footwall (Escartín & Canales, 2011). The dip of the detachment faults surface at the intersection of the seafloor can be nearly horizontal with angles measured down to 14° (e.g., Smith et al., 2014). This pursued fault activity and its shape lead to the exhumation of deep crustal and upper mantle rocks, and commonly produces spreading-parallel striations on the detachment leaving a corrugated surface (e.g., Cann et al., 1997; Escartín et al., 2003, 2017). The activity of a detachment fault at the ridge axis, or in its vicinity, produces what is known as an "oceanic core complex" (OCC; Figure 1.7), and probably develops during a magma-poor or nearly amagmatic period (e.g., Tucholke et al., 1998; Escartín et al., 2003; MacLeod et al., 2009). Maintaining the extension on the same fault during such a long period of time is aided by fault weakening in association with serpentinites formation. Although most of the extension is assumed to be accommodated by the detachment fault under magma-poor conditions, the initiation of such a fault remains unclear. Numerical models of OCCs formation indicate the importance of conjugate tectonics and magmatism in their development (Shemenda & Grocholsky, 1994; Buck et al., 2005; Bickert et al., 2020). Also, the rate of magmatic accretion at the spreading centre controls the pattern of faulting resulting from stretching. At depth, the detachment fault is proposed to root immediately above the brittle-ductile transition (Lavier et al., 2000; Escartín et al., 2003; Olive et al., 2010), and this transition is assumed to be at the base of the seismic lithosphere. This brittle-ductile transition is assumed to occur at temperatures of 700-750°C based on olivine (dunite) rheology, the principal constituent of Earth's mantle (Hirth et al., 1998). Alternatively, Escartín et al. (2003) propose that the detachment fault roots at the mantle alteration front present within the brittle crust thanks to the rheology contrast between weak serpentinites and strong peridotites. The injection of magmas into the upper brittle layer is

proposed to control the evolution of the detachment fault, while it will have no influence on it by injecting below the brittle-ductile transition (e.g., Olive et al., 2010). Nevertheless, magma injection in the ductile lithosphere will monitor the extent of exhumed gabbros by the detachment. Two types of OCCs were distinguished based on the extent and temperatures of deformation observed in the gabbro pluton exhumed as a result detachment faulting (e.g., Escartín et al., 2003).

The first type corresponds to an amagmatic extension associated to a detachment fault rooting in the cold lithosphere, and result in a weak high-temperature deformation of the exhumed gabbros (e.g., Atlantis Massif). In contrast, OCCs can form during magmatic extension with a detachment fault rooting in a melt-rich environment near the dyke-gabbro transition, resulting in a significant deformation of exhumed gabbros at high-temperature (e.g., Atlantis Bank).

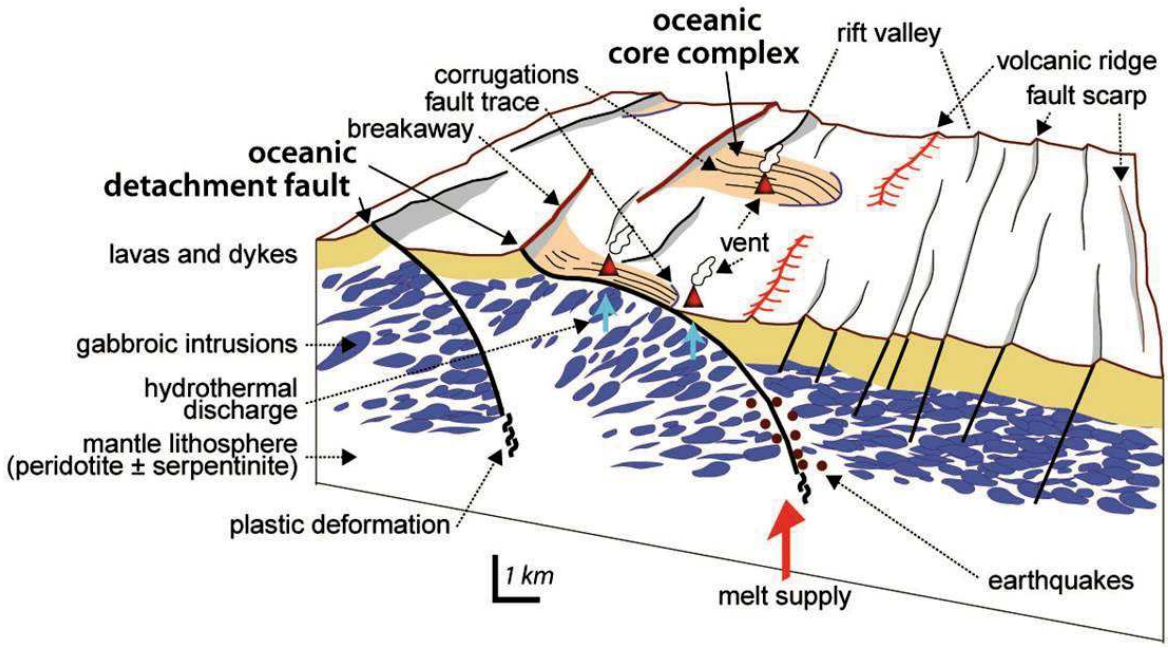

Figure 1.7 *- Schematic section showing crustal accretion at a slow-spreading centre as controlled by detachment faulting in an oceanic core complex system (Ildefonse, 2014; after Escartín & Canales, 2011).*

1.3. Intermediate and ultraslow-spreading ridges

Between the two major classes of ridges describe above intermediate-spreading ridges can display characteristics of the two endmembers depending on the magma supply (e.g., SouthEast Indian Ridge and Galapagos Ridge). These intermediate spreading ridges have expansion rates of ~40-80 mm.yr^{-1} and consist of alternations of long ridge segment with either a slow-spreading morphology or a fast-spreading morphology (Small & Sandwell, 1989; Cochran, 1991; Phipps-Morgan & Chen, 1993; Small, 1998).

At ridges spreading at rates lower than ~20 mm.yr^{-1} (e.g., SWIR and Gakkel ridge; DeMets et al., 1990, 1994), a drastic change occur in terms of ridge dynamic and morphology, in the same order as the change from fast- to slow-spreading ridges (Dick et al., 2003). The seismic crust thickness at these spreading rates is intensely decreased, probably by the depression of the upper mantle melting zone and the reduction of melt production in response to conductive cooling from the top (Reid & Jackson, 1981; Jackson et al., 1982; Bown & White, 1994; White et al., 2001). Then, variations in the mantle (composition, flow and thermal structure) and in ridge geometry will significantly influence on crustal accretion and tectonics. Ultraslow-spreading ridges are composed of "supersegments", consisting of connected magmatic and amagmatic ridge segments. The constitutive amagmatic, accretionary, segments can form in any orientation with respect to spreading, and are frequently characterized by an axial valley that possibly extends to ~50 km for ~1 km of deep (Dick et al., 2003). These important changes between slow- and ultraslow-spreading ridges result in another class of intermediate ridges displaying alternations of long segments with either slow or ultraslow properties (Dick et al., 2003).

2. Geological Setting

2.1. The Southwest Indian ridge

The Southwest Indian Ridge (SWIR) separates the African and Antarctic plates over 7700 km with a general SW-NE orientation between the Bouvet Triple Junction (BTJ, 55°S/0°40'E) and the Rodriguez Triple Junction (RTJ, 25°30'S/70°E) (Figure 1.8; e.g., Sauter & Cannat, 2010). The ridge axis is segmented by transform faults (or fracture zones) with a general ~N-S orientation in the central province that becomes NE-SW in the West. The full spreading rate is rather constant and calculated at ~14 mm.yr^{-1}, placing the ridge in the class of ultraslow-spreading ridges (e.g., Dick et al., 2003). In the vicinity of the Atlantis II Transform, the spreading is highly asymmetric with a rate of 8.5 mm.yr^{-1} to the south, and 5.5 mm.yr^{-1} to the north (Hosford et al., 2003).

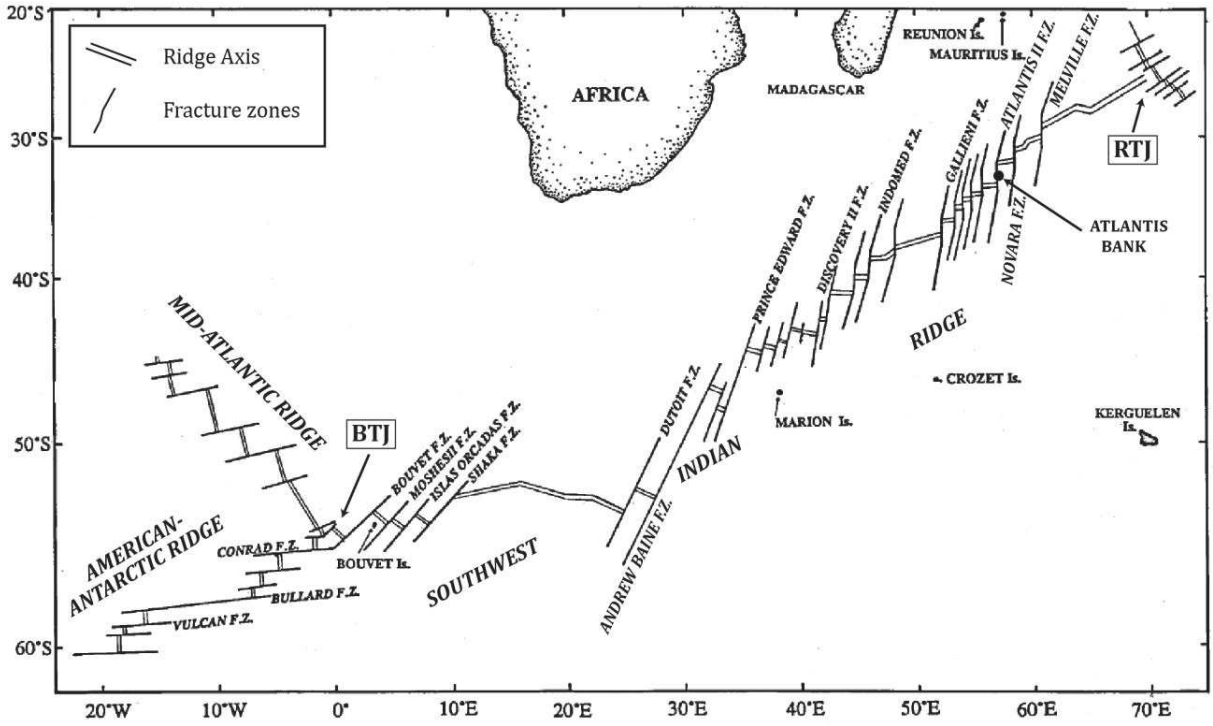

Figure 1.8 *- Position of the SWIR axis and crosscutting fracture zones (F.Z.) in the southern ocean (modified after Dick et al., 1999). The location of the SWIR edges is indicated by the boxes BTJ (Bouvet Triple Junction) and RTJ (Rodriguez Triple Junction), and the location of the Atlantis Bank is indicated by the black dot.*

Along the ridge axis, distinct geophysical provinces are observed. Two corresponds respectively to the East of the Melville fracture zone (60°E-70°E), and West of the Andrew Baine fracture zone (0°E-25°E), and the last province is the central one (Figure 1.8). In the Eastern and Western provinces, the ridge display a deep axial valley, an oblique spreading (up to 51°), sparsely developed mantle Bouger gravity anomalies and magnetic anomalies at the axis, and unsteady transform and non-transform offsets (Grindlay et al., 1992; Patriat et al., 1997; Rommevaux-Jestin et al., 1997; Cannat et al., 1999). This suggests a cold mantle associated to a thick and strong lithosphere in a magma-poor context, as corroborated by the small degree of partial fusion inferred from basalt compositions (Klein & Langmuir, 1987; Dick et al., 2003; Cannat et al., 2008). The magmatic activity of the ridge segments that compose these provinces is concentrated in some axial volcanoes separated by large regions where serpentinized mantle derived-rocks abound (e.g., Cannat et al., 2006; Sauter & Cannat, 2010). In the eastern province, to the East of the Melville transform, these large amagmatic regions form N-S corridors interpreted to result from the activity of detachment faults. The extension probably occurred by a succession of N-dipping and S-dipping detachment faults, crosscutting each other's every 1-3 Myr (Figure 1.9; Sauter et al., 2013; Cannat et al., 2019). The central province of the SWIR (30°E to 60°E) differs

by the pursued activity of transform and non-transform discontinuities, a spreading perpendicular to the axis, and important mantle Bouger gravity anomalies and magnetic anomalies at the axis (Rommevaux-Jestin et al., 1997; Cannat et al., 1999).

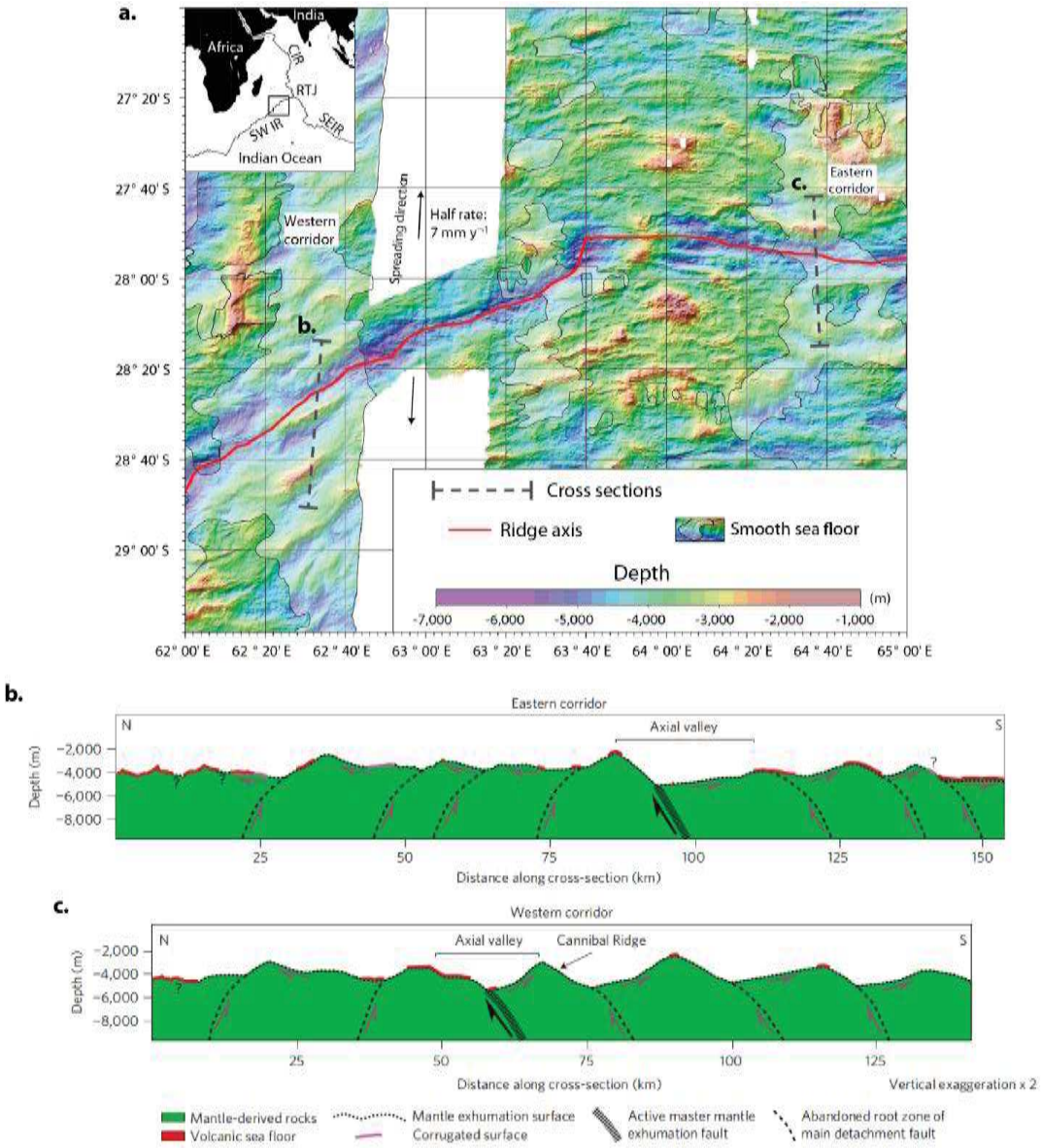

Figure 1.9 *- Smooth sea floor in the Eastern part of the SouthWest Indian Ridge. (a) Bathymetric map of the area (Sauter et al., 2013). (b) and (c) are schematic interpretative cross sections of the lithospheric extension within amagmatic corridors. The seafloor morphology is derived from bathymetric data and lithologies are from dredging data at the Southwest Indian Ridge.*

2.2. Context of formation and geology of Atlantis Bank

2.2.1. Contributions from seafloor data and geophysics

Within the ridge segment bounded by the Atlantis II and the Novara fracture zones (hereafter called Atlantis II transform and Novara transform), a submarine massif emerges from the seafloor: the Atlantis Bank (Figures 1.8 and 1.10). It is located ~73 km south of the ridge axis and extends over ~35 km in the N-S direction and is ~21 km wide (e.g., Dick et al., 1991, 2019a). The offset of the ridge axis along the Atlantis II transform is about 200 km. With its summit lying at ~700 m below sea level, the Atlantis Bank is the highest and largest of the 5-km high mountain chain flanking the West of the Atlantis II transform trough (Dick et al., 1991).

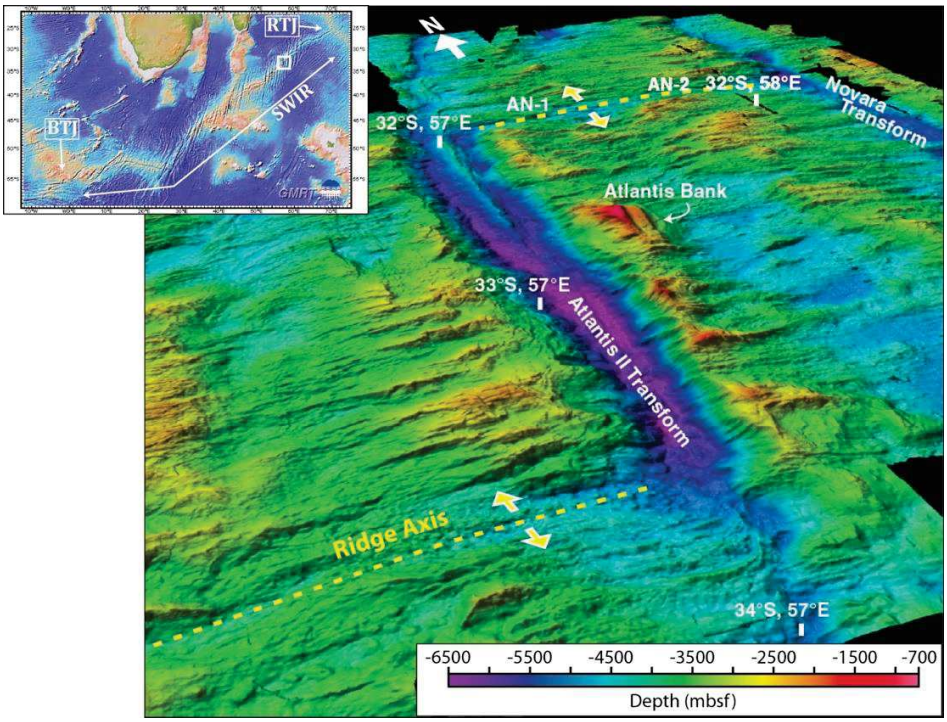

Figure 1.10 *- Bathymetric map showing the seafloor morphology in the region of the Atlantis II transform (modified after Dick et al., 2017). The inset indicate the location of the Atlantis II transform – Atlantis Bank (white square) on the SWIR (bathymetry after Ryan et al., 2009). mbsf: meters below seafloor. BTJ and RTJ are the triple junctions of Bouvet and Rodriguez, respectively.*

Its rise of about 3 km above the surrounding seafloor of the same age is explained by an uplift accommodated by a combination of a transtensional behavior of the Atlantis II transform during ca. 12 Myr, in response to a change in spreading direction, and the flexural uplift following detachment faulting (Dick et al., 1991; Baines et al., 2003; Hosford et al., 2003). The various studies performed in the area indicate that the massif corresponds to a fossil oceanic core complex (see below; e.g., Dick et al., 1991, 2019a). Magnetic anomalies measured in the

gabbroic lithologies reveal a 2.7 Myr exposure along a ~39 km long slipping fault. Their exhumation occurred between 13 Myr to 10 Myr when the ridge spreading rate accelerated to ~17 mm.yr^{-1}, mainly accommodated asymmetrically to the south at 14.1 mm.yr^{-1} (Baines et al., 2008). The summit of the Atlantis Bank is an overall flat surface extending 9 km in the N-S direction, and 4 km wide. In places, a surface of ~20 km² is found with less than 60 m of relief that indicates, together with the observation of beach cobbles, sands, and conglomerates along the Eastern flank (and at similar neighboring summits), that it corresponds to a wave-cut platform formed by erosion ca.9.5 Myr ago (Figure 1.11; e.g., Dick et al., 1991, 2019a).

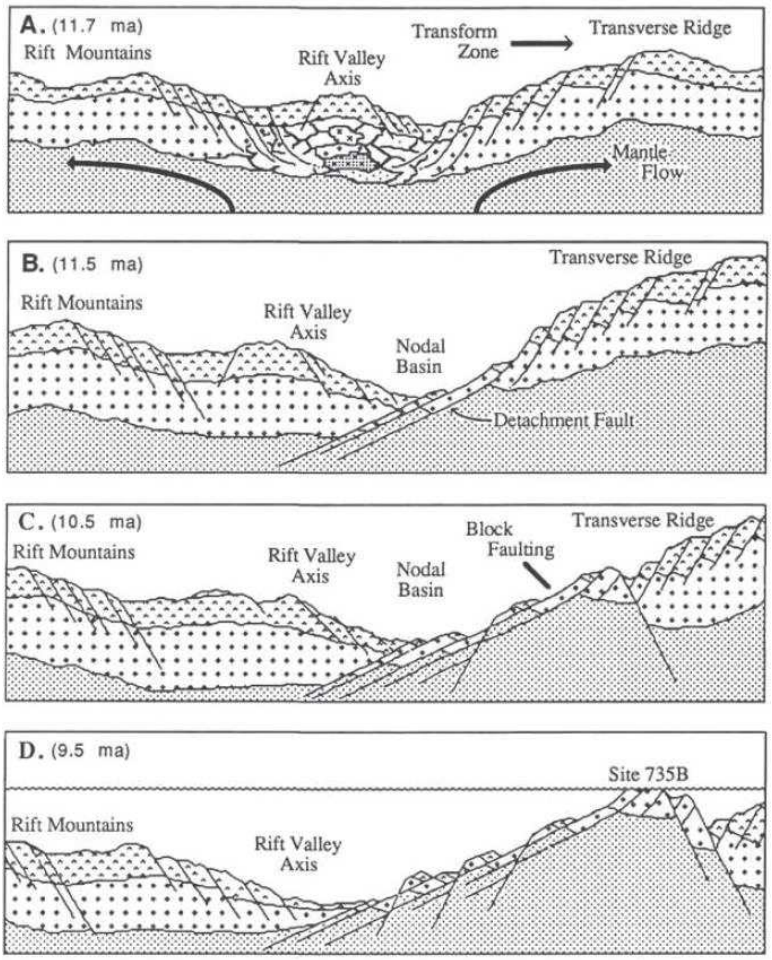

Figure 1.11 *- Schematic cross-section (N-S) depicting the tectonic evolution of the Atlantis Bank, from the accretion of the gabbro layer to it uplift in island position (Dick et al., 1991). (A) Initial symmetric spreading, possibly at the end of a magmatic pulse. (B) At some point, the shallow crust is welded to the old cold lithosphere to which the ridge axis abuts, causing formation of a detachment fault and nodal basin. (C), (D) Enhanced block uplift of the rift mountains at the ridge-transform corner forms a transverse ridge. A last step of subsidence follow this sequence, leading to the actual summit depth of ~700 mbsf. In cross-sections, the tightened dots (top)*

represent the volcanic lithologies (lavas and dikes), spaced dots (middle) represent gabbros, and the grey domain (bottom) represents mantle lithologies.

Seismic surveys in the region of the Atlantis II transform reveal a heterogeneous crustal structure, with a 3-4.5 km thick crust to the East of the Atlantis Bank (2-2.5 km of layer 2' lavas and dikes, and 1-2 km of layer 3' gabbros) and a 2.5-3 km thick "crust" in the transform valley with anomalously low velocities inferred to consist mainly of intensely serpentinized mantle rocks. Below the central region of the Atlantis Bank, seismic data indicates a thicker crust with a thinning of the layer 2 and a lower crust of 2-3 km, mainly composed of partially serpentinized mantle (Figure 1.12; Muller et al., 2000). The Moho reflector is imaged beneath the Atlantis Bank at 5 ± 1 km below seafloor (Muller et al., 2000; Dick et al., 2017).

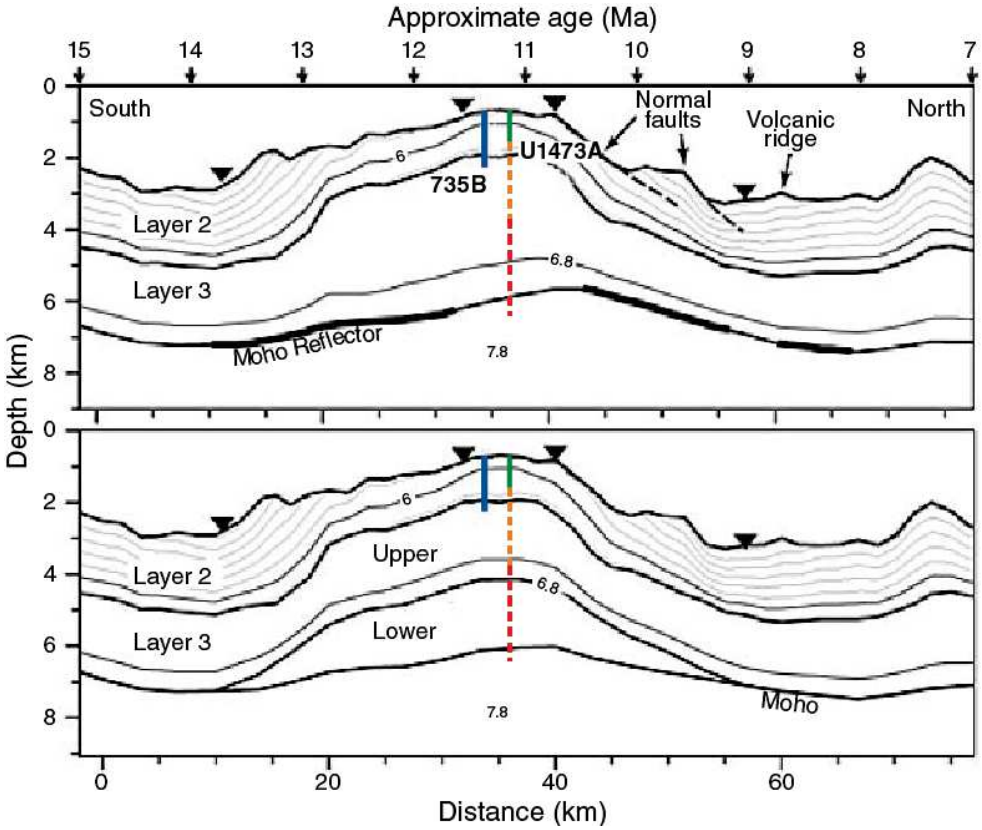

Figure 1.12 *- Velocity models at the Atlantis Bank for the N-S seismic line CAM101 (Dick et al., 2017; modified after Muller et al., 2000). The location of drilled holes (solid line; see next section) and planned drillings (dashed line) are reported.*

Fault rocks resulting from detachment faulting and more recent tectonic activity are strikingly scarce at the summit of Atlantis Bank, in contrasts to their common occurrence on the flanks of the massif. This is consistent with the uplift to an island position and subsequent erosion.

Palmiotto et al. (2013) proposed a water depth of ~100-200 m from dredged carbonates of the summit-platform edges, and algal trapped in sediments from the platform itself indicates wave base or shallower water depth (MacLeod et al., 2000; Dick et al., 2017). Also, the lack of pillow basalt occurrences on the Atlantis Bank surface is proposed to result from their removing through detachment faulting. Muller et al. (1997) and Minshull et al. (1998) proposed a thickness of 1.5-2 km for this upper unit. Indeed, the surface of the Atlantis Bank mainly consists of foliated plutonic rocks. The dominant lithology is gabbroic, and is locally overlain with limestones or carbonate-cemented pebbles conglomerates. Mainly found on the Eastern flank of the massif, the second lithology of importance consists of mixed domains of gabbros with intruding dikes (Figure 1.13a; Dick et al., 2017). This lithology indicates a magmatic activity at the ridge axis during the exhumation of the gabbro-dominated body that made up the Atlantis Bank. Only in the northern corner of the Atlantis Bank and Atlantis II transform are found dikes intruding into peridotites (Figure 1.13a and b). The classical layer 2 pillow basalts are scarce on the Atlantis Bank surface and only found in low amounts when present. This contrasts with the surrounding seafloor, to the East of the massif and the transform, where dredged samples only consist of pillow basalts (e.g., Dick et al., 2017, 2019a). The last lithology encountered at the Atlantis Bank surface consists of talc-serpentine schists inferred to correspond to the detachment fault surface (Dick et al., 2001; Miranda & John, 2010), as observed elsewhere at the Mid-Atlantic Ridge (MacLeod et al., 2002; Escartín et al., 2003; Schroeder & John, 2004). Observations and sampling on the eastern flank of the Atlantis II transform reveals the outcropping of plutonic mantle and lower-crust rocks, the latter being prominent (Dick et al., 1991). In the northwestern part of the massif, a transition from dike intruding gabbros (upslope/up in the lithostratigraphic sequence) to dike intruding peridotites (downslope/down in the lithostratigraphic sequence) is reported (Figure 1.13a and b). It is suggested to result from a waning of the magmatic activity at the ridge, and a lateral intrusion of dikes into mantle rocks near the transform fault. Locally, these dikes also intruded the talc-serpentine schists of the detachment surface (Dick et al. 2019a). The contact between the overlying olivine gabbros and lower peridotites is proposed to be intrusive, supported by the absence of tectonic contact and mylonitic or cataclastic microstructures (Figure 1.13a, c and d; Dick et al. 2019a). Sampled peridotites along the transform wall indicate a static serpentinization of medium- to coarse-grained granular lherzolites, indicative of an *in situ* intrusion. Rare dunite and troctolite samples are found in central region of the massif suggesting little primitive melt intrusion or storage up in the lower crust, and a limited melt transport through the lower crust to the upper pillow basalts almost exclusively focused in the center of the paleo-ridge segment (Dick et al. 2019a). Petrologic variations at the top and at the edges of the gabbro pluton that composes the Atlantis Bank indicate important volumes of evolved gabbros (oxide gabbros) intruding with sharp contacts the main olivine gabbro body. Over a large portion of the massif surface, a carapace of oxide gabbro mylonites is observed (e.g., Dick et al., 2019a). It is

inferred to extend over a hundred meters of thickness corresponding to the detachment fault damage zone, conformably lying beneath the talc-serpentine schists that made up the detachment fault surface.

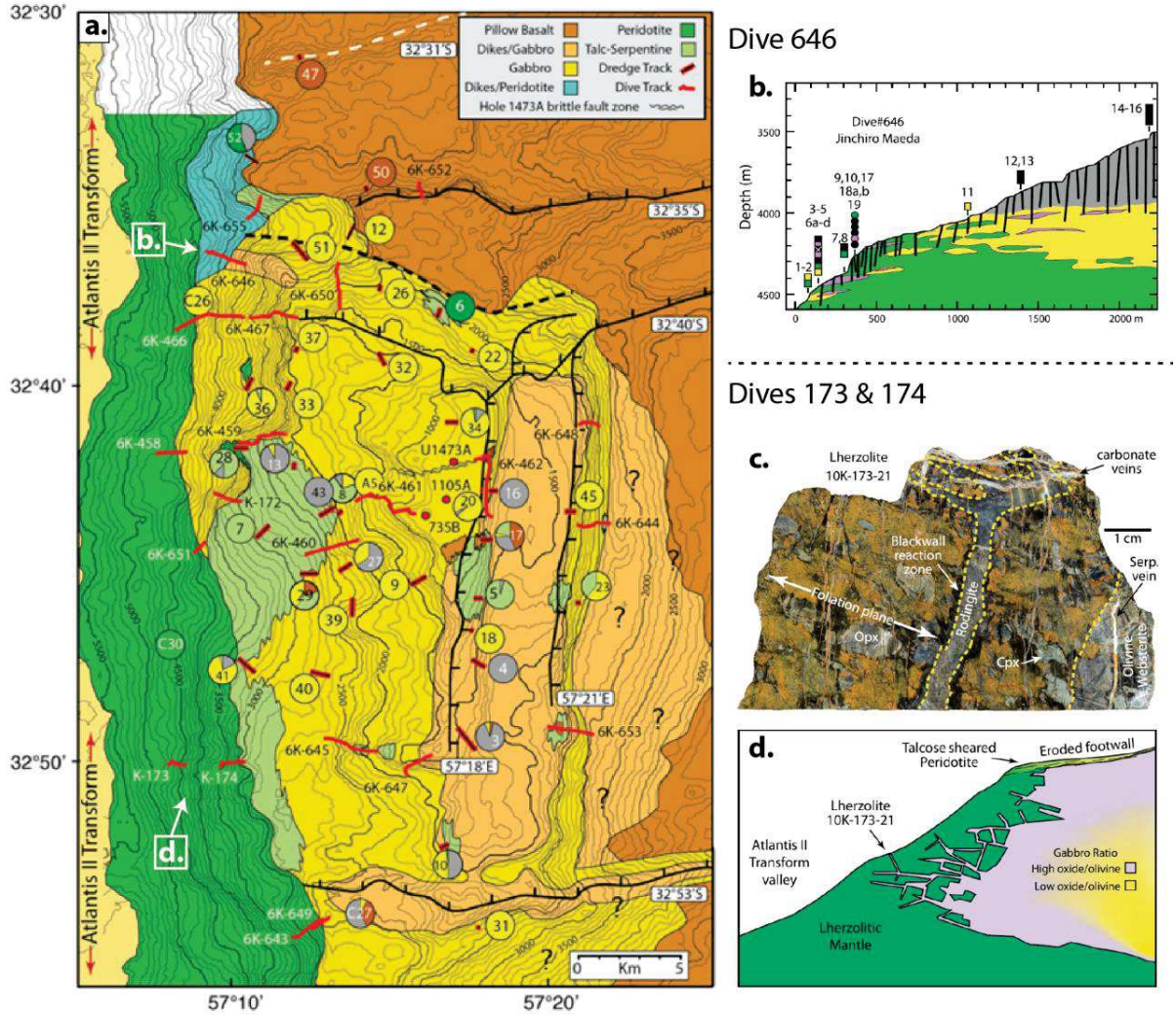

Figure 1.13 *- Lithologies and structures at the Atlantis Bank. (a) Geologic map of Atlantis Bank with dive tracks shown (modified after Dick et al., 2019a). The dashed black line indicates the detachment fault termination covered by pillow basalts, and the dashed white line the old axial volcanic ridge. Pie charts indicates the rock proportion correspond to the neighboring dive track. The three red dots in the central upper platform indicate the location of drilled holes (ODP Holes 735B and 1105A, and IODP Hole U1473A). Locations of cross-sections (b) and (d) are indicated in white. (b) Geologic interpretation of dive 646 with location of samples (Dick et al. 2019a). (c) Example of sample showing the imbricated contact between gabbro veins and lherzolites and (d) cartoon of the possible structuration of the gabbro-mantle contact (Dick et al. 2019a).*

The absence of this damage zone at the summit of the Atlantis Bank suggests that at least 100-200 m (i.e., the damage zone thickness) were eroded below the detachment surface in this region (Dick et al., 2017).

In situ sampling at the Atlantis Bank surface aiming at identifying petro-fabrics associated to deformation revealed a continued deformation of the constituting gabbroic lithologies, from hypersolidus to brittle conditions along with exhumation and strain localization (e.g., Dick et al., 1991; Miranda & John, 2010). Crystal plastic deformation is encountered at the detachment footwall and extends over a crustal thickness of ~400m below the detachment. In contrast, semi-brittle to brittle deformation is restricted to the upper 30-80 m below the detachment surface (Miranda & John, 2010). The inferred widespread ductile deformation at near-solidus conditions demonstrates an early onset of the detachment fault activity in the magmatic history, during the crystallization of gabbros. The first step of strain localization occurred with an important recrystallization of plagioclase minerals under temperatures of 910°C to 650°C. Then, dissolution-precipitation creep was accommodated by amphiboles at ~750-450°C, followed by reaction softening accommodated by chlorites at lower green-schists facies conditions (450-300°C). Finally, cataclasites and brittle fractures formed with lower temperature deformation (Miranda & John, 2010; Miranda et al., 2016).

2.2.2. Contributions from drilled holes (735B, 1105A & U1473A)

Since 1987, several drilling campaigns were conducted at the summit platform of the Atlantis Bank. The longest continuous oceanic section recovered to date was drilled in Hole 735B (e.g., Ildefonse et al., 2014). The first expedition undertaken by the ODP during Leg 118 initiated the drilling of Hole 735B from the summit platform and reached a depth of 500.7 m (Robinson et al., 1989; Dick et al., 2006). The hole was deepened to 1508 mbsf during ODP Leg 176 in 1997 with an overall high recovery of 86% (Figure 1.14a; Dick et al., 2000). In 1998, a new expedition was conducted at the Atlantis Bank during Leg 179 and ODP Hole 1105A was drilled ~1.3 km NE from Hole 735B down to 158 mbsf, again with a high recovery (~83%, Figures 1.13a and 1.14b; Pettigrew et al., 1999). Recently in winter-spring 2015-2016, the IODP expeditions 360 and 362T expanded this collection with the drilling of Hole U1473A, located 2.2 km and 1.4 km northeast to Holes 735B and 1105A, respectively (Figures 1.13a and 1.14c; Dick et al., 2019b). It was drilled to 809 mbsf with a relatively poor recovery of ~44% on the upper 469 mbsf of the hole, which turns to excellent in the lower ~200 m with 96% of recovery. Directly below a large fault zone at 411-469 mbsf, the expedition 360 scientific participants decided to drill without coring the depth interval from 481.7 mbsf to 519.2 mbsf because of very low recovery (referred as "drilled interval"; MacLeod et al., 2017).

The first striking result from these three holes is that igneous stratigraphy and mineral modes are similar, so as the dominant rock types. Drill holes reveal that the massif mainly consists of

olivine gabbros, with subordinate gabbros containing oxides, gabbros (*s.l.*), and gabbronorites (Figure 1.14; Pettigrew et al., 1999; Dick et al., 2000, 2017, 2019b). The different processes having affected the Atlantis Bank gabbros consists of combined magmatic processes, high temperature deformation, and moderate-high temperature metamorphism. This led to the heterogeneous organization of microstructures and compositions with centimeter to meter-scale variations in each lithologic unit. Hypersolidus brittle and crystal-plastic deformation are evidenced to be coeval in the three holes, pointing to an important crystallized fraction within former mushes then forming a load-bearing framework where brittle behavior is possible (Dick et al., 2019b). The major difference concerns green-schists facies and lower degree deformation with the specific occurrence of high-angle normal faults dipping to the south in Hole U1473A. The general organization of the Atlantis Bank tectono-magmatic lithostratigraphy consists of a pile of upwardly chemically differentiated olivine gabbro units (third columns in Figure 1.14). These major igneous units display a geochemical reset to a more primitive composition at the bottom of each new section. Five are identified in Hole 735B with an average thickness of 400 m, and three ~200 m to 500 m thick in Hole U1473A (Figure 1.14a and c). It corresponds to uncorrelated magmatic events emplaced into the crust. These units are composed of multiple small igneous sills of centimeter to decimeter width, with frequent crosscutting relationships. A detailed analysis of the section 2 of Hole 735B (Figure 1.14a), combining structural and petrographic characterizations together with whole rock and *in situ* mineral analyses depict a complex magmatic history. Boulanger et al. (2020) described a lower unit consisting of multiple sill intrusions (unit VI, Figure 1.14a), each with varying compositions (more or less evolved) and crystal/melt ratios, subjected to upward reactive melt percolation. This percolation of melts arising from the sills is then collected in the upper unit (unit V, Figure 1.14a) that forms progressively by differentiation. Sill intrusion is proposed to occurs every ~1 kyr and to build up the five units that constitute Hole 735B over ~200 kyr during the formation of the OCC. Observations of a well-defined layering are rare and can result from high temperature crystal-plastic deformation with or without melt in the rock (Dick et al., 2019b), or magmatic processes (magmatic flow or crystal settling; Boulanger et al., 2021).

Olivine gabbros and a great portion of oxide gabbros correspond to adcumulates, generally with less than 2% of trapped melt. In contrast the felsic veins and most of oxide gabbros formed in higher presence of melt (10-15% or higher; Natland & Dick, 2001). This inferred low amount of melt in the crystallizing mush is proposed to result from a mechanical expulsion through strong applied deviatoric stresses. The induced (evolved) melt circulation through local expulsion is consistent with the examples of reactive porous flow in crystallizing mushes, possibly leading to the formation of flow channels (e.g., Lissenberg & MacLeod, 2016; Dick et al., 2019b; Sanfilippo et al., 2020). From microstructural observations and crystallographic preferred orientations data in plagioclase, Ferrando et al. (2021) and Boulanger et al. (2021) proposed an

overall weak compaction in the coarse-grained gabbroic intervals of Hole U1473A inducing melt extraction and accumulation in locally melt-rich zones. Oxide gabbros likely formed up in the crust in lens of small extent (< 1 km) by preferential late melt migration and localization along shear zones and permeable boundaries between units (Dick et al., 2019b).

Differential erosion of the massif surface makes it difficult to correlate the lithostratigraphy between the holes. However, sub-vertical black amphibole veins along with a static replacement of the foliated gabbros are a common feature of holes in the upper hundred meters, such as the intense and pervasive crystal plastic deformation within the upper 600-700 mbsf (Figure 1.14a and c; Dick et al., 2000, 2019b). It indicates seawater penetration during the exhumation and rotation of the detachment footwall under mid-amphibolite facies conditions, and that the upper portions of holes were part of this footwall. Crystal-plastic deformation and focused late melt (Fe-Ti-rich) into shear zones are important features in the massif stratigraphy. The oxide gabbro cap inferred from dredging, and observed in both holes 735B and 1105A, is lacking in Hole U1473A, which is probably explained by its more centered position on the summit platform of the Atlantis Bank more prone to erosion. Ductile deformation is expressed in porphyroclastic and protomylonitic textures and frequently localizes in decimeter- to meter-scale ultramylonitic zones. In Hole U1473A, two thick near-continuous crystal-plastic shear zones are identified between ~150-250 mbsf and ~300-400 mbsf (MacLeod et al., 2017). Petrographic observations reveal combined deformation mechanisms in these deformed zones, varying from dislocation creep with development of crystallographic preferred orientations (Mehl & Hirth, 2008; Satsukawa et al., 2013; Gardner et al., 2020; Taufner et al., 2021) to diffusion creep and subsequent grain boundary sliding (Mehl & Hirth, 2008; Gardner et al., 2020; Taufner et al., 2021). Core section analyses reveal the preservation of magmatic textures in 42% of Hole U1473A, and most sections were subjected to crystal plasticity evidenced by undulose extinctions even in a great part of samples with magmatic textures (Figure 1.14c; MacLeod et al., 2017). The preservation of undeformed intervals in Hole 735B is much greater, representing 72% of the core (Figure 1.14a; Dick et al., 2000).

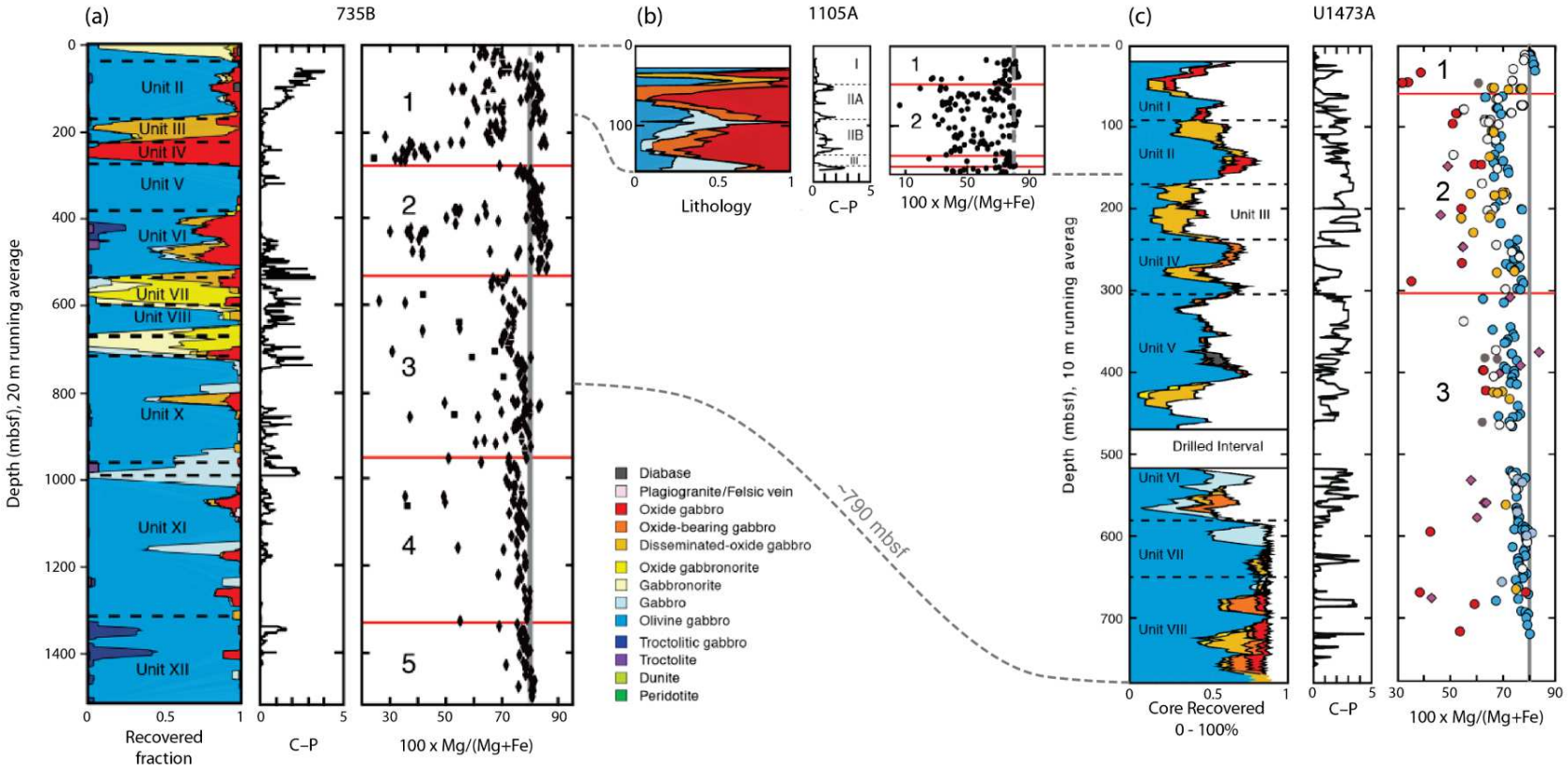

Figure 1.14 *- Lithostratigraphic, crystal-plastic fabric intensities (C–P), and whole rock Mg# (100xMg/(Mg+Fe)) variations in the two OPD holes (a) 735B and (b) 1105A, and (c) IODP Hole U1473A (modified after Dick et al., 2019b). In the third column of each hole are indicated the different gabbroic masses boundaries by the red lines and numbered from top to bottom. Note the different depth scale from (a) to (b) and (c).*

2.3. The Bracco Gabrroic Complex

2.3.1. The Alp-Apennine system and the Ligurian ophiolites

The northern and western Mediterranean domains of the Alp-Apennine belt expose several Jurassic oceanic remnants of the Alpine Tethys. This Alp-Apennine belt contains sedimentary and ophiolitic sequences belonging to this ancient ocean separating the European and African plates (dark green in Figure 1.15a; e.g., Bortolotti et al., 2001). In the Northern Apennine, ophiolites are part of the Ligurian unit consisting of a stack of tectonic slices from continental and oceanic domains. The typical stratigraphy of these Ligurian ophiolites consists of ultramafic lithologies intruded by large gabbro or gabbronorite bodies, heterogeneously covered by pillow lavas or sediments, and frequent ophiolitic breccia are found on top (e.g., Barrett & Spooner, 1977; Lemoine et al., 1987; Lagabrielle, 2009). The Ligurian unit is divided in two tectono-stratigraphic groups based on their origin: the External Ligurides of continental origin, and the Internal Ligurides of oceanic origin (Figure 1.15a; Marroni et al., 1998). The External Ligurides include calcareous sequences and ophiolitic lithologies occurring as slide blocks (olistoliths of mantle or basalt lava sequences, rare gabbros and pelagic sediments). The ultramafics are proposed to correspond to a portion of sub-continental mantle at the ocean-continent transition later exposed during thinning by continental rifting (Beccaluva et al., 1984; reviewed in Piccardo & Guarnieri, 2010). The Internal Ligurides are composed of ophiolites (serpentinized mantle peridotites, gabbros, and basalts) and the overlying pelagic sediments associated with turbidites. Depleted peridotites composing these ophiolites indicate similarities with abyssal peridotites, and are interpreted to form by MORB-type melting after asthenospheric upwelling before being cooled and accreted to the oceanic lithosphere (e.g., Rampone et al., 1996, 1997). This Internal Ligurides sequence is composed of three main tectonic units that mostly outcrop in Eastern Liguria (Decandia & Elter, 1972; Abbate et al., 1980; Marroni & Pandolfi, 2001): the Gottero unit, the Colli-Tavarone unit, and the Bracco/Val Graveglia unit (Figure 1.15b). Both Colli-Tavarone and Gottero units mostly consists of sedimentary sequences, while the Bracco/Val Graveglia unit corresponds to a preserved ophiolite with its sedimentary cover. The Internal Ligurides are characterized by a thin crustal section mainly composed of mantle peridotites and gabbros, no sheeted dike complex, overlying pillow lavas and sediments, and breccia; they resemble the crust encountered at slow- and ultraslow-spreading ridges (e.g., Cannat, 1993; Dick et al., 2003; Escartín & Canales, 2011). Lagabrielle & Cannat (1990) proposed that the exposure of mantle and lower crust lithologies were exhumed during extension at a slow-spreading ridge. More recently, other remnants of slow-spreading ridge architecture were recognized in ophiolites, particularly in the Alpine Tethys (e.g., Manatschal et al., 2011; Lagabrielle et al., 2015; Decrausaz et al., 2021).

In terms of deformation, the Internal Ligurides recorded an original high-temperature (HT) metamorphic event associated with deep crustal lithologies uplifted to the seafloor. This was followed by normal/transform faulting before the pillow basalt emplacement and sedimentary deposit. Then, orogenic deformation overprinted the latter forming NE dipping large folds and thrusts during Cretaceous to Paleocene. In the NW part of the Internal Ligurides, the pre- to middle-Eocene tectonic was recorded and consists of folding in association to a very low grade metamorphism (e.g., Bortolotti et al., 2001).

2.3.2. The Bracco-Gabbro Complex

The BGC belongs to the Internal Ligurides, and consists of a kilometer-scale layered gabbroic pluton (5 by 6 km large). It intrudes into serpentinized mantle peridotites of Jurassic age, and is associated in limited amounts to harzburgites and dunites (Figure 1.15c; Baumgartner et al., 2013; Tribuzio et al., 2016, and references therein). Extrusive pillow lava, ophiolitic breccia, and sediments are found on top of the gabbros and peridotites. The whole complex was subjected, to variable degrees, to low-temperature metamorphism leading mainly to the formation of retrograde serpentine, chlorite, prehnite, and oxides. To the SE of the BGC (toward Levanto, Figure 1.15b), dominant proportions of mantle rocks are exposed and may represent the base of the magma chamber (Cortesogno et al., 1987; Schwarzenbach et al., 2021). Gabbro (*s.s.*) is the most common lithology, and olivine-gabbros, troctolites, and plagioclase-peridotites are also documented in lesser amounts in the complex. In igneous gabbros, plagioclase is of labradorite composition (~An_{60}), clinopyroxene occur as diopside, and generally the olivine is highly serpentinized when present in these rocks. Magmatic layering is frequent in gabbroic lithologies, and marked by variations in grain sizes or in lithology, sometimes organized in lenses within the isotropic gabbro (Figure 1.16; e.g., Menna, 2009). This layering is commonly oriented NE-SW in the southern and western domains of the BGC, and changes for a NW-SE orientation in the central and northern region (Figure 1.15c).

Figure 1.15 *- Geology of the Alp-Apennine and Bracco area. (a) Geological sketch map of the Central-Western Ligurian Alps and Northern Apennine (after Rampone et al., 2020). IL: Internal Ligurides, EL: External Ligurides. (b) Geological sketch map of the Internal Ligurides unit (modified after Marroni & Pandolfi, 1996). (c) Structural sketch map of the Bracco area with location of the studied samples (modified after Menna, 2009).*

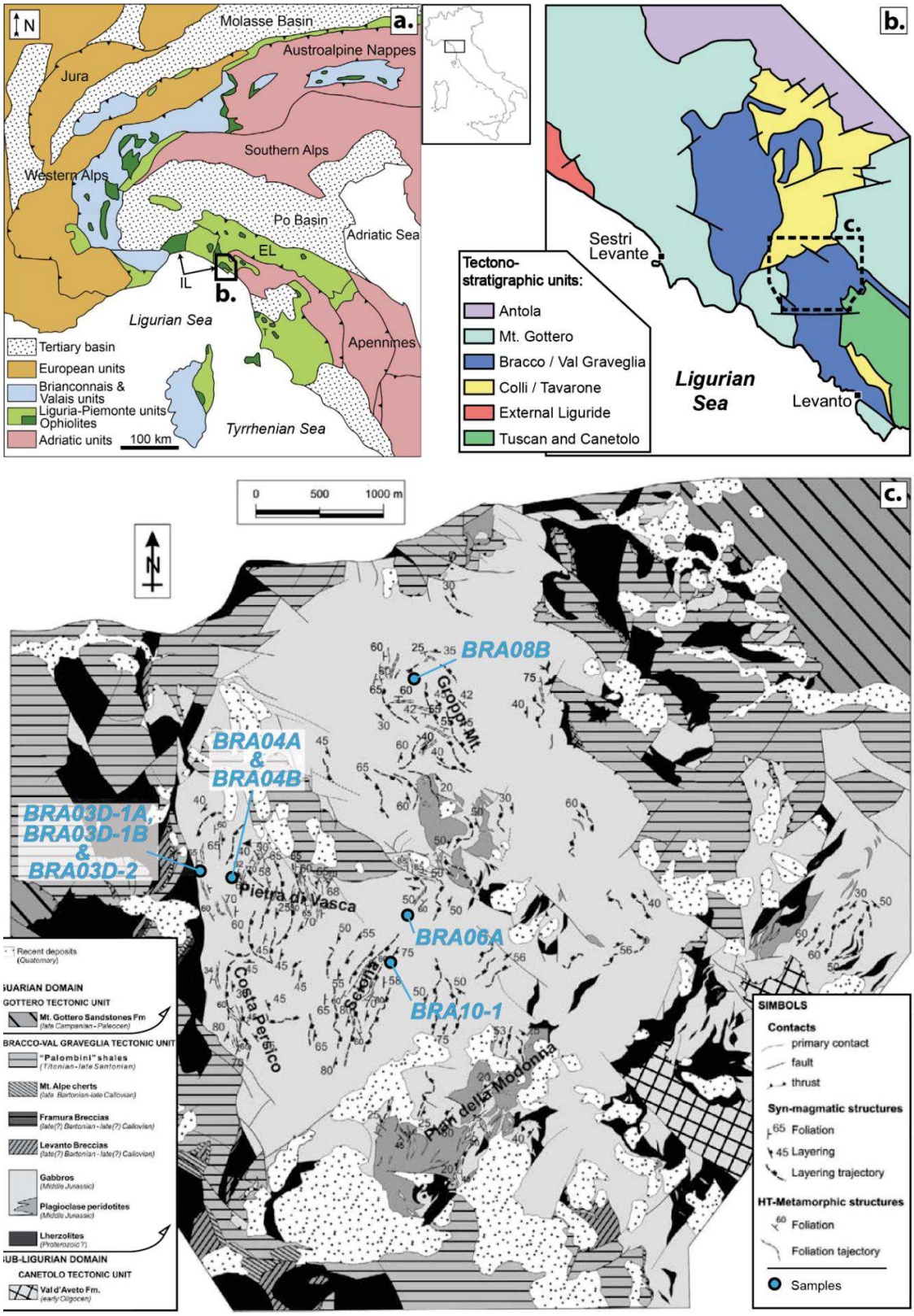
a.
N
Molasse Basin
Austroalpine Nappes
Jura
Southern Alps
Western Alps
Po Basin
Adriatic Sea
EL
IL
b.
Ligurian Sea
Apennines
Tyrrhenian Sea
Tertiary basin
European units
Brianconnais & Valais units
Liguria-Piemonte units
Ophiolites
Adriatic units
100 km
b.
Sestri Levante
c.
Tectono-stratigraphic units:
Antola
Mt. Gottero
Bracco / Val Graveglia
Colli / Tavarone
External Liguride
Tuscan and Canetolo
Ligurian Sea
Levanto
c.
0 500 1000 m
N
BRA08B
Groppo Mt.
BRA04A & BRA04B
BRA03D-1A, BRA03D-1B & BRA03D-2
Pietra di Vasca
BRA06A
Costa Perisco
BRA10-1
Monte della Madonna
Recent deposits (Quaternary)
LIGURIAN DOMAIN
GOTTERO TECTONIC UNIT
Mt. Gottero Sandstones Fm (late Campanian - Paleocen)
BRACCO-VAL GRAVEGLIA TECTONIC UNIT
"Palombini" shales (Tithonian - late Santonian)
Mt. Alpe cherts (late Bartonian-late Callovian)
Framura Breccias (late(?) Bartonian - late(?) Callovian)
Levanto Breccias (late(?) Bartonian - late(?) Callovian)
Gabbros (Middle Jurassic)
Plagioclase peridotites (Middle Jurassic)
Lherzolites (Proterozoic ?)
SUB-LIGURIAN DOMAIN
CANETOLO TECTONIC UNIT
Val d'Aveto Fm. (early Oligocen)
SIMBOLS
Contacts
primary contact
fault
thrust
Syn-magmatic structures
65 Foliation
45 Layering
Layering trajectory
HT-Metamorphic structures
60 Foliation
Foliation tajectory
Samples

Figure 1.15

In addition to the layering, a magmatic foliation is documented with a similar orientation. Subsequent mylonitic shear zones formed generally parallel to the magmatic layering/foliation during retrograde metamorphic conditions, associated mainly to the recrystallization of plagioclase and clinopyroxene (Figure 1.16a). The variation in clinopyroxene composition during recrystallization indicates sub-solidus conditions, estimated from 850°C to 950°C based on amphibole TiO_2 content within recrystallized clinopyroxene aggregates (Tribuzio et al., 2000; Montanini et al., 2008). Shear zones formed during this first phase of crystal-plastic deformation D_1 are of variable width, from tens of centimeter to tens of meter, with an increasing deformation intensity toward the core of the zone (e.g., Molli, 1996; Menna, 2009). Four types of deformed microstructures are identified associated with this D_1 phase:

(1) The fabric I corresponds to the development of a penetrative foliation in the rock, highlighted by the elongation of clinopyroxene porphyroclasts. Both plagioclase and clinopyroxene recrystallize from their edges (Figure 1.16b). This corresponds to a porphyroclastic fabric of CPF index 2 following the IODP (International Ocean Discovery Program) nomenclature used in previous chapters (Allard et al., 2021).

(2) Fabric II results from the development of pervasive S-C structures, common in D_1 shear zones (CPF index 3 to 4). These are the classical "flaser gabbros" described in alpine ophiolites, showing more or less continuous recrystallized and stretched clinopyroxene bands alternating with recrystallized plagioclase bands.

(3) Fabric III results from an increase in pervasive foliation development with the formation of millimeter-sized bands of recrystallized clinopyroxene and plagioclase (CPF index 5).

(4) The last type, Fabric IV, corresponds to very thin sub-millimeter-sized alternating plagioclase and clinopyroxene bands (finer than CPF index 5).

Both progressive and discontinuous transitions between the four fabrics can be observed in rocks, and corresponds to increasing deformation intensity (e.g., Figure 1.16b, right images; Molli, 1994; Menna, 2009). Basalt dykes and hornblende-plagioclase filled veins are not affected by deformation while cutting the D_1 shear zones, which is indicative of their younger nature (Figure 1.16a).

Static recrystallization of retrograde metamorphic phases (mainly amphiboles) is a characteristic feature of the D_2 deformation phase. By contrast to D_1 shear zones, those formed during the D_2 phase are rare. The resulting foliation consists of alternate plagioclase and amphibole bands, and is often discontinuous (Menna, 2009). The shear zones generally extend up to tens of meter with a variable thickness (< 4 m), overprinting D_1 shear zones (Figure 1.16a). Plagioclase grains are subjected to cataclasis and mechanical twinning, and grain size reduction. Amphiboles grow at the expense of clinopyroxene during this phase, more or less in a static way, leading to their parallelism with the D_1 orientation. The veins cutting the D_2 shear zones are filled with Mg-

hornblende alone or in association with tremolite-actinolite (± plagioclase, epidote, and prehnite-pumpellyite). Serpentinization is attributed to the end of this deformation phase, which is proposed to occur at ~550°C and 2 kbar and to continue below 500°C (i.e., until the onset of serpentinization; Menna, 2009).

The third and last episode of deformation D_3 consists of the replacement of former mafic phases by amphiboles (tremolite-actinolite). Narrow shear zones and crenulation cleavage are often attributed to this phase, generally found along D_2 shear zones. With the development of cataclasites, the D_3 phase probably occurred at temperatures below 500°C.

The different stages of deformation are proposed to form a continuum from syn-magmatic, granulitic conditions to amphibolitic and finally greenschist facies conditions (Menna, 2009). Although a transition from granulitic to amphibolitic conditions is observed, it may simply reflect fluid circulation (e.g., seawater) rather than changes in pressure and temperature conditions.

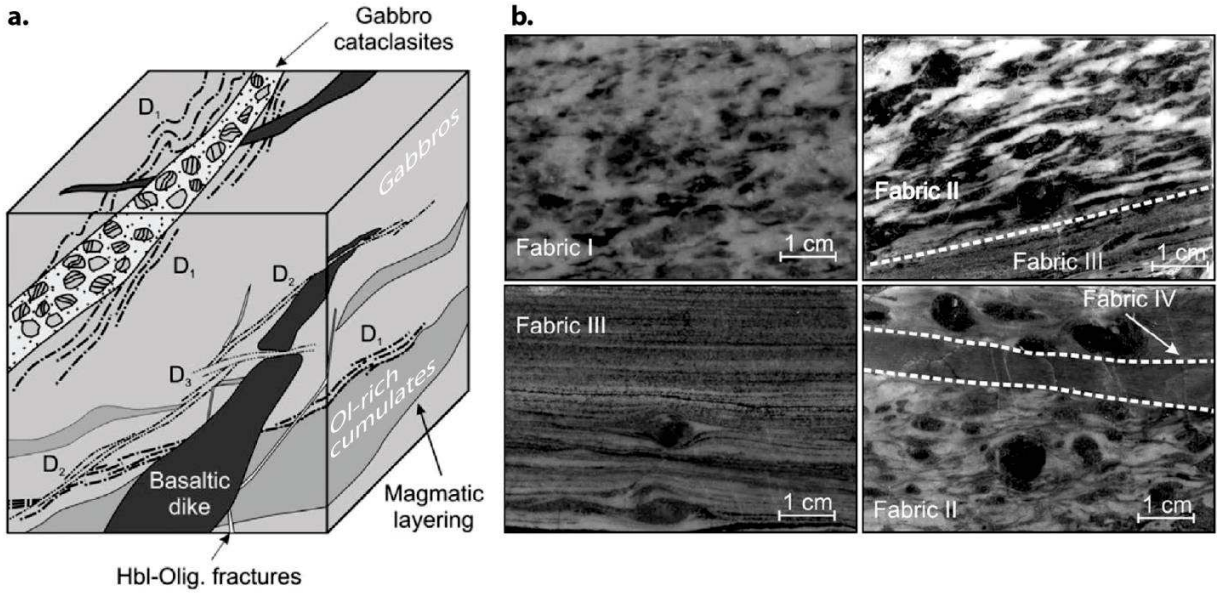

Figure 1.16 *- Deformations in the Bracco-Gabbro Complex. (a) Schematic representation of structural relations between the deformation events in the BGC (modified after Menna, 2009). (b) Macrofabrics details associated with D_1 HT phase (Menna, 2009).*

3. Deformation Processes and Accommodation

3.1. Deformation and strains: generalities

In response to a certain level of external forces, a crystal or a crystal aggregate changes of shape by a process referred to as "*deformation*". A crystal, or a solid material, subjected to deformation can be considered as a continuous body which intrinsic properties depends on pressure and temperature. The forces that apply at the surface of a crystal (or a material) are termed "*stresses*"

and are expressed in Pascals (Pa) when expressed in unit area (e.g., Poirier, 1985). It can be expressed in the form of a three-dimensional stress field with each vector describing, in the three directions of the coordinate system, the magnitude and the orientation of the stress (Figure 1.17).

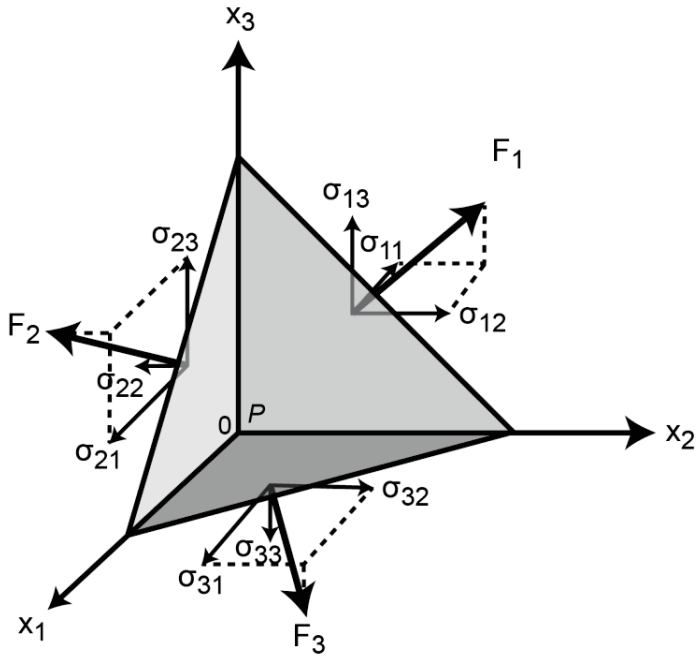

Figure 1.17 *- Applied forces to the faces of an elementary tetrahedron (modified after Poirier, 1985). The stress vectors F_1, F_2, and F_3 are orthogonal to the tetrahedron faces x_2x_3, x_1x_3, and x_1x_2 respectively. Stresses are the nine stress components σ_{ij} parallel to the coordinate axes. The three stresses $\sigma_{i=j}$ corresponds to normal stresses, orthogonal to the tetrahedron face, and the other $\sigma_{i\neq j}$ are the tangential stresses or "shear stresses", parallel to the face.*

The applied force corresponding to a "*stress vector*" (F) is described by a set of three stresses with respect to the coordinate system. The three sets of stresses associated to stress vectors (in the three directions of the coordinate system) constitute a "*stress tensor*" in the form:

$$\begin{pmatrix} \boldsymbol{\sigma_{11}} & \boldsymbol{\sigma_{21}} & \boldsymbol{\sigma_{31}} \\ \boldsymbol{\sigma_{12}} & \boldsymbol{\sigma_{22}} & \boldsymbol{\sigma_{32}} \\ \boldsymbol{\sigma_{13}} & \boldsymbol{\sigma_{23}} & \boldsymbol{\sigma_{33}} \end{pmatrix}$$

Diagonal terms σ_{11}, σ_{22}, and σ_{33} are normal stresses, acting orthogonal to the corresponding plane. The six other terms are shear stresses, acting within the considered plane, leading to the symmetry of the tensor with $\sigma_{ij} = \sigma_{ji}$. This tensor permits to entirely define the state of stress at a point *P* of a considered body (here at the origin of the coordinate system Figure 1.17). The "*principal stresses*" of the tensor: σ_1, σ_2, and σ_3 correspond to the normal stresses in a coordinate

where the shear stresses (off-diagonal terms) are equal to zero (Poirier, 1985). In geology, these principal stresses are used to describe the state of stress in deformed rocks, with σ_1 being the principal stress component, σ_2 the intermediate stress component, and σ_3 the least stress component such as $\sigma_1 > \sigma_2 > \sigma_3$.

We call the "*trace*" of a tensor the sum of the diagonal terms, which is independent to the coordinate system. Then the "*hydrostatic pressure*" *P* is:

$$\boldsymbol{P = \frac{1}{3}(\sigma_{11} + \sigma_{22} + \sigma_{33}) = \frac{1}{3}(\sigma_1 + \sigma_2 + \sigma_3)}$$

The "*mean stress*" σ_{mean} is identical to *P* only when the three principal stresses are equal. Thus, it is possible to evaluate the difference between the mean stress σ_{mean} and the normal stress σ_n, that consists of the three principal stresses, by calculation of the "*deviatoric stress*": $\sigma_{dev} = \sigma_n - \sigma_{mean}$.

The stress tensor can be decomposed into deviatoric and hydrostatic parts as:

$$\begin{pmatrix} \boldsymbol{\sigma_{11}} & \boldsymbol{\sigma_{21}} & \boldsymbol{\sigma_{31}} \\ \boldsymbol{\sigma_{12}} & \boldsymbol{\sigma_{22}} & \boldsymbol{\sigma_{32}} \\ \boldsymbol{\sigma_{13}} & \boldsymbol{\sigma_{23}} & \boldsymbol{\sigma_{33}} \end{pmatrix} = \begin{pmatrix} \boldsymbol{P} & \boldsymbol{0} & \boldsymbol{0} \\ \boldsymbol{0} & \boldsymbol{P} & \boldsymbol{0} \\ \boldsymbol{0} & \boldsymbol{0} & \boldsymbol{P} \end{pmatrix} + \begin{pmatrix} \boldsymbol{\sigma_{11} - P} & \boldsymbol{0} & \boldsymbol{0} \\ \boldsymbol{0} & \boldsymbol{\sigma_{22} - P} & \boldsymbol{0} \\ \boldsymbol{0} & \boldsymbol{0} & \boldsymbol{\sigma_{33} - P} \end{pmatrix}$$

These two components, deviatoric and hydrostatic stresses, are those considered for deforming rocks, generally with the hydrostatic term being negligible over the deviatoric one. Thus, deviatoric stresses account for most of rocks' deformation.

Through the application of forces, a crystal (or a material) is deformed, inducing the displacement of mater within. Let's consider a point x_i in the crystal that is displaced as a result of deformation along a vector $u(x_i)$. We call "*rigid-body translation*" a case where all the points inside the crystal move by the same displacement vector. When displacement vectors differ from a point to another, the deformation is not uniform and a gradient of displacement is created between neighboring points (i.e., the distance between points changes). These displacements are represented by a similar tensor than for stresses, with ε_{ij} the displacement of a vector *u* in the three directions of the coordinate system. These tensor components are:

$$\boldsymbol{\varepsilon_{ij} = \frac{1}{2}\left(\frac{\partial u_i}{\partial x_j} + \frac{\partial u_j}{\partial x_i}\right)}$$

where $\boldsymbol{\frac{\partial u_i}{\partial x_j}}$ is the infinitesimal displacement of a vector $u(x_j)$ in the direction x_j, and the tensor is:

$$\begin{pmatrix} \boldsymbol{\varepsilon_{11}} & \boldsymbol{\varepsilon_{21}} & \boldsymbol{\varepsilon_{31}} \\ \boldsymbol{\varepsilon_{12}} & \boldsymbol{\varepsilon_{22}} & \boldsymbol{\varepsilon_{32}} \\ \boldsymbol{\varepsilon_{13}} & \boldsymbol{\varepsilon_{23}} & \boldsymbol{\varepsilon_{33}} \end{pmatrix}$$

Similarly as for the stress tensor, the "*strain tensor*" is symmetrical, with the diagonal terms $\varepsilon_{i=j}$ called the "*stretches*" representing the along coordinate axes changes in length; and the off-diagonal terms $\varepsilon_{i\neq j}$ are called the "*shear strains*" and represents the changes in shape. Again, the "*principal deformation*" ε_1, ε_2, and ε_3 are used to define the internal deformation, with $\varepsilon_1 > \varepsilon_2 > \varepsilon_3$. Together, they constitute the "*strain ellipsoid*". It is defined by two ratios: $a = (\varepsilon_1 + 1) / (\varepsilon_2 + 1)$, and $b = (\varepsilon_2 + 1) / (\varepsilon_3 + 1)$. The Flinn's diagram is a representation of the shape of a deformed object in the a-b space (Figure 1.18). The shape of the strain ellipsoid relative to stresses is defined by: $k = (a - 1) / (b - 1)$. Under an elongation regime, the ellipsoid will display a cigar-like shape with a high associated k value ($k > 1$). Under a flattening regime, the ellipsoid will have a pancake-like shape with an associated low value of k ($k < 1$). Around a value of $k = 1$, the deformation is termed plane and does not produce notable change of shape of the ellipsoid.

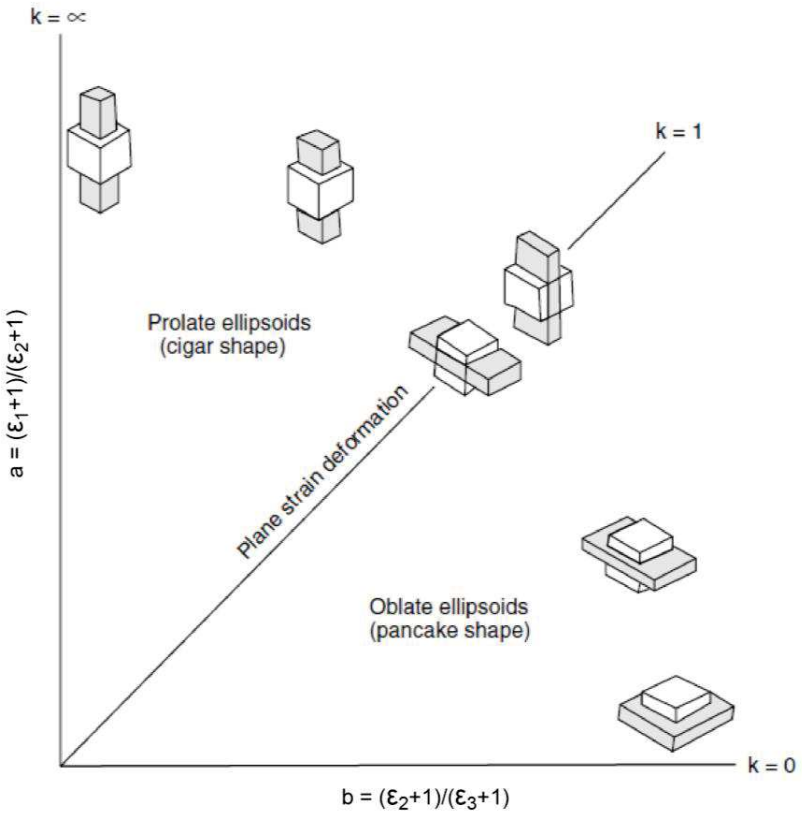

Figure 1.18 *- Flinn's diagram representing the shape of three-dimensional strains (modified after Hobbs et al., 1976).*

3.2. Deformation mechanisms

When external forces are applied to a material, the corresponding stresses and the rate at which they are applied induce different mechanical response of the material, depending on the mineral properties and the conditions under which this occur.

At low stresses, low temperature, or short time under stresses, the material display an "*elastic behavior*". It consists of an instantaneous short displacement of atoms within the material that

return to their original stable position right after the stresses cease, like a branch of a tree that almost hit you by returning abruptly to its original position (Figure 1.19). This type of deformation is recoverable, because it only involves a stretching of atomic bounds, not a breaking (Fossen, 2010). From deformation experiments, it is observed that this recovering can occur linearly or non-linearly.

As the level of stresses increases, the temperature rise, or the time during which the stresses are applied, the fraction of deformation induced is no longer recoverable (Figure 1.19). This occurs when the yield stress is reached and is termed "*plastic deformation*". The loss of elastic behavior comes from the definitive displacement of atoms from their original position in the material. The behavior of a material subjected to plastic deformation is called "*ductile*" when it accumulates permanent strain without rupture. If the rupture strength is attained by the applied stresses the material is pushed to failure. Such a material deforming by fracturing is called "*brittle*".

Plastic deformation is the term used to describe the permanent changes in shape (or size) of a material without rupture through the movement of dislocations, resulting from a continuous stress appliance beyond the elastic yield point (Fossen, 2010).

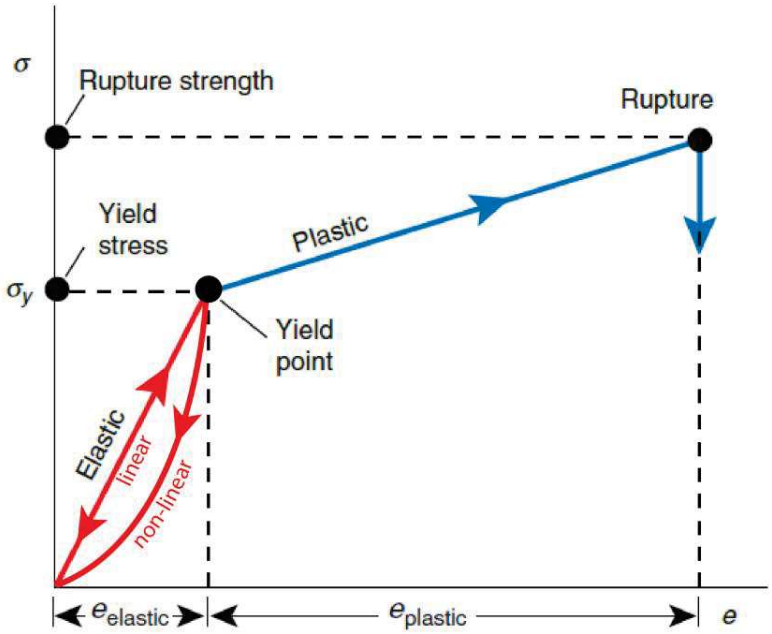

Figure 1.19 *- Stress-strain curve associated to elastic, plastic, and brittle deformation (modified after Fossen, 2010).*

3.2.1. Dislocation creep

Let's first define what a "*grain*" is: a crystallographic domain constituted of atoms arranged according to a unique scheme, with a given orientation. This scheme of organization of atoms is

the "*lattice*". An abrupt change of the lattice orientation or organization defines a grain boundary. In many rock materials it corresponds at least to a 10-15° orientation difference (e.g., Poirier, 1985). Natural crystals are seldom perfect, which materialized in the presence of defects within their lattice. These consist of "*punctual defects*" with the lack of an atom, a "*vacancy*", or the presence of an extra one, an "*interstitial*", and "*linear defects*" called "*dislocations*" (Figure 1.20). These defects that create disorder in crystal lattice will be evacuated from the lattice under a stress regime, generally toward grain boundaries. It can also organize in structures such as subgrain boundaries to release the accumulated strain (see below). Dislocations occur in two forms: "*edge dislocations*" and "*screw dislocations*". An edge dislocations constitutes the segment end of an extra-half plane in the lattice (Figure 1.20b), whereas a screw dislocation exists at the point where a part of the crystal moves of a lattice distance (Figure 1.20c).

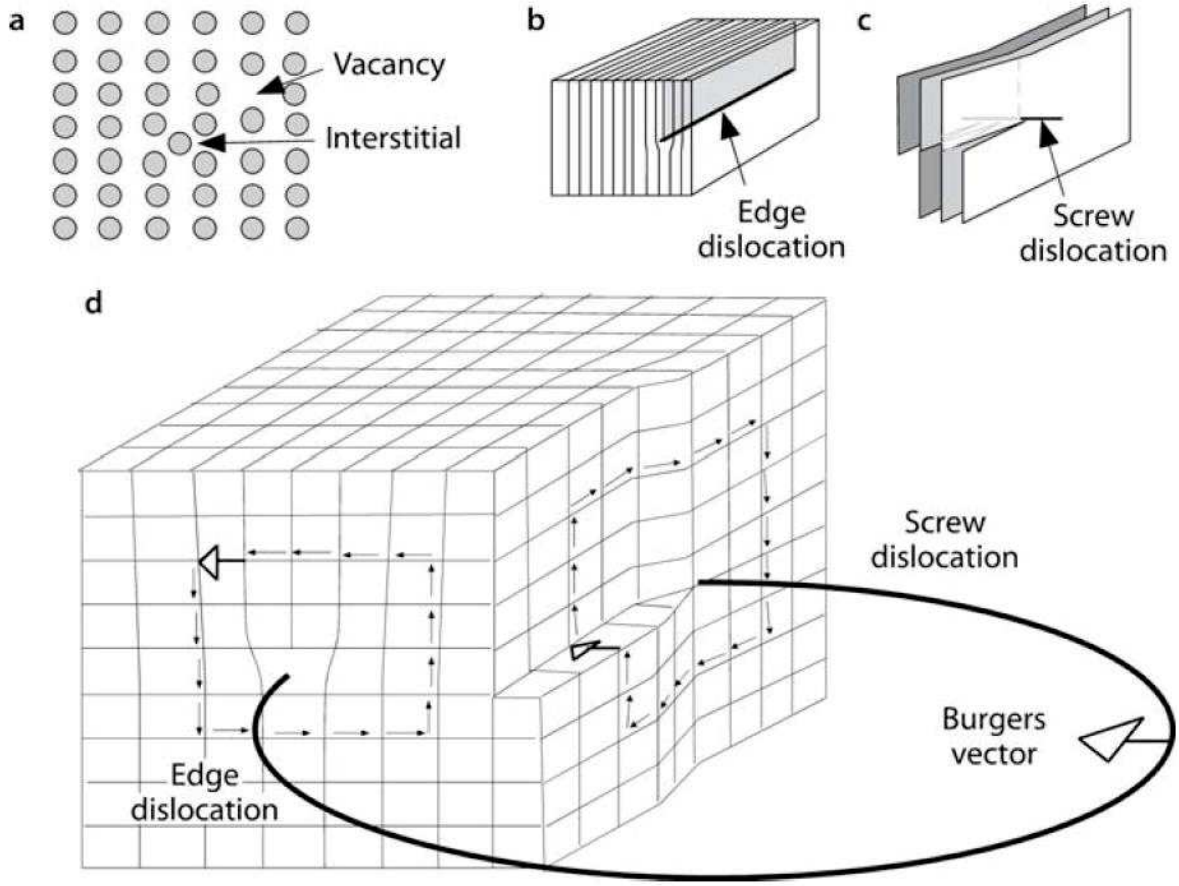

Figure 1.20 *- Defects in crystal lattices (Passchier and Trouw, 2005). (a) Example of a lattice with point defects. (b) Linear defect acting as an edge dislocation, defined by the edge of an extra half-plane in a deformed crystal lattice. (c) Linear defect acting as a screw dislocation defined by a local twisting of the lattice. (d) Edge and screw dislocations forming a loop within a crystal*

lattice. Small closed arrows around dislocations are used to define the Burgers vector orientation (open arrow) which indicates the direction of atom displacement.

Screw dislocations are therefore at a twisted region of the crystal. Also, these two types of dislocations can connect to form a "dislocation loop", which is the line bounding a closed area in which a slip occurred (Figure 1.20d and 1.21a). The vector of slip of the dislocation loop in a crystal necessarily corresponds to a vector of the Bravais lattice and is the "Burgers vector": b. An edge segment of a dislocation can only move into the glide plane defined by the dislocation line and the Burgers vector in a direction normal to the dislocation segment (Figure 1.21d).

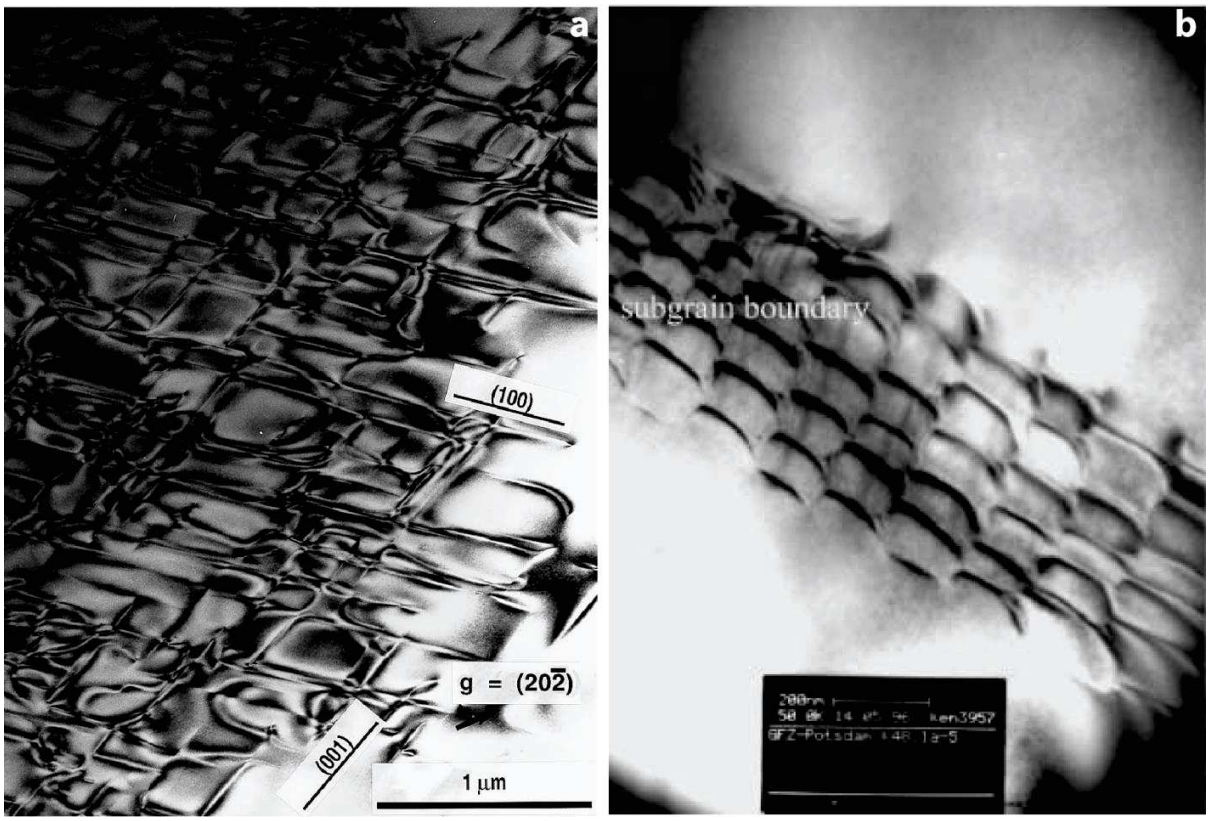

Figure 1.21 *- Transmission Electron Microscopy (TEM) microphotographs of dislocations. (a) Two set of dislocations, parallel to (001) and (100) crystallographic planes, forming numerous rectangular loops in plagioclase (Kruse & Stünitz, 1999). (b) Subgrain boundary indicative of climb in amphibole (Kenkmann & Dresen, 2002).*

Screw dislocations can theoretically move in any atomic plane that contains it in a normal direction to the dislocation segment. When reaching the boundary of the crystal, the dislocation loop is evacuated and leaves an offset of width b (Poirier, 1985). The presence and motion of dislocations distorts the crystal lattice, thus creating internal strain. The stress components of the

stress field created vary as a function of the elastic shear modulus, the length of the Burgers vector b, and the distance to the dislocation. By moving close to another, a dislocation will interact with it (e.g., attraction), and can form "walls of dislocations" by gliding in a set of parallel planes. "Tilt walls" then form by interaction of edge dislocations with similar Burgers vector. A wall composed of screw dislocations will be referred to as a "twist wall".

"*Dislocation glide*" is the term used to describe the glide of a single dislocation (Figure 1.22a). Dislocations can move only in certain crystallographic planes of the lattice with different possible slip directions. The combination of a slip direction (i.e., the Burgers vector) and a slip plane is known as a "*slip system*".

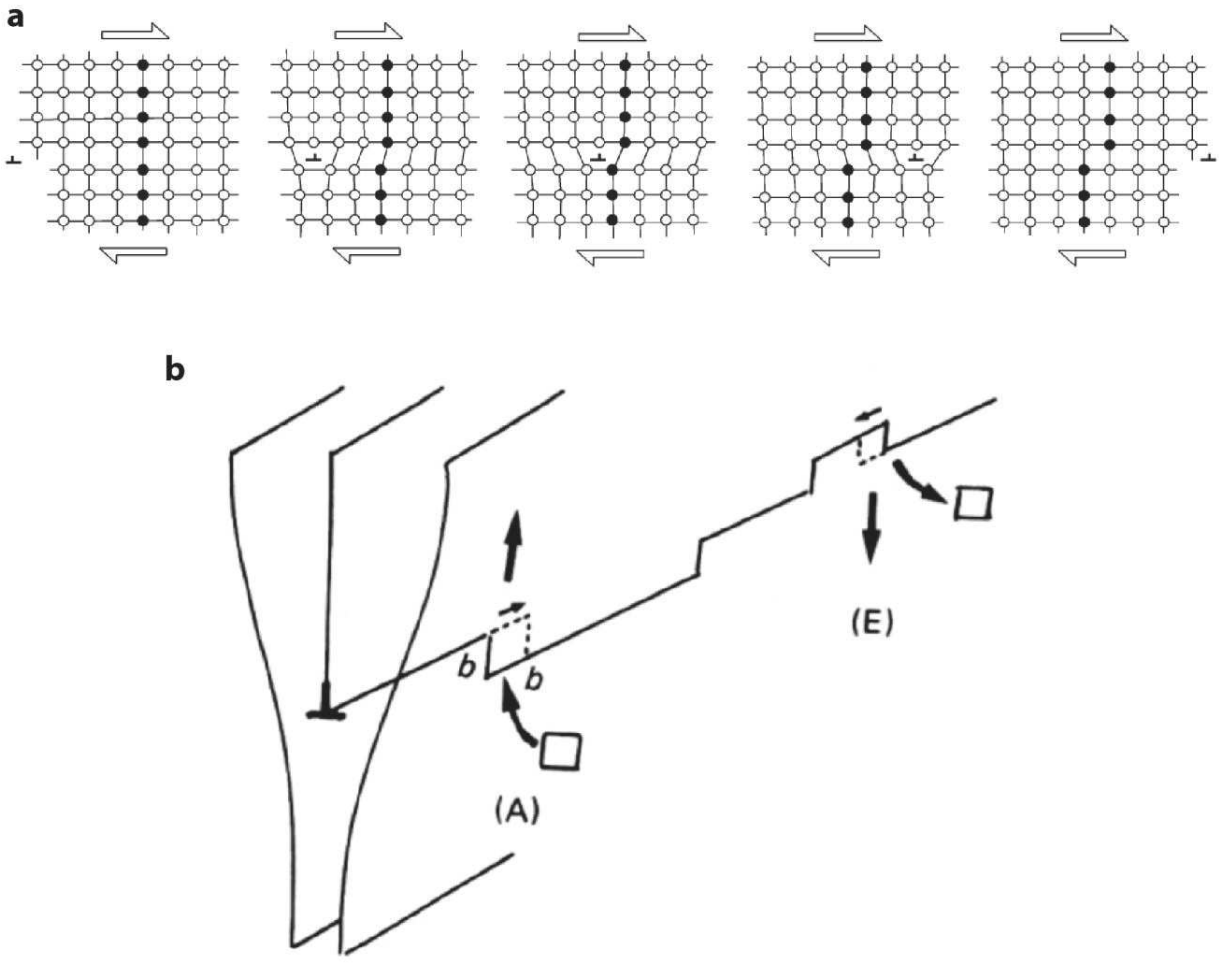

Figure 1.22 *- Displacement of dislocations in a crystal lattice. (a) Glide of an edge dislocation in a sheared crystal lattice. (b) Climb of dislocations, through the displacement of vacancies (open squares), to a plane parallel to the original glide plane to pass an obstacle (modified after Poirier, 1985). Note that the climb operates over a distance equal to b, the length of the Burgers vector, in a vertical direction in this example (straight black arrows).*

The slip systems activated during the deformation of a crystal depends on the magnitude and orientation of the stress field in the grain, which is termed the "*critical resolved shear stress*" of the slip system (i.e., the minimum energy necessary for its activation). The critical resolved shear stress strongly depends on temperature, and to a lesser extent to strain rate, differential stresses, and chemical activity of some components (e.g., water). This results in the activation of different dominant slip systems associated to varying metamorphic and stress conditions (e.g., Passchier & Trouw, 2005). When multiple slip systems operate within a crystal, dislocation can block each other, making it difficult to continue deforming the crystal by a process referred to as "*strain hardening*". To pass the obstacles that block their glide into the crystal, dislocations can "*climb*" to another plane through the migration of vacancies to the dislocation line (Figure 1.22b), and then the ductile deformation of the crystal continues. This process of dislocation glide and climb is known as "*dislocation creep*", and "*crystal-plastic deformation*" corresponds to deformation that occur by dislocation creep.

The production of dislocations during deformation of crystals produces an increase of internal strain energy. This leads to an unstable internal state, which is counterbalanced by mechanisms of dislocation annihilation. The latter continue after the deformation ceases, and the density of dislocations in crystals is reduced through this process called "*recovery*". As a result of recovery, dislocations can group and form a well-organized wall referred to as "*subgrain wall*" or "*subgrain boundary*" (Figure 1.21b and 1.22). The progressive formation of a subgrain boundary results in the misorientation between the two domains across the boundary, forming two "*subgrains*". The misorientation measured at these boundaries (< 10-15°) is lower than at "true" grain boundaries, and so is also referred to as "*low-angle grain boundaries*" in contrast to "*high-angle grain boundaries*". When formed, the subgrain boundary will acquire an orientation depending on the orientation of the slip system of the dislocations accumulated (e.g., Trépied et al., 1980). Then, it is possible to differentiate subgrain boundaries by the orientation of the rotation axis along which they formed. Tilt walls will have a rotation axis parallel to the boundary formed, and twist walls a rotation axis normal to it. Edge dislocations forming a tilt wall all have the same Burgers vector, and screw dislocations forming a twist wall consist of two sets of dislocations with different Burgers vectors. Complex walls, with an oblique rotation axis, can form by the networking of dislocations having two or more different Burgers vector. Once formed, the subgrain boundary can either migrate or evolve into a grain boundary by further migration of dislocations to it (Means & Ree, 1988).

Another type of grain boundaries exists in nature, and is of importance for this work as it is a common feature in plagioclase mineral: "*twin boundaries*". A twin is the boundary between two crystals of similar composition and structure that is defined by a twin law involving a rotation (or a reflection) around a principal lattice direction (or in a plane; Smith & Brown, 1988). Two types of twins are found: "*growth twins*" formed during the growth of the host crystal, and

"*deformation twins*" formed during deformation from the grain boundary with a wedge shape pointing to the core of the grain. During deformation at high-temperatures, similarly as for grain boundaries the twin boundaries can migrate into the grain, are limited to, and be evacuated to the grain boundary ("*twin boundary migration recrystallization*"; Vernon, 1981; Rutter, 1995). Deformation twinning alone can only accommodate a limited amount of strain and is often accompanied by other deformation processes.

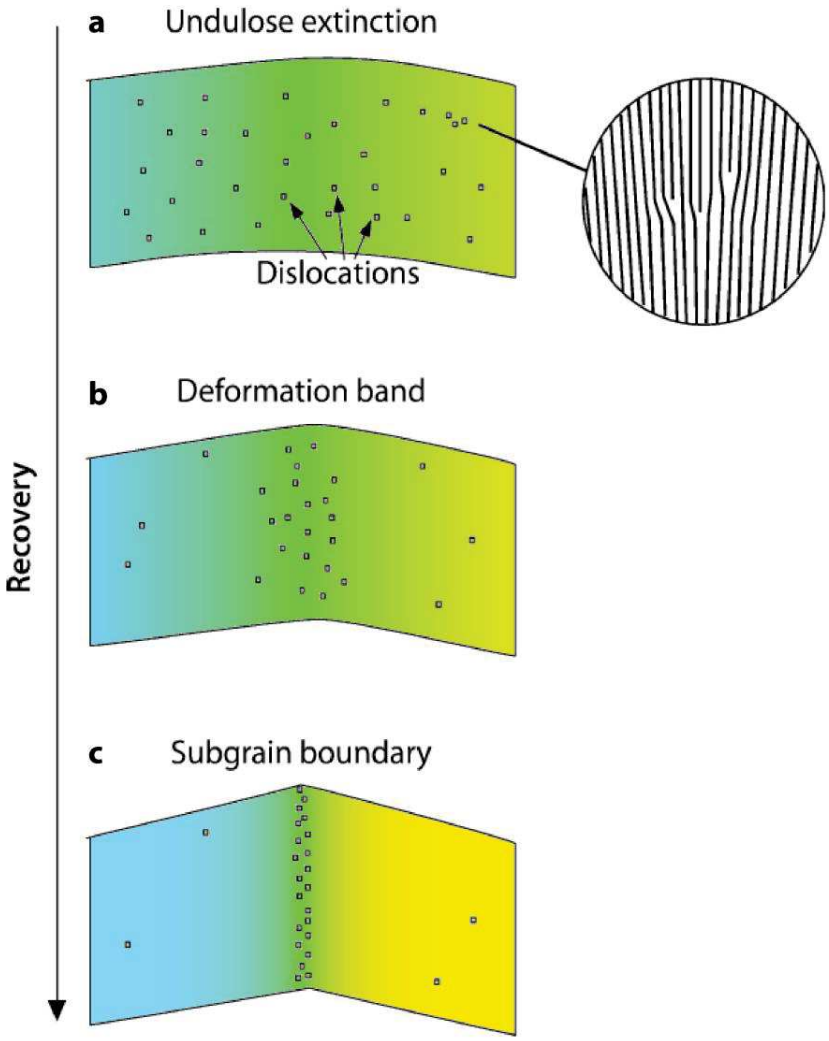

Figure 1.23 *- Edge dislocations forming a subgrain boundary by recovery (modified after Passchier & Trouw, 2005). (a) Dislocations distributed into the crystal produce the observed undulatory extinction by through the lattice torsion. (b) By a mean of internal strain energy reduction dislocations progressively gathered by recovery until (c) forming a subgrain boundary. The accumulation of dislocations to form a subgrain boundary produces a scattering of the grain orientation from one side of the boundary to the other. This change of orientation is represented by the change of color in subgrains in the sketch.*

3.2.2. Recrystallization processes

Under a given stress regime, a crystal can reduce its dislocation density by recovery, or thanks to "*grain boundary mobility*" (Gottstein & Mecking, 1985; Poirier, 1985; Jessell, 1987; Drury & Urai, 1990). One of the main variable that impacts the velocity of the boundary migration is temperature (leading to its increase), and other elements such as the misorientation at the boundary or the presence of impurities will also impact the velocity (Lücke & Stüwe, 1971; Smith et al., 1979; Poirier, 1985). This displacement of grain boundaries can occur during dynamic recrystallization or after a deformation event by static recrystallization.

Dynamic recrystallization: Bulging

In the case of a "*strain-induced boundary migration*" (SIBM), a grain with a high dislocation density with respect to its neighbors will be consumed by the latter through the absorption of its dislocations at grain boundaries (Bailey & Hirsch, 1962; Pond & Smith, 1977). The difference in internal free energy between deformed grains, associated to the dislocation density, drives the boundary migration. Then, to decrease the internal free energy of a grain, dislocation-free nuclei can emerge at its grain boundary (Figure 1.24; Bailey & Hirsch, 1962). This nucleation, referred to as *bulging*", is local as this process mainly occurs at relatively low temperatures, i.e., when the grain boundary mobility is limited. Also known as "*slow grain boundary migration*" or "*low-temperature grain boundary migration*", bulging recrystallization (BLG) corresponds to the Regime 1 evidenced in quartz aggregates by Hirth & Tullis (1992). During BLG, the bulge generally initiate at a former grain boundary or at triple junctions, and the old grain cores preserve high densities of dislocations (Urai et al., 1986; Hirth & Tullis, 1992).

Dynamic recrystallization: Subgrain rotation

The mechanism of "*subgrain rotation recrystallization*" (SGR; Regime 2 of Hirth & Tullis, 1992) results from the continuous accumulation of dislocations at subgrain boundaries, when the displacement between lattice planes is easy. It is also referred to as "*rotation recrystallization*" as documented in calcite grains by Guillopé & Poirier (1979). Achieved by dislocation glide and climb, the progressive gathering of dislocations at subgrain boundaries produces an increase of the misorientation on each side of the boundary and finally detach from the parent grain. A typical "*core-and-mantle*" structure develops similarly as when BLG intensely occurred, but the average grain size in the mantle is higher than for BLG (Figure 1.24). Also, the size and density of free dislocations of subgrains and new grains constituting the recrystallized mantle are similar (Hirth & Tullis, 1992). Subgrain rotation recrystallization alone, is not a process resulting in significant chemical changes between the parent and the recrystallized grains at low temperatures. As ionic exchanges are restricted to diffusion in the grain interior (Nabarro-Herring creep, see below), this is dependent on diffusion rate which is relatively slow at low temperatures (Yund, 1986; Yund et al., 1989; Yund & Tullis, 1991; Stünitz, 1998).

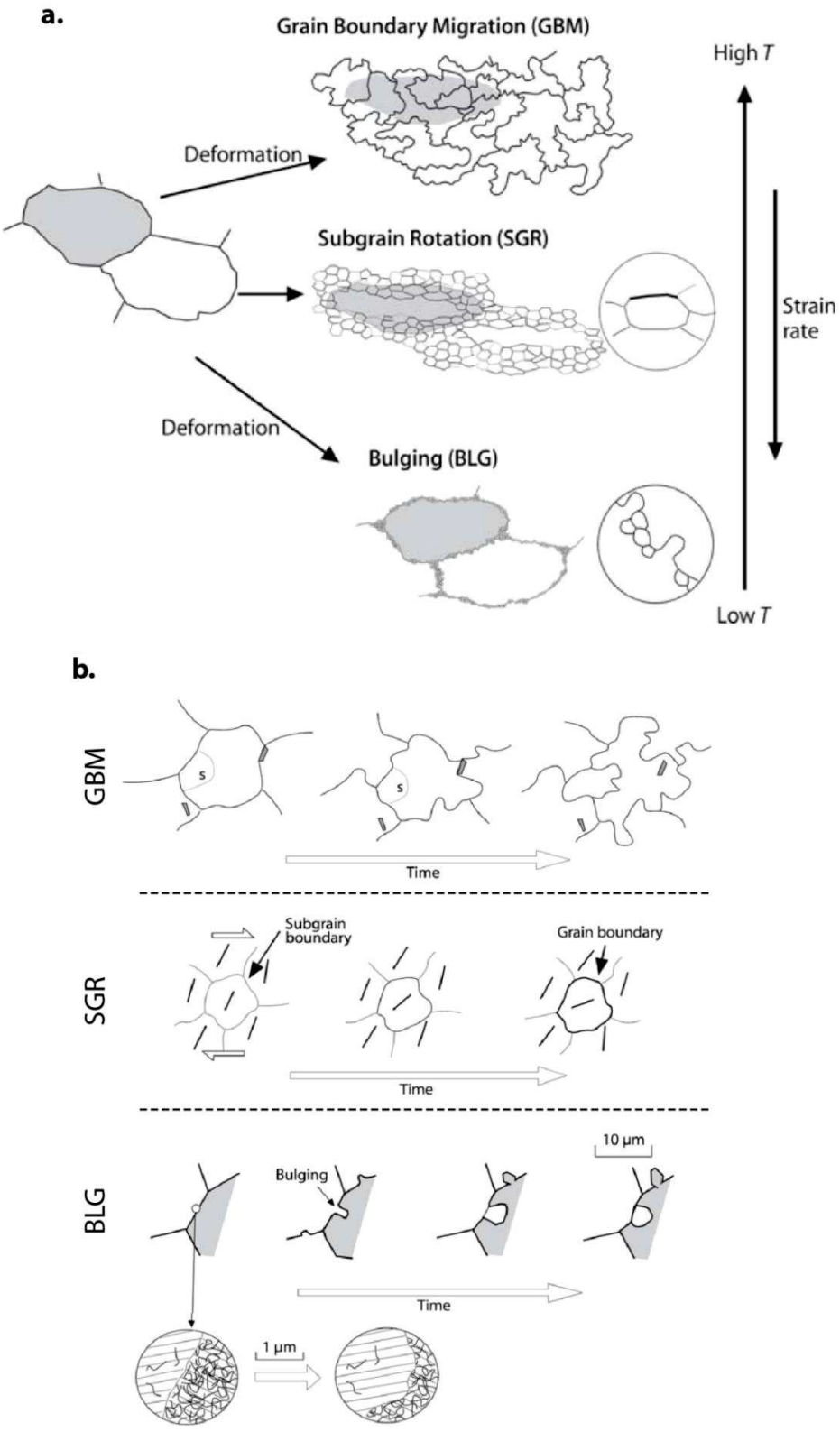
a.
Grain Boundary Migration (GBM)
High T
Deformation
Subgrain Rotation (SGR)
Strain rate
Deformation
Bulging (BLG)
Low T
b.
GBM
S
S
Time
SGR
Subgrain boundary
Grain boundary
Time
BLG
10 µm
Bulging
Time
1 µm

Figure 1.24

Figure 1.24 *- Dynamic recrystallization processes at aggregate and grain scales (modified after Passchier & Trouw, 2005). (a) Aggregate scale dynamic recrystallization processes. The grey shading represents the mater contained in the former porphyroclast. Note the resulting core-and-mantle structure of the aggregates formed by SGR and BLG. (b) Grain scale detail of the recrystallization showing the formation of subgrain boundaries (s) and new grain boundaries. Bars within subgrains formed by SGR represent their orientation. The two details associated to BLG show the migration of the grain boundary from a grain with a low dislocation density (left) to a neighbor with a high dislocation density (right).*

Dynamic recrystallization: Grain boundary migration

Owing to their enhanced mobility at high temperatures, grain boundaries in aggregates subjected to stresses can entirely sweep into a crystal to remove dislocations and subgrains. Contrasting to BLG, it corresponds to a "*fast grain boundary migration*" or "*high-temperature grain boundary migration*" (GBM; Guillopé & Poirier, 1979; Urai et al., 1986; Stipp et al., 2002). This process is the third (Regime 3) described by Hirth & Tullis (1992), also termed "*migration recrystallization*" by Guillopé & Poirier (1979). It is generally achieved in two steps, an initial SGR to create new smaller grains, followed by a rapid migration of the newly formed grain boundaries (Figure 1.24). This result in a highly lobate to amoeboid shape of the boundaries, a growth of grains formed with respect to the subgrain size, and internal strains within grains are drastically reduced. In polyphased aggregates, structures associated to the grain boundary migration can be observed such as pinning, dragging, window, and left-over-grains (Figure 1.25; Jessell, 1987). The multiple migrations of the grain boundary through the grain permit ionic exchanges between the boundary and the grain core in addition to diffusion, enabling chemical re-equilibration during recrystallization (Yund et al., 1989; Yund & Tullis, 1991; Stünitz, 1998).

Dynamic recrystallization: Grain boundary area reduction

Another process of grain boundary migration occurs during deformation. It results in the straightening of grain boundaries, generally made serrated or lobate by the operation of other recrystallization processes, together with a growth of grains. The reason for this is that grain boundaries, made up of arrays of dislocations, can be regarded as long planar defects with a significant internal free energy. Thus, the minimization of the boundary length of a grain will considerably reduce its total internal free energy (e.g., Vernon, 1976; Humphreys, 1997; Evans et al., 2001; Kruhl, 2001). This evolution to simpler boundary shapes and grain growth is the "*grain boundary area reduction*" (GBAR). Although this process is active during the deformation in parallel to the others aforementioned, it will have a greater impact on microstructures acting statically after the deformation ceased under high temperatures (Bons & Urai, 1992). If GBAR is achieved long enough at high temperatures, it will transform the microstructure to a polygonal

fabric with a majority of grains with boundaries straightened and aggregates with triple boundary junctions at ~120°.

Static recrystallization

The modification of grain structures in terms of orientation, size, and shape at high-temperatures following an episode of deformation is known as "*static recrystallization*". It combines the different processes of recovery, GBAR, and recrystallization, and is achieved in response to the free energy disequilibrium as a result of deformation.

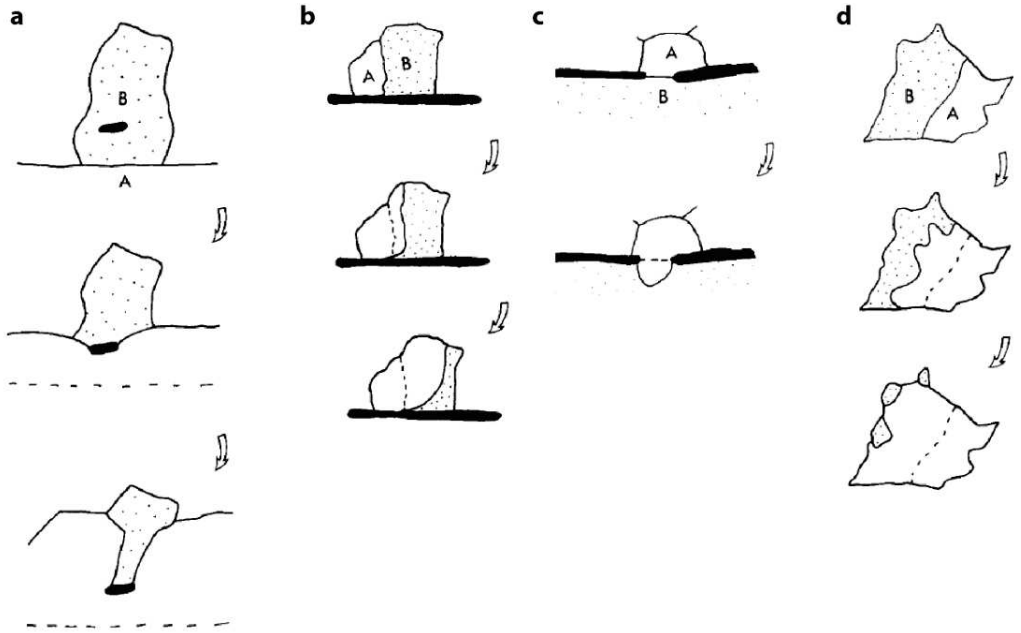

Figure 1.25 *- Formation of typical migration-associated microstructures during GBM (after Jessell, 1987). (a) Pinning microstructure formation by the migration of the boundary of grain A toward grain B, partially blocked by the presence of an obstacle in grain A (black element; e.g., grain of another phase). (b) Dragging microstructure formation through the migration of the contact boundary between grains A and B along another grain of a different phase. (c) Window microstructure formation arising from the limited boundary contact between grains A and B. (d) Migration of the boundary of grain A consuming grain B, forming left-over-grains.*

3.2.3. Diffusion creep and grain boundary sliding

Similarly to dislocation creep, "*diffusion creep*" (or "*grain-scale diffusive mass transfer*") consists of a migration within crystal lattices, but the migration concerns vacancies instead of dislocations (Knipe, 1989; Wheeler, 1992). The mass transfer occurs both within crystals by "*volume diffusion*" known as "*Nabarro-Herring creep*" and by "*grain boundary diffusion*" known as "*Coble creep*". The volume diffusion in crystals (Nabarro-Herring creep) consists of

the migration of vacancies present in the lattice, through ionic exchanges with neighboring sites, toward areas of high stress, which progressively produces a change of grains shape (Figure 1.26). This migration requires an important amount of energy, thus its rate depends on temperature. Indeed, at high temperatures the lattice vibration is higher and increases the diffusion rate of vacancies. During Coble creep, grains shape is also changed but the quantity of energy required for diffusion is lower than in volume diffusion, as vacancies are more mobile at grain boundaries. During their change of shape, grains may slide past each other. This is known as "*grain boundary sliding*" (GBS) and especially occurs in very fine-grained aggregates as the diffusion will occur over a short distance and permit this process to compete with others such as dislocation creep (e.g., Etheridge & Wilkie, 1979; Behrmann, 1985; Lloyd et al., 1992). It is also commonly known as "*granular flow*" (e.g., Boullier & Gueguen, 1975; Stünitz & Fitz Gerald, 1993; Fliervoet & White, 1995; Paterson, 1995; Kruse & Stünitz, 1999).

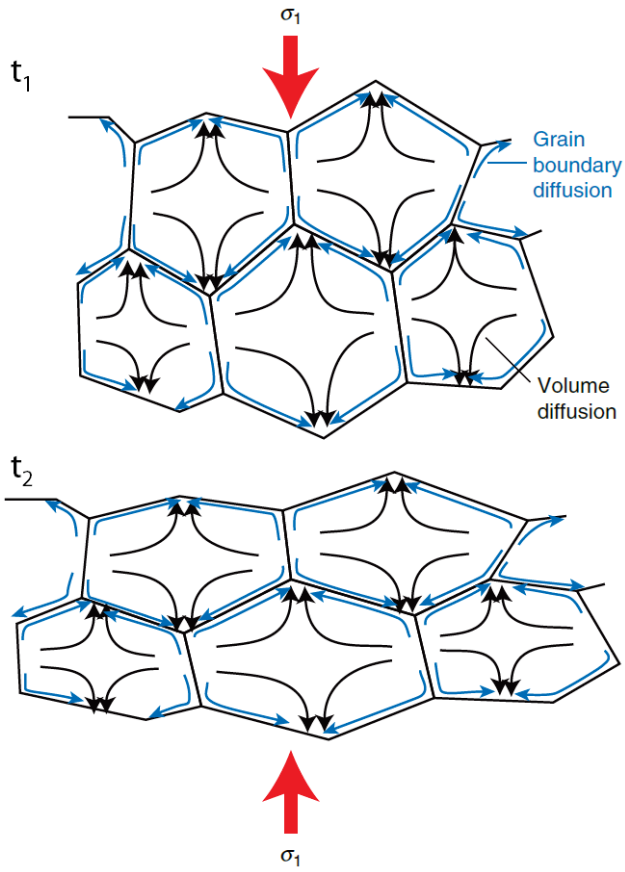

Figure 1.26 *- Diffusion creep process in grains (modified after Fossen, 2010). The transfer of vacancies operates both within grains (Nabarro-Herring creep, black arrows) and at grain boundaries (Cobble creep, blue arrows) toward areas of high stress.*

Thanks to solid state diffusion, a local increase in crystal-plastic deformation, or solution-precipitation by the circulation of a grain boundary fluid, no voids are created during this sliding. As a result of granular flow, neither shape-preferred orientation (SPO), nor crystallographic preferred orientations (CPO) are observed; instead it is inferred to progressively destroy CPO. The grain size is an important parameter to determine whether an aggregate will deform through dislocation creep or through granular flow, so granular flow enter the category of "*grain size-sensitive*" processes.

In addition to its initiation under stresses, grain boundary migration can be induced by chemical potentials which is termed "*chemically-induced grain boundary migration*" (CIGM) or "*diffusion-induced grain boundary migration*" (DIGM; Hillert & Pudry, 1978; Balluffi & Cahn, 1981; Hay & Evans, 1987). In solid solutions, CIGM is likely to occur together with recrystallization in response to equilibration with other phase(s) in presence. In this case, the combination of potentials arising from different dislocation densities and compositional difference provides an important energy for grain boundaries to migrate. Then, the resulting microstructure will be dominated by GBM. This combined effect of strain and chemical potential during recrystallization may be very effective in producing fine grains and to favor the onset of grainsize-sensitive processes like GBS (e.g., Stünitz, 1998). During metamorphism, the circulation of fluids in the deforming rock, in particular at grain boundaries can generate chemical potentials and induce diffusion creep (e.g., White et al., 2008).

3.3. The deformation of plagioclase at high temperatures

Plagioclase is the most common mineral phase within the Earth's crust, representing up to 40% of crustal minerals (Ronov & Yaroshevsky, 1969). Its pressure (P) – temperature (T) stability field encompasses highly variable conditions, which implies that it is subjected to a large spectrum of deformation mechanisms (Figure 1.27). Activities, and transitions between these mechanisms are controlled by temperature and strain rate, but also by fluids circulation and confining pressure (e.g., Debat et al., 1978; Simpson, 1985; Tullis & Yund, 1987; Fitz Gerald & Stünitz, 1993; Hirth & Tullis, 1994). For T < 500°C, plagioclase acts as a rigid mineral and deforms mainly by fracturing. Kink bands, tapered twins, and limited nucleation in small fractures can also be found in fractured grains. The transition between dominant fracturing to dislocation-accommodated deformation occurs at ~450-550°C in naturally deformed rocks (e.g., Tullis & Yund, 1977; Dell'Angelo & Tullis, 1996; Oliot et al., 2010). The temperature range at which this transition arises also depends on the texture, and on the constituting phases of the deforming rock (Tullis & Yund, 1977; Kronenberg & Shelton, 1980; Simpson, 1985; Fitz Gerald & Stünitz, 1993; Rosenberg & Stünitz, 2003; Ji, 2004). Dynamic recrystallization and grain boundary migration ("slow" and "fast") become important processes at T > 500-600°C because of the enhancement of grain boundary mobility, and of subgrain boundary formation at high

temperatures. Conversely, at lower temperatures diffusion creep could easily prevail on dislocation creep because of chemical differences accompanying recrystallization (e.g., Rosenberg & Stünitz, 2003). Although dislocation creep does not occur at $T < 500$°C, a process of dislocation generation by fracturing (easy in plagioclase because of twins) is documented and certainly encourages the transition from brittle to plastic regime (e.g., Tullis & Yund, 1985; McLaren & Pryer, 2001; Stünitz et al., 2003). Fracturing at moderate to high temperatures (600-750°C) and high-stress conditions has also been reported as an important process of grain size reduction in plagioclase grains, leading to narrow shear zone formation favoring grain-size-sensitive creep in the small-grained aggregates formed (Okudaira et al., 2015, 2017).

At upper-greenschist to amphibolite facies conditions ($T > 450$°C) the mobility of dislocations in plagioclase becomes easier and promotes their glide toward grain boundaries (Fitz Gerald & Stünitz, 1993). If dislocation mobility is low and local, the nucleation of new grains occurs at grain boundaries by bulging recrystallization (BLG), also known as "slow grain boundary migration", by a process of strain-induced boundary migration (SIGM; Bailey & Hirsch, 1962). Bulges can become (small) new grains by the formation of a subgrain boundary on their back, evolving into a grain boundary (e.g., Bell & Johnson, 1989; Oliot et al., 2014). BLG is mainly observed in plagioclase deformed between 500-550°C and ~700°C (Figure 1.27). With increasing mobility dislocations can glide faster and farther, forming subgrains (and then grains) of slightly different crystallographic orientations, or inducing large-scale fast grain boundary migration. The first mechanism, subgrain rotation recrystallization (SGR), occurs in deformed plagioclase from ~400°C to > 1000°C, especially in the range 500-750°C (Figure 1.27). Grain boundary migration recrystallization (GBM) is made possible by the high mobility of grain boundaries (Poirier & Guillopé, 1979). It is achieved by a rotation step (SGR) that is rapidly followed by the fast migration of the newly formed grain boundary, leading to large recrystallized grain sizes. GBM is naturally active from ~500°C to ~1000°C and is mostly described at 600-750°C (Figure 1.27). Note that when SGR and GBM mechanisms are active together, textures are characterized by lobate grain boundaries and small differences in overall grain sizes. Additionally, dislocation creep mechanisms are known to produce CPO, unlike diffusion creep mechanisms (Tullis & Yund, 1987; Wenk & Christie, 1991). In solid solution minerals like plagioclase, slow and fast boundary migration processes can be driven by chemical potentials occurring between neighboring grains (e.g., parent-recrystallized grains). This process is called chemically-induced grain boundary migration (CIGM; Hay & Evans, 1987) and arises from a decrease of the P-T conditions. In the dislocation creep regime, the recrystallization of grains by a process of GBM can generate compositional changes in the recrystallized grains. It arises from the migration of the high angle grain boundary within a former strained grain, which permits ionic exchanges (Na/Si and Ca/Al) with the surface of neighboring grains (e.g., Yund & Tullis, 1991). Note that SIGM and CIGM can act simultaneously during grain boundary migration (*s.l.*). In contrast,

recrystallization by SGR is not supposed to produce chemical potentials between old and new grains, as the exchanges are principally restricted to volume diffusion, usually too slow to be significant (e.g., Yund & Tullis, 1991; Stünitz, 1998).

Slip systems activities during intracrystalline deformation are documented from ~500-600°C to higher temperatures up to the solidus (Figure 1.27). Numerous slip systems have been specified after experimental deformation since the seventies (e.g., Marshall & McLaren, 1977; Scandale et al., 1983; Olsen & Kohlstedt, 1984, 1985; Montardi & Mainprice, 1987), and observed in TEM. These studies raised the general idea that slip by dislocation motion is one of the main deformation mechanisms in feldspars. Furthermore, cross slip is commonly observed and the interaction between several operating slip systems is considered as an important mechanism for dislocation multiplication (e.g., Montardi & Mainprice, 1987). An exhaustive list of slip systems documented in plagioclase to date is presented in supporting information Table S2 from Chapter III.

Based on TEM studies and CPO pattern interpretations, it appears that the main active slip systems are characterized by a slip plane that corresponds to a twinning plane, namely (010) or (001). Apart from [001](010) that is found active from ~500°C and over the largest range of temperatures, most slip systems become active at ~600°C and are well documented until 900°C (Figure 1.27).

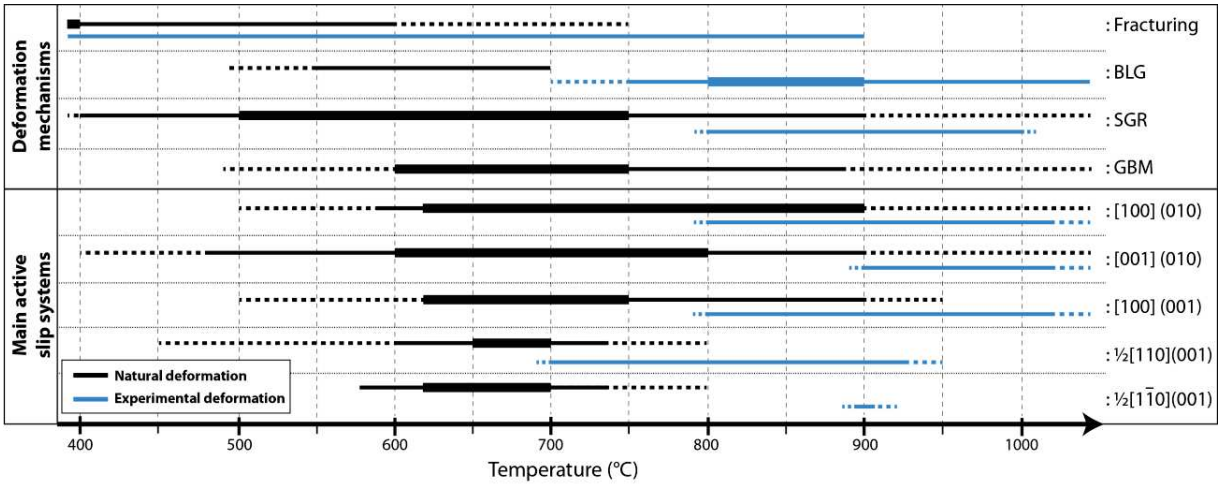

Figure 1.27 *- Plagioclase deformation mechanisms and most reported slip systems activities, plotted as a function of the temperature, for natural (black) and experimental deformation (blue). BLG: bulging recrystallization; SGR: subgrain rotation recrystallization; GBM: fast grain boundary migration recrystallization (see references in the text). GBM is not described in experimentally deformed plagioclase. The increasing importance of a deformation mechanism (or a slip system activity) is represented by the increasing thickness of the line. The full list of used references is given in supporting information Table S2 from Chapter III.*

[100](010) is one of the dominant active slip systems at high temperatures (> 800°C) while the [100](001) slip system, found active in the same range of temperatures, is less documented at high temperatures. When both [001](010) and [100](010) slip systems are observed simultaneously active, a switch of prevalence from the [001] to the [100] direction seems to occur at ~800°C. Finally, the ⟨100⟩(001) family of slip systems has been observed in a restricted range of temperatures, principally from ~600°C to 750°C. In anorthosites and gabbros, the preferred orientation of (010) is commonly interpreted as defining a foliation plane formed as a result of magmatic flow that preferentially aligns tabular plagioclase crystals (e.g., Benn & Allard, 1989; Satsukawa et al., 2013; Ji et al., 2014).

REFERENCES

Allard, M., Ildefonse, B., Oliot, É., & Barou, F. (2021). Plastic deformation of plagioclase in oceanic gabbro accreted at a slow-spreading ridge (Hole U1473A, Atlantis Bank, Southwest Indian Ridge). Journal of Geophysical Research: Solid Earth, 126, e2021JB021964. https://doi.org/10.1029/2021JB021964

Abbate, E., Bortolotti, V., Principi, G., 1980. Apennine ophiolites: a peculiar oceanic crust. In: Rocci, G. (Ed.), Special Issue on Tethyan Ophiolites, Western Area. 59–96.

Angiboust, S., Glodny, J., Oncken, O., Chopin, C., 2014. In search of transient subduction interfaces in the Dent Blanche–Sesia Tectonic System (W. Alps). Lithos 205, 298–321. https://doi.org/10.1016/j.lithos.2014.07.001

Bailey, J.E., Hirsch, P.B., 1962. The recrystallization process in some polycrystalline metals. Proceedings of the Royal Society of London. Series A. Mathematical and Physical Sciences 267, 11–30. https://doi.org/10.1098/rspa.1962.0080

Baines, A.G., Cheadle, M.J., Dick, H.J.B., Hosford Scheirer, A., John, B.E., Kusznir, N.J., Matsumoto, T., 2003. Mechanism for generating the anomalous uplift of oceanic core complexes: Atlantis Bank, southwest Indian Ridge. Geology 31, 1105. https://doi.org/10.1130/G19829.1

Baines, A.G., Cheadle, M.J., John, B.E., Schwartz, J.J., 2008. The rate of oceanic detachment faulting at Atlantis Bank, SW Indian Ridge. Earth and Planetary Science Letters 273, 105–114. https://doi.org/10.1016/j.epsl.2008.06.013

Balluffi, R.W., Cahn, J.W., 1981. Mechanism for diffusion induced grain boundary migration. Acta Metallurgica 29, 493–500. https://doi.org/10.1016/0001-6160(81)90073-0

Barrett, T.J., Spooner, E.T.C., 1977. Ophiolitic breccias associated with allochthonous oceanic crustal rocks in the East Ligurian Apennines, Italy - a comparison with observations from rifted oceanic ridges. Earth and Planetary Science Letters 35, 79–91. https://doi.org/10.1016/0012-821X(77)90031-0

Baumgartner, R.J., Zaccarini, F., Garuti, G., Thalhammer, O.A.R., 2013. Mineralogical and geochemical investigation of layered chromitites from the Bracco–Gabbro complex, Ligurian ophiolite, Italy. Contributions to Mineralogy and Petrology 165, 477–493. https://doi.org/10.1007/s00410-012-0818-5

Beccaluva, L., Macciotta, G., Piccardo, G.B., Zeda, O., 1984. Petrology of lherzolitic rocks from the Northern Apennine ophiolites. Lithos 17, 299–316. https://doi.org/10.1016/0024-4937(84)90027-6

Bédard, J.H., 1993. Oceanic crust as a reactive filter: Synkinematic intrusion, hybridization, and assimilation in an ophiolitic magma chamber, western Newfoundland. Geology 21, 77. https://doi.org/10.1130/0091-7613(1993)021<0077:OCAARF>2.3.CO;2

Bédard, J.H., 1991. Cumulate Recycling and Crustal Evolution in the Bay of Islands Ophiolite. The Journal of Geology 99, 225–249. https://doi.org/10.1086/629486

Bédard, J.H., Sparks, R.S.J., Renner, R., Cheadle, M.J., Hallworth, M.A., 1988. Peridotite sills and metasomatic gabbros in the Eastern Layered Series of the Rhum complex. Journal of the Geological Society 145, 207–224. https://doi.org/10.1144/gsjgs.145.2.0207

Behrmann, J.H., 1985. Crystal plasticity and superplasticity in quartzite; A natural example. Tectonophysics 115, 101–129. https://doi.org/10.1016/0040-1951(85)90102-7

Bell, T.H., Johnson, S.E., 1989. The role of deformation partitioning in the deformation and recrystallization of plagioclase and K-feldspar in the Woodroffe Thrust mylonite zone, central Australia. Journal of Metamorphic Geology 7, 151–168. https://doi.org/10.1111/j.1525-1314.1989.tb00582.x

Benn, K., Allard, B., 1989. Preferred Mineral Orientations Related to Magmatic Flow in Ophiolite Layered Gabbros. Journal of Petrology 30, 925–946. https://doi.org/10.1093/petrology/30.4.925

Berann, H.C., Heezen, B.C., Tharp, M., 1977. Manuscript painting of Heezen-Thrap "World ocean floor" map by Berann.

Bickert, M., Lavier, L., Cannat, M., 2020. How do detachment faults form at ultraslow mid-ocean ridges in a thick axial lithosphere? Earth and Planetary Science Letters 533, 116048. https://doi.org/10.1016/j.epsl.2019.116048

Bird, P., 2003. An updated digital model of plate boundaries: Updated model of plate boundaries. Geochemistry, Geophysics, Geosystems 4. https://doi.org/10.1029/2001GC000252

Bons, P.D., Urai, J.L., 1992. Syndeformational grain growth: microstructures and kinetics. Journal of Structural Geology 14, 1101–1109. https://doi.org/10.1016/0191-8141(92)90038-X

Bortolotti, V., Principi, G., Treves, B., 2001. Ophiolites, Ligurides and the tectonic evolution from spreading to convergence of a Mesozoic Western Tethys segment. In: Vai, G.B., Martini, I.P. (Eds.), Anatomy of an Orogen: The Apennines and Adjacent Mediterranean

Basins. Springer Netherlands, Dordrecht, 151–164. https://doi.org/10.1007/978-94-015-9829-3_11

Boudier, F., Bouchez, J.L., Nicolas, A., Cannat, M., Ceuleneer, G., Misseri, M., Montigny, R., 1985. Kinematics of oceanic thrusting in the Oman ophiolite: model of plate convergence. Earth and Planetary Science Letters 75, 215–222. https://doi.org/10.1016/0012-821X(85)90103-7

Boudier, F., Nicolas, A., Ildefonse, B., 1996. Magma chambers in the Oman ophiolite: fed from the top and the bottom. Earth and Planetary Science Letters 144, 239–250. https://doi.org/10.1016/0012-821X(96)00167-7

Boulanger, M., France, L., Deans, J.R.L., Ferrando, C., Lissenberg, C.J., von der Handt, A., 2020. Magma Reservoir Formation and Evolution at a Slow-Spreading Center (Atlantis Bank, Southwest Indian Ridge). Frontiers in Earth Science 8, 554598. https://doi.org/10.3389/feart.2020.554598

Boulanger, M., France, L., Ferrando, C., Ildefonse, B., Ghosh, B., Sanfilippo, A., Liu, C., Morishita, T., Koepke, J., Bruguier, O., 2021. Magma-Mush Interactions in the Lower Oceanic crust: Insights from Atlantis Bank Layered Series (Southwest Indian Ridge). Journal of Geophysical Research: Solid Earth 72. https://doi.org/10.1029/2021JB022331

Boullier, A.M., Gueguen, Y., 1975. SP-Mylonites: Origin of some mylonites by superplastic flow. Contributions to Mineralogy and Petrology 50, 93–104. https://doi.org/10.1007/BF00373329

Bown, J.W., White, R.S., 1994. Variation with spreading rate of oceanic crustal thickness and geochemistry. Earth and Planetary Science Letters 121, 435–449. https://doi.org/10.1016/0012-821X(94)90082-5

Brown, J.R., Karson, J.A., 1988. Variations in axial processes on the Mid-Atlantic Ridge: The median valley of the MARK area. Marine Geophysical Researches 10, 109–138. https://doi.org/10.1007/BF02424663

Buck, W.R., Lavier, L.L., Poliakov, A.N.B., 2005. Modes of faulting at mid-ocean ridges. Nature 434, 719–723. https://doi.org/10.1038/nature03358

Bullard, E., Everett, J.E., Gilbert Smith, A., 1965. The fit of the continents around the Atlantic. Philosophical Transactions of the Royal Society of London. Series A, Mathematical and Physical Sciences 258, 41–51. https://doi.org/10.1098/rsta.1965.0020

Cann, J.R., Blackman, D.K., Smith, D.K., McAllister, E., Janssen, B., Mello, S., Avgerinos, E., Pascoe, A.R., Escartín, J., 1997. Corrugated slip surfaces formed at ridge–transform intersections on the Mid-Atlantic Ridge. Nature 385, 329–332. https://doi.org/10.1038/385329a0

Cannat, M., 1993. Emplacement of mantle rocks in the seafloor at mid-ocean ridges. Journal of Geophysical Research: Solid Earth 98, 4163–4172. https://doi.org/10.1029/92JB02221

Cannat, M., Mevel, C., Maia, M., Deplus, C., Durand, C., Gente, P., Belarouchi, A., Dubuisson, G., Humler, E., Reynolds, J., 1995. Thin crust, ultramafic exposures, and rugged faulting patterns at the Mid-Atlantic Ridge (22° −24°N). Geology 23, 49–52. https://doi.org/10.1130/0091-7613(1995)023<0049:TCUEAR>2.3.CO;2

Cannat, M., Rommevaux-Jestin, C., Sauter, D., Deplus, C., Mendel, V., 1999. Formation of the axial relief at the very slow spreading Southwest Indian Ridge (49° to 69°E). Journal of Geophysical Research: Solid Earth 104, 22825–22843. https://doi.org/10.1029/1999JB900195

Cannat, M., Sauter, D., Bezos, A., Meyzen, C., Humler, E., Le Rigoleur, M., 2008. Spreading rate, spreading obliquity, and melt supply at the ultraslow spreading Southwest Indian Ridge. Geochemistry, Geophysics, Geosystems 9, n/a-n/a. https://doi.org/10.1029/2007GC001676

Cannat, M., Sauter, D., Lavier, L., Bickert, M., Momoh, E., Leroy, S., 2019. On spreading modes and magma supply at slow and ultraslow mid-ocean ridges. Earth and Planetary Science Letters 519, 223–233. https://doi.org/10.1016/j.epsl.2019.05.012

Cannat, M., Sauter, D., Ruellan, E., Okino, K., Escartin, J., Combier, V., Baala, M., 2006. Modes of seafloor generation at a melt-poor ultraslow-spreading ridge. Geology 34, 605–608. https://doi.org/10.1130/G22486.1

Cochran, J.R., 1991. Systematic variation of axial morphology along the Southeast Indian Ridge. Eos, Transactions American Geophysical Union 72, 260.

Cortesogno, L., Galbiati, B., Principi, G., 1987. Note alla '"Carta geologica delle ofioliti del Bracco"' e ricostruzione della paleogeografia Giurassico, Cretacica. Edizioni ETS.

Debat, P., Soula, J.-C., Kubin, L., Vidal, J.-L., 1978. Optical studies of natural deformation microstructures in feldspars (gneiss and pegrnatites from Occitania, southern France). Lithos 11, 133–145.

Decandia, F.A., Elter, P., 1972. La" zona" ofiolitifera del Bracco nel settore compreso fra Levanto e la Val Gravena (Apennino ligure). Società Geologica Italiana Bulletin 11, 37–64.

Decrausaz, T., Müntener, O., Manzotti, P., Lafay, R., Spandler, C., 2021. Fossil oceanic core complexes in the Alps. New field, geochemical and isotopic constraints from the Tethyan Aiguilles Rouges Ophiolite (Val d'Hérens, Western Alps, Switzerland). Swiss Journal of Geosciences 114, 3. https://doi.org/10.1186/s00015-020-00380-4

Dell'Angelo, L.N., Tullis, J., 1996. Textural and mechanical evolution with progressive strain in experimentally deformed aplite. Tectonophysics 256, 57–82. https://doi.org/10.1016/0040-1951(95)00166-2

DeMets, C., Gordon, R.G., Argus, D.F., Stein, S., 1994. Effect of recent revisions to the geomagnetic reversal time scale on estimates of current plate motions. Geophysical Research Letters 21, 2191–2194. https://doi.org/10.1029/94GL02118

DeMets, C., Gordon, R.G., Argus, D.F., Stein, S., 1990. Current plate motions. Geophysical Journal International 101, 425–478. https://doi.org/10.1111/j.1365-246X.1990.tb06579.x

Detrick, R.S., Buhl, P., Vera, E., Mutter, J., Orcutt, J., Madsen, J., Brocher, T., 1987. Multi-channel seismic imaging of a crustal magma chamber along the East Pacific Rise. Nature 326, 35–41. https://doi.org/10.1038/326035a0

Dewey, J.F., Kidd, W.S.F., 1977. Geometry of plate accretion. Geological Society of America Bulletin 88, 960. https://doi.org/10.1130/0016-7606(1977)88<960:GOPA>2.0.CO;2

Dick, H.J.B., Arai, S., Hirth, G., John, B.J., KR00-06 Scientific Party, 2001. A subhorizontal cross-section through the crust mantle boundary at the SW Indian Ridge. Geophysical Research Abstracts 3, 794.

Dick, H.J.B., Blum, P., Expedition 360 Scientists, MacLeod, C.J., 2017. Expedition 360 Summary, Proceedings of the International Ocean Discovery Program. International Ocean Discovery Program. https://doi.org/10.14379/iodp.proc.360.2017

Dick, H.J.B., Kvassnes, A.J.S., Robinson, P.T., MacLeod, C.J., Kinoshita, H., 2019a. The Atlantis Bank Gabbro Massif, Southwest Indian Ridge. Progress in Earth and Planetary Science 6, 64. https://doi.org/10.1186/s40645-019-0307-9

Dick, H.J.B., Lin, J., Schouten, H., 2003. An ultraslow-spreading class of ocean ridge. Nature 426, 405–412. https://doi.org/10.1038/nature02128

Dick, H.J.B., MacLeod, C.J., Blum, P., Abe, N., Blackman, D.K., Bowles, J.A., Cheadle, M.J., Cho, K., Ciążela, J., Deans, J.R., Edgcomb, V.P., Ferrando, C., France, L., Ghosh, B., Ildefonse, B., John, B., Kendrick, M.A., Koepke, J., Leong, J.A.M., Liu, C., Ma, Q., Morishita, T., Morris, A., Natland, J.H., Nozaka, T., Pluemper, O., Sanfilippo, A., Sylvan, J.B., Tivey, M.A., Tribuzio, R., Viegas, G., 2019b. Dynamic Accretion Beneath a Slow-Spreading Ridge Segment: IODP Hole 1473A and the Atlantis Bank Oceanic Core Complex. Journal of Geophysical Research 124, 12631–12659. https://doi.org/10.1029/2018JB016858

Dick, H.J.B., Meyer, P.S., Bloomer, S., Kirby, S., Stakes, D., Mawer, C., 1991. Proceedings of the Ocean Drilling Program, 118 Scientific Results, Proceedings of the Ocean Drilling Program. Ocean Drilling Program. https://doi.org/10.2973/odp.proc.sr.118.1991

Dick, H.J.B., Natland, J.H., Alt, J.C., Bach, W., Bideau, D., Gee, J.S., Haggas, S., Hertogen, J.G.H., Hirth, G., Holm, P.M., Ildefonse, B., Iturrino, G.J., John, B.E., Kelley, D.S., Kikawa, E., Kingdon, A., LeRoux, P.J., Maeda, J., Meyer, P.S., Miller, D.J., Naslund, H.R., Niu, Y.-L., Robinson, P.T., Snow, J., Stephen, R.A., Trimby, P.W., Worm, H.-U., Yoshinobu, A., 2000. A long in situ section of the lower ocean crust: results of ODP Leg

176 drilling at the Southwest Indian Ridge. Earth and Planetary Science Letters 179, 31–51. https://doi.org/10.1016/S0012-821X(00)00102-3

Dick, H.J.B., Natland, J.H., Ildefonse, B., 2006. Past and Future Impact of Deep Drilling in the Oceanic Crust and Mantle. Oceanography 19, 72–80. https://doi.org/10.5670/oceanog.2006.06

Dick, H.J.B., Natland, J.H., Miller, D.J., Shipboard Scientific Party, 1999. Leg 176 summary. Proceedings of the Ocean Drilling Program, Initial Reports 176.

Dietz, R.S., 1961. Continent and ocean basin evolution by spreading of the sea floor. Nature 190, 854–857.

Drury, M.R., Urai, J.L., 1990. Deformation-related recrystallization processes. Tectonophysics 172, 235–253. https://doi.org/10.1016/0040-1951(90)90033-5

Dunn, R.A., 2015. Crust and Lithospheric Structure - Seismic Structure of Mid-Ocean Ridges. Treatise on Geophysics. Elsevier, 419–451. https://doi.org/10.1016/B978-0-444-53802-4.00011-7

Escartín, J., Canales, J.P., 2011. Detachments in Oceanic Lithosphere: Deformation, Magmatism, Fluid Flow, and Ecosystems. Eos, Transactions American Geophysical Union 92, 31–31. https://doi.org/10.1029/2011EO040003

Escartín, J., Mével, C., MacLeod, C.J., McCaig, A.M., 2003. Constraints on deformation conditions and the origin of oceanic detachments: The Mid-Atlantic Ridge core complex at 15°45′N. Geochemistry, Geophysics, Geosystems 4. https://doi.org/10.1029/2002GC000472

Escartín, J., Mével, C., Petersen, S., Bonnemains, D., Cannat, M., Andreani, M., Augustin, N., Bezos, A., Chavagnac, V., Choi, Y., Godard, M., Haaga, K., Hamelin, C., Ildefonse, B., Jamieson, J., John, B., Leleu, T., MacLeod, C.J., Massot-Campos, M., Nomikou, P., Olive, J.A., Paquet, M., Rommevaux, C., Rothenbeck, M., Steinfuhrer, A., Tominaga, M., Triebe, L., Campos, R., Gracias, N., Garcia, R., 2017. Tectonic structure, evolution, and the nature of oceanic core complexes and their detachment fault zones (13°20′N and 13°30′N, Mid Atlantic Ridge). Geochemistry, Geophysics, Geosystems 18, 1451–1482. https://doi.org/10.1002/2016GC006775

Escartín, J., Smith, D.K., Cann, J., Schouten, H., Langmuir, C.H., Escrig, S., 2008. Central role of detachment faults in accretion of slow-spreading oceanic lithosphere. Nature 455, 790–794. https://doi.org/10.1038/nature07333

Etheridge, M.A., Wilkie, J.C., 1979. Grainsize reduction, grain boundary sliding and the flow strength of mylonites. Tectonophysics 58, 159–178. https://doi.org/10.1016/0040-1951(79)90327-5

Evans, B., Renner, J., Hirth, G., 2001. A few remarks on the kinetics of static grain growth in rocks. International Journal of Earth Sciences 90, 88–103. https://doi.org/10.1007/s005310000150

Expedition 335 Scientists, 2012. Deep drilling of intact ocean crust: harnessing past lessons to inform future endeavors. In: Teagle, D.A.H., Ildefonse, B., Blum, P., and the Expedition 335 Scientists, Proc. IODP, 335: Tokyo (Integrated Ocean Drilling Program Management International, Inc.). https://doi.org/10.2204/iodp.proc.335.104.2012

Ferrando, C., Basch, V., Ildefonse, B., Deans, J., Sanfilippo, A., Barou, F., France, L., 2021. Role of compaction in melt extraction and accumulation at a slow spreading center: Microstructures of olivine gabbros from the Atlantis Bank (IODP Hole U1473A, SWIR). Tectonophysics 815, 229001. https://doi.org/10.1016/j.tecto.2021.229001

Fitz Gerald, J.D., Stünitz, H., 1993. Deformation of granitoids at low metamorphic grade. I: Reactions and grain size reduction. 29.

Fliervoet, T.F., White, S.H., 1995. Quartz deformation in a very fine grained quartzo-feldspathic mylonite: a lack of evidence for dominant grain boundary sliding deformation. Journal of Structural Geology 17, 1095–1109. https://doi.org/10.1016/0191-8141(95)00007-Z

Fossen, H., 2010. Structural Geology. Cambridge university press.

Gardner, R.L., Piazolo, S., Daczko, N.R., Trimby, P., 2020. Microstructures reveal multistage melt present strain localisation in mid-ocean gabbros. Lithos 366–367, 105572. https://doi.org/10.1016/j.lithos.2020.105572

Gottstein, G., Mecking, H., 1985. Recrystallization. In: Wenk, H.R. (Ed.), Preferred Orientation in Deformed Metals and Rocks – an Introduction to Modern Texture Analysis. Academic Press, New York, 183–218.

Grindlay, N.R., Fox, P.J., Vogt, P.R., 1992. Morphology and tectonics of the Mid-Atlantic Ridge (25°–27°30′S) from Sea Beam and magnetic data. Journal of Geophysical Research: Solid Earth 97, 6983–7010. https://doi.org/10.1029/91JB02981

Guillopé, M., Poirier, J.-P., 1979. Dynamic recrystallization during creep of single-crystalline halite: An experimental study. Journal of Geophysical Research 84, 5557. https://doi.org/10.1029/JB084iB10p05557

Hasenclever, J., Theissen-Krah, S., Rüpke, L.H., Morgan, J.P., Iyer, K., Petersen, S., Devey, C.W., 2014. Hybrid shallow on-axis and deep off-axis hydrothermal circulation at fast-spreading ridges. Nature 508, 508–512. https://doi.org/10.1038/nature13174

Hay, R.S., Evans, B., 1987. Chemically induced grain boundary migration in calcite: temperature dependence, phenomenology, and possible applications to geologic systems. Contributions to Mineralogy and Petrology 97, 127–141. https://doi.org/10.1007/BF00375220

Heezen, B.C., 1960. The Rift in the Ocean Floor. Scientific American 203, 98–114.

Heezen, B.C., Tharp, M., 1965. Tectonic fabric of the Atlantic and Indian oceans and continental drift. Philosophical Transactions of the Royal Society of London. Series A, Mathematical and Physical Sciences 258, 90–106. https://doi.org/10.1098/rsta.1965.0024

Heezen, B.C., Tharp, M., 1964. VIII. Tectonic fabric of the Atlantic and Indian oceans and continental drift. Symposium on Continental Drift 258.

Heirtzler, J.R., Dickson, G.O., Herron, E.M., Pitman, W.C., Le Pichon, X., 1968. Marine magnetic anomalies, geomagnetic field reversals, and motions of the ocean floor and continents. Journal of Geophysical Research 73, 2119–2136. https://doi.org/10.1029/JB073i006p02119

Hess, H.H., 1962. History of Ocean Basins. In: Engel, A.E.J., James, H.L., Leonard, B.F. (Eds.), Petrologic Studies. Geological Society of America, USA, 599–620. https://doi.org/10.1130/Petrologic.1962.599

Hillert, M., Pudry, G.R., 1978. Chemically induced grain boundary migration. Acta Metallurgica 26, 333–340. https://doi.org/10.1016/0001-6160(78)90132-3

Hirth, G., EscartíN, J., Lin, J., 1998. The Rheology of the Lower Oceanic Crust: Implications for Lithospheric Deformation at Mid-Ocean Ridges. In: Roger Buck, W., Delaney, P.T., Karson, J.A., Lagabrielle, Y. (Eds.), Geophysical Monograph Series. American Geophysical Union, Washington, D. C., 291–303. https://doi.org/10.1029/GM106p0291

Hirth, G., Tullis, J., 1994. The brittle-plastic transition in experimentally deformed quartz aggregates. Solid Earth 99, 11731–11747.

Hirth, G., Tullis, J., 1992. Dislocation creep regimes in quartz aggregates. Journal of Structural Geology 14, 145–159.

Hobbs, B.E., Means, W.D., Williams, P., 1976. An Outline of Structural Geology, John Wiley&Sons Inc. ed. New York.

Holmes, A., 1965. Principles of physical geology, 2d ed. London.

Hosford, A., Tivey, M., Matsumoto, T., Dick, H., Schouten, H., Kinoshita, H., 2003. Crustal magnetization and accretion at the Southwest Indian Ridge near the Atlantis II fracture zone, 0-25 Ma. Journal of Geophysical Research: Solid Earth 108. https://doi.org/10.1029/2001JB000604

Humphreys, F.J., 1997. A unified theory of recovery, recrystallization and grain growth, based on the stability and growth of cellular microstructures - I. The basic model. Acta Materialia 45, 4231–4240. https://doi.org/10.1016/S1359-6454(97)00070-0

Ildefonse, B., 2014. Crustal Accretion. Earth Sciences Series. Encyclopedia of Marine Geosciences, Springer 1–7. https://doi.org/10.1007/SpringerReference_350453

Ildefonse, B., Abe, N., Godard, M., Morris, A., Teagle, D.A.H., Umino, S., 2014. Formation and Evolution of Oceanic Lithosphere: New Insights on Crustal Structure and Igneous

Geochemistry from ODP/IODP Sites 1256, U1309, and U1415. Developments in Marine Geology. Elsevier, 449–505. https://doi.org/10.1016/B978-0-444-62617-2.00017-7

Ildefonse, B., Blackman, D.K., John, B.E., Ohara, Y., Miller, D.J., MacLeod, C.J., Integrated Ocean Drilling Program Expeditions 304/305 Science Party, 2007a. Oceanic core complexes and crustal accretion at slow-spreading ridges. Geology 35, 623. https://doi.org/10.1130/G23531A.1

Ildefonse, B., Rona, P., Blackman, D., 2007b. Drilling the Crust at Mid-Ocean Ridges: An "In Depth" Perspective. Oceanography 20, 66–77. https://doi.org/10.5670/oceanog.2007.81

Jackson, H.R., Reid, I., Falconer, R.K.H., 1982. Crustal structure near the Arctic Mid-Ocean Ridge. Journal of Geophysical Research 87, 1773. https://doi.org/10.1029/JB087iB03p01773

Jessell, M.W., 1987. Grain-boundary migration microstructures in a naturally deformed quartzite. Journal of Structural Geology 9, 1007–1014. https://doi.org/10.1016/0191-8141(87)90008-3

Ji, S., 2004. A generalized mixture rule for estimating the viscosity of solid-liquid suspensions and mechanical properties of polyphase rocks and composite materials: a generalized mixture rule. Journal of Geophysical Research: Solid Earth 109. https://doi.org/10.1029/2004JB003124

Ji, S., Tongbin, S., Salisbury, M.H., Sun, S., Michibayashi, K., Zhao, W., Long, C., Liang, F., Satsukawa, T., 2014. Plagioclase preferred orientation and induced seismic anisotropy in mafic igneous rocks. Journal of Geophysical Research: Solid Earth 119, 8064–8088. https://doi.org/10.1002/2014JB011352

Karson, J.A., 1991. Accommodation Zones and Transfer Faults: Integral Components of Mid-Atlantic Ridge Extensional Systems. In: Peters, Tj., Nicolas, A., Coleman, R.G. (Eds.), Ophiolite Genesis and Evolution of the Oceanic Lithosphere, Petrology and Structural Geology. Springer Netherlands, Dordrecht, 21–37. https://doi.org/10.1007/978-94-011-3358-6_3

Karson, J.A., Dick, H.J.B., 1983. Tectonics of ridge-transform intersections at the Kane fracture zone. Marine Geophysical Researches 6, 51–98. https://doi.org/10.1007/BF00300398

Karson, J.A., Thompson, G., Humphris, S.E., Edmond, J.M., Bryan, W.B., Brown, J.R., Winters, A.T., Pockalny, R.A., Casey, J.F., Campbell, A.C., Klinkhammer, G., Palmer, M.R., Kinzler, R.J., Sulanowska, M.M., 1987. Along-axis variations in seafloor spreading in the MARK area. Nature 328, 681–685. https://doi.org/10.1038/328681a0

Kelemen, P.B., Koga, K., Shimizu, N., 1997. Geochemistry of gabbro sills in the crust-mantle transition zone of the Oman ophiolite: implications for the origin of the oceanic lower crust. Earth and Planetary Science Letters 146, 475–488. https://doi.org/10.1016/S0012-821X(96)00235-X

Kelemen, Peter.B., 1990. Reaction Between Ultramafic Rock and Fractionating Basaltic Magma I. Phase Relations, the Origin of Calc-alkaline Magma Series, and the Formation of Discordant Dunite. Journal of Petrology 31, 51–98. https://doi.org/10.1093/petrology/31.1.51

Kenkmann, T., Dresen, G., 2002. Dislocation microstructure and phase distribution in a lower crustal shear zone – an example from the Ivrea-Zone, Italy. International Journal of Earth Sciences 91, 445–458. https://doi.org/10.1007/s00531-001-0236-9

Klein, E.M., Langmuir, C.H., 1987. Global correlations of ocean ridge basalt chemistry with axial depth and crustal thickness. Journal of Geophysical Research 92, 8089. https://doi.org/10.1029/JB092iB08p08089

Knipe, R.J., 1989. Deformation mechanisms—recognition from natural tectonites. Journal of Structural Geology 11, 127–146. https://doi.org/10.1016/0191-8141(89)90039-4

Korenaga, J., Kelemen, P.B., 1997. Origin of gabbro sills in the Moho transition zone of the Oman ophiolite: Implications for magma transport in the oceanic lower crust. Journal of Geophysical Research: Solid Earth 102, 27729–27749. https://doi.org/10.1029/97JB02604

Kronenberg, A.K., Shelton, G.L., 1980. Deformation microstructures in experimentally deformed Maryland diabase. Journal of Structural Geology 2, 341–353. https://doi.org/10.1016/0191-8141(80)90022-X

Kruhl, J.H., 2001. Crystallographic control on the development of foam textures in quartz, plagioclase and analogue material. International Journal of Earth Sciences 90, 104–117. https://doi.org/10.1007/s005310000170

Kruse, R., Stünitz, H., 1999. Deformation mechanisms and phase distribution in mafic high-temperature mylonites from the Jotun Nappe, southern Norway. Tectonophysics 303, 223–249. https://doi.org/10.1016/S0040-1951(98)00255-8

Kuo, B.-Y., Forsyth, D.W., 1988. Gravity anomalies of the ridge-transform system in the South Atlantic between 31 and 34.5° S: Upwelling centers and variations in crustal thickness. Marine Geophysical Researches 10, 205–232. https://doi.org/10.1007/BF00310065

Lagabrielle, Y., 2009. Mantle exhumation and lithospheric spreading: An historical perspective from investigations in the Oceans and in the Alps-Apennines ophiolites. Italian Journal of Geosciences 279–293. https://doi.org/10.3301/IJG.2009.128.2.279

Lagabrielle, Y., Cannat, M., 1990. Alpine Jurassic ophiolites resemble the modern central Atlantic basement. Geology 18, 319–322. https://doi.org/10.1130/0091-7613(1990)018<0319:AJORTM>2.3.CO;2

Lagabrielle, Y., Vitale Brovarone, A., Ildefonse, B., 2015. Fossil oceanic core complexes recognized in the blueschist metaophiolites of Western Alps and Corsica. Earth-Science Reviews 141, 1–26. https://doi.org/10.1016/j.earscirev.2014.11.004

Lavier, L.L., Buck, W.R., Poliakov, A.N.B., 2000. Factors controlling normal fault offset in an ideal brittle layer. Journal of Geophysical Research: Solid Earth 105, 23431–23442. https://doi.org/10.1029/2000JB900108

Le Pichon, X., 1968. Sea-floor spreading and continental drift. Journal of Geophysical Research 73, 3661–3697. https://doi.org/10.1029/JB073i012p03661

Lemoine, M., Tricart, P., Boillot, G., 1987. Ultramafic and gabbroic ocean floor of the Ligurian Tethys (Alps, Corsica, Apennines): In search of a genetic model. Geology 15, 622–625. https://doi-org.insu.bib.cnrs.fr/10.1130/0091-7613(1987)15<622:UAGOFO>2.0.CO;2

Lill, G., 1961. The Mohole Project. Navigation 8, 3–11. https://doi.org/10.1002/j.2161-4296.1961.tb01999.x

Lin, J., Purdy, G.M., Schouten, H., Sempere, J.-C., Zervas, C., 1990. Evidence from gravity data for focusedmagmatic accretionalong the Mid-Atlantic Ridge. Nature 344, 627–632. https://doi.org/10.1038/344627a0

Lissenberg, C.J., MacLeod, C.J., 2016. A Reactive Porous Flow Control on Mid-ocean Ridge Magmatic Evolution. Journal of Petrology 57, 2195–2220. https://doi.org/10.1093/petrology/egw074

Lloyd, G.E., Law, R.D., Mainprice, D., Wheeler, J., 1992. Microstructural and crystal fabric evolution during shear zone formation. Journal of Structural Geology 14, 1079–1100. https://doi.org/10.1016/0191-8141(92)90037-W

Lowrie, W., 2007. Fundamentals of geophysics, 2nd ed. ed. Cambridge University Press, Cambridge ; New York.

Lücke, K., Stüwe, H.P., 1971. On the theory of impurity controlled grain boundary motion. Acta Metallurgica 19, 1087–1099. https://doi.org/10.1016/0001-6160(71)90041-1

Maclennan, J., Hulme, T., Singh, S.C., 2005. Cooling of the lower oceanic crust. Geology 33, 357. https://doi.org/10.1130/G21207.1

Maclennan, J., Hulme, T., Singh, S.C., 2004. Thermal models of oceanic crustal accretion: Linking geophysical, geological and petrological observations: OCEANIC CRUSTAL ACCRETION. Geochemistry, Geophysics, Geosystems 5, 32. https://doi.org/10.1029/2003GC000605

MacLeod, C.J., Dick, H.J., Blum, P., Expedition 360 Scientists, 2017. Site U1473A, Proceedings of the International Ocean Discovery Program. International Ocean Discovery Program. https://doi.org/10.14379/iodp.proc.360.2017

MacLeod, C.J., Escartín, J., Banerji, D., Banks, G.J., Gleeson, M., Irving, D.H.B., Lilly, R.M., McCaig, A.M., Niu, Y.-L., Allerton, S., Smith, D.K., 2002. Direct geological evidence for oceanic detachment faulting: The Mid-Atlantic Ridge, 15°45′ N. Geology 30, 879–882. https://doi.org/10.1130/0091-7613(2002)030%3C0879:DGEFOD%3E2.0.CO;2

MacLeod, C.J., Searle, R.C., Murton, B.J., Casey, J.F., Mallows, C., Unsworth, S.C., Achenbach, K.L., Harris, M., 2009. Life cycle of oceanic core complexes. Earth and Planetary Science Letters 287, 333–344. https://doi.org/10.1016/j.epsl.2009.08.016

MacLeod, C.J., Wright, W.P., Perry, C.T., Dick, H.J.B., 2000. Tectonic evolution and uplift/subsidence history of Atlantis Bank, a transverse ridge near the Atlantis II Fracture Zone, SW Indian Ridge. Eos, Transactions American Geophysical Union 81, 1129.

Manatschal, G., Sauter, D., Karpoff, A.M., Masini, E., Mohn, G., Lagabrielle, Y., 2011a. The Chenaillet Ophiolite in the French/Italian Alps: An ancient analogue for an Oceanic Core Complex? Lithos 124, 169–184. https://doi.org/10.1016/j.lithos.2010.10.017

Manatschal, G., Sauter, D., Karpoff, A.M., Masini, E., Mohn, G., Lagabrielle, Y., 2011b. The Chenaillet Ophiolite in the French/Italian Alps: An ancient analogue for an Oceanic Core Complex? Lithos 124, 169–184. https://doi.org/10.1016/j.lithos.2010.10.017

Marroni, M., Molli, G., Montanini, A., Tribuzio, R., 1998. The association of continental crust rocks with ophiolites in the Northern Apennines (Italy): implications for the continent-ocean transition in the Western Tethys. Tectonophysics 292, 43–66. https://doi.org/10.1016/S0040-1951(98)00060-2

Marroni, M., Pandolfi, L., 2001. Debris flow and slide deposits at the top of the Internal Liguride ophiolitic sequence, Northern Apennines, Italy: A record of frontal tectonic erosion in a fossil accretionary wedge. The Island Arc 10, 9–21. https://doi.org/10.1046/j.1440-1738.2001.00289.x

Marroni, M., Pandolfi, L., 1996. The deformation history of an accreted ophiolite sequence: the Internal Liguride units (Northern apennines, Italy). Geodinamica Acta 9, 13–29. https://doi.org/10.1080/09853111.1996.11417260

Marshall, D.B., McLaren, A.C., 1977. The direct observation and analysis of dislocations in experimentally deformed plagioclase feldspars. Journal of Materials Science 12, 893–903. https://doi.org/10.1007/BF00540970

McLaren, A.C., Pryer, L.L., 2001. Microstructural investigation of the interaction and interdependence of cataclastic and plastic mechanisms in Feldspar crystals deformed in the semi-brittle field. Tectonophysics 335, 15. https://doi.org/10.1016/S0040-1951(01)00042-7

Means, W.D., Ree, J.H., 1988. Seven types of subgrain boundaries in octachioropropane. Journal of Structural Geology 10, 765–770. https://doi.org/10.1016/0191-8141(88)90083-1

Mehl, L., Hirth, G., 2008. Plagioclase preferred orientation in layered mylonites: Evaluation of flow laws for the lower crust. Journal of Geophysical Research 113, B05202. https://doi.org/10.1029/2007JB005075

Menna, F., 2009. From magmatic to metamorphic deformations in a jurassic ophiolitic complex: the bracco gabbroic massif, eastern liguria (italy). Ofioliti 34, 109–130. https://doi.org/10.4454/ofioliti.v34i2.382

Mével, C., 2003. Serpentinization of abyssal peridotites at mid-ocean ridges. Comptes Rendus Geoscience 335, 825–852. https://doi.org/10.1016/j.crte.2003.08.006

Mével, C., Cannat, M., Gente, P., Marion, E., Auzende, J.M., Karson, J.A., 1991. Emplacement of deep crustal and mantle rocks on the west median valley wall of the MARK area (MAR, 23°N). Tectonophysics 190, 31–53. https://doi.org/10.1016/0040-1951(91)90353-T

Milnes, A.G., Wennberg, O.P., Skår, Ø., Koestler, A.G., 1997. Contraction, extension and timing in the South Norwegian Caledonides: the Sognefjord transect. Geological Society, London, Special Publications 121, 123–148. https://doi.org/10.1144/GSL.SP.1997.121.01.06

Minshull, T.A., Muller, M.R., Robinson, C.J., White, R.S., Bickle, M.J., 1998. Is the oceanic Moho a serpentinization front? Geological Society, London, Special Publications 148, 71–80. https://doi.org/10.1144/GSL.SP.1998.148.01.05

Miranda, E.A., Hirth, G., John, B.E., 2016. Microstructural evidence for the transition from dislocation creep to dislocation-accommodated grain boundary sliding in naturally deformed plagioclase. Journal of Structural Geology 92, 30–45. https://doi.org/10.1016/j.jsg.2016.09.002

Miranda, E.A., John, B.E., 2010. Strain localization along the Atlantis Bank oceanic detachment fault system, Southwest Indian Ridge. Geochemistry, Geophysics, Geosystems 11, 34. https://doi.org/10.1029/2009GC002646

Mock, D., Ildefonse, B., Müller, T., Koepke, J., 2021. A Reference Section Through Fast-Spread Lower Oceanic Crust, Wadi Gideah, Samail Ophiolite (Sultanate of Oman): Insights From Crystallographic Preferred Orientations. Journal of Geophysical Research: Solid Earth 126. https://doi.org/10.1029/2021JB021864

Molli, G., 1996. Pre-orogenic tectonic framework of the northern Apennine ophiolites. Eclogae Geologicae Helvetiae 89, 163–180. https://doi.org/10.5169/seals-167898

Molli, G., 1994. Microstructural features of high temperature shear zones in gabbros of the Northern Apennine Ophiolites. Journal of Structural Geology 16, 1535–1541. https://doi.org/10.1016/0191-8141(94)90031-0

Montanini, A., Tribuzio, R., Vernia, L., 2008. Petrogenesis of basalts and gabbros from an ancient continent–ocean transition (External Liguride ophiolites, Northern Italy). Lithos 101, 453–479. https://doi.org/10.1016/j.lithos.2007.09.007

Montardi, Y.A., Mainprice, D., 1987. A transmission electron microscopie study of the natural plastic defonnation of calcic plagioclases (An 68-70). Bulletin de Minéralogie 110, 1–14.

Morton, J.L., Sleep, N.H., 1985. A Mid-Ocean Ridge Thermal Model: Constraints on the volume of axial hydrothermal heat flux. Journal of Geophysical Research 90, 11345. https://doi.org/10.1029/JB090iB13p11345

Muller, M.R., Minshull, T.A., White, R.S., 2000. Crustal structure of the Southwest Indian Ridge at the Atlantis II Fracture Zone. Journal of Geophysical Research: Solid Earth 105, 25809–25828. https://doi.org/10.1029/2000JB900262

Muller, M.R., Robinson, C.J., Minshull, T.A., White, R.S., Bickle, M.J., 1997. Thin crust beneath ocean drilling program borehole 735B at the Southwest Indian Ridge? Earth and Planetary Science Letters 148, 93–107. https://doi.org/10.1016/S0012-821X(97)00030-7

Natland, J.H., Dick, H.J.B., 2001. Formation of the lower ocean crust and the crystallization of gabbroic cumulates at a very slowly spreading ridge. Journal of Volcanology and Geothermal Research 110, 191–233. https://doi.org/10.1016/S0377-0273(01)00211-6

Nicolas, A., 1995. The Mid-Oceanic Ridges. Springer Berlin Heidelberg, Berlin, Heidelberg. https://doi.org/10.1007/978-3-662-03136-0

Okudaira, T., Jeřábek, P., Stünitz, H., Fusseis, F., 2015. High-temperature fracturing and subsequent grain-size-sensitive creep in lower crustal gabbros: Evidence for coseismic loading followed by creep during decaying stress in the lower crust?: fracturing and creep in lower crust. Journal of Geophysical Research: Solid Earth 120, 3119–3141. https://doi.org/10.1002/2014JB011708

Okudaira, T., Shigematsu, N., Harigane, Y., Yoshida, K., 2017. Grain size reduction due to fracturing and subsequent grain-size-sensitive creep in a lower crustal shear zone in the presence of a CO2-bearing fluid. Journal of Structural Geology 95, 171–187. https://doi.org/10.1016/j.jsg.2016.11.001

Oliot, E., Goncalves, P., Marquer, D., 2010. Role of plagioclase and reaction softening in a metagranite shear zone at mid-crustal conditions (Gotthard Massif, Swiss Central Alps): Strain localization in granitic rocks. Journal of Metamorphic Geology 28, 849–871. https://doi.org/10.1111/j.1525-1314.2010.00897.x

Oliot, E., Goncalves, P., Schulmann, K., Marquer, D., Lexa, O., 2014. Mid-crustal shear zone formation in granitic rocks: Constraints from quantitative textural and crystallographic preferred orientations analyses. Tectonophysics 612–613, 63–80. https://doi.org/10.1016/j.tecto.2013.11.032

Olive, J.-A., Behn, M.D., Tucholke, B.E., 2010. The structure of oceanic core complexes controlled by the depth distribution of magma emplacement. Nature Geoscience 3, 491–495. https://doi.org/10.1038/ngeo888

Olsen, T.S., Kohlstedt, D.L., 1985. Natural deformation and recrystallization of some intermediate plagioclase feldspars. Tectonophysics 111, 107–131. https://doi.org/10.1016/0040-1951(85)90067-8

Olsen, T.S., Kohlstedt, D.L., 1984. Analysis of dislocations in some naturally deformed plagioclase feldspars. Physics and Chemistry of Minerals 11, 153–160. https://doi.org/10.1007/BF00387845

Palmiotto, C., Corda, L., Ligi, M., Cipriani, A., Dick, H.J.B., Douville, E., Gasperini, L., Montagna, P., Thil, F., Borsetti, A.M., Balestra, B., Bonatti, E., 2013. Nonvolcanic tectonic islands in ancient and modern oceans: Nonvolcanic Tectonic Islands. Geochemistry, Geophysics, Geosystems 14, 4698–4717. https://doi.org/10.1002/ggge.20279

Passchier, C.W., Trouw, R.A.J., 2005. Microtectonics. Springer Science & Business Media.

Paterson, M.S., 1995. A theory for granular flow accommodated by material transfer via an intergranular fluid. Tectonophysics 245, 135–151. https://doi.org/10.1016/0040-1951(94)00231-W

Patriat, P., Sauter, D., Munschy, M., Parson, L., 1997. A Survey of the Southwest Indian Ridge Axis Between Atlantis II Fracture Zone and the Indian Ocean Triple Junction: Regional Setting and Large Scale Segmentation. Marine Geophysical Researches 19, 457–480. https://doi.org/10.1023/A:1004312623534

Pettigrew, T., Casey, J., Miller, D., Araki, E., Boissonnas, R., Busby, R., Einaudi, F., Gerdom, M., Guo, Z., Hopkins, H., 1999. Leg 179 summary. ODP, Texas A and M Univ., USA.

Phipps-Morgan, J., Chen, Y.J., 1993. The genesis of oceanic crust: Magma injection, hydrothermal circulation, and crustal flow. Journal of Geophysical Research: Solid Earth 98, 6283–6297. https://doi.org/10.1029/92JB02650

Piccardo, G.B., Guarnieri, L., 2010. Alpine peridotites from the Ligurian Tethys: an updated critical review. International Geology Review 52, 1138–1159. https://doi.org/10.1080/00206810903557829

Poirier, J.P., 1985. Creep of crystals: high-temperature deformation processes in metals, ceramics and minerals, Cambridge University Press. Cambridge.

Pond, R.C., Smith, D.A., 1977. On the absorption of dislocations by grain boundaries. Philosophical Magazine 36, 353–366. https://doi.org/10.1080/14786437708244939

Quick, J.E., Denlinger, R.P., 1993. Ductile deformation and the origin of layered gabbro in ophiolites. Journal of Geophysical Research: Solid Earth 98, 14015–14027. https://doi.org/10.1029/93JB00698

Rampone, E., Borghini, G., Basch, V., 2020. Melt migration and melt-rock reaction in the Alpine-Apennine peridotites: Insights on mantle dynamics in extending lithosphere. Geoscience Frontiers 11, 151–166. https://doi.org/10.1016/j.gsf.2018.11.001

Rampone, E., Hofmann, A.W., Piccardo, G.B., Vannucci, R., Bottazzi, P., Ottolini, L., 1996. Trace element and isotope geochemistry of depleted peridotites from an N-MORB type

ophiolite (Internal Liguride, N. Italy). Contributions to Mineralogy and Petrology 123, 61–76. https://doi.org/10.1007/s004100050143

Rampone, E., Piccardo, G.B., Vannucci, R., Bottazzi, P., 1997. Chemistry and origin of trapped melts in ophiolitic peridotites. Geochimica et Cosmochimica Acta 61, 4557–4569. https://doi.org/10.1016/S0016-7037(97)00260-3

Reid, I., Jackson, H.R., 1981. Oceanic spreading rate and crustal thickness. Marine Geophysical Researches 5, 165–172. https://doi.org/10.1007/BF00163477

Robinson, P.T., Von Herzen, R., et al., 1989. Proceedings of the Ocean Drilling Program, Initial Reports, 118: College Station, TX (Ocean Drilling Program). Proceedings of the Ocean Drilling Program, Initial Reports. https://doi.org/doi:10.2973/odp.proc.ir.118.1989

Rommevaux-Jestin, C., Deplus, C., Patriat, P., 1997. Mantle Bouguer Anomaly Along an Ultra Slow-Spreading Ridge: Implications for Accretionary Processes and Comparison with Results from Central Mid-Atlantic Ridge. Marine Geophysical Researches 19, 481–503. https://doi.org/10.1023/A:1004269003009

Ronov, A., Yaroshevsky, A., 1969. Chemical composition of the Earth's crust. GMS 13, 37–57.

Rosenberg, C.L., Stünitz, H., 2003. Deformation and recrystallization of plagioclase along a temperature gradient: an example from the Bergell tonalite. Journal of Structural Geology 25, 389–408. https://doi.org/10.1016/S0191-8141(02)00036-6

Rutter, E.H., 1995. Experimental study of the influence of stress, temperature, and strain on the dynamic recrystallization of Carrara marble. Journal of Geophysical Research: Solid Earth 100, 24651–24663. https://doi.org/10.1029/95JB02500

Ryan, W.B.F., Carbotte, S.M., Coplan, J.O., O'Hara, S., Melkonian, A., Arko, R., Weissel, R.A., Ferrini, V., Goodwillie, A., Nitsche, F., Bonczkowski, J., Zemsky, R., 2009. Global Multi-Resolution Topography synthesis: global multi-resolution topography synthesis. Geochemistry, Geophysics, Geosystems 10, n/a-n/a. https://doi.org/10.1029/2008GC002332

Sanfilippo, A., MacLeod, C.J., Tribuzio, R., Lissenberg, C.J., Zanetti, A., 2020. Early-Stage Melt-Rock Reaction in a Cooling Crystal Mush Beneath a Slow-Spreading Mid-Ocean Ridge (IODP Hole U1473A, Atlantis Bank, Southwest Indian Ridge). Frontiers in Earth Science 8, 579138. https://doi.org/10.3389/feart.2020.579138

Satsukawa, T., Ildefonse, B., Mainprice, D., Morales, L.F.G., Michibayashi, K., Barou, F., 2013. A database of plagioclase crystal preferred orientations (CPO) and microstructures – implications for CPO origin, strength, symmetry and seismic anisotropy in gabbroic rocks. Solid Earth 4, 511–542. https://doi.org/10.5194/se-4-511-2013

Sauter, D., Cannat, M., 2010. The ultraslow spreading Southwest Indian Ridge. In: Rona, P.A., Devey, C.W., Dyment, J., Murton, B.J. (Eds.), Geophysical Monograph Series. American

Geophysical Union, Washington, D. C., 153–173. https://doi.org/10.1029/2008GM000843

Sauter, D., Cannat, M., Rouméjon, S., Andreani, M., Birot, D., Bronner, A., Brunelli, D., Carlut, J., Delacour, A., Guyader, V., MacLeod, C.J., Manatschal, G., Mendel, V., Ménez, B., Pasini, V., Ruellan, E., Searle, R., 2013. Continuous exhumation of mantle-derived rocks at the Southwest Indian Ridge for 11 million years. Nature Geoscience 6, 314–320. https://doi.org/10.1038/ngeo1771

Scandale, E., Gandais, M., Willaime, C., 1983. Transmission electron microscopic study of experimentally deformed k-feldspar single crystals: The (010)[001], (001)1/2[-110]1/2[-112] and(1-11)1/2[110] slip systems. Physics and Chemistry of Minerals 9, 182–187. https://doi.org/10.1007/BF00308376

Schroeder, T., John, B.E., 2004. Strain localization on an oceanic detachment fault system, Atlantis Massif, 30°N, Mid-Atlantic Ridge. Geochemistry, Geophysics, Geosystems 5, n/a-n/a. https://doi.org/10.1029/2004GC000728

Schwarzenbach, E.M., Vogel, M., Früh-Green, G.L., Boschi, C., 2021. Serpentinization, Carbonation, and Metasomatism of Ultramafic Sequences in the Northern Apennine Ophiolite (NW Italy). Journal of Geophysical Research: Solid Earth 126. https://doi.org/10.1029/2020JB020619

Shemenda, A.I., Grocholsky, A.L., 1994. Physical modeling of slow seafloor spreading. Journal of Geophysical Research: Solid Earth 99, 9137–9153. https://doi.org/10.1029/93JB02995

Simpson, C., 1985. Deformation of granitic rocks across the brittle-ductile transition. Journal of Structural Geology 7, 503–511. https://doi.org/10.1016/0191-8141(85)90023-9

Singh, S.C., Crawford, W.C., Carton, H., Seher, T., Combier, V., Cannat, M., Pablo Canales, J., Düsünür, D., Escartin, J., Miguel Miranda, J., 2006. Discovery of a magma chamber and faults beneath a Mid-Atlantic Ridge hydrothermal field. Nature 442, 1029–1032. https://doi.org/10.1038/nature05105

Sinton, J.M., Detrick, R.S., 1992. Mid-ocean ridge magma chambers. Journal of Geophysical Research 97, 197. https://doi.org/10.1029/91JB02508

Sleep, N.H., 1975. Formation of oceanic crust: Some thermal constraints. Journal of Geophysical Research 80, 4037–4042. https://doi.org/10.1029/JB080i029p04037

Small, C., 1998. Global Systematics of Mid-Ocean Ridge Morphology. In: Roger Buck, W., Delaney, P.T., Karson, J.A., Lagabrielle, Y. (Eds.), Geophysical Monograph Series. American Geophysical Union, Washington, D. C., 1–25. https://doi.org/10.1029/GM106p0001

Small, C., Sandwell, D.T., 1989. An abrupt change in ridge axis gravity with spreading rate. Journal of Geophysical Research 94, 17383. https://doi.org/10.1029/JB094iB12p17383

Smith, D.A., Rae, C.M.F., Grovenor, C.R.M., 1979. Grain-boundary migration. Grain Boundary Structure and Kinetics. New York, 450.

Smith, D.K., Schouten, H., Dick, H.J.B., Cann, J.R., Salters, V., Marschall, H.R., Ji, F., Yoerger, D., Sanfilippo, A., Parnell-Turner, R., Palmiotto, C., Zheleznov, A., Bai, H., Junkin, W., Urann, B., Dick, S., Sulanowska, M., Lemmond, P., Curry, S., 2014. Development and evolution of detachment faulting along 50 km of the Mid-Atlantic Ridge near 16.5°N. Geochemistry, Geophysics, Geosystems 15, 4692–4711. https://doi.org/10.1002/2014GC005563

Smith, J.V., Brown, W.L., 1988. Feldspar Minerals. Springer Berlin Heidelberg, Berlin, Heidelberg. https://doi.org/10.1007/978-3-642-72594-4

Stipp, M., Stünitz, H., Heilbronner, R., Schmid, S.M., 2002. The eastern Tonale fault zone: a 'natural laboratory' for crystal plastic deformation of quartz over a temperature range from 250 to 700°C. Journal of Structural Geology 24, 1861–1884. https://doi.org/10.1016/S0191-8141(02)00035-4

Stünitz, H., 1998. Syndeformational recrystallization - dynamic or compositionally induced? Contributions to Mineralogy and Petrology 131, 219–236. https://doi.org/10.1007/s004100050390

Stünitz, H., Fitz Gerald, J.D., 1993. Deformation of granitoids at low metamorphic grade. II: Granular flow in albite-rich mylonites. Tectonophysics 221, 299–324. https://doi.org/10.1016/0040-1951(93)90164-F

Stünitz, H., Fitz Gerald, J.D., Tullis, J., 2003. Dislocation generation, slip systems, and dynamic recrystallization in experimentally deformed plagioclase single crystals. Tectonophysics 372, 215–233. https://doi.org/10.1016/S0040-1951(03)00241-5

Taufner, R., Viegas, G., Faleiros, F.M., Castellan, P., Silva, R., 2021. Deformation mechanisms of granulite-facies mafic shear zones from hole U1473A, Atlantis Bank, Southwest Indian Ridge (IODP Expedition 360). Journal of Structural Geology 149, 104380. https://doi.org/10.1016/j.jsg.2021.104380

Tivey, M.K., 2007. Generation of Seafloor Hydrothermal Vent Fluids and Associated Mineral Deposits. Oceanography 20, 50–65. https://doi.org/10.5670/oceanog.2007.80

Tolstoy, M., Harding, A.J., Orcutt, J.A., 1993. Crustal thickness on the Mid-Atlantic Ridge: Bull's-eye gravity anomalies and focused accretion. Science 262, 726–729. https://doi.org/10.1126/science.262.5134.726

Trépied, L., Doukhan, J.C., Paquet, J., 1980. Subgrain boundaries in quartz theoretical analysis and microscopic observations. Physics and Chemistry of Minerals 5, 201–218. https://doi.org/10.1007/BF00348570

Tribuzio, R., Garzetti, F., Corfu, F., Tiepolo, M., Renna, M.R., 2016. U–Pb zircon geochronology of the Ligurian ophiolites (Northern Apennine, Italy): Implications for continental

breakup to slow seafloor spreading. Tectonophysics 666, 220–243. https://doi.org/10.1016/j.tecto.2015.10.024

Tribuzio, R., Tiepolo, M., Vannucci, R., 2000. Evolution of gabbroic rocks of the Northern Apennine ophiolites (Italy): Comparison with the lower oceanic crust from modern slow-spreading ridges. Special Paper 349: Ophiolites and Oceanic Crust: New Insights from Field Studies and the Ocean Drilling Program. Geological Society of America, 129–138. https://doi.org/10.1130/0-8137-2349-3.129

Tucholke, B.E., Lin, J., Kleinrock, M.C., 1998. Megamullions and mullion structure defining oceanic metamorphic core complexes on the Mid-Atlantic Ridge. Journal of Geophysical Research: Solid Earth 103, 9857–9866. https://doi.org/10.1029/98JB00167

Tullis, J., Yund, R.A., 1987. Transition from cataclastic flow to dislocation creep of feldspar: Mechanisms and microstructures. 5.

Tullis, J., Yund, R.A., 1985. Dynamic recrystallization of feldspar: A mechanism for ductile shear zone formation. Geology 13, 238–241.

Tullis, J., Yund, R.A., 1977. Experimental deformation of dry westerly granite. Journal of Geophysical Research 82, 5705–5718. https://doi.org/10.1029/JB082i036p05705

Urai, J.L., Means, W.D., Lister, G.S., 1986. Dynamic recrystallization of minerals. In: Hobbs, B.E., Heard, H.C. (Eds.), Geophysical Monograph Series. American Geophysical Union, Washington, D. C., 161–199. https://doi.org/10.1029/GM036p0161

Vernon, R.H., 1981. Optical microstructure of partly recrystallized calcite in some naturally deformed marbles. Tectonophysics 78, 601–612. https://doi.org/10.1016/0040-1951(81)90031-7

Vernon, R.H., 1976. Deformation, Recovery and Recrystallisation Processes. Metamorphic Processes. Springer Netherlands, Dordrecht, 148–172. https://doi.org/10.1007/978-94-015-1109-4_6

Vine, F.J., 1966. Spreading of the Ocean Floor: New Evidence. Science 154, 1405–1415. https://doi.org/10.1126/science.154.3755.1405

Vine, F.J., Matthews, D.H., 1963. Magnetic anomalies over oceanic ridges. Nature 199, 947–949.

Wegener, A., 1912. Die Entstehung der Kontinente. Geologische Rundschau 3, 276–292. https://doi.org/10.1007/BF02202896

Wenk, H.-R., Christie, J.M., 1991. Comments on the interpretation of deformation textures in rocks. Journal of Structural Geology 13, 1091–1110. https://doi.org/10.1016/0191-8141(91)90071-P

Wheeler, J., 1992. Importance of pressure solution and coble creep in the deformation of polymineralic rocks. Journal of Geophysical Research: Solid Earth 97, 4579–4586. https://doi.org/10.1029/91JB02476

White, R.S., McKenzie, D., O'Nions, R.K., 1992. Oceanic crustal thickness from seismic measurements and rare earth element inversions. Journal of Geophysical Research 97, 19683. https://doi.org/10.1029/92JB01749

White, R.S., Minshull, T.A., Bickle, M.J., Robinson, C.J., 2001. Melt Generation at Very Slow-Spreading Oceanic Ridges: Constraints from Geochemical and Geophysical Data. Journal of Petrology 42, 1171–1196. https://doi.org/10.1093/petrology/42.6.1171

White, R.W., Powell, R., Baldwin, J.A., 2008. Calculated phase equilibria involving chemical potentials to investigate the textural evolution of metamorphic rocks. Journal of Metamorphic Geology 26, 181–198. https://doi.org/10.1111/j.1525-1314.2008.00764.x

Yund, R.A., 1986. Interdiffusion of N a S i - CaA1 in Peristerite. Physics and Chemistry of Minerals 13, 11–16. https://doi.org/10.1007/BF00307308

Yund, R.A., Quigley, J., Tullis, J., 1989. The effect of dislocations on bulk diffusion in feldspars during metamorphism. Journal of Metamorphic Geology 7, 337–341. https://doi.org/10.1111/j.1525-1314.1989.tb00601.x

Yund, R.A., Tullis, J., 1991. Compositional changes of minerals associated with dynamic recrystallizatin. Contributions to Mineralogy and Petrology 108, 346–355. https://doi.org/10.1007/BF00285942

CHAPTER II

ANALYTICAL METHODS

1. Sampling

1.1. Hole U1473A

During expedition IODP 360 at the Atlantis Bank (winter 2015-2016), a collection of 116 samples were recovered onboard from drilled core sections by Benoît Ildefonse. Then in 2019, it was supplemented by 11 samples collected by myself during a mission at the Kochi Core Center (Japan). Samples were collected between 11.3 and 786.5 mbsf (meters below sea floor), with an average spacing of 5.5 m. All these samples are from the "working half" of drilled core sections, targeting variably deformed zones in Hole U1773A for the purpose of establishing a global picture of the gabbroic lower oceanic crust deformation in a (ultra-) slow-spreading context.

Onboard, the recovered core sections were split along a plane orthogonal to the foliation, when present, or in general in a way to have the most complete representation of existing features in both halves (MacLeod et al., 2017). Thus, the cut face of core sections on which thin sections used were made, is the plane orthogonal to the foliation (ZY plane in core reference frame, Figure 2.1). Drilled cores in Hole U1473A correspond to 9.5 m long cores of 5.87 cm of diameter. Each core is composed of ~1.4-1.5 m long sections numbered from top to bottom. The top of sections have an associated depth reported in Core Composite depth below Sea Floor (CCSF, in meter), corresponding to a sum of cores length which take into account unrecovered intervals in sections (see MacLeod et al. (2017) for details). For the sake of simplicity, I used "Meters Below Seafloor" (mbsf) for the core or sample depth in this manuscript. The selected samples are then named using the name of the core and the name of the section to which they belong, and their depth in this section. In addition, the number of the expedition, the name of the drilled hole, the method of drilling (R) and the used core half are indicated (W), such as the type of sample (depending of the analyses intended, ex: TSB), ex: 360_U1473A_69R_5_W 73/76 TSB. For simplicity, samples are only named by their core (I), section (II), and top depth (III, CCSF depth) in this manuscript: I_II_III. In case where two samples are from a same depth interval, or if several domains in the same sample are analyzed separately, a final letter (A, B, or C) is added, ex: 69_5_73_B.

Thin sections were realized by Christophe Nevado and Doriane Delmas at Geosciences Montpellier. Thin sections are ~30 µm thick and have a high-quality polished surface obtained through both mechanical and chemical polishing. This is critical for high quality electron backscatter diffraction analyses.

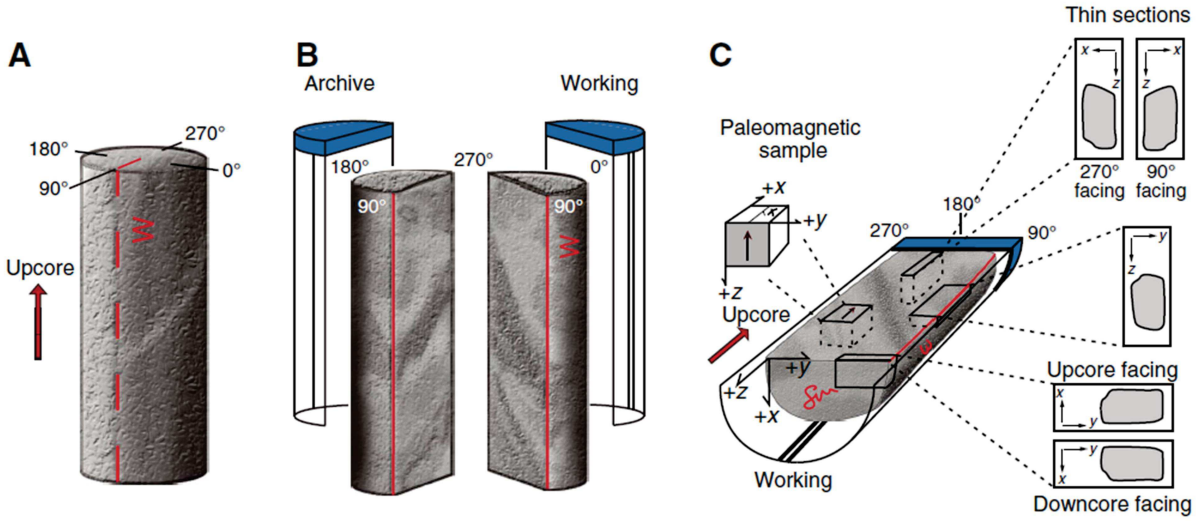

Figure 2.1 *- Core reference frame associated to splitting, and thin sections orientations (MacLeod et al., 2017).*

1.2. Bracco Gabbroic Massif

During a one-week fieldwork conducted in the Bracco-Gabbro Complex in the Internal Ligurides by Émilien Oliot and myself, I collected a suite of eighteen samples. These gabbroic samples display in total 16 deformed and 3 undeformed domains. The sampled deformed microstructures vary from protomylonites to ultramylonites, often with a well-defined foliation. A total of six samples were taken in place, and the rest corresponds to floating hand samples. When sampled in place, the foliation plane orientation and dip was measured in deformed samples. Samples taken from the same outcrop have identical numbers (ex: 03), and a letter was added to differentiate them (ex: 03D). An ultimate number was added to differentiate thin sections from the same samples (ex: 03D-1), associated to different microstructures. Similarly as for samples from Hole U1473A, thin sections (n=22) were made at Geosciences Montpellier, after being cut in the plane orthogonal to the foliation, and parallel to the lineation.

2. Electron Backscattered Diffraction

2.1. Equipment and acquisition parameters

Electron Backscatter Diffraction (EBSD) analyses were all performed at Geosciences Montpellier on 113 microstructural domains from Hole U1473A with two different Scanning Electron Microscopes (SEM) and equipped EBSD detectors, depending on the step size wanted. Concerning the Bracco ophiolite, eight microstructural domains were analyzed. Most of the analyses were done with the CamScan X500FE Crystal Probe SEM equipped with the Oxford Instrument Nordlys® detector that was changed for the Symmetry® detector after about a half of

samples were analyzed. The preferential use of this instrument resides in the fact that it is equipped of a FEG (Field Emission Gun) in terms of source of electrons, allowing a high resolution for measurements. Microstructural domains with coarser grain sizes were analyzed with the Jeol 5600 SEM equipped with the Oxford Instrument NordlysNano EBSD detector with a larger step size (generally higher than 20 µm). This instrument is equipped of a tungsten filament as the source of electron. The scanning resolution was adapted to the grain size in the analyzed samples, with the objective to have a step size of about a third of the size of smallest grains. Overall the step size used varies between 1.6 to 30 µm, and was mainly around 5-10 µm as a great part of samples display small recrystallized grain sizes. The diffraction pattern acquisition was achieved at a working distance of 25 mm, an indexing speed of 140 Hz, an acceleration voltage of 20 kV, and a probe current of 10 nA. The indexing rate was relatively high, 90% on average, and ranges from 73% in intensely altered domains to 98% in pristine domains. Finally, the size of the mapped area varies together with the grain size (and chosen step size) for analytical time requirements. It principally consists of 1-2 cm² areas in domains of reduced grain sizes, or to the entire thin section (~3-3.5 cm²) in coarse-grained domains. Regarding the acquisition, 59 samples of Hole U1473A were already analyzed at the beginning of my PhD project, and I did the 54 remaining analyses. I this EBSD data set, ~10-15 samples were analyzed with the Crystal Probe – Nordlys couple and the rest with the Crystal Probe – Symmetry couple with systematic EDS (Energy Dispersive Spectroscopy) associated chemical analysis. The resolution of chemical maps is similar to the associated EBSD maps. The eight EBSD maps on samples from the Bracco ophiolite were similarly analyzed with the Crystal Probe – Symmetry couple with EDS.

2.2. Principle of the method

The EBSD technic permits through SEM the analysis of the crystallography of a material (metals, alloys, ceramics, ice, rocks…). Measurements are conducted by sending high-energy electrons at the surface of the material through a stationary electron beam. The induced diffraction of electrons at the surface forms an Electron Backscattered Pattern (EBSP), sometimes referred to as Backscattered Kikuchi Pattern (BKP). The electrons under Bragg configuration form the EBSP that is detected on the fluorescence (or phosphor) screen of the EBSD detector. An angle of 70° between the electron beam and the analyzed surface is used after Monte-Carlo simulations demonstrated improved backscatter diffraction under these conditions. Furthermore, this minimizes the effect on diffraction of the different mineral species present and provides a clear EBSP (e.g., Dudarev et al., 1995; Reimer, 1998). The EBSP obtained is characteristic of both the crystallographic structure (i.e., a mineral species) and the orientation in the analyzed region. A set of EBSP acquired in a region of a sample permit to analyze, among other crystallographic characteristics, the phase distribution, grain boundaries, or intragranular deformation (e.g.,

Baudin, 2010). The first observation of diffraction patterns formation in backscatter mode under electronic bombing of a material surface was reported by Nishikawa and Kikuchi through transmission electron microscopy (TEM; Nishikawa & Kikuchi, 1928). The EBSP consists of a set of bright bands forming prominent distinct zones when they overlap, the zone axes, and is a gnomonic projection of the crystal lattice on the flat phosphor screen (Figure 2.1). The Kikuchi lines that bounds Kikuchi bands corresponds to the pair of the diffraction cones formed by diffraction of electrons on a set of parallel lattice planes (i.e., a family of planes). Generally, several Kikuchi bands are imaged by diffraction and the angles between the plane normal orientations are the interplanar angles. The angular width of Kikuchi bands $\{hkl\}$ corresponds to the double of the Bragg angle ϑ_{hkl}, and then the band width is linked to the space in-between lattice planes by Bragg's law (e.g., Schwartz, 2009):

$$2 \cdot d_{hkl} \cdot sin\,(\vartheta_{hkl}) = n \cdot \lambda\,,$$

where n is the order of reflection and λ the wavelength of the incident electron beam, depending on the accelerating voltage of the SEM. A decrease in the accelerating voltage results in an increase in electron wavelength, and then in a widening of the Kikuchi bands, to the first order by the inverse of the voltage square root.

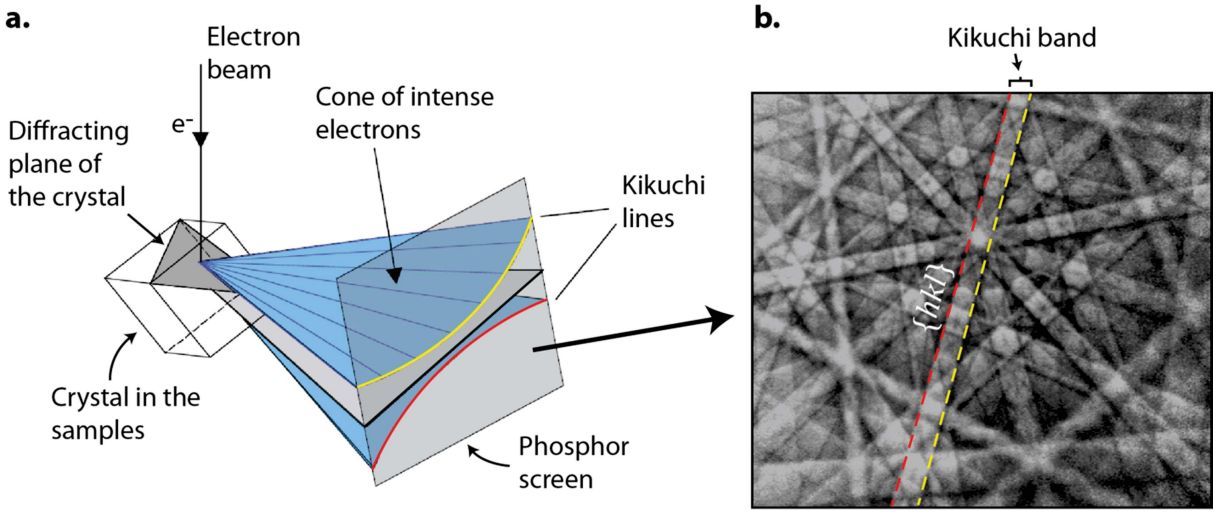

Figure 2.2 *- Principle of electron diffraction and formation of an Electron Backscattered Pattern (modified after Schwarzer et al., 2009). (a) Schematic representation of the induced diffraction of electrons on a plane of a crystal lattice, and its capture on a phosphor screen. (b) Example of an Electron Backscattered Pattern in cadium bombed at 20 keV captured by the EBSD detector. Note that the Kikuchi lines (in yellow and red) formed by the two diffracting cones (in blue in (a)) are the edges of the Kikuchi band. Each Kikuchi band corresponds to a specific {hkl} plane of the crystal lattice.*

In the generated EBSP, the zone axes (intersections of Kikuchi bands) positions are independent of the accelerating voltage used, and characteristic of the crystal symmetry and orientation. Then, the determination of positions and width of some bands in the pattern is sufficient for the characterization of the analyzed region of a material. Still, the analysis of EBSP by computers remains a hard task as it is generally noisy and because the Kikuchi bands are diffuse broad bands, not straight, with heterogeneous intensity distributions. For this reason a special processing is performed, using the Hough transform (a derived transformation of the Randon transform; e.g., Radon, 1917; Hough, 1962). The Hough transform consists of a change from the image coordinate system (x, y) to that of the Hough space (ρ, ϑ):

$$\rho = x \cdot \cos(\vartheta) + y \cdot \sin(\vartheta)$$

Thus, a straight line in the image space (x, y) is transformed to a single point (ρ, ϑ) in Hough space, easier to detect, by using the perpendicular distance (ρ) of the Kikuchi band from the origin, and its angle (ϑ) with respect to the x axis (Figure 2.3). Once the EBSP is indexed by the computer, the crystal lattice orientation is known, such as the crystal symmetry (i.e., the phase is determined; Baudin, 2010).

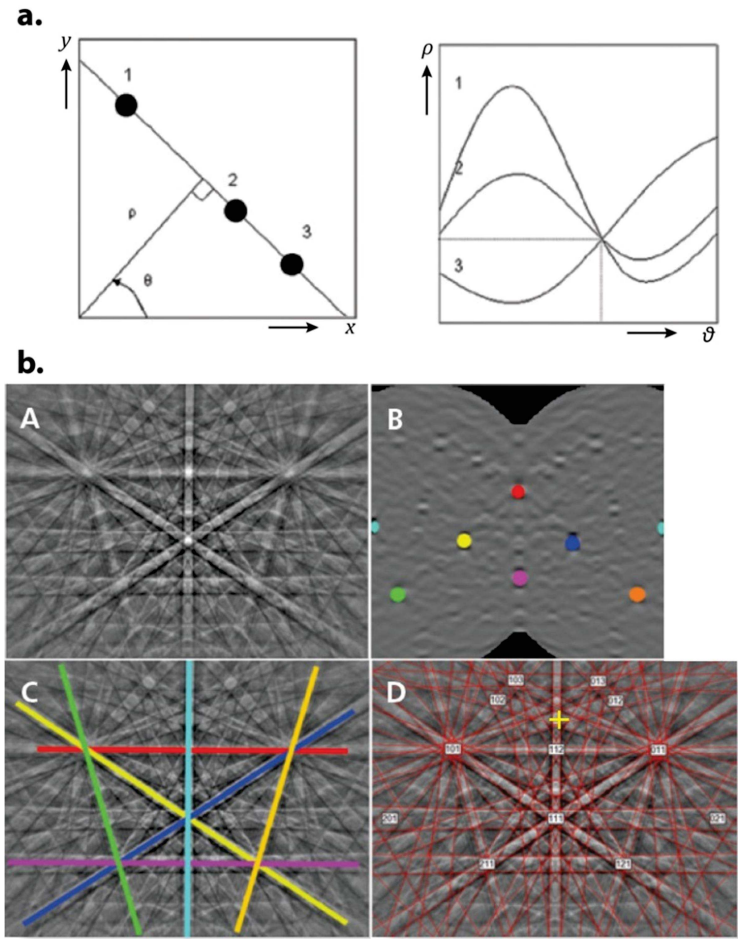

Figure 2.3 *- Transformation from image to Hough space (modified after Oxford Instruments documentation, 2020). (a) Conversion of lines into points in Hough space. (b) Identification of Kikuchi bands of the diffraction pattern (EBSP) through the Hough transform. A: acquired diffraction pattern. B: Identification and coloring of points (i.e., the transformed Kikuchi bands) corresponding to peaks in the Hough space. C: Fitting of bands corresponding to the peaks identified in Hough space. D: Final indexed diffraction pattern with Kikuchi lines shown (red), such as the pattern center (yellow cross).*

2.3. Initial data processing

Data acquisition was performed with the Oxford Instrument AZtecHKL softeware, and the initial processing was performed with the CHANNEL 5 Tango program. The AztecHKL processing consists on the montage of the EBSD map through the fitting of neighboring analyzed fields edges (fields of ~500 µm²) using the inverse pole figure (IPF) orientation map. Then, data are exported in a "*.cpr" file (Channel Project File) to be opened in CHANNEL 5. The program Tango is used to do a first step of noise reduction by eliminating wild spikes (i.e., isolated pixels incorrectly indexed), followed by a low level (level 6) of zero solutions pixels (i.e., pixels where the EBSP have not been indexed) correction, from the information of at least 6 neighboring pixels. Then the project is saved and exported as a "*.ctf" file (Channel Text File) to be processed with the Matlab® MTEX toolbox (version 5.3.1, e.g., Mainprice et al., 2015). For a few number of samples, a correction of bad indexed pixels between clinopyroxene and orthopyroxene was performed before the project was exported using the chemical information obtained by the EDS analysis conducted in parallel to the EBSD analysis. The list of phases to index during the acquisition depended on the samples, but the following phases were always present: olivine, clinopyroxene, plagioclase, magnetite, orthopyroxene, and ilmenite.

All the data processing used to produce maps and pole figures was done with MTEX. My objective was to generate a generic script to process uniformly the large set of EBSD data acquired to produce a consistent database. All EBSD data were processed with the depth in the hole pointing downward in maps and pole figures to image the variation of texture orientation in Hole U1473A. The script used was originally provided by Benoît Ildefonse, and further developed and completed by myself for the purpose of the project (see next sections). Only pixels with mean angular deviations (i.e., the angle between the acquired diffraction pattern and the indexing solution) below 1°, and grains containing more than 5 pixels have been considered in data sets. The grain segmentation angle used to identify grain boundaries is 10°. Misorientations lower than 2° between two neighboring pixels are not been considered when discussing misorientation characteristics (Trimby et al., 1998). For the orientation analysis (pixels and grains) the method implemented in MTEX uses the Euler angles φ_1, ϕ and φ_2 (Mainprice et al., 2015). This method was introduced by Bunge (1982), and utilizes the Euler angles to fit the three axes *X*, *Y* and *Z* of the reference specimen coordinate system K_A to the axes *X'*, *Y'* and *Z'* of the crystal coordinate system K_B (Figure 2.4a). The successive rotations are achieved as follow: a rotation of φ_1 around the *Z'* axis (Figure 2.4b), a rotation of ϕ around the *X'* axis (Figure 2.4c), and a rotation of φ_2 around the *Z'* again (Figure 2.4d).

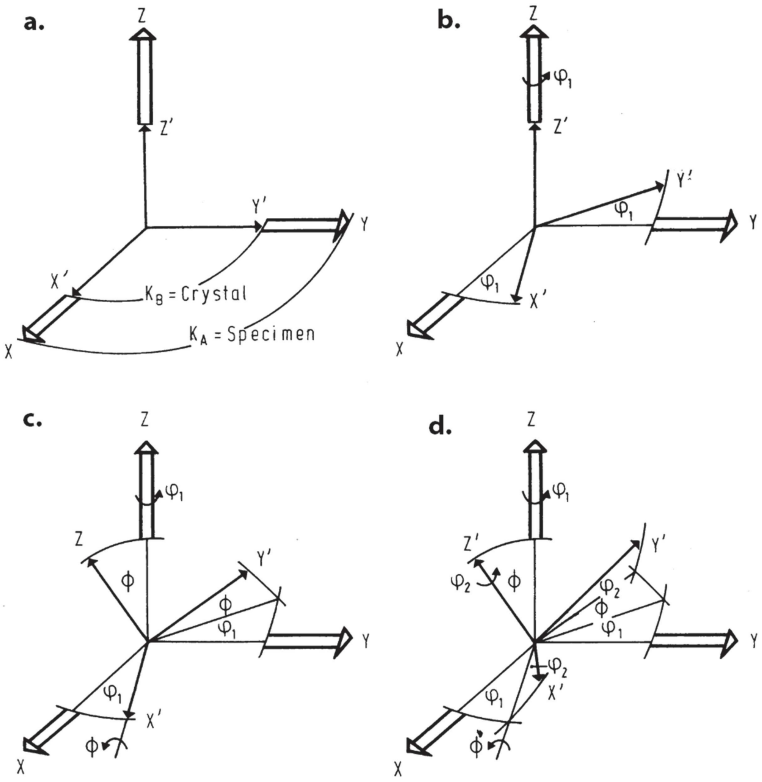

Figure 2.4 *- Definition of the Euler angles and application of rotations (after Bunge, 1982). From the initial state (a), three rotations are applied: (b) of φ_1 around Z', (c) of ϕ around X', and (c) of φ_2 around Z'.*

With this definition, we can define the rotation *g* applied for each crystals of the analyzed area:

$$g = \{ \varphi_1, \phi, \varphi_2 \}$$

This permit to represent the rotation of each crystal of the sample in the three-dimensional Euler space (φ_1, ϕ, and φ_2; Bunge, 1982).

Important parameters in the EBSD analysis are based on the orientation of pixels, and on the difference in orientation (i.e., the misorientation) between neighboring pixels. The most important is the Orientation Distribution Function (ODF), which characterizes crystal orientations in a sample. The ODF is a function depending on *g*:

$$\frac{\Delta V(g)}{V} = f(g)\, \mathrm{d}g,$$

where $dg = (\sin(\phi) \cdot d\varphi_1 \cdot d\phi \cdot d\varphi_2) / 8\pi^2$ is the rotational invariant volume element of the orientation variation from which the ODFs are normalized (Mainprice et al., 2015). Then, *g* represents an orientation and *V(g)* is the volume portion of the ODF. For EBSD analyzes, we consider $V(g) = 1$ so that the diffraction volume is similar at each point. $\Delta V(g)$ is defined as the volume portion of a crystal with an orientation within a volume element *dg* of *g*, and *V* being the total volume of crystals of the considered phase in all the sample. Thus the ODF provides

information about the area fraction of crystals of a phase having a similar (or close) crystallographic orientation.

To evaluate the ODF and its meaning in a sample, the texture index J_{ODF} can be used. This index is defined as:

$$\boldsymbol{J_{ODF} = \int |f(g)|^2 dg = \|f\|^2_{L^2}}$$

The mathematical definition of the texture index J_{ODF} involves the square of *f*, defining it as a function of L2-norm (Mainprice et al., 2015). In case of a uniform distribution (i.e., no preferred orientation of crystals in the phase), $J = 1$. When a crystallographic orientation extensively prevails on others *J* tends toward ∞. However, in general a value of $J > 10$ results from a low number of analyzed grains and is statistically meaningless. When J_{ODF} is noticeably higher than 1 and statistically meaningful, the considered phase is said to have a crystallographic preferred orientation (CPO). In the regard of low number of analyzed grains, Satsukawa et al. (2013) proposed a limit of 100 analyzed plagioclase grains for a statistical meaning of the computed J_{ODF} values (Figure 2.5a). However, the distribution of J_{ODF} values remains noticeably variable between 100 to 1000 grains. Based on the dataset acquired during my PhD, it clearly appears that a number of analyzed plagioclase grains below 1000 produce abnormal J_{ODF} values (Figure 2.5b). Also, from 1500 to 3000 measured grains, differences in calculated R^2 associated to linear regressions are high and close from each other, and the dispersion of data is lower. This indicates that a limit of 1000 analyzed grains is reasonable. Thus, the following analyses on J_{ODF} values are performed on samples where > 1000 grains were analyzed. Another type of texture index, J_{MDF}, can be used and derived from the Misorientation Distribution Function (MDF). Rather than the similarity in orientation between crystals of a phase, the MDF is based on the difference in orientation. As this index is not of use in this manuscript it will not be further detailed.

In 2005, Skemer et al. introduced another index of strength for crystallographic fabrics: the Misorientation index (M index). It is based on the difference between a theoretical uniform distribution and the distribution of uncorrelated misorientation angles for a considered phase. The M index can be defined for a uniform distribution $f^{(U)}(\theta)$ and a measured distribution $f^{(M)}(\theta)$ in a general form as follow:

$$\boldsymbol{M = \frac{1}{2} \int |f^{(U)}(\theta) - f^{(M)}(\theta)| \, d\theta = \frac{1}{2} \left\| f^{(U)} - f^{(M)} \right\|_{L^1}}$$

It is also possible to define it in a discretized form through a reference table for defining the uniform distribution $\boldsymbol{D_i^{(U)}}$ and a histogram with a 1° bin width for the measured distribution$\boldsymbol{D_i^{(M)}}$:

$$\boldsymbol{M = \frac{\theta_{max}}{2n} \sum_{i=1}^{n} | D_i^{(U)} - D_i^{(M)} |}$$

The M index is then the L1-norm of the difference between the uniform and the measured distributions. This M index varies from 0 for a random misorientation distribution to 1 for a single orientation fabric (Skemer et al., 2005).

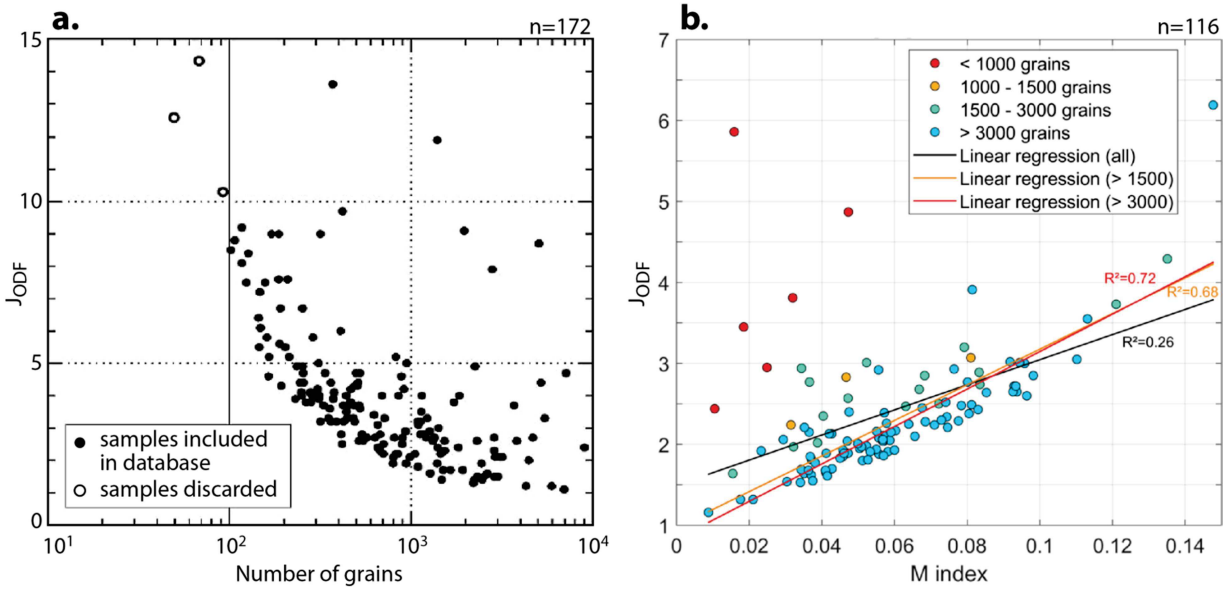

Figure 2.5 *- Statistical evolution of J_{ODF} values. (a) Evolution of J_{ODF} values with the number of analyzed grains (after Satsukawa et al., 2013). (b) Evolution of J_{ODF} values with the M index and the number of grains (this study). Samples with less than 1000 measured grains display abnormal values of J_{ODF} with respect to M index values. Note that the M index is not affected by the number of measured grains (Skemer et al., 2005). Linear regressions suggest that above 1000 analyzed grains the calculated J_{ODF} values can be considered meaningful.*

For convenience we used pole figures representations of CPO rather than ODF and MDF representation, as it consists of a stereographic projection in the specimen (i.e., the sample) reference frame. An operation through a Radon transform of the ODF is applied to define the pole density *P* of pole figures, for unit axes ±*h* and a unit direction *r* (Mainprice et al., 2015):

$$\boldsymbol{P(\pm h, \mathbf{r}) = \frac{1}{2\pi} \int_{(\pm \mathbf{g}h=r)} f(g)\mathbf{d}g}$$

The function component $P(\pm\boldsymbol{h}, \circ)$ corresponds to the pole figure, with ±*h* being a unit axis parameter in crystal coordinates. In the same way, $P(\circ, \boldsymbol{r})$ corresponds to the inverse pole figure, as ***r*** is a unit axis parameter in specimen coordinates. These unit vectors can be expressed in spherical pole angles (α, β), with α the polar angle varying in [0, 180], and β the azimuthal angle varying in [0, 360]. The fabric strength associated to a ***h***-pole figure $P(\boldsymbol{h}, \circ)$ can be calculated by:

$$\boldsymbol{PfJ} = \int |\boldsymbol{P(h,r)}|^2 \, \mathbf{d}\boldsymbol{r} = \|\boldsymbol{P}\|_{L^2}^2$$

PfJ is then a rotationally invariant functional of *P*, as d***r*** = sin *α dα dβ / 4π* is the rotationally invariant surface element of the unit sphere. The texture index of the pole figure *PfJ* evolves similarly as the J index, being equal to 1 for a random distribution, and tending toward high values in case of well define CPOs.

Pole figures have been used for to interpret CPO in samples. The data plotted corresponds to average grain orientations which permit to give the same weight to all grains in the sample, regardless to their size. Plotting CPO calculated on the basis of pixels orientations instead of average grain orientations results on the over-representation of large grains orientation. Another representation of pixel (or grain) orientations is the inverse pole figure (IPF), where orientations are regarded in the crystallographic coordinate system. Then, three IPF are classically used in the *X*, *Y*, and *Z* sample directions (cf. figure 2.4 and related explanations), and indicate which crystallographic axes in the analyzed mineral are parallel to sample directions.

2.4. Twins processing

In order to work with "true" grains instead of twinned domains when considering grain average orientation data set in samples, twins in grains must be identified and separated from grain boundaries. This concerns mainly plagioclase grains, but also clinopyroxene and ilmenite mineral phases.

The first step is the identification of twin boundaries through their misorientation angle and boundary axis and/or plane. In plagioclase, a majority of twin boundaries forms on the (010) plane by a rotation of 180°, namely the Albite twins. Other common twins are: the Manebach twin forming along the (001), the Ala twin occurring along the [100] direction, the Pericline twin along [010], and the Carlsbad twin along [001] (e.g., Smith, 1974). The plot of misorientation axes of grain boundaries with a misorientation of 180° ± 5° indicates the possible twin boundaries present in the sample (Figure 2.6a). We see in this example that potentially all the five families of plagioclase twin boundaries seem to be present in samples, and that those around (010) and or [010] are dominant. The selection of pixels belonging to grain boundaries with a 180° misorientation that corresponds to the known plagioclase twin axes indicates a dominance of Albite and Pericline twins in grains (Figure 2.6b and c). We can evaluate here the necessity to select twin boundaries on both their misorientation angle and rotation axis or plane, rather than to restrict the analysis to misorientation angles (compare IPF plot in figure 2.6a and b). After the twin boundaries are identified, they are eliminated and the twinned domains merged into a single host grain (Figure 2.6d). After the merging process the number of grains can be drastically changed, as in this example where is drops from 2709 to 559 grains. In terms of orientation, the merged grain is attributed a mean orientation corresponding to the largest twin domain merged into it (Figure 2.6d).

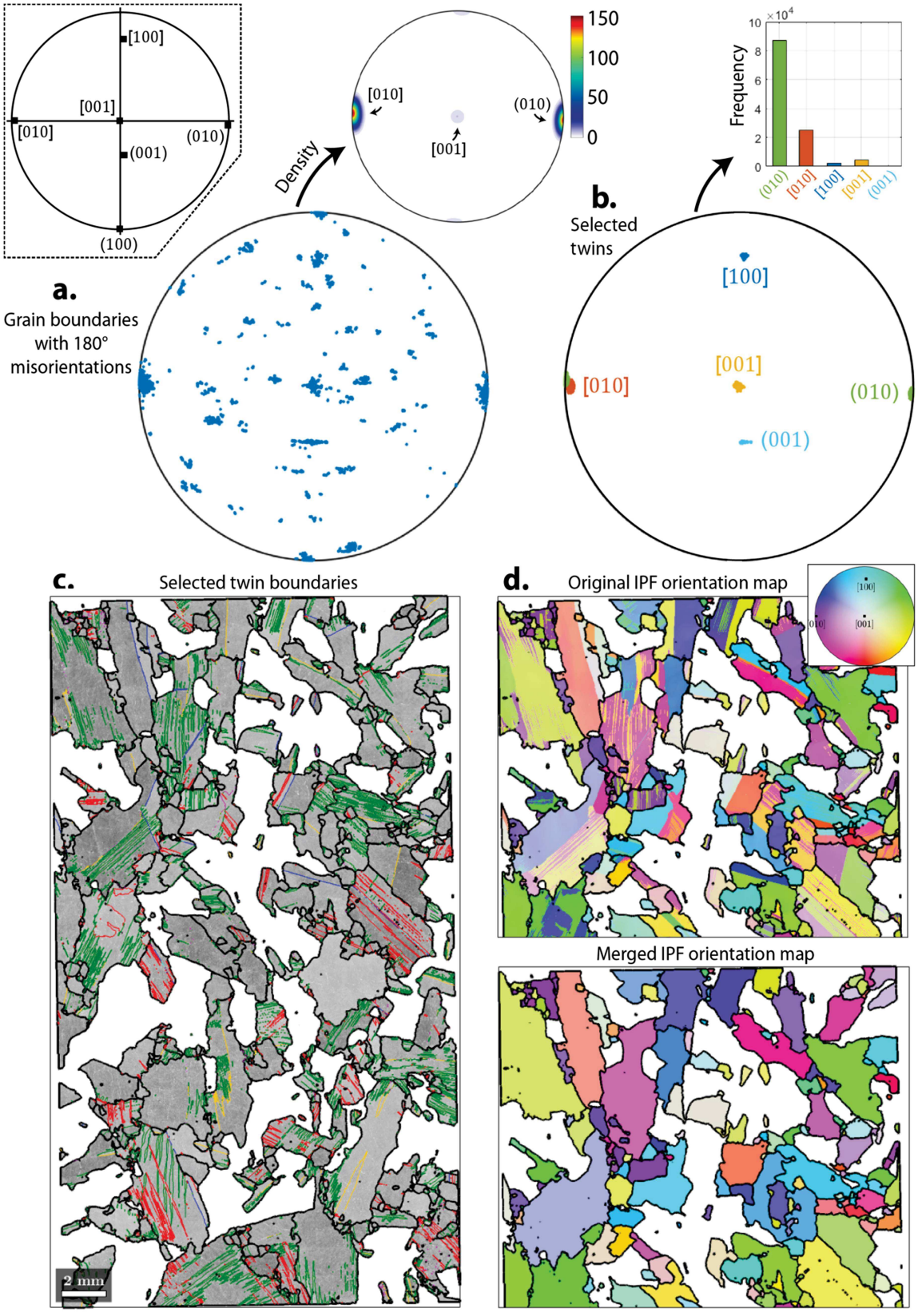
[100]
[001]
[010]
(010)
(001)
(100)
Density
150
100
50
0
[010]
[001]
(010)
Frequency
×10^4
10
8
6
4
2
0
(010)
[010]
[100]
[001]
(001)
a.
Grain boundaries with 180° misorientations
b.
Selected twins
[100]
[001]
[010]
(010)
(001)
c.
Selected twin boundaries
d.
Original IPF orientation map
[100]
[010]
[001]
Merged IPF orientation map
2 mm

Figure 2.6

Figure 2.6 *- Twin boundary selection in plagioclase, example in sample 88_5_117 (subophitic olivine-gabbro). (a) IPF plot of all boundary pixels with a 180° misorientation, and plot of associated densities of clustering. The upper left inset indicates the orientation of the main crystallographic axes and planes in the IPF plot. (b) Selected pixels corresponding to twin boundaries in plagioclase. Their respective proportions are shown in the upper right histogram. Note the dominant proportions of Albite and Pericline twins. (c) Grain boundaries identified as twins on top of the band contrast map. Note the correspondence of colors with (b). (d) Orientation map with IPF coloring in the x direction for original pixel orientation and average grain orientation after twin merging. The color key of orientations is given in the top right corner. In both maps the thick black lines correspond to the considered grain boundaries after twin merging into their host grain.*

This stage of twin identification and merging is important for further analyses such as CPO based on average grain orientation data set, but also for grain size and shape characterizations.
The same processing was performed in clinopyroxene and ilmenite grains. In clinopyroxene the two twin axes [100] and [001] were considered. Note that generally the number of twins was limited in grains. Regarding ilmenite three axes where selected: $[11\bar{2}0]$, $[2\bar{1}\bar{1}0]$, and $[\bar{1}2\bar{1}0]$. In contrast to clinopyroxene, ilmenite grains are intensely twinned and sample 3_1_86 (containing ~29% of ilmenite) is a good example of this with the change from 30732 to 6545 grains after twin merging. The resulting grain maps have been checked by comparison with direct observations in thin section and thanks to IPFs maps.

2.5. Detection of recrystallized grains and porphyroclasts

To quantify the deformation intensity in samples, an important information is the amount of recrystallization in the constituting phases and in the entire sample. During the deformation and recrystallization of minerals, grains detach in two groups with different characteristics: porphyroclast grains, and recrystallized grains. Porphyroclasts grains are generally of comparable size than the original undeformed grains (or slightly smaller. Note that this may be incorrect for grains recrystallized through GBM, see chapter III for details), have significant accumulated internal strain, and have complex grain boundary shapes. In contrast, recrystallized grains have generally a reduced internal strain, a small size, and simple shaped grain boundaries (e.g., Tarasiuk et al., 2002; Alvi et al., 2003, 2004; Mirzadeh et al., 2012). It should be noted here that these characteristics may be modified in case of a continuous deformation over evolving conditions (P-T-fluids) or simply with the occurrence of a second episode of deformation after recrystallization (e.g., strain hardening in grains). Alternatively, high temperatures conditions to the wane of deformation could favor recovery processes, progressively erasing recrystallization features.

Two main approaches have been proposed in the literature, one based on image quality (IQ) of the acquired EBSP, and the other utilizes the crystal orientation variations (i.e., misorientations). The analysis through IQ rely on its dependence on the near-surface defect content of the material, being lower in recrystallized regions (higher IQ) as defects have been significantly evacuated from grains. However, both methods have important limitations to consider. Indeed, the IQ method is dependent, among others, on mineral phase, the crystal orientation, and the surface roughness of the material. On the other hand, misorientation-based methods depends on the angular resolution of the EBSD that is generally in the range 0.5-1.0° (Dziaszyk et al., 2010).

The method used here is based on the misorientation analysis, partly, and on two other parameters of shape and size. This choice relies mainly on the fact that the material studied is polyphased, and that the relative strength of the different phases results in topographic differences at the surface of the sample after being polished. Also, with the IQ method the quality of images will be additionally affected by alteration that can occur in pyroxene and olivine grains in the sample suite. Ultimately, a simple selection through grain size only was not chosen for reproducibility because of the varying grain sizes in the sample suite. The chosen misorientation parameter is based on the misorientation of pixels within a grain to the mean orientation of the grain, and is referred to as the "mis2mean" (Figure 2.7a). For each samples, the recrystallized fraction was calculated using the Grain Orientation Spread (GOS), corresponding to the average of the mis2mean in a grain. The GOS indicates the state of deformation within grains, and have low values in poorly deformed grains, and high values in strongly deformed grains (Figure 2.7a and b). Another parameter can be use, based on the average misorientation between a pixel (the kernel) and its neighbors (first order neighbors used here), known as the Kernel Average Misorientation (KAM; Figure 2.7c). To use this parameter at grain level, the Grain Average Misorientation (GAM, or Grain Average KAM (GKAM)) is calculated by averaging the KAM in grains (Figure 2.7d). In experimental deformation of steel it has been used efficiently the same way as the GOS, the GAM displaying lower values in recrystallized grains than in porphyroclasts in these studies (e.g., Dziaszyk et al., 2010; Mirzadeh et al., 2012). However, this parameter was not chosen for the recrystallized fraction estimation as it is always observed with an inverse evolution compared to the GOS with higher GAM values in small grains (opposed to smaller GOS values; compare figure 2.7b and d). Higher GAM values in small grains is explained by the fact that deformation continued after recrystallization, producing strain within recrystallized grains; and arises from the fact that deformation is localized within grains. This is what indicates both the mis2mean and KAM maps (Figure 2.7a and c). The localized nature of deformation within grains results in a higher density of misorientation in small grains than in larger ones as the latter contains larger undeformed regions.

The calibration was performed on tens of samples with varying recrystallized fractions, phase proportions and recrystallized grain sizes.

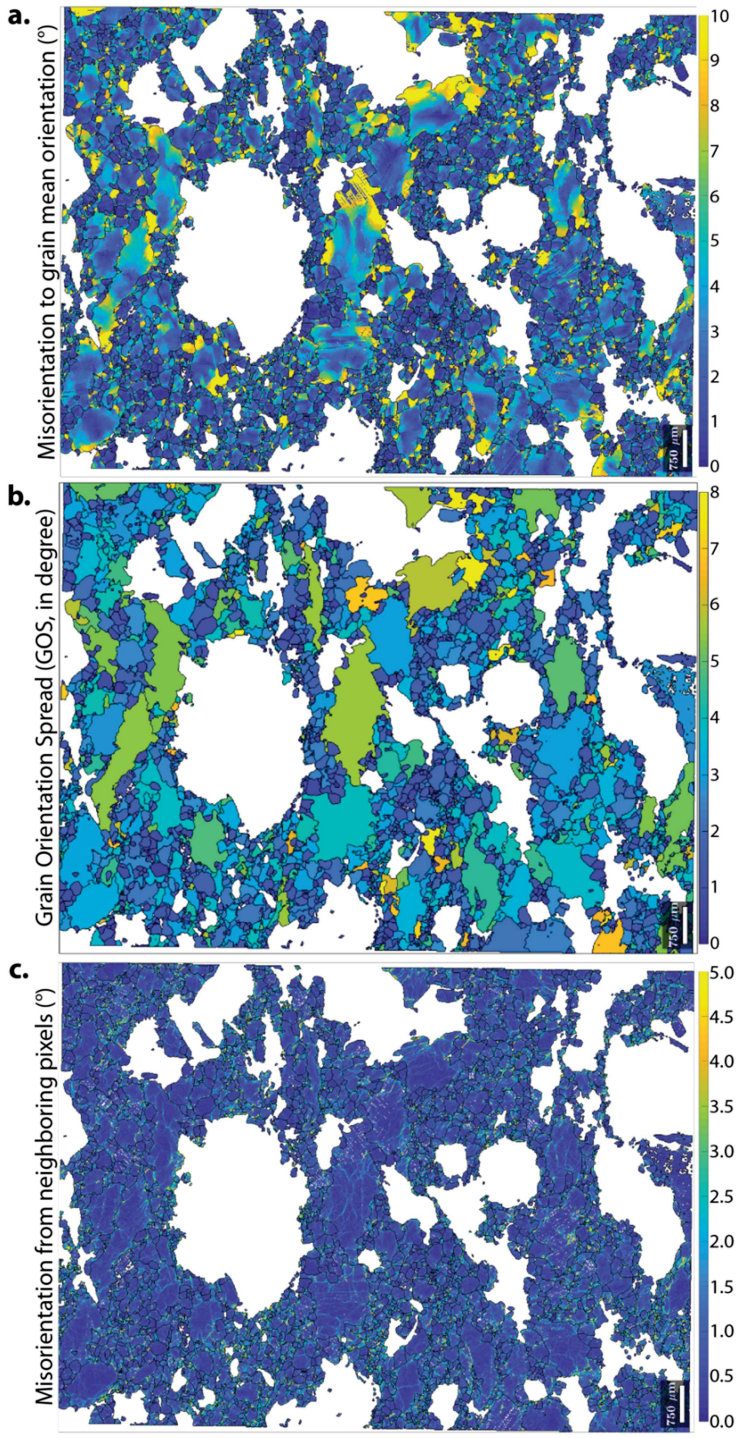

Figure 2.7 *- Parameters used for recrystallized fraction estimation. Presented for plagioclase grains from the porphyroclastic olivine-gabbro 16_1_121_B. See text for details.*

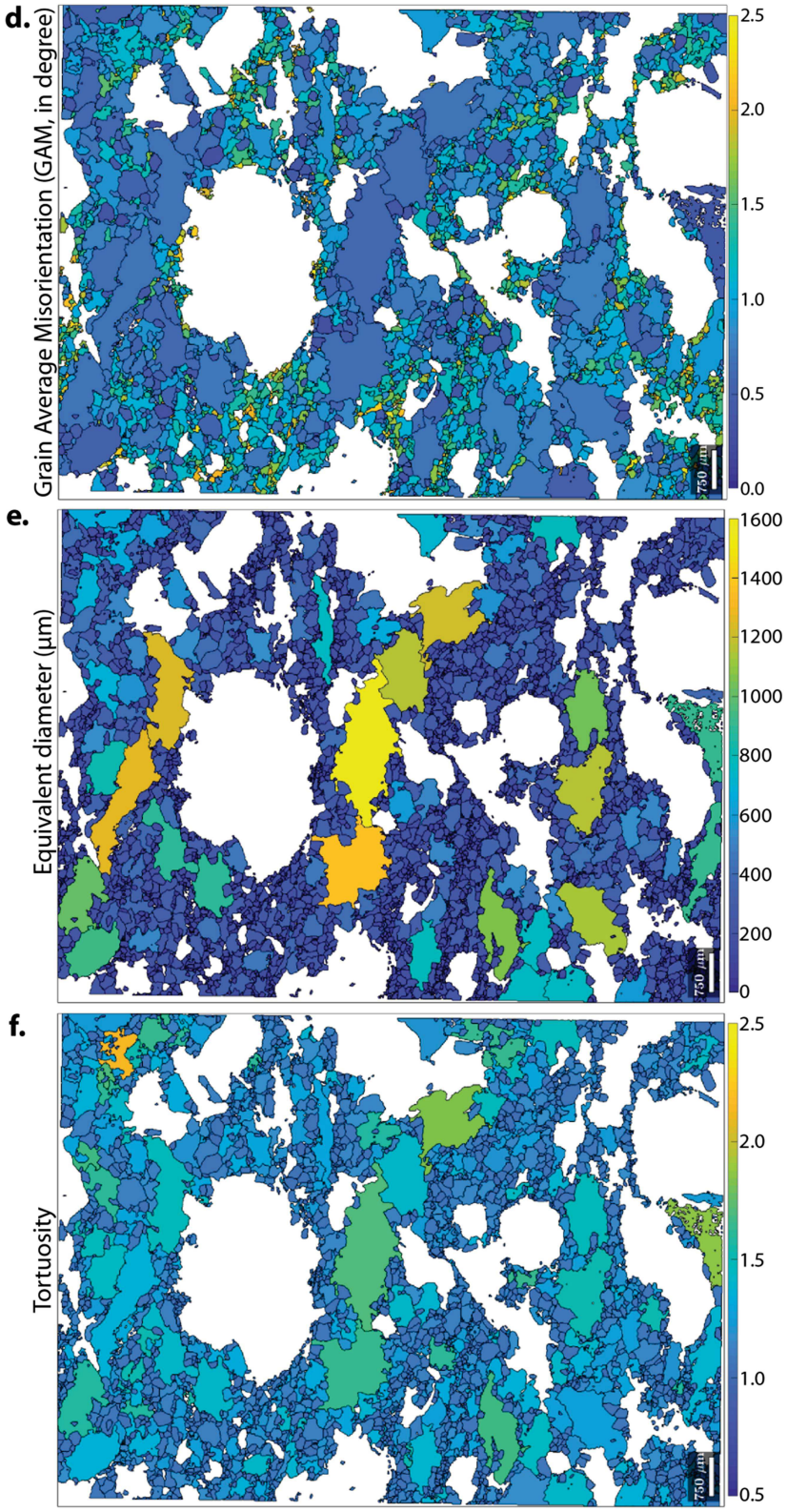

Figure 2.7 (continued)

This results in the choice of a unique value for each parameter, for all phases. The GOS-based recrystallized fraction corresponds to grains with a GOS < 2°, a size < 700 µm, and a tortuosity < 1.4. For the grain size, the parameter used is the equivalent diameter, which corresponds to the diameter of a disk of the same area as the grain (Figure 2.7e). The tortuosity is a shape parameter defined as the ratio between the grain perimeter and the convex hull perimeter. The convex hull perimeter corresponds to the envelope of the grain, in the same way an elastic film would cover the surface of a walnut. The tortuosity is 1 when a grain has no boundary irregularities, and increases as the grain boundary is getting lobate or serrated (Figure 2.7f). Concerning the GOS, values of the same order (1-3°) are reported for recrystallized fraction estimation in aluminum alloy and in steel (e.g., Alvi et al., 2003; Dziaszyk et al., 2010; Mirzadeh et al., 2012). The obtained value for the total recrystallization fraction is considered as a lower bound.

2.6. Intragranular misorientation analyses

Intragranular misorientations consist of misorientations measured between 2° and 10°. The upper value correspond to the segmentation angle chosen to define grains, and the lower value correspond to the confidence bound assumed with respect to the angular resolution of the EBSD (Trimby et al., 1998). The analysis of intragranular misorientations permits to investigate the subgrain structures formed in grains as a result of deformation. The density of subgrain structures formed into a grain provides a proxy of its internal strain, as this reflects the activation of slip systems to reduce dislocation density in the grain (see chapter I, section 3). An approximation of the active slip systems that formed subgrain boundaries is possible through the characterization of the misorientation axis of the boundaries (Trépied et al., 1980; Lloyd et al., 1997). An example is provided in plagioclase grains from the porphyroclastic olivine-gabbro 16_1_121_B in figure 2.8. In this example, plagioclase grains display a strong maximum of misorientation rotation axes (MRA) around the [100] axis at subgrain boundaries (Figure 2.8a). In parallel, pole figures indicate a CPO characterized by the alignment of crystal (010) planes close to the foliation orientation, and the clustering of [100] axes in the (010) plane (Figure 2.8b). It is possible to plot on a map the subgrain boundaries calculated in plagioclase grains (Figure 2.8b), as well as to highlight the subgrain boundaries with their misorientation axis being [100] (Figure 2.8c). In most crystal symmetries, a “tilt” subgrain boundary (build-up by edge dislocations) has its MRA lying within the slip plane of the slip system which formed it, and for a “twist” boundary (build-up by screw dislocations) the MRA is orthogonal to the slip plane (except in plagioclase of triclinic symmetry where it oblique). In case of a tilt wall, the Burgers vector is orthogonal to the misorientation axis and also lies in the slip plane. Then if we assume that the identified subgrain boundaries are “tilt” and we consider the alignment of (010) planes close the foliation, we can deduce that subgrain boundaries result from the activity of the [001](010) slip system (e.g., Kruse et al., 2001)

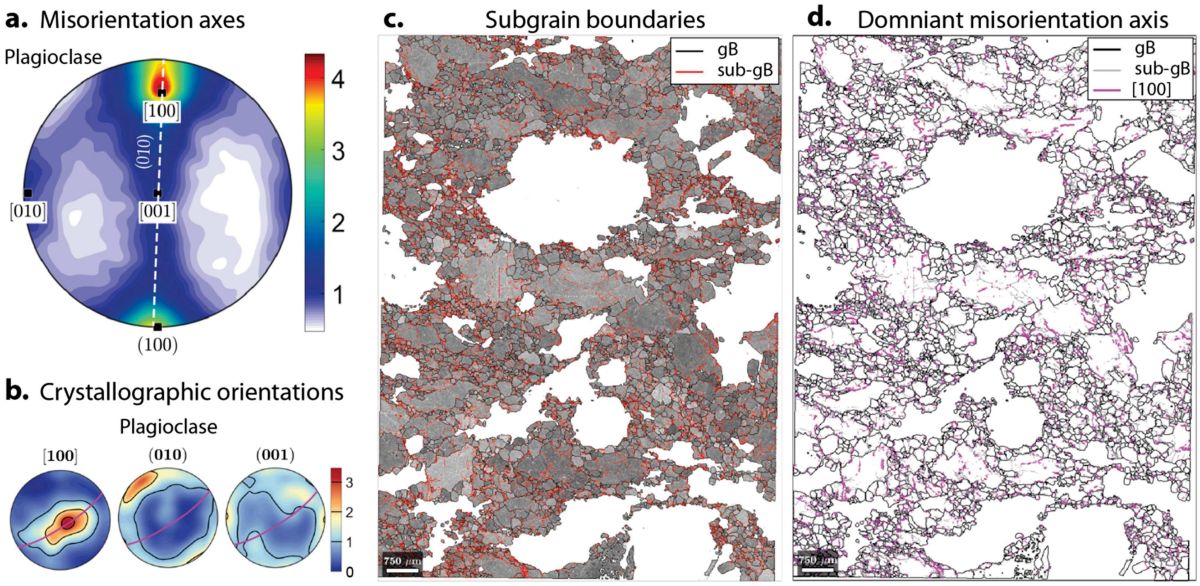

Figure 2.8 *- Misorientations and crystallographic orientations in plagioclase grains from porphyroclastic olivine-gabbro 16_1_121_B. (a) Misorientation rotation axes at subgrain boundaries plot in crystal coordinates. The three principal crystallographic directions are plotted so as the trace of the (010) plane. (b) Pole figures of average grain orientations. The trace of the (010) plane of plagioclase is indicated in purple, and is very close to the foliation plane in the rock. (c) Subgrain boundaries (red) on top of a band contrast map in plagioclase. (d) Map showing the identified subgrain boundaries with a [100] misorientation rotation axis (purple).*

3. Electron Probe Micro-Analyses

3.1. Equipment and acquisition parameters

Quantitative mineral chemical analyses were performed in collaboration with Pierre Lanari at the Institute of Geological Sciences of the University of Bern using a JEOL JXA 8200 superprobe instrument. A total of six quantitative maps were acquired in samples from Hole U1473A, and five other maps for the Bracco ophiolite study. Thin sections were carbon coated to ensure the electron evacuation onto the sample surface during measurements. Measurements were done with an accelerating voltage at 15 keV and a beam current of 20 nA for spot analyses and 100 nA for mapping. For spot analyses, background corrected count rates were calibrated using synthetic and natural standards including albite (Na), forsterite (Mg), anorthite (Ca, Al), orthoclase (Si, K), magnetite (Fe) pyrolusite (Mn), rutile (Ti), Ni-metal (Ni) and spinel (Cr). X-ray maps were calibrated using a set of spot analyses acquired in the mapped area and used as internal standards. All elements but Ni, P, S, Ti, and Mn were analyzed by a wavelength dispersive X-ray spectrometer (WDS), whereas the five other were analyzed by an energy dispersive X-ray

spectrometer (EDS). The step size was adapted for each map to the length of the area to be mapped and to the grain size. The size of mapped area varies from ~7 mm² to 30 m².

3.2. Principle of the method

An analysis through an Electron Probe Micro-Analyzer (EPMA, also called microprobe) consists on the emission of a focused electrons beam that will hit the surface of a sample, and the collection of the X-ray photons emitted. Within the electron gun, the heat of a tungsten filament cathode to 2700°K generates electrons that are bombed orthogonal to the samples surface. The collision of electrons at the surface of the sample induces the excitation of atoms which release their energy by the emission of characteristic X-ray photons, secondary electrons, backscattered electrons, etc. (Figure 2.9). The wavelength of emitted X-rays is detected in the WDS (or/and EDS) collectors that analyze and quantify the X-ray spectra to determine elements. WDS spectrometers and the sample are spatially organized to respect Bragg's law. Typically, modern microprobes are composed of five WDS. To achieve the analysis of nine elements it is then required to do two passes of acquisition. The order of element measurements is of importance as some like Na, K and Ca (light elements) produce a local diffusion of electrons, and have to be measured first.

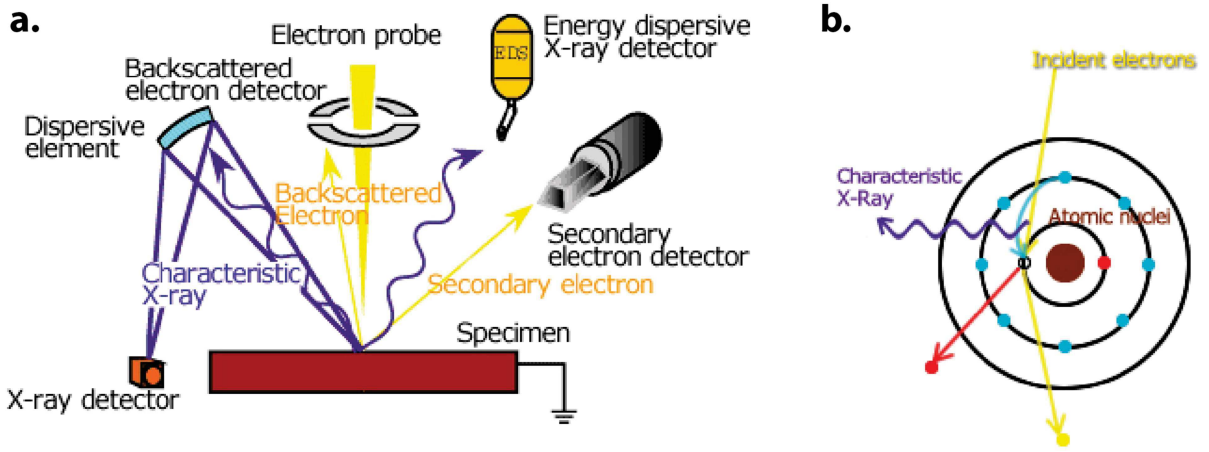

Figure 2.9 *- Principle of the EPMA analysis. (a) Schematic representation of the EPMA analysis with the incident electron beam producing electrons and X-ray emission by hitting the specimen (or sample) surface then collected in detectors. (b) Interaction of electrons with atoms at the surface of the sample producing an X-ray emission characteristic of the excited atom.*

3.3. Quantitative compositional maps processing

Data and maps used in this project were processed using XMAPTOOLS 3.4.1 (Lanari et al., 2014, 2019). The first steps during the analysis consist of scanning a sample area, in which spot analyses are performed for calibration. Through a binary diagram selection, the different phases in the map are identified by their chemistry (Figure 2.10a and b). Once the pixels are classified by phase, the use of spot analyses permit to calibrate pixel values and to recalculate them into oxide weight percent (wt.%; Figure 2.10c). During this calibration, all elements (except P and S) are checked and corrected from background when needed. Once the pixels of a phase have been calibrate, it is possible to calculate the structural formulae of the phase and then to display the results in terms of element per formula unit. In additions, classical ratio such as the *X*Mg (*X*Mg = Mg / (Mg + Fe ± Mn)) or $An_{\%}$ or *X*an (*X*an = Ca / (Ca + Na + K)) are automatically computed in the same time. The objectives of quantitative chemical mapping in my PhD project were to characterize chemical variations in phases, identify phase compositions, and extract bulk composition for thermodynamic modeling. The bulk composition extraction of the mapped area required to merge back pixels separated in the phases to which they belong after being calibrated (i.e., all pixels are considered, and they are expressed in wt.%). The composition extracted is intended to be representative of the whole rock composition. Then, the bulk composition measured in the sample in 2D needed to be extrapolated in 3D. To do so, the volume of each phase is necessary to correct the 2D bulk composition. This correction requires the phases densities are known as the final bulk composition correspond to the sum of the wt.% of each phase multiply by the ratio between the density of the phase and the bulk density of the sample (Lanari & Engi, 2017). The extracted bulk composition is given in wt.%.

Figure 2.10 *- Selection of phases in XMAPTOOLS in sample 88_5_117. (a) Presentation of measured pixels in a binary diagram of Ca versus Mg elements (in counts) with user manual selection (colors), and associated pixel density indicating the family of phases. (b) Map obtained through phase selection performed in (a). NaM corresponds to unselected pixels (<<1%). Selected phases are here, from group 1 to 6: olivine, orthopyroxene, clinopyroxene, amphibole, plagioclase, and pyrite. (c) Ca element map with spot analyses location on top (cross and purple circles). The scale bar length is 2 mm.*

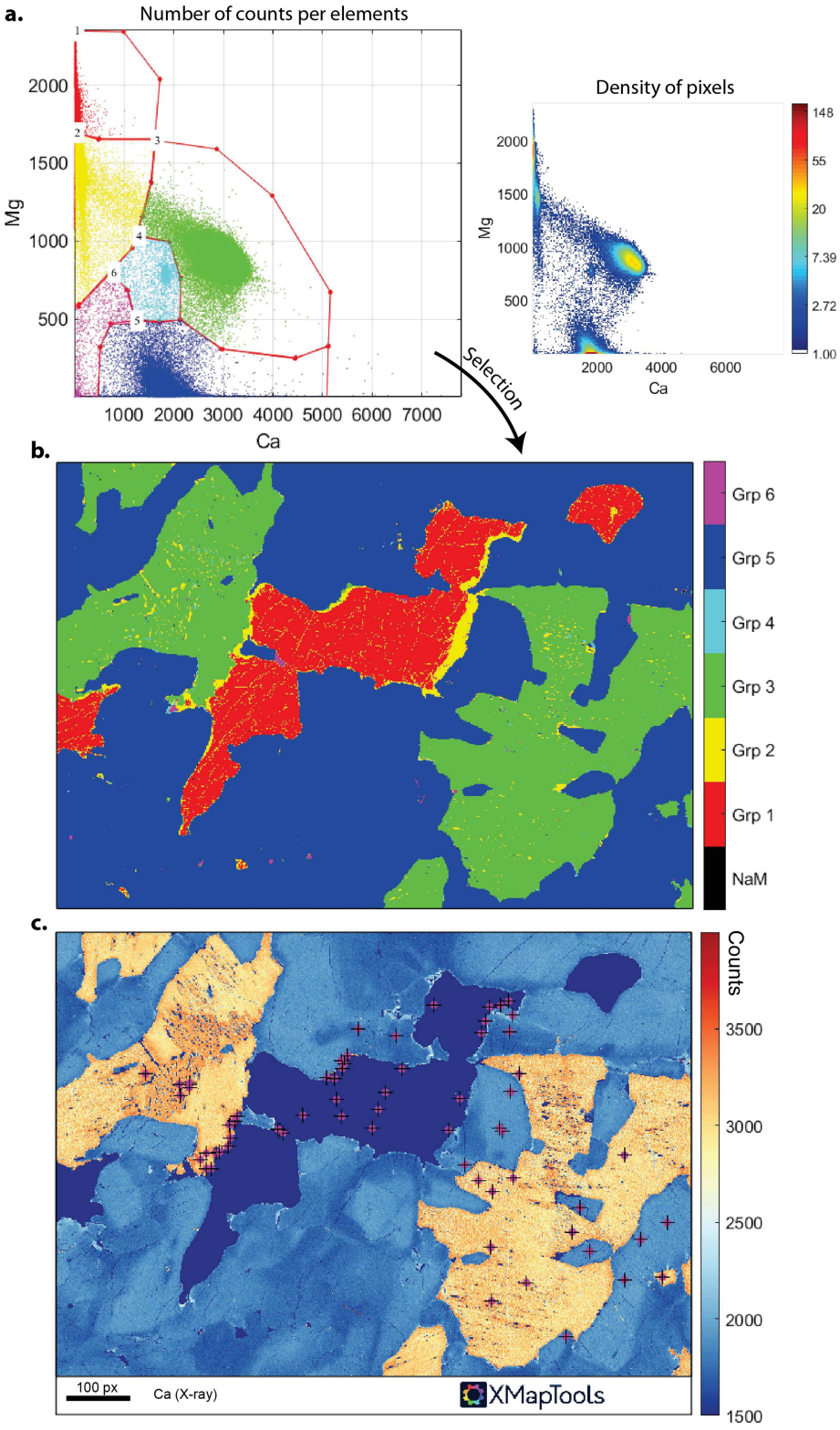
a.
Number of counts per elements
Mg
Ca
Density of pixels
Selection
b.
Grp 6
Grp 5
Grp 4
Grp 3
Grp 2
Grp 1
NaM
c.
Counts
100 px
Ca (X-ray)
XMapTools

Figure 2.10

3.4. Mineral thermometry

Mineral thermometry was investigated in a selection of samples with the amphibole-plagioclase thermometer B of Holland & Blundy (1994), as implemented in XMAPTOOLS. This thermometer is based on compositions of plagioclase and amphibole pairs through the reaction:

$$\underset{\text{Edenite}}{NaCa_2Mg_5(AlSi_3)Si_4O_{22}(OH)_2} + \underset{\text{Albite}}{NaAlSi_3O_8} = \underset{\text{Richterite}}{Na(CaNa)Mg_5Si_8O_{22}(OH)_2} + \underset{\text{Anorthite}}{CaAl_2Si_2O_8}$$

This reaction involves exchanges of Na, Ca, Al, and Si elements in the amphibole and plagioclase structure and in-between. This thermometer is especially efficient under high-temperature conditions when Anorthite-rich plagioclase dominates (Holland & Blundy, 1994), which is the case of the studied gabbroic lithologies. The thermometer is a revised version of Spear (1980) that is intended for quart-bearing rocks. It should be used for plagioclase within *X*an > 0.1 and < 0.9, and for amphiboles with $\boldsymbol{X_{Na}^{M4}} > 0.03$, $Al^{VI} < 1.8$ per formula unit (p.f.u.), and Si ∈ [6.0, 7.7] p.f.u.:

$$\boldsymbol{T = \frac{78.44 + Y_{ab-an} - 33.6 \cdot X_{Na}^{M4} - (66.8 - 2.92 \cdot P) \cdot X_{Al}^{M2} + 78.5 \cdot X_{Al}^{T1} + 9.4 \cdot X_{Na}^{A}}{0.0721 - R \cdot \ln\left(\frac{27 \cdot X_{Na}^{M4} \cdot X_{Si}^{T1} \cdot X_{an}^{plag}}{64 \cdot X_{Ca}^{M4} \cdot X_{Al}^{T1} \cdot X_{ab}^{plag}}\right)}}$$

Where: $Y_{ab\text{-}an}$ = 3.0 kJ for X_{ab} > 0.5, or $Y_{ab\text{-}an} = 12.0 \cdot (2 \cdot X_{ab} - 1) + 3.0$ kJ

The calculated temperature (*T*) is in Kelvins, the pressure (*P*) is in kbar, and the $\boldsymbol{X_{\alpha}^{\beta}}$ terms corresponds to molar fractions of elements (or ratio) α in a crystallographic site (or a phase) β. The authors indicate a standard uncertainty of ±35-40°C on the calculated temperature, but the standard deviation calculated from histograms considering all pixels of amphiboles was used instead (fall in the range ~30-70°C for analyzed samples).

3.5. Thermodynamic modeling

After being extracted from quantitative compositional maps, bulk compositions were used for thermodynamic modeling of pressure-temperature-fluids (P-T-f) conditions of equilibrium of mineralogical assemblages. This was performed in the NCK$Fe^{2+}Fe^{3+}$MASHT system (Na_2O-CaO-K_2O-FeO-Fe_2O_3-MgO-Al_2O_3-SiO_2-H_2O-TiO_2) with the Perple_X 6.9.1 software suite (Connolly, 2005, 2009). Perple_X is a collection of programs intended for calculations of phase diagrams, phase equilibria, and thermodynamic data. Calculations performed to determine the P-T-f stability conditions of a system (bulk composition & mineral assemblage) are based on the minimization of free Gibbs energy. This arises from the Gibbs stability criterions describing the state of equilibrium of a system for a minimum Gibbs energy (e.g., Gibbs, 1928). Any variations in terms of P, T, or chemistry will increase the Gibbs energy of a system. In other words, in the

view of thermodynamics, the best arises when nothing happens. Then for a fixed chemical composition of a system, it is possible to compute the associated P and T having the lowest Gibbs energy.

The internally-consistent thermodynamic database used for calculations is from Holland & Powell (2011). Models of solid-solutions are from Green et al. (2016) for clinopyroxenes, melt, amphiboles, and garnets, White et al. (2014) for orthopyroxenes and biotites, White et al. (2000) for ilmenites, Holland & Powell (1998) for olivines, White et al. (2002) for spinels, and Fuhrman & Lindsley (1988) for feldspars. Although more recent models from Holland et al. (2018) are available concerning pyroxenes, amphiboles, melt, biotite, olivine, spinel, and garnet, the choice of using older solid-solution models results from the different tests performed to evaluate the consistency of the modeled pseudo-sections. The accuracy of the results was evaluated both in terms of geological/petrological significance of the modeled pseudo-section together with the ability of Perple_X to produce well defined assemblage fields with these models (model convergence). Attempts to produce pseudo-sections with addition of Mn in the system were unsuccessful because of the complexity it implies for amphibole solid-solution models. The element Ti was added to the system as it is of importance for amphiboles. Because it is only incorporated in models of ilmenite, amphibole, and biotite, this resulted in the presence of ilmenite in all the pseudo-sections at modeled conditions. Some runs with the complete exclusion of ilmenite from the system demonstrated important changes in stabilized amphiboles compositions (±15% in *X*Mg and ±1.0 in Si p.f.u.), completely out of the range of measurements (comparatively as with ilmenite). From the frequent observation of Fe-Ti oxides (ilmenite and magnetite mainly) the sampled gabbroic rocks (and more generally drilled at the Atlantis Bank; e.g., Dick et al., 2019), and the very low amounts of modeled ilmenite (< 1%), it was chosen to keep ilmenite in the stabilized assemblage.

The following describes the different steps leading to the interpreted pseudo-sections:

(1) Modeling of a preliminary P-T pseudo-section in NCKFMAST system ($Fe_{tot.}$ = FeO) to test the convergence of models with the current system composition (Figure 2.11a). At this step, no amphibole and biotite are stabilized in the assemblage (anhydrous system).

(2) Modeling of a T-M(H_2O) pseudo-section to quantify the amount of H_2O present in the system (Figure 2.11b). The calibration of the H_2O content is based on the comparison between predicted and measured modes of amphiboles (the hydrated phase in samples), and is tested at 1 kbar, 2 kbar, and 3 kbar.

(3) The H_2O content estimated is added to the system and a second P-T pseudo-section is modeled in the NCKFMASHT system (Figure 2.11c). The model convergence is again evaluated with predicted phase modes and compositions in the assemblage fields.

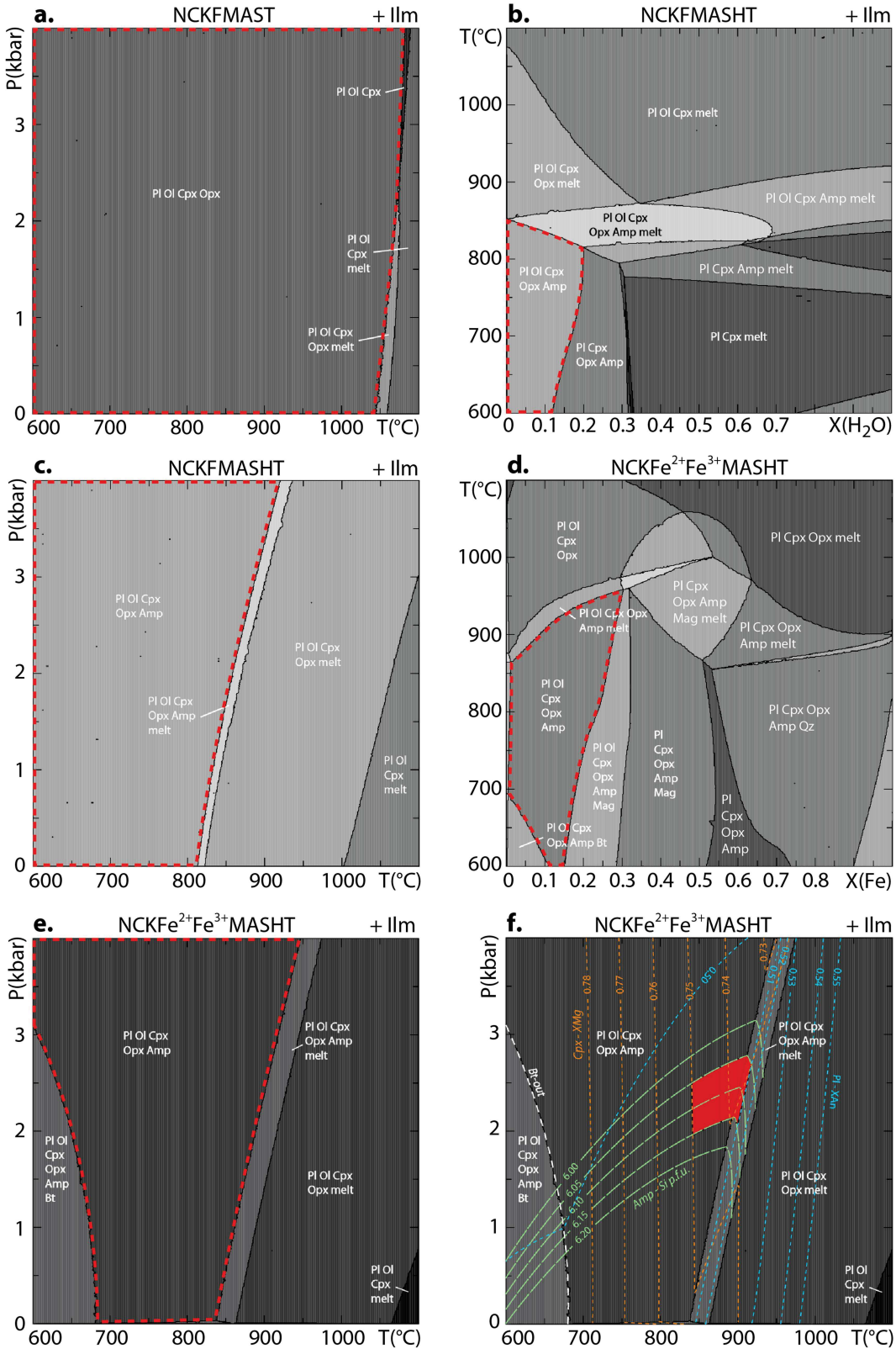
a.
NCKFMAST
+ Ilm
P(kbar)
T(°C)
Pl Ol Cpx
Pl Ol Cpx Opx
Pl Ol Cpx melt
Pl Ol Cpx Opx melt
b.
NCKFMASHT
+ Ilm
T(°C)
Pl Ol Cpx melt
Pl Ol Cpx Opx melt
Pl Ol Cpx Amp melt
Pl Ol Cpx Opx Amp melt
Pl Ol Cpx Opx Amp
Pl Cpx Amp melt
Pl Cpx melt
Pl Cpx Opx Amp
X(H2O)
c.
NCKFMASHT
+ Ilm
P(kbar)
T(°C)
Pl Ol Cpx Opx Amp
Pl Ol Cpx Opx melt
Pl Ol Cpx Opx Amp melt
Pl Ol Cpx melt
d.
NCKFe2+Fe3+MASHT
T(°C)
Pl Ol Cpx Opx
Pl Cpx Opx melt
Pl Cpx Opx Amp Mag melt
Pl Ol Cpx Opx Amp melt
Pl Cpx Opx Amp melt
Pl Ol Cpx Opx Amp
Pl Cpx Opx Amp Qz
Pl Ol Cpx Opx Amp Mag
Pl Cpx Opx Amp Mag
Pl Ol Cpx Opx Amp Bt
Pl Cpx Opx Amp
X(Fe)
e.
NCKFe2+Fe3+MASHT
+ Ilm
P(kbar)
T(°C)
Pl Ol Cpx Opx Amp
Pl Ol Cpx Opx Amp melt
Pl Ol Cpx Opx Amp Bt
Pl Ol Cpx Opx melt
Pl Ol Cpx melt
f.
NCKFe2+Fe3+MASHT
+ Ilm
P(kbar)
T(°C)
Cpx - XMg
Bt-out
Pl-XAn
Amp Si p.f.u.
Pl Ol Cpx Opx Amp
Pl Ol Cpx Opx Amp melt
Pl Ol Cpx Opx Amp Bt
Pl Ol Cpx Opx melt
Pl Ol Cpx melt

Figure 2.11

Figure 2.11 *- Construction of a phase diagrams with Perple_X, example for the protomylonitic olivine gabbro 9_5_19_A. (a) P-T phase diagram in the NCKFMAST system. The dashed-red line indicates the field of the paragenesis at modeled conditions. (b) T-M(H2O) diagram indicating the evolution of assemblage stability fields with the amount of water in the system and the temperature. Note that the maximum value at X(H2O) = 1 is fixed at 0.2 moles. (c) P-T phase diagram in the NCKFMASHT system. The addition of H2O in the system permitted the stabilization of amphibole and lowered the solidus to 800-900°C. (d) T-X(Fe) diagram showing of assemblage stability fields with temperature and varying proportions of FeO and Fe2O3. The x-axis varies from Fetot. = FeO at x = 0, to Fetot. = Fe2O3 at x = 1. The value corresponding to the best fit between predicted and measured compositions of pyroxenes and amphiboles serves to recalculate the proportion of FeO and Fe2O3 of the system. (e) The final P-T phase diagram in the NCKFe2+Fe3+MASHT system. (f) Plot of isopleths of modes and compositions of phases in the phase diagram, here Si p.f.u. in amphibole, XMg in clinopyroxene, and Xan in plagioclase are shown. The region of the diagram assumed to represent the stability conditions of the analyzed mineral assemblage is displayed in red.*

(4) Similarly as the H_2O content is estimated, the "true" FeO and Fe_2O_3 contents are deduced from pyroxene and amphibole compositions (models that integrates Fe^{3+} in the mineral structure) within a T-X(Fe) pseudo-section (Figure 2.11d). This diagram displays the evolution of phase modes and composition according to the ratio of FeO and Fe_2O_3 of the system. Again, three pseudo-sections are modeled from 1 kbar to 3 kbar.
(5) Finally, the last pseudo-section is calculated back in a P-T diagram in NCKFe^{2+}Fe^{3+}MASHT (Figure 2.11e). For this system, isopleths of phase compositions and modes are calculated and plotted in the diagram to find the stability conditions of the modelled paragenesis (Figure 2.11f). For mafic phases (clinopyroxene, orthopyroxene, and olivine) the *X*Mg ratio is used, in association with the Si p.f.u. in amphibole, and in plagioclase the *X*an is used. The region of the diagram where the observed mineral assemblage is predicted with the closest mineral modes and compositions is assumed to correspond to the stability conditions.
From observations of biotite in olivine gabbros (Nozaka et al., 2019), we use the biotite-out line as a lower temperature limit in the modeled phase diagrams (e.g., Figure 2.11e and f).

REFERENCES

Alvi, M.H., Cheong, S.W., Weiland, H., Rollett, A.D., 2004. Recrystallization and Texture Development in Hot Rolled 1050 Aluminum. Materials Science Forum 467–470, 357–362. https://doi.org/10.4028/www.scientific.net/MSF.467-470.357

Alvi, M.H., Cheong, S.W., Weiland, H., Rollett, A.D., 2003. Microstructural evolution during recrystallization in hot rolled Aluminum Alloy 1050. In Proc. 1st Intl. Symp. on Metallurgical Modeling for Aluminum Alloys, TMS, Pittsburgh 191–197.

Baudin, T., 2010. Analyse EBSD - Principe et cartographies d'orientations. 24.

Bunge, H.J., 1982. Texture Analysis in Materials Science: Mathematical Methods. Butterworths.

Connolly, J.A.D., 2009. The geodynamic equation of state: What and how: geodynamic equation of state-what and how. Geochemistry, Geophysics, Geosystems 10, n/a-n/a. https://doi.org/10.1029/2009GC002540

Connolly, J.A.D., 2005. Computation of phase equilibria by linear programming: A tool for geodynamic modeling and its application to subduction zone decarbonation. Earth and Planetary Science Letters 236, 524–541. https://doi.org/10.1016/j.epsl.2005.04.033

Dick, H.J.B., MacLeod, C.J., Blum, P., Abe, N., Blackman, D.K., Bowles, J.A., Cheadle, M.J., Cho, K., Ciążela, J., Deans, J.R., Edgcomb, V.P., Ferrando, C., France, L., Ghosh, B., Ildefonse, B., John, B., Kendrick, M.A., Koepke, J., Leong, J.A.M., Liu, C., Ma, Q., Morishita, T., Morris, A., Natland, J.H., Nozaka, T., Pluemper, O., Sanfilippo, A., Sylvan, J.B., Tivey, M.A., Tribuzio, R., Viegas, G., 2019. Dynamic Accretion Beneath a Slow-Spreading Ridge Segment: IODP Hole 1473A and the Atlantis Bank Oceanic Core Complex. Journal of Geophysical Research 124, 12631–12659. https://doi.org/10.1029/2018JB016858

Dudarev, S.L., Rez, P., Whelan, M.J., 1995. Theory of electron backscattering from crystals. Physical Review B 51, 3397–3412. https://doi.org/10.1103/PhysRevB.51.3397

Dziaszyk, S., Payton, E.J., Friedel, F., Marx, V., Eggeler, G., 2010. On the characterization of recrystallized fraction using electron backscatter diffraction: A direct comparison to local hardness in an IF steel using nanoindentation. Materials Science and Engineering: A 527, 7854–7864. https://doi.org/10.1016/j.msea.2010.08.063

Fuhrman, M.L., Lindsley, D.H., 1988. Ternary-feldspar modeling and thermometry. American Mineralogist 73, 201–215.

Gibbs, J.W., 1928. The Collected Works of J. Willard Gibbs, vol. I, Thermodynamics. Yale University Press.

Green, E.C.R., White, R.W., Diener, J.F.A., Powell, R., Holland, T.J.B., Palin, R.M., 2016. Activity-composition relations for the calculation of partial melting equilibria in metabasic rocks. Journal of Metamorphic Geology 34, 845–869. https://doi.org/10.1111/jmg.12211

Holland, T.J.B., Blundy, J., 1994. Non-ideal interactions in calcic amphiboles and their bearing on amphibole-plagioclase thermometry. Contributions to Mineralogy and Petrology 116, 433–447. https://doi.org/10.1007/BF00310910

Holland, T.J.B., Green, E.C.R., Powell, R., 2018. Melting of Peridotites through to Granites: A Simple Thermodynamic Model in the System KNCFMASHTOCr. Journal of Petrology 59, 881–900. https://doi.org/10.1093/petrology/egy048

Holland, T.J.B., Powell, R., 2011. An improved and extended internally consistent thermodynamic dataset for phases of petrological interest, involving a new equation of state for solids. Journal of Metamorphic Geology 29, 333–383. https://doi.org/10.1111/j.1525-1314.2010.00923.x

Holland, T.J.B., Powell, R., 1998. An internally consistent thermodynamic data set for phases of petrological interest. Journal of Metamorphic Geology 16, 309–343. https://doi.org/10.1111/j.1525-1314.1998.00140.x

Hough, P.V.C., 1962. Methods and means for recognizing complex patterns. Patent and Trademark Office.

Kruse, R., Stünitz, H., Kunze, K., 2001. Dynamic recrystallization processes in plagioclase porphyroclasts. Journal of Structural Geology 23, 1781–1802. https://doi.org/10.1016/S0191-8141(01)00030-X

Lanari, P., Engi, M., 2017. Local Bulk Composition Effects on Metamorphic Mineral Assemblages. Reviews in Mineralogy and Geochemistry 83, 55–102. https://doi.org/10.2138/rmg.2017.83.3

Lanari, P., Vho, A., Bovay, T., Airaghi, L., Centrella, S., 2019. Quantitative compositional mapping of mineral phases by electron probe micro-analyser. Geological Society, London, Special Publications 478, 39–63. https://doi.org/10.1144/SP478.4

Lanari, P., Vidal, O., De Andrade, V., Dubacq, B., Lewin, E., Grosch, E.G., Schwartz, S., 2014. XMapTools: A MATLAB®-based program for electron microprobe X-ray image processing and geothermobarometry. Computers & Geosciences 62, 227–240. https://doi.org/10.1016/j.cageo.2013.08.010

Lloyd, G.E., Farmer, A.B., Mainprice, D., 1997. Misorientation analysis and the formation and orientation of subgrain and grain boundaries. Tectonophysics 279, 55–78. https://doi.org/10.1016/S0040-1951(97)00115-7

MacLeod, C.J., Dick, H.J.B., Blum, P., Expedition 360 Scientists, 2017. Expedition 360 methods, Proceedings of the International Ocean Discovery Program. International Ocean Discovery Program. https://doi.org/10.14379/iodp.proc.360.2017

Mainprice, D., Bachmann, F., Hielscher, R., Schaeben, H., 2015. Descriptive tools for the analysis of texture projects with large datasets using MTEX : strength, symmetry and components. Geological Society, London, Special Publications 409, 251–271. https://doi.org/10.1144/SP409.8

Mirzadeh, H., Cabrera, J.M., Najafizadeh, A., Calvillo, P.R., 2012. EBSD study of a hot deformed austenitic stainless steel. Materials Science and Engineering: A 538, 236–245. https://doi.org/10.1016/j.msea.2012.01.037

Nishikawa, S., Kikuchi, S., 1928. Diffraction of Cathode Rays by Calcite. Nature 122, 726–726. https://doi.org/10.1038/122726a0

Nozaka, T., Akitou, T., Abe, N., Tribuzio, R., 2019. Biotite in olivine gabbros from Atlantis Bank: Evidence for amphibolite-facies metasomatic alteration of the lower oceanic crust. Lithos 348–349, 105176. https://doi.org/10.1016/j.lithos.2019.105176

Radon, J., 1917. Über die Bestimmung von Funktionen durch ihre Integralwerte längs gewisser Mannigfaltigkeiten. Berichte über die Verhandlungen der Königlich-Sächsischen Akademie der Wissenschaften zu Leipzig, Mathematisch-Physische Klasse 27, 262–277. https://doi.org/10.1090/psapm/027/692055

Reimer, L., 1998. Scanning Electron Microscopy, Springer Series in Optical Sciences. Springer Berlin Heidelberg, Berlin, Heidelberg. https://doi.org/10.1007/978-3-540-38967-5

Satsukawa, T., Ildefonse, B., Mainprice, D., Morales, L.F.G., Michibayashi, K., Barou, F., 2013. A database of plagioclase crystal preferred orientations (CPO) and microstructures – implications for CPO origin, strength, symmetry and seismic anisotropy in gabbroic rocks. Solid Earth 4, 511–542. https://doi.org/10.5194/se-4-511-2013

Schwartz, A.J., Kumar, M., Adams, B.L., Field, D.P. (Eds.), 2009. Electron backscatter diffraction in materials science, 2nd ed. ed. Springer, New York.

Schwarzer, R.A., Field, D.P., Adams, B.L., Kumar, M., Schwartz, A.J., 2009. Present State of Electron Backscatter Diffraction and Prospective Developments. In: Schwartz, A.J., Kumar, M., Adams, B.L., Field, D.P. (Eds.), Electron Backscatter Diffraction in Materials Science. Springer US, Boston, MA, 1–20. https://doi.org/10.1007/978-0-387-88136-2_1

Skemer, P., Katayama, I., Jiang, Z., Karato, S., 2005. The misorientation index: Development of a new method for calculating the strength of lattice-preferred orientation. Tectonophysics 411, 157–167. https://doi.org/10.1016/j.tecto.2005.08.023

Smith, J.V., 1974. Twins and Related Structures. Feldspar Minerals, 2 Chemical and Textural Properties. Springer-Verlag Berlin Heidelberg, 303–398.

Spear, F.S., 1980. NaSi ⇌ CaAI Exchange EquilibriumBetween Plagioclase and Amphibole. Contributions to Mineralogy and Petrology 72, 34–41.

Tarasiuk, J., Gerber, Ph., Bacroix, B., 2002. Estimation of recrystallized volume fraction from EBSD data. Acta Materialia 50, 1467–1477. https://doi.org/10.1016/S1359-6454(02)00005-8

Trépied, L., Doukhan, J.C., Paquet, J., 1980. Subgrain boundaries in quartz theoretical analysis and microscopic observations. Physics and Chemistry of Minerals 5, 201–218. https://doi.org/10.1007/BF00348570

Trimby, P.W., Prior, D.J., Wheeler, J., 1998. Grain boundary hierarchy development in a quartz mylonite. Journal of Structural Geology 20, 917–935. https://doi.org/10.1016/S0191-8141(98)00026-1

White, R.W., Powell, R., Clarke, G.L., 2002. The interpretation of reaction textures in Fe-rich metapelitic granulites of the Musgrave Block, central Australia: constraints from mineral equilibria calculations in the system K2O-FeO-MgO-Al2O3-SiO2-H2O-TiO2-Fe2O3. Journal of Metamorphic Geology 20, 41–55. https://doi.org/10.1046/j.0263-4929.2001.00349.x

White, R.W., Powell, R., Holland, T.J.B., Johnson, T.E., Green, E.C.R., 2014. New mineral activity-composition relations for thermodynamic calculations in metapelitic systems. Journal of Metamorphic Geology 32, 261–286. https://doi.org/10.1111/jmg.12071

White, R.W., Powell, R., Holland, T.J.B., Worley, B.A., 2000. The effect of TiO2 and Fe2O3 on metapelitic assemblages at greenschist and amphibolite facies conditions, mineral equilibria calculations in the system K2O-FeO-MgO-Al2O3-SiO2-H2O-TiO2-Fe2O3. Journal of Metamorphic Geology 18, 497–511. https://doi.org/10.1046/j.1525-1314.2000.00269.x

CHAPTER III

DEFORMATION OF GABBRO DRILLED IN HOLE U1473A AT THE ATLANTIS BANK (SOUTHWEST INDIAN RIDGE)

Foreword: ***An essential aspect of the work conducted in this PhD project was the description and identification of the different microstructures and their origins. This was performed on a collection of 127 thin sections from Hole U1473A, and little was presented for the purpose of the article constituting the second part of this chapter. This first part aims at providing a more exhaustive and documented description of the different microstructures studied.***

1. Microstructures and petrography of hole U1473A samples

The selected samples mainly consists of olivine-gabbros (> 5 vol% of olivine), oxide-gabbros (> 1vol% oxides), olivine-oxide-gabbros, and gabbros (Figure 3.1a and 3.2a). The principal minerals in these rocks are plagioclase (~60 vol%), clinopyroxene (~25 vol%), and olivine (~5 vol%; Figure 3.2b). Within the 127 samples, a total of 143 microstructural domains were recognized. Each domain is characterized by a homogeneous microstructure (i.e., constant deformation intensity and homogenous lithology) over a whole thin section, or a part of it. In this chapter and in the following, the IODP classification of the deformation intensity into different indices was used (e.g., MacLeod et al., 2017). The crystal plastic fabric index (CPF index) ranges from 0 to 5 for the different microstructures with 0: undeformed, 1: foliated, 2: porphyroclastic, 3: protomylonitic, 4: mylonitic; 5: ultramylonitic. Most of microstructural domains (~72%) correspond to porphyroclastic (CPF index 2) to mylonitic (CPF index 4) textures (Figure 3.1b and 3.2c). Only 6 microstructural domains sampled display an ultramylonitic texture, with either gradual or sharp contact with the host matrix. The less deformed microstructural domains are found mainly in the lower part of Hole U1473A (< 550 mbsf), where deformation is generally localized (Figure 3.2c). Foliations resulting from plastic deformation exhibit low to medium dip angles, mainly ranging from 5° to 40°, and this observation is also valid for shear zones (Figure 3.2d). In terms of retrograde alterations, it is also evaluate through indexing of samples from unaltered or very weakly altered (index 0) to strongly altered (index 4). It is often limited in the studied samples with a half to a third of samples unaltered to weakly altered, although it can be important locally (Figure 3.2e). This alteration consists of retrograde minerals associated to amphibolitic and greenschist facies principally, as demonstrated by the presence of green amphibole, colorless amphibole, and chlorite. These minerals are observed to occur in veins often orthogonal to the foliation and after clinopyroxene for green amphibole, after clinopyroxene and green amphibole for colorless amphibole, and in cracks (sometimes parallel to amphibole veins) within the plagioclase matrix and after clinopyroxene for chlorite.

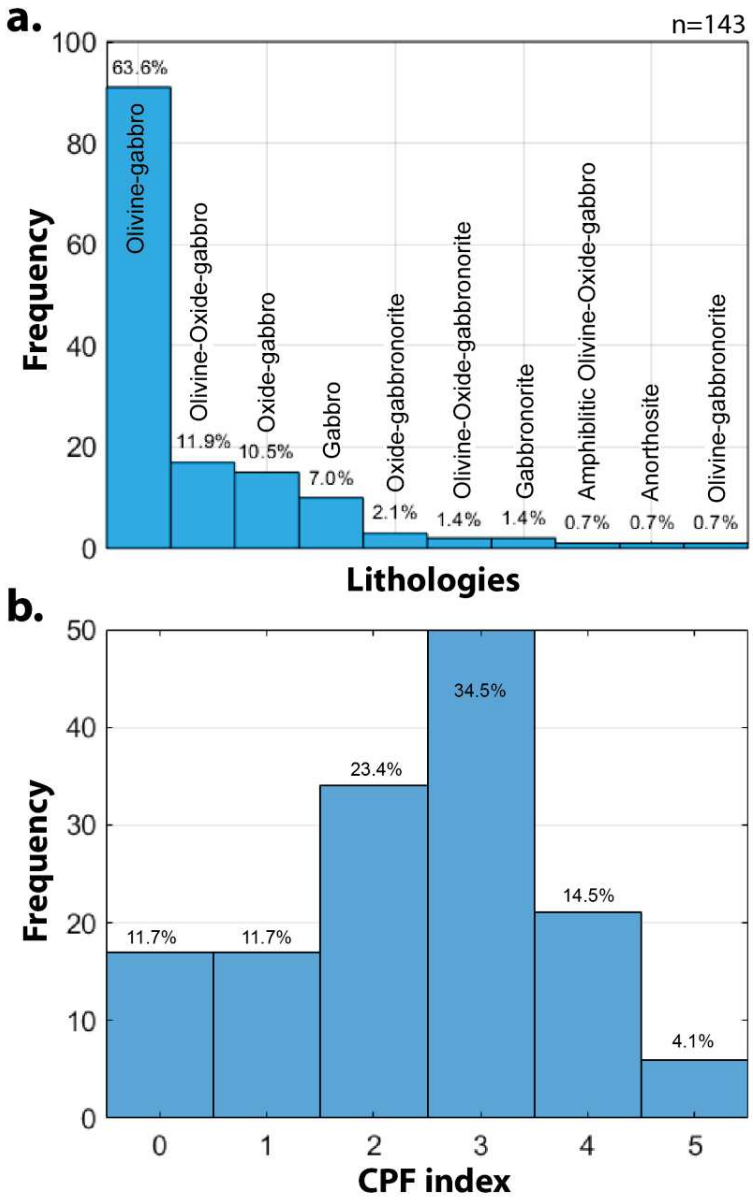

Figure 3.1 *- Sampled microstructural domains from Hole U1473A. (a) Fraction of studied microstructural domains expressed as their lithology. (b) Fraction of studied microstructural domains expressed as their CPF index (see text).*

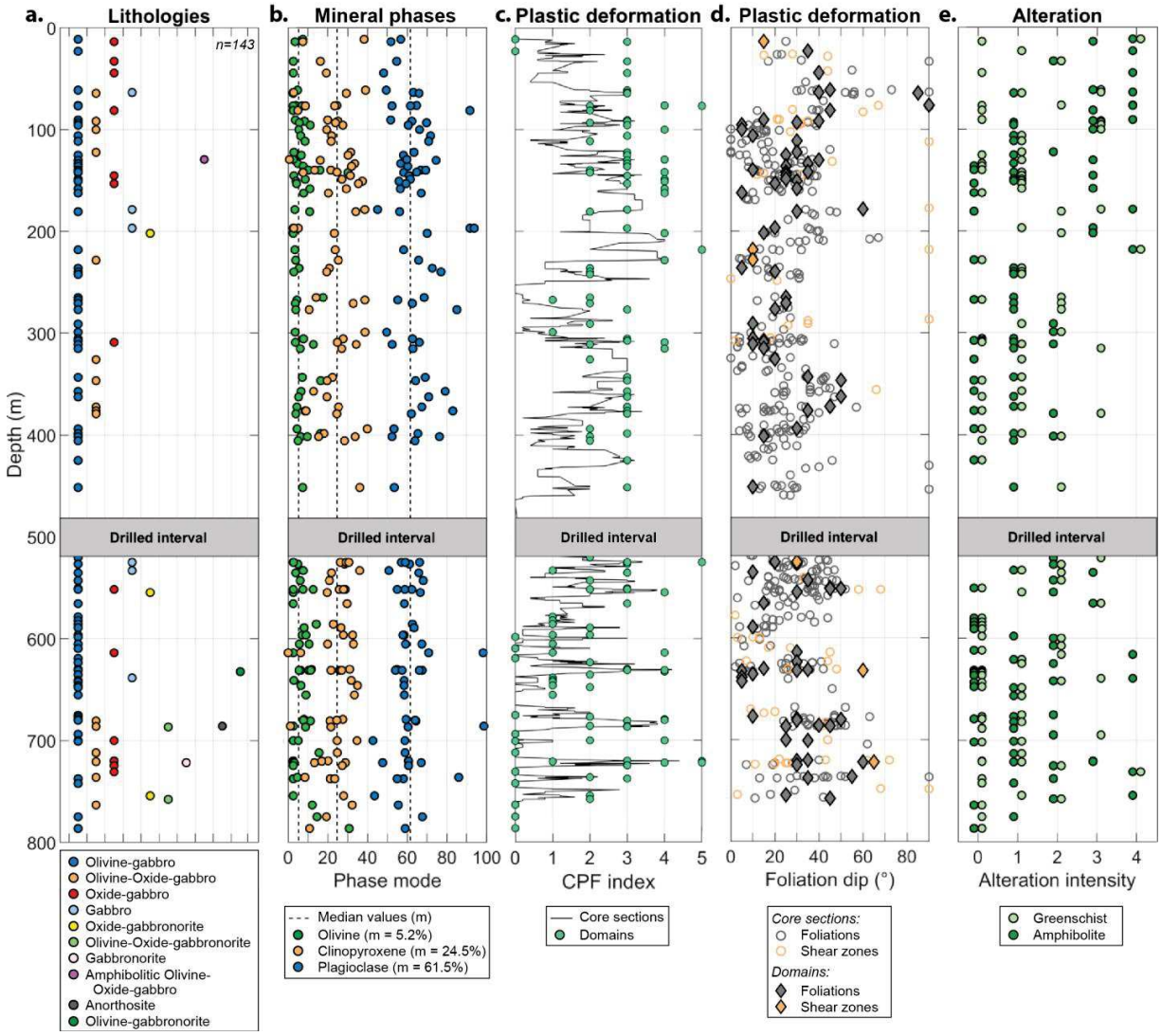

Figure 3.2 *- Along depth variations of the principal petrographic characteristics of the studied microstructural domains in Hole U1473A. (a) Lithologies. (b) Mineral modal proportion evolution with depth in the hole. (c) Depth of sampled microstructural domains and associated deformation intensity (CPF index). The line refers to the CPF index defined by expedition 360 scientists on all core sections, and circles to studied microstructural domains. (d)Plastic fabrics foliations dip from the horizontal in the hole. Diamonds corresponds to studied domains, and open circles to expedition 360 scientists' observations. (e) Alteration intensity and inferred associated metamorphic facies from mineral occurrences. The alteration intensity is indexed as follow: 0: absent or very weak, 1: weak, 2: moderate, 3: moderate to strong, 4: strong. The drilled interval is a cored but not recovered interval.*

1.1. Magmatic microstructure

The sampled undeformed magmatic microstructures are subophitic olivine-gabbro to troctolites (Figure 3.3). They are characterized by tabular to granular plagioclase grains penetrating into clinopyroxene oikocrysts, and accompanied by skeletal to granular olivine grains. Growth twins in plagioclase grains are common, as well as the occurrence of tapered twins which indicate that an incipient deformation affected these rocks (Figure 3.3b, d, e, f, and g). Also, some tapered twins are observed to have thicken after being formed, which is indicative of high temperatures during their formation (Figure 3.3g).

Figure 3.3 *- Microphotographs of representative undeformed magmatic microstructures in the sampled olivine-gabbros and troctolites from Hole U1473A. Plane polarized light microphotographs are presented in (a), (c), and (h), others are cross-polarized light. (a) to (d), and (h) are thin section scale microphotographs showing subophitic microstructures. (e) to (f) are microphotograph details in subophitic olivine gabbros. Mineral abbreviations in this and in the following figures are from Whitney & Evans (2010).*

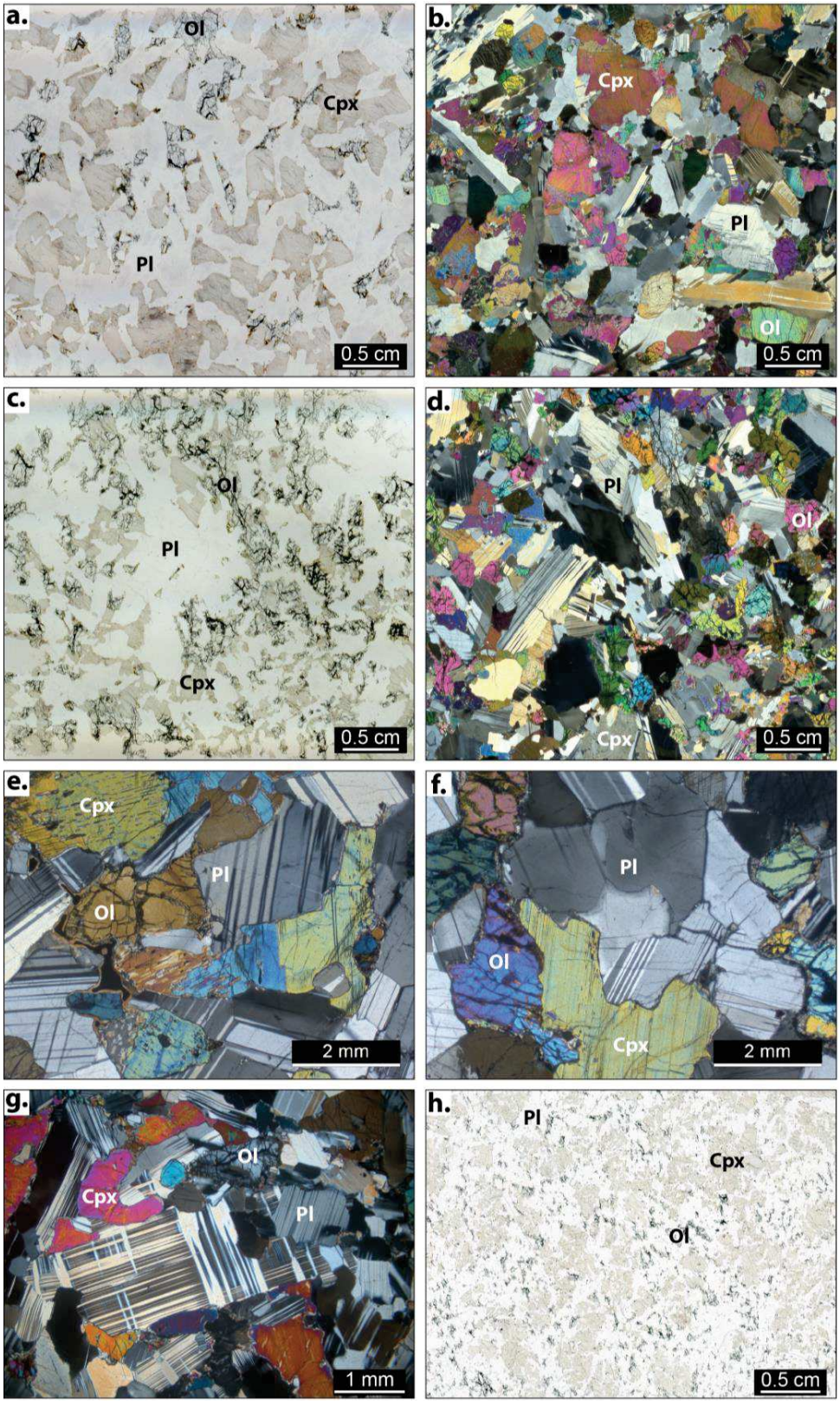
a.
Ol
Cpx
Pl
0.5 cm
b.
Cpx
Pl
Ol
0.5 cm
c.
Ol
Pl
Cpx
0.5 cm
d.
Pl
Ol
Cpx
0.5 cm
e.
Cpx
Pl
Ol
2 mm
f.
Pl
Ol
Cpx
2 mm
g.
Ol
Cpx
Pl
1 mm
h.
Pl
Cpx
Ol
0.5 cm

Figure 3.3

Grain size variations in undeformed gabbros have been sampled, usually displaying sharp contacts, and sometimes variations in textures from granular to subophitic (Figure 3.4a – d). Observations indicate the presence of late melt products such as orthopyroxene often rimming olivine grains (Figure 3.4e), and brown amphibole frequently rimming oxides (mostly ilmenite and magnetite; Figure 3.4f). Oxides themselves are late melt products as nicely demonstrated by their occurrence at clinopyroxene rims (Figure 3.4g) and their incorporation within the clinopyroxene margin (Figure 3.4h and i). Note that oxide bearing gabbros are inferred to form from more evolved melts that are shown to circulate within the crystallizing pluton and to induce melt-rock reaction (e.g., Dick et al., 2019), as illustrated by the examples given in Figure 3.4f and h. Finally, some apatite grains are found in samples, often in the presence of oxides (Figure 3.4j).

Figure 3.4 *- Microphotographs of representative of grain size variations and late melt products in the sampled undeformed magmatic microstructures. Plane polarized light microphotographs are presented in (a), (c), (f), (g), and (h), others are cross-polarized light. (a)-(b) are thin section scale microphotographs and (c)-(d) detailed microphotographs showing grain size variations in olivine gabbros. (e) Microphotograph pointing the presence of orthopyroxene at olivine rim, and (f) the presence of brown amphibole at oxide grains rims as a result of late melts crystallization. (g) to (i) are microphotographs at thin section scale showing the occurrence of oxides in gabbros, frequently distributed at clinopyroxene rims. (j) Apatite grains in the oxide-gabbro presented in (h) and (i).*

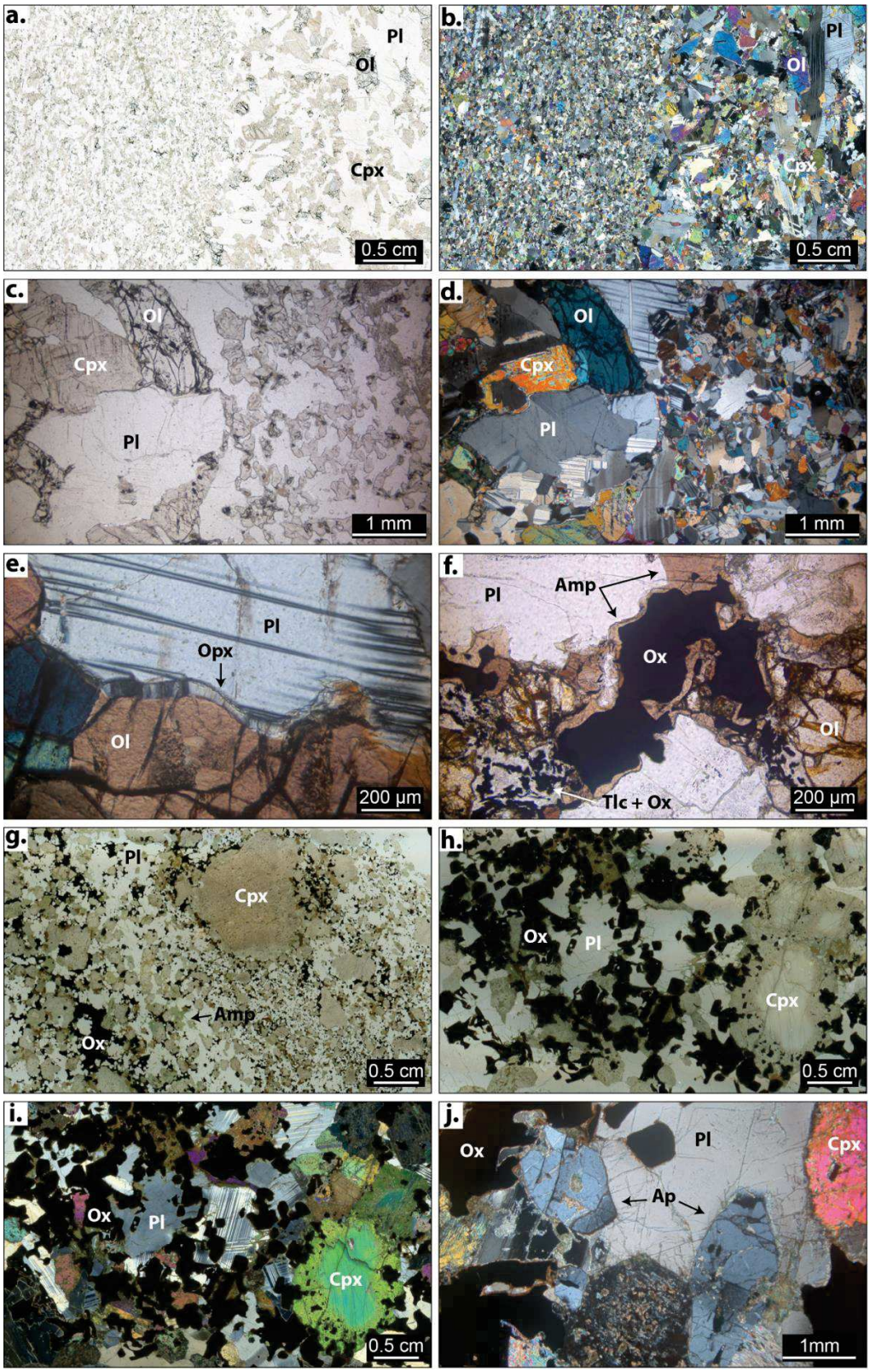
a.
Pl
Ol
Cpx
0.5 cm
b.
Pl
Ol
Cpx
0.5 cm
c.
Ol
Cpx
Pl
1 mm
d.
Ol
Cpx
Pl
1 mm
e.
Pl
Opx
Ol
200 µm
f.
Pl
Amp
Ox
Ol
Tlc + Ox
200 µm
g.
Pl
Cpx
Amp
Ox
0.5 cm
h.
Ox
Pl
Cpx
0.5 cm
i.
Ox
Pl
Cpx
0.5 cm
j.
Ox
Pl
Cpx
Ap
1mm

Figure 3.4

1.2. Deformation-related microstructures

The principal deformation mechanism observed in samples is dislocation creep as shown by the widespread occurrence of intragranular deformation and recrystallized grains in the main phases (plagioclase, clinopyroxene, and olivine; Figure 3.5). Porphyroclastic to ultramylonitic microstructures are very common in the hole and were the most sampled for this project (Figure 3.2c). Plagioclase grains are frequently strongly recrystallized and textural observations suggest that recrystallization occurred by subgrain rotation recrystallization (e.g., Poirier & Guillopé, 1979; Figure 3.5a – c). Locally, some gabbros present a fine-grained matrix of polygonal plagioclase grains, attesting to grain boundary area reduction (e.g., Kruhl, 2001; Figure 3.5d). Recrystallization also occurs in clinopyroxene and olivine grains, although it is less developed than in plagioclase (Figure 3.5e – h). In addition, the large olivine porphyroclasts frequently display undulose extinction (Figure 3.5g and h).

Figure 3.5 *- Representative cross-polarized light microphotographs showing dislocation creep in plagioclase, clinopyroxene, and olivine. (a) Typical porphyroclastic to protomylonitic microstructure characterize by a strong recrystallization of plagioclase. (b) and (c): Subgrain rotation recrystallization of plagioclase grains. (d) Polygonal fabric in plagioclase grains testifying for grain static recrystallization. (e) and (f): Subgrain rotation recrystallization of clinopyroxene. (g) and (h): Subgrain rotation recrystallization of olivine and undulose extinction in olivine porphyroclasts. Indices 1 and 2 refer to porphyroclasts and recrystallized grains, respectively.*

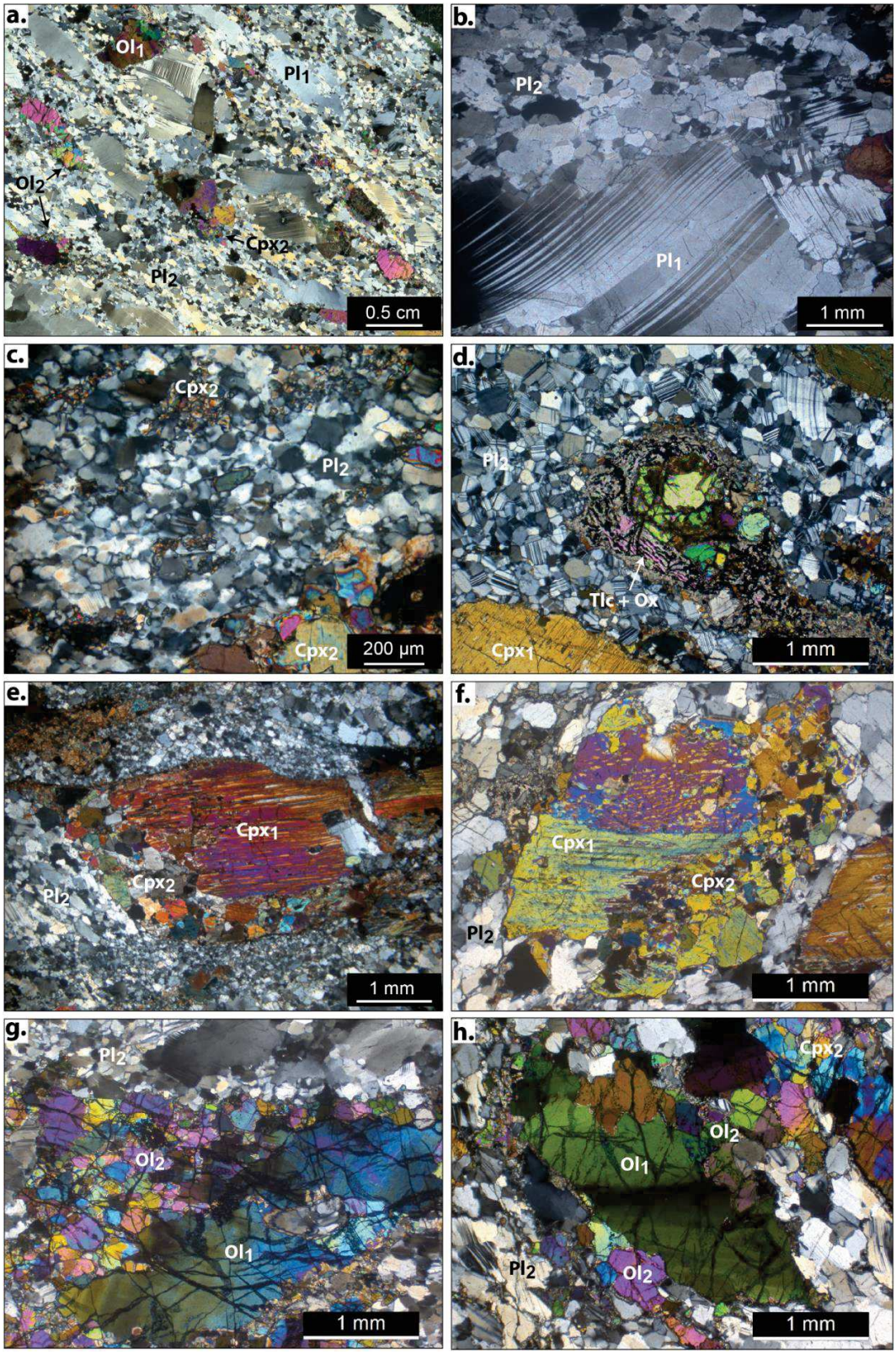
a.
Ol1
Pl1
Ol2
Cpx2
Pl2
0.5 cm
b.
Pl2
Pl1
1 mm
c.
Cpx2
Pl2
Cpx2
200 µm
d.
Pl2
Tlc + Ox
Cpx1
1 mm
e.
Cpx1
Cpx2
Pl2
1 mm
f.
Cpx1
Cpx2
Pl2
1 mm
g.
Pl2
Ol2
Ol1
1 mm
h.
Cpx2
Ol2
Ol1
Pl2
Ol2
1 mm

Figure 3.5

The recrystallization of clinopyroxene commonly results in the formation of elongated aggregates, often accompanied by the nucleation of brown amphibole, sometimes oxides, at recrystallized grain boundaries junctions (Figure 3.6a – e). Microstructures in protomylonites to ultramylonites are defined by a progressive rearrangement in plagioclase-rich bands alternating with clinopyroxene-rich bands (Figure 3.6a – f). The localization of deformation in associated in some samples to the occurrence of apatite grains, or sometimes titanite (Figure 3.6g and h).
band.

Figure 3.6 *- Microstructures associated to intense recrystallization in the studied gabbroic samples. Microphotographs are plane-polarized light except in (f) and (g). (a) Recrystallized clinopyroxene grains forming tails at the edge of clinopyroxene porphyroclasts and elongated aggregates where oxides occur at grain boundary junctions. The upper right inset is a reflected light image showing the oxide grains (in white). (b) Clinopyroxene porphyroclasts with a recrystallized tail where brown amphibole occur at grain boundary junctions. (c) and (d): representative microstructures in mylonites and ultramylonites of the sample suite, respectively, showing an arrangement in plagioclase-rich and clinopyroxene-rich bands. (e) and (f): Ultramylonite (shear zone: SZ) cutting into a gabbro mylonite. Note the important grain size reduction in the shear zone and the ubiquitous presence of oxide grains mixed with the very fine plagioclase grains. (g) Local occurrence of titanite, and (h) of apatite in a protomylonitic band.*

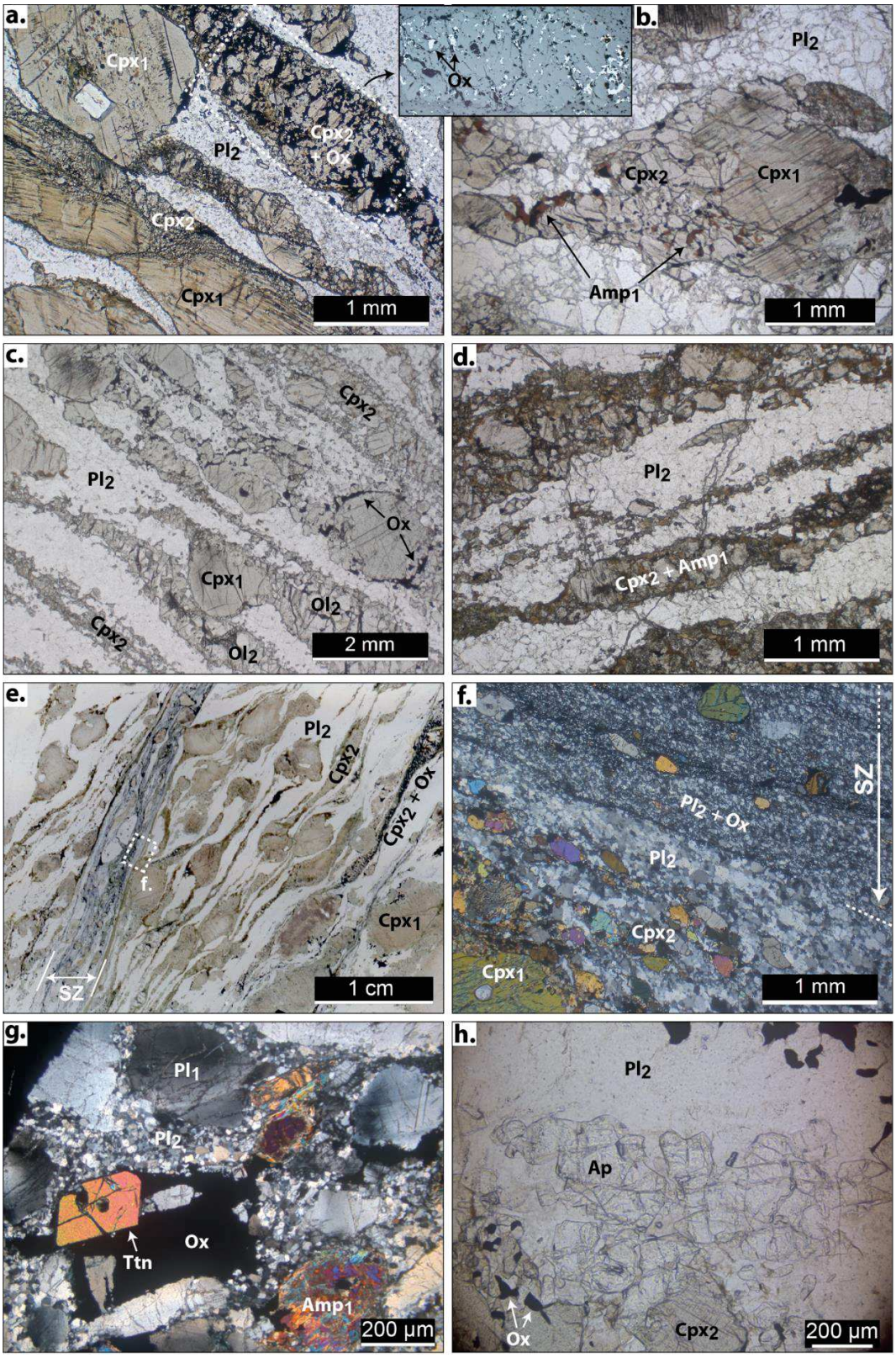
a.
Cpx1
Ox
Pl2
Cpx2 + Ox
Cpx2
Cpx1
1 mm
b.
Pl2
Cpx2
Cpx1
Amp1
1 mm
c.
Cpx2
Pl2
Ox
Cpx1
Ol2
Cpx2
Ol2
2 mm
d.
Pl2
Cpx2 + Amp1
1 mm
e.
Pl2
Cpx2
Cpx2 + Ox
f.
Cpx1
SZ
1 cm
f.
SZ
Pl2 + Ox
Pl2
Cpx2
Cpx1
1 mm
g.
Pl1
Pl2
Ox
Ttn
Amp1
200 µm
h.
Pl2
Ap
Ox
Cpx2
200 µm

Figure 3.6

Later brittle-ductile deformation is found crosscutting through both undeformed and deformed samples, often forming very thin bands consisting of fine-grained recrystallized plagioclase and clinopyroxene (± green amphibole; Figure 3.7a – f). In their vicinity, plagioclase grains can exhibit undulose extinction while grains farther from the recrystallized band are free of deformation (Figure 3.7a). Sometimes a sense of shear from one side of the band to the other can be deduced from the occurrence of small recrystallized tails of clinopyroxene (Figure 3.7e and f). It can also be accompanied by the retrograde alteration of clinopyroxene that is observed mixed with brownish-green amphibole (Figure 3.7e and f). This brittle-ductile deformation can be intense in some samples and form a very fine-grained matrix of plagioclase grains in which porphyroclasts are fractured (Figure 3.7g and h). Note that recrystallization is likely to occur by bulging in these thin deformed bands (e.g., Bailey & Hirsch, 1962; Figure 3.7b and g).

Figure 3.7 *- Highly localized brittle-ductile deformation observed in gabbroic samples from Hole U1473A. Microphotographs are cross-polarized light except in (c) and (e). (a) and (b): Very thin recrystallized plagioclase band cutting through a formerly undeformed subophitic olivine-gabbro. Note that the recrystallization of plagioclase in the deformed band seems to occur by bulging (see text). (c) and (d): Similar thin deformed band occurring in a porphyroclastic olivine-gabbro. Both plagioclase and clinopyroxene form very-fine grains in the deformed band. (e) and (f): Thin deformed band in a protomylonitic gabbro. In this sample the deformation is accompanied by the formation of a very fine-grained tail of clinopyroxene and brownish-green amphibole. (g) Fine-grained plagioclase matrix and fractured plagioclase porphyroclasts. Note the occurrence in the porphyroclasts' fractures of fine plagioclase grains similar to those that constitute the matrix. (h) Large plagioclase grain deformed by a set of sub-vertical fractures, and slip on it twins (sub-horizontal). Note the bending of twins in the vicinity of fractures.*

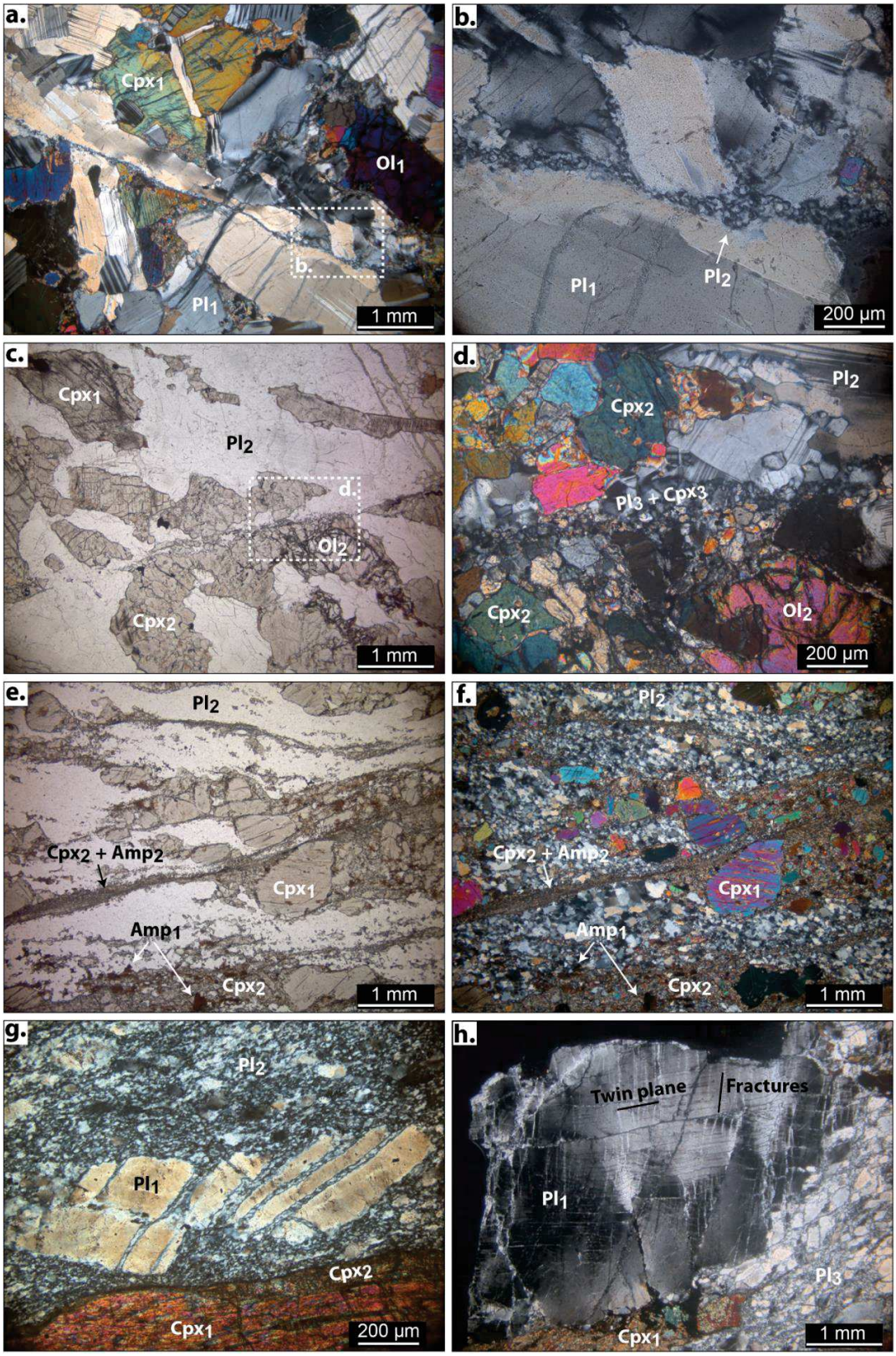
a.
Cpx1
Ol1
b.
Pl1
1 mm
b.
Pl1
Pl2
200 µm
c.
Cpx1
Pl2
d.
Ol2
Cpx2
1 mm
d.
Pl2
Cpx2
Pl3 + Cpx3
Cpx2
Ol2
200 µm
e.
Pl2
Cpx2 + Amp2
Cpx1
Amp1
Cpx2
1 mm
f.
Pl2
Cpx2 + Amp2
Cpx1
Amp1
Cpx2
1 mm
g.
Pl2
Pl1
Cpx2
Cpx1
200 µm
h.
Twin plane
Fractures
Pl1
Pl3
Cpx1
1 mm

Figure 3.7

1.3. Alteration-related microstructures

Secondary clinopyroxene grains growing within the former clinopyroxene grains in elongated digitated shapes into cleavages are observed in samples, and inferred to form by static alteration (e.g., MacLeod et al., 2017; Figure 3.8a and b). Olivine grains are observed with an assemblage of talc and oxides (principally magnetite) consuming them from their edges (Figure 3.8c). In some samples this occurs together with a lower grade serpentinization of the olivine grain (Figure 3.8d). Note that the magnetite grains often arrange in bands that forms during serpentinization (Figure 3.8c, 3.8d, and 3.5d). Pale green amphibole is found after clinopyroxene, replacing it from the edges or sometimes through filled fractures/veins cutting through samples (Figure 3.8e – g). The amphibole grains can be also found after talc at olivine rims, and are later replaced by chlorite under lower grade metamorphic conditions (Figure 3.8e, g, h, i). Note that chlorite also occurs in cracks formed into the plagioclase matrix, often following grain boundaries (Figure 3.8h). Finally, olivine has been rarely found replaced by clay minerals such as iddingsite (Figure 3.8j).

Figure 3.8 *- Representative alteration-related microstructures. (a) and (b): Static alteration in clinopyroxene giving rise to secondary clinopyroxene. (c) and (d): Retrograde talc associated to oxides (magnetite mainly) after olivine, and (d) serpentine after olivine. (e) Retrograde green amphibole after clinopyroxene, also occurring in veins into fractured plagioclase, and chlorite after amphibole. (f) Vein of amphibole sub-orthogonal to the foliation. Note the presence of a parallel set of chlorite-filled cracks around the amphibole vein. (g) Fractures/veins filled with green amphibole and chlorite. The alteration progresses from the vein through proximal clinopyroxene grains. Chlorite is found principally in halos around olivine (appearing as black granular aggregates), and to a lesser extent around amphibole. (h) Chlorite-filled cracks formed into the recrystallized plagioclase matrix. Note the preferential localization of cracks at plagioclase grain boundaries. (i) Amphibolite to greenschist sequence of alteration of olivine grains with talc and oxides, followed by green amphibole, and finally by chlorite. (j) Clay minerals (iddingsite) after olivine, the later alteration product observed in the sample suite.*

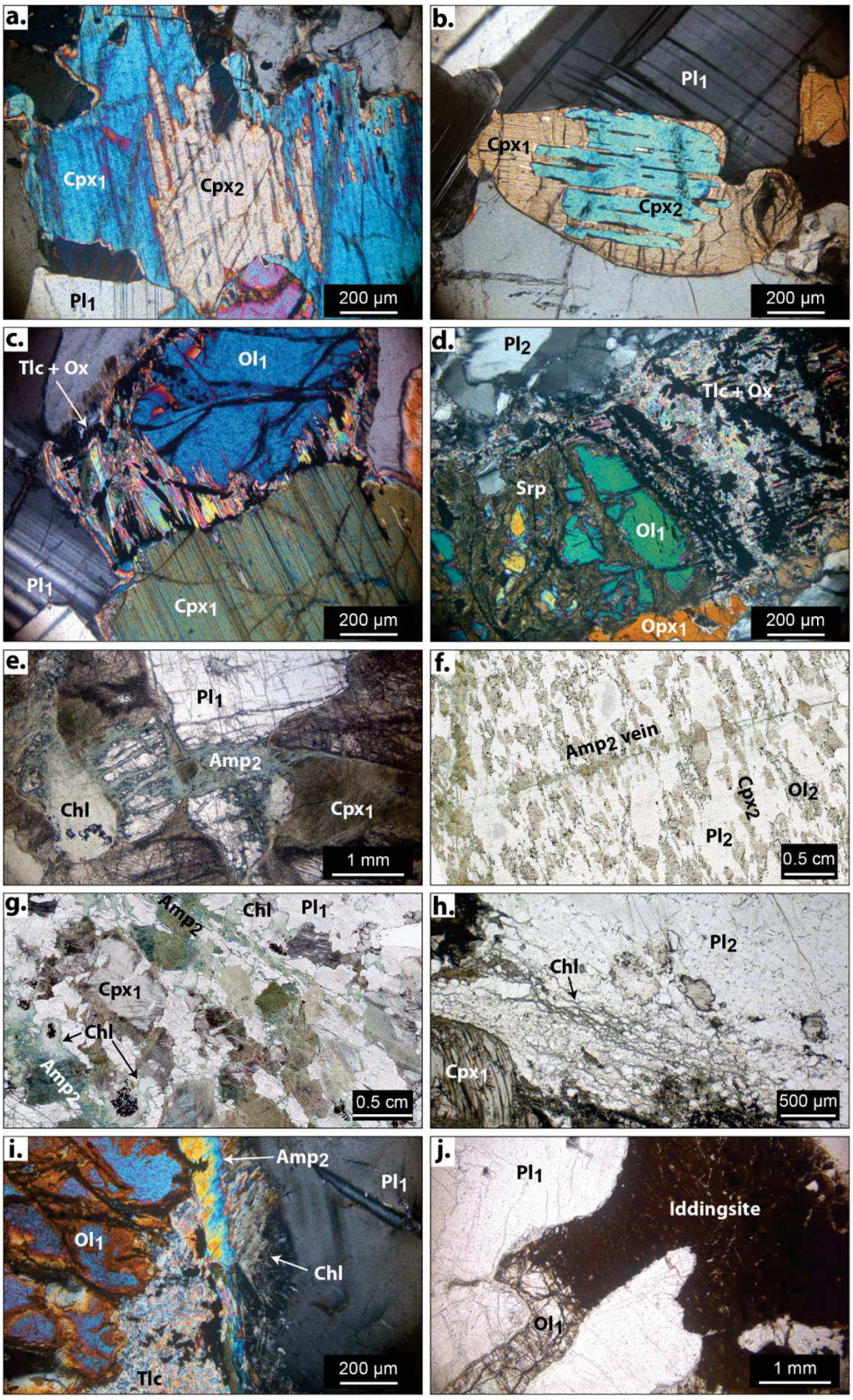
a.
Cpx1
Cpx2
Pl1
200 µm
b.
Pl1
Cpx1
Cpx2
200 µm
c.
Tlc + Ox
Ol1
Pl1
Cpx1
200 µm
d.
Pl2
Tlc + Ox
Srp
Ol1
Opx1
200 µm
e.
Pl1
Amp2
Chl
Cpx1
1 mm
f.
Amp2 vein
Cpx2
Ol2
Pl2
0.5 cm
g.
Amp2
Chl
Pl1
Cpx1
Chl
Amp2
0.5 cm
h.
Pl2
Chl
Cpx1
500 µm
i.
Amp2
Pl1
Ol1
Chl
Tlc
200 µm
j.
Pl1
Iddingsite
Ol1
1 mm

Figure 3.8

REFERENCES

Bailey, J.E., Hirsch, P.B., 1962. The recrystallization process in some polycrystalline metals. Proceedings of the Royal Society of London. Series A. Mathematical and Physical Sciences 267, 11–30. https://doi.org/10.1098/rspa.1962.0080

Dick, H.J.B., MacLeod, C.J., Blum, P., Abe, N., Blackman, D.K., Bowles, J.A., Cheadle, M.J., Cho, K., Ciążela, J., Deans, J.R., Edgcomb, V.P., Ferrando, C., France, L., Ghosh, B., Ildefonse, B., John, B., Kendrick, M.A., Koepke, J., Leong, J.A.M., Liu, C., Ma, Q., Morishita, T., Morris, A., Natland, J.H., Nozaka, T., Pluemper, O., Sanfilippo, A., Sylvan, J.B., Tivey, M.A., Tribuzio, R., Viegas, G., 2019. Dynamic Accretion Beneath a Slow-Spreading Ridge Segment: IODP Hole 1473A and the Atlantis Bank Oceanic Core Complex. Journal of Geophysical Research 124, 12631–12659. https://doi.org/10.1029/2018JB016858

Kruhl, J.H., 2001. Crystallographic control on the development of foam textures in quartz, plagioclase and analogue material. International Journal of Earth Sciences 90, 104–117. https://doi.org/10.1007/s005310000170

MacLeod, C.J., Dick, H.J.B., Blum, P., Expedition 360 Scientists, 2017. Site U1473A, Proceedings of the International Ocean Discovery Program. International Ocean Discovery Program. https://doi.org/10.14379/iodp.proc.360.2017

Poirier, J.-P., Guillopé, M., 1979. Deformation induced recrystallization of minerals. Bulletin de Minéralogie 102, 67–74. https://doi.org/10.3406/bulmi.1979.7256

Whitney, D.L., Evans, B.W., 2010. Abbreviations for names of rock-forming minerals. American Mineralogist 95, 185–187. https://doi.org/10.2138/am.2010.3371

JGR Solid Earth

RESEARCH ARTICLE
10.1029/2021JB021964

Special Section:
Ophiolites and Oceanic Lithosphere, with a focus on the Samail ophiolite in Oman

Plastic Deformation of Plagioclase in Oceanic Gabbro Accreted at a Slow-Spreading Ridge (Hole U1473A, Atlantis Bank, Southwest Indian Ridge)

Maël Allard[1], Benoît Ildefonse[1], Émilien Oliot[1], and Fabrice Barou[1]

[1]Géosciences Montpellier, Université de Montpellier, CNRS, Montpellier, France

Key Points:

- Deformation led to the progressive dynamic recrystallization of plagioclase, forming both highly localized and pervasive mylonitic zones
- Dislocation creep produced overall weak crystallographic preferred orientations of plagioclase grains, weakened further in ultramylonites
- The prevalence of the identified active slip systems changes with cooling, during crystallographic preferred orientations development and subgrain boundaries formation

Supporting Information:

Supporting Information may be found in the online version of this article.

Correspondence to:

M. Allard,
mael.allard@umontpellier.fr

Citation:

Allard, M., Ildefonse, B., Oliot, É., & Barou, F. (2021). Plastic deformation of plagioclase in oceanic gabbro accreted at a slow-spreading ridge (Hole U1473A, Atlantis Bank, Southwest Indian Ridge). *Journal of Geophysical Research: Solid Earth*, *126*, e2021JB021964. https://doi.org/10.1029/2021JB021964

Received 27 FEB 2021
Accepted 28 SEP 2021

Abstract Crustal architecture at slow-spreading oceanic ridges results from complex interactions between magmatism, hydrothermalism, and tectonics. IODP Hole U1473A was drilled during Expeditions 360 and 362T at the summit of the Atlantis Bank, a gabbroic massif exhumed at the Southwest Indian Ridge. In this study, we identify and quantify plastic deformation processes in gabbroic lithologies and active slip systems in plagioclase from 115 microstructural domains throughout Hole U1473A. We describe deformed zones using petrographic observations and electron backscattered diffraction analyses made all along the core. Ductile deformation is widespread, and in places strongly localized in mylonitic and ultramylonitic zones. Plagioclase represents ~60% of rock's volume and is the dominant phase accommodating deformation in samples. It shows strong dynamic recrystallization accommodated by subgrain rotation in the dislocation creep regime, forming a fine-grained matrix. Electron backscattered diffraction analyses reveal weak to moderate crystallographic preferred orientations of plagioclase as a result of plastic deformation and strain localization, producing a fabric characterized by (010) parallel to the foliation plane and [100] parallel to the lineation. The fabric strength is first increasing from slightly deformed lithologies to mylonites before decreasing significantly in ultramylonites. This could be explained by orientation scattering after recrystallization, and a change of active slip systems. Subsequent granular flow has likely occurred in some samples. A detailed investigation of intracrystalline misorientations measured at plagioclase subgrain boundaries reveals the activity of four dominant slip systems: [001](010), [100](001), ½[110](001), and ½[$1\bar{1}0$](001). These slip systems reflect decreasing temperatures during CPO development and subgrain wall formation.

Plain Language Summary Crustal architecture of slow-spreading oceanic crust results from complex interactions between magmatism, hydrothermalism, and tectonics. In this study, we identify and quantify plastic deformation processes in gabbroic lithologies and active slip systems in plagioclase from 115 intervals throughout Hole U1473A, drilled at the Atlantis Bank gabbroic massif. We describe deformed zones using petrographic observations, crystallographic orientations analyses, and intragranular deformation analyses made all along the core. Plagioclase represents ~60% of rock's volume and is the dominant phase accommodating deformation in samples. The weak crystallographic preferred orientations measured in plagioclase result from ductile deformation and strain localization. The intensity of crystallographic preferred orientations increases as deformation increases in samples, before decreasing in the most intensely deformed samples. This could be explained by orientation scattering after recrystallization, and a change of active slip systems. Subsequent grain-size-sensitive processes and chemical diffusion have likely occurred in some samples. A detailed investigation of intracrystalline deformations measured in plagioclase grain reveals the activity of four dominant slip systems in addition to the one that produced the crystallographic orientations. These slip systems reflect decreasing temperatures during the deformation of the studied gabbroic lithologies, related to the tectonic activity at the ridge.

1. Introduction

Plastic deformation and recrystallization processes of minerals control the rheological behavior of the lower continental and oceanic crusts during their tectonic history. Deformation of polyphase rocks like granites and gabbros occur over a wide range of temperatures, pressures, strain rates, and fluid conditions. In these rocks plagioclase is ubiquitous, constituting a third to a half of the whole mineralogical assemblage, and is

stable in most crustal conditions (up to ~1–1.5 GPa/~30–40 km, e.g., Newton & Kennedy, 1968). In igneous mafic rocks, plagioclase is the main component and often corresponds to the weaker phase of the mineral assemblage below near-solidus conditions (e.g., Ji, 2004; Kronenberg & Shelton, 1980). Thus, plagioclase plays a key role in crustal rheology, and understanding its mechanical and microstructural behavior is critical (e.g., Rybacki & Dresen, 2004).

In plagioclase grains, internal plastic deformation occurring at high temperatures (>500°–600°C) leads to subgrain rotation (SGR) recrystallization and subsequent (fast) grain boundary migration (GBM) recrystallization (e.g., Drury & Urai, 1990; Kruse et al., 2001; Poirier & Guillopé, 1979; Urai et al., 1986). This usually induces the development of crystallographic preferred orientations (CPO), through dislocation creep, reflecting the activity of syn-deformation slip systems (e.g., Wenk & Christie, 1991). The main slip systems identified by transmission electron microscopy (TEM) observations in plagioclase are those that slip on the principal twin planes, namely (010) and (001), and the most commonly reported one is [001](010) (e.g., Gandais & Willaime, 1984; Montardi & Mainprice, 1987; Olsen & Kohlstedt, 1984).

Slow spreading ridges represent more than 55% of mid-ocean ridges on Earth, and generate about 20% of the global ocean floor (Teagle et al., 2012). At slow-spreading ridges, the development of detachment faults leads to the exhumation of deep crustal and upper-mantle lithologies (e.g., Cannat, 1993), and to the development of oceanic core complexes (OCC; e.g., Escartín & Canales, 2011). OCC are accessible key locations for understanding the relations between high-temperature magmatic processes, cooling, and tectonics occurring at the ridge axis within deep rocks. At the Southwest Indian Ridge, the Atlantis Bank consists of a pluri-kilometer scale gabbro pluton exhumed through an OCC system at 11–13 Ma, and is of great interest for submersible explorations, dredging, and drilling since 1987 (Blum et al., 2017; Dick et al., 2000; Dick, MacLeod, et al., 2019; Pettigrew et al., 1999). Multiple expeditions drilled three deep holes since 1987: ODP Hole 735B (Dick et al., 2000) and Hole 1105A (Pettigrew et al., 1999), and IODP Hole U1473A (Blum et al., 2017; Dick, MacLeod, et al., 2019), for a maximum penetration depth of ~1.5 km. Plastic deformation of the constituting minerals is widespread and penetrative in the uppermost part of the massif (first 500–600 m) before being more heterogeneous and localized down section. The onset of this plastic deformation occurs early in the magmatic accretion history, under hyper solidus conditions, and continues at lower temperature, down to the ductile-brittle conditions. In IODP Hole U1473A, it forms two thick crystal-plastic shear zones at least 100 m large in the upper ~500 m. By contrast, the lower ~300 m show more localized shear zones in a slightly deformed framework (MacLeod et al., 2017).

Our study aims to characterize plastic deformation in gabbroic rocks from the drill core recovered at the Atlantis Bank OCC in IODP Hole U1473A. After reviewing the deformation mechanisms acting in plagioclases in relation with active slip systems, we evaluate the active deformation mechanisms and slip systems and their evolution during cooling in the context of crustal accretion and lower crust–upper mantle denudation through a detachment fault at a slow-spreading ridge. A suite of 102 samples was taken along Hole U1473A in variably plastically deformed gabbroic lithologies; it is characterized by very limited amounts of retrograde alterations and can therefore be used for primary structures analysis. We combine core and thin section observations for textural and mineralogical identifications, and complement these with detailed Electron Backscattered Diffraction (EBSD) mapping.

2. Deformation Mechanisms of Plagioclase

Plagioclase is the most common mineral phase within the Earth's crust, representing up to 40% of crustal minerals (Ronov & Yaroshevsky, 1969). Its pressure-temperature (P-T) stability field encompasses highly variable conditions, which implies that it is subjected to a large spectrum of deformation mechanisms (Figure 1). Activities, and transitions between these mechanisms are controlled by temperature and strain rate, but also by fluids circulation and confining pressure (e.g., Debat et al., 1978; Fitz Gerald & Stünitz, 1993; Hirth & Tullis, 1994; Simpson, 1985; Tullis & Yund, 1987). For $T < 500$°C, plagioclase acts as a rigid mineral and deforms mainly by fracturing. Kink bands, tapered twins, and limited nucleation in small fractures can also be found in fractured grains. The transition between dominant fracturing to dislocation-accommodated deformation occurs at ~450°–550°C in naturally deformed rocks (e.g., Dell'Angelo & Tullis, 1996; Oliot et al., 2010; Tullis & Yund, 1977). The temperature range at which this transition arises also depends on the

texture, and on the constituting phases of the deforming rock (Fitz Gerald & Stünitz, 1993; Ji, 2004; Kronenberg & Shelton, 1980; Rosenberg & Stünitz, 2003; Simpson, 1985; Tullis & Yund, 1977). Dynamic recrystallization and grain boundary migration ("slow" and "fast") become important processes at $T > 500°–600°C$ because of the enhancement of grain boundary mobility, and of subgrain boundary formation at high temperatures. Conversely, at lower temperatures diffusion creep could easily prevail on dislocation creep because of chemical differences accompanying recrystallization (e.g., Rosenberg & Stünitz, 2003). Although dislocation creep does not occur at $T < 500°C$, a process of dislocation generation by fracturing (easy in plagioclase because of twins) is documented and certainly encourages the transition from brittle to plastic regime (McLaren & Pryer, 2001; Stünitz et al., 2003; Tullis & Yund, 1985). Fracturing at moderate to high temperatures (600°–750°C) and high-stress conditions has also been reported as an important process of grain size reduction in plagioclase grains, leading to narrow shear zone formation favoring grain-size-sensitive creep in the small-grained aggregates formed (Okudaira et al., 2015, 2017).

At upper-greenschist to amphibolite facies conditions ($T > 450°C$) the mobility of dislocations in plagioclase becomes easier and promotes their glide toward grain boundaries (Fitz Gerald & Stünitz, 1993). If dislocation mobility is low and local, the nucleation of new grains occurs at grain boundaries by bulging recrystallization (BLG), also known as "slow grain boundary migration," by a process of strain-induced boundary migration (SIGM, Bailey & Hirsch, 1962). Bulges can become (small) new grains by the formation of a subgrain boundary on their back, evolving into a grain boundary (e.g., Bell & Johnson, 1989; Oliot et al., 2014). BLG is mainly observed in plagioclase deformed between 500°–550°C and ~700°C (Figure 1). With increasing mobility dislocations can glide faster and farther, forming subgrains (and then grains) of slightly different crystallographic orientations, or inducing large-scale fast grain boundary migration. The first mechanism, subgrain rotation recrystallization (SGR), occurs in deformed plagioclase from ~400°C to >1000°C, especially in the range 500°–750°C (Figure 1). Grain boundary migration recrystallization (GBM) is made possible by the high mobility of grain boundaries (Poirier & Guillopé, 1979). It is achieved by a rotation step (SGR) that is rapidly followed by the fast migration of the newly formed grain boundary, leading to large recrystallized grain sizes. GBM is naturally active from ~500°C to ~1000°C and is mostly described at 600°–750°C (Figure 1). Note that when SGR and GBM mechanisms are active together, textures are characterized by lobate grain boundaries and small differences in overall grain sizes. Additionally, dislocation creep mechanisms are known to produce CPO, unlike diffusion creep mechanisms (Tullis & Yund, 1987; Wenk & Christie, 1991). In solid solution minerals like plagioclase, slow and fast boundary migration processes can be driven by chemical potentials occurring between neighboring grains (e.g., parent-recrystallized grains). This process is called chemically induced grain boundary migration (CIGM, Hay & Evans, 1987) and arises from a decrease of the P-T conditions. In the dislocation creep regime, the recrystallization of grains by a process of GBM can generate compositional changes in the recrystallized grains. It arises from the migration of the high angle grain boundary within a former strained grain, which permits ionic exchanges (Na/Si and Ca/Al) with the surface of neighboring grains (e.g., Yund & Tullis, 1991). Note that SIGM and CIGM can act simultaneously during grain boundary migration (*s.l.*). By contrast, recrystallization by SGR is not supposed to produce chemical potentials between old and new grains, as the exchanges are principally restricted to volume diffusion, usually too slow to be significant (e.g., Stünitz, 1998; Yund & Tullis, 1991).

Slip systems activities during intracrystalline deformation are documented from ~500°C to 600°C to higher temperatures up to the solidus (Figure 1). Numerous slip systems have been specified after experimental deformations since the seventies (e.g., Marshall & McLaren, 1977; Montardi & Mainprice, 1987; Olsen & Kohlstedt, 1985; 1984; Scandale et al., 1983), and observed in TEM. These studies raised the general idea that slip by dislocation motion is one of the main deformation mechanisms in feldspars. Furthermore, cross slip is commonly observed and the interaction between several operating slip systems is considered as an important mechanism for dislocation multiplication (e.g., Montardi & Mainprice, 1987). An exhaustive list of slip systems documented in plagioclase to date is presented in Table S1 in Supporting Information S1.

Based on TEM studies and CPO pattern interpretations, it appears that the main active slip systems are characterized by a slip plane that corresponds to a twinning plane, namely (010) or (001). Apart from [001](010) that is found active from ~500°C and over the largest range of temperatures, most slip systems become active at ~600°C and are well documented until 900°C (Figure 1). [100](010) is one of the dominant active slip systems at high temperatures (>800°C) while the [100](001) slip system, found active in the same range

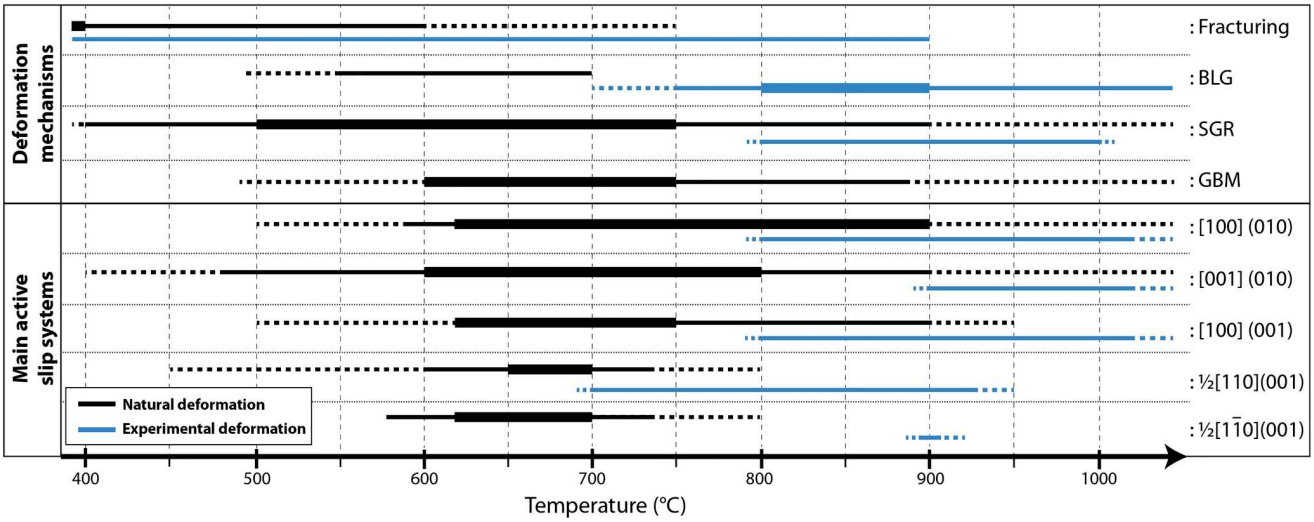

Figure 1. Plagioclase deformation mechanisms and most reported slip systems activities, plotted as a function of the temperature, for natural (black) and experimental deformations (blue). BLG: bulging recrystallization; SGR: subgrain rotation recrystallization; GBM: fast grain boundary migration recrystallization (see references in the text). GBM is not described in experimentally deformed plagioclase. The increasing importance of a deformation mechanism (or a slip system activity) is represented by the increasing thickness of the line. The full list of used references is given in Table S2 in Supporting Information S2.

of temperatures, is less documented at high temperatures. When both [001](010) and [100](010) slip systems are observed simultaneously active, a switch of prevalence from the [001] to the [100] direction seems to occur at ~800°C. Finally, the <110>(001) family of slip systems has been observed in a restricted range of temperatures, principally from ~600°C to 750°C. In anorthosites and gabbros, the preferred orientation of (010) is commonly interpreted as defining a foliation plane formed as a result of magmatic flow that preferentially aligns tabular plagioclase crystals (e.g., Benn & Allard, 1989; Ji et al., 2014; Satsukawa et al., 2013).

3. Geological Setting and IODP Hole U1473A

The ultraslow-spreading Southwest Indian Ridge (SWIR) has a full spreading rate of ~14 mm/yr (e.g., Hosford et al., 2003). Located 79–116 km south of the ridge axis, the Atlantis Bank (32° 42.3622′S, 57° 16.6880′E) is a pluri-kilometric gabbroic pluton bordered on its western flank by the north-south Atlantis II Transform (Figure 2a). This massif is an OCC exhumed by detachment faulting at 11–13 Ma. Lying at 700 m below sea level, the summit of the Atlantis Bank is a flat surface corresponding to a wave-cut platform, eroded ~9.5 Ma ago (Figure 2a, Dick et al., 1991). Although the surface of the Atlantis Bank is not a typical detachment surface, the presence of talc-serpentine schists around the massif is documented (e.g., Baines et al., 2003; Dick, Kvassnes, et al., 2019), as well as low-angle dipping ductile shear zones located in the upper parts of ODP Hole 735B and IODP Hole U1473A (Dick et al., 2000; Dick, Kvassnes, et al., 2019). These shear zones predominantly display normal sense of shear in the upper 50 and ~450 m of holes U1473A and 735B, respectively, before becoming reverse at greater depths (Dick, MacLeod, et al., 2019).

IODP Hole U1473A was drilled from the summit of the Atlantis Bank to 809.4 m below seafloor (mbsf) during IODP Expeditions 360 and 362T (Blum et al., 2017; Dick, Kvassnes, et al., 2019). The two other holes drilled between 1987 and 1998, are located 1–2 km away from Hole U1473A: ODP Hole 735B (1508 mbsf, Dick et al., 2000) and ODP Hole 1105A (158 mbsf, Pettigrew et al., 1999). Sections recovered from these three holes consist of olivine-gabbros with minor oxide (-bearing) gabbros, gabbros, and troctolites (Figure 2b, Dick et al., 2000; Pettigrew et al., 1999).

In gabbroic lithologies from Hole U1473A, ductile deformation is frequent, particularly in the upper 500 mbsf. This upper section displays porphyroclastic to protomylonitic textures, in which meter-scale ultramylonites zones are common (Figure 2c). Two important and near-continuous zones of intense crystal-plastic deformation are located between 150 and 250 mbsf, and between 300 and 400 mbsf (MacLeod et al., 2017). The deeper part of Hole U1473A (from 500–600 to ~800 mbsf, Figure 2c) is affected by

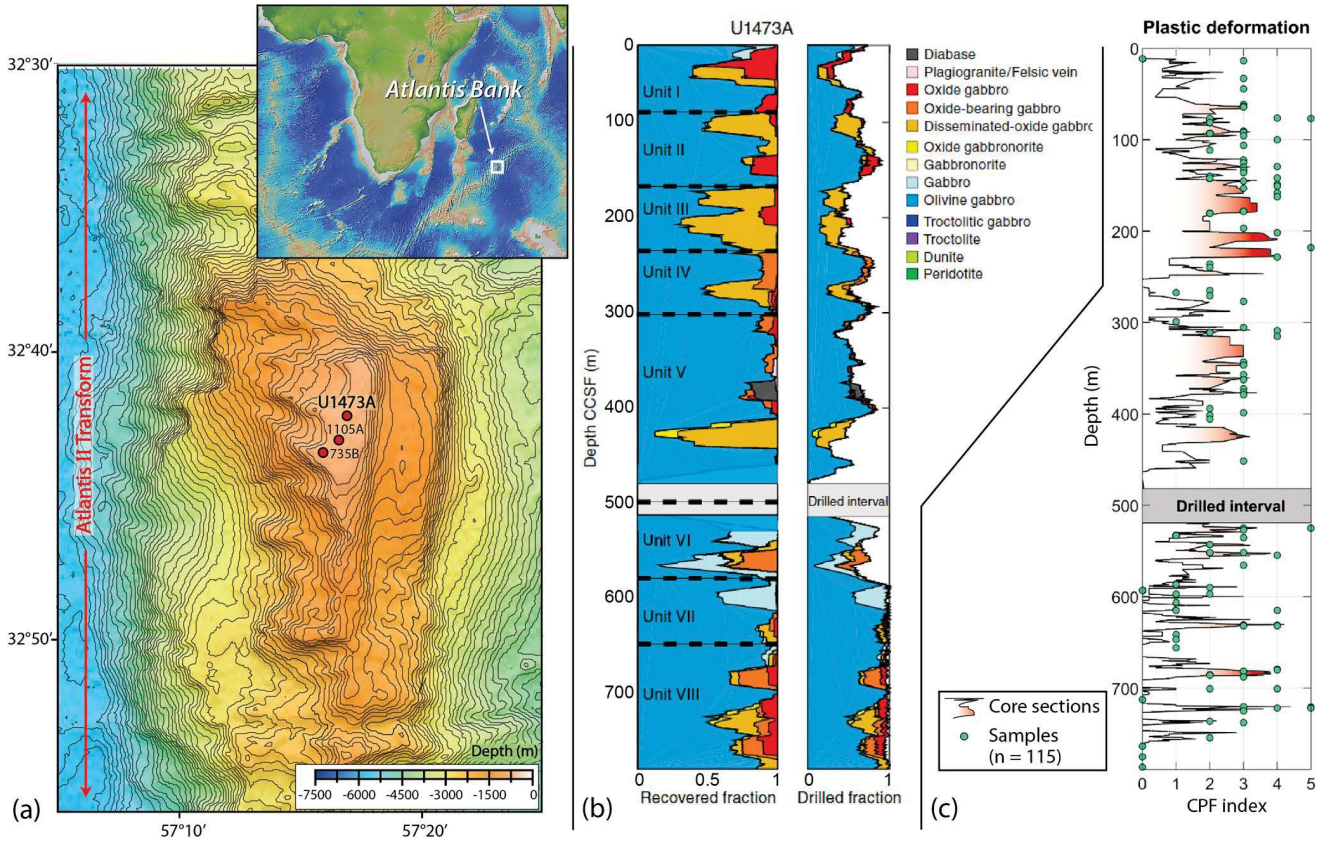

Figure 2. Location and characteristics of interests of Hole U1473A. (a) Bathymetric map of the Atlantis Bank, modified after Dick et al. (2017). The inset displays the location of the Atlantis Bank at the SWIR (Ryan et al., 2009) ; (b) Lithologies from Hole U1473A, after MacLeod et al. (2017); (c) Moving average of the apparent deformation intensity (crystal plastic fabrics (CPF)) inferred from macroscopic core observations (running average on five depth intervals, see MacLeod et al., 2017), and position along the depth of all studied samples with their CPF index. The drilled interval (481.7–519.2 mbsf) was drilled without coring. The red color below the curve highlights the deformed zones. CPF index: 0 = undeformed, 1 = foliated, 2 = porphyroclastic, 3 = protomylonitic, 4 = mylonitic, 5 = ultramylonitic. "n" is the number of analyzed depth intervals.

more localized ductile deformation, with thin high-strain zones that are heterogeneously distributed in a framework of undeformed to porphyroclastic gabbroic lithologies. These shear zones are centimeter-scale ultramylonites to rare meter-scale mylonites. Shipboard observations reveal that 42% of the core presents preserved magmatic textures. The qualitative categorization of crystal-plastic fabrics (CPF), ranging from 0 to 5 (CPF index: 0 = undeformed, 1 = foliated, 2 = porphyroclastic, 3 = protomylonitic, 4 = mylonitic, 5 = ultramylonitic), shows that deformed zones are characterized by 32% of porphyroclastic to protomylonitic textures, and 13% of mylonitic to ultramylonitic textures (Figure 2c, MacLeod et al., 2017).

The whole ductile deformation history within the Atlantis Bank appears to have occurred continuously from hyper-solidus conditions to lower temperatures while successive igneous gabbroic intrusions were emplaced. This is described as a process of dynamic accretion, characteristic of slow-spreading ridges with low to intermediate magmatism (Dick, MacLeod, et al., 2019).

Conditions for ductile deformation at the Atlantis Bank result in multiple deformation stages. Two dominant types of deformation are identified: solid-state deformation through dislocation creep, and melt-assisted deformation through both melt-rock reactions and dislocation creep. A first stage of solid-state deformation (Stage 1) led to the recrystallization of former igneous plagioclase, pyroxenes, and olivine grains. It is documented at 907°–1093°C (median = 1026°C; Gardner et al., 2020) and ~860°–940°C (Mehl & Hirth, 2008) in Hole 735B, at 862–910°C in submersible samples from the Atlantis Bank surface (Miranda & John, 2010). Following this initial solid-state deformation stage, two melt-assisted deformation episodes are reported in the presence of melt (grouped in Stage 2). The first episode (Stage 2a) occurred at 846°–969°C (median at 949° and 906°C; Gardner et al., 2020), and the second (Stage 2b) at 817°–1000°C, mainly from ~800 to 900°C

(Gardner et al., 2020; Taufner et al., 2021). A lower temperature solid-state event (Stage 3) is documented in mylonites at 740°–840°C (median at 780°C in Miranda et al., 2016, and 795°C in Miranda & John, 2010). An ultimate stage of solid state–semi-brittle deformation (Stage 4) is recorded mainly in plagioclase-amphibole bearing mylonites/ultramylonites at 665 ± 40°C (Miranda & John, 2010).

4. Methods

A collection of 102 gabbroic rock samples (115 microstructural domains) were taken for this study between 11.3 and 786.5 mbsf (average spacing of 6.8 m, Figure 2c) in Hole U1473A, targeting intervals with crystal-plastic deformation. These studied microstructural domains are mainly attributed to a continuum of deformation from early Stage 1 to Stage 3 under solid-state conditions. Some highly deformed domains display textural similarities with domains associated to stage 2 deformations. Some of the studied mylonites and ultramylonites may have undergone deformation in the presence of melt. Finally, the plagioclase-amphibole ultramylonites formed during late Stage 4. Core sections were split onboard to maximize the expression of dipping structures on the cut face (e.g., foliation) while maintaining representative features in both core section halves (MacLeod et al., 2017). Hence the plane of analysis is orthogonal to the foliation, and the lineation is generally not known but is deduced from the plagioclase CPO. Sample names (I_II_III) indicate the core number (I), the number of the section in the core (II), the top depth in the section in cm (III). A letter (A, B, or C) identifying the microstructural domain is added at the end when several domains were analyzed at the same depth or in the same sample.

4.1. EBSD Analyses

Crystallographic analyses were performed with the electron backscatter diffraction (EBSD) technique, using the CamScan X500FE Crystal Probe SEM, equipped with the Oxford instruments Nordlys®, and later on, Symmetry® EBSD detector, and the Jeol 5600 SEM equipped with the Oxford instrument NordlysNano EBSD detector at Geosciences Montpellier lab. The diffraction pattern acquisition was achieved at a working distance of 25 mm, an indexing speed of 140 Hz, an acceleration voltage of 20 kV, and a probe current of 10 nA. The scanning resolution was chosen as a function of the mean minimum grain size of each analyzed sample and finally varies from 2.5 to 30 μm (average resolution: 10 μm). The indexing rate is relatively high on raw maps ranging from 73% to 98%, with a large majority of samples around 90%. Thin section mapping was generally done on areas of 1–2 cm^2, and on whole thin sections for the five coarse-grained samples considered in this study.

4.2. EBSD Data Processing

Data processing was performed on 115 microstructural domains with the MTEX Matlab® toolbox (version 5.3.1, e.g., Mainprice et al., 2015), to calculate pole figures, inverse pole figures (IPF), and parameters indicative of the fabric strength: the J index and pole figure index PfJ, derived from the orientation density function (ODF), and the M index derived from uncorrelated misorientations. J varies from one for random orientations to infinity for a single orientation (e.g., Bunge, 1982). PfJ is expressed as an integral of the ODF, calculated for a unit axis given in crystal coordinates and a unit direction in specimen coordinates, and varies the same way as J index (e.g., Mainprice et al., 2015). M index is defined as the difference between the distribution of measured uncorrelated misorientation angles and the distribution of uncorrelated misorientation angles of a random fabric, and varies from zero for a random fabric to one for a single orientation fabric (Skemer et al., 2005). Calculated parameters for each analyzed sample are given in Table S3 in Supporting Information S2.

Only pixels with mean angular deviations (i.e., the angle between the acquired diffraction pattern and the indexing solution) below 1°, and grains containing more than five pixels have been considered in data sets. The grain segmentation angle used is 10°. Misorientations lower than 2° between two neighboring pixels have not been considered (Trimby et al., 1998). Average grain orientations were used for calculation of pole figures and orientation parameters, instead of the pixel orientation data set, in order to give equivalent weights to all grains, regardless of their size. The twinned plagioclase grains are reconstructed by identifying the twin boundaries and merging twinned domains within a same grain for grain orientation analysis.

Twins are identified from their boundary angle (>175°) and a rotation in (010) and (001), and around [010] and [001]. The orientation of the largest twin domain is attributed to the reconstructed grain.

Recrystallized grains were automatically selected using the following parameters: (a) a grain orientation spread (GOS) <2°, which corresponds to the average of the misorientations between each pixel in a grain and the grain mean orientation (e.g., Brewer et al., 2009); (b) a tortuosity <1.4 (ratio between the grain perimeter and the convex hull perimeter); and (c) an equivalent diameter <700 μm (diameter of a circle of the same area as the grain). These threshold values were chosen due to their good reproducibility in the sample suite, and give a lower bound for the amount of recrystallization in samples. Calculated recrystallized fractions were then systematically optically checked to prevent possible errors. EBSD maps also allowed us to calculate the phase modal amounts in each analyzed domains. In the following, medians and interquartile ranges (i.e., the interval between the first and third quartiles of a data set) are used to evaluate the evolution of the recrystallized fraction in analyzed microstructural domains with increasing deformation.

4.3. Misorientations Analysis

The deformation of grains and their recrystallization results in orientation relations characterized by specific rotation axes and associated rotation angles, known as misorientations (e.g., Wheeler et al., 2001). The misorientation axis and angle distributions between porphyroclasts and their neighboring recrystallized grains, indicative of the deformation mechanism, have been measured (e.g., Jiang et al., 2000; Kruse et al., 2001; Svahnberg & Piazolo, 2010). The rotation axes of misorientations measured within grains are used to determine the type of subgrains (e.g., tilt or twist) and the possible slip systems having produced these misorientations (e.g., Lloyd et al., 1997). The analysis of correlated and uncorrelated misorientation angle distribution is performed after the twin boundaries have been merged into their host grain to focus on other boundaries. Another misorientation parameter use is the GOS, which is the average of the deviation between the orientations of pixels within a grain from the mean orientation of the grain.

Plagioclase slip planes (010) and (001) can be considered as the easiest slip planes in the sense that they intersect the smallest number of tetrahedra-O bonds of the framework structure (Gandais & Willaime, 1984; Ji et al., 1988; Tullis, 1983). In order to look at active slip directions on these planes, we selected in each analyzed domains two groups of grains: one with (001) parallel to the analyzed plane of the thin section (plane orthogonal to Z), and a second for (010) being parallel to the analyzed plane. A tolerance angle of 15° was arbitrarily taken. Misorientation rotation axes observed in these planes indicates the type of dislocation associated with the measured misorientations: edge dislocations if they belong to the selected plane and screw dislocations if they are orthogonal to it. The burgers vectors of these dislocation systems can then be deduced from the orientation relationship between the misorientation axis, the inspected plane, and the structural orientation. Then, as explained in Kruse et al. (2001) we will consider a slip system to be well orientated for glide if its Burgers vectors is close to the lineation and within the foliation plane. The plagioclase structure is assumed to be $C\bar{1}$ due to their compositional range varying from andesine to labradorite and to their thermal context (Smith, 1984).

5. Sample Descriptions

Analyzed microstructural domains (115 on 102 samples) consist of 70 olivine gabbros, 14 oxide gabbros (oxide content >1%), 13 olivine oxide gabbros, 8 gabbros, 3 gabbronorites, 3 oxide gabbronorites, 2 amphibolitic metagabbros, 1 anorthosite, and 1 oxide gabbronorite. The average mineralogical assemblage in all lithologies consists of plagioclase (Pl, ~50%), clinopyroxene (Cpx, ~30%), subordinate olivine (Ol, ~5–10%) and orthopyroxene (Opx, ~2–5%), and minor oxides (Ox) and amphiboles (Amph, Table S3 in Supporting Information S2). Microstructural evolutions occur without significant petrological changes, with relatively constant average modes of plagioclase. Conversely, modes of clinopyroxene and olivine decrease as the deformation increases in samples, from 27%–30% to ~20% in clinopyroxene and from ~10% to the disappearance of olivine. This is accompanied by a rise of amphibole modes (~3%–~14%) and of orthopyroxene (~1.5%–~5%).

Alteration is weak in the selected sample suite, principally associated with veinlets and almost exclusively restricted to the upper half of Hole U1473A. These veinlets, mainly filled by green amphiboles, rarely by

chlorite, are observed in 31 samples located in the upper 570 mbsf. The veinlets are orthogonal to the trace of the foliation in 22 samples and oblique in the others.

Plagioclase found in Hole U1473A gabbroic lithologies has a composition ranging between andesine and labradorite (An_{36} to An_{71}), with more An rich compositions in gabbros and olivine-gabbros (An_{40} to An_{71}) than in oxide-bearing-gabbros (An_{36} to An_{45}, Dick, Kvassnes, et al., 2019; Nguyen et al., 2018; Nozaka et al., 2019). A decrease of 2%–3% in An content is measured from the core to rims in some samples, as well as in partially albitized gabbros where it decreases to An_{32} (Nozaka et al., 2019). Clinopyroxene is augite; its Mg# varies from 0.48 to 0.86 with a mean at 0.74 in gabbros and olivine-gabbros, and 0.70 in oxide-bearing-gabbros (Dick, Kvassnes, et al., 2019; Nguyen et al., 2018; Nozaka et al., 2019). The Mg# of olivines varies from 0.46 to 0.80 in all gabbroic rocks (Dick, Kvassnes, et al., 2019; Nguyen et al., 2018; Nozaka et al., 2019). Orthopyroxene is hypersthene, and has a Mg# varying from 0.56 to 0.79, with a mean at 0.67 (Dick, Kvassnes, et al., 2019; Nozaka et al., 2019).

One hundred and seven analyzed microstructural domains (over 115) are plastically deformed, and 72 corresponds to CPF indices 3 to 5 (protomylonites to ultramylonites). Dynamic recrystallization of plagioclase, clinopyroxene, and olivine is the main deformation accommodation mechanism observed within the studied domains (Figure 3). Recrystallized minerals constitute at least 50% of modes in a majority of the analyzed domains (Figure 4). Accordingly, core and mantle structures around magmatic porphyroclasts are widespread, and nucleation bands in grains-scale fractures or thin section-scale fractures occur in plagioclase. In the following sections, deformation mechanisms are identified by both optical observations and EBSD analyses.

5.1. Undeformed Domains (CPF Index 0, Figure 3a)

Microstructural domains with no apparent (or very limited) plastic deformation varies from fine to coarse grained. Textures are generally granular in fine-grained domains (~100–150 μm) with subequant grain shapes, and subophitic in coarse-grained domains (0.5 mm–1.5 cm) with laths of subhedral plagioclases that penetrate pyroxenes oikocrysts, and anhedral olivine (Figure 3a). In these microstructures the analyzed domains consist of five olivine gabbros, two olivine oxide gabbros, and 1 gabbronorite. The mineralogical assemblage contains on average plagioclase (59.2%), clinopyroxene (27.1%), olivine (10.8%), orthopyroxene (2.0%), and minor amphiboles and oxides (<1%). Plastic deformation is not completely absent, as indicated by limited undulatory extinction in plagioclase, clinopyroxene, and olivine crystals, sometimes accompanied by tapered twins in plagioclase (Figure 3a). Grain boundaries are straight or lobate. A magmatic foliation is observed in fine-grained granular domains through the discrete shape preferred orientation of plagioclase and clinopyroxene grains. This is not observed in domains of coarser grain sizes, possibly because of the limited number of grains at thin section scale.

5.2. Foliated Domains (CPF Index 1, Figure 3b)

The original subophitic or granular texture is partly preserved in the foliated domains; only a limited amount of deformation is accommodated by pyroxene and olivine, and the grain size is medium (0.1–0.5 cm, Figure 3b). In these microstructures the analyzed domains consist of eight olivine gabbros, one oxide gabbro, and 1 gabbro. These lithologies contain on average plagioclase (60.9%), clinopyroxene (30.2%), olivine (4.0%), amphibole (3.3%), orthopyroxene (1.6%), and minor oxides (<1%). Plagioclase porphyroclasts (Pl_1; see Figure 5) show undulatory extinction and some subgrain boundaries, tapered deformation twins, grain boundary migration, and grain boundaries are lobate and sometimes serrated (e.g., Figures 5a and 5d). Dynamic recrystallization is ~40% of the whole mineral assemblage (Figure 4a) and the calculated fractions of recrystallized plagioclase (Pl_2), 44%, are positively skewed with an IR = 42.2% (the median is closer to the first quartile than to the third one, Figure 4b). The grain size of Pl_2 grains is variable (50–250 μm), on average ~140 μm. Deformation is largely accommodated by plagioclase and leads to the loss of the lath shape of primary plagioclase and the formation of inequigranular aggregates of recrystallized Pl_2 grains (Figure 3b).

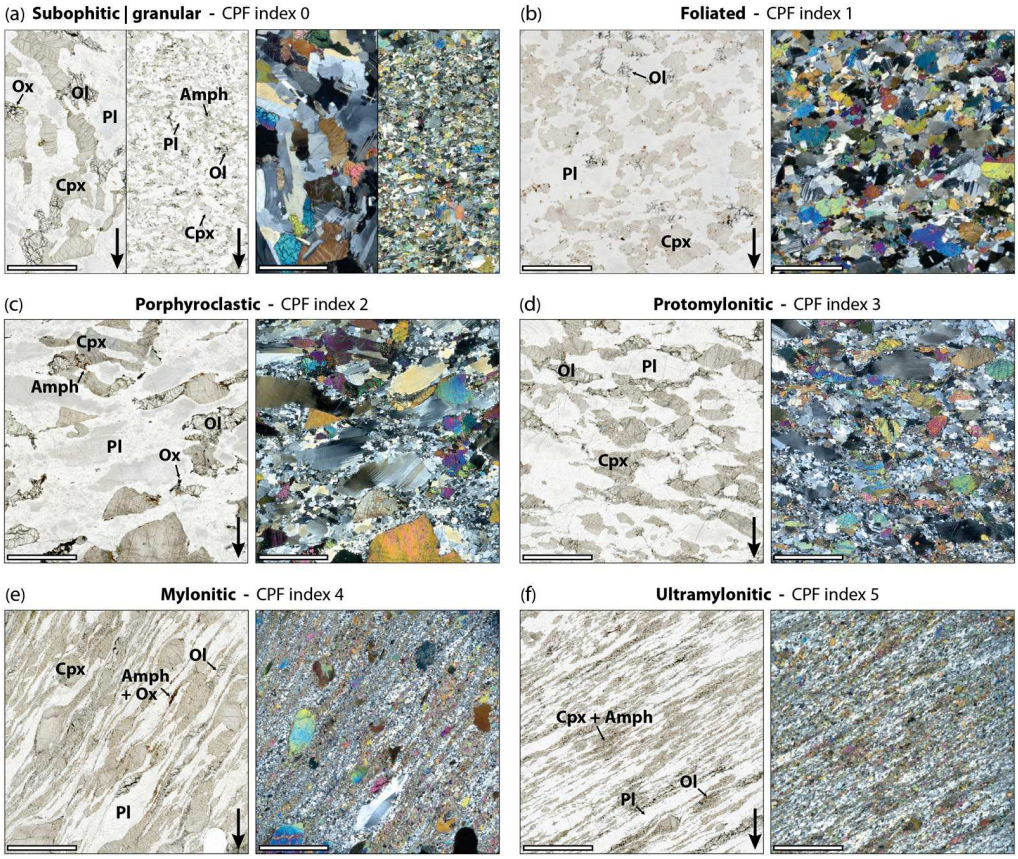

Figure 3. Representative microstructures observed in studied intervals from Hole U1473A. (a) Undeformed subophitic microstructural domain 88_5_117 and granular domain 66_1_96; (b) Foliated domain 70_7_6; (c) Porphyroclastic domain 13_2_59; (d) Protomylonitic domain 50_2_43; (e) Mylonitic domain 69_5_73_A; (f) Ultramylonitic domain 58_5_79_C. In each subfigure sections, on the left are plane-polarized light microphotographs, and on the right cross-polarized light microphotographs. The scale bar length is 5 mm. The bottom-right arrows indicate the down hole direction in the rock. Pl: Plagioclase; Cpx: Clinopyroxene; Ol: Olivine, Amph: Amphibole, Ox: Oxide.

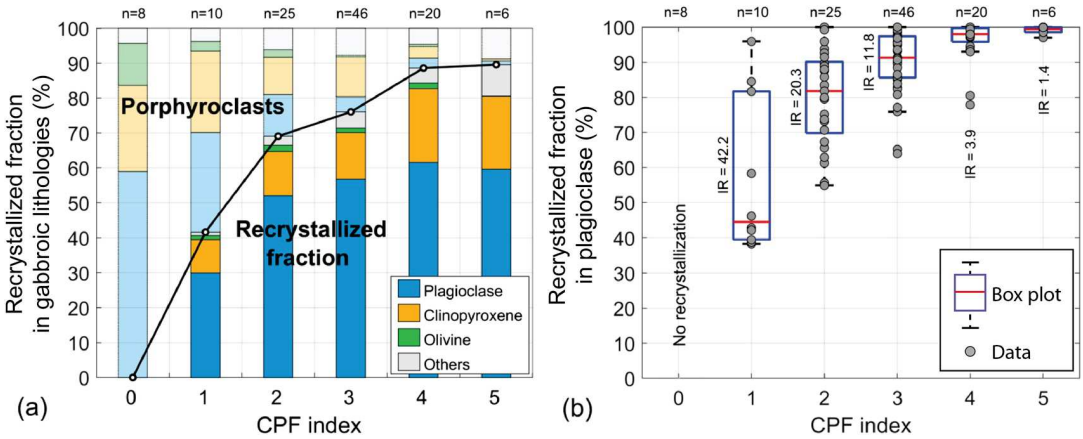

Figure 4. Modal proportions of recrystallized minerals deduced from EBSD maps and plotted as a function of the CPF indices of microstructural domains. (a) Evolution of the recrystallized fraction in studied domains (black curve) and superimposed cumulative histograms of recrystallized fractions (bottom) and porphyroclast fractions (top, translucent) within main constitutive phases. "Others" correspond to orthopyroxene, oxide, and amphibole. All values are medians of normal distributions, and "*n*" is the number of analyzed microstructural domains. (b) Boxplots showing the proportions of the recrystallized fraction in plagioclase. "IR" is the interquartile range of the data set. Blue boxes contain 50% of the data located between the first (25%) and third (75%) quartiles. The red line is the median value and the whiskers (dotted line) extend within ±2.7 σ for normally distributed data sets. Data points outside of the whiskers are not considered.

5.3. Porphyroclastic Domains (CPF Index 2, Figure 3c)

The original subophitic or granular texture is lost in porphyroclastic domains. Recrystallization of plagioclase and olivine grains induces the development of millimeter-sized, weakly foliated porphyroclastic aggregates forming core and mantle structures (Figures 3c, 5d and 5f). Clinopyroxene recrystallizes from its edges, but to a lesser extent than in plagioclase and olivine (Figure 3c). In these microstructures the analyzed domains consist of 20 olivine gabbros, 2 oxide gabbros, 1 olivine oxide gabbro, 1 oxide gabbronorite, and 1 anorthosite. Mineral proportions are on average plagioclase (66.5%), clinopyroxene (22.4%), olivine (5.7%), amphibole (2.6%), orthopyroxene (2.1%), and minor oxides (<1%). Pl_1 grains display tapered twins, grain boundary migration, frequent undulatory extinction, and subgrain boundaries (Figure 5a, 5d and 5f). Pl_1 grain boundaries are usually serrated, sometimes lobate. Pl_2 grain size usually ranges from 70 to 100 μm (median = 89 μm). Pl_2 grain boundaries are often lobate, and tapered twins are common. Grain boundary migration and undulatory extinction are often found in olivine grains (Figure 5b). Recrystallization rises to ~70% overall (Figure 4a) and is ~82% in plagioclase (Figure 4b). In these textures, the recrystallized fraction distribution is negatively skewed (median close to the third quartile) with a high IR (20.3%).

5.4. Protomylonitic Domains (CPF Index 3, Figure 3d)

In protomylonitic textures, plagioclase tends to be highly recrystallized and forms a connected fine-grained matrix in which magmatic clinopyroxene and olivine porphyroclasts continue to dynamically recrystallize from their edges (Figure 3d). The foliation is well defined by recrystallized aggregates of clinopyroxenes and olivines, and elongated porphyroclasts of plagioclases and clinopyroxenes (Figure 3d). In these microstructures the analyzed domains consist of 24 olivine gabbros, 8 oxide gabbros, 8 olivine oxide gabbros, 5 gabbros, and 1 olivine oxide gabbronorite. The mineralogical assemblage contains on average plagioclase (63.1%), clinopyroxene (23.2%), amphibole (5.1%), orthopyroxene (3.2%), olivine (3.1%), and oxides (~2%). Pl_1 grain boundaries are mostly serrated, whereas the Pl_2 grain boundaries are lobate or curvilinear. Both frequently contain tapered deformation twins. Subgrain boundaries in Pl_1 porphyroclasts are widespread, and sometimes present in large Pl_2 grains (200–300 μm, e.g., Figure 5d). Some microstructural domains display minor evidence of grain boundary migration forming small new grains (10–20 μm) closed by subgrain boundaries, while others are indicative of static recrystallization microstructures in plagioclase grains (Figures 5g and 5h). Subgrain boundaries are found in olivine grains, and in recrystallized clinopyroxene aggregates occurring together with grain boundary migration (Figure 5c, 5e and 5f). The Pl_2 grain size ranges from 50 to 100 μm (median = 69 μm). Recrystallization reaches ~75% overall (Figure 4a) and ~91% in plagioclase (Figure 4b). Recrystallized fractions of plagioclase are normally arranged and the IR is low (IR = 11.8%, Figure 4b).

5.5. Mylonitic Domains (CPF Index 4, Figure 3e)

A strong foliation characterizes mylonitic domains due to the dynamic recrystallization of an important fraction of clinopyroxene and olivine, in addition to plagioclase, in elongated sigmoid aggregates (Figure 3e). This foliation consists of alternating plagioclase-rich and clinopyroxene-rich slightly undulating bands. In these microstructures the analyzed domains consist of 12 olivine gabbros, 2 oxide gabbros, 2 olivine oxide gabbros, 2 oxide gabbronorites, 1 gabbronorite, and 1 amphibolitic metagabbro. The mineralogical assemblage is on average plagioclase (61.7%), clinopyroxene (23.3%), amphibole (6.2%), orthopyroxene (4.3%), olivine (2.9%), and others including oxides (<2%). Pl_2 grain boundaries are mostly curvilinear while Pl_1 grain boundaries are mostly serrated. Tapered twins and subgrain boundaries are common in grains larger than 0.5 mm. The recrystallized fraction is ~88% (Figure 4a) and rises to ~97% in plagioclase (Figure 4b). Data are normally arranged and associated with a low IR (IR = 3.9%, Figure 4b). The Pl_2 grain size is 30–70 μm (median = 52 μm) and decreases to 10–20 μm in localized shear bands (e.g., Figure 5e).

5.6. Ultramylonitic Domains (CPF Index 5, Figure 3f)

Ultramylonitic textures are characterized by an almost complete dynamic recrystallization of all grains and a straight layering formed by nearly continuous plagioclase-rich bands that alternate with clinopyroxene-rich bands (Figure 3f). In these microstructures the analyzed domains consist of 2 gabbros, one olivine

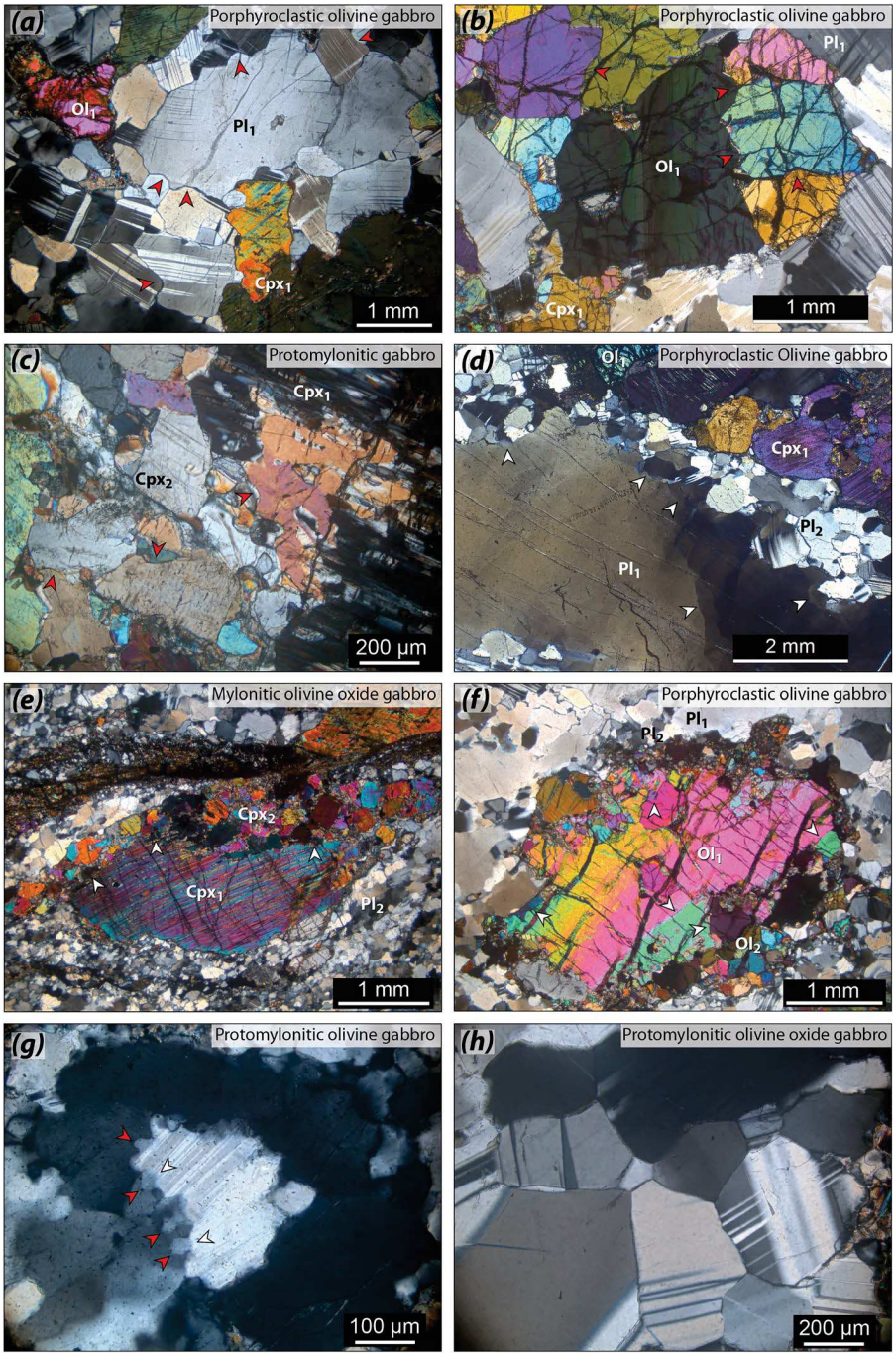

Figure 5. Cross-polarized microphotographs of representative microstructures and recrystallization mechanisms, observed in studied intervals from Hole U1473A. (a–c) Evidence of grain boundary migration in (a) plagioclase (Pl), (b) olivine (Ol), and (c) clinopyroxene (Cpx). The indices "1" and "2" indicate primary grains and recrystallized grains, respectively. Red arrows indicate boundary migration. Note the frequent occurrence of tapered twins in plagioclase grains. (d–f) Evidence of subgrain rotation recrystallization in (d) plagioclase, (e) clinopyroxene, and (f) olivine, forming core and mantle structures. Note that parent grains display undulatory extinction. White arrows indicate subgrain boundaries. (g) Evidence of bulging recrystallization in plagioclase forming a core and mantle structure. Note that most of the bulges are closed by a subgrain boundary (white arrows). (h) Polygonal fabric and related 120°-triple junctions of plagioclase, testifying for static recrystallization. Note the systematic occurrence of tapered twins.

gabbro, one oxide gabbro, 1 gabbronorite, and 1 amphibolitic metagabbro. The mineralogical assemblage contains on average plagioclase (59.1%), clinopyroxene (20.4%), amphibole (14.4%), orthopyroxene (5.3%), and minor olivine and retrograde phases (other than amphibole; <1%). Pl_2 grains have lobate to serrated boundaries, and tapered deformation twins and subgrain boundaries are frequent. Ultramylonitic deformation is frequently highly localized at a very small scale (from 0.5 mm to 1–2 mm thick bands), although it can occur at the pluri-decimeter scale (as in sample 58_5_79_C, Figure 3f). Recrystallization reaches ~90% overall (Figure 4a) and is complete in plagioclase (Figure 4b), with a very low IR (IR = 1.4%, Figure 4b). The size of Pl_2 grains ranges from 15 to 30 μm (median = 21 μm), and sometimes 5–10 μm in shear bands.

6. EBSD Analysis of Plagioclase

6.1. Crystallographic Preferred Orientations

In the undeformed (CPF index 0) and foliated (CPF index 1) microstructural domains, misorientation maps indicate little intra-grain deformation (e.g., Figure 6a). In undeformed microstructures, CPO are generally random in coarse-grained domains and can be strong in fine-grained domains (Figures 6a and 7a). Note that the number of analyzed grains in coarse-grained domains is not statistically significant; hence the resulting CPO is not necessarily representative of the sampled domain. In fine-grained undeformed domains, the foliation is parallel to the preferred orientation of plagioclase (010) planes, accompanied by an orthogonal girdle (rarely a point maximum) of [100] axis, which aligns in the magmatic foliation (Figures 6a and 7a). The foliation and the preferred orientation of plagioclase (010) are generally sub parallel, so the preferred orientation of (010) in plagioclase is used in pole figures as a proxy to the foliation (pink great circles, Figures 6a and 7a). Foliated domains (CPF index 1) display similar CPO patterns as fine-grained undeformed domains with a weaker fabric strength (Figure 7b).

The increase of plastic deformation results in progressive recrystallization (Figures 3 and 4), especially in plagioclase, accompanied by the widespread development of subgrain boundaries in grains (Figures 6d and 6e). These subgrains first form in porphyroclasts (CPF indices 2 and 3, Figures 6b and 6c), but as deformation progresses, they also develop in the larger recrystallized grains (CPF indices 4 and 5, Figure 6c–6e). From CPF indices 2 to 5, typical CPO has (010) lying close to the foliation plane and [100] aligned in this plane (Figures 6b–6e, and 7c–7f). Point maxima are most common for both (010) and [100], although girdle distributions can be found. (001) commonly forms girdles orthogonal to the foliation. Seven protomylonitic to ultramylonitic domains (CPF indices 3 to 5) show an alignment of (001) close to the foliation rather than (010) (e.g., Figures 7d and 7f, samples 6_2_128 and 81_6_117_B). In all analyzed domains, the transition from porphyroclastic to mylonitic samples (CPF indices 2 to 4) is accompanied by the development of a lineation well-defined by the preferred alignment of [100] (Figures 6 and 7).

Considering the parent-child grains relationships, we observe in porphyroclastic to mylonitic domains (CPF indices 2 to 4) a strong similarity in crystallographic orientations (e.g., Figures 6b and 6c). It is referred to as a "host-controlled" orientation of recrystallized grains. Among the 88 analyzed microstructural domains containing porphyroclasts (CPF indices 1 to 5), 52 domains display similar CPO patterns in porphyroclasts and recrystallized grains, and the preferred orientations of at least [100] and (010) are similar in 63 domains (e.g., Figures 6b and 6c). The CPO patterns display no similarities between porphyroclasts and recrystallized grains in only 16 domains.

All studied domains through IODP Hole U1473A show relatively weak CPO as indicated by low values of J and M indices, usually below 3 and 0.09 respectively (Figures 8a and 8b). The evolution of the CPO strength as a function of the CPF index is significantly different for the two strength indices. Median J values indicate a smooth decrease of CPO strength from ~3.0 in CPF index 0 to ~1.8 in CPF index 5, passing through ~2.3 in CPF index 2 (Figure 8a). High IR values of the J distribution, 0.82 in CPF index 0 and 0.69–0.87 in CPF indices 2 to 4, indicate a large dispersion from one sample to another. IR values strongly decrease in ultramylonites (CPF index 5), and the distribution of J is positively skewed from CPF indices 1 to 5. Analyzed domains with less than 1000 grains (orange data in Figure 8a) are excluded from statistics because of the abnormally high J values calculated for them (Figure S1 in Supporting Information S1 and Table S3 in Supporting Information S2).

Median M values are low, below 0.07 overall; they slightly increase from CPF indices 1 to 4 and then decrease from CPF indices 4 to 5 (Figure 8b). The statistic distribution ranges (i.e., IR) are large, 0.06 in CPF

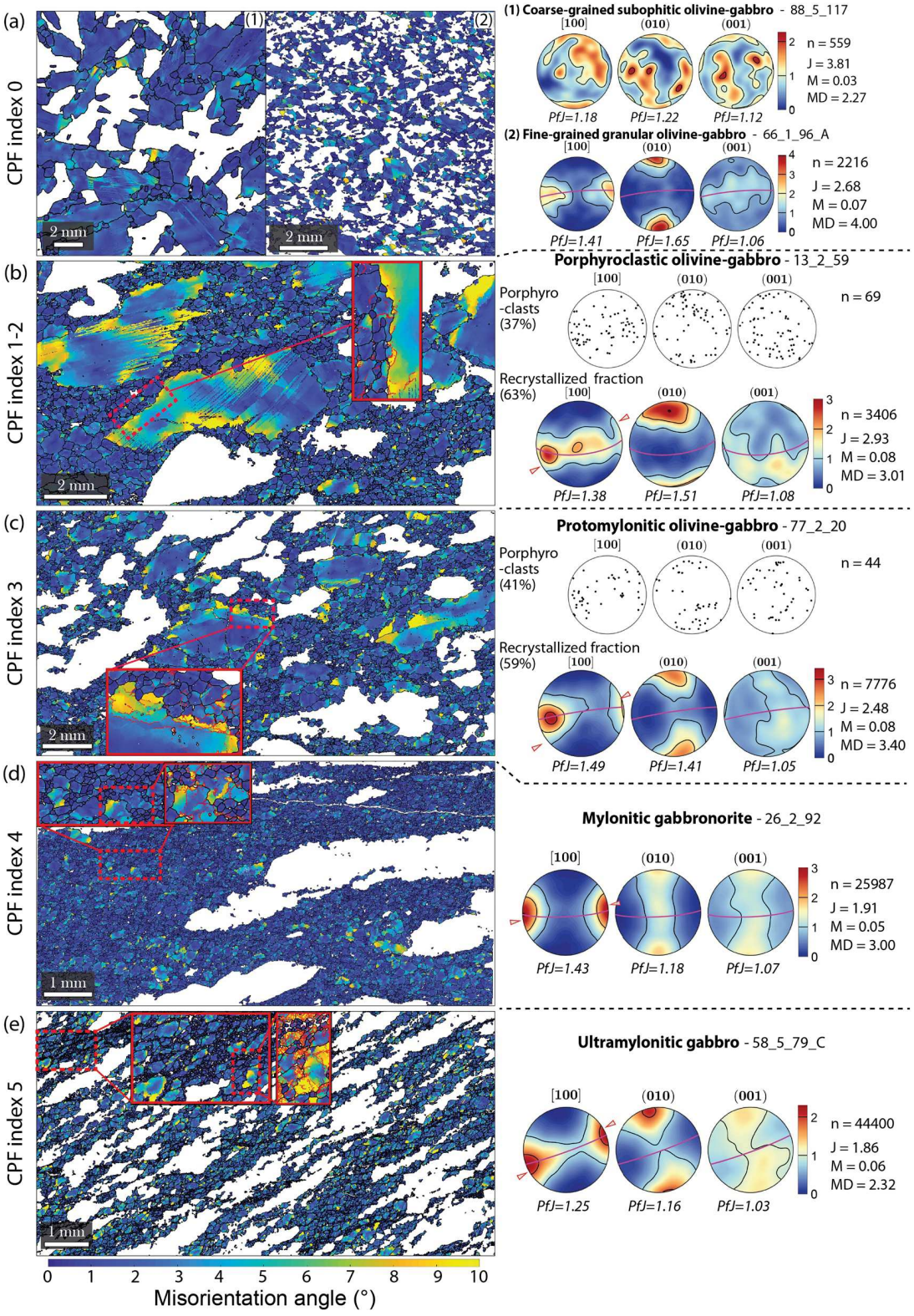
(a)
CPF index 0
(1)
(2)
2 mm
2 mm
(1) Coarse-grained subophitic olivine-gabbro - 88_5_117
[100] (010) (001)
PfJ=1.18 PfJ=1.22 PfJ=1.12
n = 559
J = 3.81
M = 0.03
MD = 2.27
(2) Fine-grained granular olivine-gabbro - 66_1_96_A
[100] (010) (001)
PfJ=1.41 PfJ=1.65 PfJ=1.06
n = 2216
J = 2.68
M = 0.07
MD = 4.00
(b)
CPF index 1-2
2 mm
Porphyroclastic olivine-gabbro - 13_2_59
Porphyro -clasts (37%)
[100] (010) (001)
n = 69
Recrystallized fraction (63%)
[100] (010) (001)
PfJ=1.38 PfJ=1.51 PfJ=1.08
n = 3406
J = 2.93
M = 0.08
MD = 3.01
(c)
CPF index 3
2 mm
Protomylonitic olivine-gabbro - 77_2_20
Porphyro -clasts (41%)
[100] (010) (001)
n = 44
Recrystallized fraction (59%)
[100] (010) (001)
PfJ=1.49 PfJ=1.41 PfJ=1.05
n = 7776
J = 2.48
M = 0.08
MD = 3.40
(d)
CPF index 4
1 mm
Mylonitic gabbronorite - 26_2_92
[100] (010) (001)
PfJ=1.43 PfJ=1.18 PfJ=1.07
n = 25987
J = 1.91
M = 0.05
MD = 3.00
(e)
CPF index 5
1 mm
Ultramylonitic gabbro - 58_5_79_C
[100] (010) (001)
PfJ=1.25 PfJ=1.16 PfJ=1.03
n = 44400
J = 1.86
M = 0.06
MD = 2.32
0 1 2 3 4 5 6 7 8 9 10
Misorientation angle (°)

Figure 6.

index 0 and 0.04 in CPF index 4 and they usually overlap from one CPF index to another. The data distribution is negatively skewed from CPF indices 1 to 3, and rather normal from 4 to 5.

The M index indicate higher CPO strength for fine-grained magmatic samples (CPF index 0, gray data points Figure 8b). The evolution of J and M indices with increasing CPF indices from 1 to 5 shows a bell-shaped distribution. The peak maximum of this distribution is at CPF indices 2–3 for J and 3–4 for M (taking into account the complete overlap of the neighboring distributions).

6.2. Misorientation Analysis

Deformation at high temperature induces storage of energy in strained grains that is released up by the creep of crystal defects toward the grain boundary and can arrange in subgrain structures. Produced by the dislocation motion through slip systems, they are characterized by a local rotation specific to the dislocations that they are made up of Amelinckx and Dekeyser (1959). These rotations and axes along which they arrange are indicative of the activated slip systems (e.g., Lloyd et al., 1997).

Intracrystalline misorientation analysis indicates dominant amounts of low angle correlated misorientations (<10°) within grains in 77 microstructural domains (e.g., Figure 6 and Figure S2 in Supporting Information S1). This is observed from CPF indices 0 to 5, and predominates in protomylonitic to ultramylonitic domains (CPF indices 3 to 5). In the 38 other microstructural domains, similar amounts of low and high angle misorientations (<10° and 150°–180°, respectively) are observed. Fifty nine domains indicate more than 20% of misorientations in the class 0°–10°, and 88 domains indicate more than 10% of misorientations in that class. This strongly suggests that the main active mechanism is SGR (e.g., Poirier & Guillopé, 1979). Displayed in inverse pole figure, the rotation axes of intracrystalline misorientations are always preferentially arranged around the [100] axis, sometimes with variations of up to 20° toward the north pole (Figure S2 in Supporting Information S1 and Figure 9a, top). Other misorientation axes are present at subgrain boundaries but are less common. The misorientation axis and the slip direction in slip systems are orthogonal, or at least at high angle for edge dislocations in plagioclase (e.g., Kruse et al., 2001). Then, by considering the [100](010) slip system inferred from pole figures (Figures 6 and 7), the misorientation axis displayed in inverse pole figure should be different from [100]. Consistently with the pole figures (Figures 6 and 7), misorientation rotation axes at grain boundaries are preferentially located around (010) (Figure S2 in Supporting Information S1 and Figure 9a, middle and bottom). Then as (010) is the plane parallel to the foliation in almost all analyzed domains, it is possible that subgrain boundaries, with a [100] misorientation axis, mainly consist of tilt boundaries, while grain boundaries, with a [010] misorientation axis, consist of twist boundaries.

The analysis of misorientations related to recrystallization was performed on 52 plagioclase porphyroclast-recrystallized mantle pairs in 33 microstructural domains of variably deformed textures (CPF indices 1 to 4), mainly porphyroclastic and protomylonitic (CPF indices 2 and 3). Rotation axes of misorientations at parent grains boundaries (Figure 9a, middle) correspond to a mix of those of misorientations at subgrain boundaries (Figure 9a, top) and at recrystallized grains boundaries, dominantly along the (010) plane (Figure 9a, bottom). At parent grains boundaries, ubiquitous high misorientations indicate a general scattering of the neighboring recrystallized grains (Figure 9b). Two groups of misorientations are distinguished: (a) with boundary segments of 10°–60° angles and (b) with 120°–180° angles (Figure 9b). Group 1 is found in 35 porphyroclast-recrystallized mantle pairs (over 52 analyzed) and combines with group 2 in 30 pairs. 17 pairs display a non-zero flat misorientation profile from ~10° to 100°, increasing for higher misorientations (>120°). In these pairs, a major part of grain boundaries are twin boundaries (misorientations of 180°). The two types of profiles (one with groups 1 and 2, and the other with only the group 2) are also observed by looking at differences in orientations between parent grains and their second- and third-order neighbors.

Figure 6. Maps of misorientations from grain average orientation in plagioclase, and associated pole figures (average grain orientation data, lower hemisphere, equal-area projection) measured in representative domains from CPF indices 0 to 5. The trace of (010) in plagioclase (defined by the principal eigen-vector of the orientation tensor) is represented by the pink great circles, and the orientation of the trace of the foliation measured in samples, when observed with confidence, is indicated by the red arrows at the periphery of [100] pole figures. The white color in maps corresponds to other phases, and red limits in insets are subgrain boundaries. Contour intervals are multiples of a uniform distribution, and the minimum density is set to zero for comparison between analyzed domains. Maps and pole figures are presented respectively with the depth increasing from the top to the bottom and from north to south pole. "*n*" is the number of grains, "J" is the J index, "M" is the M index, "MD" is the maximum density, and "PfJ" are the pole densities of each pole figures (see text for explanations). Indicated percentages in (c and d) are area fractions of porphyroclasts and recrystallized grains.

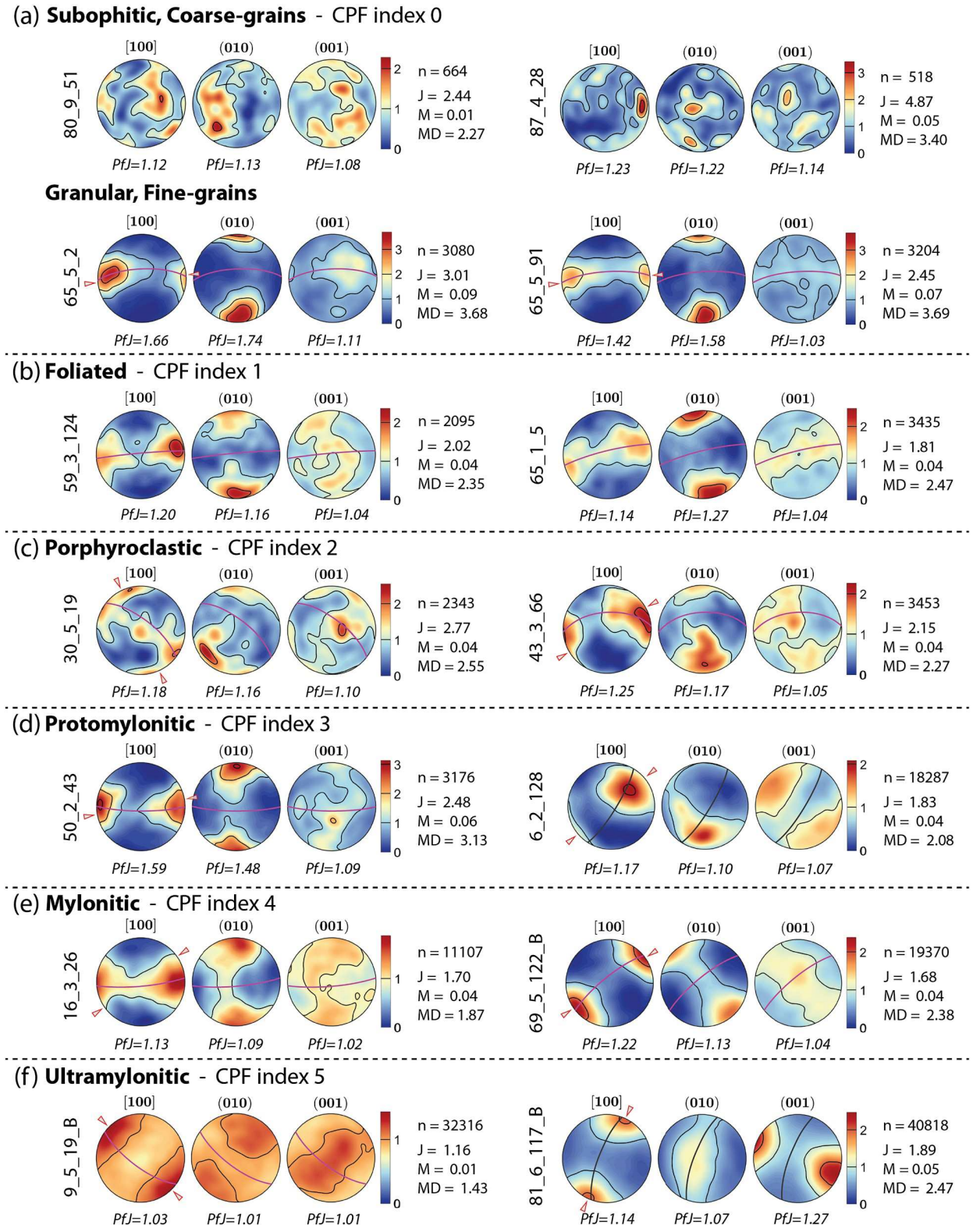
(a) Subophitic, Coarse-grains - CPF index 0
80_9_51
[100] (010) (001)
n = 664
J = 2.44
M = 0.01
MD = 2.27
PfJ=1.12 PfJ=1.13 PfJ=1.08
87_4_28
[100] (010) (001)
n = 518
J = 4.87
M = 0.05
MD = 3.40
PfJ=1.23 PfJ=1.22 PfJ=1.14
Granular, Fine-grains
65_5_2
[100] (010) (001)
n = 3080
J = 3.01
M = 0.09
MD = 3.68
PfJ=1.66 PfJ=1.74 PfJ=1.11
65_5_91
[100] (010) (001)
n = 3204
J = 2.45
M = 0.07
MD = 3.69
PfJ=1.42 PfJ=1.58 PfJ=1.03
(b) Foliated - CPF index 1
59_3_124
[100] (010) (001)
n = 2095
J = 2.02
M = 0.04
MD = 2.35
PfJ=1.20 PfJ=1.16 PfJ=1.04
65_1_5
[100] (010) (001)
n = 3435
J = 1.81
M = 0.04
MD = 2.47
PfJ=1.14 PfJ=1.27 PfJ=1.04
(c) Porphyroclastic - CPF index 2
30_5_19
[100] (010) (001)
n = 2343
J = 2.77
M = 0.04
MD = 2.55
PfJ=1.18 PfJ=1.16 PfJ=1.10
43_3_66
[100] (010) (001)
n = 3453
J = 2.15
M = 0.04
MD = 2.27
PfJ=1.25 PfJ=1.17 PfJ=1.05
(d) Protomylonitic - CPF index 3
50_2_43
[100] (010) (001)
n = 3176
J = 2.48
M = 0.06
MD = 3.13
PfJ=1.59 PfJ=1.48 PfJ=1.09
6_2_128
[100] (010) (001)
n = 18287
J = 1.83
M = 0.04
MD = 2.08
PfJ=1.17 PfJ=1.10 PfJ=1.07
(e) Mylonitic - CPF index 4
16_3_26
[100] (010) (001)
n = 11107
J = 1.70
M = 0.04
MD = 1.87
PfJ=1.13 PfJ=1.09 PfJ=1.02
69_5_122_B
[100] (010) (001)
n = 19370
J = 1.68
M = 0.04
MD = 2.38
PfJ=1.22 PfJ=1.13 PfJ=1.04
(f) Ultramylonitic - CPF index 5
9_5_19_B
[100] (010) (001)
n = 32316
J = 1.16
M = 0.01
MD = 1.43
PfJ=1.03 PfJ=1.01 PfJ=1.01
81_6_117_B
[100] (010) (001)
n = 40818
J = 1.89
M = 0.05
MD = 2.47
PfJ=1.14 PfJ=1.07 PfJ=1.27

Figure 7.

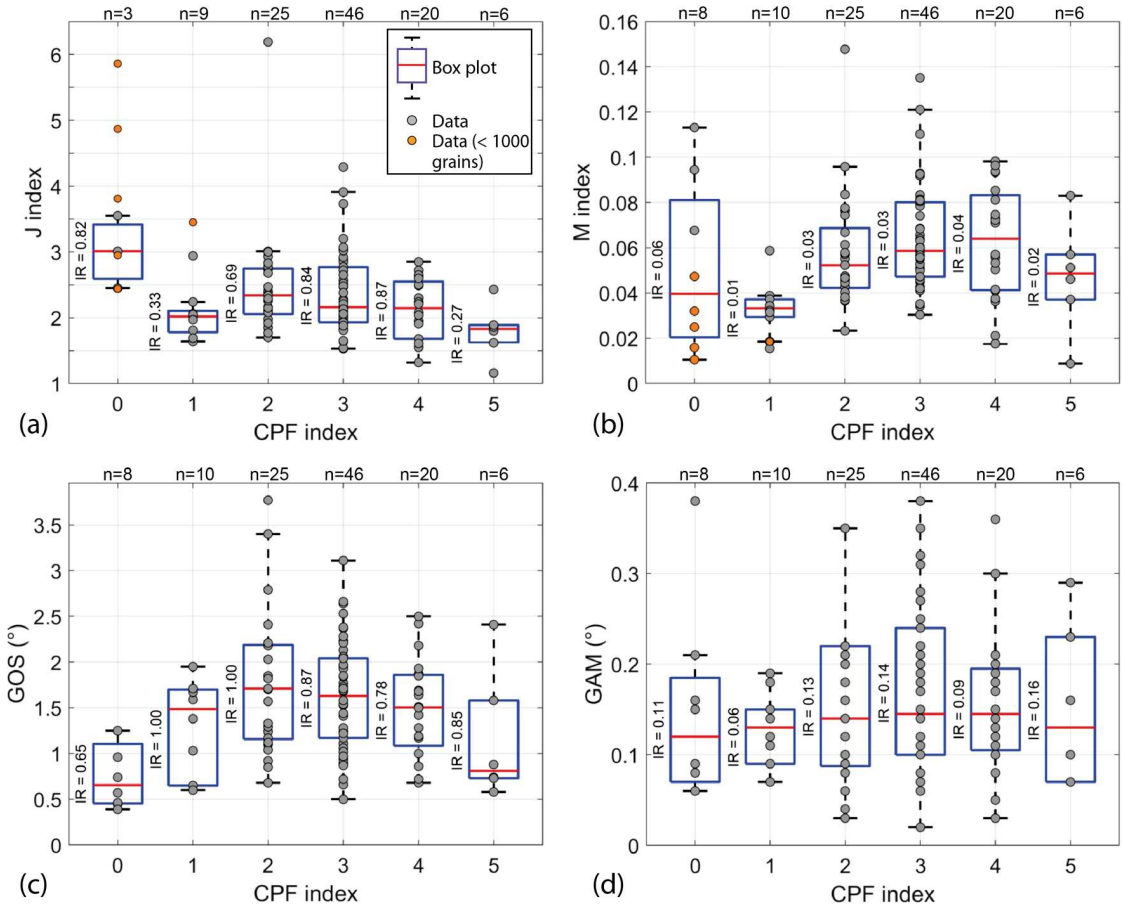

Figure 8. Fabric strength and misorientations indices of plagioclase grains. (a) J index and (b) M index evolution with CPF index in plagioclase. Note that orange data (<1000 grains) are excluded from J index statistics (see text). Box plot parameters, "IR" and "*n*" are detailed in the legend of Figure 4. (c) Average grain orientation spread (GOS) for plagioclase in the analyzed samples. It indicates the degree of torsion of the lattice at grain scale. (d) Mean of grain average misorientations (GAM) of plagioclase in the analyzed samples. It indicates the degree of local misorientations in grains. Average grain orientation data are used in these graphics and both porphyroclasts and recrystallized grains are considered.

However, when present group 1 is usually wider and shifted toward higher misorientations (40°–90°). No correlation was found between parent grains crystallographic orientations and the dispersion of crystallographic orientations of neighboring recrystallized grains. Other correlations with the textural position of parent grains (within the recrystallized matrix of plagioclase, or on contact with other phases) or the size of recrystallized grains have not been observed either.

Plagioclase grain deformation increases with increasing recrystallization in analyzed domains. GOS median values display a positively skewed distribution from CPF indices 0 to 5, with values ranging from ~0.65° to ~1.7°. The statistic distribution is characterized by an important dispersion with IR values ranging from 0.65° to 1.00°, and overlapping between CPF indices (Figure 8c and Table S3 in Supporting Information S2). A decrease of GOS values is observed in grains from ultramylonites (CPF index 5), where the median grain size is significantly reduced (21 μm; Table S3 in Supporting Information S2). Although median GAM values show a weak linear increase toward CPF index 4, the overlap between all IR does not permit to establish a clear tendency (Figure 8d and Table S3 in Supporting Information S2). Median GAM values are low and

Figure 7. Pole figures of plagioclase (average grain orientation data, lower hemisphere, equal-area projection) measured in representative domains in gabbros from CPF indices 0 to 5. The trace of the (010) plane in plagioclase is represented by the pink great circles, the trace of the (001) by the black great circles in (d and f), and the orientation of the trace of the foliation measured in thin section, when observed with confidence, is indicated by the red arrows at the periphery of [100] pole figures. The minimum density in pole figures is set to zero for direct comparison between analyzed domains. The parameters are the same as in Figure 6.

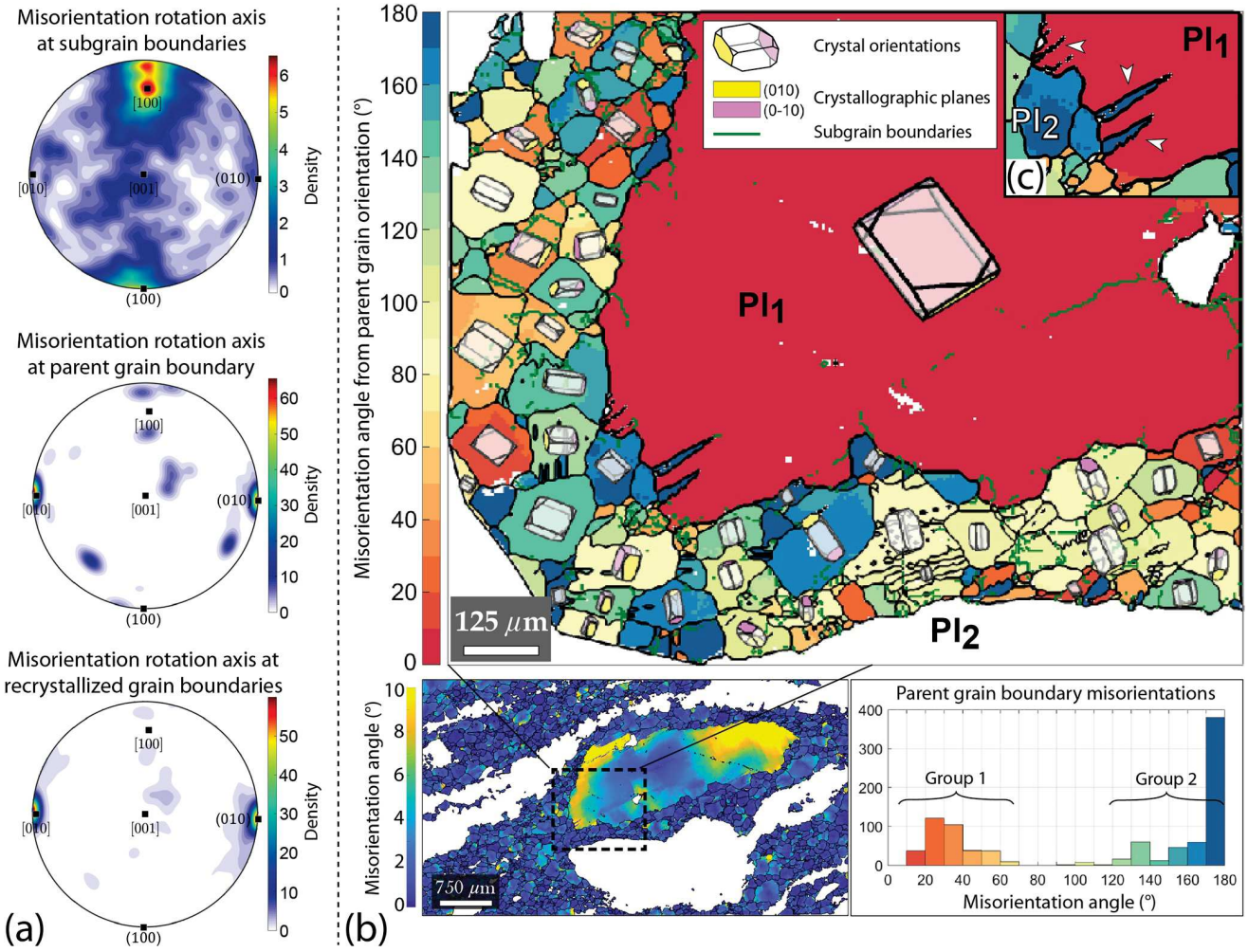

Figure 9. Representative porphyroclast-recrystallized mantle pair misorientation relations in plagioclase, microstructural domain 69_5_17 (CPF index 3). (a) IPF (antipodal, equal angle projection) of misorientation rotation axes at subgrain boundaries (top), parent grain boundary (middle), and recrystallized grain boundaries (bottom). (b) Misorientations between the plagioclase parent porphyroclast (red; Pl_1) and the recrystallized grains (red, green to blue colors; Pl_2), superimposed by oriented crystal shapes and subgrain boundaries (green limits). The bottom left misorientation map from grain average orientation in plagioclase indicates the analyzed region. The histogram shows parent grain boundary misorientations from its mean orientation. (c) Close-up showing tapered twins (white arrows) at the periphery of the parent grain (Pl_1).

ranges from 0.12° to ~0.14° with large IR values ranging from 0.06° to 0.16°. Again, the overlap between the statistic distributions is important (Figure 8d). A peculiar observation is that the GAM values are systematically higher in recrystallized grains than in magmatic porphyroclasts (Figure S3 in Supporting Information S1). This is explained by the localized nature of intragranular misorientations in grains, leading to higher measured misorientation density (hence a higher GAM) in newly and small recrystallized grains than in old and larger porphyroclasts.

7. Discussion

7.1. Lithologies and Deformation Intensity

As already reported by Miranda and John (2010) in dive samples from the surface of the Atlantis Bank, no differences in terms of deformation intensity (CPF indices) are observed between the sampled oxide-free and oxide-bearing lithologies. In addition to this observation, the increase in deformation intensity occurs with limited mineral modal changes (Figure 4a and Table S3 in Supporting Information S2), generalizing

these authors' conclusion to gabbroic lithologies in general that the primary rock composition has no influence on strain localization.

7.2. Crystallographic Preferred Orientations and Deformation Mechanisms of Plagioclase

Fine-grained granular domains (CPF index 0, Figure 7a) display CPO with a [100](010) fabric, interpreted as resulting from magmatic flow (e.g., Benn & Allard, 1989; Ji et al., 2014; Satsukawa et al., 2013). Although coarse-grained subophitic domains shown herein display no clear CPO (CPF index 0; e.g., Figures 6a and 7a), it is documented in coarse-grained olivine gabbros from Hole U1473A by Boulanger et al. (2021). The onset of plastic deformation in sampled domains (CPF indices 1 to 5) also results in the development of a [100](010) CPO (Figures 6b–6e and 7b–7f) with a common "host-controlled" relation between porphyroclasts and recrystallized grains (Figures 6b and 6c). The presence of a CPO in porphyroclasts from deformed domains could then result from the direct deformation of porphyroclasts leading to their reorientation; or from the preferential localization of deformation in intervals with a preexisting magmatic fabric. This magmatic fabric would define a "soft" orientation of crystals (Burg et al., 1986; Schmid, 1994) favoring the activity of the [100](010) slip system, or more generally [*hkl*](010). Note that a few analyzed domains (CPF indices 2 to 5) indicates CPO patterns consistent with the [100](001) slip system (Figures 7d and 7f, and possibly Figure 6d). Similar CPO have already been reported in the SWIR mylonites (Mehl & Hirth, 2008) and other OCC (e.g., Hansen et al., 2013; Harigane et al., 2008).

Overall, the intensity of plagioclase CPO is weak (Figures 8a and 8b). Similar fabric strength in gabbros mylonites are reported by Miranda et al. (2016) at the footwall of the Atlantis Bank, and by Mehl and Hirth (2008) in Hole 735B, who also measured higher strength in plagioclase monophase layers. The calculated CPO strength in plagioclase aggregates is weak in gabbroic rocks in general, except in some magmatic foliated gabbros (e.g., Satsukawa et al., 2013). CPO in deformed rocks, even when weak, is often interpreted as resulting from dislocation creep (e.g., Mehl & Hirth, 2008; Urai et al., 1986). Dynamic recrystallization processes via dislocation creep occurs within grain aggregates of the same type, at interphase boundaries (e.g., Poirier, 1985). Texturally, the general tendency of monomineralic banding arrangement forming a strain-induced foliation plane in samples from Hole U1473A could be consistent with a deformation dominated by dislocation creep (Figure 3) and enhances strain localization (e.g., Kenkmann & Dresen, 2002). Consistently, the increase of J index values from CPF indices 1 to 2, and of M index from CPF indices 1 to 4 are indicative of the building of a CPO, highlighting that the deformation occur in the dislocation creep regime (Figures 8a and 8b). The limited number of grains in coarse-grained undeformed domains (CPF index 0) does not allow to be conclusive about the evolution of the fabric strength from CPF indices 0 to 1 concerning the J index. However, the M index, which is not dependent of the number of analyzed grains by contrast to the J index (Skemer et al., 2005), seems to display an increase of the fabric strength from CPF indices 0 to 4 (for CPF index 0 the comparison is made with coarse-grained domains as they most probably corresponds to the protoliths of the deformed domains, see orange data in Figure 8b).

At hyper-solidus conditions, olivine crystals are the first to undergo plastic deformation (Yoshinobu & Hirth, 2002), and in hot geothermal lower crustal sections plagioclase is usually weaker than olivine and clinopyroxene (e.g., Homburg et al., 2010; Kronenberg & Shelton, 1980). The studied microstructures are consistent with these observations, and indicate that because of its important proportion (~60%), plagioclase accommodates alone most of rock's deformation (e.g., Ji et al., 2000). The evolution of the fabric strength presented in Figures 8a and 8b show a decrease in ultramylonites. This decrease is possibly an effect of the progressive SGR recrystallization, first occurring in porphyroclasts and continuing within the recrystallized grains as indicated by the important proportions of subgrain boundaries observed in recrystallized grains of mylonites and ultramylonites (e.g., Figures 6d and 6e). This effect of the progressive recrystallization can combine with the change in the dominant active slip system at decreasing deformation temperatures to produce the observed fabric strength decrease. Other mechanisms than dislocation creep could also account for this fabric strength decrease, such as the heterogeneous nucleation of amphibole grains (up to ~14% in ultramylonites) or the activation of diffusion creep thanks to hydrothermal fluid circulation (e.g., Mehl & Hirth, 2008; Nozaka et al., 2019). In addition, the reduced grain size in ultramylonites (median = 21 μm) and the likely decrease in deformation temperature in the presence of hydrothermal fluids, which must induce significant chemical potential gradients, could favor the activity of grain-size-sensitive processes such as

granular flow (e.g., Mehl & Hirth, 2008; Oliot et al., 2010, 2014; Paterson, 1995; Stünitz & Fitz Gerald, 1993). Granular flow is likely to have occurred in the microstructural domain 9_5_19_B, corresponding to a plagioclase-amphibole bearing narrow ultramylonite, displaying a very weak CPO (Figure 7f). Kenkmann and Dresen (2002) proposed that in fine-grained mafic mylonites, fluid-assisted diffusion and dislocation creep are activated together to accommodate grain-boundary sliding. Chemical potentials are also known to enhance diffusion processes such as CIGM, which is a strain softening process (Hay & Evans, 1987; Hirth & Tullis, 1992; Urai et al., 1986). Other studies in gabbros deformed in OCC systems also proposed the activation of grain-size-sensitive processes such as grain boundary sliding to explain the observation of weak CPO in highly deformed samples (e.g., Harigane et al., 2008; Mehl & Hirth, 2008; Miranda et al., 2016).

Seven of the 115 microstructural domains with a foliation parallel to (001) in plagioclase rather than the common (010) are characterized by high amphibole contents (11%–28%), and by a high oxide content (ilmenite: 11%, and magnetite: 10%) in another domain. The median recrystallized grain size in all these studied domains is ∼30 μm. In mylonites and ultramylonites from the Godzilla Megamullion (Parece Vela Basin, Philippine Sea), Harigane et al. (2011) proposed a transition from dislocation creep to grain-size-sensitive creep with decreasing temperature to explain the change from [100](010) to [100](001) slip systems in CPO patterns. For the same reasons as in ultramylonites, a transition to a grain-size-sensitive creep such as granular flow could explain the transition from a CPO pattern to another. However, an alternative explanation that does not require a change in deformation mechanism, also linked to deformation temperature, is that the dominant active slip system changed. As shown in Figure 1, the activity of the [100](010) slip system is documented over a large range of high temperatures (∼600°–900°C), and a decreasing temperature (<750°C) during deformation could favor the activity of other slip systems, here [100](001), at the expense of the former one. Then, these domains could correspond to intervals deformed during the later solid state–semi-brittle deformation episode at 665 ± 40°C (Miranda & John, 2010). This hypothesis is better consistent than a switch in CPO patterns arising from a change in deformation mechanism, with the majority of ultramylonites displaying clear CPO patterns indicating [100](010) slip, although granular flow may also have occurred.

7.3. Dynamic Recrystallization Processes of Plagioclase

In deformed domains (CPF indices 2 to 5), core-mantle structures develop because of extensive recrystallization of the main phases (e.g., Figures 3c, 3d and 5d–5f). Subgrain boundaries in plagioclase porphyroclasts (Figures 5d and 7b–7e) are associated with dominant frequencies of low-angle misorientations (<10°), representing 20% of all misorientations in 59 analyzed domains and 10% in 88 domains (Figure S2 in Supporting Information S1). A host-controlled relationship between magmatic parent and recrystallized grains is inferred from the CPO of most domains (e.g., Figures 7b and 7c). Finally, the ubiquitous presence of recrystallized grains with 20°–60° of misorientation from the parent grain (group 1, Figure 9b) is consistent with a progressive rotation of the newly formed grains to the parent grain. All these observations argue in favor of SGR as the main recrystallization mechanism in plagioclase. This recrystallization process in plagioclase grains is commonly described in Atlantis Bank mylonites (Gardner et al., 2020; Mehl & Hirth, 2008; Miranda et al., 2016; Miranda & John, 2010; Taufner et al., 2021).

Important fractions of high misorientations can be found at the direct contact between parent and recrystallized grains (group 2, 100°–180°). This might indicate that recrystallization initiated within microcracks (e.g., Escher & Gottstein, 1998; Kruse et al., 2001; Okudaira et al., 2017), or by SGR from a twinned domain of the parent grain. In the later, the misorientation between the twinned domains would be 180° (e.g., Figure 9c). Then, grains achieving a rotation of 60° from a twinned domain (reference orientation at 180°) would be measured with a misorientation of 120° with respect to the parent grain orientation (reference orientation at 0°). This could be consistent with the widespread observation of tapered twins in plagioclase grains (e.g., Figure 5a, 5b, 5d and 9c). Concerning microfracturing, this produces nuclei that rapidly grow by grain boundary migration, resulting in arbitrary misorientations from their parent grain. However, the limitation of this hypothesis in our samples resides in the widespread observation of a crystallographic control on the formation of recrystallized grains (Figure 9a), best consistent with the formation of new grains by progressive SGR (Lloyd et al., 1997). In addition, grains with a high angle misorientation to the parent grain (group 2, Figure 9b) are heterogeneously distributed. One would expect these grains to be aligned if

nucleation occurred along microcracks. However, it is a possible mechanism for the very first stages of shear-band development in 4 porphyroclastic to protomylonitic domains (CPF indices 2 and 3, microstructural domains 34_2_98, 44_1_105_B, 67_1_73 and 67_7_110_A, Figure S4 in Supporting Information S1 and Table S3 in Supporting Information S2), where thin and straight recrystallized bands (100–150 μm large) are found within large porphyroclasts (450–500 μm).

In a context of continuous deformation from hyper-solidus to lower grade metamorphic conditions (granulite to amphibolite), one may expect that recrystallized grains continued to deform after they detached from their parent grain. This is observed in analyzed domains with an increasing development of subgrain boundaries from porphyroclastic to ultramylonitic textures (CPF indices 2 to 5, Figure 6b–6e), and by the general observation of higher GAM values in recrystallized grains than in porphyroclasts (Figure S3 in Supporting Information S1). It indicates an intracrystalline hardening of grains as recrystallization progresses, together with a general grain size reduction. This strain hardening arising during dislocation creep could then favor the activation of other deformation mechanisms such as grain-size-sensitive process and chemical diffusion (i.e., granular flow).

In 38 microstructural domains (mostly CPF indices 0 to 2), plagioclase grain boundaries are lobate and the recrystallized grain size is higher than in samples showing evidence of dominant SGR (120–300 μm, e.g., Figure 5a). Also, the fraction of low angle misorientations (>10°) is small compared to higher misorientations, attesting for GBM.

The dominant recrystallization mechanism varies with the extent of deformation, but also varies with depth (Figure 10a). SGR is ubiquitous throughout the hole whereas GBM is dominant at CPF indices 1 and 2 in the lower parts of the hole (~500–800 mbsf). In this lower interval, SGR is dominantly observed in zones of more intense and localized deformation (CPF indices >3; Figures 10a and 10b) as already observed in granulitic submersible mylonite samples by Miranda and John (2010). The recrystallized grain size associated with SGR in localized zones from this lower interval is on average 49 μm (±25 μm), about 20 μm smaller than for the upper interval, where it is of 72 μm (±28 μm) (Figures 10b and 10c), and third time smaller than for GBM recrystallized grains (on average 167 μm ± 88 μm). This is consistent with the fact that areas of reduced grain size by dynamic recrystallization, here SGR, associated with a CPO (acting as a local geometrical softening) are known to induce softening, enhancing strain localization (Ji & Mainprice, 1990; Tullis & Yund, 1985; Urai et al., 1986).

Together with the common observation of undulose extinction in grains from undeformed microstructural domains (Figure 6a), this suggests that plastic deformation started early, during post-magmatic stages (Dick, MacLeod, et al., 2019). The range of activity of GBM and SGR in plagioclase is rather similar at high temperatures (>600°C, Figure 1), so differences in the temperature of deformation between the upper and lower parts of the hole cannot explain the change in recrystallization mechanisms. Variations in strain are likely to account for the transition between GBM (lower strain and/or strain rate) and SGR (higher strain and/or strain rate). Differential stress calculations performed in recrystallized plagioclase grains support this hypothesis, as previously described in Mehl and Hirth (2008), using the Twiss (1977) equation for recrystallized grain size paleopiezometer. For recrystallized grains resulting from GBM (average grain size of ~167 μm) this calculation gives differential stresses of ~32 MPa, while for recrystallized grains resulting from SGR (average grain size of ~65 μm) the calculation yield a paleostress of ~61 MPa. Furthermore, the average recrystallized grain sizes associated with SGR vary between the upper part (~72 μm) and lower part (~49 μm) of the hole (Figures 9b and 9c). Thus, the more pervasive ductile deformation in the upper interval indicates lower differential stresses (~57 MPa above 500 mbsf) than in the lower interval (~74 MPa below 500 mbsf) where deformation is mostly localized.

The rare occurrence of BLG in plagioclase is mainly documented in domains from the upper 200 m of Hole U1473A, and a different temperature of deformation is likely as BLG is documented *ad maximam* at ~700°C while SGR occurs at least up to ~900°C in naturally deformed plagioclase aggregates (Figure 1). This could suggest that the lowest temperature deformation event (<700°C; Miranda & John, 2010) is important in the upper 200 m of the hole. The widespread crystal plastic deformation in the upper 500–600 mbsf of Hole U1473A is interpreted to result from the activity of the detachment fault that exhumed the gabbroic pluton forming nowadays the Atlantis Bank (MacLeod et al., 2017).

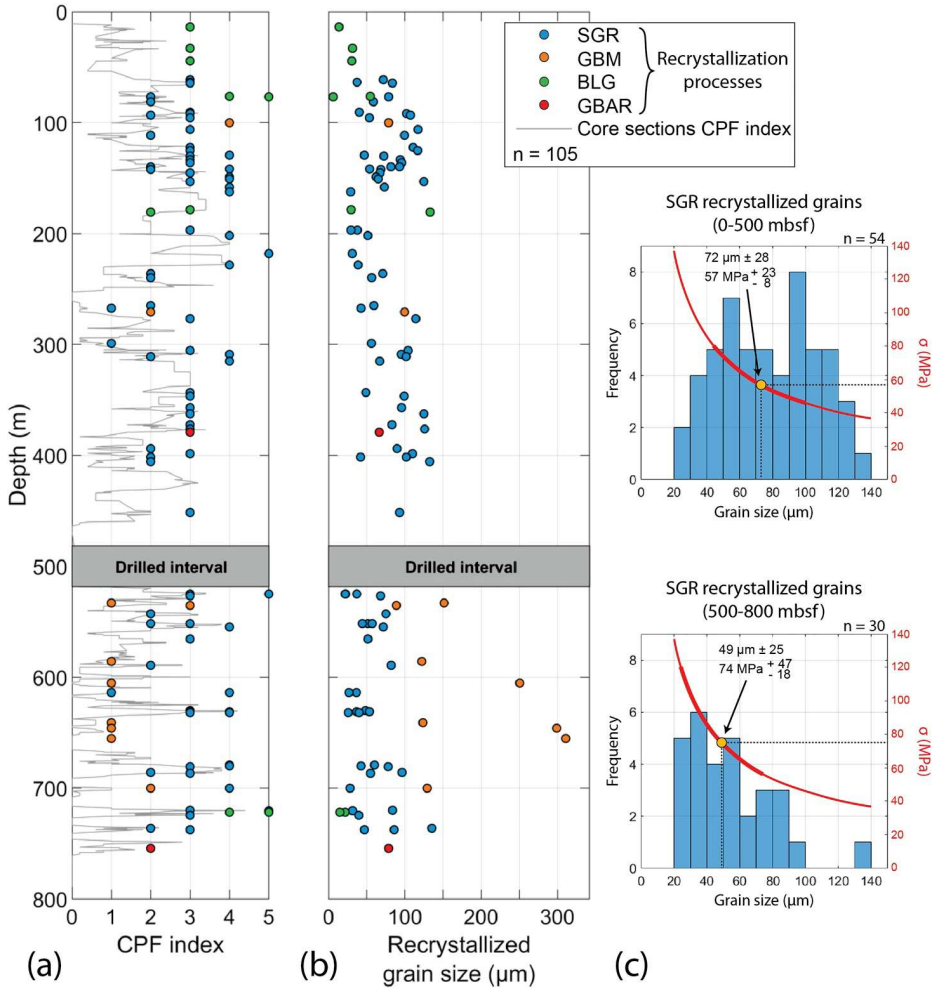

Figure 10. Recrystallization processes and associated grain sizes in plagioclase grains. (a) Dominant recrystallization processes in plagioclase as a function their CPF index along depth in Hole U1473A. The gray line corresponds to the CPF index of core sections (see Figure 2c). (b) Recrystallized grain size and associated recrystallization processes along depth. Recrystallization processes: SGR: subgrain rotation; GBM: grain boundary migration; BLG: bulging; GBAR: grain boundary area reduction (i.e., static recrystallization). (c) Histograms of recrystallized grain sizes associated with SGR recrystallization. The red curve corresponds to associated differential stresses calculated with Twiss (1977) equation for recrystallized grain size paleopiezometer. The geometric mean grain size and the associated paleostress are represented by the orange dots. The bold part of the red curve corresponds to paleostresses related to the standard deviation around the mean grain size. "*n*" is the number of analyzed microstructural domains.

7.4. Slip Systems Activity During Crystal-Plastic Deformation

A majority of microstructural domains display a foliation subparallel to the preferred orientation of plagioclase (010), associated with a lineation on [100] (Figures 6 and 7). This suggests the activity of the [100](010) slip system during crystal-plastic deformation. The analysis of misorientation rotation axes at subgrain boundaries in plagioclase indicates a strong maximum at or near [100] in all microstructural domains (e.g., Figure 9a). Previous studies of slip systems in plagioclase indicate that [100] is the misorientation rotation axis associated with the edge segments of [001](010) dislocation system (e.g., Kruse et al., 2001; Svahnberg & Piazolo, 2010). Similar observations are documented in mylonites of the Kane OCC (Mid-Atlantic ridge, e.g., Hansen et al., 2013). However, pole figures of a majority of analyzed domains are characterized by the preferred orientation of (010) for the foliation and [100] for the lineation, consistent with the activity of the [100](010) slip system. The ubiquitous [100] misorientation axis on subgrain boundaries must indicate the activity of the [001](010) slip system that does not reflect in the CPO. The observation of different slip

systems at subgrain boundaries than the one inferred from CPO was also reported by Mehl and Hirth (2008) and Svahnberg and Piazolo (2010) in plagioclase. Mehl and Hirth (2008) proposed that porphyroclasts subgrain boundaries are not dominantly composed of the easiest slip systems, or that the critical resolved shear stress of slip systems is not the only parameter to control the development of the CPO. The general observation of an "host-controlled" relation between porphyroclasts and recrystallized grains, the presence of a CPO with a similar slip plane in igneous textures (CPF index 0) and in deformed samples (CPF indices 1 to 5, Figure 6), and the parallelism between this slip plane and the foliation suggest a general "soft" orientation of porphyroclasts in studied domains. This supports the activity of slip systems different from the easiest one in porphyroclasts, with [001](010) dominantly observed at subgrain boundaries, while the dominant slip system producing the CPO is [100](010).

Further analyses of misorientations aiming at the active slip systems identification in plagioclase grains are conducted through the selection of grains with, respectively, their (010) and (001) planes parallel to the analyzed plane (see Section 4.3 in Methods). In the first group (i.e., (001) parallel to the plane of analysis), 79 microstructural domains show a clustering of misorientation axes around [101] dominantly, and [001] (Figure 11a). In many domains the maximum is centered on [101] but extends toward [001], and can form a semi-girdle between the [001] and [201] directions (aligned in (010)). [101] is nearly orthogonal to (001), thus misorientations result from the motion of screw dislocations. Direct identification of the Burgers vector of the corresponding dislocations system is not straightforward as any direction orthogonal to the misorientation axis is possible (Lloyd et al., 1997). As explained in Section 4.3 the closest directions to the lineation are considered the better candidates for glide. The possible slip directions comprised in (001) are: [100], ½[110], and ½[1$\bar{1}$0] (e.g., Kruse et al., 2001; Marshall & McLaren, 1977). Deformation in Hole U1473A mainly occurs as reverse shearing, so the lineation (here parallel to [100] of plagioclase) should be close to the shear direction. Then, the three slip directions are likely by considering that ½[110] and ½[1$\bar{1}$0] could be activated simultaneously. A second maximum is found in 31 domains, usually associated with the previous one, clustering around [100] (Figure 11a). This maximum lies in the (001) plane, and can thus be related to edge dislocations. Possible slip directions are: ½[110] and ½[1$\bar{1}$0], and it is proposed that both slip systems were active for the same reason as for the [101] misorientation axis.

The second group of grains (i.e., (010) parallel to the plane of analysis) shows a maximum of misorientation axes on [100] (93 microstructural domains, Figure 11b). This direction is within the (010) plane, sub-parallel to the foliation, and results from the activity of the [001](010) slip system. A sub-maximum is found around the [010] direction (38 microstructural domains). In that case, misorientations are orthogonal to the slip plane (010) and correspond to screw dislocations. The possible slip directions are: [100], [001], [201], and

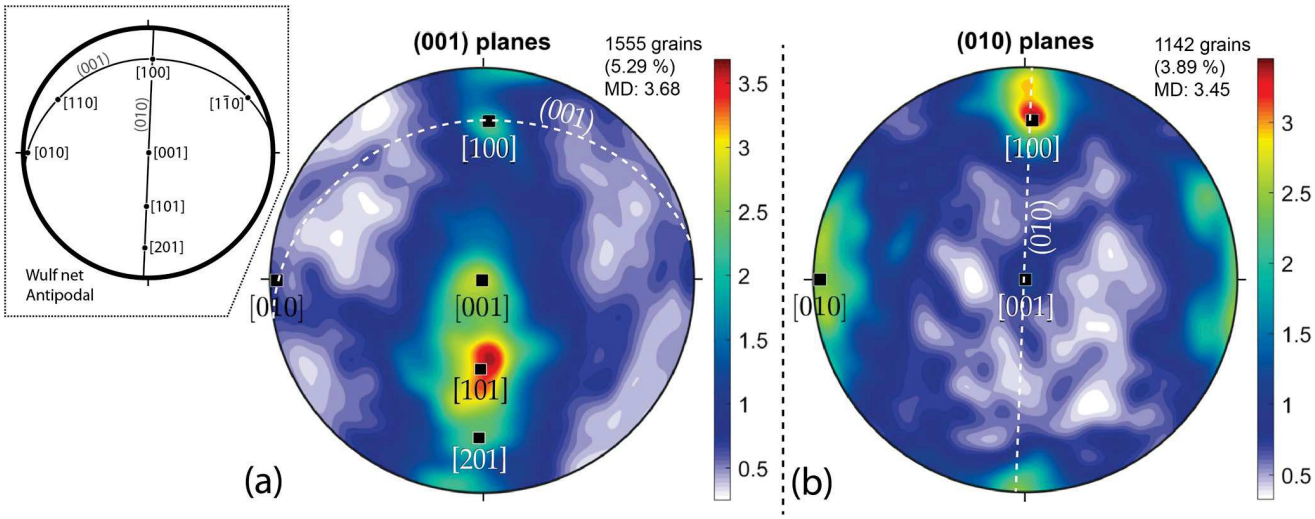

Figure 11. Typical IPF (antipodal, equal angle projection) showing misorientation rotation axes at subgrain boundaries in grains with (a) their (001) plane and (b) their (010) plane parallel to the plane of analysis (microstructural domain 69_5_17). The corresponding percentage of grains in the domain is indicated, MD is the maximum density. The top left inset indicates the location of the discussed crystallographic directions and planes (modified after Kruse et al., 2001).

[101] (e.g., Kruse et al., 2001; Marshall & McLaren, 1977). The directions [201] and [100] are the most likely due to their geometrical relationship to the lineation in the studied domains (parallel to [100]), whereas [101] and [001] are at high angle from the [100] direction. In addition, the [100] slip direction corresponds to the [100](010) slip system that produced the CPO. However, the [101] and [001] directions cannot be completely ruled out only based on their high angle to the lineation.

In summary, the dominant active slip systems identified with misorientations are: [100](001), ½[110](001), ½[1 $\bar{1}$0](001), and [001](010); and other possible slip systems of secondary importance are: [100](010) or [201](010), or less likely [001](010) or [101](010).

The slip systems identified both in porphyroclasts and recrystallized grains are indicative of different temperature ranges for active crystal plasticity. The most common slip systems in the sample suite is [100](010). It is documented over a wide range of temperatures, and corresponds to the slip system dominantly observed at the highest temperatures (~900°C, Figure 1). Documented as dominant from 600°C to 800°C, [001](010) is the main slip system active at subgrains (Figure 1). Both may have operated simultaneously in plagioclase grains from the onset of crystal plasticity during the first episode of solid state deformation from ~1000° to ~860°C, leading to the observed CPO and dominant subgrain boundaries development (Gardner et al., 2020; Mehl & Hirth, 2008; Miranda & John, 2010). The two other important slip systems identified at subgrain boundaries are ½[110](001) and ½[1 $\bar{1}$0](001). Their range of activity is documented for lower temperatures than the two others: mainly ~600° to 700°–750°C for ½[110](001), and mainly <600°–700°C for ½[1 $\bar{1}$0](001) (Figure 1). Finally, the [100](001) slip system observed in CPO patterns of a few microstructural domains is mainly active from ~600° to 750°C and documented up to ~900°C (Figure 1). The rising activity of these three slip systems gliding in (001) could possibly be related to the latest episode of mylonitization <700°C (Miranda & John, 2010) as their presence seems limited and confined at subgrain boundaries (except for [100](001), see Section 7.2).

8. Conclusion

Crystal-plastic deformation of plagioclase is common in the gabbroic lithologies of IODP Hole U1473A, and results in foliated to ultramylonitic textures. The sampled lithologies indicate a progressive monomineralic banding arrangement as plagioclase dynamic recrystallization increases until it is complete in ultramylonites, together with a general decrease of the recrystallized grain size. Plastic deformation in these rocks is dominated by dislocation creep, which reflects in plagioclase by the development of a CPO produced by the [100](010) slip system, and locally by [100](001). This second CPO produced by the [100](001) slip system is interpreted to arise from lower temperature of deformations (<700°C) rather than a change in deformation mechanism. The intensity of the CPO is weaker in ultramylonites as indicated by lower J and M indices values. This decrease in intensity is interpreted to possibly arise from the scattering of grain orientation during recrystallization and a change in slip system activity during lower temperature deformations. For a fraction of the analyzed domains, a change in the main active deformation mechanism made feasible by reduced grain size and hydrothermal fluid circulation is likely. Diffusion and grain-size-sensitive processes, in combination or individually, would then have produced a randomization of the CPO.

Recrystallization in plagioclase grains results from progressive subgrain rotation as evidenced by (a) the orientation relationship between magmatic parent grains and their neighboring recrystallized mantles, (b) the widespread observation of subgrain boundaries and intracrystalline misorientations (<10°), and (c) the crystallographic control on recrystallized grains boundaries. SGR is dominant throughout Hole U1473A, although in the lowermost 300 m it is more associated to areas of localized deformations when GBM prevails away from these localized shear zones. SGR in these localized domains produce smaller recrystallized grains than in the upper part of the hole where the deformation is pervasive. This results in higher estimated differential stresses in the lower part of Hole U1473A, ~20 MPa above the value calculated for the upper part.

The detailed analysis of misorientations within plagioclase grains reveals the activity of four dominant slip systems in addition to [100](010) that produced the CPO: [001](010), [100](001), ½[110](001), and ½[1 $\bar{1}$0](001). The activity of the two main slip systems, [100](010) and [001](010), is most probably related to an episode of solid state deformation at high temperatures (860°–1000°C). By contrast, the three other could

correspond to the episode of moderate deformation temperatures (650°–700°C) in the semi-brittle ductile regime, possibly occurring later during the exhumation history of the Atlantis Bank.

Data Availability Statement

The data set is accessible in the PANGEAE data repository (https://doi.org/10.1594/PANGAEA.932302).

Acknowledgments
This research used samples and data provided by the International Ocean Discovery Program. The authors thank the members of the IODP Expedition 360 Science Party, the captain and crew of the JOIDES Resolution, and the staff at the Kochi Core Center. The authors thank C. Nevado and D. Delmas for careful thin section preparation. E. Schettino is acknowledged for EBSD measurements during his internship in Montpellier, and M. Boulanger for the access to EBSD data in three fine-grained olivine gabbro samples. The authors thank R. Hielscher, R. Kilian, and A. Tommasi for their help with MTEX. H. Stünitz, A. Tommasi, and D. Mainprice are acknowledged for fruitful discussions. The authors are also grateful for the substantial improvements provided by two anonymous reviewers and the editor S. Parman. This study was funded by IODP-France.

References

Amelinckx, S., & Dekeyser, W. (1959). The structure and properties of grain boundaries. In Seitz, F., & Turnbull, D. (Eds.), *Solid state physics* (Vol. 8, pp. 325–499). Elsevier. https://doi.org/10.1016/S0081-1947(08)60482-8

Bailey, J. E., & Hirsch, P. B. (1962). The recrystallization process in some polycrystalline metals. *Proceedings of the Royal Society of London—Series A: Mathematical and Physical Sciences*, *267*(1328), 11–30. https://doi.org/10.1098/rspa.1962.0080

Baines, A. G., Cheadle, M. J., Dick, H. J. B., Scheirer, A. H., John, B. E., Kusznir, N. J., & Matsumoto, T. (2003). Mechanism for generating the anomalous uplift of oceanic core complexes: Atlantis Bank, Southwest Indian Ridge. *Geology*, *31*(12), 1105. https://doi.org/10.1130/G19829.1

Bell, T. H., & Johnson, S. E. (1989). The role of deformation partitioning in the deformation and recrystallization of plagioclase and K-feldspar in the Woodroffe Thrust mylonite zone, central Australia. *Journal of Metamorphic Geology*, *7*(2), 151–168. https://doi.org/10.1111/j.1525-1314.1989.tb00582.x

Benn, K., & Allard, B. (1989). Preferred mineral orientations related to magmatic flow in ophiolite layered gabbros. *Journal of Petrology*, *30*(4), 925–946. https://doi.org/10.1093/petrology/30.4.925

Blum, P., Dick, H. J., MacLeod, C. J., & Expedition 360 Scientists. (2017). *Hole U1473A remediation operations, Expedition 362T*. International Ocean Discovery Program. https://doi.org/10.14379/iodp.proc.360.2017

Boulanger, M., France, L., Ferrando, C., Ildefonse, B., Ghosh, B., Sanfilippo, A., et al. (2021). Magma-Mush Interactions in the Lower Oceanic Crust: Insights From Atlantis Bank Layered Series (Southwest Indian Ridge). *Journal of Geophysical Research: Solid Earth*, *126*(9). https://doi.org/10.1029/2021jb022331

Brewer, L. N., Field, D. P., & Merriman, C. C. (2009). Mapping and assessing plastic deformation using EBSD. In Schwartz, A. J., Kumar, M., Adams, B. L., & Field, D. P. (Eds.), *Electron backscatter diffraction in materials science* (pp. 251–262). Boston, MA: Springer US. https://doi.org/10.1007/978-0-387-88136-2_18

Bunge, H. J. (1982). *Texture analysis in materials science: Mathematical methods*. Butterworth. https://doi.org/10.1016/C2013-0-11769-2

Burg, J. P., Wilson, C. J. L., & Mitchell, J. C. (1986). Dynamic recrystallization and fabric development during the simple shear deformation of ice. *Journal of Structural Geology*, *8*(8), 857–870. https://doi.org/10.1016/0191-8141(86)90031-3

Cannat, M. (1993). Emplacement of mantle rocks in the seafloor at mid-ocean ridges. *Journal of Geophysical Research: Solid Earth*, *98*(B3), 4163–4172. https://doi.org/10.1029/92JB02221

Debat, P., Soula, J.-C., Kubin, L., & Vidal, J.-L. (1978). Optical studies of natural deformation microstructures in feldspars (gneiss and pegrnatites from Occitania, southern France). *Lithos*, *11*(2), 133–145. https://doi.org/10.1016/0024-4937(78)90004-x

Dell'Angelo, L. N., & Tullis, J. (1996). Textural and mechanical evolution with progressive strain in experimentally deformed aplite. *Tectonophysics*, *256*(1–4), 57–82. https://doi.org/10.1016/0040-1951(95)00166-2

Dick, H. J. B., Blum, P., MacLeod, C. J., & Expedition 360 Scientists. (2017). *Expedition 360 summary*. International Ocean Discovery Program. https://doi.org/10.14379/iodp.proc.360.2017

Dick, H. J. B., Kvassnes, A. J. S., Robinson, P. T., MacLeod, C. J., & Kinoshita, H. (2019). The Atlantis Bank Gabbro Massif, Southwest Indian Ridge. *Progress in Earth and Planetary Science*, *6*(1), 64. https://doi.org/10.1186/s40645-019-0307-9

Dick, H. J. B., MacLeod, C. J., Blum, P., Abe, N., Blackman, D. K., Bowles, J. A., et al. (2019). Dynamic accretion beneath a slow-spreading ridge segment: IODP Hole 1473A and the Atlantis Bank oceanic core complex. *Journal of Geophysical Research*, *124*(12), 12631–12659. https://doi.org/10.1029/2018JB016858

Dick, H. J. B., Meyer, P. S., Bloomer, S., Kirby, S., Stakes, D., & Mawer, C. (1991). *Proceedings of the Ocean Drilling Program, 118 Scientific Results* (Vol. 118). Ocean Drilling Program. https://doi.org/10.2973/odp.proc.sr.118.1991

Dick, H. J. B., Natland, J. H., Alt, J. C., Bach, W., Bideau, D., Gee, J. S., et al. (2000). A long in situ section of the lower ocean crust: Results of ODP Leg 176 drilling at the Southwest Indian Ridge. *Earth and Planetary Science Letters*, *179*(1), 31–51. https://doi.org/10.1016/S0012-821X(00)00102-3

Drury, M. R., & Urai, J. L. (1990). Deformation-related recrystallization processes. *Tectonophysics*, *172*(3–4), 235–253. https://doi.org/10.1016/0040-1951(90)90033-5

Escartín, J., & Canales, J. P. (2011). Detachments in oceanic lithosphere: Deformation, magmatism, fluid flow, and ecosystems. *Eos, Transactions American Geophysical Union*, *92*(4), 31. https://doi.org/10.1029/2011EO040003

Escher, C., & Gottstein, G. (1998). Nucleation of recrystallization in boron doped Ni3Al. *Acta Materialia*, *46*(2), 525–539. https://doi.org/10.1016/S1359-6454(97)00264-4

Fitz Gerald, J. D., & Stünitz, H. (1993). Deformation of granitoids at low metamorphic grade. I: Reactions and grain size reduction. *Tectonophysics*, *221*(3–4), 269–297. https://doi.org/10.1016/0040-1951(93)90163-E

Gandais, M., & Willaime, C. (1984). Mechanical properties of feldspars. In Brown, W. L. (Ed.), *Feldspars and Feldspathoids* NATO ASI Series (Series C: Mathematical and Physical Sciences) (Vol. 137, pp. 207–246). Dordrecht: Springer. https://doi.org/10.1007/978-94-015-6929-3_6

Gardner, R. L., Piazolo, S., Daczko, N. R., & Trimby, P. (2020). Microstructures reveal multistage melt present strain localisation in mid-ocean gabbros. *Lithos*, *366–367*, 105572. https://doi.org/10.1016/j.lithos.2020.105572

Hansen, L. N., Cheadle, M. J., John, B. E., Swapp, S. M., Dick, H. J. B., Tucholke, B. E., & Tivey, M. A. (2013). Mylonitic deformation at the Kane oceanic core complex: Implications for the rheological behavior of oceanic detachment faults: Rheology of Kane Oceanic Core Complex. *Geochemistry, Geophysics, Geosystems*, *14*(8), 3085–3108. https://doi.org/10.1002/ggge.20184

Harigane, Y., Michibayashi, K., & Ohara, Y. (2008). Shearing within lower crust during progressive retrogression: Structural analysis of gabbroic rocks from the Godzilla Mullion, an oceanic core complex in the Parece Vela backarc basin. *Tectonophysics*, *457*(3–4), 183–196. https://doi.org/10.1016/j.tecto.2008.06.009

Harigane, Y., Michibayashi, K., & Ohara, Y. (2011). Deformation and hydrothermal metamorphism of gabbroic rocks within the Godzilla Megamullion, Parece Vela Basin, Philippine Sea. *Lithos*, *124*(3–4), 185–199. https://doi.org/10.1016/j.lithos.2011.02.001

Hay, R. S., & Evans, B. (1987). Chemically induced grain boundary migration in calcite: Temperature dependence, phenomenology, and possible applications to geologic systems. *Contributions to Mineralogy and Petrology*, *97*(1), 127–141. https://doi.org/10.1007/BF00375220

Hirth, G., & Tullis, J. (1992). Dislocation creep regimes in quartz aggregates. *Journal of Structural Geology*, *14*(2), 145–159. https://doi.org/10.1016/0191-8141(92)90053-Y

Hirth, G., & Tullis, J. (1994). The brittle-plastic transition in experimentally deformed quartz aggregates. *Solid Earth*, *99*(B6), 11731–11747. https://doi.org/10.1029/93JB02873

Homburg, J. M., Hirth, G., & Kelemen, P. B. (2010). Investigation of the strength contrast at the Moho: A case study from the Oman Ophiolite. *Geology*, *38*(8), 679–682. https://doi.org/10.1130/G30880.1

Hosford, A., Tivey, M., Matsumoto, T., Dick, H., Schouten, H., & Kinoshita, H. (2003). Crustal magnetization and accretion at the Southwest Indian Ridge near the Atlantis II fracture zone, 0–25 Ma. *Journal of Geophysical Research*, *108*(B3). https://doi.org/10.1029/2001JB000604

Ji, S. (2004). A generalized mixture rule for estimating the viscosity of solid-liquid suspensions and mechanical properties of polyphase rocks and composite materials. *Journal of Geophysical Research*, *109*(B10). https://doi.org/10.1029/2004JB003124

Ji, S., & Mainprice, D. (1990). Recrystallization and Fabric Development in Plagioclase. *The Journal of Geology*, *98*(1), 65–79. https://doi.org/10.1086/629375

Ji, S., Mainprice, D., & Boudier, F. (1988). Sense of shear in high-temperature movement zones from the fabric asymmetry of plagioclase feldspars. *Journal of Structural Geology*, *10*(1), 73–81. https://doi.org/10.1016/0191-8141(88)90129-0

Ji, S., Tongbin, S., Salisbury, M. H., Sun, S., Michibayashi, K., Zhao, W., et al. (2014). Plagioclase preferred orientation and induced seismic anisotropy in mafic igneous rocks. *Journal of Geophysical Research: Solid Earth*, *119*, 8064–8088. https://doi.org/10.1002/2014JB011352

Ji, S., Wirth, R., Rybacki, E., & Jiang, Z. (2000). High-temperature plastic deformation of quartz-plagioclase multilayers by layer-normal compression. *Journal of Geophysical Research*, *105*(B7), 16651–16664. https://doi.org/10.1029/2000JB900130

Jiang, Z., Prior, D. J., & Wheeler, J. (2000). Albite crystallographic preferred orientation and grain misorientation distribution in a low-grade mylonite: Implications for granular flow. *Journal of Structural Geology*, *22*(11–12), 1663–1674. https://doi.org/10.1016/S0191-8141(00)00079-1

Kenkmann, T., & Dresen, G. (2002). Dislocation microstructure and phase distribution in a lower crustal shear zone—An example from the Ivrea-Zone, Italy. *International Journal of Earth Sciences*, *91*(3), 445–458. https://doi.org/10.1007/s00531-001-0236-9

Kronenberg, A. K., & Shelton, G. L. (1980). Deformation microstructures in experimentally deformed Maryland diabase. *Journal of Structural Geology*, *2*(3), 341–353. https://doi.org/10.1016/0191-8141(80)90022-X

Kruse, R., Stünitz, H., & Kunze, K. (2001). Dynamic recrystallization processes in plagioclase porphyroclasts. *Journal of Structural Geology*, *23*(11), 1781–1802. https://doi.org/10.1016/S0191-8141(01)00030-X

Lloyd, G. E., Farmer, A. B., & Mainprice, D. (1997). Misorientation analysis and the formation and orientation of subgrain and grain boundaries. *Tectonophysics*, *279*(1–4), 55–78. https://doi.org/10.1016/S0040-1951(97)00115-7

MacLeod, C. J., Dick, H. J. B., Blum, P., & Expedition 360 Scientists. (2017). Southwest Indian ridge lower crust and moho. In *Proceedings of the International Ocean Discovery Program* (Vol. 360). College Station, TX: International Ocean Discovery Program. https://doi.org/10.14379/iodp.proc.360.2017

Mainprice, D., Bachmann, F., Hielscher, R., & Schaeben, H. (2015). Descriptive tools for the analysis of texture projects with large datasets using MTEX : Strength, symmetry and components. *Geological Society, London, Special Publications*, *409*(1), 251–271. https://doi.org/10.1144/SP409.8

Marshall, D. B., & McLaren, A. C. (1977). The direct observation and analysis of dislocations in experimentally deformed plagioclase feldspars. *Journal of Materials Science*, *12*(5), 893–903. https://doi.org/10.1007/BF00540970

McLaren, A. C., & Pryer, L. L. (2001). Microstructural investigation of the interaction and interdependence of cataclastic and plastic mechanisms in Feldspar crystals deformed in the semi-brittle field. *Tectonophysics*, *335*, 15. https://doi.org/10.1016/S0040-1951(01)00042-7

Mehl, L., & Hirth, G. (2008). Plagioclase preferred orientation in layered mylonites: Evaluation of flow laws for the lower crust. *Journal of Geophysical Research*, *113*(B5), B05202. https://doi.org/10.1029/2007JB005075

Miranda, E. A., Hirth, G., & John, B. E. (2016). Microstructural evidence for the transition from dislocation creep to dislocation-accommodated grain boundary sliding in naturally deformed plagioclase. *Journal of Structural Geology*, *92*, 30–45. https://doi.org/10.1016/j.jsg.2016.09.002

Miranda, E. A., & John, B. E. (2010). Strain localization along the Atlantis Bank oceanic detachment fault system, Southwest Indian Ridge. *Geochemistry, Geophysics, Geosystems*, *11*(4), 34. https://doi.org/10.1029/2009GC002646

Montardi, Y. A., & Mainprice, D. (1987). A transmission electron microscopie study of the natural plastic defonnation of calcic plagioclases (An 68–70). *Bulletin de Mineralogie*, *110*(1), 1–14. https://doi.org/10.3406/bulmi.1987.8022

Newton, M. S., & Kennedy, G. C. (1968). Jadeite, analcite, nepheline, and albite at high temperatures and pressures. *American Journal of Science*, *266*(8), 728–735. https://doi.org/10.2475/ajs.266.8.728

Nguyen, D., Morishita, T., Soda, Y., Tamura, A., Ghosh, B., Harigane, Y., et al. (2018). Occurrence of felsic rocks in oceanic gabbros from IODP Hole U1473A: Implications for evolved melt migration in the lower oceanic crust. *Minerals*, *8*(12), 583. https://doi.org/10.3390/min8120583

Nozaka, T., Akitou, T., Abe, N., & Tribuzio, R. (2019). Biotite in olivine gabbros from Atlantis Bank: Evidence for amphibolite-facies metasomatic alteration of the lower oceanic crust. *Lithos*, *348–349*, 105176. https://doi.org/10.1016/j.lithos.2019.105176

Okudaira, T., Jeřábek, P., Stünitz, H., & Fusseis, F. (2015). High-temperature fracturing and subsequent grain-size-sensitive creep in lower crustal gabbros: Evidence for coseismic loading followed by creep during decaying stress in the lower crust? *Journal of Geophysical Research: Solid Earth*, *120*(5), 3119–3141. https://doi.org/10.1002/2014JB011708

Okudaira, T., Shigematsu, N., Harigane, Y., & Yoshida, K. (2017). Grain size reduction due to fracturing and subsequent grain-size-sensitive creep in a lower crustal shear zone in the presence of a CO_2-bearing fluid. *Journal of Structural Geology*, *95*, 171–187. https://doi.org/10.1016/j.jsg.2016.11.001

Oliot, E., Goncalves, P., & Marquer, D. (2010). Role of plagioclase and reaction softening in a metagranite shear zone at mid-crustal conditions (Gotthard Massif, Swiss Central Alps): Strain localization in granitic rocks. *Journal of Metamorphic Geology*, *28*(8), 849–871. https://doi.org/10.1111/j.1525-1314.2010.00897.x

Oliot, E., Goncalves, P., Schulmann, K., Marquer, D., & Lexa, O. (2014). Mid-crustal shear zone formation in granitic rocks: Constraints from quantitative textural and crystallographic preferred orientations analyses. *Tectonophysics*, *612–613*, 63–80. https://doi.org/10.1016/j.tecto.2013.11.032

Olsen, T. S., & Kohlstedt, D. L. (1984). Analysis of dislocations in some naturally deformed plagioclase feldspars. *Physics and Chemistry of Minerals*, *11*(4), 153–160. https://doi.org/10.1007/BF00387845
Olsen, T. S., & Kohlstedt, D. L. (1985). Natural deformation and recrystallization of some intermediate plagioclase feldspars. *Tectonophysics*, *111*(1–2), 107–131. https://doi.org/10.1016/0040-1951(85)90067-8
Paterson, M. S. (1995). A theory for granular flow accommodated by material transfer via an intergranular fluid. *Tectonophysics*, *245*(3–4), 135–151. https://doi.org/10.1016/0040-1951(94)00231-W
Pettigrew, T. L., Casey, J. F., & Miller, D. J. (1999). *Proc. ODP, Init. Repts*. (p. 179). Retrieved From http://www-odp.tamu.edu/publications/179_IR/179TOC.HTM
Poirier, J. P. (1985). *Creep of crystals: High-temperature deformation processes in metals, ceramics and minerals*. Cambridge University Press.
Poirier, J. P., & Guillopé, M. (1979). Deformation induced recrystallization of minerals. *Bulletin de Mineralogie*, *102*(2), 67–74. https://doi.org/10.3406/bulmi.1979.7256
Ronov, A., & Yaroshevsky, A. (1969). Chemical composition of the Earth's crust. *GMS*, *13*, 37–57.
Rosenberg, C. L., & Stünitz, H. (2003). Deformation and recrystallization of plagioclase along a temperature gradient: An example from the Bergell tonalite. *Journal of Structural Geology*, *25*(3), 389–408. https://doi.org/10.1016/S0191-8141(02)00036-6
Ryan, W. B. F., Carbotte, S. M., Coplan, J. O., O'Hara, S., Melkonian, A., Arko, R., et al. (2009). Global multi-resolution topography synthesis. *Geochemistry, Geophysics, Geosystems*, *10*(3). https://doi.org/10.1029/2008GC002332
Rybacki, E., & Dresen, G. (2004). Deformation mechanism maps for feldspar rocks. *Tectonophysics*, *382*(3–4), 173–187. https://doi.org/10.1016/j.tecto.2004.01.006
Satsukawa, T., Ildefonse, B., Mainprice, D., Morales, L. F. G., Michibayashi, K., & Barou, F. (2013). A database of plagioclase crystal preferred orientations (CPO) and microstructures- implications for CPO origin, strength, symmetry and seismic anisotropy in gabbroic rocks. *Solid Earth*, *4*(2), 511–542. https://doi.org/10.5194/se-4-511-2013
Scandale, E., Gandais, M., & Willaime, C. (1983). Transmission electron microscopic study of experimentally deformed k-feldspar single crystals: The (010)[001], 0011/2[-110]1/2[-112] and(1-11)1/2[110] slip systems. *Physics and Chemistry of Minerals*, *9*(3–4), 182–187. https://doi.org/10.1007/BF00308376
Schmid, S. M. (1994). Textures of geological materials: Computer model predictions versus empirical interpretations based on rock deformation experiments and field studies. In Bunge, H. J., Siegesmund, S., Skrotzki, W., & Weber, K. (Eds.), *Texture of geological materials*. (pp. 279–301). Oberursel: Deutsch gesellschaft für materialkunde.
Simpson, C. (1985). Deformation of granitic rocks across the brittle-ductile transition. *Journal of Structural Geology*, *7*(5), 503–511. https://doi.org/10.1016/0191-8141(85)90023-9
Skemer, P., Katayama, I., Jiang, Z., & Karato, S. (2005). The misorientation index: Development of a new method for calculating the strength of lattice-preferred orientation. *Tectonophysics*, *411*(1–4), 157–167. https://doi.org/10.1016/j.tecto.2005.08.023
Smith, J. V. (1984). Phase relations of plagioclase feldspars. In Brown, W. L. (Ed.), Feldspars and Feldspathoids (Series C: Mathematical and Physical Sciences) (Vol. 137, pp. 55–94). Dordrecht: Springer. https://doi.org/10.1007/978-94-015-6929-3_2
Stünitz, H. (1998). Syndeformational recrystallization—Dynamic or compositionally induced? *Contributions to Mineralogy and Petrology*, *131*(2–3), 219–236. https://doi.org/10.1007/s004100050390
Stünitz, H., & Fitz Gerald, J. D. (1993). Deformation of granitoids at low metamorphic grade. II: Granular flow in albite-rich mylonites. *Tectonophysics*, *221*(3–4), 299–324. https://doi.org/10.1016/0040-1951(93)90164-F
Stünitz, H., Fitz Gerald, J. D., & Tullis, J. (2003). Dislocation generation, slip systems, and dynamic recrystallization in experimentally deformed plagioclase single crystals. *Tectonophysics*, *372*(3–4), 215–233. https://doi.org/10.1016/S0040-1951(03)00241-5
Svahnberg, H., & Piazolo, S. (2010). The initiation of strain localisation in plagioclase-rich rocks: Insights from detailed microstructural analyses. *Journal of Structural Geology*, *32*(10), 1404–1416. https://doi.org/10.1016/j.jsg.2010.06.011
Taufner, R., Viegas, G., Faleiros, F. M., Castellan, P., & Silva, R. (2021). Deformation mechanisms of granulite-facies mafic shear zones from Hole U1473A, Atlantis Bank, Southwest Indian Ridge (IODP Expedition 360). *Journal of Structural Geology*, *149*, 104380. https://doi.org/10.1016/j.jsg.2021.104380
Teagle, D. A. H., Ildefonse, B., Blum, P., & Expedition 335 Scientists. (2012). *Deep drilling of intact ocean crust: Harnessing past lessons to inform future endeavors*. Integrated Ocean Drilling Program. https://doi.org/10.2204/iodp.proc.335.2012
Trimby, P. W., Prior, D. J., & Wheeler, J. (1998). Grain boundary hierarchy development in a quartz mylonite. *Journal of Structural Geology*, *20*(7), 917–935. https://doi.org/10.1016/S0191-8141(98)00026-1
Tullis, J. (1983). Deformation of feldspars. In Ribbe, P. H. (Ed.), *Feldspar mineralogy* (pp. 297–323). Mineral Society of America. https://doi.org/10.1515/9781501508547-018
Tullis, J., & Yund, R. A. (1977). Experimental deformation of dry westerly granite. *Journal of Geophysical Research*, *82*(36), 5705–5718. https://doi.org/10.1029/JB082i036p05705
Tullis, J., & Yund, R. A. (1985). Dynamic recrystallization of feldspar: A mechanism for ductile shear zone formation. *Geology*, *13*, 238–241. https://doi.org/10.1130/0091-7613(1985)13<238:DROFAM>2.0.CO;2
Tullis, J., & Yund, R. A. (1987). Transition from cataclastic flow to dislocation creep of feldspar: Mechanisms and microstructures. *Geology*, *15*(7), 606–609. https://doi.org/10.1130/0091-7613(1987)15<606:TFCFTD>2.0.CO;2
Twiss, R. J. (1977). Theory and applicability of a recrystallized grain size paleopiezometer. In Wyss, M. (Ed.), *Stress in the Earth* (pp. 227–244). Birkhäuser, Basel: Contributions to Current Research in Geophysics (CCRG). https://doi.org/10.1007/978-3-0348-5745-1_13
Urai, J. L., Means, W. D., & Lister, G. S. (1986). Dynamic recrystallization of minerals. In Hobbs, B. E., & Heard, H. C. (Eds.), Geophysical Monograph Series (Vol. 36, pp. 161–199). Washington, D. C.: American Geophysical Union. https://doi.org/10.1029/GM036p0161
Wenk, H. R., & Christie, J. M. (1991). Comments on the interpretation of deformation textures in rocks. *Journal of Structural Geology*, *13*(10), 1091–1110. https://doi.org/10.1016/0191-8141(91)90071-P
Wheeler, J., Prior, D., Jiang, Z., Spiess, R., & Trimby, P. (2001). The petrological significance of misorientations between grains. *Contributions to Mineralogy and Petrology*, *141*(1), 109–124. https://doi.org/10.1007/s004100000225
Yoshinobu, A. S., & Hirth, G. (2002). Microstructural and experimental constraints on the rheology of partially molten gabbro beneath oceanic spreading centers. *Journal of Structural Geology*, *24*(6–7), 1101–1107. https://doi.org/10.1016/S0191-8141(01)00094-3
Yund, R. A., & Tullis, J. (1991). Compositional changes of minerals associated with dynamic recrystallizatin. *Contributions to Mineralogy and Petrology*, *108*(3), 346–355. https://doi.org/10.1007/BF00285942

References From the Supporting Information

Ague, D. M., Wenk, H. R., & Wenk, E. (1990). Deformation microstructures and lattice orientations of plagioclase in Gabbros from central Australia. In Duba, A. G., Durham, W. B., Handin, J. W., & Wang, H. F. (Eds.), Geophysical Monograph Series (Vol. 56, pp. 173–186). Washington, D. C.: American Geophysical Union. https://doi.org/10.1029/GM056p0173

Baratoux, L., Schulmann, K., Ulrich, S., & Lexa, O. (2005). Contrasting microstructures and deformation mechanisms in metagabbro mylonites contemporaneously deformed under different temperatures (c. 650°C and c. 750°C). *The Geological Society of London*, *243*, 97–125.

Barreiro, J. G., Lonardelli, I., Wenk, H. R., Dresen, G., Rybacki, E., Ren, Y., & Tomé, C. N. (2007). Preferred orientation of anorthite deformed experimentally in Newtonian creep. *Earth and Planetary Science Letters*, *264*(1–2), 188–207. https://doi.org/10.1016/j.epsl.2007.09.018

Barreiro, J. G., Wenk, H.-R., & Vogel, S. (2015). Texture and elastic anisotropy of a mylonitic anorthosite from the Morin Shear Zone (Quebec, Canada). *Journal of Structural Geology*, *71*, 100–111. https://doi.org/10.1016/j.jsg.2014.07.021

Cross, A. J. (2015). *Microstructural evolution under non-steady state deformation in mid-crustal ductile shear zones, (Doctoral dissertation)*. University of Otago. Retrieved from http://hdl.handle.net/10523/5608

Díaz-Azpiroz, M., Lloyd, G. E., & Fernández, C. (2011). Deformation mechanisms of plagioclase and seismic anisotropy of the Acebuches metabasites (SW Iberian massif). *Geological Society, London, Special Publications*, *360*(1), 79–95. https://doi.org/10.1144/SP360.5

Egydio-Silva, M., & Mainprice, D. (1999). Determination of stress directions from plagioclase fabrics in high grade deformed rocks (Além Paraíba shear zone, Ribeira fold belt, southeastern Brazil). *Journal of Structural Geology*, *21*(12), 1751–1771. https://doi.org/10.1016/S0191-8141(99)00121-2

Egydio-Silva, M., Vauchez, A., Bascou, J., & Hippertt, J. (2002). High-temperature deformation in the Neoproterozoic transpressional Ribeira belt, southeast Brazil. *Tectonophysics*, *352*(1–2), 203–224. https://doi.org/10.1016/S0040-1951(02)00197-X

Fukuda, J., & Okudaira, T. (2013). Grain-size-sensitive creep of plagioclase accompanied by solution–precipitation and mass transfer under mid-crustal conditions. *Journal of Structural Geology*, *51*, 61–73. https://doi.org/10.1016/j.jsg.2013.03.006

Gandais, M., & Willaime, C. (1984). Mechanical properties of feldspars. In Brown, W. L. (Ed.), *Feldspars and Feldspathoids* NATO ASI Series (Series C: Mathematical and Physical Sciences) (Vol. 137, pp. 207–246). Dordrecht: Springer. https://doi.org/10.1007/978-94-015-6929-3_6

Hansen, L. N., Cheadle, M. J., John, B. E., Swapp, S. M., Dick, H. J. B., Tucholke, B. E., & Tivey, M. A. (2013). Mylonitic deformation at the Kane oceanic core complex: Implications for the rheological behavior of oceanic detachment faults: Rheology of Kane Oceanic Core Complex. *Geochemistry, Geophysics, Geosystems*, *14*(8), 3085–3108. https://doi.org/10.1002/ggge.20184

Heidelbach, F., Post, A., & Tullis, J. (2000). Crystallographic preferred orientation in albite samples deformed experimentally by dislocation and solution precipitation creep. *Journal of Structural Geology*, *22*(11–12), 1649–1661. https://doi.org/10.1016/S0191-8141(00)00072-9

Homburg, J. M., Hirth, G., & Kelemen, P. B. (2010). Investigation of the strength contrast at the Moho: A case study from the Oman Ophiolite. *Geology*, *38*(8), 679–682. https://doi.org/10.1130/G30880.1

Jensen, L. N., & Starkey, J. (1985). Plagioclase microfabrics in a ductile shear zone from the Jotun Nappe, Norway. *Journal of Structural Geology*, *7*(5), 527–539.

Jerabek, P., Stünitz, H., Heilbronner, R., Lexa, O., & Schulmann, K. (2007). Microstructural-deformation record of an orogen-parallel extension in the Vepor Unit, West Carpathians. *Journal of Structural Geology*, *29*(11), 1722–1743. https://doi.org/10.1016/j.jsg.2007.09.002

Ji, S. (2004). A generalized mixture rule for estimating the viscosity of solid-liquid suspensions and mechanical properties of polyphase rocks and composite materials. *Journal of Geophysical Research*, *109*(B10). https://doi.org/10.1029/2004JB003124

Ji, S., & Mainprice, D. (1988). Natural deformation fabrics of plagioclase: Implications for slip systems and seismic anisotropy. *Tectonophysics*, *147*(1–2), 145–163. https://doi.org/10.1016/0040-1951(88)90153-9

Ji, S., & Mainprice, D. (1990). Recrystallization and Fabric Development in Plagioclase. *The Journal of Geology*, *98*(1), 65–79. https://doi.org/10.1086/629375

Ji, S., Jiang, Z., Rybacki, E., Wirth, R., Prior, D., & Xia, B. (2004). Strain softening and microstructural evolution of anorthite aggregates and quartz–anorthite layered composites deformed in torsion. *Earth and Planetary Science Letters*, *222*(2), 377–390. https://doi.org/10.1016/j.epsl.2004.03.021

Ji, S., Mainprice, D., & Boudier, F. (1988). Sense of shear in high-temperature movement zones from the fabric asymmetry of plagioclase feldspars. *Journal of Structural Geology*, *10*(1), 73–81. https://doi.org/10.1016/0191-8141(88)90129-0

Ji, S., Wirth, R., Rybacki, E., & Jiang, Z. (2000). High-temperature plastic deformation of quartz-plagioclase multilayers by layer-normal compression. *Journal of Geophysical Research*, *105*(B7), 16651–16664. https://doi.org/10.1029/2000JB900130

Ji, S., Zhao, X., Zhao, P., de Grologie, D., & de Montrral (1994). On the measurement of plagioclase lattice preferred orientations. *Journal of Structural Geology*, *16*(12), 1711–1718. https://doi.org/10.1016/0191-8141(94)90136-8

Jiang, Z., Prior, D. J., & Wheeler, J. (2000). Albite crystallographic preferred orientation and grain misorientation distribution in a low-grade mylonite: Implications for granular flow. *Journal of Structural Geology*, *22*(11–12), 1663–1674. https://doi.org/10.1016/S0191-8141(00)00079-1

Kanagawa, K., Shimano, H., & Hiroi, Y. (2008). Mylonitic deformation of gabbro in the lower crust: A case study from the Pankenushi gabbro in the Hidaka metamorphic belt of central Hokkaido, Japan. *Journal of Structural Geology*, *30*(9), 1150–1166. https://doi.org/10.1016/j.jsg.2008.05.007

Kendrick, J. E., Lavallée, Y., Mariani, E., Dingwell, D. B., Wheeler, J., & Varley, N. R. (2017). Crystal plasticity as an indicator of the viscous-brittle transition in magmas. *Nature Communications*, *8*(1), 1926. https://doi.org/10.1038/s41467-017-01931-4

Kruhl, J. H. (1987). Preferred lattice orientations of plagioclase from amphibolite and greenschist facies rocks near the Insubric Line (Western Alps). *Tectonophysics*, *135*, 233–242.

Kruse, R., & Stünitz, H. (1999). Deformation mechanisms and phase distribution in mafic high-temperature mylonites from the Jotun Nappe, southern Norway. *Tectonophysics*, *303*(1–4), 223–249. https://doi.org/10.1016/S0040-1951(98)00255-8

Kruse, R., Stünitz, H., & Kunze, K. (2001). Dynamic recrystallization processes in plagioclase porphyroclasts. *Journal of Structural Geology*, *23*(11), 1781–1802. https://doi.org/10.1016/S0191-8141(01)00030-X

Lafrance, B., John, B. E., & Scoates, J. S. (1996). Syn-emplacement recrystallization and deformation microstructures in the Poe Mountain anorthosite, Wyoming. *Contributions to Mineralogy and Petrology*, *122*(4), 431–440. https://doi.org/10.1007/s004100050139

Lapworth, T., Wheeler, J., & Prior, D. J. (2002). The deformation of plagioclase investigated using electron backscatter diffraction crystallographic preferred orientation data. *Journal of Structural Geology*, *24*(2), 387–399. https://doi.org/10.1016/S0191-8141(01)00057-8

MacLeod, C. J., Dick, H. J. B., Blum, P., & Expedition 360 Scientists. (2017). Southwest Indian ridge lower crust and moho. In *Proceedings of the International Ocean Discovery Program* (Vol. 360). College Station, TX: International Ocean Discovery Program. https://doi.org/10.14379/iodp.proc.360.2017

Marshall, D. B., & McLaren, A. C. (1977a). Deformation mechanisms in experimentally deformed plagioclase feldspars. *Physics and Chemistry of Minerals*, *1*(4), 351–370.
Marshall, D. B., & McLaren, A. C. (1977b). The direct observation and analysis of dislocations in experimentally deformed plagioclase feldspars. *Journal of Materials Science*, *12*(5), 893–903. https://doi.org/10.1007/BF00540970
Mehl, L., & Hirth, G. (2008). Plagioclase preferred orientation in layered mylonites: Evaluation of flow laws for the lower crust. *Journal of Geophysical Research*, *113*(B5), B05202. https://doi.org/10.1029/2007JB005075
Michibayashi, K., Harigane, Y., Ohara, Y., Muto, J., & Okamoto, A. (2014). Rheological properties of the detachment shear zone of an oceanic core complex inferred by plagioclase flow law: Godzilla Megamullion, Parece Vela back-arc basin, Philippine Sea. *Earth and Planetary Science Letters*, *408*, 16–23. https://doi.org/10.1016/j.epsl.2014.10.005
Miranda, E. A., Hirth, G., & John, B. E. (2016). Microstructural evidence for the transition from dislocation creep to dislocation-accommodated grain boundary sliding in naturally deformed plagioclase. *Journal of Structural Geology*, *92*, 30–45. https://doi.org/10.1016/j.jsg.2016.09.002
Montardi, Y. A., & Mainprice, D. (1987). A transmission electron microscopie study of the natural plastic defonnation of calcic plagioclases (An 68–70). *Bulletin de Mineralogie*, *110*(1), 1–14. https://doi.org/10.3406/bulmi.1987.8022
Oliot, E., Goncalves, P., Schulmann, K., Marquer, D., & Lexa, O. (2014). Mid-crustal shear zone formation in granitic rocks: Constraints from quantitative textural and crystallographic preferred orientations analyses. *Tectonophysics*, *612–613*, 63–80. https://doi.org/10.1016/j.tecto.2013.11.032
Olsen, T. S., & Kohlstedt, D. L. (1984). Analysis of dislocations in some naturally deformed plagioclase feldspars. *Physics and Chemistry of Minerals*, *11*(4), 153–160. https://doi.org/10.1007/BF00387845
Olsen, T. S., & Kohlstedt, D. L. (1985). Natural deformation and recrystallization of some intermediate plagioclase feldspars. *Tectonophysics*, *111*(1–2), 107–131. https://doi.org/10.1016/0040-1951(85)90067-8
Pearce, F. D., Rondenay, S., Sachpazi, M., Charalampakis, M., & Royden, L. H. (2012). Seismic investigation of the transition from continental to oceanic subduction along the western Hellenic Subduction Zone. *Journal of Geophysical Research*, *117*(B7). https://doi.org/10.1029/2011JB009023
Prasannakumar, V., & Lloyd, G. (2007). Development of crystal lattice preferred orientation and seismic properties in Bhavani shear zone, Southern India. *Journal of the Geological Society of India*, *70*(282–296), 26.
Rosenberg, C. L., & Stünitz, H. (2003). Deformation and recrystallization of plagioclase along a temperature gradient: An example from the Bergell tonalite. *Journal of Structural Geology*, *25*(3), 389–408. https://doi.org/10.1016/S0191-8141(02)00036-6
Scandale, E., Gandais, M., & Willaime, C. (1983). Transmission electron microscopic study of experimentally deformed k-feldspar single crystals: The (010)[001], 0011/2[-110]1/2[-112] and(1-11)1/2[110] slip systems. *Physics and Chemistry of Minerals*, *9*(3–4), 182–187. https://doi.org/10.1007/BF00308376
Shigematsu, N., & Tanaka, H. (2000). Dislocation creep of *ne-grained recrystallized plagioclase under low-temperature conditions. *Journal of Structural Geology*, *22*(1), 65–79. https://doi.org/10.1016/S0191-8141(99)00132-7
Siegesmund, S., Helming, K., & Kruse, R. (1994). Complete texture analysis of a deformed amphibolite: Comparison between neutron diffraction and U-stage data. *Journal of Structural Geology*, *16*(1), 131–142. https://doi.org/10.1016/0191-8141(94)90024-8
Stünitz, H., Fitz Gerald, J. D., & Tullis, J. (2003). Dislocation generation, slip systems, and dynamic recrystallization in experimentally deformed plagioclase single crystals. *Tectonophysics*, *372*(3–4), 215–233. https://doi.org/10.1016/S0040-1951(03)00241-5
Svahnberg, H., & Piazolo, S. (2010). The initiation of strain localisation in plagioclase-rich rocks: Insights from detailed microstructural analyses. *Journal of Structural Geology*, *32*(10), 1404–1416. https://doi.org/10.1016/j.jsg.2010.06.011
Terry, M. P., & Heidelbach, F. (2006). Deformation-enhanced metamorphic reactions and the rheology of high-pressure shear zones, Western Gneiss Region, Norway. *Journal of Metamorphic Geology*, *24*(1), 3–18. https://doi.org/10.1111/j.1525-1314.2005.00618.x
White, J. C. (1990). Albite deformation within a basal ophiolite shear zone. *Geological Society, London, Special Publications*, *54*(1), 327–333. https://doi.org/10.1144/GSL.SP.1990.054.01.29
Xie, Y., Wenk, H. -R., & Matthies, S. (2003). Plagioclase preferred orientation by TOF neutron diffraction and SEM-EBSD. *Tectonophysics*, *370*(14), 269–286. https://doi.org/10.1016/S0040-1951(03)00191-4

Journal of Geophysical Research: Solid Earth

Supporting Information for

Plastic Deformation of Plagioclase in Oceanic Gabbro Accreted at a Slow-Spreading Ridge (Hole U1473A, Atlantis Bank, Southwest Indian Ridge)

Maël Allard, Benoît Ildefonse, Émilien Oliot, and Fabrice Barou

Géosciences Montpellier, Université de Montpellier, CNRS, Montpellier, France

Supporting Information S1

Contents of this file

Introduction

The following supporting information includes a literature compilation of the observed active slip systems in plagioclase grains and associated temperatures of deformation (Tables S1 & S2). The main characteristics of the sample suite used in this study are given in Table S3. During IODP expedition 360 in 2016, Benoît Ildefonse collected 116 samples that were complemented by 11 samples collected by Maël Allard and Benoît Ildefonse in 2019 at the Kochi Core Center (Kochi University, JAMSTEC, Japan). The relation between calculated J index and M index values and the number of analyzed grains is provided for the sample suite (Figure S1). Further grain misorientation characteristics are reported for plagioclase (Figure S2 and S3). An example of a microstructure in which grain nucleation in microcracks is likely is presented in Figure S4.

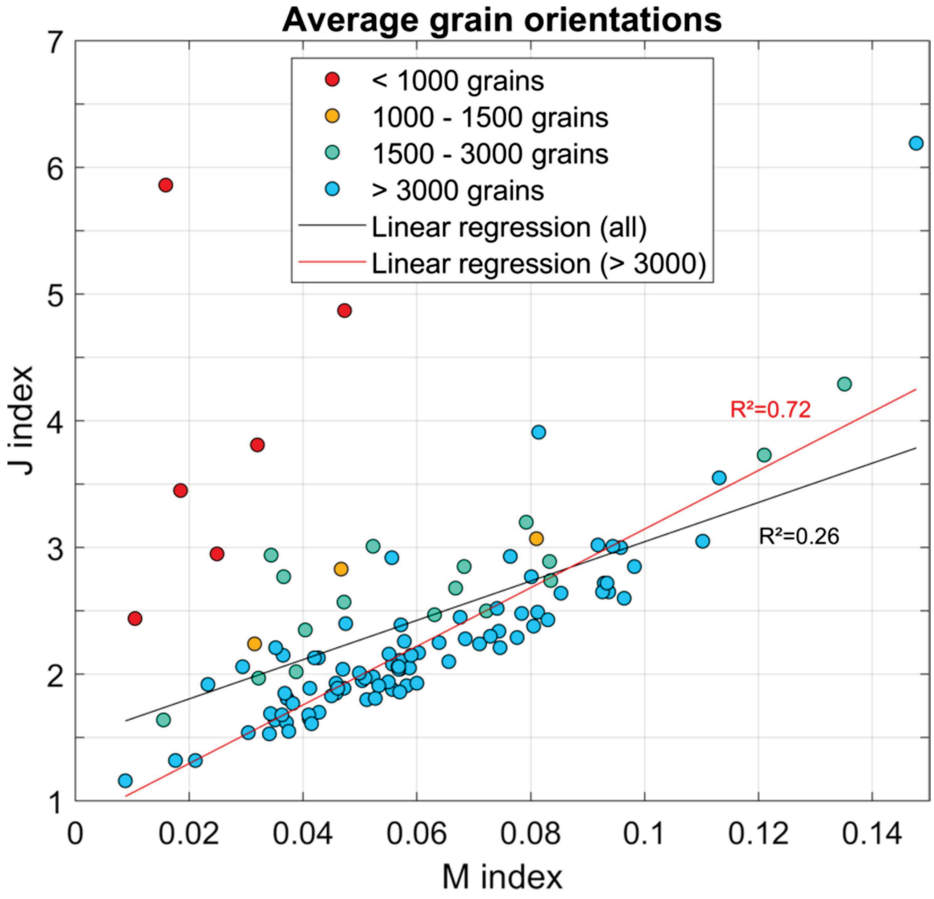

Figure S1. Relation between the M index and the J index, in relation with the number of analyzed grains in plagioclase.

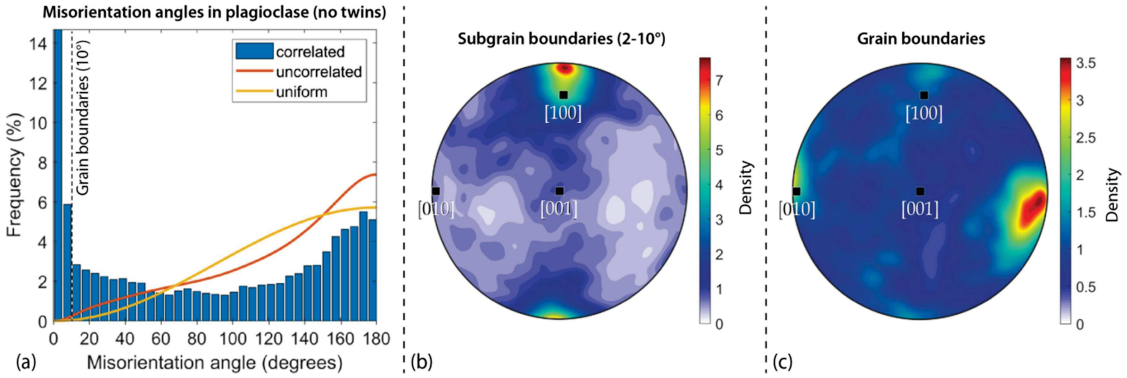

Figure S2. Representative misorientations characteristics in plagioclase, microstructural domain 13_2_59 (see associated pole figures in Figure 6b). (a) Misorientation angle distribution histogram, all grains are considered (porphyroclasts and recrystallized grains). (b) and (c) inverse pole figures (IPF, antipodal, equal area projection) showing the misorientation axes distributions at subgrain boundaries and at grain boundaries, respectively.

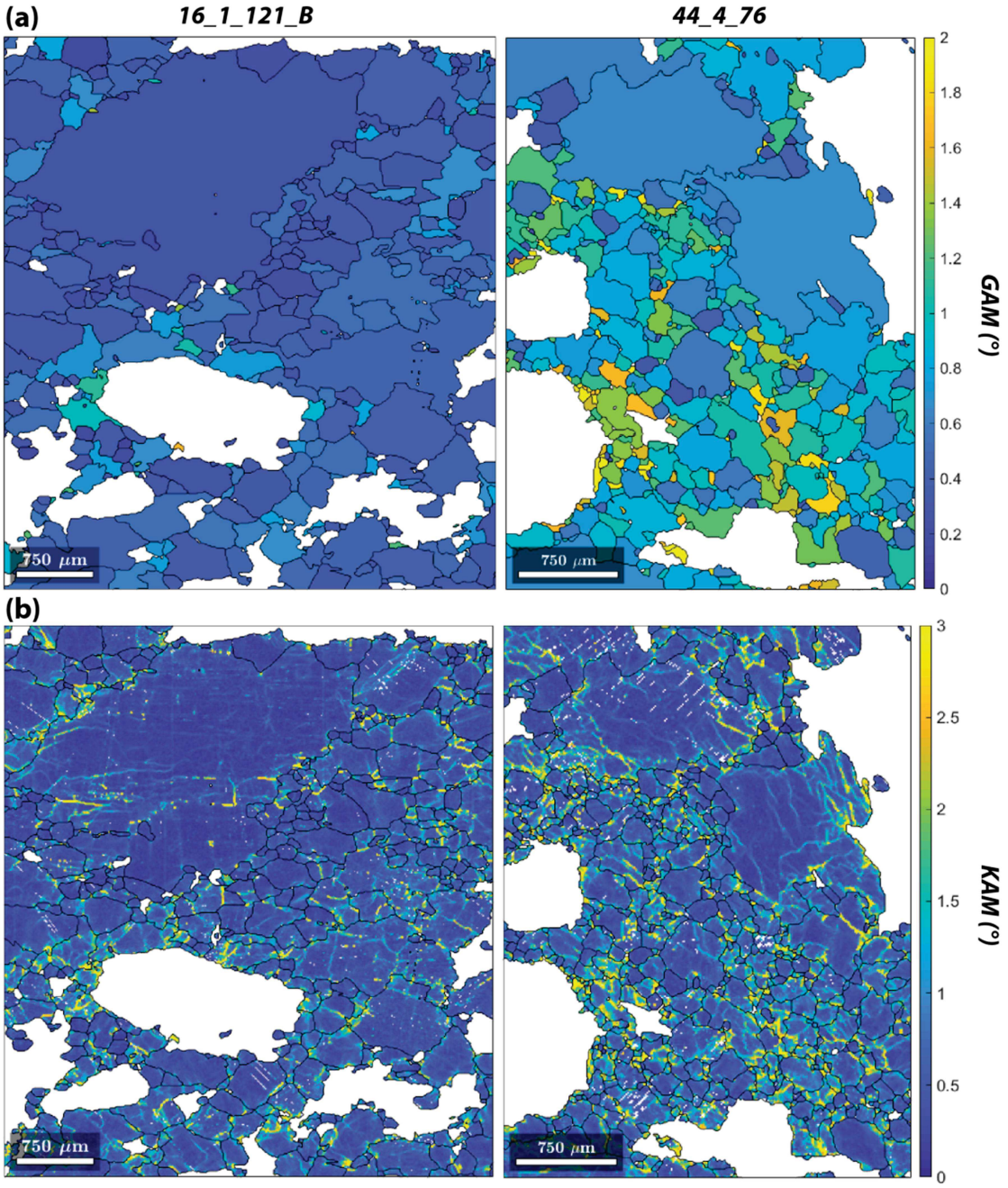

Figure S3. Representative misorientation characteristics in plagioclase grains, examples from the porphyroclastic domains 16_1_121_B and 44_4_76. (a) Grain Average Misorientation (GAM) maps representing the mean intragranular misorientation in grains. (b) Kernel Average Misorientation (KAM) maps representing local misorientations between neighboring pixels. Note the general measurement of higher GAM values in small grains (recrystallized) by contrast to large grains (porphyroclasts). This results from the localized nature of misorientations in grains. The white color corresponds to other phases.

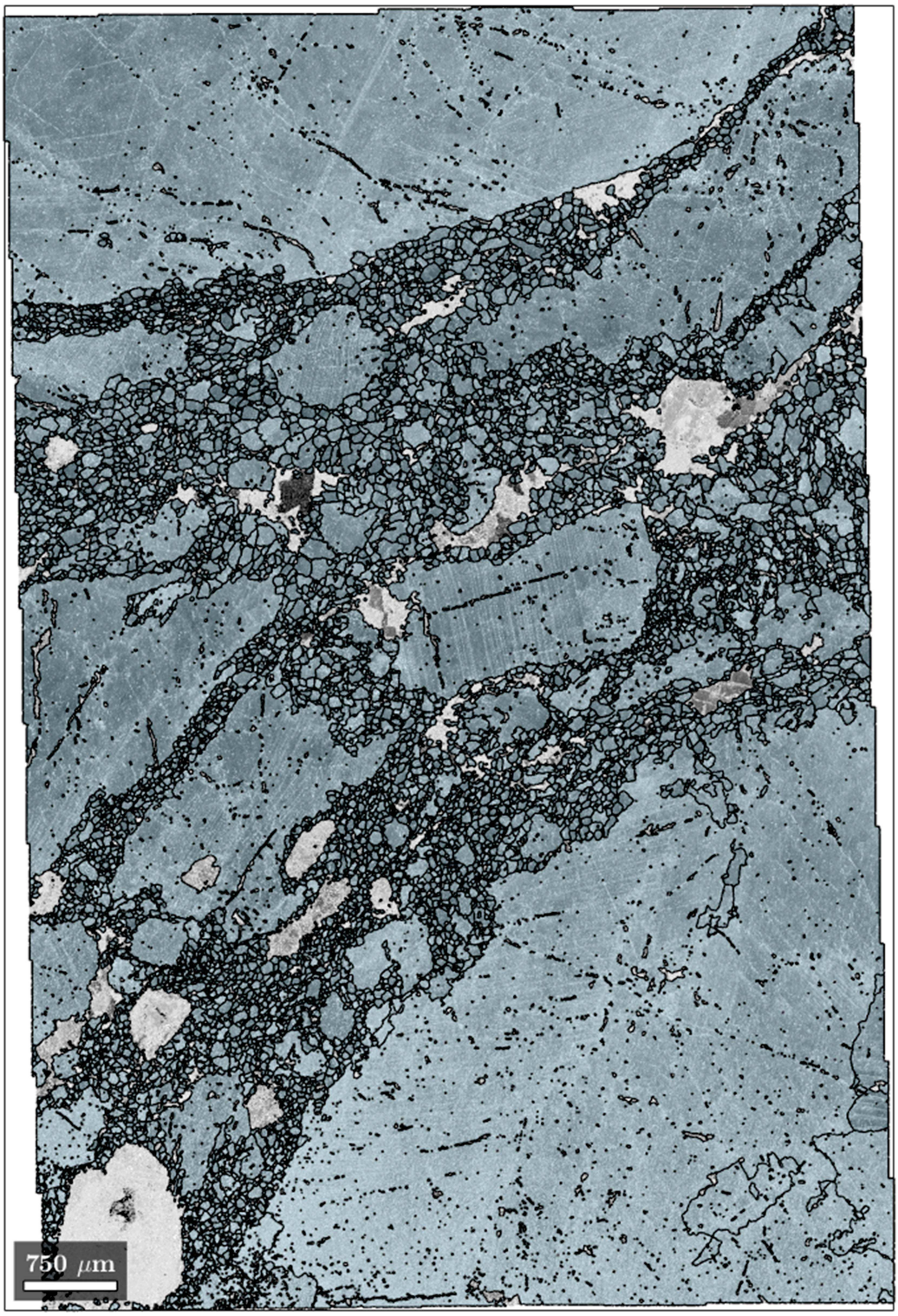

Figure S4. Band contrast map superimposed by plagioclase grain boundaries (without twins), showing a typical texture with nuclei nucleation in microcracks (microstructural domain 67_7_110_A). Light grey areas are other phases.

b	Slip plane 1	Slip plane 2	Slip plane 3
[001]	(010)	$(1\bar{2}0)$	-
[100]	(010)	(001)	-
[101]	(010)	$(11\bar{1})$	$(13\bar{1})$
[201]	(010)	-	-
½ [110]	(001)	$(1\bar{1}\bar{1})$	-
½ $[1\bar{1}0]$	(001)	$(11\bar{1})$	-
½ [111]	$(10\bar{1})$	-	-
½ $[1\bar{1}1]$	$(10\bar{1})$	-	-
½ $[1\bar{1}2]$	(110)	$(20\bar{1})$	(021)
½ $[\bar{1}12]$	$(13\bar{1})$	-	-
½ [112]	$(11\bar{1})$	$(20\bar{1})$	-
[102]	$(20\bar{1})$	-	-

Table S1. Known plagioclase slip systems (Kruse et al., 2001; Marshall and McLaren, 1977; Montardi and Mainprice, 1987; Olsen and Kohlstedt, 1985, 1984; Scandale et al., 1983; Stünitz et al., 2003). "*b*" are Burgers vectors. The two dominant slip systems are in red, the secondary ones are in green, and the tentative ones are in black. Because slip systems are presented according to their slip direction, only corresponding slip planes are colored.

Supporting Information S2

Temperature (°C)	Slip systems						Deformation	References
250-400	[010](001)						natural	Prasannakumar & Lloyd, 2007
300-450	no dis. cr.						natural	Jiang et al., 2000
380-480	no dis. cr.						natural	Jerabek et al., 2007
400-500	[001](010)						natural	Kruhl, 1987
400-510	no dis. cr.						natural	Fukuda & Okudaira, 2013
490	no dis. cr.						natural	Oliot et al., 2014
< 500	½[110](001)						natural	*Shigematsu & Tanaka, 2000
500-650	[100](001)						natural	Terry & Heidelbach, 2006
500-700	[100](001)	[010](001)					natural	Kruhl, 1987
500-700	no dis. cr.						natural	Lapworth et al., 2002
500-850	[100](010)						natural	Homburg et al., 2010
500-950	[001](010)	[100](010)					natural	*Ji & Mainprice, 1988
580-620	[100](010)						natural	Rosenberg & Stünitz, 2003
590-610	$[1\bar{1}0](112)$	$[110](1\bar{1}2)$	$[1\bar{1}0](001)$				natural	Pearce et al., 2011
600	[100](021)						natural	Jensen & Starkey, 1985
600-700	[001](010)	[100](001)	$½[1\bar{1}1](011)$	$[101](10\bar{1})$			natural	*Montardi & Mainprice, 1987
600-950	[001](010)						natural	Ji & Mainprice, 1990
620-670	[100](010)						natural	Rosenberg & Stünitz, 2003
620-650	[100](001)						natural	Siegesmund et al., 1994
630-750	[001](010)						natural	Barreiro et al., 2015
650	$[1\bar{1}0](001)$	$½[1\bar{1}2](20\bar{1})$	$½[1\bar{1}2](021)$				natural	Baratoux et al., 2005
655	[100](010)	[100](001)					natural	Díaz-Azpiroz et al., 2011
650-850	[100](010)						natural	Michibayashi et al., 2014
650-850	[100](010)	[100](001)					natural	Michibayashi et al., 2014
650-850	[100](001)						natural	Michibayashi et al., 2014
675-700	⟨110⟩(001)						natural	Svahnberg & Piazolo, 2010
670-700	$½[1\bar{1}0](001)$						natural	Kanagawa et al., 2008
700	[001](010]	½⟨110⟩(001)					natural	*Kruse et al., 2001
700	[001](010)	$½[1\bar{1}0](001)$					natural	*Kruse & Stünitz, 1999
700	½[110](001)						experimental	*Gandais & Willaime, 1984
≥700	[001](010)	[101](010)	$[101](12\bar{1})$				natural & exp.	*Gandais & Willaime, 1984

Table S2. Plagioclase slip systems inferred by transmission electron microscopy (*) and inferred from EBSD analyses (CPO or misorientations). Slip systems indicated in grey are uncertain. "dis. cr.": dislocation creep.

>700	[001](010)	½[110](001)					natural	*Ague et al., 1990
700-750	[001](010]						natural	Egydio-Silva & Mainprice, 1999
700-800	[001](010)	½[110](001)	½[1$\bar{1}$0](001)	½[110](1$\bar{1}\bar{1}$)	½[1$\bar{1}$0](11$\bar{1}$)	[101](010)	natural	*Olsen & Kohlstedt, 1984
720	[100](001)						natural	Díaz-Azpiroz et al., 2011
720	[100](010)	[100](001)					natural	Díaz-Azpiroz et al., 2011
740-840	[$\bar{1}$00](011)	⟨110⟩{111}					natural	Miranda et al, 2016
750	[100](010)	[100](001)					natural	Baratoux et al., 2005
750-850	[100](010)	[001](010)					natural	Hansen et al., 2013
750-900	[001](010)	[111](01$\bar{1}$)	[012](02$\bar{1}$)	[012](1$\bar{2}$1)			natural	Ji et al., 1994
750-900	[100](010)						natural	Xie et al., 2003
750-950	[001](010)	[100](010)					natural	Ji et al., 1988
800	½[111](10$\bar{1}$)						experimental	*Marshall & McLaren, 1977b
800	½[001]($\bar{1}$30)	½[001]($\bar{1}$20)					experimental	*Marshall & McLaren, 1977b
800	½[111](10$\bar{1}$)	½[1$\bar{1}$1](10$\bar{1}$)					experimental	*Marshall & McLaren, 1977b
800	½[201](11$\bar{2}$)	½[201](13$\bar{2}$)	½[$\bar{1}$11](13$\bar{2}$)	½[201](010)	[100](010)	[101](10$\bar{1}$)	experimental	*Marshall & McLaren, 1977b
800	½[111](10$\bar{1}$)	½[1$\bar{1}$1](10$\bar{1}$)	[100](001)				experimental	*Marshall & McLaren, 1977a
800	[110](10$\bar{1}$)						experimental	*Marshall & McLaren, 1977a
800-950	[100](010)	[100](001)					natural	Mehl & Hirth, 2008
810-880	[100](010)	[001](010)					natural	Egydio-Silva et al., 2002
850-1050	[101](010)	[001](010)	½[112](20$\bar{1}$)				natural	*White, 1990
900	[001](010)	½[110](001)	½[1$\bar{1}$0](001)				experimental	*Stünitz et al., 2003
900	[100](001)						experimental	Cross, 2015
900	⟨100⟩{001}						experimental	*Heidelbach et al., 2000
≥900	½[110](001)						experimental	*Gandais & Willaime, 1984
940-950	[001](010)	⟨110⟩(001)	⟨110⟩(111)				experimental	Kendrick et al., 2017
950-1200	[100](010)	[001](010)	[100](001)				experimental	*Barreiro et al., 2007
1000-1200	[100](010)						experimental	*Ji et al., 2000
1050	[100](010)	[001](010)					natural	Lafrance et al., 1996
1100-1200	[100](010)						experimental	Ji et al., 2004

Table S2. (continued)

Micro-structural domains	Mean Depth CSF-A (m)	Lithology	Main phase modes					CPF index	Plagioclase texture indices		Mean GOS (°)			Mean GAM (°)			Pl rec. grain size (µm)	Number of Pl grains
			Pl	*Cpx*	*Ol*	*Opx*	*Amph*		*J index*	*M index*	*Pl*	*Cpx*	*Ol*	*Pl*	*Cpx*	*Ol*		
2_2_46	11.36	olivine gabbro	57%	38%	5%	0%	0%	0	5.86	0.016	1.72	1.43	1.25	0.06	0.12	1.86	-	314
3_1_86	13.68	oxide gabbro	52%	7%	1%	2%	8%	3	1.89	0.041	1.41	0.73	0.96	0.21	0.22	2.32	14	10313
5_1_93	32.95	oxide gabbro	55%	16%	0%	1%	5%	3	2.04	0.047	2.23	0.93	0.45	0.38	0.43	4.18	31	9521
6_2_128	44.41	oxide gabbro	48%	19%	0%	0%	29%	3	1.83	0.045	1.96	0.79	0.82	0.25	0.28	3.28	30	18287
8_1_31	61.34	olivine gabbro	49%	39%	2%	1%	8%	3	2.13	0.043	2.53	1.44	1.65	0.35	0.41	-	72	5182
8_2_122	63.59	gabbro	63%	3%	0%	0%	34%	3	2.06	0.057	2.13	0.58	-	0.32	0.39	2.71	37	13056
8_3_48	64.35	olivine oxide gabbro	66%	29%	0%	2%	2%	3	3.05	0.110	2.21	1.19	-	0.25	0.34	-	84	10088
9_4_120	76.35	olivine gabbro	65%	24%	1%	7%	3%	4	2.30	0.073	2.42	0.98	0.75	0.42	0.50	3.00	55	9528
9_5_19_A	76.77	olivine gabbro	62%	23%	4%	4%	6%	2	2.74	0.084	3.77	1.55	2.40	0.35	0.46	3.48	79	2838
9_5_19_B	76.77	amphibolitic metagabbro	52%	9%	0%	0%	39%	5	1.16	0.009	0.58	0.44	-	0.16	0.17	-	6	32316
10_1_81	81.24	oxide gabbro	92%	5%	0%	0%	1%	2	6.19	0.148	3.40	0.96	-	0.52	0.65	-	59	6690
11_1_47	90.60	olivine gabbro	52%	20%	1%	1%	26%	3	1.53	0.034	1.77	0.77	0.59	0.18	0.22	2.18	40	18645
11_2_18	91.80	olivine oxide gabbro	62%	25%	6%	1%	3%	3	1.89	0.047	1.53	0.72	0.80	0.14	0.21	1.46	102	6729
11_3_20	93.27	olivine gabbro	70%	24%	3%	2%	1%	2	1.98	0.052	1.24	0.71	0.89	0.12	0.19	0.74	107	5454
11_4_108	95.65	olivine gabbro	61%	28%	9%	1%	2%	3	1.97	0.051	1.71	0.84	0.93	0.10	0.15	1.13	53	8631
12_1_27	100.09	olivine oxide gabbro	66%	19%	3%	2%	9%	4	2.64	0.085	1.64	0.76	0.53	0.14	0.18	1.67	79	5823

Table S3. List of analyzed microstructural domains. CSF-A: core composite depth below seafloor (see MacLeod et al. (2017) for details). Samples names (I_II_III) indicate the core number (I), the number of the section in the core (II), and the top depth in the section in cm (III). The different microstructures analyzed in the same sample or depth interval are indicate by the addition of the letters A, B or C. Pl: plagioclase; Cpx: clinopyroxene; Ol: olivine; Opx: orthopyroxene; Amph: amphibole; CPF index: Crystal-plastic fabrics index, ranging from 0 (not deformed), to 5 (ultramylonite); GOS: Grain Orientation Spread; GAM: Grain Average Misorientation (mean value of grain average kernel misorientations). Note that the J index is not given for samples with less than 1000 grains because of the abnormally high calculated values (see supporting information Figure S1). Texture indices J and M are calculated from average grain orientation data set. "Pl rec.": plagioclase recrystallized grains.

12_5_45	106.20	olivine gabbro	72%	22%	4%	2%	-	3	2.28	0.069	1.84	0.94	0.89	0.22	0.32	2.03	117	12672
13_2_59	111.44	olivine gabbro	71%	22%	6%	1%	-	2	2.93	0.076	1.71	0.99	1.17	0.12	0.19	1.26	100	5140
14_3_16	122.34	olivine oxide gabbro	63%	31%	0%	2%	-	3	2.10	0.066	1.93	1.10	0.92	0.24	0.32	2.23	111	12087
14_5_9	125.15	olivine gabbro	58%	30%	4%	4%	4%	3	2.25	0.064	2.06	1.09	1.06	0.28	0.35	2.57	117	4983
15_1_46	129.40	amphibolitic metagabbro	60%	1%	0%	0%	40%	4	2.72	0.093	2.18	0.68	-	0.30	0.35	-	47	9615
15_1_128	130.21	olivine gabbro	75%	16%	1%	3%	5%	3	2.15	0.059	1.97	0.89	0.78	0.15	0.22	1.64	73	9191
15_4_45	133.37	olivine gabbro	57%	34%	2%	4%	3%	3	1.91	0.058	1.68	1.03	0.86	0.12	0.15	1.82	94	14348
15_6_25	136.14	olivine gabbro	60%	32%	5%	2%	-	3	2.17	0.060	1.85	1.09	1.05	0.17	0.24	1.57	96	6646
16_1_121_A	139.84	olivine gabbro	67%	22%	8%	3%	1%	2	2.11	0.057	1.70	0.88	0.86	0.21	0.30	2.00	93	5928
16_1_121_B	139.84	olivine gabbro	69%	13%	13%	2%	1%	2	2.40	0.048	1.85	1.10	1.21	0.22	0.31	2.49	82	3890
16_3_26	141.84	olivine gabbro	65%	25%	5%	3%	2%	4	2.65	0.094	1.87	0.76	0.72	0.15	0.21	0.25	54	11107
16_3_60	142.19	olivine gabbro	58%	8%	28%	3%	3%	2	1.70	0.043	1.71	0.83	0.66	0.10	0.16	1.09	69	6392
16_5_73	145.27	oxide gabbro	61%	31%	0%	1%	6%	3	1.64	0.035	1.73	0.84	0.78	0.15	0.22	1.70	67	3384
17_1_54	148.86	olivine gabbro	62%	27%	6%	2%	3%	4	2.24	0.071	1.85	0.86	0.76	0.17	0.24	1.93	62	7254
17_2_99	150.77	olivine gabbro	56%	37%	1%	2%	3%	4	2.08	0.056	2.50	1.08	1.05	0.36	0.44	2.89	65	6614
17_4_52	153.12	oxide gabbro	59%	35%	2%	3%	1%	3	2.04	0.057	2.64	1.55	1.45	0.57	0.62	3.23	125	9963
18_1_13	158.15	olivine gabbro	57%	29%	8%	3%	3%	4	1.95	0.050	1.93	0.97	0.92	0.19	0.26	1.99	73	4952
18_4_19	162.40	olivine gabbro	67%	20%	5%	3%	4%	4	1.68	0.036	1.42	0.54	0.47	0.19	0.26	1.43	29	14832
20_1_112	178.54	gabbro	45%	39%	1%	3%	12%	3	1.54	0.030	2.37	0.99	0.80	0.38	0.45	3.01	30	16894
21_1_56	180.69	olivine gabbro	56%	34%	8%	1%	-	2	2.08	0.061	2.79	1.60	2.30	0.68	0.71	1.46	133	7899
23_1_7_A	196.90	gabbro	92%	5%	0%	0%	3%	3	1.93	0.046	1.28	0.61	1.77	0.11	0.20	0.00	38	12369
23_1_7_B	196.90	gabbro	94%	3%	0%	1%	2%	3	2.01	0.050	3.11	1.20	-	0.31	0.39	3.24	29	12141
23_4_54	201.84	oxide gabbronorite	70%	23%	0%	2%	5%	4	2.49	0.081	1.51	0.55	0.54	0.21	0.26	0.90	51	8676
25_2_35	218.07	olivine gabbro	58%	24%	1%	2%	15%	5	1.62	0.037	1.58	0.78	0.49	0.23	0.30	2.01	31	11426
26_2_92	228.34	olivine oxide gabbro	66%	25%	1%	6%	1%	4	1.91	0.053	1.69	0.97	0.91	0.18	0.26	1.59	39	25987
27_1_51	236.14	olivine gabbro	73%	21%	3%	1%	2%	2	1.85	0.046	1.57	1.01	0.75	0.08	0.14	0.00	71	12786
27_4_5	239.78	olivine gabbro	77%	19%	0%	1%	2%	2	2.16	0.055	1.82	0.93	1.17	0.22	0.28	1.89	57	9615
30_1_22	264.96	olivine gabbro	69%	14%	15%	1%	1%	2	2.39	0.057	2.18	1.33	0.98	0.16	0.23	3.00	59	7193

Table S3. (continued)

30_2_110	267.33	olivine gabbro	55%	39%	2%	1%	3%	1	2.06	0.029	1.70	1.16	1.19	0.14	0.21	1.49	43	9488
30_5_19	270.77	olivine gabbro	63%	33%	1%	0%	3%	2	2.77	0.037	1.71	0.90	0.90	0.20	0.30	1.48	100	2343
31_2_89	276.82	olivine gabbro	85%	11%	1%	0%	2%	3	3.73	0.121	1.69	1.43	1.38	0.20	0.25	2.32	114	2677
33_5_3	299.02	olivine gabbro	50%	39%	1%	1%	10%	1	2.94	0.034	1.59	0.88	0.73	0.15	0.19	1.26	56	2122
34_2_98	305.48	olivine gabbro	63%	28%	5%	2%	2%	3	2.57	0.047	1.24	0.52	0.38	0.11	0.19	0.84	104	2102
34_5_75	308.96	oxide gabbro	66%	25%	1%	5%	3%	4	2.50	0.072	1.50	0.88	1.07	0.10	0.14	0.86	95	2133
34_6_129	311.00	olivine gabbro	52%	34%	10%	1%	2%	2	2.35	0.040	2.21	0.89	0.87	0.18	0.25	2.61	102	2387
35_2_42	315.14	olivine gabbro	63%	27%	4%	3%	3%	4	2.85	0.098	1.28	0.82	1.09	0.20	0.27	1.38	67	4201
38_2_	343.37	olivine gabbro	69%	22%	5%	1%	2%	3	2.52	0.074	1.11	0.87	0.75	0.08	0.15	0.62	49	5369
38_4_52	346.66	olivine oxide gabbro	64%	20%	14%	1%	0%	3	2.89	0.083	1.54	0.99	1.22	0.10	0.20	0.99	99	2975
39_4_108	357.06	olivine gabbro	79%	13%	4%	1%	3%	3	2.21	0.035	1.17	0.71	0.71	0.10	0.17	0.29	96	4101
40_1_85	362.58	olivine gabbro	71%	20%	3%	2%	5%	3	4.29	0.135	2.28	1.21	1.72	0.18	0.28	2.21	125	1616
41_1_96	372.39	olivine oxide gabbro	67%	25%	2%	3%	1%	3	2.85	0.068	1.06	1.06	0.93	0.07	0.13	0.42	83	2019
41_4_68	376.34	olivine oxide gabbro	83%	9%	6%	1%	1%	3	3.20	0.079	0.66	0.44	0.52	0.11	0.15	1.23	126	1843
41_6_56	379.11	olivine oxide gabbro	62%	25%	1%	3%	9%	3	1.65	0.041	1.02	0.82	0.81	0.06	0.12	0.73	66	10709
43_3_66	394.11	olivine gabbro	53%	40%	2%	2%	3%	2	2.15	0.037	1.10	0.75	0.84	0.10	0.17	0.46	90	3453
43_7_39	398.67	olivine gabbro	65%	18%	14%	2%	1%	3	2.47	0.063	1.28	0.84	0.83	0.07	0.15	0.47	110	2636
44_1_105_A	401.58	olivine gabbro	76%	15%	4%	2%	3%	2	1.85	0.037	0.92	0.69	0.75	0.06	0.11	0.28	102	5133
44_1_105_B	401.58	olivine gabbro	52%	34%	7%	3%	3%	2	1.92	0.023	1.29	0.76	0.87	0.09	0.16	0.78	42	6216
44_4_76	405.66	olivine gabbro	64%	28%	2%	4%	2%	2	3.01	0.052	1.04	0.80	0.85	0.14	0.17	0.97	133	1515
50_2_43	451.56	olivine gabbro	53%	36%	5%	3%	2%	3	2.77	0.080	1.71	0.91	0.82	0.15	0.21	1.25	93	3176
58_5_79_A	525.06	gabbro	66%	26%	0%	1%	6%	3	1.81	0.053	2.38	0.93	0.59	0.27	0.32	3.11	37	30622
58_5_79_B	525.06	gabbro	57%	29%	0%	4%	10%	5	1.80	0.051	2.41	0.99	0.59	0.29	0.34	2.90	22	23353
58_5_79_C	525.06	gabbro	59%	31%	0%	3%	7%	5	1.86	0.057	0.74	0.61	0.55	0.10	0.12	0.45	22	44400
58_6_108	527.09	olivine gabbro	61%	28%	2%	4%	4%	3	2.72	0.093	2.66	1.05	0.85	0.38	0.45	2.57	68	4269
59_3_124	533.15	gabbro	51%	36%	5%	3%	5%	1	2.02	0.039	1.03	0.76	0.77	0.18	0.22	0.66	151	2095
59_5_71	535.36	olivine gabbro	66%	22%	1%	1%	10%	3	1.94	0.055	2.04	1.00	0.94	0.17	0.24	2.52	89	10703
60_4_40	542.95	olivine gabbro	68%	21%	4%	3%	4%	2	2.26	0.058	2.41	1.17	0.66	0.22	0.30	3.94	75	3227

Table S3. (continued)

61_3_73_A	551.66	olivine gabbro	55%	29%	5%	9%	1%	3	2.92	0.056	1.58	0.89	0.64	0.11	0.18	2.02	52	5339
61_3_73_B	551.66	olivine gabbro	62%	26%	10%	1%	1%	2	2.34	0.074	2.41	1.17	0.66	0.22	0.30	3.94	44	3599
61_3_73_C	551.66	oxide gabbro	59%	28%	0%	12%	1%	3	3.02	0.092	1.28	0.67	0.66	0.07	0.12	0.87	57	7858
61_5_112	554.69	oxide gabbronorite	67%	20%	0%	9%	4%	4	2.04	0.057	1.68	0.92	0.94	0.10	0.18	1.75	72	6365
62_6_71	565.61	olivine gabbro	59%	30%	0%	3%	9%	3	3.02	0.092	0.88	0.87	0.61	0.06	0.10	0.27	52	2747
65_1_5	586.53	olivine gabbro	63%	23%	12%	2%	1%	1	1.81	0.037	0.65	0.42	0.53	0.09	0.12	0.56	122	3435
65_3_73	590.02	olivine gabbro	63%	27%	6%	4%	1%	2	2.47	0.045	2.03	1.30	1.36	0.16	0.25	0.73	82	1791
65_5_2	593.04	olivine gabbro	64%	26%	5%	3%	1%	0	3.01	0.094	1.72	1.43	1.25	0.06	0.12	1.86	-	5322
65_5_79	593.09	gabbronorite	54%	35%	4%	5%	1%	0	3.55	0.113	1.41	0.73	0.96	0.21	0.22	2.32	-	3459
65_5_91	593.10	olivine gabbro	57%	30%	9%	3%	1%	0	2.45	0.068	2.23	0.93	0.45	0.38	0.43	4.18	-	11669
66_1_96_A	597.18	olivine gabbro	58%	28%	5%	1%	8%	2	2.68	0.067	1.17	1.09	1.30	0.06	0.10	1.17	-	2216
66_1_96_B	597.18	olivine gabbro	58%	32%	6%	1%	2%	1	3.45	0.019	0.60	0.36	0.26	0.07	0.13	0.00	-	699
67_1_73	606.33	olivine gabbro	59%	33%	3%	1%	4%	1	1.64	0.016	0.60	0.50	0.41	0.09	0.12	0.00	251	2314
67_7_110_A	614.91	oxide gabbro	98%	0%	0%	0%	1%	1	1.69	0.034	1.38	0.97	1.00	0.12	0.20	1.09	37	9847
67_7_110_B	614.91	oxide gabbro	71%	6%	0%	0%	18%	4	1.55	0.038	1.00	0.53	0.35	0.12	0.16	0.58	27	26792
69_5_17	630.80	olivine gabbro	55%	31%	9%	3%	2%	3	1.93	0.060	0.94	0.48	0.37	0.14	0.17	0.55	48	15421
69_5_73_A	631.10	olivine gabbro	54%	26%	8%	6%	6%	4	1.32	0.021	1.17	1.08	1.33	0.12	0.19	0.90	40	14897
69_5_73_B	631.10	olivine gabbro	57%	27%	9%	3%	4%	3	2.13	0.042	1.41	1.13	1.93	0.12	0.22	1.54	26	5510
69_5_122_A	631.86	olivine gabbro	68%	26%	4%	1%	1%	3	2.06	0.057	1.22	0.71	0.65	0.11	0.15	0.74	37	9511
69_5_122_B	631.86	olivine gabbro	66%	22%	3%	6%	3%	4	1.68	0.041	0.68	0.51	0.43	0.13	0.16	1.63	54	19370
70_5_98	641.47	olivine gabbro	58%	32%	0%	4%	6%	1	2.05	0.059	1.95	0.90	0.73	0.19	0.25	1.91	124	7287
71_2_67	646.83	olivine gabbro	58%	35%	4%	2%	1%	1	1.97	0.032	1.67	0.96	0.92	0.11	0.16	1.40	299	1673
74_2_110	655.93	olivine gabbro	59%	33%	6%	1%	0%	1	2.24	0.032	1.71	0.75	0.56	0.15	0.22	1.44	311	1112
76_5_69	679.25	olivine gabbro	59%	28%	5%	4%	3%	4	2.60	0.096	1.00	0.57	0.50	0.11	0.15	0.64	60	12135
77_1_78	680.12	olivine gabbro	64%	24%	5%	4%	2%	4	2.21	0.075	1.19	0.51	0.49	0.05	0.07	1.17	43	20950
77_2_20	681.48	olivine oxide gabbro	64%	21%	9%	3%	3%	3	2.48	0.078	0.90	0.54	0.45	0.02	0.07	0.00	78	10964
78_4_131	687.71	olivine oxide gabbronorite	60%	22%	6%	6%	6%	3	3.91	0.081	0.50	0.37	1.05	0.06	0.08	0.31	55	7180
78_4_48	685.91	Anorthosite	99%	1%	0%	0%	0%	2	2.29	0.078	0.85	0.70	0.81	0.04	0.07	0.74	96	3152

Table S3. (continued)

79_7_25_A	700.70	olivine gabbro	43%	25%	0%	12%	0%	4	1.32	0.018	0.86	0.48	-	0.08	0.11	-	28	10320
79_7_25_B	700.70	oxide gabbro	59%	35%	3%	3%	0%	2	2.83	0.047	1.33	0.77	0.28	0.10	0.15	0.55	129	1204
80_9_51	712.62	olivine oxide gabbro	59%	25%	13%	0%	3%	0	2.44	0.011	0.74	0.46	0.46	0.16	0.18	0.03	-	664
81_6_65	720.35	oxide gabbro	61%	20%	0%	7%	1%	3	1.88	0.056	0.97	0.69	0.63	0.19	0.21	0.92	84	8577
81_6_109	720.79	oxide gabbro	61%	17%	0%	11%	11%	5	2.43	0.083	0.73	0.66	0.28	0.07	0.10	0.25	32	10488
81_6_117_A	721.84	gabbronorite	67%	13%	0%	12%	5%	5	1.89	0.046	0.88	0.65	0.56	0.07	0.12	0.45	22	40818
81_6_117_B	721.84	gabbronorite	48%	29%	1%	11%	12%	4	1.61	0.042	0.72	0.49	0.44	0.03	0.06	0.18	15	44555
82_3_106	724.95	oxide gabbro	61%	27%	0%	8%	3%	3	2.65	0.093	0.87	0.57	0.44	0.07	0.13	0.46	40	9597
83_6_8	736.23	olivine oxide gabbro	86%	8%	2%	3%	0%	2	3.00	0.096	1.12	0.97	1.48	0.03	0.08	0.70	135	4564
83_7_57_A	737.75	olivine gabbro	58%	21%	0%	17%	0%	3	2.38	0.081	0.72	0.41	0.36	0.10	0.13	0.06	86	8112
83_7_57_B	737.75	olivine gabbro	55%	23%	0%	13%	0%	3	3.07	0.081	1.44	0.98	0.91	0.08	0.12	0.85	47	1289
85_3_105	754.33	oxide gabbronorite	44%	28%	0%	1%	15%	2	1.77	0.038	0.68	0.70	0.93	0.03	0.06	0.32	79	3807
87_4_28	763.64	olivine oxide gabbro	56%	32%	10%	2%	1%	0	4.87	0.047	1.39	0.75	0.74	0.15	0.21	1.39	-	518
88_5_117	775.14	olivine gabbro	68%	19%	12%	1%	0%	0	3.81	0.032	0.70	0.45	0.39	0.08	0.12	0.47	-	559
89_6_47	786.55	olivine gabbro	59%	11%	28%	1%	1%	0	2.95	0.025	0.74	0.50	0.57	0.09	0.14	0.56	-	676

Table S3. (continued)

CHAPTER IV

HIGH-TEMPERATURE DEFORMATION AND RETROGRADE STRAIN LOCALIZATION DURING COOLING AND EXHUMATION OF GABBROIC PLUTON IN AN OCEANNIC CORE COMPLEC (HOLE U1473A, ATLANTIS BANK, SOUTHWEST INDIAN RIDGE)

High-temperature deformation and retrograde strain localization during cooling and exhumation of a gabbroic pluton in an Oceanic Core Complex (Hole U1473A, Atlantis Bank, Southwest Indian Ridge)

Maël Allard [1], Émilien Oliot [1], Pierre Lanari [2], Benoît Ildefonse [1]

[1] Geosciences Montpellier, University of Montpellier, CNRS, Montpellier, France
[2] Institute of Geological Sciences, University of Bern, Bern, Switzerland

To be submitted to the Journal of Metamorphic Geology

KEYWORDS: Gabbro, EBSD, EPMA, Thermodynamic modeling, Atlantis Bank, Oceanic core complex

1. Introduction

The important role of deformation in crustal accretion is a well-documented characteristic at slow- and ultraslow-spreading ridges. The progressive strain localization along long-lived low-angle detachment faults leads to the development of oceanic core complexes (OCC) at spreading centers and the exhumation of lower oceanic units. In slow-spreading ridges, these exhumed lithologies have the potential to provide important constraints regarding the interaction between magmatic accretion, deformation, and melt/fluid circulation during the generation of oceanic crust. The Atlantis Bank is a ~600 km^3 large gabbro pluton exposed at the bottom of the ocean at the Southwest Indian Ridge (e.g., Dick et al., 1991, 2019a). It was exhumed within an OCC at ~12 Ma and is today located ~73 km away from the ridge axis. This submarine massif has been the subject of several scientific drilling and dredging expeditions since the late 80's (Pettigrew et al., 1999; Dick et al., 2000, 2019b; Blum et al., 2017). Three cores were drilled during these expeditions for a total of ~2500 m of gabbroic lithologies in ODP Hole 735B (Dick et al., 2000), ODP Hole 1105A (Pettigrew et al., 1999), and IODP Hole U1473A (Blum et al., 2017; Dick et al., 2019b). Crystal plastic deformation is documented as widespread and penetrative in the uppermost 500–600 m of the Atlantis Bank whereas deformation becomes more heterogeneous and localized deeper in the massif. The onset of plastic deformation is observed early in the crystallizing mush, and continues under lower temperature conditions, down to the ductile-brittle transition (e.g., Cannat, 1991; Miranda & John, 2010; MacLeod et al., 2017a; Dick et al., 2019b; Gardner et al., 2020; Allard et al., 2021 ; Taufner et al., 2021). In targeted depth intervals from ODP Hole 735B and IODP Hole U1473A, recent studies documented both High-Temperature (HT) solid-state and melt-present deformation stages (Gardner et al., 2020; Taufner et al., 2021). These studies highlight complex interactions between melt circulation and strain localization

inducing changes in the deformation regime and associated rheology during crust formation and the development of the OCC.

This study aims at giving insights on the evolution of deformation conditions (*P*–*T*–fluid) accompanying strain localization at the Atlantis Bank during accretion and subsequent exhumation of the lower oceanic gabbro. We selected six samples with representative microstructures ranging from undeformed to ultramylonitic from Hole U1473A and conducted detailed petrographic and quantitative texture analyses. Relations between recrystallization, intragranular deformation, and chemical changes in grains are investigated through Electron Backscatter Diffraction analyses (EBSD) and Electron Probe Micro-Analyses (EPMA). Ultimately, we used phase equilibrium modeling to investigate the *P*–*T*–Fluid conditions associated to the microstructure formation through the variably deformed samples.

2. Geological setting

The Southwest Indian Ridge (SWIR) is an ultraslow-spreading ridge with a full spreading rate of ~14 mm.yr^{-1} (asymmetrically spreading at 8.5 mm.yr^{-1} to the south and 5.5 mm.yr^{-1} to the north; e.g., Hosford et al., 2003). Located 73-116 km south of the ridge axis, the Atlantis Bank is a pluri-kilometric gabbroic pluton bordered on its western flank by the north-south Atlantis II Transform fault (Figure 4.1a). This submarine massif is a 11-13 Ma old OCC emerging from ~3000 m to ~700 m of the seafloor, and its summit is a flat surface corresponding to a wave-cut platform, eroded ~9.5 Ma ago (Figure 4.1a; Dick et al., 1991). Although the surface of the Atlantis Bank is not a typical detachment fault surface, the presence of talc-serpentine schists around the massif is documented (e.g., Baines et al., 2003; Dick et al., 2019a) together with low-angle dipping ductile shear zones located in the upper parts of ODP Hole 735B and IODP Hole U1473A (Dick et al., 2000, 2019b). These shear zones predominantly display normal sense of shear in the upper 50 m and ~450 m of holes U1473A and 735B, respectively, before becoming reverse at greater depths (Dick et al., 2019b). IODP Hole U1473A was drilled from the summit of the Atlantis Bank to 809.4 mbsf during IODP Expeditions 360 and 362T (Blum et al., 2017; Dick et al., 2019b). Two other holes drilled between 1987 and 1998, are located 1–2 km away from Hole U1473A: ODP Hole 735B (1508 mbsf; Dick et al., 2000) and ODP Hole 1105A (158 mbsf; Pettigrew et al., 1999). Sections recovered from these three holes consist of olivine-gabbro with minor oxide (-bearing) gabbro, gabbro, and troctolites (Figure 4.1b; Pettigrew et al., 1999; Dick et al., 2000, 2019b). Gabbroic lithologies from Hole U1473A are frequently affected by ductile deformation, particularly in the upper 500 mbsf where porphyroclastic to protomylonitic textures evolving in meter-scale ultramylonites are common (Figure 4.1c). Two important and near-continuous zones of intense crystal-plastic deformation are located in the depth intervals ~150-250 mbsf and ~300-400 mbsf (Figure 4.1c; MacLeod et al., 2017a). The deeper part of Hole U1473A (from 500-600 to ~800 mbsf, Figure 4.1c) is affected by more localized ductile

deformation, with thin high-strain zones heterogeneously distributed in a framework of undeformed to porphyroclastic gabbroic lithologies. These shear zones consist of centimeter-scale ultramylonites to rare meter-scale mylonites. Shipboard observations reveal magmatic textures preserved in 42% of core sections. The qualitative categorization of crystal-plastic fabrics by their deformation intensities (CPF index), ranging from 0 to 5 (CPF index: 0 = undeformed, 1 = foliated, 2 = porphyroclastic, 3 = protomylonitic, 4 = mylonitic, 5 = ultramylonitic), shows that deformed zones are characterized by 32% of porphyroclastic to protomylonitic textures, and 13% of mylonitic to ultramylonitic textures (Figure 4.1c; MacLeod et al., 2017a).

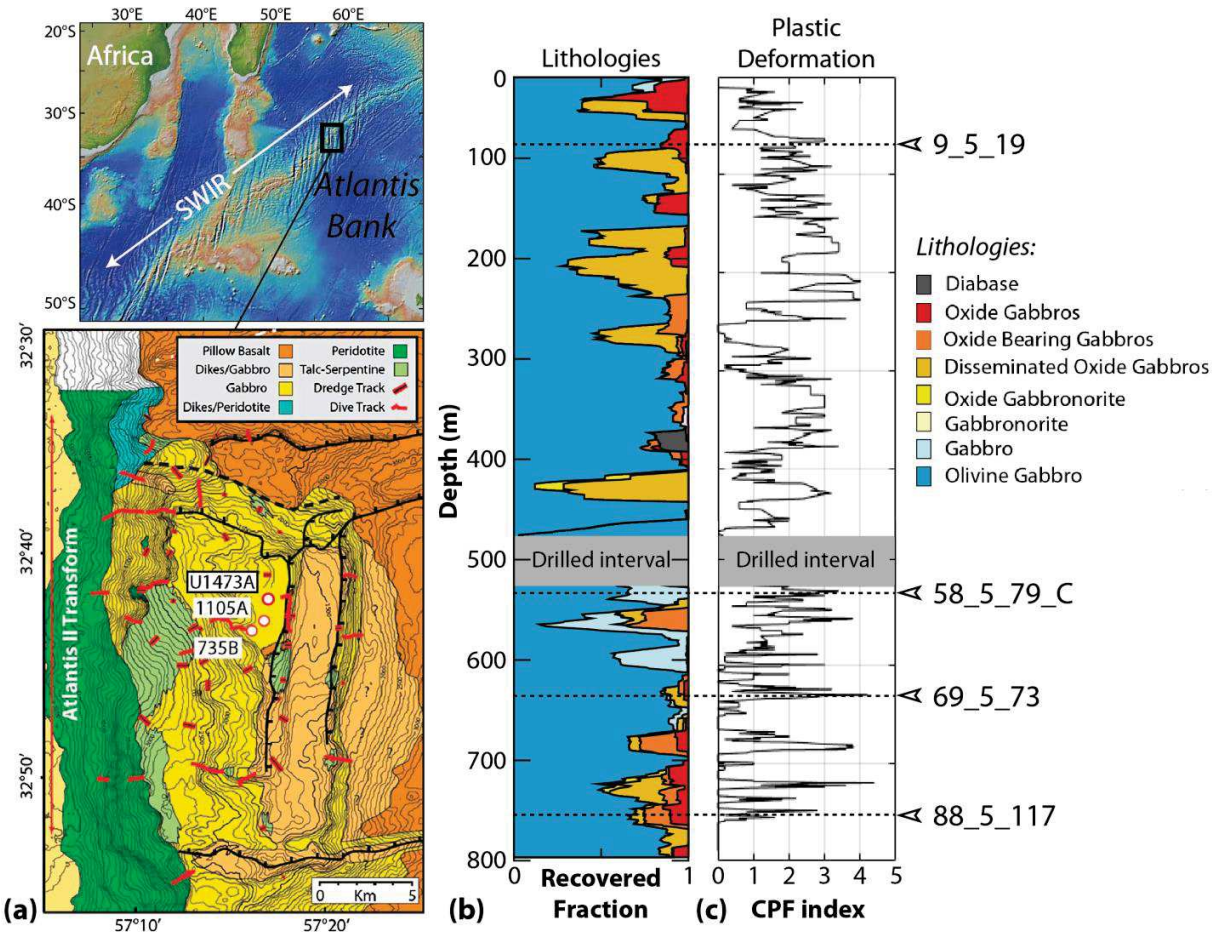

Figure 4.1 *- Location and characteristics of Hole U1473A. (a) Location of the Atlantis Bank at the Southwest Indian Ridge (SWIR; Bathymetric map after Ryan et al. (2009), and geologic map of Atlantis Bank, modified after Dick et al. (2019a). (b) Lithologies from Hole U1473A, after MacLeod et al. (2017a). (c) Moving average of the apparent deformation intensity, i.e. the crystal plastic fabrics (CPF) inferred from macroscopic core observations (running average on five depth intervals, see MacLeod et al. (2017b). CPF index: 0 = undeformed, 1 = foliated, 2 =*

porphyroclastic, 3 = protomylonitic, 4 = mylonitic, 5 = ultramylonitic. Sample locations are given by arrow heads in (c).

The whole ductile deformation history within the Atlantis Bank appears to have occurred continuously from hyper-solidus conditions to lower temperatures while successive igneous gabbroic intrusions were emplaced. This is described as a process of dynamic accretion, characteristic of slow-spreading ridges with low to intermediate magmatism (Dick et al., 2019b). Conditions for ductile deformation at the Atlantis Bank result in multiple deformation stages. Two dominant types of deformation are identified: solid-state deformation through dislocation creep, and melt-assisted deformation through both melt-rock reactions and dislocation creep. A first stage of solid-state deformation (Stage 1) led to the recrystallization of former igneous plagioclase, pyroxenes, and olivine grains. It is documented at 907-1093°C (median=1026°C; Gardner et al., 2020) and ~860-940°C (Mehl & Hirth, 2008) in Hole 735B, at 862-910°C in submersible samples from the Atlantis Bank surface (Miranda & John, 2010). Following this initial solid-state deformation stage, two melt-assisted deformation episodes are reported in the presence of melt (grouped in Stage 2). The first episode (Stage 2a) occurred at 846-969°C (median at 949°C and 906°C; Gardner et al., 2020), and the second (Stage 2b) at 817-1000°C, mainly from ~800 to 900°C (Gardner et al., 2020; Taufner et al., 2021). A lower temperature solid-state event (Stage 3) is documented in mylonites at 740-840°C (median at 780°C in Miranda et al., 2016, and 795°C in Miranda & John 2010). An ultimate stage of solid state – semi-brittle deformation (Stage 4) is recorded mainly in plagioclase-amphibole bearing mylonites/ultramylonites at 665±40°C (Miranda & John, 2010).

3. Methods

3.1. Sampling strategy

Five samples containing microstructures related to variable strain intensities were selected mainly in the lower part, below ~520 mbsf, of Hole U1473A (Figure 4.1b, 4.1c, and 4.2). These samples are representative endmembers of microstructures encountered in Hole U1473A (Allard et al., 2021). Two pairs of samples in intervals *9_5_19* and *69_5_73* permit to study the processes responsible for strain localization in different conditions of strain intensity and fluid circulation. Sampling was performed on core sections that were previously split onboard during the drilling expedition so that the two resulting halves maintains representative features (MacLeod et al., 2017b). In each sample, the thin sections used herein are orthogonal to the foliation. Sample names (I_II_III) indicate the core number (I), the number of the section in the core (II), and the top depth in the section in cm (III). A letter (A, B, or C) identifying a particular microstructural domain is added at the end of the sample names when several domains were analyzed at the same depth or in the same sample. For clarity in the following text, interval names are written in italic

(e.g., *9_5_19*) while microstructural domains are in written in regular font and identified by a final letter (e.g., 9_5_19_A).

3.2. Mineral chemistry

Quantitative mineral chemical analyses were carried out at the Institute of Geological Sciences of the University of Bern using a JEOL JXA 8200 superprobe instrument. Thin sections were polished to ~30 µm and carbon coated. Measurements were performed using an accelerating voltage of 15 kV, a beam current of 10–20 nA for spot analyses and 100 nA for mapping. For spot analyses, background corrected count rates were calibrated using synthetic and natural standards including albite (Na), forsterite (Mg), anorthite (Ca, Al), orthoclase (Si, K), magnetite (Fe) pyrolusite (Mn), rutile (Ti), Ni-metal (Ni) and spinel (Cr). X-ray maps were calibrated using a set of spot analyses acquired in the mapped area and used as internal standards. A total of six maps were acquired (Figure S4.1 and Table S4.1) and analyzed using XMapTools 3.4.1 (Lanari et al., 2014, 2019). Representative mineral compositions were estimated through the maximum clustering density of pixel compositions. Local bulk compositions used for thermodynamic modeling were obtained using XMapTools after a normalization to oxide weight percentage and a density correction (Lanari & Engi, 2017).

3.3. Crystallographic preferred orientations

Electron backscatter diffraction (EBSD) analyses were performed at Geosciences Montpellier, University of Montpellier, using a CamScan X500FE Crystal Probe SEM, equipped with an Oxford instruments Symmetry® EBSD detector. The diffraction pattern acquisition was achieved at a working distance of 25 mm, an indexing speed of 140 Hz, an acceleration voltage of 20 kV, and a probe current of 10 nA. The scanning resolution was chosen as a function of the size of the analyzed grains and ranged from 1.6 µm to 11 µm in deformed domains. It was of 20 µm in the undeformed sample (Table S4.1). EBSD quantitative maps were acquired in the domains analyzed at the EPMA (Figure S4.1), and the main processing results are provided in the general annexes Figure SG.1.

EBSD data were processed using the MTEX Matlab® toolbox (version 5.3.1; e.g., Mainprice et al., 2015) to calculate misorientations, pole figures, and parameters indicative of fabric strength. The later consist of the J index, deriving from the orientation density function (ODF), and the M index, deriving from uncorrelated misorientations (Bunge, 1982; Skemer et al., 2005). The J index value varies from 1 to infinity for a random to a single orientation fabric, respectively. The M index is the difference between the distribution of uncorrelated misorientation angles measured and the one corresponding to a random fabric, and varies from 0 for a random fabric to 1 for a single orientation fabric. Pixels with mean angular deviations (i.e., the angle between the acquired diffraction pattern and the indexing solution) higher than 1° are removed from the

dataset. The grain segmentation angle is set to 10° and only grains containing at least 5 pixels are considered. Pole figures and orientation parameters are calculated for average grain orientation data to give equivalent weight to all grains (i.e., avoiding a dependency to their size). A special treatment is performed in plagioclase grains to identify twins and merge twinned domains into their host grains, and then the average orientation of the largest twin is attributed to the reconstructed grain. Grain boundaries characterized by an angle of 180° ± 5° and a rotation in (010) or (001), or around [100], [010] or [001] are considered as twins.

3.4. Mineral thermometry and thermodynamic modeling

Equilibrium temperatures have been first evaluated by conventional mineral thermometry for amphibole-plagioclase pairs using the Holland & Blundy (1994) thermometer as implemented in XMAPTOOLS (Lanari et al., 2013, 2014). Temperatures were calculated for a pressure of 150 MPa. The average compositions for amphibole and plagioclase used for calculating the temperature conditions correspond to texturally concordant grains.

Thermodynamic modeling was performed in the NCK$Fe^{2+}Fe^{3+}$MASHT system (Na_2O-CaO-K_2O-FeO-Fe_2O_3-MgO-Al_2O_3-SiO_2-H_2O-TiO_2) using Perple_X 6.9.1 (Connolly, 2005), a collection of programs for calculations of phase diagrams, phase equilibria, and thermodynamic data. Determination of *P*–*T*–fluid stability conditions of a considered mineralogical assemblage with a given bulk composition was computed using free Gibbs energy minimizations (e.g., Connolly, 2005, 2009). The internally-consistent thermodynamic database used for calculations is from Holland & Powell (2011). Models of solid-solutions are from Green et al. (2016) for clinopyroxene, melt, amphibole, White et al. (2014) for orthopyroxene garnet, and biotite, White et al. (2000) for ilmenite, Holland & Powell (1998) for olivine, White et al. (2002) for spinel, and Fuhrman & Lindsley (1988) for feldspars. From observations of retrograde biotite reported by Nozaka et al. (2019) in olivine gabbros from Hole U1473A, we use the biotite-out curve as a lower limit in the modeled phase diagrams as no biotite was observed in the studied samples. Local bulk compositions used for phase diagram calculations were extracted from quantitative chemical maps by taking, in each analyzed domain, the area considered as the most representative of the equilibrated magmatic or metamorphic assemblage. This approach is valid in the case of well equilibrated mineral assemblages for which local bulk compositions can be used to estimate formation *P*–*T* conditions (e.g., Lanari & Duesterhoeft, 2019; Lanari & Hermann, 2021). Estimations of H_2O content was performed through *T*–M_{H_2O} phase diagrams (*T*–*X* diagram with *X* varying from 0 to 0.2 moles of H_2O). The assumed H_2O content in samples was estimated based on the modes of amphiboles, the main hydrated phase in samples. Afterward, the FeO–Fe_2O_3 relative contents were regarded in a *T*–X_{Fe3+} phase diagrams (*T*–*X* diagram with *X* varying from $Fe_{tot.}$=FeO to $Fe_{tot.}$=Fe_2O_3 corresponding to X_{Fe3+} = 0 to X_{Fe3+} = 1). The assumed FeO and Fe_2O_3 molar proportions were obtained by comparison of measured

(normalized) and modeled Mg/(Mg+Fe_{tot}±Mn) (with $Fe_{tot.}$ corresponding to the measured Fe content expressed as Fe^{2+}) in clinopyroxene, amphibole, and orthopyroxene. The final preferred stability conditions of an assemblage then correspond to the *P–T* stability field where mineral modes and compositions best fit the measurements. The estimated depth given in phase diagrams is calculated for an ideal lithosphere composed of 50% of gabbros and 50% of partially serpentinized mantle peridotites.

4. Results

4.1. Petrographic observations

Analyzed microstructural domains consist of an undeformed subophitic olivine gabbro, five porphyroclastic to ultramylonitic olivine gabbros, and a plagioclase-amphibole bearing ultramylonite (Figures 4.1c, 4.2, and 4.3). The spatial distribution of deformation structures at the core section scale is heterogeneous, either absent or pervasive along long intervals or highly localized (Figure 4.2; e.g., Allard et al., 2021). In each depth interval *9_5_19* and *69_5_73*, two pairs of microstructural domains corresponding to strain gradients end-members were studied at the thin section scale (Figures 4.2b, 4.2c, 4.3a, and 4.3b). Mineral modes and grain sizes in each analyzed domain are detailed in Table 4.1. Mineral abbreviations are after Whitney & Evans (2010).

Late deformation features are observed in some samples. It mainly corresponds to green amphibole veins (green Amp_2) orthogonal to the foliation, inducing the alteration of clinopyroxene in their vicinity (within ~1 mm from the veins).

Figure 4.2 *- Studied intervals from Hole U1473A. (a) to (d): Core section photographs (left), sketch of macrostructures (middle), and relative strain intensity (i.e., CPF index) estimated at the middle of the core section (right) of studied depth intervals. Mineral abbreviations in this and in the following figures are from Whitney & Evans (2010).*

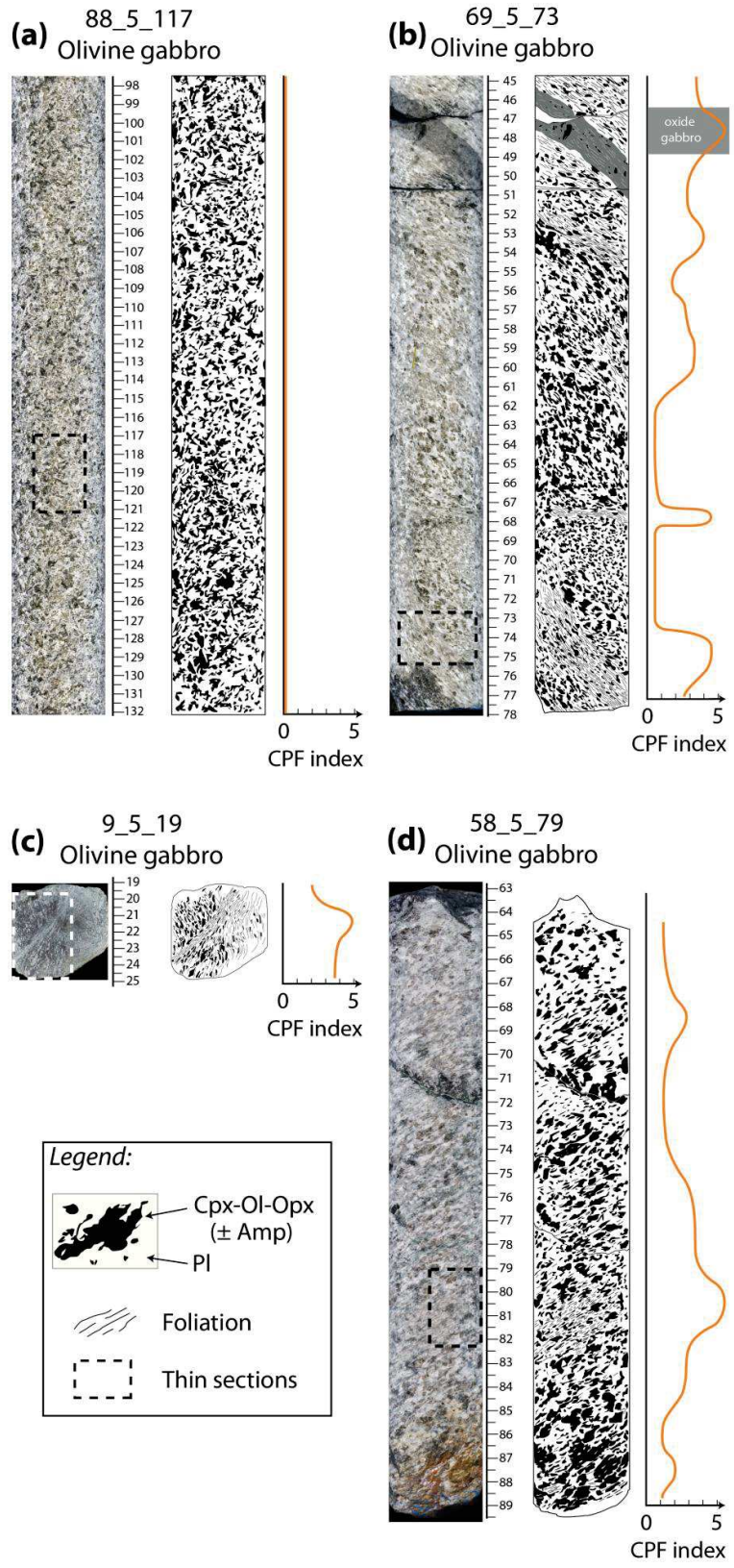
(a) 88_5_117
Olivine gabbro
(b) 69_5_73
Olivine gabbro
oxide gabbro
(c) 9_5_19
Olivine gabbro
(d) 58_5_79
Olivine gabbro
0
5
CPF index
Legend:
Cpx-Ol-Opx
(± Amp)
Pl
Foliation
Thin sections

Figure 4.2

4.1.1. Undeformed microstructure (CPF index 0)

Sample 88_5_117 was taken from a large undeformed interval of medium grain size (Figure 4.2a). The analyzed domain is a coarse-grained (2-2.5 mm) subophitic olivine gabbro mainly composed of plagioclase, clinopyroxene, and olivine (Figure 4.3c and Table 4.1). Plagioclase (Pl_1) often occurs with elongated lath shapes frequently embedded in clinopyroxene oikocrysts. Tapered twins and undulose extinction are widespread, grain boundaries are straight to lobate and boundary migration is observed. Clinopyroxene (Cpx_1) oikocrysts display only limited undulose extinction. Olivine grains (Ol_1) are of granular to skeletal shape and rarely display undulose extinction. Small grains of orthopyroxene (Opx_1) occur essentially at olivine rims, less commonly at clinopyroxene rims, and as exsolution lamellae in clinopyroxene and at intergrowth junctions. Amphibole (Amp_1; < 1%) is rare and occurrences are limited to Cpx_1 rims.

4.1.2. Porphyroclastic microstructure (CPF index 2)

The core section in the interval *69_5_73* is variably deformed (Figure 4.2b). Strain localization is gradual in some areas (e.g., from 66 to 45 cm; Figure 4.2b) and more localized in others (e.g., from 67 to 68 cm and 71 to 76 cm Figure 4.2b). Microstructural domain 69_5_73_B corresponds to a slightly deformed olivine gabbro studied at the margin of a 3 cm-thick localized high-strained zone (69_5_73_A; Figure 4.2b and Table 4.1). The porphyroclastic microstructure is characterized by an important dynamic recrystallization of plagioclase, and to a lesser extent, of olivine and clinopyroxene (Figure 4.3d). Plagioclase porphyroclasts (Pl_1; 0.7-1 mm) have serrated grain boundaries, display undulose extinction and subgrain boundaries. Recrystallized plagioclase grains (Pl_2; 90–150 µm) have lobate to straight grain boundaries, and constitute the fine matrix of the rock. Clinopyroxene and olivine porphyroclasts (Cpx_1 and Ol_1) display undulose extinction and recrystallize in fined-grained aggregates (Cpx_2 and Ol_2, 80–100 µm). Fine-grained orthopyroxene and brown amphibole (Opx_1 and Amp_1; ~80 µm) are very common at olivine grain boundaries, usually mixed with small recrystallized olivine grains (Ol_2). Similarly, very fine-grained orthopyroxene and amphibole (Opx_1 and Amp_1; ~40 µm) are found at Cpx_2 grain boundary junctions (Figure 4.3d*). Orthopyroxene also forms fine-grained elongated aggregates and can occur in Cpx_1 lamellae. Finally, small apatite grains are observed in the microstructural domain 69_5_73_B.

4.1.3. Protomylonitic microstructure (CPF index 3)

Domain 9_5_19_A is a foliated protomylonitic olivine gabbro, studied at the margin of a highly localized shear zone (domain 9_5_19_B). The shear zone orientation is orthogonal to the foliation in domain 9_5_19_A, and the contact is sharp (Figures 4.2c and 4.3b). Plagioclase (Pl_1) in protomylonitic microstructure is nearly completely recrystallized in elongated medium grains (Pl_2, 200–300 µm) with straight to lobate grain boundaries, in which undulose extinction is

frequent (Figure 4.3e and Table 4.1). Magmatic clinopyroxenes (Cpx_1) are rare and most is recrystallized (Cpx_2), constituting elongated aggregates often mixed with small Ol_2 and Opx_1 grains (~150 µm), and small brown amphibole (Amp_1; ~90 µm).

4.1.4. Mylonitic microstructure (CPF index 4)

Crosscutting with a progressive to sharp contact the porphyroclastic microstructure 69_5_73_B, the domain 69_5_73_A is a fine-grained mylonite (Figures 4.2b, 4.3a, and 4.3f). The mineralogical assemblage is similar but modal amounts differ, especially for plagioclase which varies from 60 to 49 vol% (Table 4.1). Mylonitic foliation is well developed and is constituted by alternating Pl_2-rich bands, elongated recrystallized Cpx_2 or Ol_2 aggregates, and very fine-grained (30–40 µm) polymineralic ribbons of Cpx-Ol-Opx-brown Amp (Figures 4.2b, 4.3a, 4.3f, 4.3f*, and Table 4.1). Dynamic recrystallization of all phases is important, and only a few magmatic Pl_1 and Cpx_1 porphyroclasts remain. Fine grained Pl_2 (70–80 µm), constituting the matrix of the rock, have lobate to straight boundaries and display some undulose extinction. Tapered twins in Pl_2 are also rare. At grain boundary junctions in some Pl_2-rich bands, we observe the presence of fine Opx_1 (30–40 µm). Core-and-mantle structures are still observed in fine-grained (70–80 µm) Cpx_2 aggregates. Very fine brown Amp_1 grains (30–40 µm) are widespread at Cpx_2 boundary junctions, at times accompanied by small Opx_1 and/or Ol_2 grains. Similarly in recrystallized Ol_2 aggregates of medium grain size (100–120 µm), small Opx_1 (35–40 µm) are common along grain boundaries and at the aggregate rims. Finally, the polymineralic ribbons consist of a mixture of equant to slightly elongated grains of all phases. Apatite is observed as accessory mineral in the domain (<< 1%).

4.1.5. Ultramylonitic microstructures (CPF index 5)

The two studied ultramylonitic microstructures consist of a fine-grained foliated gabbro (domain 58_5_79_C), and a very fine-grained amphibolite (domain 9_5_19_B). Both are at different depths in the hole but occur in intervals where deformation is rather homogeneous and pervasive overs tens of meters (Figures 4.1b and c).

Microstructural domain 9_5_19_B

Domain 9_5_19_B corresponds to a 1–2 mm wide localized shear zone composed of plagioclase, green amphibole, and highly amphibolitized clinopyroxene (Figures 4.3b, 4.3g, and Table 4.1). The larger plagioclase grains are comparable in size to recrystallized Pl_2 from the adjacent protomylonitic domain 9_5_19_A (Figures 4.2c, 4.3e and 4.3g). In 9_5_19_B, Pl_2 grains are of medium size (~120 µm on average, and up to ~400 µm) and their grain boundaries are often serrated, sometimes lobate. In the ultramylonite, Pl_3 grains are dominantly very fine-grained (~8 µm) with simple equant shapes in general (Figure 4.3g*). Green Amp_2 occur both as large (~100 µm) and small grains (~20 µm), in the shear zone core and at its margin. Small Amp_2 grains are

commonly elongated parallel to the shear zone plane, and grain boundaries are serrated to straight. Close to the shear zone margin, rare small bands and aggregates of very fine-grained Cpx_3 are observed, always surrounded by green amphiboles. Elsewhere, clinopyroxene occurs as small Cpx_2 clasts (~200 µm) and is being replaced by green amphibole. No olivine or orthopyroxene were found in this shear zone.

Microstructural domain 58_5_79_C

The ultramylonitic domain 58_5_79_C is composed of Pl_2 and Cpx_2 arranged as alternating, nearly continuous thin monomineralic bands (Figures 4.2d, 4.3h and Table 4.1). Dynamic recrystallization is almost complete for both phases. Plagioclase grains Pl_2 (~100 µm) are elongated with serrated to straight boundaries. A second group of very fine, equant, recrystallized Pl_3 (~20 µm) occur in narrow C'-bands within Pl_2-rich bands (Figure 4.3h, 4.3h*, and Table 4.1). Clinopyroxene mainly occurs as medium-grained Cpx_2 (~130 µm) ribbon aggregates, displaying sometimes a preserved core of magmatic Cpx_1. The C'-bands observed in plagioclase continue into Cpx_2 aggregate and forms very fine-grained Cpx_3 (~20 µm). Very fine-grained brown amphiboles (Amp_1) are widespread at grain boundary junctions (similarly as in domains 65_5_73_A and _B), and Opx_1 is also present as exsolution in Cpx_1 lamellae (Table 4.1). Locally, an additional type of colorless amphiboles (Amp_2) occurs, mainly at Cpx_2 aggregate rims, and is sometimes observed around Amp_1, or within Cpx_2 grain boundaries. Finally, talc occurs as a retrograde mineral around fine-grained aggregates of recrystallized Opx_2 and Ol_2. Chlorite occurs within small fractures, mainly in plagioclase monophase bands, and rimming the Amp_2 grains and talc-orthopyroxene rich domains.

Table 4.1 *- Mineral modal compositions and grain sizes (in µm) of analyzed microstructural domains. Mineral abbreviations are after Whitney & Evans (2010); Opq: opaque minerals (ilmenite & magnetite); n.o: not observed. Regarding amphibole and orthopyroxene, grain sizes are only given for the most widespread family of grains, when modes exceed 5% (see text).*

Microstructural domains		*Pl*	*Cpx*	*Ol*	*Opx*	*Amp*	*Opq*	*Tlc*
Phase modes								
88_5_117	Undeformed	59	26	12	2	< 1	n.o.	n.o.
69_5_73_B	Porphyroclastic	60	20	11	3	4	< 1	n.o.
9_5_19_A	Protomylonitic	58	23	4	7	8	< 1	n.o.
69_5_73_A	Mylonitic	49	24	13	7	6	< 1	n.o.
9_5_19_B	Ultramylonitic	43	10	n.o.	n.o.	47	n.o.	n.o.
58_5_79_C	Ultramylonitic	52	28	3	4	8	< 1	5
Grain sizes (µm)								
88_5_117	Igneous grains	2000–2500	2000–2500	1800–2000	n.o.	n.o.		
69_5_73_B	Porphyroclasts	700–1000	1500–2000	600	n.o.	n.o.		
	Recryst. grains	90–150	80–90	100 & 350	40 & 80	40 & 80		
9_5_19_A	Porphyroclasts	n.o.	1100	n.o.	n.o.	n.o.		
	Recryst. grains	200–300	250	150	150	90		
69_5_73_A	Porphyroclasts	1000	600	n.o.	n.o.	n.o.		
	Recryst. grains	70–80	70–80	100	30–40	30–40		
	Mixed domain	n.o.	30–40	30–40	30–40	30–40		
9_5_19_B	Porphyroclasts	120	120–200	n.o.	n.o.	10 0		
	Recryst. grains	8	10	n.o.	n.o.	20		
58_5_79_C	Porphyroclasts	n.o.	650	n.o.	n.o.	n.o.		
	Recryst. grains	100	130	n.o.	40	35		
	C’ bands	20	20	n.o.	n.o.	n.o.		

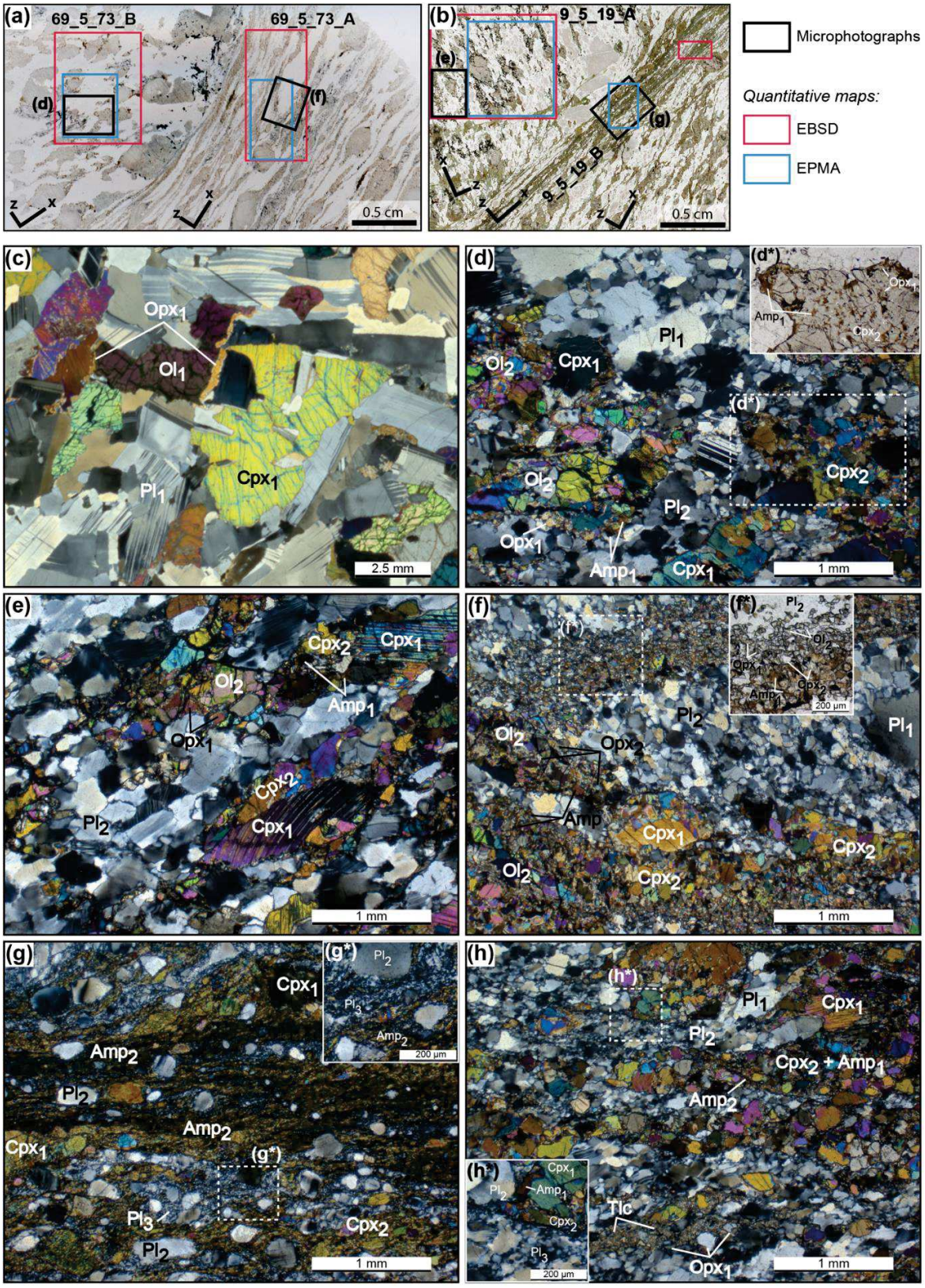
(a)
69_5_73_B
69_5_73_A
(d)
(f)
0.5 cm
(b)
9_5_19_A
(e)
(g)
9_5_19_B
0.5 cm
Microphotographs
Quantitative maps:
EBSD
EPMA
(c)
Opx1
Ol1
Pl1
Cpx1
2.5 mm
(d)
(d*)
Opx1
Amp1
Cpx2
Pl1
Ol2
Cpx1
(d')
Cpx2
Ol2
Pl2
Opx1
Amp1
Cpx1
1 mm
(e)
Cpx2
Cpx1
Ol2
Amp1
Opx1
Cpx2
Pl2
Cpx1
1 mm
(f)
(f')
(f*)
Pl2
Ol2
Opx1
Cpx2
Amp
200 µm
Pl2
Pl1
Ol2
Opx2
Amp
Cpx1
Cpx2
Ol2
Cpx2
1 mm
(g)
(g*)
Pl2
Pl3
Amp2
200 µm
Cpx1
Amp2
Pl2
Amp2
Cpx1
(g*)
Pl3
Pl2
Cpx2
1 mm
(h)
(h*)
Pl1
Cpx1
Pl2
Cpx2 + Amp1
Amp2
(h*)
Cpx1
Pl2
Amp1
Cpx2
Pl3
200 µm
Tlc
Opx1
1 mm

Figure 4.3

Figure 4.3 *- Representative microstructures observed in the studied intervals 69_5_73 and 9_5_19. (a) and (b) Plane-polarized photographs of 69_5_73 and 9_5_19 intervals, respectively, displaying locations of following microphotographs and maps (indicated by rectangles). (c) to (h) cross-polarized images of representative microstructures in analyzed domains, plane-polarized details in (d*) and (f*). Corresponding microstructural domains in this study are: (c) 88_5_117, (d) 69_5_73_B, (e) 9_5_19_A, (f) 69_5_73_A, (g) 9_5_19_B, and (h) 58_5_79_C.*

4.2. Mineral chemistry

Chemical compositions measured in the undeformed domain 88_5_117 are considered as the reference for primary phase compositions arising from the gabbro crystallization. Phase compositions in the studied microstructural domains are relatively homogenous overall. The exception to this is microstructural domain 9_5_19_B (i.e., the narrow ultramylonitic plagioclase-amphibole bearing shear zone) where chemical compositions of constituting minerals are significantly different.

4.2.1. Plagioclase composition

Measured chemical compositions of plagioclase indicate variations associated both with magma crystallization and with plastic deformation. Igneous plagioclase grains from undeformed domain 88_5_117 have labradorite compositions with important core to rim variations in anorthite content ($An_{\%}$ or *X*an = Ca/(Ca+Na+K)), from An_{62} to An_{54} respectively (Figure 4.4a). Locally at plagioclase grain boundary junctions and especially at olivine and orthopyroxene grain boundaries, a local increase up to An_{73} is observed (Figure 4.4a and b).

In deformed domains 69_5_73_A, 69_5_73_B, and 58_5_79_C, recrystallized grains (formed by the first stage of recrystallization, called R1) indicate igneous rim-like compositions of $An_{52\text{-}57}$ (Figure 4.4a). Porphyroclasts and recrystallized porphyroclast cores from domains 69_5_73_A and 69_5_73_B have compositions similar to undeformed igneous cores of domain 88_5_117, testifying to a magmatic origin. Again, a local increase in anorthite content up to $An_{72\text{-}73}$ is observed at the grain boundaries with olivine and orthopyroxene (Figure 4.4a, c and d). In the interval *69_5_73*, a general decrease of the anorthite content (An_{58} to An_{54} in the domain A, and $An_{56\text{-}57}$ to $An_{53\text{-}54}$ in the domain B) is observed from one side of the quantitative maps to the other (Figure S4.2 and S4.3).

Studied domains from interval *9_5_19* differ in compositions from the other analyzed intervals, with lower anorthite content measured in grains (Figure 4.4a). A striking difference in domain 9_5_19_A is the lack of chemical variations in plagioclase grains. Moreover, the rise of anorthite content at olivine-orthopyroxene edges is not observed in this interval. This interval is located up in Hole U1473A (76.8 mbsf) in contrast to others (< 520 mbsf), so a different magmatic origin of the protolith is possible. The plagioclase-amphibole ultramylonite 9_5_19_B contains plagioclase

porphyroclasts with an andesine composition (~An_{46}), similar to the recrystallized Pl_2 grains composition in the protomylonitic domain 9_5_19_A (Figure 4.4a and e). A second episode of dynamic recrystallization (called R2) led to the formation of Pl_3 grains, characterized by an important decrease of anorthite content down to An_{34} (Figure 4.4a and e).

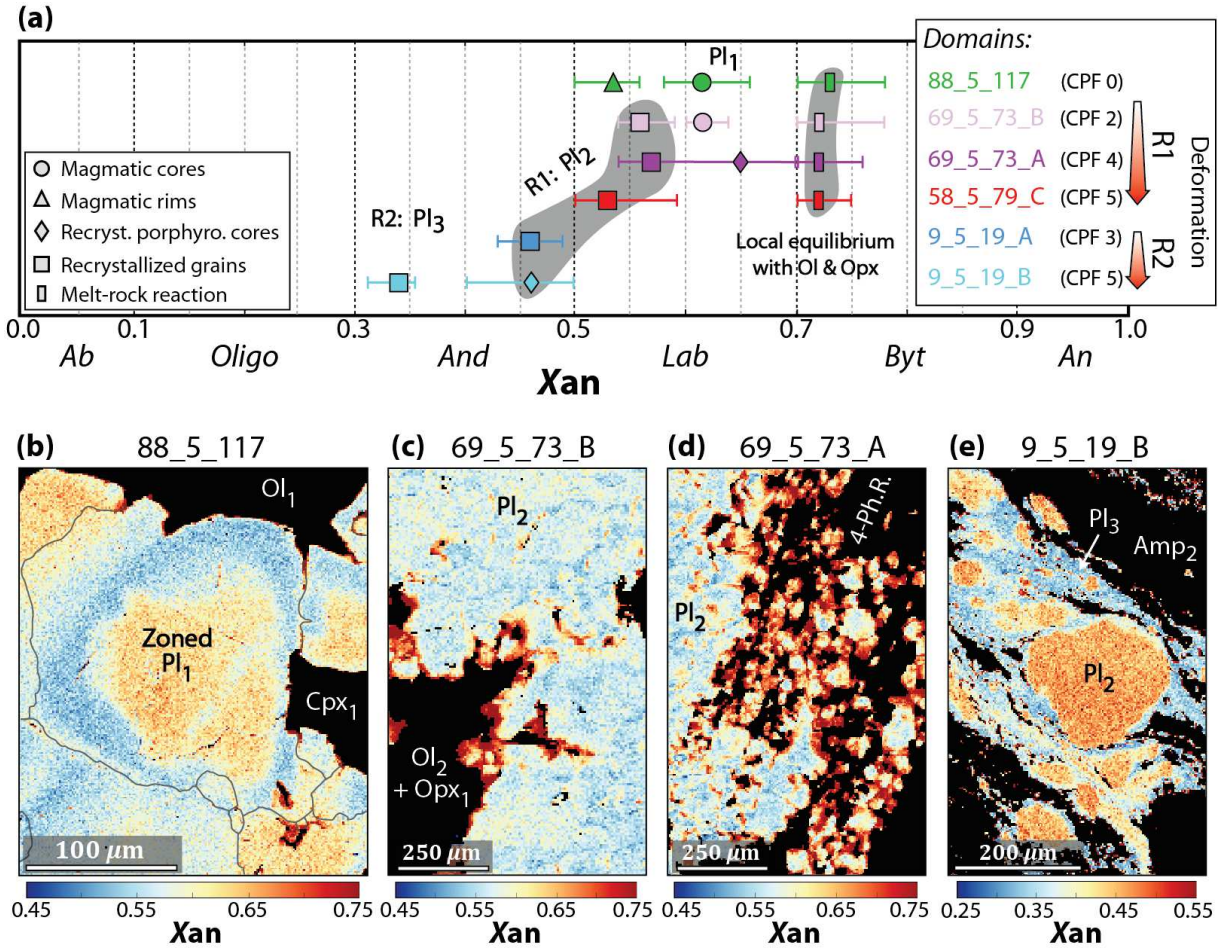

Figure 4.4 *- Plagioclase chemical compositions in studied microstructural domains. (a) Synthesis of compositions of plagioclase grains expressed as their Anorthite content. The two successive episodes of deformation associated with dynamic recrystallization are referred to as R1 and R2. Grey shaded areas group texturally consistent chemical compositions. CPF is the crystal plastic fabric intensity. Oligo: oligoclase, And: andesine, Lab: labradorite, Byt: bytownite. (b) to (e) Compositional maps of anorthite content in the studied microstructural domains, note the change in Xan range from (b), (c), and (d) to (e). Dark-grey lines in (b) correspond to grain boundaries. (d) Detail at the contact of a four-phase ribbon (4-Ph.R., see Figure 4.3f) presented in Figure 4.3f*.*

4.2.2. Pyroxene composition

Pyroxene encountered in the studied microstructural domains consists mainly for clinopyroxene of augite igneous grains and diopside recrystallized grains, and for orthopyroxene of enstatite (Figure 4.5a).

Clinopyroxene composition

Igneous clinopyroxene grains (or grain cores) display *X*Mg (*X*Mg = Mg/(Mg+Fe+Mn)) ratios similar to recrystallized grains, mainly ranging from 0.77 to 0.83, except in domain 9_5_19_A where it is calculated below 0.75 in all grain types (Figure 4.5b). In the undeformed domain 88_5_117, the core to rim decrease in *X*Mg is accompanied by a decrease in Cr and Al contents.
Overall, dynamic recrystallization of clinopyroxene in deformed domains is also accompanied by an important decrease of Al and Cr contents, together with a significant increase of Ca and Si contents (Figure 4.5b, 4.5c, and S4.4). Variations in *X*Mg are more complex in deformed samples. Although recrystallized porphyroclasts have generally higher Mg and Fe contents in their core than at their rims, their relative contents are highly variable (in particular from one side to the other of the analyzed area). This results in the occurrence of grains with a core to rim decrease in *X*Mg such as in igneous grains from the undeformed domain 88_5_117, and others with a reverse zoning (Figure 4.5d). Recrystallized porphyroclast from domains 69_5_73_B, 69_5_73_A, and 58_5_79_C display intermediate compositions between igneous cores and recrystallized grains (Figure 5b). The Ca content in these recrystallized porphyroclasts increases with the intensity of deformation in the domain.
In the protomylonitic domain 9_5_19_A, clinopyroxenes have different compositions than those of other studied domains, with both lower *X*Mg ratio and Ca content. Porphyroclasts from the ultramylonitic domain 9_5_19_B corresponds to partly recrystallized, but most importantly, amphibolitized grains, hence the difference in composition with Cpx in other domains.

Orthopyroxene composition

Compositional zoning is also observed in orthopyroxene grains, especially in Al and Ca contents, and *X*Mg, and appears to be controlled by grain boundaries or particular textural environments. For example, in clinopyroxene lamellae (e.g., domain 9_5_19_A; Figure 4.5e), orthopyroxene displays Ca, Mg and Al contents that are higher than in matrix grains. In orthopyroxene surrounding olivine, a systematic decrease of ~0.3-0.4 wt.% in Al_2O_3 is observed toward the olivine contact (Figure S4.5). Generally in deformed domains (e.g. 58_5_79_C, 9_5_19_A, 69_5_73_A, and 69_5_73_B), a core to rim decrease in Ca content is observed and the Al content is sometimes slightly higher in cores than in rims (e.g., domain 9_5_19_A; Figure 4.5e). Locally, in the ultramylonitic domain 58_5_79_C, the Ca content of orthopyroxene is lower if talc is present (Figure S4.5).

In the undeformed domain 88_5_117, *X*Mg of orthopyroxene is 0.78, and decreases in deformed domains to 0.67 (domain 9_5_19_A) and 0.74-0.76 (domain 58_5_79_C and interval *69_5_73*). Low *X*Mg are also measured at the contact with Cpx_2 junctions (e.g., domain 69_5_73_B, Figure 4.5f) or at the contact with an olivine of lower *X*Mg (e.g., domain 69_5_73_B; Figure S4.5). By contrast, the measured *X*Mg ratio is higher in association with talc (e.g., domain 58_5_79_C). By considering intervals *58_5_79* and *69_5_*73 the decrease of *X*Mg values seems linked to the increase of plastic deformation. Again, phase compositions in the interval *9_5_19* differ from other samples. Finally, the anorthite content decrease in plagioclase grains form on side of the mapped area to the other in the two domains of the interval *69_5_73* is accompanied by the decrease of *X*Mg of clinopyroxene from 0.80 to 0.74-0.75 (Figure S4.2 and S4.3).

Figure 4.5 *- Chemical compositions of pyroxene in the studied microstructural domains. (a) Pyroxene compositions represented in the pyroxene quadrilateral (after Morimoto, 1988). Note the shift toward diopside composition of recrystallized grains with respect to igneous grains. Marker colors correspond to the studied microstructural domains (b) XMg variations against* Ca^{M2} *in clinopyroxenes. Grey shaded areas group texturally consistent chemical compositions. CPF is the crystal plastic fabric intensity. (c) to (f): Quantitative chemical maps of CaO content (c) and XMg ratio (d) in clinopyroxene, and* Al_2O_3 *content (e) and XMg ratio (f) in orthopyroxene. The black color in chemical maps mainly corresponds to plagioclase. Large clinopyroxene grains in (e) and (f) are indicated in dark grey. Sample names are indicated on top of each map together with the phase of interest. wt. %: oxide weight percent.*

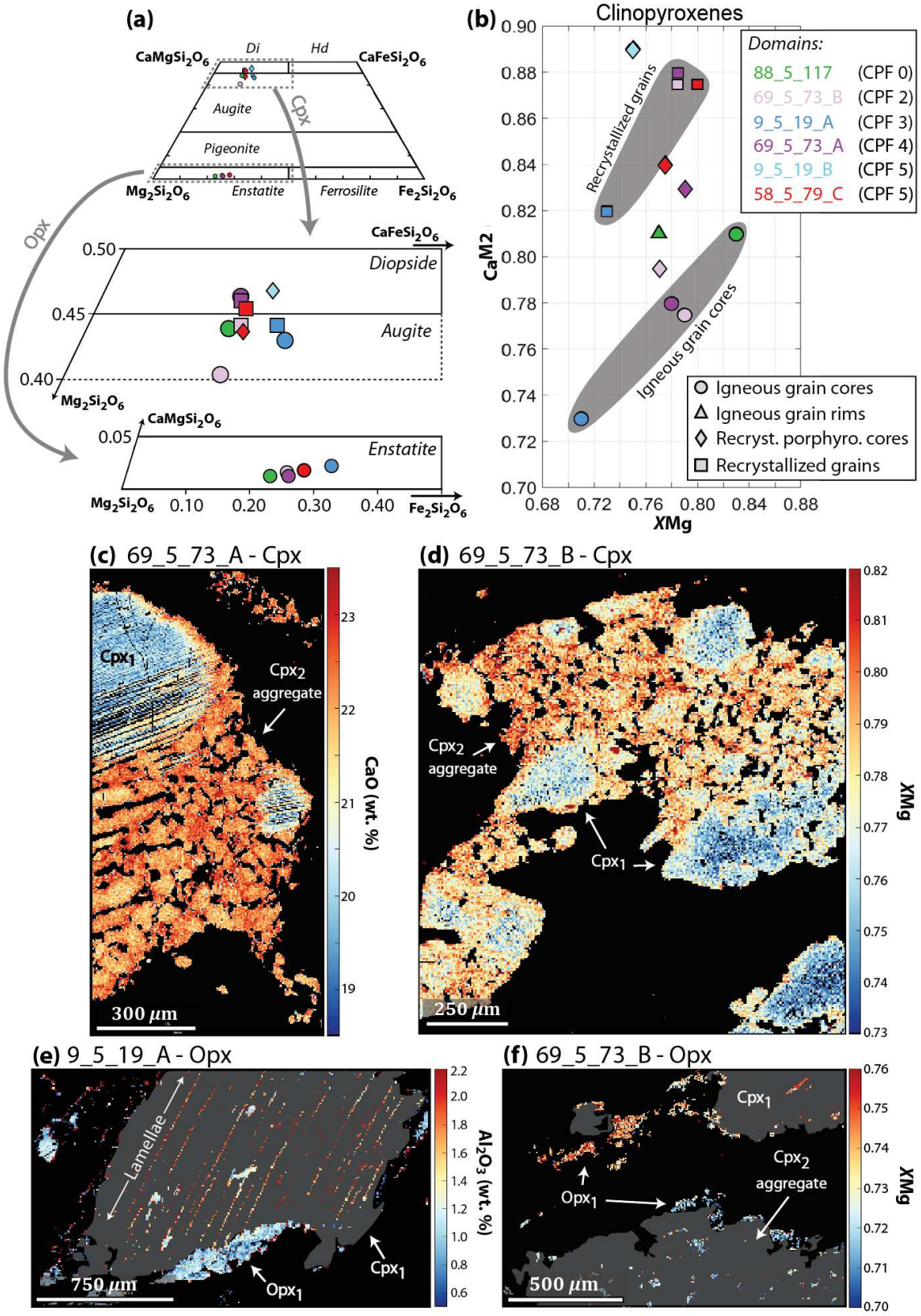
(a)
Di
Hd
CaMgSi2O6
CaFeSi2O6
Augite
Cpx
Pigeonite
Mg2Si2O6
Enstatite
Ferrosilite
Fe2Si2O6
Opx
0.50
0.45
0.40
Diopside
Augite
0.05
Enstatite
0.10
0.20
0.30
0.40
(b)
Clinopyroxenes
Domains:
88_5_117 (CPF 0)
69_5_73_B (CPF 2)
9_5_19_A (CPF 3)
69_5_73_A (CPF 4)
9_5_19_B (CPF 5)
58_5_79_C (CPF 5)
Recrystallized grains
Igneous grain cores
CaM2
XMg
Igneous grain cores
Igneous grain rims
Recryst. porphyro. cores
Recrystallized grains
(c) 69_5_73_A - Cpx
Cpx1
Cpx2 aggregate
300 μm
CaO (wt. %)
(d) 69_5_73_B - Cpx
Cpx2 aggregate
Cpx1
250 μm
XMg
(e) 9_5_19_A - Opx
Lamellae
Cpx1
Opx1
750 μm
Al2O3 (wt. %)
(f) 69_5_73_B - Opx
Cpx1
Opx1
Cpx2 aggregate
500 μm
XMg

Figure 4.5

4.2.3. Olivine composition

Olivine is the third mineral of importance in the studied gabbroic lithologies and displays no significant grain-scale compositional zoning. Measured Forsterite content ($Fo_{\%}$ or *X*fo=Mg/(Mg+Fe+Mn)) decreases from Fo_{74} in the undeformed domain 88_5_117 to $Fo_{0.67\text{-}0.72}$ in the studied deformed domains (Figure 4.6a). In the mylonitic domain 69_5_73_A, the neo-formed grains present in the four phase ribbons have higher *X*Mg ratio than the rest of the grains in the domain (Figure 4.6a, 4.6c, and 4.3f). In the interval *69_5_73*, the forsterite content in grains is observed to evolve from one side to the other in the analyzed domains (Figure 4.6b, 4.6c, S4.2 and S4.3). Textural relations with other phases do not provide a key to understand these chemical evolutions.

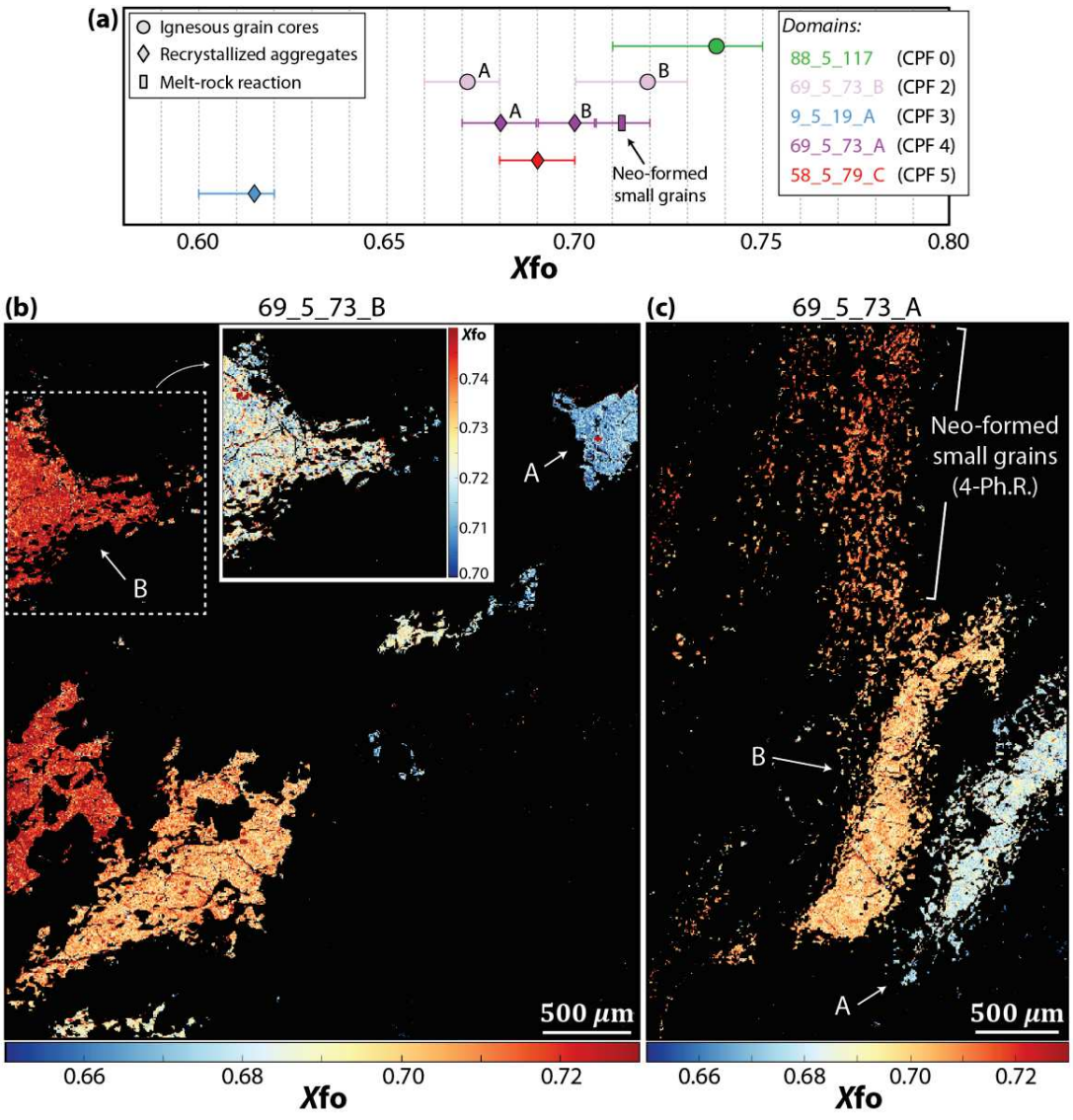

Figure 4.6 *- Olivine chemical compositions expressed as forsterite content. (a) Measured Xfo in each studied structural domain. CPF is the crystal plastic fabric intensity, and letters (A and B) refers to annotated grains in (b) and (c). (b) and (c) Quantitative compositional maps of Xfo in Olivine in porphyroclastic 69_5_73_B and mylonitic 69_5_73_A domains, respectively. The inset in (b) supports the lack of chemical variations from the magmatic core to the surrounding recrystallized rim. The black color corresponds mainly to plagioclase and clinopyroxene (see Figure S4.2 and S4.3).*

4.2.4. Amphibole composition

Several amphibole types are observed in the studied intervals, namely brown amphiboles of magmatic origin, and green and colorless amphiboles of retrograde metamorphic origin. Pargasitic brown amphibole is encountered in all domains except 9_5_19_B, edenitic green amphibole is observed in the protomylonitic to ultramylonitic domains of the interval *9_5_19*, and actinolitic colorless amphibole is found in the ultramylonitic domain 58_5_79_C (Figure 4.7a and b).

Calculated Si content expressed in apfu (atom per formula unit) in pargasite ranges from ~5.8 to ~6.3 and *X*Mg ratio is bracketed between 0.67 and ~0.76. Very similar compositions are found in the two microstructural domains analyzed in the interval *69_5_73*. Pargasite grains in deformed microstructural domains display notable decrease in *X*Mg ratio (- ~0.6) and Al content (Al_2O_3 ~2 wt.%) from the margin to the inside of Cpx_2 recrystallized aggregates (Figure 4.7c). This is often accompanied by slight increase in Cr content (Cr_2O_3 + ~0.2 wt.%). In the protomylonitic domain 9_5_19_A, a core to rim decrease of Ti contents is measured in conjunction with a small increase of Si and *X*Mg values.

Edenite grains from the interval *9_5_19* have similar compositions, either in the protomylonitic domain or in the ultramylonitic shear band, with an *X*Mg of ~0.65 and a Si content of ~6.70 apfu (Figure 4.7b). However, chemical variations are observed in the ultramylonite 9_5_19_B when Edenite grains coexist with Cpx_1 grains (amphibolitized), displaying a decrease in Al (mainly), K and Na contents at their contacts, and an increase of Si and *X*Mg (e.g., Figure 4.7b and d).

Actinolite observed in the ultramylonitic shear band 58_5_79_C is characterized by the highest calculated Si (~7.80 apfu), whereas observed *X*Mg is like in the other domains (~0.77; Figure 4.7a). The increase of Cr content in actinolite in Cpx_2 aggregates is small, and the main chemical variations concern Al and K contents that are higher in contact with the ubiquitous pargasite.

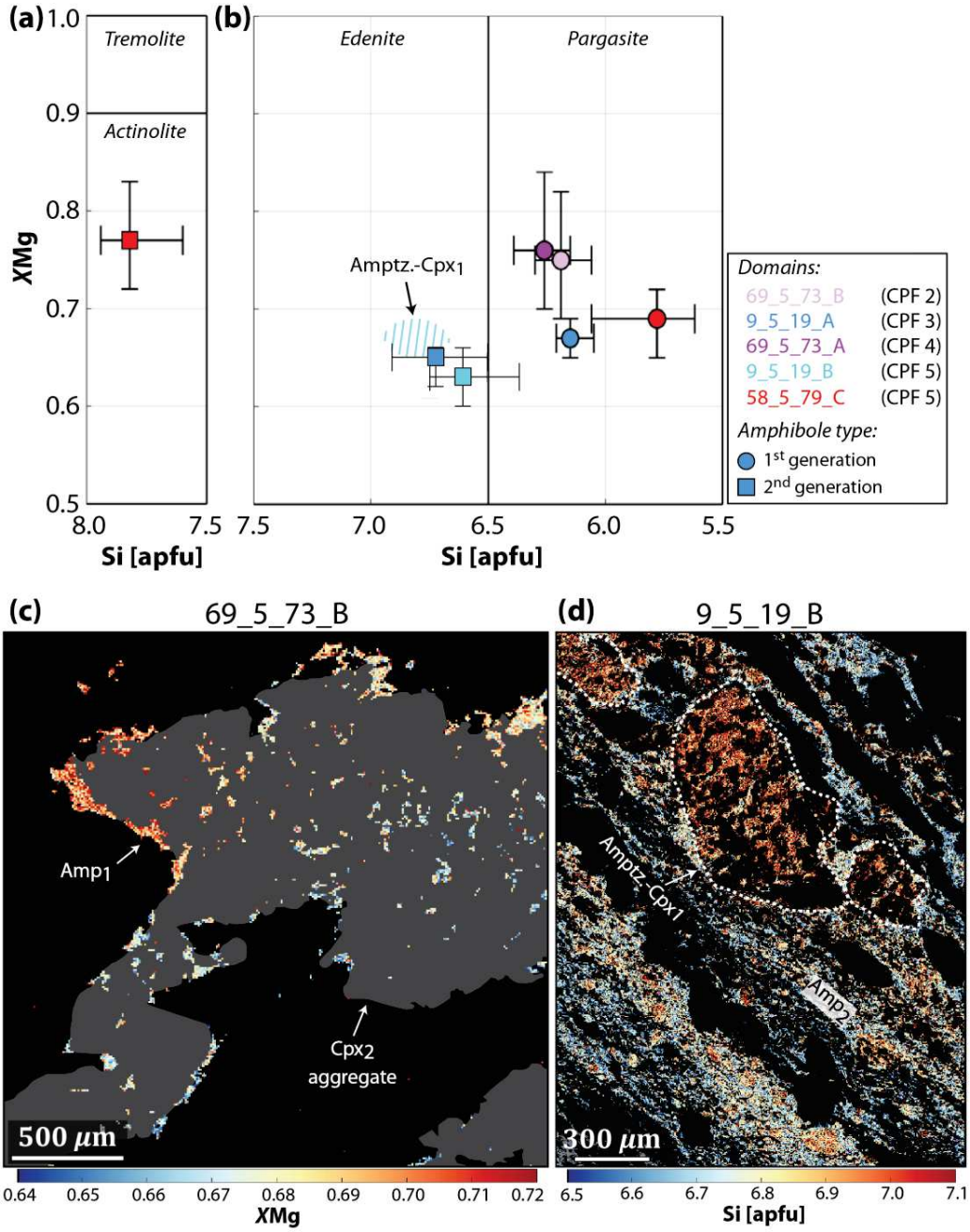

Figure 4.7 *- Calcic amphibole chemical compositions. (a) Low sodi-potassic calcic amphiboles diagram. (b) High sodi-potassic calcic amphiboles diagram. Diagrams after Leake et al (1997). The hatched region in (b) corresponds to edenite replacing Cpx_1 grains (amphibolitization; Amptz.-Cpx_1). CPF is the crystal plastic fabric intensity. (c) and (d): Quantitative composition maps of XMg in pargasite and Si apfu in edenite, respectively. The black color mainly corresponds to plagioclase. Note that the area shown in (c) is also presented for clinopyroxene in Figure 4.5d. In the ultramylonite 9_5_19_B in (d), the highest values of Si apfu are found in highly amphibolitized Cpx_1 marked by the white dashed contours.*

4.3. Mineral thermometry and phase equilibrium modeling

4.3.1. Plagioclase-amphibole mineral thermometry

Mineral thermometry was performed for the plagioclase-amphibole compositions presented in Table 4.2 at a pressure of 150 MPa. Selected plagioclase corresponds to recrystallized grains (Pl_2, and Pl_3 in 9_5_19_B), and amphiboles are considered as formed during deformation (or in its direct continuity) due to their textural occurrence (i.e., occurring at Cpx_2 grain boundaries, see section 4.1). The calculated temperatures in the studied domains indicate two episodes of deformation: a first high temperature granulitic event at ~840-850 °C, associated to the development of porphyroclastic to mylonitic microstructures, and a second amphibolitic episode at ~630-670 °C linked to the ultramylonites formation.

Table 4.2 *- Representative compositions of amphiboles and element ratio for plagioclases used for mineral thermometry. Note that temperatures calculated for secondary amphibole consider the same compositions for plagioclase than for the other type of amphibole of the same domain. And: Andesine, Lab: Labradorite. See Methods for details.*

Weight %	***Porphyroclastic***	***Protomylonitic***	***Mylonitic***	***Ultramylonitic***		Secondary amphiboles	
	69_5_73_B	**9_5_19_A**	**69_5_73_A**	**9_5_19_B**	**58_5_79_C**	**9_5_19_A**	**58_5_79_C**
Amphibole	*Pargasite*	*Pargasite*	*Pargasite*	*Edenite*	*Pargasite*	*Edenite*	*Actinolite*
SiO_2	42.36	40.93	43.43	46.49	47.33	47.45	51.31
Al_2O_3	11.66	12.03	12.29	12.34	12.91	11.44	2.79
TiO_2	3.21	3.97	3.06	2.56	0.10	1.17	0.06
FeO	10.37	11.77	9.35	11.59	8.94	13.46	10.70
MgO	13.90	12.92	13.88	11.16	14.35	13.92	18.14
MnO	0.14	0.15	0.22	0.22	0.24	0.06	0.36
CaO	11.73	10.81	11.97	10.95	11.87	11.29	11.08
Na_2O	2.74	3.04	2.26	3.18	1.28	2.28	0.75
K_2O	0.43	0.16	0.27	0.01	0.30	0.12	0.06
Cr_2O_3	0.14	0.01	0.20	0.09	0.00	0.00	0.01
Total	96.72	95.80	96.48	98.68	97.32	101.18	95.31
Plagioclase	*Lab*	*And*	*Lab*	*And*	*Lab*	*And*	*Lab*
*X*ab	0.43	0.54	0.43	0.65	0.46	0.54	0.46
*X*an	0.56	0.46	0.56	0.35	0.54	0.46	0.54
T (°C)	838 ± 34	851 ± 41	841 ± 65	718 ± 30	634 ± 56	698 ± 74	676 ± 41

4.3.2. Thermodynamic modeling

Phase diagrams calculations are presented for all the studied deformed domains to assess the evolution of deforming conditions associated to the different microstructures. The bulk compositions used in these calculations are presented in Table 4.3 and are considered representative of the analyzed domains from petrographic observations.

Table 4.3 *- Local bulk compositions used for thermodynamic modeling (see text).*

Weight	***Porphyroclastic***	***Protomylonitic***	***Mylonitic***	***Ultramylonitic***	
%	**69_5_73_B**	**9_5_19_A**	**69_5_73_A**	**9_5_19_B**	**58_5_79_C**
SiO_2	50.68	52.30	49.66	50.93	53.88
Al_2O_3	17.82	17.42	15.62	14.81	16.99
TiO_2	0.36	0.62	0.50	0.62	0.30
FeO	5.98	6.71	7.88	9.02	3.72
Fe_2O_3	0.42	0.48	0.27	0.16	0.36
MgO	9.78	8.06	11.79	8.61	7.22
CaO	11.92	10.85	11.83	11.31	14.30
Na_2O	2.88	3.51	2.32	3.77	3.02
K_2O	0.08	0.07	0.07	0.09	0.04
H_2O	0.07	0.14	0.13	0.82	0.20
Total	99.99	100.16	100.07	99.69	100.03

Porphyroclastic domain 69_5_73_B

The paragenesis observed in thin section Pl_2+Cpx_2+Ol_2+Opx_2+Amp_2+Opq is predicted to be stable at 881 ± 34 °C and 125 ± 20 MPa (Figure 4.8a). The stability field is constrained by both mineral modal proportions and mineral compositions, and by the intersection of Si apfu and *X*Mg isopleths of amphibole. Measured and predicted modes and compositions are in very good agreement for all phases (see bottom right table in figure 4.8a). The highest differences are found for plagioclase and correspond to an excess of only 2-3 vol%. From 1100 °C to the solidus, the predicted melt fractions are low overall and the crystallization of the very last melt fraction in the rock forms orthopyroxene (< 4 vol% of melt) and pargasite amphibole (< 2% of melt; Figure 4.8b). This is highly consistent with the petrographic observations of Opx_2 both rimming olivine grains and within Ol_2 recrystallized mantles, and the presence of Amp_2 within Cpx_2 recrystallized aggregates. The stability field of the paragenesis is large, and bounded by the apparition of biotite and melt at low and high temperatures, respectively, and by the apparition of garnet at pressures higher than 600 MPa (Figure 4.8c). Plagioclase and clinopyroxene igneous grain core compositions are found stable together at > 1050 °C and > 250 MPa with a melt fraction of 6-12

vol%. This gives a general *P–T* path for deformation/crystallization before late local equilibration in presence of orthopyroxene and amphibole at 881 °C and 125 MPa.

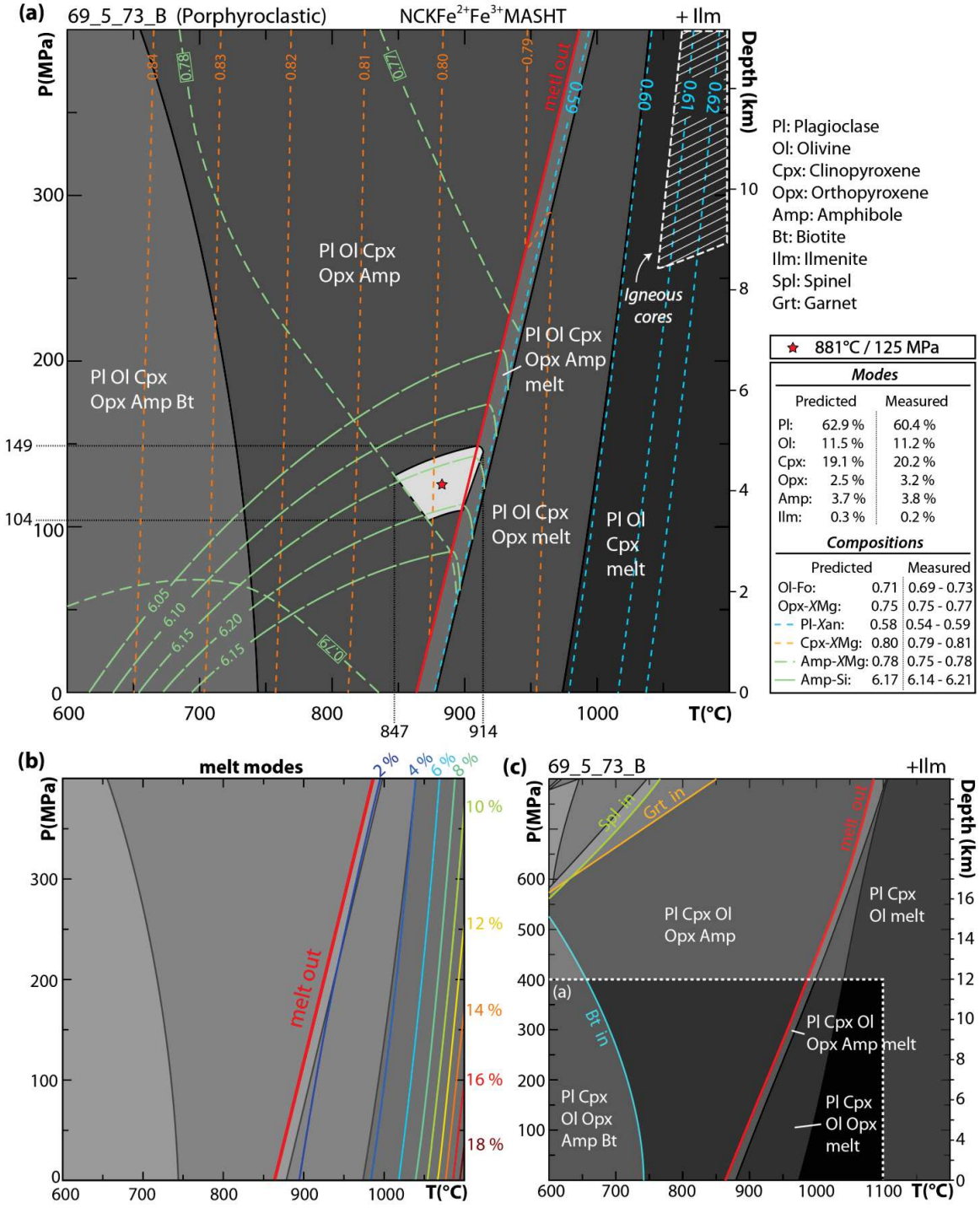

Figure 4.8 *- P–T phase diagrams for the porphyroclastic olivine gabbro 69_5_73_B. The white area in (a) indicates the preferred range of stability conditions, and the red star (center of the domain) represents the assumed P–T conditions. The white hatched area indicates the conditions*

where plagioclase and clinopyroxene igneous grain core compositions are reproduced in the model. The comparison between predicted mineral modes and compositions corresponding to the red star are presented in bottom right table. Note that the predicted Xan values remain > 0.58 below ~850 °C, and that ilmenite is present in the entire diagram. (b) Evolution of melt modes in the calculated phase diagram (in volume %). (c) Phase diagram of (a) calculated for broader ranges of P and T. It indicates the evolution of assemblage stability fields outside the bounds of (a) (white-dashed rectangle).

Protomylonitic domain 9_5_19_A

The phase diagram calculated for the olivine gabbro 9_5_19_A predict a stability of the paragenesis Pl_2+Cpx_2+Ol_2+Opx_2+Amp_2+Opq at 874 ± 40 °C and 235 ± 25 MPa (Figure 4.9a).

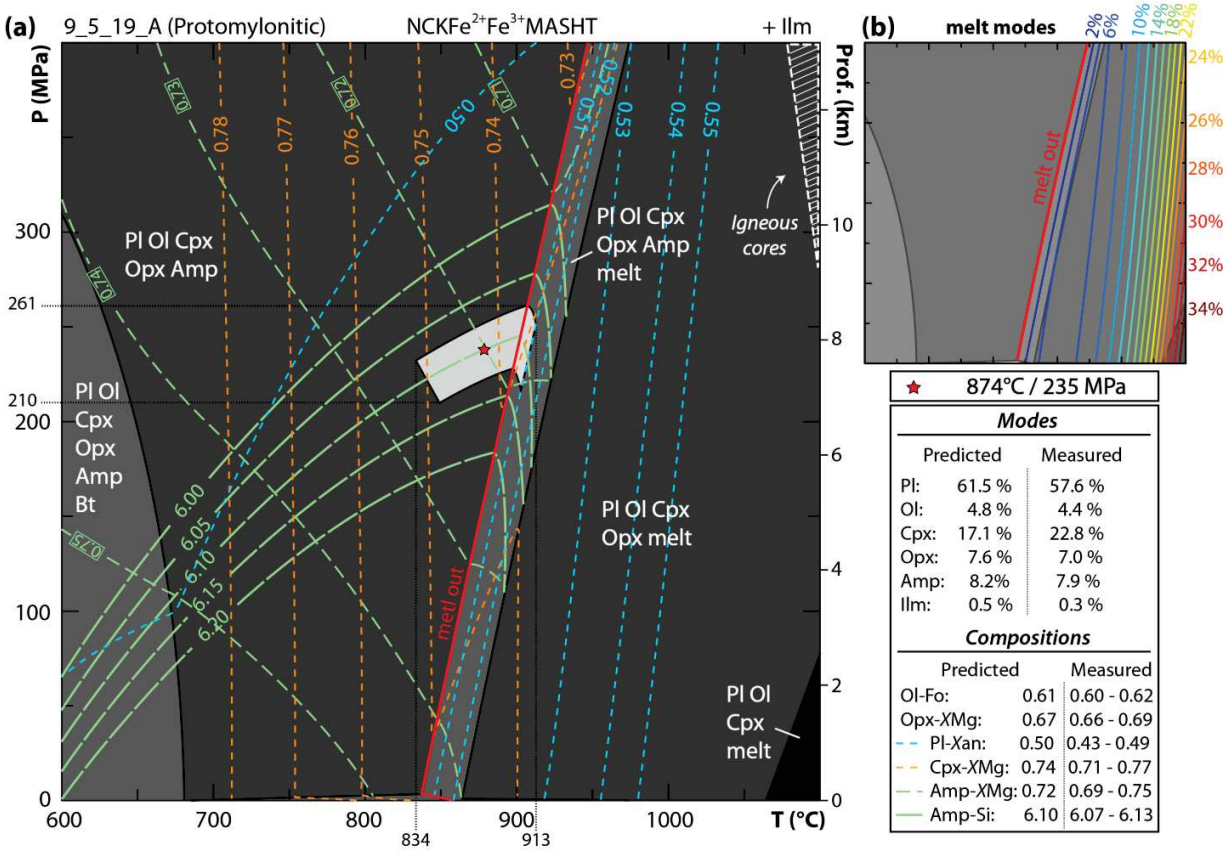

Figure 4.9 *- Phase diagram for the protomylonitic olivine gabbro 9_5_19_A. (a) P–T phase diagram and (b) evolution of melt fractions in the diagram. The white hatched area in (a) indicates the conditions where igneous clinopyroxene grain core compositions are met in the diagram. For phase abbreviations and details see Figure 4.8.*

The general shape of the phase diagram is similar to the one calculated for 69_5_73_B, and has the same evolution at higher pressures and temperatures presented in Figure 4.8b. The main differences is a lower *T* for the solidus in this domain and the width of the field where amphibole and melt coexist due to higher amount of water in the local bulk composition of 9_5_19_A (Figure 4.9 and Table 4.3). The stability field is determined by phase modes and compositions, and is bounded by pargasite amphibole Si apfu in terms of pressure. Modeled plagioclase and clinopyroxene modes appear to differ by up to 4% and 5%, respectively, from the measured modes but their predicted compositions are in line with the observations. Amphibole is predicted to be stable for low melt fractions (< 4 vol%) whereas the melt fraction is relatively high in presence of orthopyroxene at elevated temperatures (up to ~30%; Figure 4.9b). Igneous clinopyroxene grain core compositions are found stable together at > 1080 °C and > 280 MPa in the presence of variable amounts of melt (16–28 vol%).

Mylonitic domain 69_5_73_A

The mylonitic domain 69_5_73_A crosscutting the porphyroclastic olivine gabbro 69_5_73_B is predicted to be stable at 867 ± 38 °C and 155 ± 16 MPa for the paragenesis Pl_2+Cpx_2+Ol_2+Opx_2+Amp_2+Opq (Figure 4.10a).

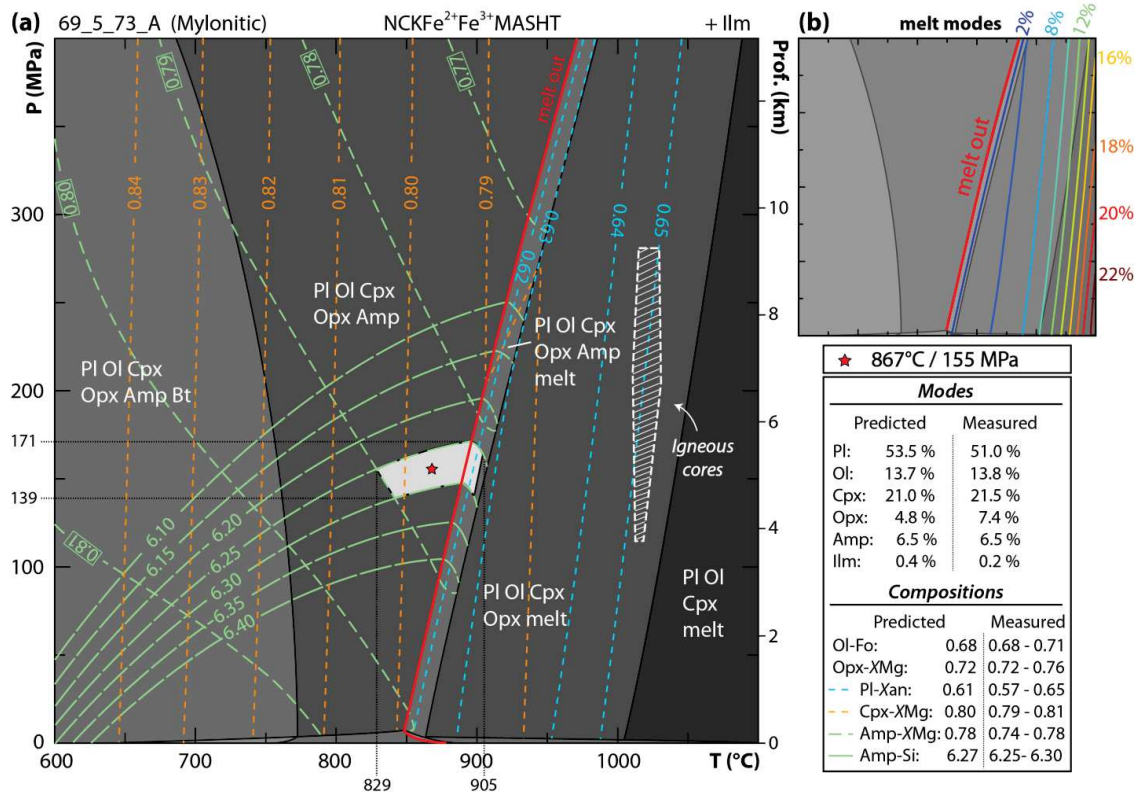

Figure 4.10 *- Phase diagram for the mylonitic olivine gabbro 69_5_73_A. (a) P–T phase diagram and (b) evolution of melt fractions in the diagram. The white hatched area in (a)*

indicates the conditions where both plagioclase and clinopyroxene igneous core compositions are met in the diagram.

This phase diagram shares again high similarities with those calculated for the two previous microstructural domains. The predicted mineral stability field is narrow in terms of pressure, defined by the Si apfu content measured and predicted for pargasite amphiboles, and represents accurately the measured modes and phase compositions. The highest difference concerns the mineral modes of plagioclase and orthopyroxene with differences of 1.5% and 2.5%, respectively (table in Figure 4.10). As observed in domain 69_5_73_B, the melt mode rapidly decreases in the diagram (< 1050 °C), and orthopyroxene forms in the presence of ~10 vol% of melt (Figure 4.10b), while amphibole forms with the latest ~2 vol% of melt. Igneous plagioclase and clinopyroxene gains core compositions of are found stable together at 1010-1030 °C and 115-280 MPa in the presence of ~8 vol% of melt.

Mylonitic domain 58_5_79_C

The stability conditions in the mylonitic domain 58_5_79_C are calculated for a local bulk composition extracted from a subdomain of the quantitative chemical map (Figure S4.6). This subdomain excludes the local presence of talc and olivine that are anecdotic in this sample. In the phase diagram, the field where the predicted mineral modes and compositions best fit the measurements correspond to the light grey field in the center of the diagram of Figure 4.11a with the stable assemblage Pl_2+Cpx_2+Opx_2+Amp_2+Ilm+melt. This stability field contains a few percent of melt (maximum ~2 vol%) in addition to the observed minerals (Figure 4.11b). The predicted stability conditions that best fit the measurements occur at 782 ± 50 °C and 132 ± 50 MPa. Deviations are assumed based on the ranges of measured compositions and modes within the field in the center of the diagram. In this domain, the modeled amphibole is actinolite (Amp_2, see previous sections) and formed from the crystallization of the latest melt fraction.

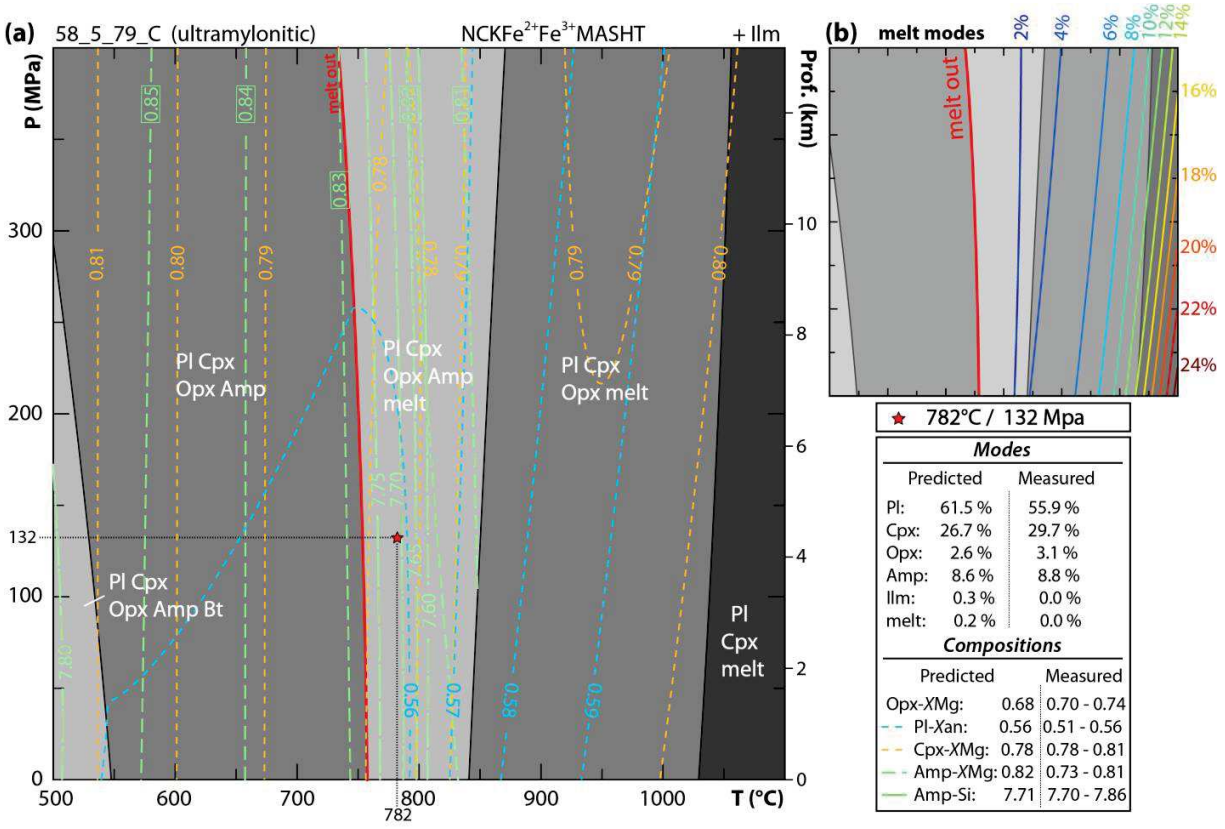

Figure 4.11 *- Phase diagram for the ultramylonitic gabbro 58_5_79_C. (a) P–T phase diagram and (b) evolution of melt fractions in the diagram. Note that the lower limit on temperature is 100 °C lower than in the previous diagrams, and that the modeled amphibole is actinolite instead of pargasite.*

Ultramylonitic domain 9_5_19_B

The ultramylonitic domain 9_5_19_B stability conditions are modeled in a *T–X* section by assuming that it formed by strain localization and hydrous fluid circulation within a domain similar to 9_5_19_A. Chemical changes in bulk composition of the two domains mainly consist on an hydration accompanied by a decrease of SiO_2, Al_2O_3, and Fe_2O_3 and a gain of FeO (≤ 2.5 wt.% for all cited elements). This metasomatism occurs in a range of ~270 °C and ~130 MPa before modeling the observed assemblage in the ultramylonite 9_5_19_B at ~700 °C and ~100 MPa. Two fields are considered in this *T–X* phase diagram, one corresponding to the observed mineral compositions (blue field and star A in Figure 4.11) with the assemblage Pl+Cpx+Amp+Ol±Bt±Ilm, and another one where the observed modes are reproduced by the model (purple field and star B in Figure 4.11) with the assemblage Pl+Cpx+Amp±Bt±Ilm. Note that the modeled amphiboles are actinolites and have compositions closed to the measurements at star B conditions (i.e., at the ultramylonite bulk composition; see table B in Figure 4.11). The

observation of modeled mineral compositions and modes reproducing observations at different locations of the phase diagram suggest local disequilibrium within the ultramylonitic domain. Although the water content in the ultramylonite is high, it indicates a water-rich (~1 ox. wt.%) but non-saturated environment (Table 4.3).

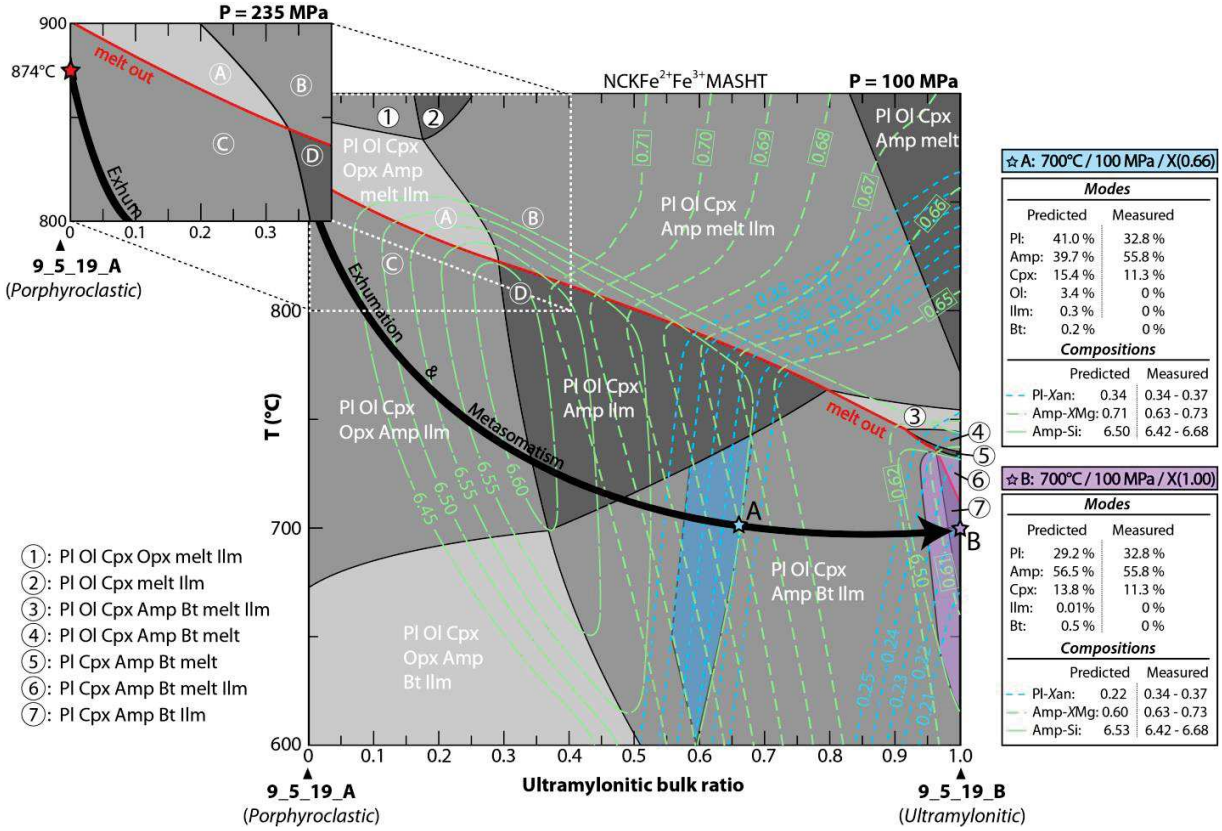

Figure 4.12 *- T–X Phase diagram modeling the evolution from the composition of the porphyroclastic domain 9_5_19_A (left) to the one of the ultramylonitic domain 9_5_19_B (right). The bulk composition of the ultramylonitic domain was calculated without the high-andesitic plagioclase cores (Pl_2; Figure S4.7). The blue domain represents the field where measured compositions are met, and the blue star (A) is the preferred condition. The top right table indicates modeled modes and compositions at this point. The purple domain represents the field corresponding to measured modes (and in a lesser extend to amphibole compositions), and the purple star (B) is the preferred condition. The bottom right table indicates modeled mineral modes and compositions at this point. The black arrow indicates the proposed path associated to metasomatism and strain localization leading to the formation of the ultramylonite (9_5_19_B) starting from the porphyroclastic host domain (9_5_19_A) during exhumation. The top left inset corresponds to the T–X phase diagram calculated at 235 MPa (stability condition modeled for 9_5_19_A), and the red star indicate the modeled stability temperatures. The letters A, B, C, and D indicate the corresponding assemblage field in the large diagram section.*

4.4. Crystallographic preferred orientations and intracrystalline deformation

Electron backscattered diffraction (EBSD) analyses were performed in all the studied domains to evaluate crystallographic preferred orientations (CPO) and quantify grain sizes (see Table 4.1) and intragranular deformations. Phase maps of the analyzed areas in each microstructural domain are given in figure S4.8. It should be noted here that the EBSD data used are part of the large dataset published and discussed in Allard et al. (2021).

Deformation gradient in the interval 69_5_73

The studied interval *69_5_73* presents a sharp gradient in deformation, marked by the crosscutting of a mylonitic domain (69_5_73_A) into a porphyroclastic domain (69_5_73_B; Figure 4.3a).

Crystallographic orientations measured in the porphyroclastic domain 69_5_73_B indicate preferred orientations of medium intensities in all phases (Figure 4.13a). Texture indices calculated in this domain range from 1.90 to 3.14 for the J index, and from 0.02 to 0.08 for the M index. The highest values correspond to clinopyroxene, amphibole, and olivine CPO. Pole figures indicate an alignment of the [100] axes in plagioclase and [001] axes in both olivine and amphibole parallel to the lineation (Figure 4.3a and 4.13a). CPO in plagioclase, olivine, and amphibole are characterized by the clustering of (010) planes (also (100) planes in amphibole) parallel to the foliation. Clinopyroxene and orthopyroxene pole figures indicate a general East-West preferred orientation (in the thin section reference frame) of (010) planes at angle (30-40°) from the foliation plane. The detailed analysis of Cpx_2 recrystallized aggregates indicates very low intragranular deformations in Amp_1 and Opx_1 by contrast to Cpx_2 grains, and the associated CPO are very similar for the three minerals (Figure 4.14a and b). The (010) planes of the three minerals are parallel to the plane of elongation of the Cpx_2 recrystallized aggregate, and their [100] axes (or orthogonal direction to (100) in clinopyroxene) are in the direction of elongation. Note that these CPO are rather similar to that obtained by considering all clinopyroxene, orthopyroxene, and amphibole grains in the analyzed area (Figure 4.13a). At recrystallized rims of Ol_1, Opx_1 grains present at Ol_2 boundary junctions display weak internal deformations (Figure 4.14c). Pole figures in Opx_1 and Ol_2 grains from the Ol_1 rims display strong CPO (Figure 4.14d). The (010) planes in both Opx_1 and Ol_2 are subparallel to each other and the [100] axes in Opx_1 are close to the [001] axes in Ol_2. Note that the Ol_2 grains CPO at the Ol_1 rim is similar to the CPO corresponding to all olivine grains in the analyzed area (Figure 4.13a and 4.14d). Also, Opx_1 grains CPO observed at the Ol_1 rim is orthogonal to that observed in Opx_1 from recrystallized Cpx_2 aggregates (Figure 4.13b and 4.14d). CPO in recrystallized Opx_1 grains seems strongly influenced by the phase within which they occur.

The neighboring mylonitic domain 69_5_73_A displays random to weak CPO in all phases (Figure 4.13b). Calculated J index and M index are low (> 1.32 and > 0.02, respectively), and are

maximum in plagioclase and amphibole. The [001] axes in amphibole, and less distinctly the [100] axes in plagioclase and olivine, are parallel to the lineation. With low clustering densities, the (010) planes in plagioclase, clinopyroxene, and olivine, and the (100) planes in amphibole are parallel to the foliation (Figure 4.13b). A detailed analysis of the four-phase ribbons (see section 4.1.4) reveals very weak intragranular deformation in the constitutive minerals (Cpx_2-Ol_2-Amp_1-Opx_1; Figure 4.14e). CPO of medium intensity are measured in Cpx_2 and Amp_1 with texture index J values of ~2.3-2.4 and M index values of 0.04-0.05 (Figure 4.14f). By contrast, olivine and orthopyroxene CPO are weak to random and the associated texture index J is below ~1.4 and the M index below 0.01 (Figure 4.14f). Pole figures patterns indicate the alignment of the [001] axes in Amp_1 parallel to the lineation, and the (100) plane in Cpx_2 and (100) planes in Amp_1 are parallel to the foliation (Figure 4.14f). The CPO in Ol_2 and Opx_1 are less clear, however the [100] axes in olivine and [010] axes in orthopyroxene seems globally aligned with the lineation. In the Cpx_2 recrystallized aggregates, CPO of Cpx_2, Ol_2, Amp_1, and Opx_1 display similar relations as in in the porphyroclastic domain 69_5_73_B. The (010) planes of all grains are parallel to the plane of elongation of the Cpx_2 aggregate (and to the foliation), and the [100] axes in orthopyroxene and olivine (and orthogonal direction to (100) in clinopyroxene), and [001] axes in amphibole are parallel to the long axis of the aggregate (i.e., the lineation). Similarly to domain 69_5_73_B, the CPO patterns of Opx_1 and Amp_1 grains within the Cpx_2 recrystallized aggregates are different from that observed in Ol_2 recrystallized aggregates.

Overall, misorientation maps for both domains indicate very weak internal deformations in small Opx_1 and Amp_1 grains present at grain boundary junctions in recrystallized aggregates. These grains frequently display dihedral angles, embayment, and occurrence as mineral film at grain boundaries (Figure 4.14g).

Deformation gradient in the interval 9_5_19

In the interval *9_5_19* a strong and abrupt gradient of deformation is observed between the protomylonitic domain 9_5_19_A and the crosscutting domain 9_5_19_B (Figure 4.3b).

The microstructural domain 9_5_19_A is characterized by well-defined CPO in minerals overall (Figure 4.13c). Texture index J values range from 1.52 to 2.65 and M index values from 0.01 to 0.05, and the strongest fabric intensities are measured in plagioclase and orthopyroxene. The [100] axes of plagioclase and olivine, and [001] axes in clinopyroxene, orthopyroxene, and amphibole are oriented parallel to the lineation (Figure 4.3b and 4.13c). Plagioclase and olivine (001) planes and orthopyroxene and amphibole (100) planes are parallel to the foliation.

The plagioclase-amphibole ultramylonitic shear zone 9_5_19_B indicate a weakening of the CPO in plagioclase grains with an associated J index value of 1.16 and M index of 0.01 (Figure 4.13d). Corresponding pole figures display a poorly defined CPO with [100] axes parallel to the lineation and (010) planes parallel to the foliation. Amphiboles are indicative of a relatively strong fabric

intensity (the strongest one calculated in the sample suite) with a texture index J value of 2.21 and a M index value of 0.07. Pole figures indicate well defined CPO patterns with the alignment of [001] axes and (100) planes respectively parallel to the lineation and the foliation. The analysis of a ~200 µm wide plagioclase monomineralic band within the shear zone indicate the alignment of the [100] axis with the lineation, similarly as in pole figures calculated by considering all grains in the map, but unlike the CPO of all grains the foliation is then not clearly associated to (010). Instead, (001) could be more likely as a preferred slip plane associated to the foliation, although it preferred orientation is very weak and poorly defined (Figure 4.13d, 4.15a, and 4.15b). The associated texture indices J and M are slightly higher for this monomineralic band than for the whole mapped area. In a plagioclase-amphibole mixed band, the CPO patterns and texture indices values are similar to those observed for all the mapped area (Figure 4.13d and 4.15c).

Ultramylonitic domain 58_5_79_C

The well-defined foliation in the microstructural domain 58_8_79_C is associated with random to weak fabric intensities in all mineral phases (Figure 4.13e). The J index ranges from 1.08 to 1.18 and M index from 0.00 to 0.01 except for plagioclase which have higher values at 1.86 and 0.06 respectively. Pole figures show the alignment of [100] axes in plagioclase and [001] axes in amphibole parallel to the lineation, and (100) planes in clinopyroxene orthogonal to it (Figure 4.13e and 4.15d). The (010) planes in plagioclase and the (100) planes in orthopyroxene and amphibole are parallel (subparallel for orthopyroxene and amphibole) to the foliation plane. The analysis of a Cpx_2 elongated recrystallized aggregate indicates the alignment of [001] clinopyroxene and amphibole axes and [100] orthopyroxene axes orthogonal to the elongation direction of the aggregate (Figure 4.15d, and e). Both (100) poles of clinopyroxene and amphibole planes are parallel to the elongation axis. Fabric intensities are strong with J index values at ~2.3-3.0 and M index values at 0.06-0.10. This strongly differs from the texture indices calculated for all grains in each phase. Although the other aggregates made of recrystallized Cpx_2 in the analyzed domain display similar characteristics in terms of fabric strength and CPO relations between phases, the orientation of CPO differs from an aggregate to another. This explains the random CPO calculated by considering all grains from all aggregates together. Intragranular misorientations measured in Cpx_2, Amp_1, and Opx_1 within Cpx_2 recrystallized aggregates are medium to low, which differs from observations made in microstructural domain from interval *69_5_73*. Analyzed plagioclase monophase bands display very close CPO patterns than that observed in the whole mapped area, and the associated fabric intensities are slightly higher (e.g., Figure 4.13e and 4.15f).

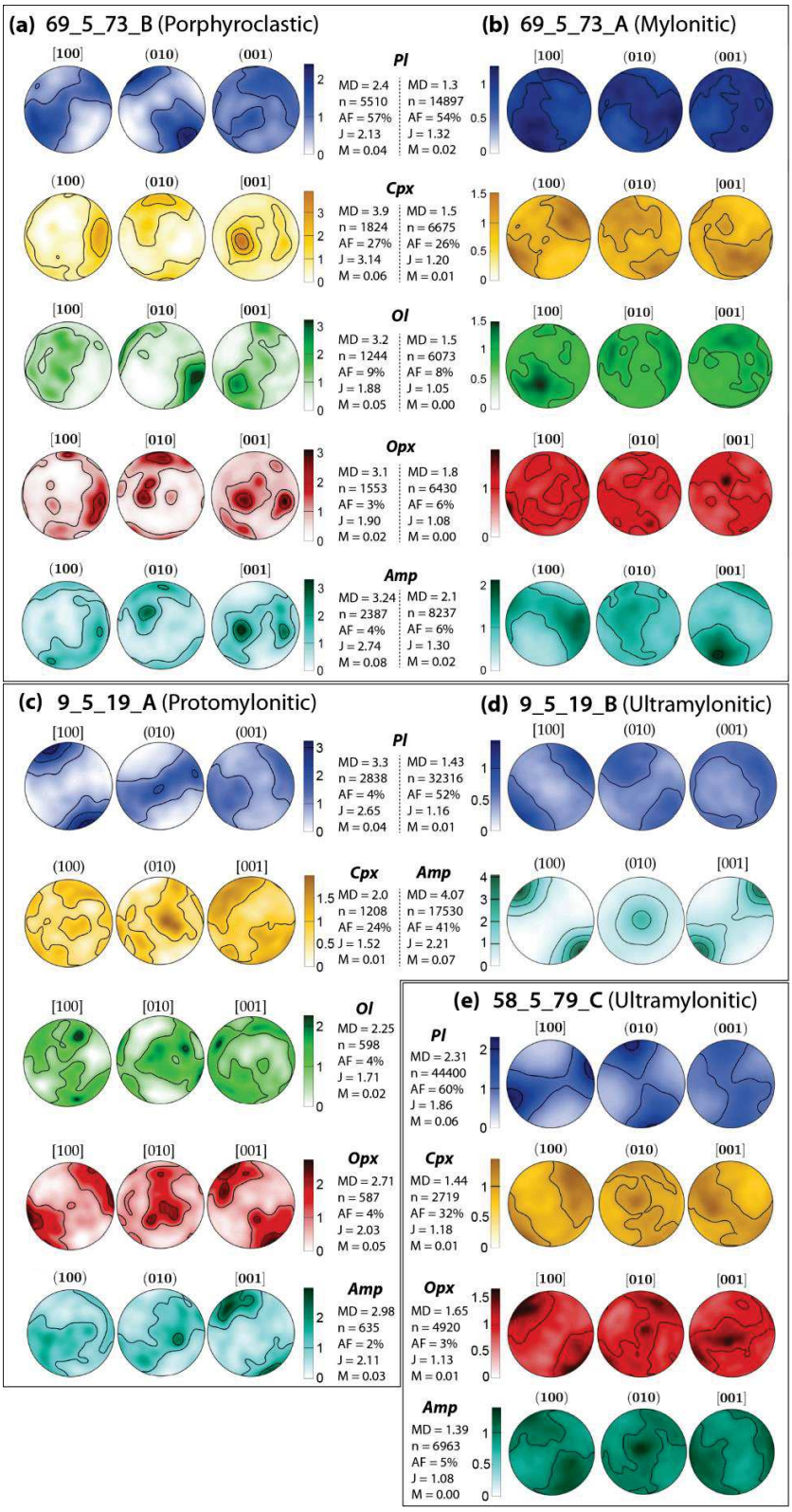
(a) 69_5_73_B (Porphyroclastic)
(b) 69_5_73_A (Mylonitic)
Pl
MD = 2.4
n = 5510
AF = 57%
J = 2.13
M = 0.04
MD = 1.3
n = 14897
AF = 54%
J = 1.32
M = 0.02
Cpx
MD = 3.9
n = 1824
AF = 27%
J = 3.14
M = 0.06
MD = 1.5
n = 6675
AF = 26%
J = 1.20
M = 0.01
Ol
MD = 3.2
n = 1244
AF = 9%
J = 1.88
M = 0.05
MD = 1.5
n = 6073
AF = 8%
J = 1.05
M = 0.00
Opx
MD = 3.1
n = 1553
AF = 3%
J = 1.90
M = 0.02
MD = 1.8
n = 6430
AF = 6%
J = 1.08
M = 0.00
Amp
MD = 3.24
n = 2387
AF = 4%
J = 2.74
M = 0.08
MD = 2.1
n = 8237
AF = 6%
J = 1.30
M = 0.02
(c) 9_5_19_A (Protomylonitic)
(d) 9_5_19_B (Ultramylonitic)
Pl
MD = 3.3
n = 2838
AF = 4%
J = 2.65
M = 0.04
MD = 1.43
n = 32316
AF = 52%
J = 1.16
M = 0.01
Cpx
MD = 2.0
n = 1208
AF = 24%
J = 1.52
M = 0.01
Amp
MD = 4.07
n = 17530
AF = 41%
J = 2.21
M = 0.07
Ol
MD = 2.25
n = 598
AF = 4%
J = 1.71
M = 0.02
Opx
MD = 2.71
n = 587
AF = 4%
J = 2.03
M = 0.05
Amp
MD = 2.98
n = 635
AF = 2%
J = 2.11
M = 0.03
(e) 58_5_79_C (Ultramylonitic)
Pl
MD = 2.31
n = 44400
AF = 60%
J = 1.86
M = 0.06
Cpx
MD = 1.44
n = 2719
AF = 32%
J = 1.18
M = 0.01
Opx
MD = 1.65
n = 4920
AF = 3%
J = 1.13
M = 0.01
Amp
MD = 1.39
n = 6963
AF = 5%
J = 1.08
M = 0.00

Figure 4.13

Figure 4.13 *- Pole figures calculated on average grain orientation data for the studied deformed microstructural domains (lower hemisphere, equal-area projection). Contour intervals are multiples of a uniform distribution, and the minimum density is set to zero for comparison between pole figures. Concerning amphibole pole figures for the microstructural domain 9_5_19_A, only grains outside the amphibole vein are selected (see Figure 4.3b). Colors in pole figures correspond to phase colors in maps (Figures 4.14 and 4.15). MD: maximum density, n: number of grains, AF: area fraction, J: J index, M: M index.*

Figure 4.14 *- Details on misorientations and crystallographic preferred orientations in mineral. (a) Phase map of the selected recrystallized clinopyroxene aggregate from microstructural domain 69_5_73_B, and associated intragranular misorientation maps (misorientation from grain average orientation) in clinopyroxene, amphibole, and orthopyroxene. (b) Pole figures of Cpx_2, Amp_1, and Opx_1 grains from the selected region in (a) (pole figures and parameters details are given in figure 4.13). (c) Phase map of the selected olivine porphyroclast and recrystallized aggregate from microstructural domain 69_5_73_B, and associated intragranular misorientation maps in olivine and orthopyroxene. (d) Pole figures for Ol_2 and Opx_1 grains from the Ol_1 recrystallized rim of (c). (e) Phase map within a four-phases ribbon from microstructural domain 69_5_73_A and associated intragranular misorientation maps in Cpx_2, Ol_2, Amp_1, and Opx_1. (f) Pole figures associated to grains presented in misorientation maps in (h). (g) Phase map details displaying grain shape characteristics for Opx_1 and Amp_1 within Ol_2 and Cpx_2 recrystallized aggregates, respectively, and the local occurrence of Ol_2 grains in Cpx_2 recrystallized aggregates. Arrows indicate dihedral angles and embayment shapes in Opx_1, mineral film of Amp_1 at Cpx_2 grain boundaries, and Amp_1 nucleus at Cpx_2 triple/quadriple grain junctions. Note the very weak intragranular misorientations (i.e., deformations) in the Cpx_2, Ol_2, Amp_1, and Opx_1 grains presented here.*

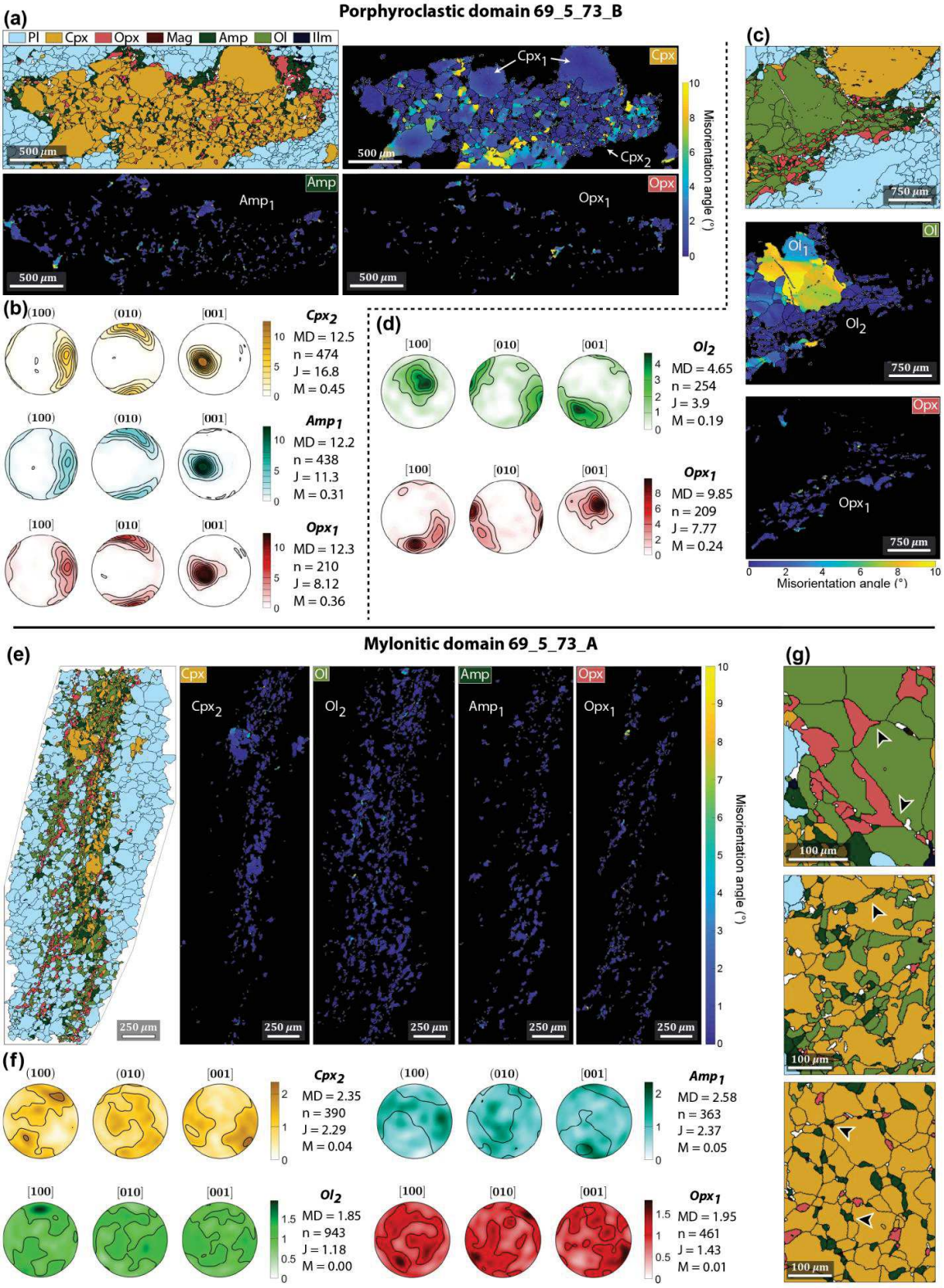
(a)
Porphyroclastic domain 69_5_73_B
Pl Cpx Opx Mag Amp Ol Ilm
500 µm
Cpx
Cpx1
Cpx2
Misorientation angle (°)
Amp
Amp1
Opx
Opx1
(b)
(100) (010) [001]
Cpx2
MD = 12.5
n = 474
J = 16.8
M = 0.45
Amp1
MD = 12.2
n = 438
J = 11.3
M = 0.31
Opx1
MD = 12.3
n = 210
J = 8.12
M = 0.36
(c)
750 µm
Ol
Ol1
Ol2
Opx
Opx1
Misorientation angle (°)
(d)
Ol2
MD = 4.65
n = 254
J = 3.9
M = 0.19
Opx1
MD = 9.85
n = 209
J = 7.77
M = 0.24
Mylonitic domain 69_5_73_A
(e)
250 µm
Cpx
Cpx2
Ol
Ol2
Amp
Amp1
Opx
Opx1
Misorientation angle (°)
(f)
Cpx2
MD = 2.35
n = 390
J = 2.29
M = 0.04
Amp1
MD = 2.58
n = 363
J = 2.37
M = 0.05
Ol2
MD = 1.85
n = 943
J = 1.18
M = 0.00
Opx1
MD = 1.95
n = 461
J = 1.43
M = 0.01
(g)
100 µm

Figure 4.14

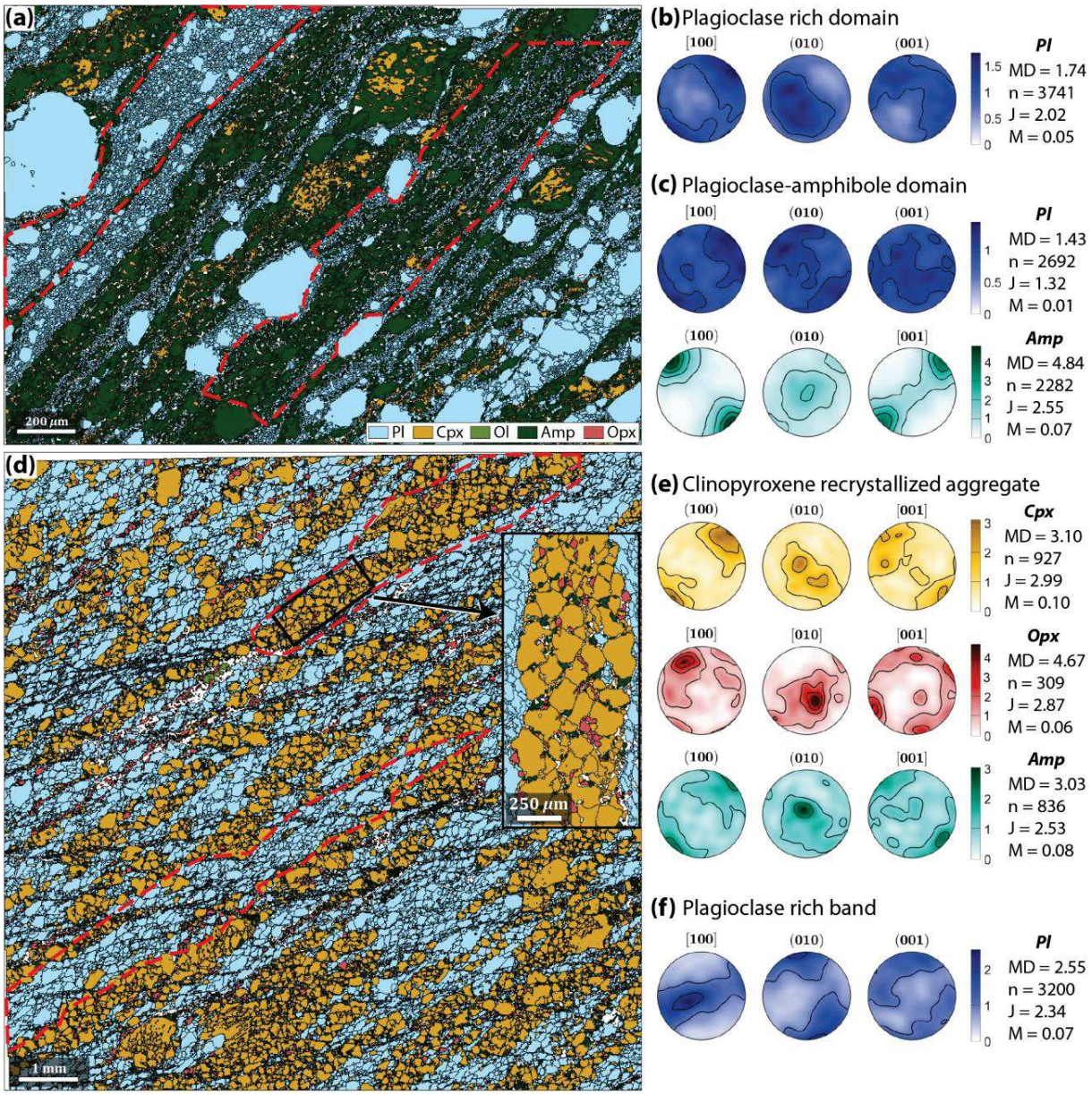

Figure 4.15 *- Detailed CPO analysis in specific mineral bands. (a) Phase map of the ultramylonitic domain 9_5_19_B. (b) and (c): Pole figures associated to the contoured bands (red) in (a). (d) Phase map of the ultramylonitic domain 58_5_79_C. (e) and (f): Pole figures associated to the contoured domains in (d).*

5. Discussion

5.1. Multiple episodes of ductile deformation

The studied domains display extensive recrystallization of mineral, associated to medium to weak or random CPO. Furthermore, recrystallization is accompanied by varying strain intensities,

chemical changes, and in some cases by later retrograde deformations. The following sections depict the characteristics and timing of deformations observed in the sampled intervals, occurring as a result of extension during accretion at the ridge axis and subsequent exhumation within an oceanic core complex.

5.1.1. Early crystal-plastic deformations

The first episode of deformation, well recorded in the sampled domains 69_5_73_B and 9_5_19_A, occurs in the dislocation creep regime as shown by the frequent observation of undulose extinction and subgrain boundaries in grains (mainly in plagioclase and olivine; e.g., Figure 4.3d and e). The intense recrystallization in plagioclase, less significant in olivine and clinopyroxene, results from subgrain rotation recrystallization (e.g., Drury & Urai, 1990; Kruse et al., 2001; Poirier & Guillopé, 1979; Urai et al., 1986), as previously described in Allard et al. (2021). Consistently, CPO of medium intensity are measured in line with the kinematic directions for the three main phases of theses rocks, namely plagioclase, clinopyroxene, and olivine (Figure 4.13a and c). Pole figures of plagioclase suggest the activity of the [100](010) slip system in the domain 69_5_73_B, and together with [100](001) in domain 9_5_19_A. Pole figures in clinopyroxene are not consistent with any known slip or twin system. Chemical analyses indicate compositional changes in clinopyroxene grains (69_5_73_B and 9_5_19_A) and plagioclase grains (69_5_73_B) between the igneous porphyroclasts and their recrystallized mantles (Figure 4.4 and 4.5). These variations in composition are of the order of those observed from core to rims in the undeformed olivine gabbro 88_5_117 (Figure 4.4a and b). Although these core-rim variations could be associated to diffusion, similar observations in undeformed olivine gabbros from Atlantis Bank are reported and interpreted as the result of met-rock interaction due to the circulation of a melt in a crystallizing mush (e.g., Sanfilippo et al., 2020). A demonstration of melt-rock interaction is the local increase of anorthite content in plagioclase in direct contact with Ol_2 and Opx_1 (± Amp_1) in the microstructural domain 69_5_73_B and the more strongly deformed domains 69_5_73_A and 58_5_79_C (Figure 4.4). From the observation of a similar paragenesis between the undeformed domain and the two porphyroclastic and protomylonitic domains (69_5_73_B and 9_5_19_A), and comparable chemical variations, we posit that variations in chemistry from porphyroclast to recrystallized grain in deformed domains also result from melt-rock interactions. The origin of the melt is probably external, from deeper in the crust, as its composition is less evolved than the one inferred to have formed the main paragenesis (higher Ca content and *X*Mg ratio in reaction products). Thermodynamic modeling in these deformed domains predicts concordant Pl_1 and Cpx_1 igneous grain core compositions in presence of melt (> 6 vol% in domain 69_5_73_B and > 18% in domain 9_5_19_A) at temperatures > 1050 °C and pressures > 250-300 MPa (Figures 4.8a and 4.9a). In the further deformed domain 69_5_73_A, where Pl_1 and Cpx_1 igneous porphyroclasts are also preserved, concordant grain

core compositions fall in the range of 1010-1030 °C and 115-280 MPa (Figure 4.10a). Moreover, significant core-rim variations in plagioclase anorthite content are measured in recrystallized Pl_2 grains from domain 69_5_73_B and _A (e.g., Figure 4.16).

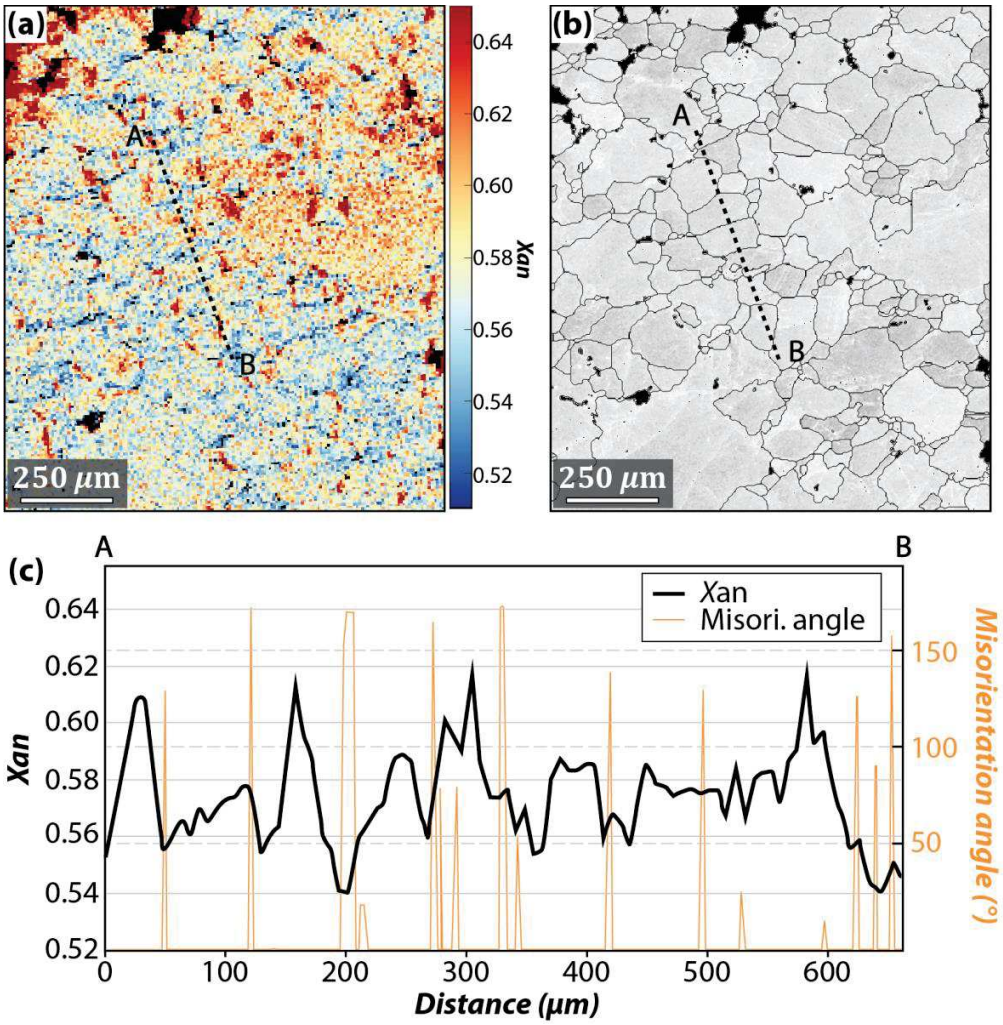

Figure 4.16 *- Core-rim variations in plagioclase Anorthite content in recrystallized grains from domain 69_5_73_B. (a) Composition map of Anorthite content in plagioclase. (b) Plagioclase grain map on top of band contrast image. The black color in maps corresponds to other minerals. (c) Composition profile (black) and misorientation profile (orange) in plagioclase grains corresponding to the A-B transect presented in (a) and (b). The superimposition of the composition profile on top of the misorientation profile highlights the dramatic drop of anorthite content at grain boundaries.*

The highest anorthite contents measured in Pl_2 grain cores match compositions measured in Pl_1 igneous porphyroclasts, but the anorthite fraction decreases by 5 mol% to 8% at grain boundaries.

This dramatic drop in anorthite content appears to be restricted to grain boundaries, which could suggest the presence of a melt film at the grain boundary interfaces, producing melt-rock reactions that can account for these chemical variations (e.g., Lissenberg & MacLeod, 2016; Sanfilippo et al., 2020). The modeled mineral composition of plagioclase, assuming a closed system, is not predicted lower than An_{58-59} (Figure 4.8a), which could suggest an external chemical perturbation to account for the measured An_{54-56} at grain boundaries. These observations are also valid for the domain 69_5_73_A, where measured anorthite content at grain boundaries are at An_{54-57} while the lowest predicted value in the phase diagram is An_{62} (Figure 4.10a). Melt circulation, and induced melt-rock interactions, in these rocks would also be consistent with the observation of gradually decreasing *X*Mg ratio in olivine, clinopyroxene, orthopyroxene, and amphibole grains, and anorthite content in plagioclase grains (both porphyroclast and recrystallized grains for all minerals) toward the mylonite contact in 69_5_73_B (e.g., Figure 4.3a, 4.6a, 4.6b, and S4.2), and away from it in 69_5_73_A (e.g., Figure 4.3a, 4.6a, 4.6c, and S4.2). These thin section scale variations would then result from the former presence of several melt channels.

The final paragenesis of the rock is predicted to be stable at 881 °C – 125 MPa and 874 °C – 235 MPa, respectively in the porphyroclastic and protomylonitic domains (Figure 4.8 and 4.9). Interestingly, the stability conditions calculated for the domain 9_5_19_A are similar to those calculated for 69_5_73_B although their bulk and mineral compositions differ (lower anorthite content in plagioclase and *X*Mg in pyroxenes, amphibole, and olivine for 9_5_19_A). Also, the interval *9_5_19* is located higher up in Hole U1473A (76.8 mbsf) in contrast to the other studied domains (below ~520 mbsf), and must correspond to the emplacement of evolved melt lenses up in the oceanic crust as indicated by the presence of other high emplacements of evolved lithologies at Atlantis Bank (e.g., Dick et al., 2019b). The lack of chemical variations in plagioclase grains of that interval could then attest to an absence of melt circulation in the higher portion of the hole. The final paragenesis observed in these domains consists of orthopyroxene and amphibole (and minor oxides) in addition to primary olivine, plagioclase and clinopyroxene. Textural analyses suggest a magmatic origin for these two new minerals, already proposed in gabbroic lithologies at the Atlantis Bank (e.g., Gao et al., 2006, 2007; Gardner et al., 2020; Gillis & Meyer, 2001; Taufner et al., 2021), which is supported by measured CPO and intragranular misorientations (Figure 4.14), and thermodynamic modeling (Figures 4.8 to 4.10). Absence or very low intragranular deformations in Opx_1 and Amp_1 grains together with CPO intimately related to that of the recrystallized aggregate (clinopyroxene and/or olivine) in which they occur is indicative of epitaxial growth (e.g., Gardner et al., 2020; Shelley, 1994; Figure 4.14a-f). Then, the episode of crystal-plastic deformation resulting in the recrystallization of plagioclase, olivine, and clinopyroxene occurred before the crystallization (or at its onset) of orthopyroxene and

amphibole in the rock. The formation of these two minerals and of Pl_2 with compositions different to Pl_1 porphyroclatst is proposed to result from the reaction:

$$Ol_a+Pl_a+melt_a \rightarrow Opx_b+Amp_b+Pl_b+melt_b$$

at Ol_1 rims, and by:

$$Cpx_a+Pl_a+melt_a \rightarrow Opx_b+Amp_b+Pl_b+melt_b$$

within the Cpx_2 aggregates (e.g., Gardner et al., 2020). From the calculated phase diagrams, igneous grain core compositions are predicted to be stable in presence of melt above ~1050 °C, which is 50-60 °C higher than the apparition of orthopyroxene in 69_5_73_B, and in the presence of 2–3 vol% of orthopyroxene in 9_5_19_A. Thus, we propose that the first episode of crystal-plastic deformation occurred at temperatures of 1000–1050 °C and between 200 to 300 MPa (~6–10 km of depth). This is consistent with the predicted melt fractions at these conditions, from 6–8 vol% to 14–20%, that enable dominant crystal plasticity in the crystallized framework of the deforming mush (e.g., Costa et al., 2009; Picard et al., 2013), also in line with the fact that dislocation creep is often described as the dominant deformation mechanism in partially molten rocks (e.g., Bussod & Christie, 1991; Hirth & Kohlstedt, 1995).Previous studies on Atlantis Bank gabbros proposed a similar range of temperatures for the solid-state recrystallization of plagioclase, clinopyroxene, and olivine, from 800-850 °C to ~1090 °C and 220–270 MPa (Mehl & Hirth, 2008; Miranda & John, 2010; Gardner et al., 2020; Taufner et al., 2021), leading to the development of CPO in these minerals. Allard et al. (2021) documented the ubiquitous development of CPO in deformed gabbroic lithologies sampled in Hole U1473A, demonstrating the major role of crystal plasticity at the Atlantis Bank. Only the study of Gardner et al. (2020) reported an early isochemical recrystallization stage, while others indicate lower anorthite contents in recrystallized Pl_2 grains and lower *X*Mg ratio in recrystallized Cpx_2 and Ol_2 grains, suggesting that this early isochemical stage may not be a widespread feature at the Atlantis Bank, or rarely preserved.

5.1.2. Subsequent strain localization and progressive CPO randomization

The two mylonitic and ultramylonitic domains 69_5_73_A and 58_5_79_C have mineral assemblages similar to the less deformed domains described in the previous section. Mineral compositions are very similar to those in domain 69_5_73_B, and the same textural characteristics are observed (e.g., epitaxial Amp_1 and Opx_2 in Ol_1 recrystallized rims and Cpx_2 recrystallized aggregates; Table 4.1 and Figures 4.4a and 4.5b). These two domains differ from the less deformed ones by higher strain intensities, but associated weaker to random CPO measured in almost all minerals (Figure 4.13b and e). Only plagioclase grain from domain 58_5_79_C indicates medium fabric intensities associated with a clear [100](010) CPO pattern. The detailed analysis of Pl_2 monomineral bands within the rock indicates higher fabric intensities

(of the same order as in 69_5_73_B and 9_5_19_A), as already reported in other studies of plagioclase monomineral bands (e.g., Getsinger et al., 2013), with orientations very similar to the general one, which strongly suggests that the studied microstructure was produced by dislocation creep (Figures 4.13e, 4.15d, and 4.15f). This is also valid for the strongly elongated Cpx_2 aggregates with the exception that the CPO is different from one aggregate to another, sometimes with (001) sub-parallel to the foliation and [100] parallel to the lineation, or with (010) parallel to the foliation (e.g., Figure 4.14e, 4.15d and 4.15e). Allard et al. (2021) reported high intragranular deformations in recrystallized Pl_2 grains from this domain and proposed subgrain rotation recrystallization as the main deformation mechanism followed by strain hardening in grains. Then the general loss of CPO in clinopyroxene (and associated CPO in orthopyroxene and amphibole) can be explained by the isolation of internally crystallographically-consistent elongated recrystallized aggregates. This would also explain the weaker CPO strength measured by considering all Pl_2 recrystallized bands than within individual bands. The observation of moderately deformed Amp_1 and Opx_1 grains present in Ol_1 recrystallized rims and Cpx_2 recrystallized aggregates contrasts with observations made in less deformed domains. This indicates that crystal-plastic deformation continued after the crystallization of Amp_1 and Opx_1, most likely in a melt-absent environment.

Weak to random CPO are measured in all minerals in the mylonitic domain 69_5_73_A although CPO patterns remain consistent with the microstructure. This strongly suggests the progressive loss of a former CPO during strain localization and further recrystallization. The chemical evolutions in minerals associated to recrystallization are identical to that measured in the neighboring domain 69_5_73_B (Figure 4.4, 4.5 and 4.6), and very similar stability conditions are calculated for the final paragenesis, only with ~20 °C and 30 MPa of difference (Figure 4.10a). This argues for of a simple difference in terms of strain localization between the two domains (from 69_5_73_B to 69_5_73_A), and informs on the heterogeneous, anastomosed, distribution of high-temperature crystal-plastic deformation in Hole U1473A (e.g., Figures 4.2b and 4.3a). Although the chemical differences between igneous porphyroclasts and recrystallized grains are similar to those measured in domain 69_5_73_B, the amount of melt in domain 69_5_73_A was higher. This is demonstrated by the formation of several fine-grained four-phase ribbons (Ol_2-Cpx_2-Opx_1-Amp_1) as a result of melt-rock interaction reactions, and mixed aggregates of Cpx_2, Ol_2, and Amp_1 (e.g., Figure 4.14e and g). At the contact of these ribbons plagioclase grain size is reduced, probably by second phase pinning, the second phases being the melt-rock products (e.g., Mehl & Hirth, 2008). Because of higher strains in this domain and the resulting reduced grain sizes, larger amount of melt could have circulated at grain boundary interfaces and potentially channelized locally where the four-phase ribbons formed. This is consistent with various field observations, experiments, and numerical modeling demonstrating the key role of highly strained zones on melt circulation (e.g., Llorens et al., 2019; Qi et al., 2018;

Schulmann et al., 2008). The reduced grain size and larger amount of melt in this domain would have favored a change of deformation mechanism during strain localization to melt-assisted grain boundary sliding (e.g., Paterson, 2001; Stuart et al., 2018; Gardner et al., 2020), producing the progressive randomization of crystallographic preferred orientations.

This episode of strain localization under nearly isochemical conditions would then have occurred both in presence and in absence of melt, depending on depth intervals in the Hole U1473A, and is proposed to equilibrate at 867 °C and 155 MPa (~5 km of depth) when orthopyroxene and amphibole form.

5.1.3. Fluid-assisted strain localization

The presence of retrograde fluids during deformation is evident in the two ultramylonitic domains 58_5_79_C and 9_5_19_B. In domain 58_5_79_C, it results on the formation of actinolite (Amp_2) in replacement of the former pargasite (Amp_1), or in replacement of Cpx_3 grains formed in C'-like bands within Cpx_2 recrystallized aggregates, and talc after Opx_1 and Ol_2 (Figure 4.17).

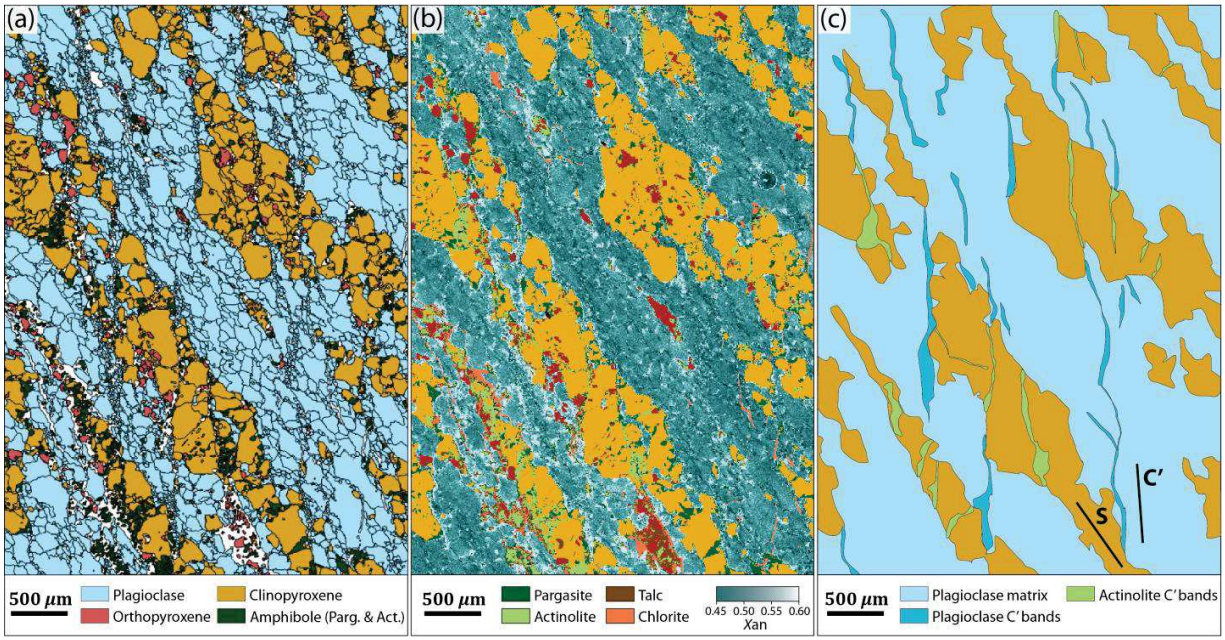

Figure 4.17 *- Strain localization and formation of C' bands in plagioclase and clinopyroxene in domain 58_5_79_C. (a) EBSD phase map. (b) EMPA phase map superimposed by plagioclase Anorthite content map (blue colors). (c) Sketch highlighting the occurrence of C' bands of recrystallized fine-grained Pl_2, prolonged by Actinolite-filled bands in clinopyroxene aggregates. Actinolite is retrograde and likely formed preferentially in these bands through enhanced fluid circulation at fine grain boundaries. S: foliation; C': shear bands of C' orientation. Note that the two generations of amphiboles are differentiated in (b) but not in (a), and that talc and chlorite are represented in the EPMA map (b) in addition to minerals presented in (a) (not indexed at the*

EBSD). The phase map of the whole analyzed area showing the anastomosed organization of these C' bands is provided in Figure S4.6.

An ultimate retrograde stage (in greenschist facies) is recorded in the stability field of chlorite that occurs at orthopyroxene and talc rims, and in microcracks within the plagioclase matrix. This retrograde alteration in the domain explains the lower stability conditions obtained at 782 °C and 132 MPa (4-5 km of depth), at which actinolite is predicted to be stable instead of pargasite similarly as in the interval *69_5_73* and the domain 9_5_19_A. Occurrence of actinolite in thin C' bands within Cpx_2 aggregates (in continuity to C' bands within Pl_2 grains) likely result from a preferential fluid circulation in these fine-grains bands (~20 µm in Cpx_3; Figure 4.17 and Table 4.1).

The ultramylonite 9_5_19_B significantly differs from the other studied deformed domains in the sample suite. The high amount of edenitic amphiboles in the rock (Amp_2; 41%) indicates an important fluid circulation, predicted in a water unsaturated environment, during strain localization. This produced a metasomatism leading to the replacement of former Cpx_1 and high-andesite (An_{46}) Pl_2 grains by edenite (Amp_2) and low-andesite (An_{34}) Pl_3. The very fine grain size (~8 µm) and the loss of CPO in Pl_3 grains together with the inferred fluid circulation strongly suggest granular flow as the main deformation mechanism in the domain (e.g., Boullier & Gueguen, 1975; Stünitz & Fitz Gerald, 1993; Paterson, 1995; Mehl & Hirth, 2008). By contrast, the medium CPO measured in edenitic Amp_2 and their shape preferred orientation indicates an oriented growth (Figures 4.13d and 4.15a). To model the conditions of formation of this plagioclase-amphibole shear zone, we tested the hypothesis of an initiation of strain localization in a domain similar to the neighboring 9_5_19_A (Figure 4.12). This corresponds to a progressive hydration of the rock enhanced by increasing strain and the resulting grain size reduction in minerals. The final composition of the shear zone is encountered at ~700 °C and 100 MPa (~3.5 km), and the model suggests that fluid circulation continued under similar conditions before producing the observed modes. This amphibolite mylonitization episode was already reported by Miranda & John (2010) as a result of retrograde ductile-brittle deformation, and determined at 665 ± 40 °C by mineral thermometry. The origin for these hydrous fluids is most likely hydrothermal as inferred from the observation of black amphibole veins in the upper hundred meters of holes drilled at the Atlantis Bank (Dick et al., 2000, 2019b).

5.1.4. Timing of deformation under HT conditions in the Atlantis Bank oceanic core complex

We propose that the widespread observation of solid-state crystal plastic deformations in Hole U1473A leading to the development of foliated (to porphyroclastic?) microstructures in olivine gabbro with well-defined CPO resulted from far-field forces associated to the ridge spreading

under granulitic conditions (Figure 4.18a). The range of temperature for these deformations is likely comprised between 1260 °C to > 1030 °C, which corresponds to the differentiation and percolation of the primitive melt giving rise to Ti-rich melt as proposed by Boulanger et al. (2020). An anastomosed network of mylonites and ultramylonites formed under similar conditions by focused strain localization (both solid-state and melt-present) associated to weaker CPO. This is proposed to be associated to the capture of the gabbroic pluton by the detachment fault below the ridge axis as a result of asymmetric spreading (Figure 4.18b). The progressive exhumation of the gabbro pluton in the OCC continues with further strain localization through dominant dislocation creep in granulite-amphibolite metamorphic conditions (Figure 4.18c). Locally, seawater penetration within the fractured exhuming crust accompanied strain localization in narrow shear zones cross-cutting higher grade foliations (Figure 4.18d).

Figure 4.18 *- Synthetic summary of the deformation history observed at the Atlantis Bank through Hole U1473A core sections. At each stage from crystallization (a) to retrograde hydrated conditions we propose a schematic cross-section at the ridge axis showing the progressive development of the OCC, a synthetic sketch showing the relations between deformation episodes and melt/fluid circulations, an example of microstructure (EBSD grain map) and plagioclase pole figures, and the associated quantitative chemical map (EPMA combined phase chemical variations map). The depth interval at which deformation structures are observed in the hole is indicated by the orange star and the arrow and brackets along the depth scale. Initial stage after Dick et al. (2019a) and final stage after Baines et al. (2008). See text for details.*

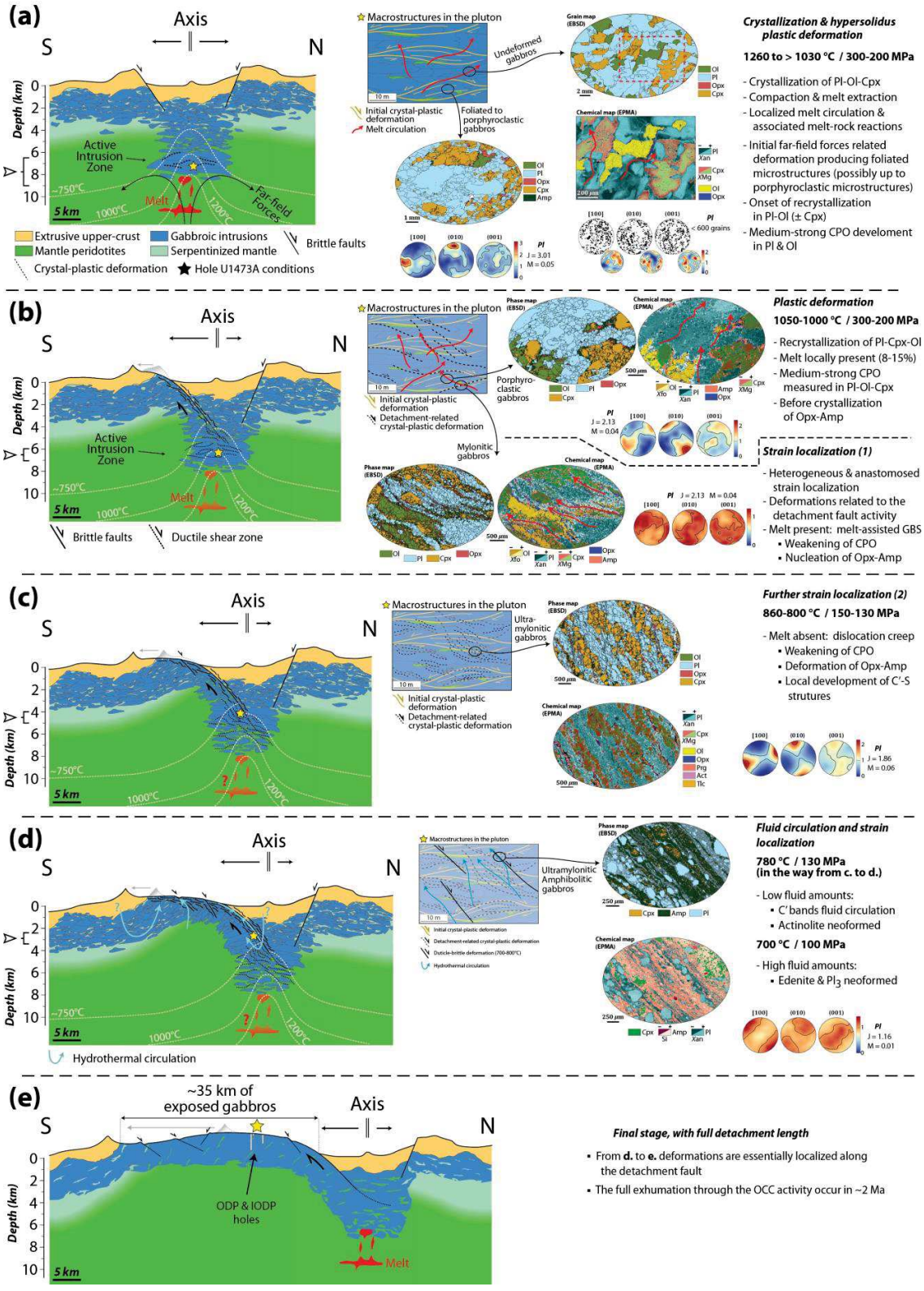
(a)
Axis
S
N
Depth (km)
Active Intrusion Zone
~750°C
1000°C
1200°C
Melt
Far-field Forces
5 km
Extrusive upper-crust
Gabbroic intrusions
Brittle faults
Mantle peridotites
Serpentinized mantle
Crystal-plastic deformation
Hole U1473A conditions
Macrostructures in the pluton
Undeformed gabbros
Foliated to porphyroclastic gabbros
Initial crystal-plastic deformation
Melt circulation
Grain map (EBSD)
Chemical map (EPMA)
Crystallization & hypersolidus plastic deformation
1260 to > 1030 °C / 300-200 MPa
- Crystallization of Pl-Ol-Cpx
- Compaction & melt extraction
- Localized melt circulation & associated melt-rock reactions
- Initial far-field forces related deformation producing foliated microstructures (possibly up to porphyroclastic microstructures)
- Onset of recrystallization in Pl-Ol (± Cpx)
- Medium-strong CPO develoment in Pl & Ol
(b)
Axis
S
N
Depth (km)
Active Intrusion Zone
~750°C
1000°C
1200°C
Melt
5 km
Brittle faults
Ductile shear zone
Macrostructures in the pluton
Initial crystal-plastic deformation
Detachment-related crystal-plastic deformation
Porphyro-clastic gabbros
Mylonitic gabbros
Phase map (EBSD)
Chemical map (EPMA)
Plastic deformation
1050-1000 °C / 300-200 MPa
- Recrystallization of Pl-Cpx-Ol
- Melt locally present (8-15%)
- Medium-strong CPO measured in Pl-Ol-Cpx
- Before crystallization of Opx-Amp
Strain localization (1)
- Heterogeneous & anastomosed strain localization
- Deformations related to the detachment fault activity
- Melt present: melt-assisted GBS
▪ Weakening of CPO
▪ Nucleation of Opx-Amp
(c)
Axis
S
N
Depth (km)
~750°C
1000°C
1200°C
5 km
Macrostructures in the pluton
Ultra-mylonitic gabbros
Initial crystal-plastic deformation
Detachment-related crystal-plastic deformation
Phase map (EBSD)
Chemical map (EPMA)
Further strain localization (2)
860-800 °C / 150-130 MPa
- Melt absent: dislocation creep
▪ Weakening of CPO
▪ Deformation of Opx-Amp
▪ Local development of C'-S strutures
(d)
Axis
S
N
Depth (km)
~750°C
1000°C
1200°C
5 km
Hydrothermal circulation
Macrostructures in the pluton
Ultramylonitic Amphibolitic gabbros
Phase map (EBSD)
Chemical map (EPMA)
Fluid circulation and strain localization
780 °C / 130 MPa
(in the way from c. to d.)
- Low fluid amounts:
▪ C' bands fluid circulation
▪ Actinolite neoformed
700 °C / 100 MPa
- High fluid amounts:
▪ Edenite & Pl3 neoformed
(e)
~35 km of exposed gabbros
Axis
S
N
Depth (km)
ODP & IODP holes
Melt
5 km
Final stage, with full detachment length
▪ From d. to e. deformations are essentially localized along the detachment fault
▪ The full exhumation through the OCC activity occur in ~2 Ma

Figure 4.18

6. Conclusions

Gabbroic lithologies from Hole U1473A display widespread porphyroclastic to ultramylonitic microstructures resulting from successive stages of crystal-plastic deformation. The progressive recrystallization of plagioclase, clinopyroxene, and olivine is associated with well-defined CPO in porphyroclastic to protomylonitic microstructural domains. A primary recrystallization episode is proposed to onset at temperatures > 1030 °C as result of far-field forces. Then recrystallization strongly intensifies to form porphyroclastic to protomylonitic microstructures at ~1000-1050 °C and 200-300 MPa as the detachment fault penetrates the active intrusion zone, and is supported by petrographic evidence and phase equilibrium modeling. At similar conditions, the studied microstructures testify to a melt circulation associated to increasing strain in some depth intervals. Melt-rock reactions led to the formation of secondary plagioclase, olivine, orthopyroxene, and amphibole grains with epitaxial growth, together with a strong weakening of CPO in all minerals through melt-assisted grain boundary sliding. In other depth intervals, crystal-plastic deformation continued under purely solid-state conditions, leading to an intense recrystallization and grain size reduction together with an intragranular strain hardening in plagioclase grains. Medium intensity CPO are measured in plagioclase recrystallized grains while clinopyroxene grains CPO are strongly controlled by the monomineralic banding in which they are measured. Phase equilibrium modeling and the deformation patterns of orthopyroxene and amphibole melt-rock reaction products indicate granulitic conditions for deformation at 867 °C and 155 MPa. An ultimate episode of brittle-ductile deformation in the presence of hydrous fluids resulted in the formation of narrow plagioclase-edenite shear zones. This intense circulation of fluids during strain localization led to the retrograde alteration of clinopyroxene into edenite, and to edenite grain nucleation at plagioclase grain boundaries. CPO measured in plagioclase are random or extremely weak, indicative of fluid-assisted grain boundary sliding. Strain localization in presence of hydrous fluids is predicted stable at ~700 °C and 100 MPa by thermodynamic modeling. The four episodes of deformation identified in this study represent the main HT deformations episodes that occurred at the Atlantis Bank in Hole U1473A as a continuum from hypersolidus conditions resulting from ridge spreading, followed by lower grade granulitic to amphibolitic conditions.

REFERENCES

Allard, M., Ildefonse, B., Oliot, E., Barou, F. (2021). Plastic deformation of plagioclase in oceanic gabbro accreted at a slow-spreading ridge (Hole U1473A, Atlantis Bank, Southwest Indian Ridge). Journal of Geophysical Research: Solid Earth, 126, e2021JB021964. https://doi.org/10.1029/2021JB021964

Baines, A.G., Cheadle, M.J., Dick, H.J.B., Hosford Scheirer, A., John, B.E., Kusznir, N.J., Matsumoto, T., 2003. Mechanism for generating the anomalous uplift of oceanic core

complexes: Atlantis Bank, southwest Indian Ridge. Geology 31, 1105. https://doi.org/10.1130/G19829.1

Baines, A.G., Cheadle, M.J., John, B.E., Schwartz, J.J., 2008. The rate of oceanic detachment faulting at Atlantis Bank, SW Indian Ridge. Earth and Planetary Science Letters 273, 105–114. https://doi.org/10.1016/j.epsl.2008.06.013

Blum, P., Dick, H.J.B., MacLeod, C.J., Expedition 360 Scientists, 2017. Hole U1473A remediation operations, Expedition 362T, Proceedings of the International Ocean Discovery Program. International Ocean Discovery Program. https://doi.org/10.14379/iodp.proc.360.2017

Boulanger, M., France, L., Deans, J.R.L., Ferrando, C., Lissenberg, C.J., von der Handt, A., 2020. Magma Reservoir Formation and Evolution at a Slow-Spreading Center (Atlantis Bank, Southwest Indian Ridge). Frontiers in Earth Science 8, 554598. https://doi.org/10.3389/feart.2020.554598

Boullier, A.M., Gueguen, Y., 1975. SP-Mylonites: Origin of some mylonites by superplastic flow. Contributions to Mineralogy and Petrology 50, 93–104. https://doi.org/10.1007/BF00373329

Bunge, H.J., 1982. Texture Analysis in Materials Science: Mathematical Methods. Butterworths.

Bussod, G.Y., Christie, J.M., 1991. Textural Development and Melt Topology in Spinel Lherzolite Experimentally Deformed at Hypersolidus Conditions. Journal of Petrology Special_Volume, 17–17. https://doi.org/10.1093/petrology/Special_Volume.2.17

Cannat, M., 1991. Plastic deformation at an oceanic spreading ridge: a microstructural study of Site 735 gabbros (southwest Indian Ocean). In: Von Herzen, R., Robinson, P.T., Proceedings of the Ocean Drilling Program, Scientific Results. College Station, TX (Ocean Drilling Program), 399–408.

Connolly, J.A.D., 2009. The geodynamic equation of state: What and how: geodynamic equation of state-what and how. Geochemistry, Geophysics, Geosystems 10, n/a-n/a. https://doi.org/10.1029/2009GC002540

Connolly, J.A.D., 2005. Computation of phase equilibria by linear programming: A tool for geodynamic modeling and its application to subduction zone decarbonation. Earth and Planetary Science Letters 236, 524–541. https://doi.org/10.1016/j.epsl.2005.04.033

Costa, A., Caricchi, L., Bagdassarov, N., 2009. A model for the rheology of particle-bearing suspensions and partially molten rocks. Geochemistry, Geophysics, Geosystems 10, 13. https://doi.org/10.1029/2008GC002138

Dick, H.J.B., Kvassnes, A.J.S., Robinson, P.T., MacLeod, C.J., Kinoshita, H., 2019a. The Atlantis Bank Gabbro Massif, Southwest Indian Ridge. Progress in Earth and Planetary Science 6, 64. https://doi.org/10.1186/s40645-019-0307-9

Dick, H.J.B., MacLeod, C.J., Blum, P., Abe, N., Blackman, D.K., Bowles, J.A., Cheadle, M.J., Cho, K., Ciążela, J., Deans, J.R., Edgcomb, V.P., Ferrando, C., France, L., Ghosh, B., Ildefonse, B., John, B., Kendrick, M.A., Koepke, J., Leong, J.A.M., Liu, C., Ma, Q., Morishita, T., Morris, A., Natland, J.H., Nozaka, T., Pluemper, O., Sanfilippo, A., Sylvan, J.B., Tivey, M.A., Tribuzio, R., Viegas, G., 2019b. Dynamic Accretion Beneath a Slow-Spreading Ridge Segment: IODP Hole 1473A and the Atlantis Bank Oceanic Core Complex. Journal of Geophysical Research 124, 12631–12659. https://doi.org/10.1029/2018JB016858

Dick, H.J.B., Meyer, P.S., Bloomer, S., Kirby, S., Stakes, D., Mawer, C., 1991. Proceedings of the Ocean Drilling Program, 118 Scientific Results, Proceedings of the Ocean Drilling Program. Ocean Drilling Program. https://doi.org/10.2973/odp.proc.sr.118.1991

Dick, H.J.B., Natland, J.H., Alt, J.C., Bach, W., Bideau, D., Gee, J.S., Haggas, S., Hertogen, J.G.H., Hirth, G., Holm, P.M., Ildefonse, B., Iturrino, G.J., John, B.E., Kelley, D.S., Kikawa, E., Kingdon, A., LeRoux, P.J., Maeda, J., Meyer, P.S., Miller, D.J., Naslund, H.R., Niu, Y.-L., Robinson, P.T., Snow, J., Stephen, R.A., Trimby, P.W., Worm, H.-U., Yoshinobu, A., 2000. A long in situ section of the lower ocean crust: results of ODP Leg 176 drilling at the Southwest Indian Ridge. Earth and Planetary Science Letters 179, 31–51. https://doi.org/10.1016/S0012-821X(00)00102-3

Drury, M.R., Urai, J.L., 1990. Deformation-related recrystallization processes. Tectonophysics 172, 235–253. https://doi.org/10.1016/0040-1951(90)90033-5

Fuhrman, M.L., Lindsley, D.H., 1988. Ternary-feldspar modeling and thermometry. American Mineralogist 73, 201–215.

Gao, Y., Hoefs, J., Hellebrand, E., von der Handt, A., Snow, J.E., 2007. Trace element zoning in pyroxenes from ODP Hole 735B gabbros: diffusive exchange or synkinematic crystal fractionation? Contributions to Mineralogy and Petrology 153, 429–442. https://doi.org/10.1007/s00410-006-0158-4

Gao, Y., Hoefs, J., Przybilla, R., Snow, J.E., 2006. A complete oxygen isotope profile through the lower oceanic crust, ODP Hole 735B. Chemical Geology 233, 217–234. https://doi.org/10.1016/j.chemgeo.2006.03.005

Gardner, R.L., Piazolo, S., Daczko, N.R., Trimby, P., 2020. Microstructures reveal multistage melt present strain localisation in mid-ocean gabbros. Lithos 366–367, 105572. https://doi.org/10.1016/j.lithos.2020.105572

Getsinger, A.J., Hirth, G., Stünitz, H., Goergen, E.T., 2013. Influence of water on rheology and strain localization in the lower continental crust: Water, Rheology, and Strain Localization. Geochemistry, Geophysics, Geosystems 14, 2247–2264. https://doi.org/10.1002/ggge.20148

Gillis, K.M., Meyer, P.S., 2001. Metasomatism of oceanic gabbros by late stage melts and hydrothermal fluids: Evidence from the rare earth element composition of amphiboles. Geochemistry, Geophysics, Geosystems 2, 30. https://doi.org/10.1029/2000GC000087

Green, E.C.R., White, R.W., Diener, J.F.A., Powell, R., Holland, T.J.B., Palin, R.M., 2016. Activity-composition relations for the calculation of partial melting equilibria in metabasic rocks. Journal of Metamorphic Geology 34, 845–869. https://doi.org/10.1111/jmg.12211

Hirth, G., Kohlstedt, D.L., 1995. Experimental constraints on the dynamics of the partially molten upper mantle: Deformation in the diffusion creep regime. Journal of Geophysical Research: Solid Earth 100, 1981–2001. https://doi.org/10.1029/94JB02128

Holland, T.J.B., Blundy, J., 1994. Non-ideal interactions in calcic amphiboles and their bearing on amphibole-plagioclase thermometry. Contributions to Mineralogy and Petrology 116, 433–447. https://doi.org/10.1007/BF00310910

Holland, T.J.B., Powell, R., 2011. An improved and extended internally consistent thermodynamic dataset for phases of petrological interest, involving a new equation of state for solids. Journal of Metamorphic Geology 29, 333–383. https://doi.org/10.1111/j.1525-1314.2010.00923.x

Holland, T.J.B., Powell, R., 1998. An internally consistent thermodynamic data set for phases of petrological interest. Journal of Metamorphic Geology 16, 309–343. https://doi.org/10.1111/j.1525-1314.1998.00140.x

Hosford, A., Tivey, M., Matsumoto, T., Dick, H., Schouten, H., Kinoshita, H., 2003. Crustal magnetization and accretion at the Southwest Indian Ridge near the Atlantis II fracture

zone, 0-25 Ma. Journal of Geophysical Research: Solid Earth 108. https://doi.org/10.1029/2001JB000604

Kruse, R., Stünitz, H., Kunze, K., 2001. Dynamic recrystallization processes in plagioclase porphyroclasts. Journal of Structural Geology 23, 1781–1802. https://doi.org/10.1016/S0191-8141(01)00030-X

Kvassnes, A.J.S., Robinson, P.T., MacLeod, C.J., Kinoshita, H., Dick, H.J.B., 2019. The Atlantis Bank Gabbro Massif, Southwest Indian Ridge. Progress in Earth and Planetary Science 6, 70. https://doi.org/10.1186/s40645-019-0307-9

Lanari, P., Duesterhoeft, E., 2019. Modeling Metamorphic Rocks Using Equilibrium Thermodynamics and Internally Consistent Databases: Past Achievements, Problems and Perspectives. Journal of Petrology 60, 19–56. https://doi.org/10.1093/petrology/egy105

Lanari, P., Engi, M., 2017. Local Bulk Composition Effects on Metamorphic Mineral Assemblages. Reviews in Mineralogy and Geochemistry 83, 55–102. https://doi.org/10.2138/rmg.2017.83.3

Lanari, P., Hermann, J., 2021. Iterative thermodynamic modelling—Part 2: Tracing equilibrium relationships between minerals in metamorphic rocks. Journal of Metamorphic Geology 39, 651–674. https://doi.org/10.1111/jmg.12575

Lanari, P., Riel, N., Guillot, S., Vidal, O., Schwartz, S., Pêcher, A., Hattori, K.H., 2013. Deciphering high-pressure metamorphism in collisional context using microprobe mapping methods: Application to the Stak eclogitic massif (northwest Himalaya). Geology 41, 111–114. https://doi.org/10.1130 / g33523.1

Lanari, P., Vho, A., Bovay, T., Airaghi, L., Centrella, S., 2019. Quantitative compositional mapping of mineral phases by electron probe micro-analyser. Geological Society, London, Special Publications 478, 39–63. https://doi.org/10.1144/SP478.4

Lanari, P., Vidal, O., De Andrade, V., Dubacq, B., Lewin, E., Grosch, E.G., Schwartz, S., 2014. XMapTools: A MATLAB®-based program for electron microprobe X-ray image processing and geothermobarometry. Computers & Geosciences 62, 227–240. https://doi.org/10.1016/j.cageo.2013.08.010

Leake, B.E., Woolley, A.R., Arps, A.R., Birch, W.D., Gilbert, M.C., Grice, J.D., Hawthorne, F.C., Kato, A., Kisch, H.J., Krivovichev, V.G., Linthout, K., Laird, J., Mandarino, J.A., Maresch, W.V., Nickel, E.H., Rock, N.M.S., Schumacher, J.C., Smith, D.C., Stephenson, N.C.N., Ungaretti, L., Whittaker, E.J.W., Youzhi, G., 1997. Nomenclature of amphiboles Report of the Subcommittee on Amphiboles of the International Mineralogical Association Commission on New Minerals and Mineral Names. The Canadian Mineralogist 35, 219–246.

Lissenberg, C.J., MacLeod, C.J., 2016. A Reactive Porous Flow Control on Mid-ocean Ridge Magmatic Evolution. Journal of Petrology 57, 2195–2220. https://doi.org/10.1093/petrology/egw074

Llorens, M.-G., Gomez-Rivas, E., Ganzhorn, A.-C., Griera, A., Steinbach, F., Roessiger, J., Labrousse, L., Walte, N.P., Weikusat, I., Bons, P.D., 2019. The effect of dynamic recrystallisation on the rheology and microstructures of partially molten rocks. Journal of Structural Geology 118, 224–235. https://doi.org/10.1016/j.jsg.2018.10.013

MacLeod, C.J., Dick, H.J.B., Blum, P., Expedition 360 Scientists, 2017a. Site U1473A, Proceedings of the International Ocean Discovery Program. International Ocean Discovery Program. https://doi.org/10.14379/iodp.proc.360.2017

MacLeod, C.J., Dick, H.J.B., Blum, P., Expedition 360 Scientists, 2017b. Expedition 360 methods, Proceedings of the International Ocean Discovery Program. International Ocean Discovery Program. https://doi.org/10.14379/iodp.proc.360.2017

Mainprice, D., Bachmann, F., Hielscher, R., Schaeben, H., 2015. Descriptive tools for the analysis of texture projects with large datasets using MTEX : strength, symmetry and components. Geological Society, London, Special Publications 409, 251–271. https://doi.org/10.1144/SP409.8

Mehl, L., Hirth, G., 2008. Plagioclase preferred orientation in layered mylonites: Evaluation of flow laws for the lower crust. Journal of Geophysical Research 113, B05202. https://doi.org/10.1029/2007JB005075

Miranda, E.A., John, B.E., 2010. Strain localization along the Atlantis Bank oceanic detachment fault system, Southwest Indian Ridge. Geochemistry, Geophysics, Geosystems 11, 34. https://doi.org/10.1029/2009GC002646

Morimoto, N., 1988. Nomenclature of Pyroxenes. Mineralogy and Petrology 39, 55–76. https://doi.org/10.1007/BF01226262

Nozaka, T., Akitou, T., Abe, N., Tribuzio, R., 2019. Biotite in olivine gabbros from Atlantis Bank: Evidence for amphibolite-facies metasomatic alteration of the lower oceanic crust. Lithos 348–349, 105176. https://doi.org/10.1016/j.lithos.2019.105176

Paterson, M.S., 2001. A granular flow theory for the deformation of partially molten rock. 335, 51–61. https://doi.org/10.1016/S0040-1951(01)00045-2

Paterson, M.S., 1995. A theory for granular flow accommodated by material transfer via an intergranular fluid. Tectonophysics 245, 135–151. https://doi.org/10.1016/0040-1951(94)00231-W

Pettigrew, T., Casey, J., Miller, D., Araki, E., Boissonnas, R., Busby, R., Einaudi, F., Gerdom, M., Guo, Z., Hopkins, H., 1999. Leg 179 summary. ODP, Texas A and M Univ., USA.

Picard, D., Arbaret, L., Pichavant, M., Champallier, R., Launeau, P., 2013. The rheological transition in plagioclase-bearing magmas: rheological transition in magmas. Journal of Geophysical Research: Solid Earth 118, 1363–1377. https://doi.org/10.1002/jgrb.50091

Poirier, J.-P., Guillopé, M., 1979. Deformation induced recrystallization of minerals. Bulletin de Minéralogie 102, 67–74. https://doi.org/10.3406/bulmi.1979.7256

Qi, C., Hansen, L.N., Wallis, D., Holtzman, B.K., Kohlstedt, D.L., 2018. Crystallographic Preferred Orientation of Olivine in Sheared Partially Molten Rocks: The Source of the "a-c Switch." Geochemistry, Geophysics, Geosystems 19, 316–336. https://doi.org/10.1002/2017GC007309

Ryan, W.B.F., Carbotte, S.M., Coplan, J.O., O'Hara, S., Melkonian, A., Arko, R., Weissel, R.A., Ferrini, V., Goodwillie, A., Nitsche, F., Bonczkowski, J., Zemsky, R., 2009. Global Multi-Resolution Topography synthesis: global multi-resolution topography synthesis. Geochemistry, Geophysics, Geosystems 10, n/a-n/a. https://doi.org/10.1029/2008GC002332

Sanfilippo, A., MacLeod, C.J., Tribuzio, R., Lissenberg, C.J., Zanetti, A., 2020. Early-Stage Melt-Rock Reaction in a Cooling Crystal Mush Beneath a Slow-Spreading Mid-Ocean Ridge (IODP Hole U1473A, Atlantis Bank, Southwest Indian Ridge). Frontiers in Earth Science 8, 579138. https://doi.org/10.3389/feart.2020.579138

Schulmann, K., Martelat, J.-E., Ulrich, S., Lexa, O., Štípská, P., Becker, J.K., 2008. Evolution of microstructure and melt topology in partially molten granitic mylonite: Implications for rheology of felsic middle crust. Journal of Geophysical Research 113, B10406. https://doi.org/10.1029/2007JB005508

Shelley, D., 1994. Spider texture and amphibole preferred orientations. Journal of Structural Geology 16, 709–717. https://doi.org/10.1016/0191-8141(94)90120-1

Skemer, P., Katayama, I., Jiang, Z., Karato, S., 2005. The misorientation index: Development of a new method for calculating the strength of lattice-preferred orientation. Tectonophysics 411, 157–167. https://doi.org/10.1016/j.tecto.2005.08.023

Stuart, C.A., Meek, U., Daczko, N.R., Piazolo, S., Huang, J.-X., 2018. Chemical Signatures of Melt–Rock Interaction in the Root of a Magmatic Arc. Journal of Petrology 59, 321–340. https://doi.org/10.1093/petrology/egy029

Stünitz, H., Fitz Gerald, J.D., 1993. Deformation of granitoids at low metamorphic grade. II: Granular flow in albite-rich mylonites. Tectonophysics 221, 299–324. https://doi.org/10.1016/0040-1951(93)90164-F

Taufner, R., Viegas, G., Faleiros, F.M., Castellan, P., Silva, R., 2021. Deformation mechanisms of granulite-facies mafic shear zones from hole U1473A, Atlantis Bank, Southwest Indian Ridge (IODP Expedition 360). Journal of Structural Geology 149, 104380. https://doi.org/10.1016/j.jsg.2021.104380

Urai, J.L., Means, W.D., Lister, G.S., 1986. Dynamic recrystallization of minerals. In: Hobbs, B.E., Heard, H.C. (Eds.), Geophysical Monograph Series. American Geophysical Union, Washington, D. C., 161–199. https://doi.org/10.1029/GM036p0161

White, R.W., Powell, R., Clarke, G.L., 2002. The interpretation of reaction textures in Fe-rich metapelitic granulites of the Musgrave Block, central Australia: constraints from mineral equilibria calculations in the system K2O-FeO-MgO-Al2O3-SiO2-H2O-TiO2-Fe2O3. Journal of Metamorphic Geology 20, 41–55. https://doi.org/10.1046/j.0263-4929.2001.00349.x

White, R.W., Powell, R., Holland, T.J.B., Johnson, T.E., Green, E.C.R., 2014. New mineral activity-composition relations for thermodynamic calculations in metapelitic systems. Journal of Metamorphic Geology 32, 261–286. https://doi.org/10.1111/jmg.12071

White, R.W., Powell, R., Holland, T.J.B., Worley, B.A., 2000. The effect of TiO2 and Fe2O3 on metapelitic assemblages at greenschist and amphibolite facies conditions, mineral equilibria calculations in the system K2O-FeO-MgO-Al2O3-SiO2-H2O-TiO2-Fe2O3. Journal of Metamorphic Geology 18, 497–511. https://doi.org/10.1046/j.1525-1314.2000.00269.x

Whitney, D.L., Evans, B.W., 2010. Abbreviations for names of rock-forming minerals. American Mineralogist 95, 185–187. https://doi.org/10.2138/am.2010.3371

ANNEXES

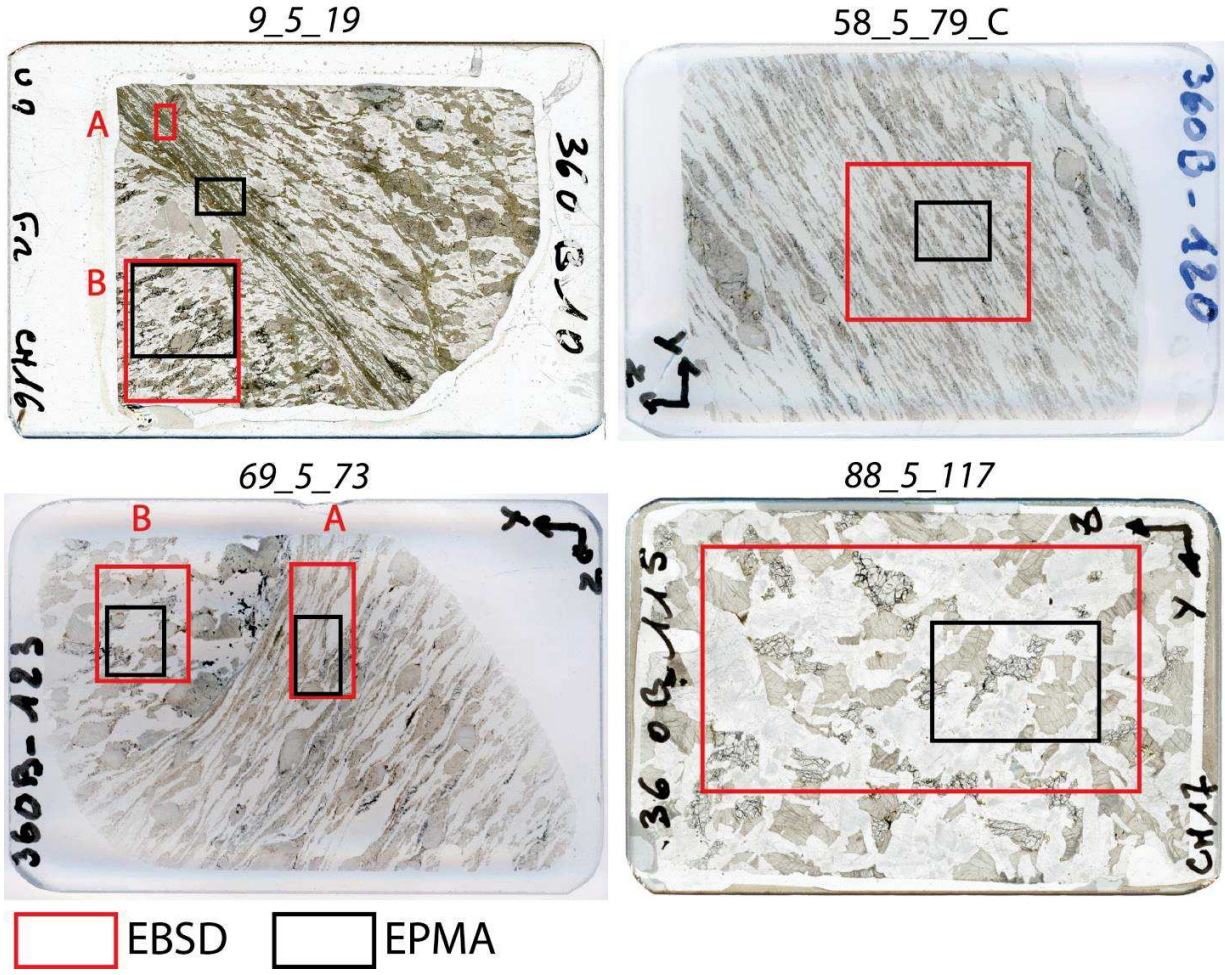

Figure S4.1 *- Thin section microphotographs and location of quantitative maps (EBSD and EPMA.*

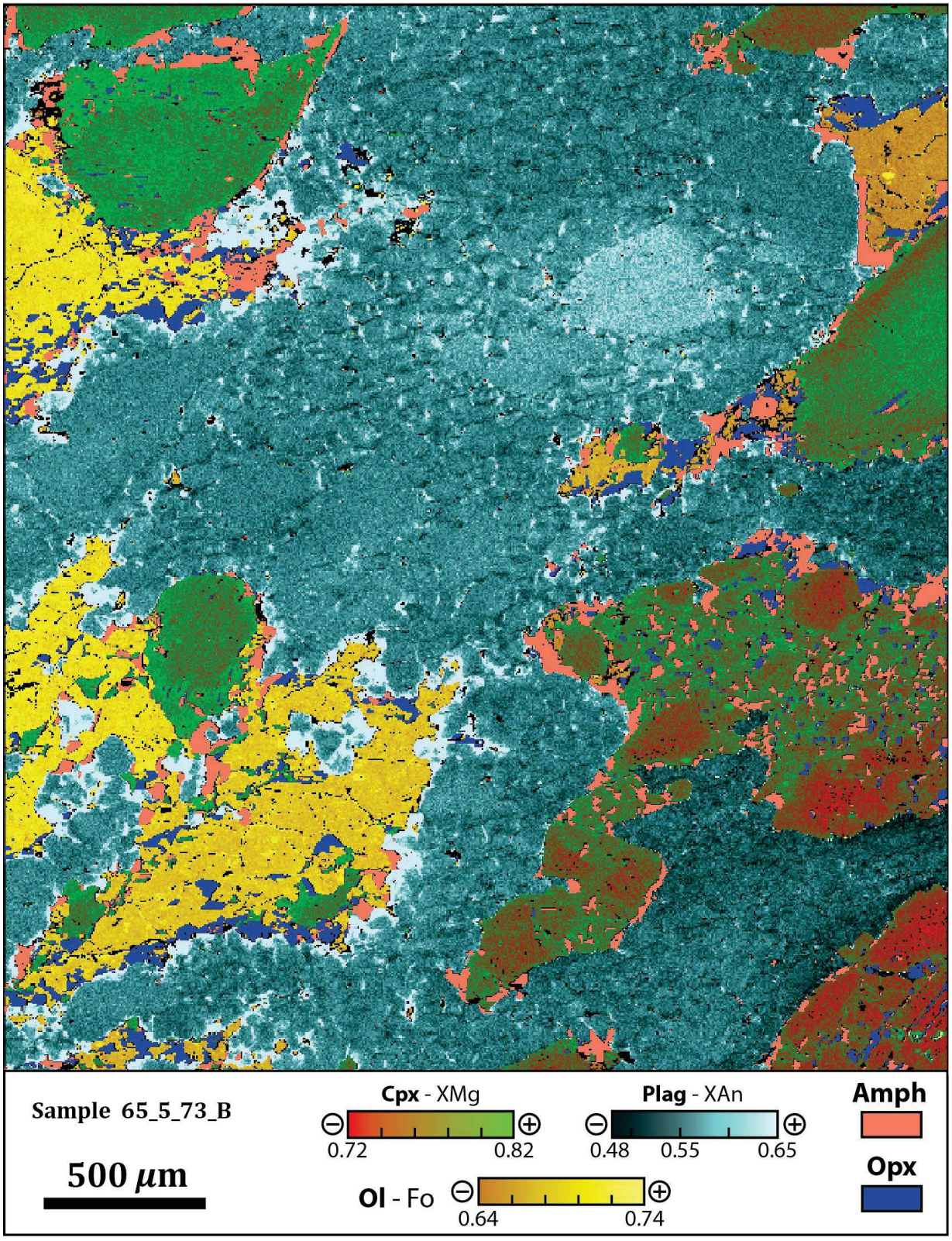

Figure S4.2 - *Compiled quantitative composition map sample 65_5_73_B.*

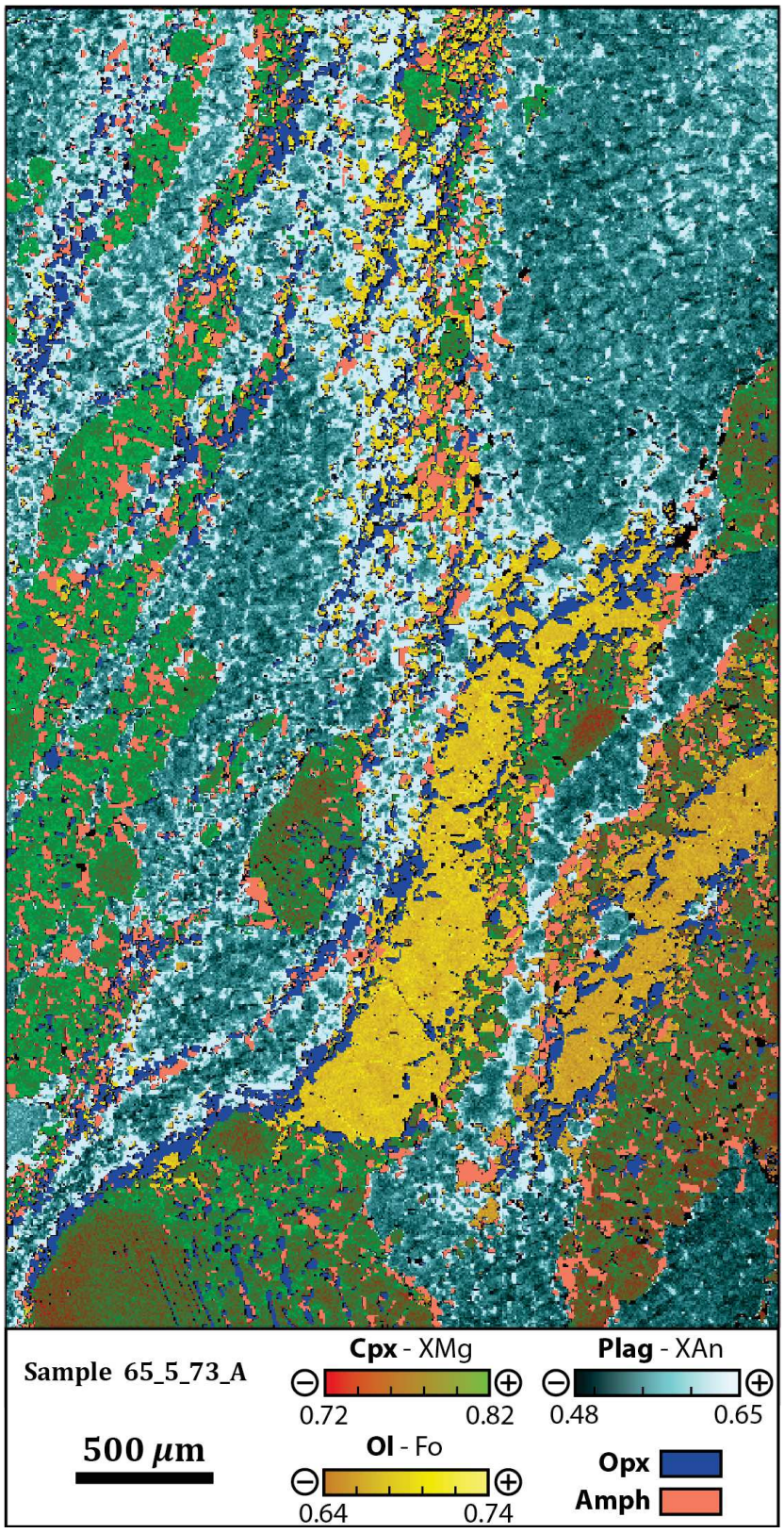

Figure S4.3 *- Compiled quantitative composition map sample 65_5_73_A.*

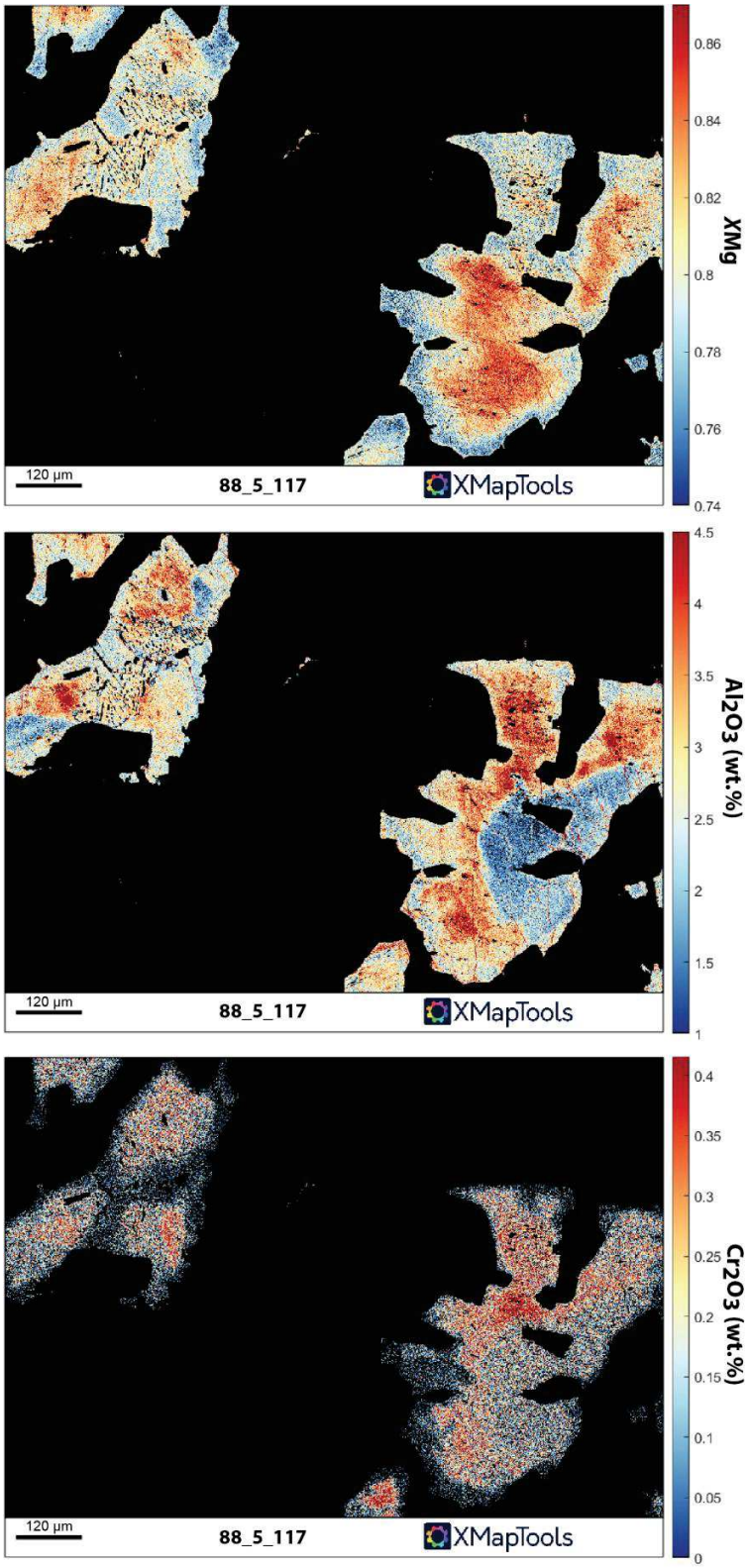

Figure S4.4 *- Quantitative chemical maps in clinopyroxene grains from the studied samples.*

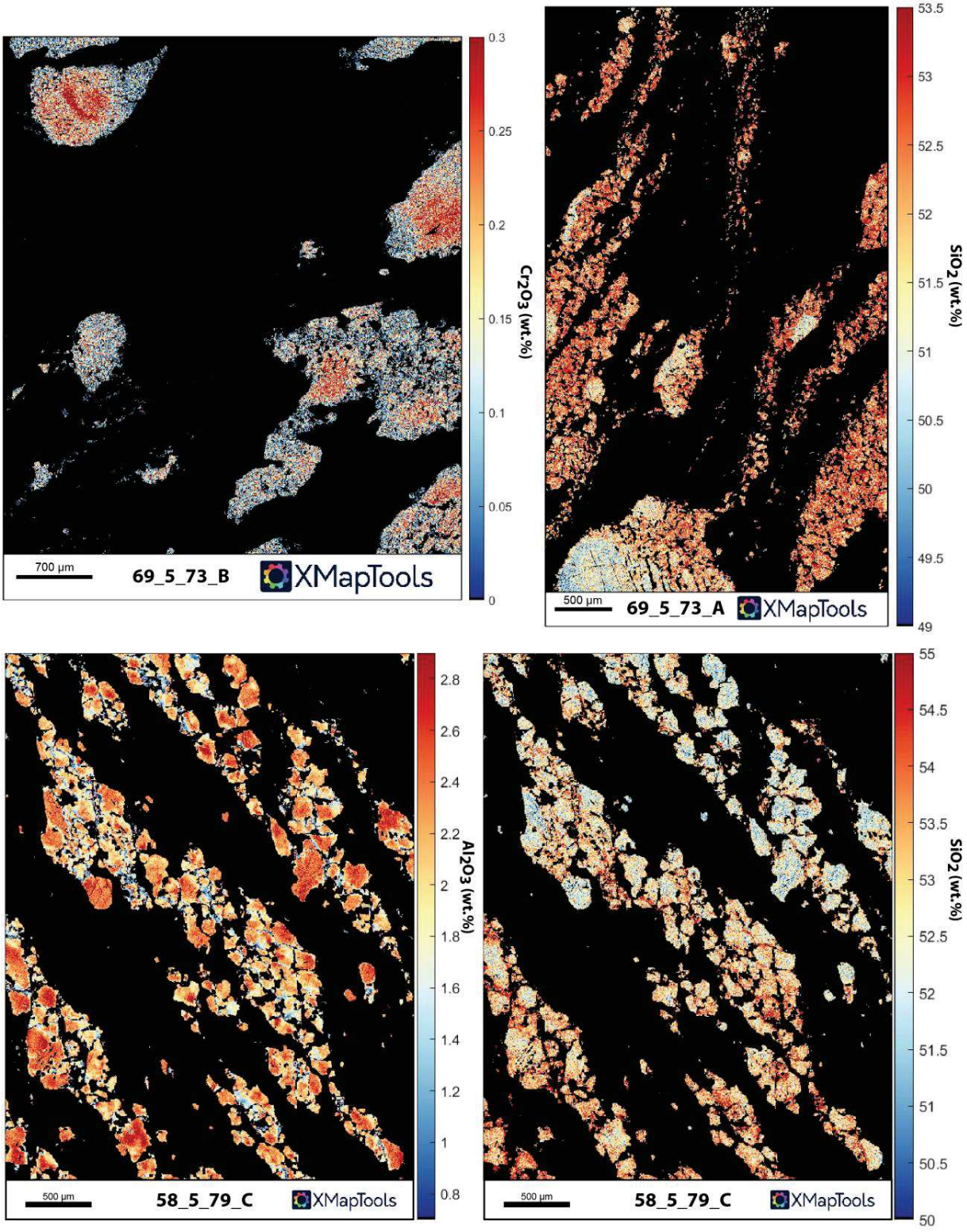

Figure S4.4 (continued)

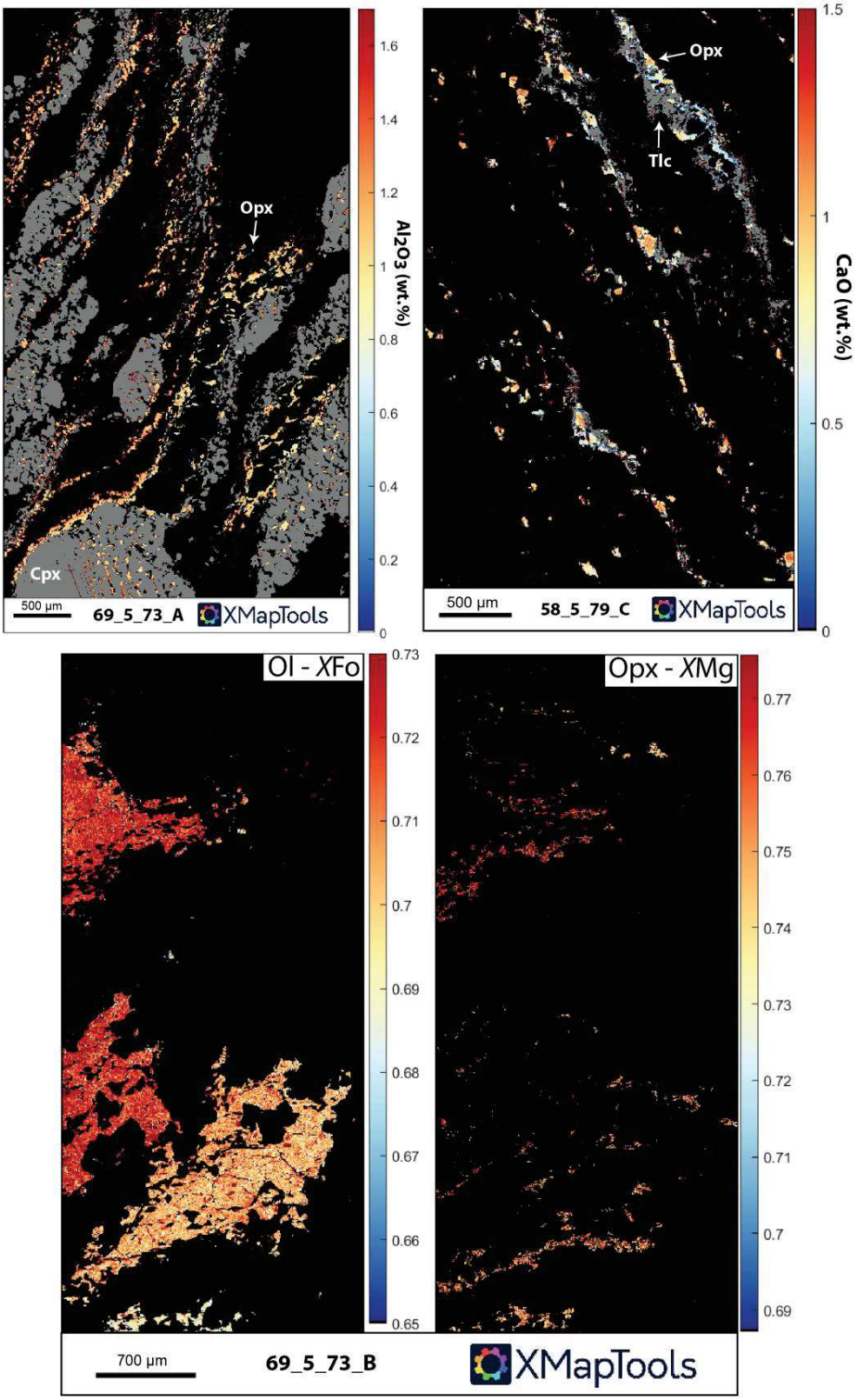

Figure S4.5 *- Quantitative chemical maps in orthopyroxene grains from the studied samples.*

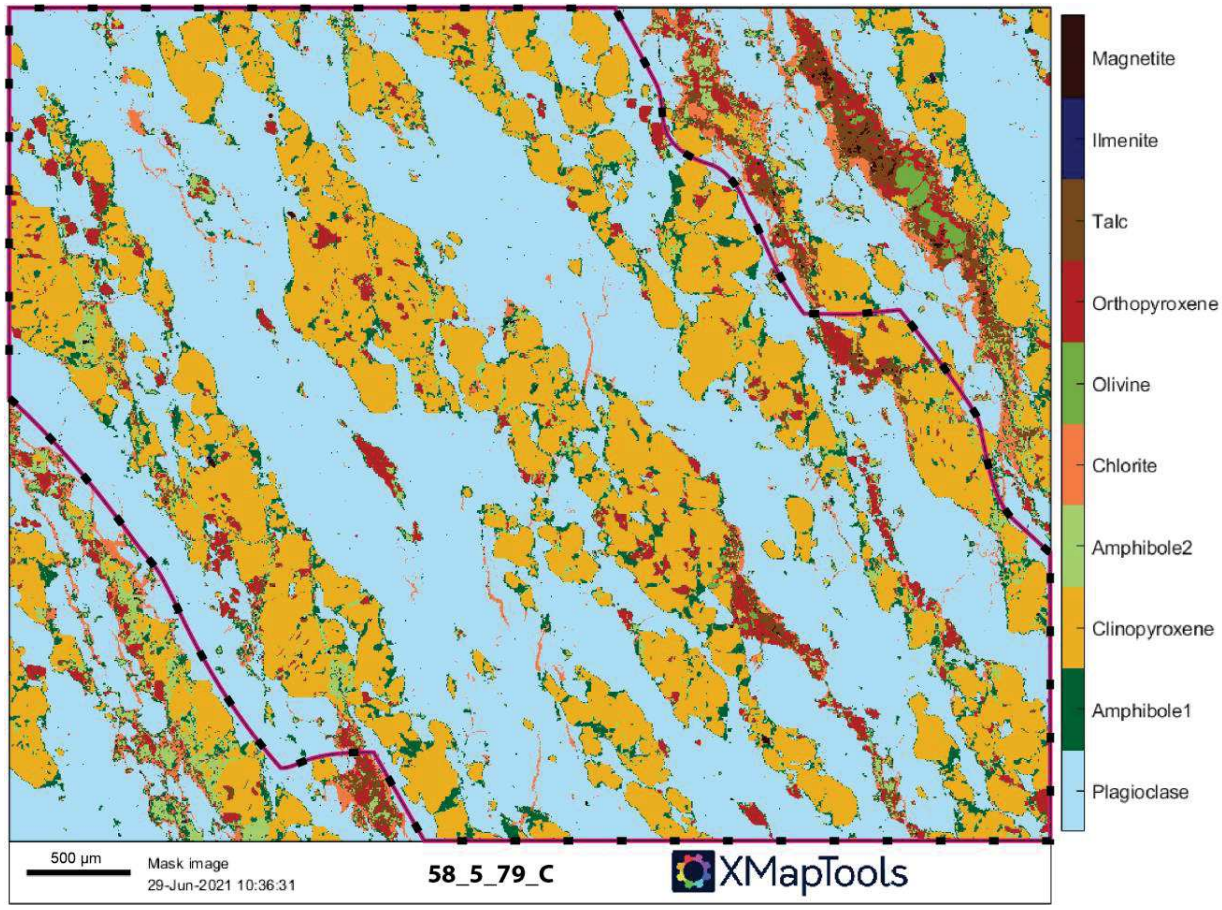

Figure S4.6 *- Sub-region selected for bulk composition extraction in sample 58_5_79_C and used in thermodynamic modeling. Amphibole1 and amphibole2 refer to pargasite and actinolite, respectively.*

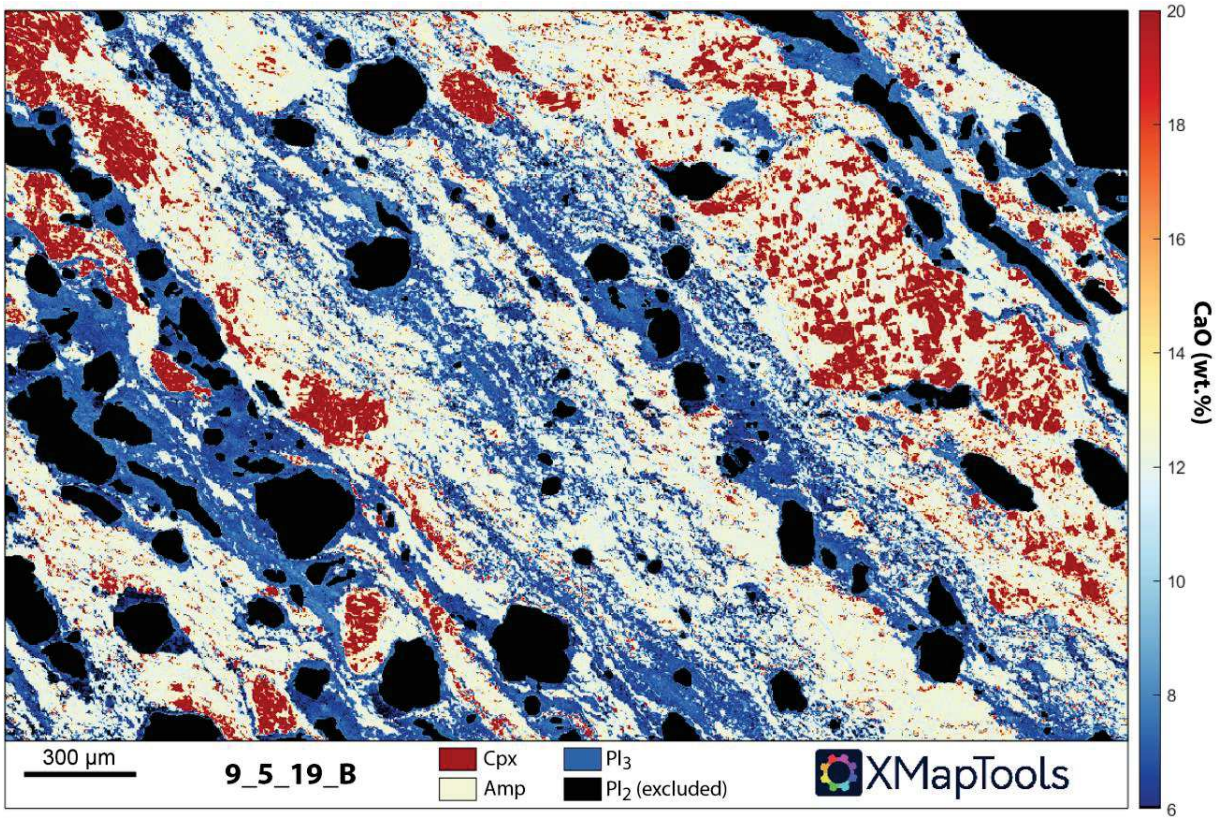

Figure S4.7 *- Sub-region selected for bulk composition extraction in sample 58_5_79_C and used in thermodynamic modeling. Note that most of the selection consists of the removing of Ca-rich plagioclase porphyroclasts.*

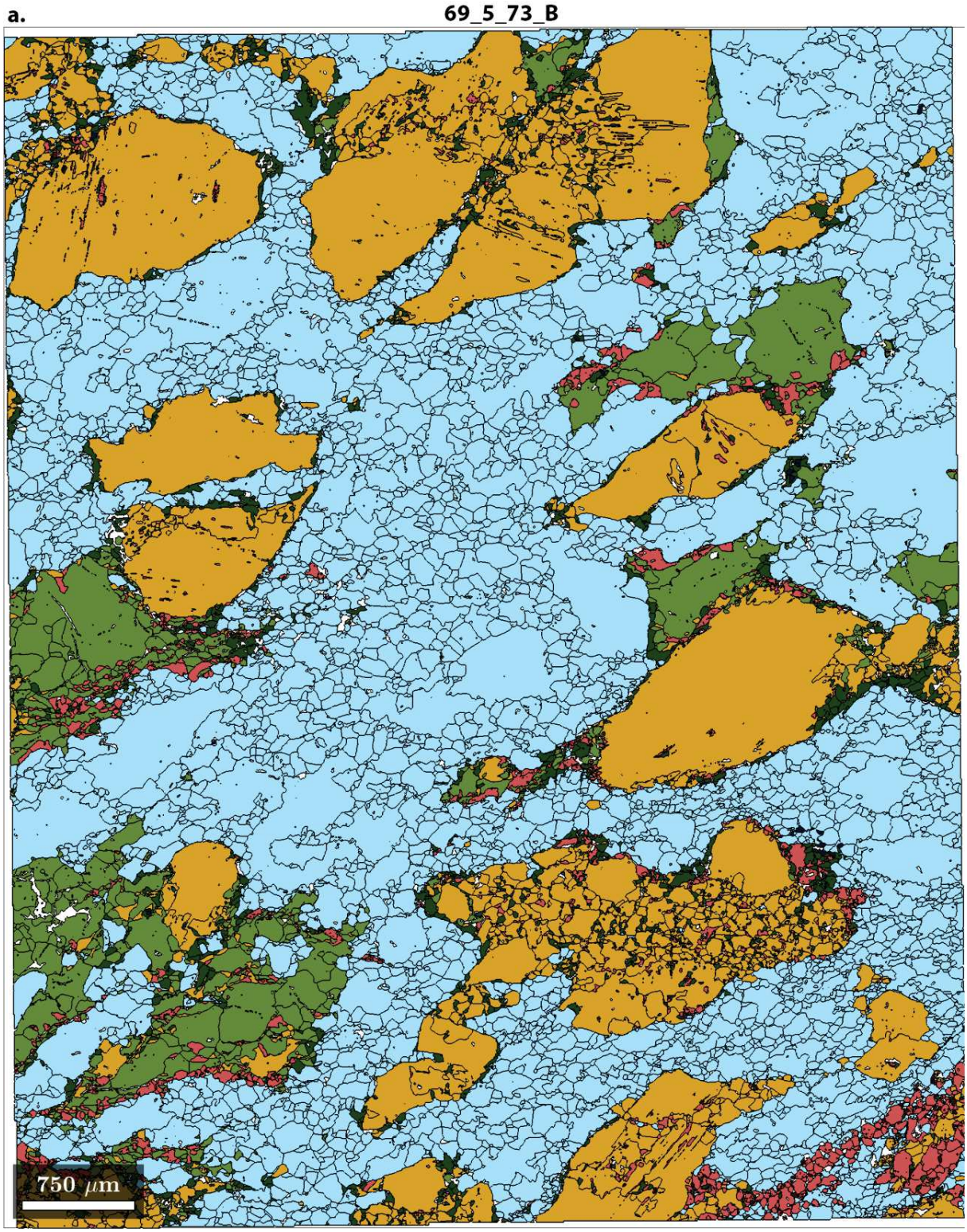

Figure S4.8 *- EBSD phase maps of the studied domains.*

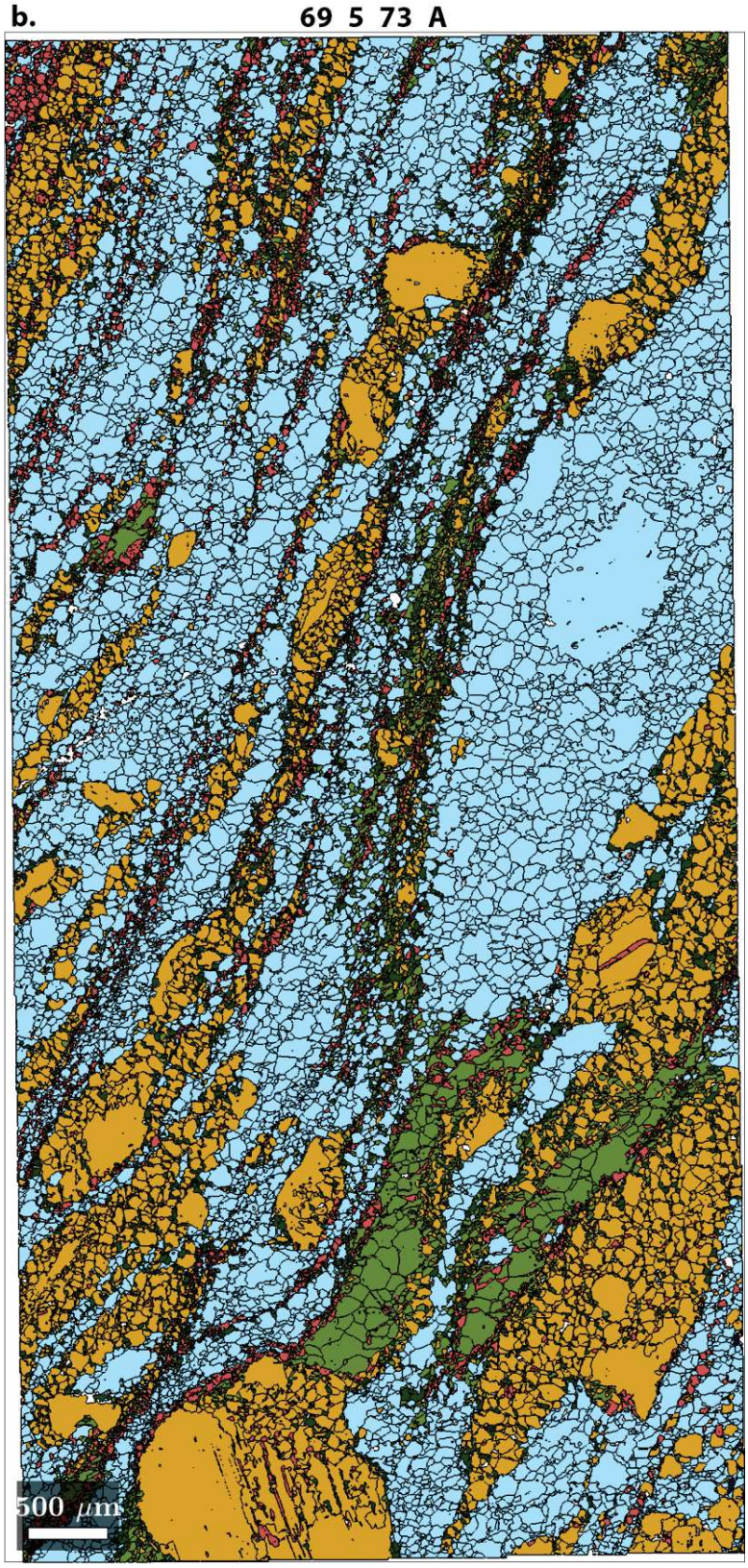

Figure S4.8 (continued)

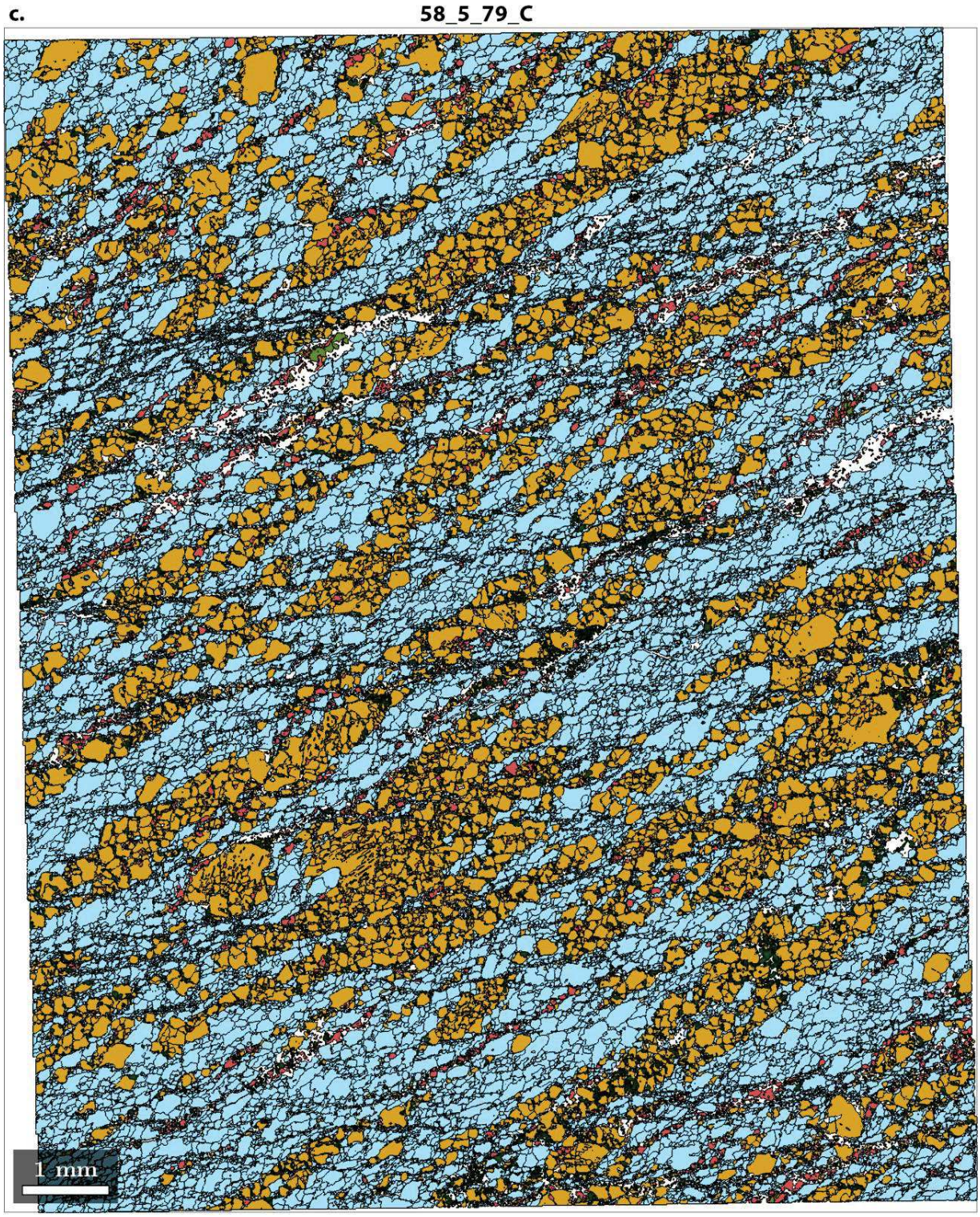

Figure S4.8 (continued)

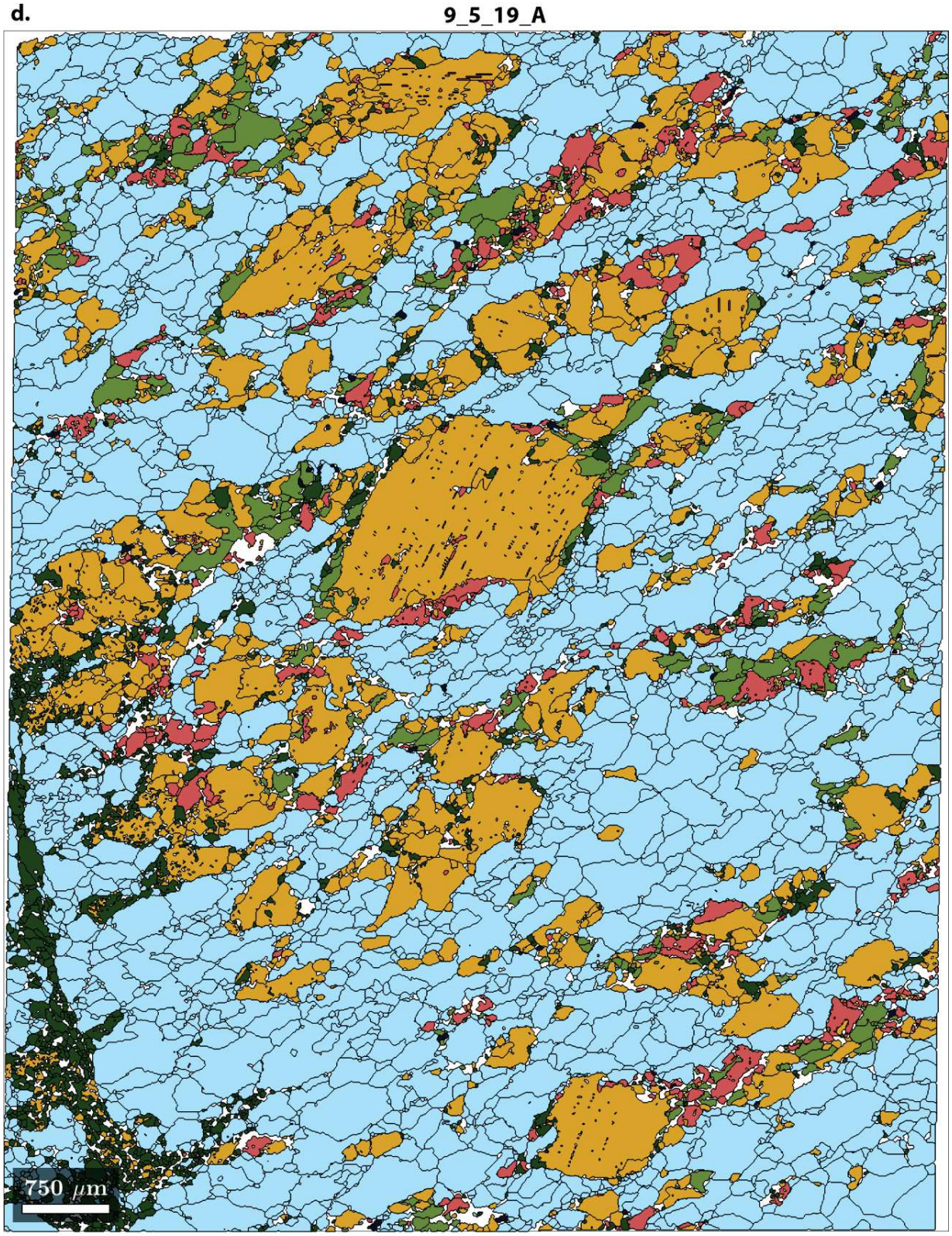

Figure S4.8 (continued)

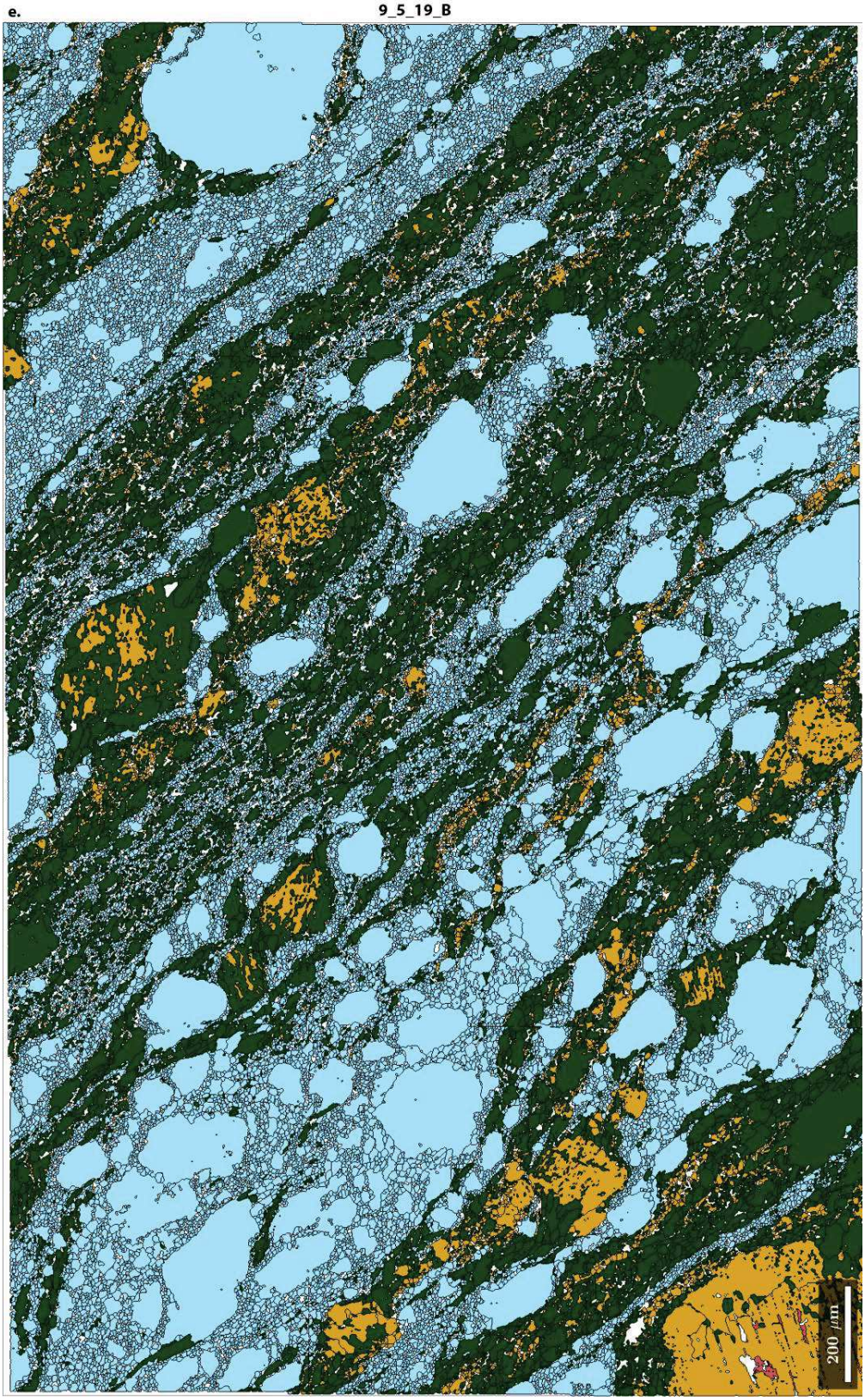

Figure S4.8 (continued)

Table S4.1 *- Parameters of acquisition for quantitative maps.*

	69_5_73_A	**69_5_73_B**	**9_5_19_A**	**9_5_19_B**	**88_5_117**	**58_5_79_C**
EBSD						
Step size	3 µm	3.7 µm	11 µm	1.6 µm	20 µm	5 µm
Field width	1552 px	1733 px	735 px	1774 px	1599 px	2733 px
Field height	3210 px	2164 px	934 px	1113 px	920 px	2242 px
Acquisition time	7.0 ms	7.0 ms	24.4 ms	24.4 ms	7.0 ms	7.0 ms
Indexation rate	95.3 %	96.4 %	94.5 %	93.1 %	97.0 %	91.7 %
EPMA						
Step size	5 µm	7 µm	10 µm	3 µm	12 µm	5 µm
Field width	600 px	600 px	700 px	1000 px	1000 px	1000 px
Field height	1024 px	678 px	600 px	650 px	700 px	800 px

CHAPTER VI

THE BRACCO-GABBRO COMPLEX: A TETHYSIAN EXAMPLE OF DETACHMENT FAULTING AT SLOW-SPREADING RIDGE (INTERNAL LIGURIDES, NORTHERN APENNINES)

Foreword: ***This chapter aims at drawing comparisons between the Bracco-Gabbro complex, an ancient oceanic core complex, and a modern one studied in the previous chapters, the Atlantis Bank. This is performed through field work, structural analyses and petro-geochemical analyses to characterize the type and distribution of structures encountered at the scale of an entire gabbro massif. Ideas developed in this preliminary version of an article will be further discussed later in the version that will be submitted for publication. Furthermore, it will be complemented by thermodynamic modeling for more accurate temperature, pressure, and fluid conditions estimates.***

1. Introduction

The study of ophiolites provides easily accessible analogue observations to modern mid-ocean ridges. It offers the opportunity to investigate in details the tectono-magmatic processes operating at spreading axes. The Bracco-Gabbro Complex (BGC) is one of the largest ophiolitic sequences exposed in the Internal Ligurides (Northern Apennines; e.g., Marroni et al., 1998). It corresponds to a preserved portion of the Jurassic slow-spreading Western Tethys exhumed on the seafloor within an Oceanic Core Complex (OCC; e.g., Menna, 2009). The gabbro pluton which constitutes the core of this complex exposes heterogeneously distributed magmatic foliations and layering, and highly localized granulitic shear zones (e.g., Molli, 1994, 1996; Menna, 2009). Previous studies proposed that the genesis of these structures is coeval, and that the whole deformation history, from granulitic to greenschist conditions, developed continuously during the OCC formation. Although the sets of structures observed in the complex have been extensively studied (e.g., Molli, 1994, 1996; Menna, 2009), the detailed analysis of the deformation mechanisms in high-grade shear zones is lacking.

The study presented here is intended to complement the characterization of high-grade shear zones of the Bracco complex, and to compare their nature to those exposed at modern oceanic ridges. We selected seven gabbro samples representative of the deformed structures observed on the field, with textures ranging from porphyroclastic to ultramylonitic. An end-member sample representative of the low-grade structures, widespread in the complex was also selected. Petrographic and microstructural analyses were performed in these samples through Electron Probe Micro-Analyses (EPMA) and Electron Backscatter Diffraction (EBSD) analyses, respectively. These measurements aim at providing insights on the deformation mechanisms operating during the formation of these structures, and on the temperature at which they occur.

2. Geological setting

2.1. The Alp-Apennine system and the Ligurian ophiolites

The northern and western Mediterranean domains of the Alp-Apennine belt expose several Jurassic oceanic remnants of the Alpine Tethys. This Alp-Apennine belt contains sedimentary

and ophiolitic sequences belonging to this ancient ocean separating the European and African plates (dark green in Figure 5.1a; e.g., Bortolotti et al., 2001). In the Northern Apennine, ophiolites are part of the Ligurian unit consisting of a stack of tectonic slices from continental and oceanic domains. The typical stratigraphy of these Ligurian ophiolites consists of ultramafic lithologies intruded by large gabbro or gabbronorite bodies, heterogeneously covered by pillow lavas or sediments, and frequent ophiolitic breccia are found on top (e.g., Barrett & Spooner, 1977; Lemoine et al., 1987; Lagabrielle, 2009). The Ligurian unit is divided in two tectono-stratigraphic groups based on their origin: the External Ligurides of continental origin, and the Internal Ligurides of oceanic origin (Figure 5.1a; Marroni et al., 1998). The External Ligurides include calcareous sequences and ophiolitic lithologies occurring as slide blocks (olistoliths of mantle or basalt lava sequences, rare gabbros and pelagic sediments). The ultramafics are proposed to correspond to a portion of sub-continental mantle at the ocean-continent transition later exposed during thinning by continental rifting (Beccaluva et al., 1984; reviewed in Piccardo & Guarnieri, 2010). The Internal Ligurides are composed of ophiolites (serpentinized mantle peridotites, gabbros, and basalts) and the overlying pelagic sediments associated with turbidites. Depleted peridotites composing these ophiolites indicate similarities with abyssal peridotites, and are interpreted to form by MORB-type melting after asthenospheric upwelling before being cooled and accreted to the oceanic lithosphere (e.g., Rampone et al., 1996, 1997). This Internal Ligurides sequence is composed of three main tectonic units that mostly outcrop in Eastern Liguria (Decandia & Elter, 1972; Abbate et al., 1980; Marroni & Pandolfi, 2001): the Gottero unit, the Colli-Tavarone unit, and the Bracco/Val Graveglia unit (Figure 5.1b). Both Colli-Tavarone and Gottero units mostly consists of sedimentary sequences, while the Bracco/Val Graveglia unit corresponds to a preserved ophiolite with its sedimentary cover. The Internal Ligurides are characterized by a thin crustal section mainly composed of mantle peridotites and gabbros, no sheeted dike complex, overlying pillow lavas and sediments, and breccia; they resemble the crust encountered at slow- and ultraslow-spreading ridges (e.g., Cannat, 1993; Dick et al., 2003; Escartín & Canales, 2011). Lagabrielle & Cannat (1990) proposed that the exposure of mantle and lower crust lithologies were exhumed during extension at a slow-spreading ridge. More recently, other remnants of slow-spreading ridge architecture were recognized in ophiolites, particularly in the Alpine Tethys (e.g., Manatschal et al., 2011; Lagabrielle et al., 2015; Decrausaz et al., 2021).

In terms of deformation, the Internal Ligurides recorded an original high-temperature (HT) metamorphic event associated with deep crustal lithologies uplifted to the seafloor. This was followed by normal/transform faulting before the pillow basalt emplacement and sedimentary deposit. Then, orogenic deformation overprinted the latter forming NE dipping large folds and thrusts during Cretaceous to Paleocene. In the NW part of the Internal Ligurides, the pre- to

middle-Eocene tectonic was recorded and consists of folding in association to a very low grade metamorphism (e.g., Bortolotti et al., 2001).

2.2. The Bracco-Gabbro Complex

The BGC belongs to the Internal Ligurides, and consists of a kilometer-scale layered gabbroic pluton (5 by 6 km large). It intrudes into serpentinized mantle peridotites of Jurassic age, and is associated in limited amounts to harzburgites and dunites (Figure 5.1c; Baumgartner et al., 2013; Tribuzio et al., 2016, and references therein). Extrusive pillow lava, ophiolitic breccia, and sediments are found on top of the gabbros and peridotites. The whole complex was subjected, to variable degrees, to low-temperature metamorphism leading mainly to the formation of retrograde serpentine, chlorite, prehnite, and oxides. To the SE of the BGC (toward Levanto, Figure 5.1b), dominant proportions of mantle rocks are exposed and may represent the base of the magma chamber (Cortesogno et al., 1987; Schwarzenbach et al., 2021). Gabbro (*s.s.*) is the most common lithology, and olivine-gabbros, troctolites, and plagioclase-peridotites are also documented in lesser amounts in the complex. In igneous gabbros, plagioclase is of labradorite composition (~An_{60}), clinopyroxene occur as diopside, and generally the olivine is highly serpentinized when present in these rocks. Magmatic layering is frequent in gabbroic lithologies, and marked by variations in grain sizes or in lithology, sometimes organized in lenses within the isotropic gabbro (Figure 5.2; e.g., Menna, 2009). This layering is commonly oriented NE-SW in the southern and western domains of the BGC, and changes for a NW-SE orientation in the central and northern region (Figure 5.1c).

Figure 5.1 *- Geology of the Alp-Apennine and Bracco area. (a) Geological sketch map of the Central-Western Ligurian Alps and Northern Apennine (after Rampone et al., 2020). IL: Internal Ligurides, EL: External Ligurides. (b) Geological sketch map of the Internal Ligurides unit (modified after Marroni & Pandolfi, 1996). (c) Structural sketch map of the Bracco area with location of the studied samples (modified after Menna, 2009).*

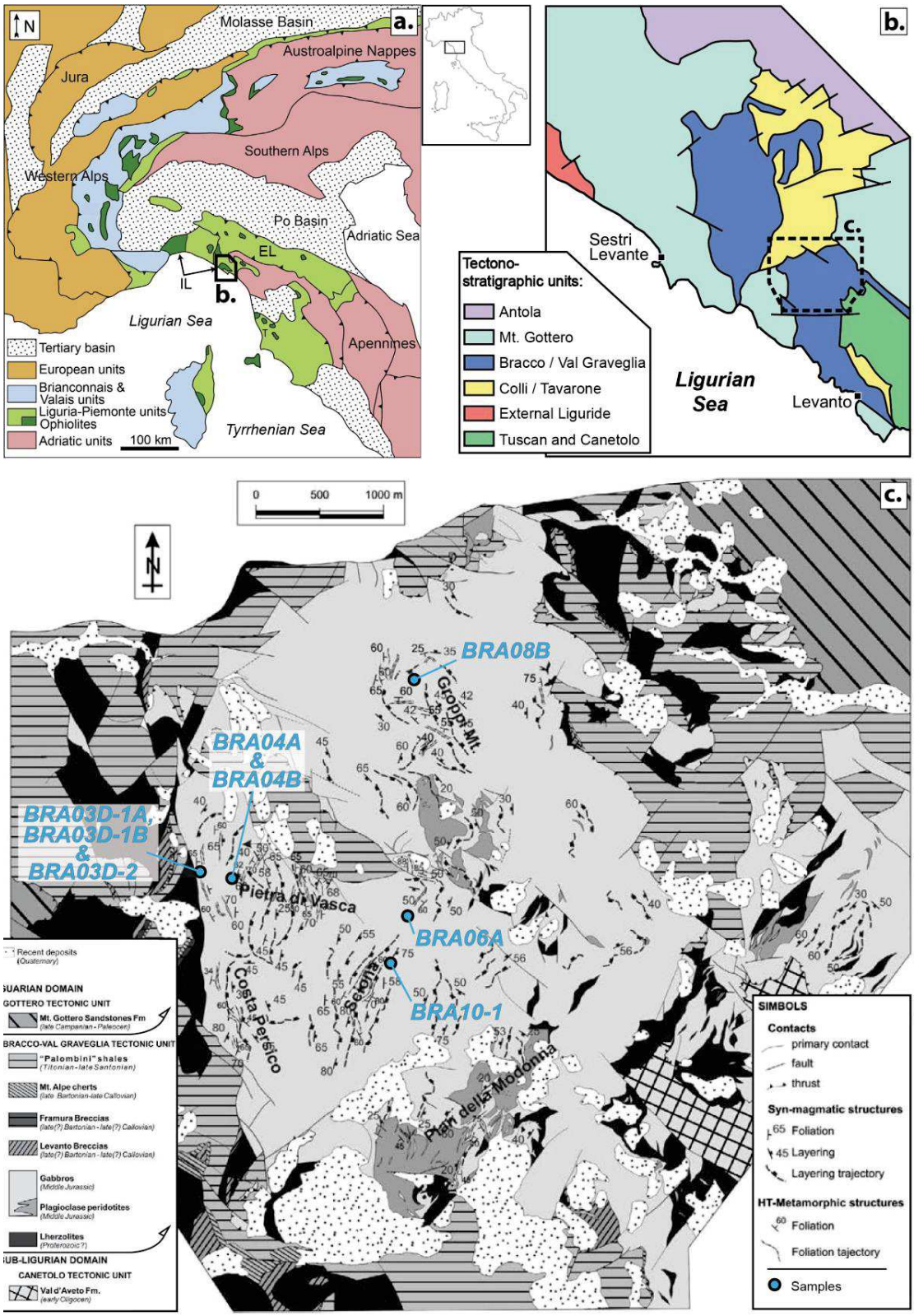
a.
b.
c.
N
Molasse Basin
Austroalpine Nappes
Jura
Southern Alps
Western Alps
Po Basin
Adriatic Sea
EL
IL
Ligurian Sea
Apennines
Tyrrhenian Sea
Tertiary basin
European units
Brianconnais & Valais units
Liguria-Piemonte units
Ophiolites
Adriatic units
100 km
Sestri Levante
Levanto
Ligurian Sea
Tectono-stratigraphic units:
Antola
Mt. Gottero
Bracco / Val Graveglia
Colli / Tavarone
External Liguride
Tuscan and Canetolo
0 500 1000 m
BRA08B
BRA04A & BRA04B
BRA03D-1A, BRA03D-1B & BRA03D-2
BRA06A
BRA10-1
Groppo di Mt.
Pietra di Vasca
Costa Persico
Scogna
Pian della Madonna
Recent deposits (Quaternary)
LIGURIAN DOMAIN
GOTTERO TECTONIC UNIT
Mt. Gottero Sandstones Fm (late Campanian - Paleocen)
BRACCO-VAL GRAVEGLIA TECTONIC UNIT
"Palombini" shales (Tithonian-late Santonian)
Mt. Alpe cherts (late Bartonian-late Callovian)
Framura Breccias (late(?) Bartonian - late(?) Callovian)
Levanto Breccias (late(?) Bartonian - late(?) Callovian)
Gabbros (Middle Jurassic)
Plagioclase peridotites (Middle Jurassic)
Lherzolites (Proterozoic?)
SUB-LIGURIAN DOMAIN
CANETOLO TECTONIC UNIT
Val d'Aveto Fm. (early Oligocen)
SIMBOLS
Contacts
primary contact
fault
thrust
Syn-magmatic structures
Foliation
Layering
Layering trajectory
HT-Metamorphic structures
Foliation
Foliation tajectory
Samples

Figure 5.1

In addition to the layering, a magmatic foliation is documented with a similar orientation. Subsequent mylonitic shear zones formed generally parallel to the magmatic layering/foliation during retrograde metamorphic conditions, associated mainly to the recrystallization of plagioclase and clinopyroxene (Figure 5.2a). The variation in clinopyroxene composition during recrystallization indicates sub-solidus conditions, estimated from 850°C to 950°C based on amphibole TiO_2 content within recrystallized clinopyroxene aggregates (Tribuzio et al., 2000; Montanini et al., 2008). Shear zones formed during this first phase of crystal-plastic deformation D_1 are of variable width, from tens of centimeter to tens of meter, with an increasing deformation intensity toward the core of the zone (e.g., Molli, 1996; Menna, 2009). Four types of deformed microstructures are identified associated with this D_1 phase:

(1) The fabric I corresponds to the development of a penetrative foliation in the rock, highlighted by the elongation of clinopyroxene porphyroclasts. Both plagioclase and clinopyroxene recrystallize from their edges (Figure 5.2b). This corresponds to a porphyroclastic fabric of CPF index 2 following the IODP (International Ocean Discovery Program) nomenclature used in previous chapters (Allard et al., 2021).

(2) Fabric II results from the development of pervasive S-C structures, common in D_1 shear zones (CPF index 3 to 4). These are the classical "flaser gabbros" described in alpine ophiolites, showing more or less continuous recrystallized and stretched clinopyroxene bands alternating with recrystallized plagioclase bands.

(3) Fabric III results from an increase in pervasive foliation development with the formation of millimeter-sized bands of recrystallized clinopyroxene and plagioclase (CPF index 5).

(4) The last type, Fabric IV, corresponds to very thin sub-millimeter-sized alternating plagioclase and clinopyroxene bands (finer than CPF index 5).

Both progressive and discontinuous transitions between the four fabrics can be observed in rocks, and corresponds to increasing deformation intensity (e.g., Figure 5.2b, right images; Molli, 1994; Menna, 2009). Basalt dykes and hornblende-plagioclase filled veins are not affected by deformation while cutting the D_1 shear zones, which is indicative of their younger nature (Figure 5.2a).

Static recrystallization of retrograde metamorphic phases (mainly amphiboles) is a characteristic feature of the D_2 deformation phase. By contrast to D_1 shear zones, those formed during the D_2 phase are rare. The resulting foliation consists of alternate plagioclase and amphibole bands, and is often discontinuous (Menna, 2009). The shear zones generally extend up to tens of meter with a variable thickness (< 4 m), overprinting D_1 shear zones (Figure 5.2a). Plagioclase grains are subjected to cataclasis and mechanical twinning, and grain size reduction. Amphiboles grow at the expense of clinopyroxene during this phase, more or less in a static way, leading to their parallelism with the D_1 orientation. The veins cutting the D_2 shear zones are filled with Mg-

hornblende alone or in association with tremolite-actinolite (± plagioclase, epidote, and prehnite-pumpellyite). Serpentinization is attributed to the end of this deformation phase, which is proposed to occur at ~550°C and 2 kbar and to continue below 500°C (i.e., until the onset of serpentinization; Menna, 2009).

The third and last episode of deformation D_3 consists of the replacement of former mafic phases by amphiboles (tremolite-actinolite). Narrow shear zones and crenulation cleavage are often attributed to this phase, generally found along D_2 shear zones. With the development of cataclasites, the D_3 phase probably occurred at temperatures below 500°C.

The different stages of deformation are proposed to form a continuum from syn-magmatic, granulitic conditions to amphibolitic and finally greenschist facies conditions (Menna, 2009). Although a transition from granulitic to amphibolitic conditions is observed, it may simply reflect fluid circulation (e.g., seawater) rather than changes in pressure and temperature conditions.

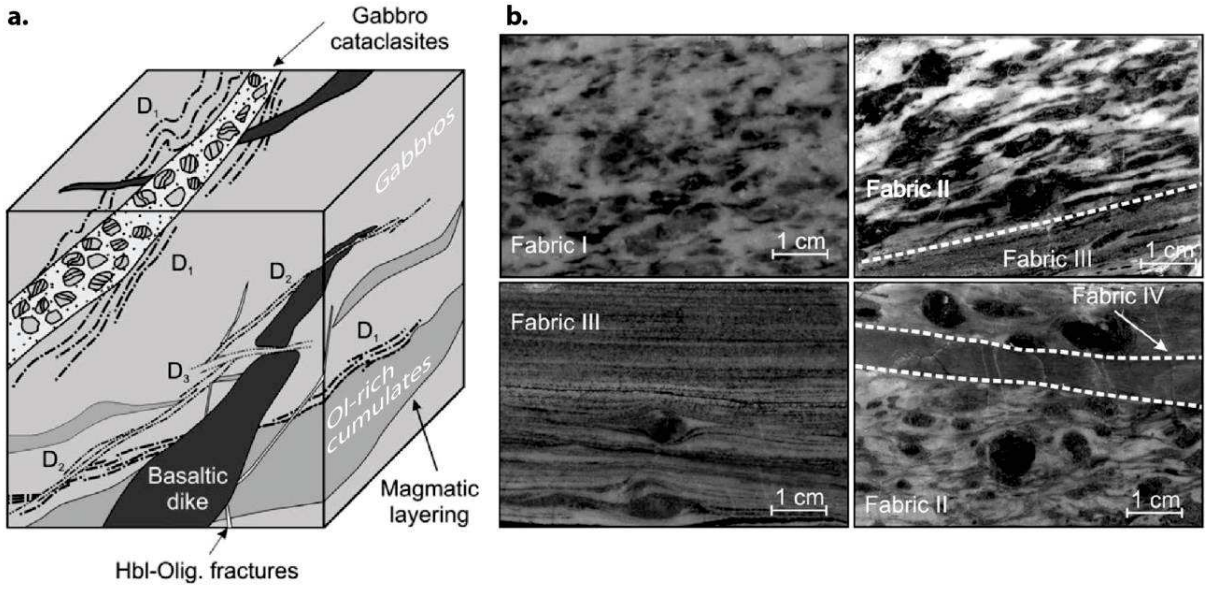

Figure 5.2 *- Deformations in the Bracco-Gabbro Complex. (a) Schematic representation of structural relations between the deformation events in the BGC (modified after Menna, 2009). (b) Macrofabrics details associated with D_1 HT phase (Menna, 2009).*

3. Methods

3.1. Sampling and measurements

A collection of eight gabbroic rock samples from the BGC was selected for this study. It consists of a coarse-grained isotropic gabbro crosscut by a low-grade brittle-ductile structure (BRA10-1), a porphyroclastic gabbro (Fabric I; BRA03D-2), a protomylonites (Fabric II; BRA04B), a mylonite (Fabric II; BRA04A), and four ultramylonites (Fabric III; BRA03D-1A and -1B,

BRA06A, BRA08B). The porphyroclastic to ultramylonitic samples are associated with the D_1 event and are likely to have been superimposed by the D_2 event. When sampled *in situ*, the orientation and dip of the foliation plane were measured, then samples were cut in the foliation and parallel to the stretching lineation (XZ plane of the finite deformation). The analysis of structural measurements was performed using the Stereonet® software (Allmendinger et al., 2011), with contours intervals set to 0.5 and a significance level of 2.

3.2. Mineral chemistry

Quantitative mineral chemical analyses were performed at the Institute of Geological Sciences of the University of Bern using a JEOL JXA 8200 superprobe instrument. A total of five quantitative maps were acquired in four samples: BRA03D-1A and -1B, BRA04A, BRA08B, and BRA10-1 (Figure S5.1). Thin sections were carbon coated to ensure the electron evacuation onto the sample surface during measurements. Measurements were performed using an accelerating voltage of 15 kV, a beam current of 10–20 nA for spot analyses and 100 nA for mapping. For spot analyses, background corrected count rates were calibrated using synthetic and natural standards including albite (Na), forsterite (Mg), anorthite (Ca, Al), orthoclase (Si, K), magnetite (Fe) pyrolusite (Mn), rutile (Ti), Ni-metal (Ni) and spinel (Cr). X-ray maps were calibrated using a set of spot analyses acquired in the mapped area and used as internal standards. The step size was adapted for each map to the length of the area to be mapped and to grain sizes and varies from 2 µm to 7 µm (Table S5.1). Quantitative chemical map processing was performed with XMapTools as well as structural formulae calculation (Lanari et al., 2014, 2019).

3.3. Crystallographic preferred orientations

Electron backscatter diffraction (EBSD) analyses were performed at Geosciences Montpellier, University of Montpellier, using a CamScan X500FE Crystal Probe SEM, equipped with an Oxford instruments Symmetry® EBSD detector. Eight quantitative maps were acquired in seven samples BRA03D-1A, BRA03D-1B, BRA03D-2, BRA04A, BRA04B, BRA06A, and BRA08B (Figure S5.1), and the main processing results are provided in the general annexes Figure SG.2. The diffraction pattern acquisition was achieved at a working distance of 25 mm, an indexing speed of 140 Hz, an acceleration voltage of 20 kV, and a probe current of 10 nA. The scanning resolution was chosen as a function of the size of the analyzed grains and ranges from 3.5 µm to 7 µm. Because of alteration in samples, the indexation rate is variable and ranges from 50% to 81% (Table S5.1).

EBSD data were processed with the MTEX Matlab® toolbox (version 5.3.1, e.g., Mainprice et al., 2015) to calculate misorientations, pole figures, and parameters indicative of fabric strength. The later consist of the J index, deriving from the orientation density function (ODF), and the M index, deriving from uncorrelated misorientations (Bunge, 1982; Skemer et al., 2005). The J

index value varies from 1 for a random fabric to high values for a single orientation fabric. The M index is the difference between the distribution of uncorrelated misorientation angles measured and the distribution corresponding to a random fabric, and varies from 0 for a random fabric to 1 for a single orientation fabric. Pixels with mean angular deviations (i.e., the angle between the acquired diffraction pattern and the indexing solution) higher than 1° are removed from the dataset. The grain segmentation angle is set to 10° and only grains containing at least 5 pixels are considered. Pole figures and orientation parameters are calculated for average grain orientation data to give equivalent weight to all grains (i.e., avoiding a dependency to their size). A special treatment is performed in plagioclase grains to identify and merge twins into their host grains, and then the orientation of the largest twin is attributed to the reconstructed grain. The grain boundaries considered as twins are characterized by an angle of 180° ± 5° and a rotation in (010) or (001), or around [100], [010] or [001].

3.4. Mineral thermometry

Equilibrium temperatures were evaluated by mineral thermometry for plagioclase-amphibole pairs using the Holland & Blundy (1994) thermometer implemented in XMapTools (Lanari et al., 2013, 2014). Temperatures were calculated for a pressure of 150 MPa. The average and local (texturally concordant) compositions for amphibole and plagioclase were used.

3.5. Paleostress calculations

Differential stress calculation was performed using the Twiss (1977) equation for recrystallized grain size paleopiezometer: $\sigma = B \cdot d^{-0.68}$, where $\boldsymbol{\sigma}$ is the differential stress (in MPa), B is a parameter depend to the crystal symmetry and the active Burgers vector, and d is the grain size (in mm). A value of B = 9.6 was used in calculations, as it is proposed to better reflect the glide on the [100] direction in plagioclase (Mehl & Hirth, 2008), which is consistent with the calculated Crystallographic Preferred Orientation (CPO) in analyzed samples. Data from the literature compared to those of this study also display CPO suggesting a glide in the [100] direction in plagioclase, and deformed mainly by dislocation creep.

4. Results

4.1. Field data

Structural measurements were performed over the BGC on two types of structures: High-Grade Foliations (HGF) associated with D_1 (often with a D_2 overprint) and Low-Grade Faults (LGF; probably D_3-related or lower grade). Overall, the complex is characterized by a widespread occurrence of gabbros with isotropic magmatic textures (granular/"eufotide" to foliated), where grain size variations are common at the meter scale (Figure 5.3a). These are extensively cut by sets of LGF, while the HGF are only sparsely observed. LGF generally extend up to tens of

meters in length for a few millimeters in width, rarely centimetric, frequently forming a partly anastomosed network (Figure 5.3b, c, and d). The fault itself is filled by an assemblage of calcic and hydrous minerals. When observed, HGF rarely extend more than 10-15 m in length, and generally consist of 1-3 m thick deformed zones, with evolving deformation intensity (Figure 5.3e and f).

Figure 5.3 *- Macrostructures in gabbros of the Bracco-Gabbro Complex. (a) Isotropic fine- to medium-grained gabbros with lenses of coarse-grained gabbros. (b) Anastomosed set of Low-Grade Faults (LGF) in isotropic gabbros. The bottom inset is a sketch of structures. (c) and (d): Detail photographs of LGF. The dashed lines in (d) highlight the prominent LGF-filling. (e) and (f): High-grade foliations with variable deformation intensities (Fabric I to III).*

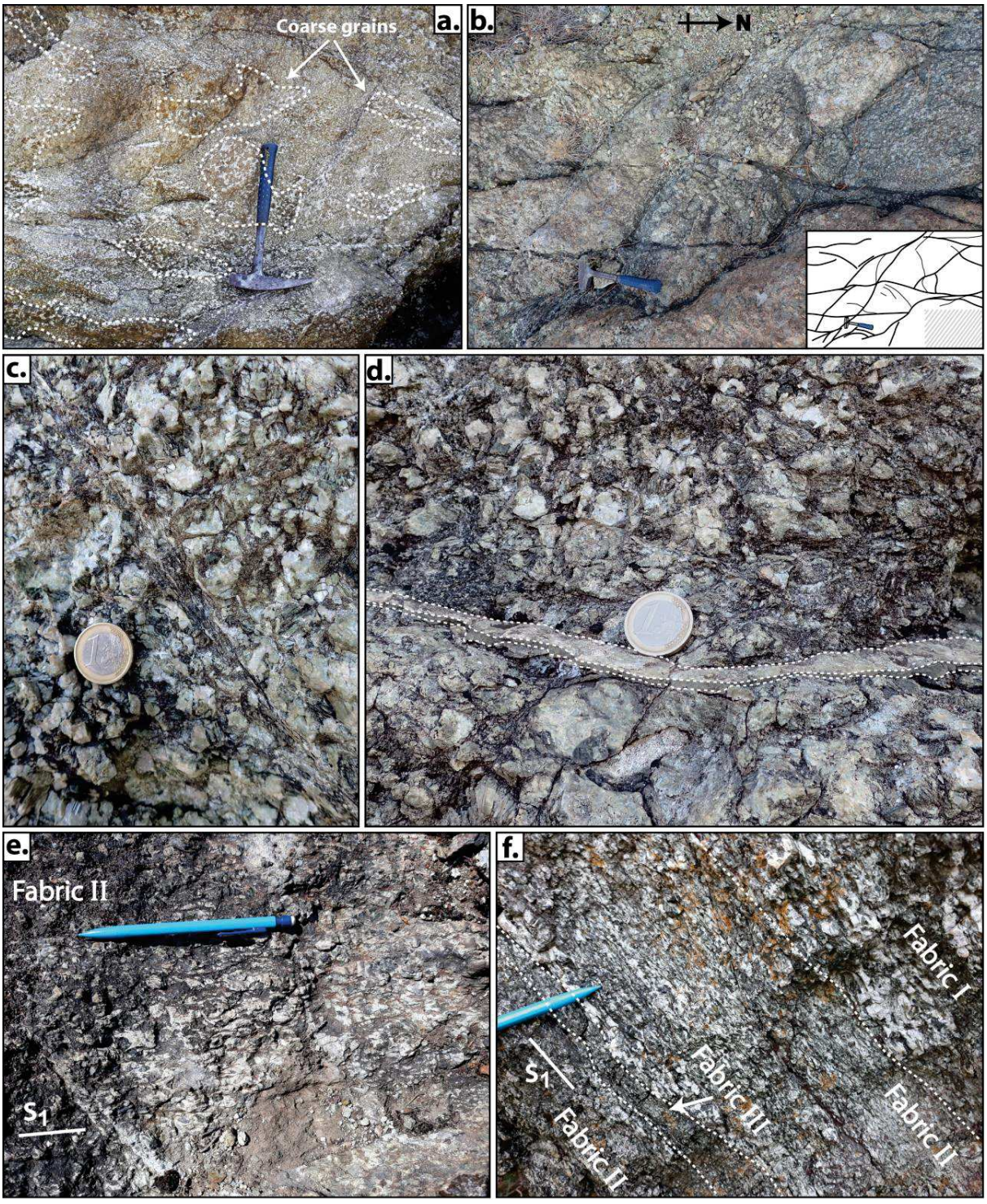
a.
Coarse grains
b.
N
c.
d.
e.
Fabric II
S1
f.
Fabric I
S1
Fabric III
Fabric II
Fabric II

Figure 5.3

Low-Grade Faults

On the basis of 502 measurements we identified two main sets of LGF, oriented NW-SE principally dipping to the E, and NE-SW principally dipping to the NW (Figure 5.4). The NW-SE group is the most commonly observed in the complex except in the central area (Figure 5.4b – e). It is found dominantly striking N330-350° and dipping 70°NE in the northern area (Figure 5.4b), and N330-340° dipping 50°NE in the western and southern areas (Figure 5.4c and d). In these western and southern areas, the LGF patterns are more scattered and strike variations are observed up to N300° or N30° for this NW-SE group. Regarding the second group, oriented NE-SW, it is observed in three of the studied areas and is absent in the north (Figure 5.4b – e). It strikes N220-250° and dips 30-60°NW in the central area (Figure 5.4c), and N240-250° with a steeper dip of 50-60°NW in the western and southern areas (Figure 5.4d and e). In the central area, a small group of five structures is measured N15-30°, dipping 60-80°E instead of W-dipping. No stretching lineation have been observed and measured.

High-Grade Foliations

In the studied areas, only 50 measurements of HGF were performed because of the few occurrences of these structures by contrast to LGF (Figure 5.4a). About half of the HGF were measured in the northern area, and form two main groups trending NW-SE and N-S. No HGF were observed in the southern area. The general orientation of these foliations is variable at the scale of the Bracco complex, although it is observed quite homogeneous at smaller scale in the northern and western areas (Figure 5.4b – d). The NW-SE trending group of foliations is equally measured striking N300-330° and N140-150°, both dipping 70-80°, to the E and to the W, respectively (Figure 5.4b – d). These NW-SE foliations are mostly encountered in the northern area. The N-S group is found striking N350°-N10° dipping 40-50°E in the western area, and striking N180-190° dipping ~80°W in the northern and southern areas (Figure 5.4b – d). Other scattered foliation orientations were measured in the studied areas, and vary from ~N30° to ~N100°.

Figure 5.4 *- Structural measurements in the Bracco area. (a) Structural sketch map with measurements and contouring of studied zones (modified after Menna, 2009). The inset locates the studied area at the scale of the Bracco-Levanto unit. LGF: Low-grade faults, HGF: High-grade foliations. (b) to (f): Stereograph of measured LGF (poles to plane displayed) and HGF (foliation planes displayed) in Monte Groppi – Passo del Bracco (c), Sciona (d), Pietra di Vasca (e), and Costa Persico (f) (lower hemisphere stereo net, equal-area projection). Concerning HGF, the red and green planes correspond to the identified dominant families. n: number of measurements. Data measurements are presented in Table S5.2.*

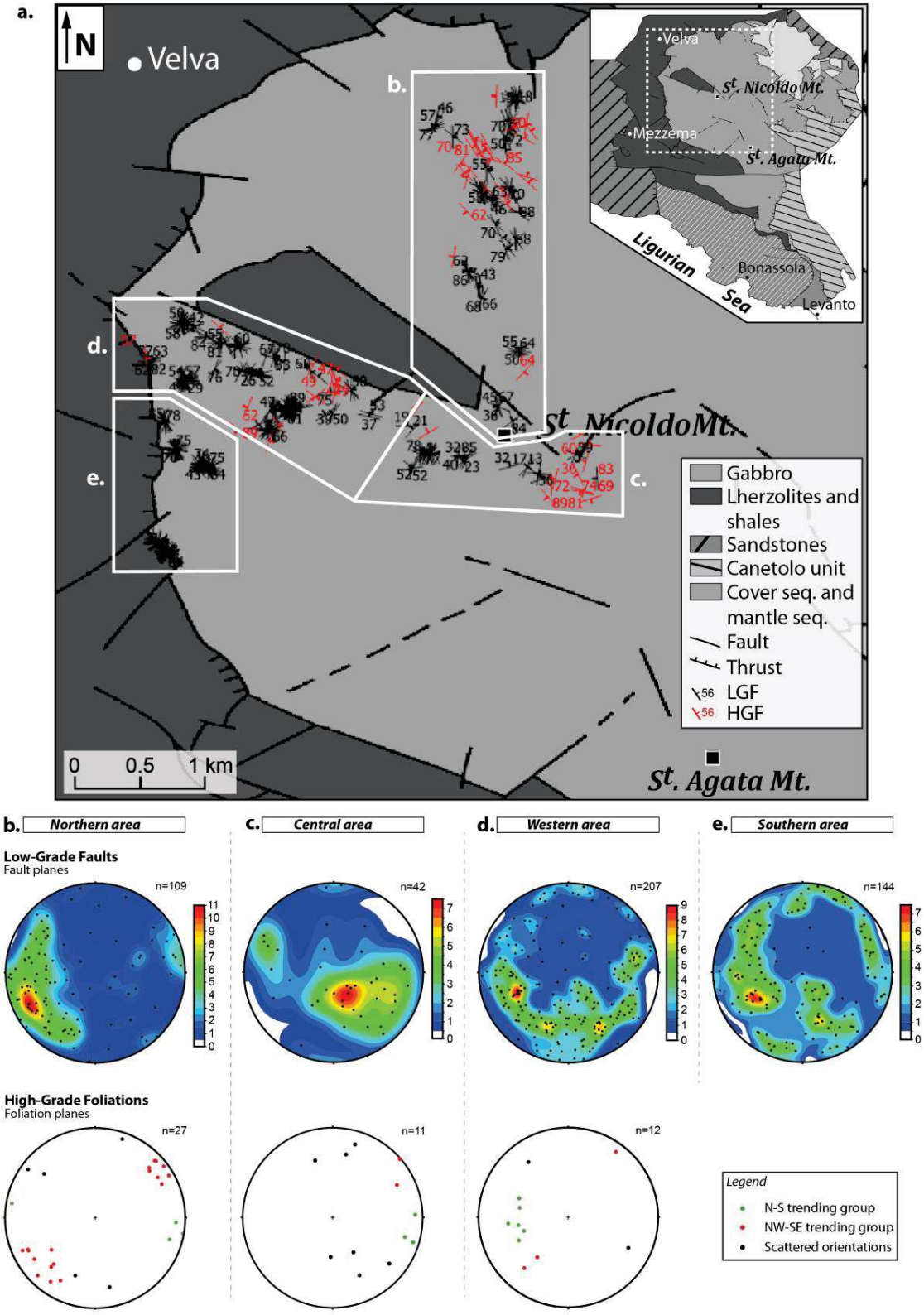
a.
N
Velva
b.
c.
d.
e.
St. Nicoldo Mt.
St. Agata Mt.
Mezzema
Ligurian Sea
Bonassola
Levanto
Gabbro
Lherzolites and shales
Sandstones
Canetolo unit
Cover seq. and mantle seq.
Fault
Thrust
LGF
HGF
0 0.5 1 km
b. Northern area
c. Central area
d. Western area
e. Southern area
Low-Grade Faults
Fault planes
n=109
n=42
n=207
n=144
High-Grade Foliations
Foliation planes
n=27
n=11
n=12
Legend
N-S trending group
NW-SE trending group
Scattered orientations

Figure 5.4

4.2. Petrographic observations

4.2.1. Ductile-Brittle structures: Low-Grade Faults

Observation in thin section of the ductile-brittle structures corresponding to the LGF show that they cut through the igneous plagioclase (Pl_1) and clinopyroxene (Cpx_1) grains (mineral abbreviations are after Whitney & Evans, 2010). The mineral assemblage found within the LGF in sample BRA10-1 consists of chlorite (~56 vol%) and prehnite (~36 vol%) dominantly, and of calcite (~2-5 vol%; Figure 5.5a, 5.5b and Table 5.1). Often, calcite is found in the core of the fault, and the rest is an alternation of prehnite and chlorite rich bands. Low amounts of pumpellyite are documented in the fault core (~2-3 vol%) as well as in plagioclase grains in contact with the fault. Locally plagioclase grains are found recrystallized (Pl_2) at the contact of these structures (Figure 5.5b). Calcite grains are sometimes indicative of shear within the LGF through their sigmoid shape and undulose extinction. Also, the rimming prehnite grains often display undulose extinction (inset in Figure 5.5b). Ultimately, calcite grains usually contain tabular thick twins, frequently accompanied by a set of oblique (less commonly parallel) thin twins. The different fractures observed in samples are found cutting through all phases, even those constituting the LGF (Figure 5.5a and b).

4.2.2. Porphyroclastic microstructure (Fabric I)

The porphyroclastic gabbro BRA03D-2 (Fabric I) is part of a HGF evolving into an ultramylonite (Fabric III, sample BRA03D-1) over a few centimeters (Figure 5.5c). The sample is composed of plagioclase (~46 vol%), clinopyroxene (~27 vol%), chlorite (~20 vol%), brown amphibole (~4 vol%), and minor titanite (< 1vol%; Table 5.1). The metamorphic mineralogical assemblage associated with the deformation is Pl-Cpx-brown Amp, with both plagioclase and clinopyroxene recrystallized in small grains (Pl_2 and Cpx_2, ~30 µm; Table 5.1). Recrystallization of Pl_1 is extensive (~85 vol%), and Pl_2 grains constitute the rock matrix. Recrystallization is more limited in Cpx_1 grains (~30 vol%) and essentially forms Cpx_2 tails at Cpx_1 margins, or elongated Cpx_2 aggregates (Figure 5.5d and Table 5.1). Brown Amp_1 occurs at Cpx_2 grain boundary junctions and at Cpx_1 or chlorite tails and margin. Chlorite occurs as large grains of similar size to Cpx_1 or to Cpx_2 aggregates (~0.5-1 mm; Figure 5.5d and Table 5.1), and corresponds to *in situ* replacement of clinopyroxene during retrograde metamorphic conditions.

4.2.3. Protomylonitic and Mylonitic microstructures (Fabric II)

The protomylonitic sample BRA04B and mylonitic sample BRA04A come from the same high-grade structure with a general C'-S arrangement. These samples represent the gradient of deformation intensity at the margin of a shear zone, which corresponds to a grain size reduction together with the progressive thinning of the Pl_2- and Cpx_2-rich bands formed. The mineral assemblage is plagioclase (~60 vol%), clinopyroxene (~17 vol%), and chlorite (~20 vol%), with

minor brown amphibole and oxides (titanite-rutile, < 1-2 vol%; Table 5.1). Similarly to the porphyroclastic sample BRA03D-2, chlorite mainly occurs as *in situ* replacement of clinopyroxene grains. Brown Amp_1 is present within Cpx_2 aggregates and less frequently at Cpx_1 boundaries, and is often replaced by chlorite (Figure 5.5e). Note that oxide gains are sometimes associated to Amp_1 in Cpx_2 aggregates. Some quartz grains are observed locally within chlorite aggregates in the protomylonite BRA04B. In the latter, recrystallization is almost complete in Pl (~95 vol%), and result in grain sizes that are heterogeneously arranged with anastomosed very fine-grain bands (Pl_2: 55-60 µm) and lenses of coarser grains (~200 µm; Figure 5.5f and Table 5.1). About a half of Cpx_1 grains (~3-6 mm) are recrystallized in medium-grain size (~100-200 µm) elongated tails at Cpx_1 margins or in elongated aggregates. In the mylonite BRA04A, similar recrystallized fractions are observed while the sizes of Cpx_1 grains and both Pl_2 and Cpx_2 grains are smaller than in BRA04B (Cpx_1: 0.7-2 mm, Cpx_2: 20-30 µm, and Pl_2: 25-30 µm and 100-200 µm; Table 5.1).

4.2.4. Ultramylonitic microstructures (Fabric III)

The ultramylonites BRA03D-1A and -1B, BRA06A, and BRA08B are characterized by very fine grain sizes and an alternation of Pl_2- and Cpx_2-rich bands, tens of micrometers thick. The sample BRA08B slightly differs from this with larger, millimeter-sized bands. The mineral assemblage of these ultramylonites comprises mostly plagioclase (40-60 vol%) and clinopyroxene (~3-8 vol% in BRA03D-1B, and 15-25 vol% for the other samples; Table 5.1). In samples BRA03D-1A and -1B, the amount of brownish-green Amp_2 is high (~21 vol% in -1A, and 40 vol% in -1B) and results from the retrograde replacement of clinopyroxene grains (Figure 5.5g). In sample BRA03D-1A, chlorite occurs also as a retrograde *in situ* replacement of clinopyroxene grains. In other samples but BRA03D-1B, chlorite grains form thin bands replacing the former clinopyroxene and brownish-green Amp_2, and are often accompanied by small titanite grains (Figure 5.5h). In sample BRA08B, brown Amp_1 is also found at Cpx_2 grain boundaries (Figure 5.5h). Pl_2 grain size varies from 20-25 µm in samples BRA06A and BRA08B to 15-20 µm in samples BRA03D-1A and -1B. $RCpx_2$ grain size mainly ranges from 25 µm to 50 µm overall (Table 5.1). Finally, some apatite grains (~1 vol%) are found in the two analyzed domains of BRA03D-1, often located in the Pl_2-rich bands.

Table 5.1 *- Mineral modal compositions and grain sizes (in µm) in studied samples. Mineral abbreviations in this and in the following tables are from Whitney & Evans (2010). LGF: low-grade fault. n.o.: not observed*

Microstructural domains		*Pl*	*Cpx*	*Amp*	*Chl*	*Prh*	*Pmp*	*Cal*
Phase modes								
BRA10-1	LGF (only)	n.o.	n.o.	n.o.	56	36	2-3	2-5
BRA03D-2	Porphyroclastic	46	27	4	20	n.o.	n.o.	n.o.
BRA04B	Protomylonitic	56	22	2-3	18	n.o.	n.o.	n.o.
BRA04A	Mylonitic	61	17	1-2	20	n.o.	n.o.	n.o.
BRA03D-1A	Ultramylonitic	39	7-8	21	31	n.o.	n.o.	n.o.
BRA03D-1B	Ultramylonitic	57	2-3	40	n.o.	n.o.	n.o.	n.o.
BRA06A	Ultramylonitic	54	15	2	29	n.o.	n.o.	n.o.
BRA08B	Ultramylonitic	59	23	< 1	17	n.o.	n.o.	n.o.
Grain sizes (µm)								
BRA03D-2	Porphyroclasts	2000-4000	1500-2500	n.o.	500-1000			
	Recryst. grains	30	30	20	n.o.			
BRA04B	Porphyroclasts	n.o.	3000-6000	n.o.	500-2000			
	Recryst. grains	55-60 & 200	100-200	25	n.o.			
BRA04A	Porphyroclasts	n.o.	700-2000	n.o.	n.o.			
	Recryst. grains	25-30 & 100-200	20-30	15	n.o.			
BRA03D-1A	Porphyroclasts	n.o.	250-500	n.o.	300-2000			
	Recryst. grains	15-20	30	10	n.o.			
BRA03D-1B	Porphyroclasts	n.o.	200	250-300	n.o.			
	Recryst. grains	15	20-25	15	n.o.			
BRA06A	Porphyroclasts	n.o.	220	n.o.	n.o.			
	Recryst. grains	25	25-50	12	n.o.			
BRA08B	Porphyroclasts	n.o.	150-250	n.o.	n.o.			
	Recryst. grains	20	20	13	n.o.			
	Coarser bands	150	n.o.	n.o.	n.o.			

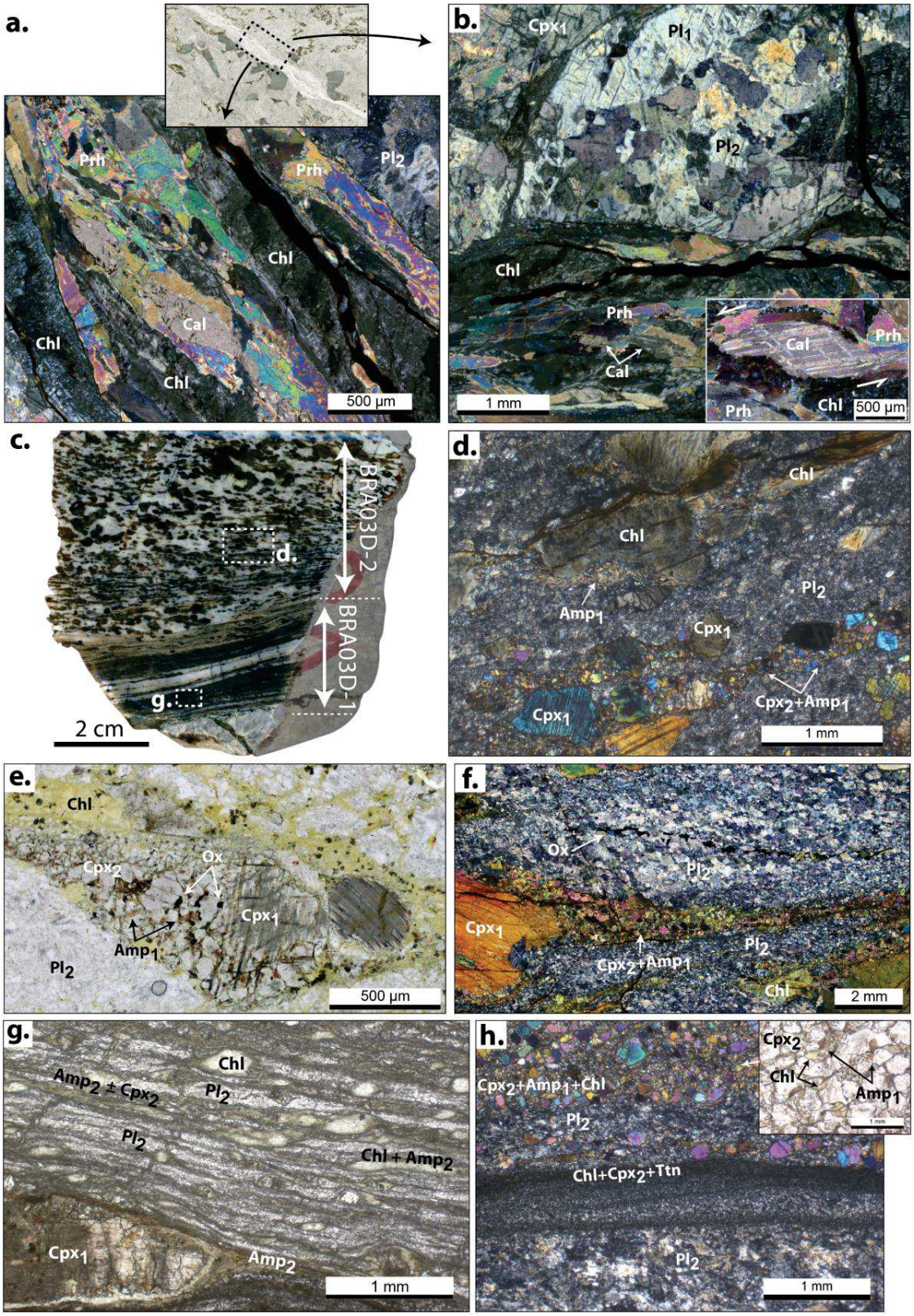
a.
Prh
Prh
Pl2
Chl
Cal
Chl
Chl
500 µm
b.
Cpx1
Pl1
Pl2
Chl
Prh
Cal
1 mm
Cal
Prh
Prh
Chl
500 µm
c.
d.
BRA03D-2
BRA03D-1
g.
2 cm
d.
Chl
Chl
Amp1
Pl2
Cpx1
Cpx1
Cpx2+Amp1
1 mm
e.
Chl
Cpx2
Ox
Cpx1
Amp1
Pl2
500 µm
f.
Ox
Pl2
Cpx1
Cpx2+Amp1
Pl2
Chl
2 mm
g.
Chl
Amp2 ± Cpx2
Pl2
Pl2
Chl + Amp2
Cpx1
Amp2
1 mm
h.
Cpx2+Amp1+Chl
Cpx2
Chl
Amp1
Pl2
Chl+Cpx2+Ttn
Pl2
1 mm

Figure 5.5

Figure 5.5 *- Representative microstructures in studied samples. (a) and (b): Detail microphotographs in the LGF and its vicinity in the isotropic gabbro BRA10-1 (cross-polarized light). Mineral abbreviations in this and in the following figures are from Whitney & Evans (2010). Note the presence of recrystallized plagioclase grains rimming the LGF. The inset in (a) (plane-polarized light) indicates the location of microphotographs in the thin section. The inset in (b) shows a calcite grain with a sigmoid shape indicative of sinistral shear, and rimming bended prehnite grains (cross-polarized light). (c) Photograph of the porphyroclastic to ultramylonitic gabbro BRA03D with the location of the studied domains 1B and 2. (d) Representative microstructure in the porphyroclastic gabbro BRA03D-2 (cross-polarized light). Note the similarity in shape and size between large clinopyroxene and chlorite grains. (e) Microphotograph detail of a* Cpx_2 *recrystallized aggregate formed at a* Cpx_1 *margin and mantling chlorite in the mylonite BRA04A (plane-polarized light). (f) Representative microphotograph in the protomylonite BRA04B showing lenses of large recrystallized* Pl_2 *grains in a very fine-grained* Pl_2 *matrix (cross-polarized light). (g) Fine grain alternation of chlorite-amphibole and plagioclase bands in the ultramylonite BRA03D-1B (plane-polarized light). (h) Representative microphotograph at the contact between recrystallized clinopyroxene-rich and plagioclase-rich bands. The inset shows the presence of amphibole and chlorite grains at recrystallized clinopyroxene grain boundaries.*

4.3. Mineral Chemistry

4.3.1. Plagioclase composition

Plagioclase grain compositions measured in samples are consistent with a retrograde alteration during their tectonic history. Nevertheless, primary compositions are preserved in some domains of analyzed rocks, indicating an anorthite composition of An_{91} for igneous grains ($An_{\%}$ or $\boldsymbol{X}An$ = Ca/(Ca+Na+K); Figure 5.6a and b). In the vicinity of the LGF, Pl_1 grains composition is strongly modified with a loss in Ca content (down to An_{02}) and Al content, and a gain in Na and Si contents. In deformed samples, Pl_2 is Andesine and the measured anorthite contents are very homogeneous, ranging from An_{47} to An_{49} (Figure 5.6a, 5.6c and Table 5.2). In bands associated with chlorite and/or Amp_2, Pl_2 grains display higher K, Si and Na contents together with lower Al and Ca contents. In these bands, Pl_3 is albite with measured anorthite contents of $An_{05\text{-}07}$ (Figure 5.6c)

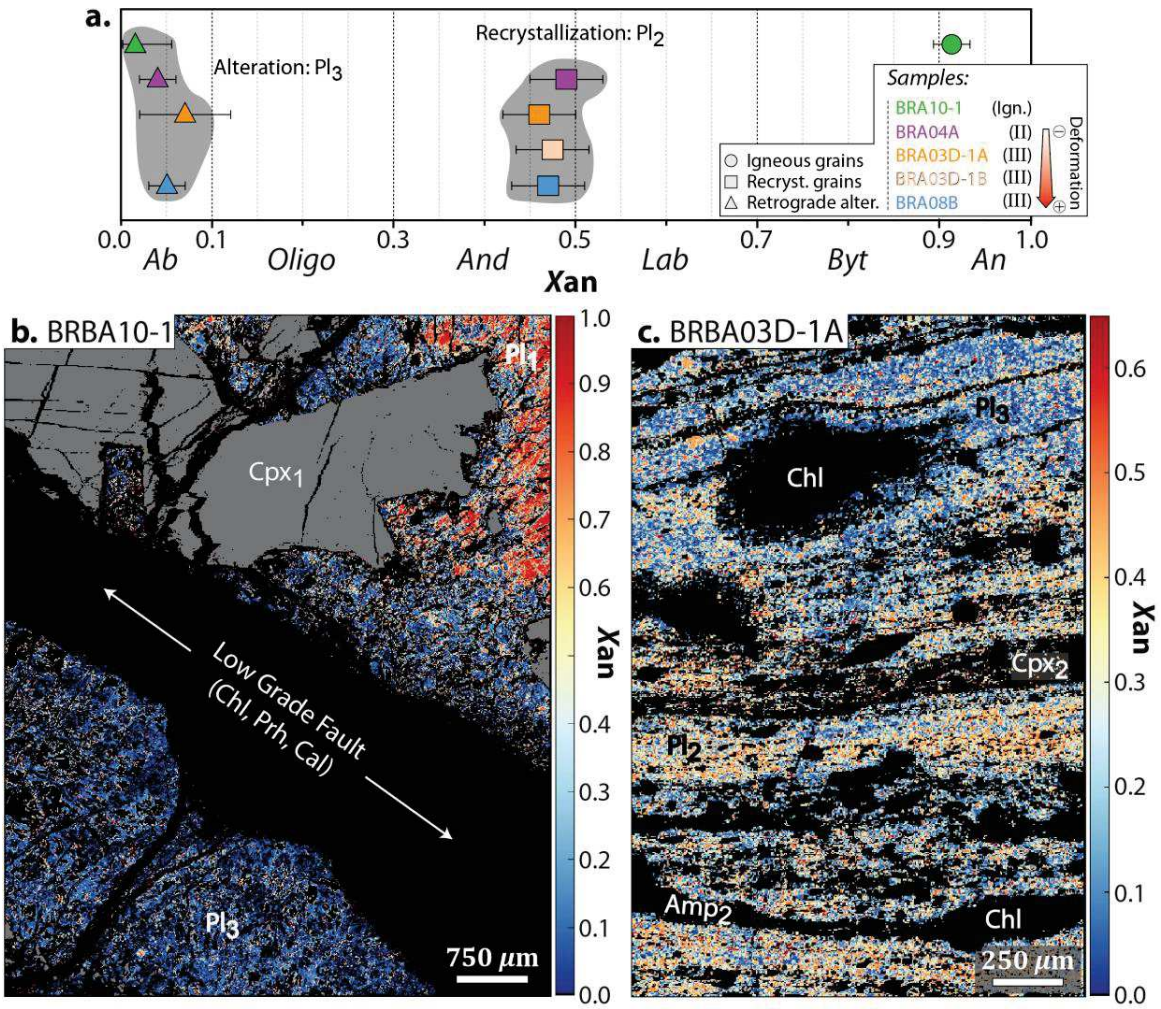

Figure 5.6 *- Plagioclase chemical compositions in studied samples. (a) Synthesis of plagioclase grains compositions expressed as their anorthite content, highlighting differences in compositions between igneous grains, recrystallized grains, and grains subjected to retrograde alteration. Note that K_2O content is found lower than 5% in all samples, except in BRA03D-1A where ~20 vol% of grains correspond to K-feldspars (see Figure S5.2). Ign.: igneous grains; II and III refer to fabric types (see text). (b) and (c) are maps of anorthite content in the vicinity of a LGF in BRA10-1, and in the ultramylonite BRA03D-1A. The grey color in (b) corresponds to clinopyroxene grains. Indices 1, 2 and 3 indicate, respectively, porphyroclasts, recrystallized, and altered grains.*

4.3.2. Clinopyroxene composition

The clinopyroxene analyzed in the sample suite is diopside (Figure 5.7a and Table 5.2). Chemical variations are observed from igneous/porphyroclast grains to recrystallized grains. During dynamic recrystallization Cpx_2 grains are enriched in CaO and SiO_2, and depleted in Al_2O_3 and FeO (Figure 5.7b – e). Because of this depletion in FeO during recrystallization, the *X*Mg ratio is often increasing with recrystallization up to 0.80-0.82 (*X*Mg = Mg/(Mg+Fe_{tot}+Mn), with $Fe_{tot.}$ corresponding to the measured Fe content expressed as Fe^{2+}; Figure 5.7b). Igneous grains preserve domains with high *X*Mg = 0.87-0.88, and associated core to rim zonation is not always clear (Figure 5.7f). The preservation of magmatic characteristics in BRA10-1 Cpx_1 grains is also shown by the zonation in Cr content (Figure 5.7g). Finally, cores of Cpx_2 porphyroclasts in sample BRA08B display compositions closer to Cpx_2 grains than igneous Cpx_1 cores except for the Ca content (Figure 5.7b – d).

Figure 5.7 *- Pyroxene chemical compositions in studied samples. (a) Analyzed pyroxene grains in the pyroxene quadrilateral diagram (after Morimoto, 1988). Ign.: igneous grains; II and III refer to fabric types (see text). (b) and (c): compositional variations from igneous to recrystallized clinopyroxene grains. (d) to (g): compositional quantitative maps of* Ca^{M2} *and* Al_2O_3 *contents, XMg ratio, and Cr2O3 content in clinopyroxene grains. Indices 1 and 2 indicate, respectively, porphyroclasts and recrystallized grains.*

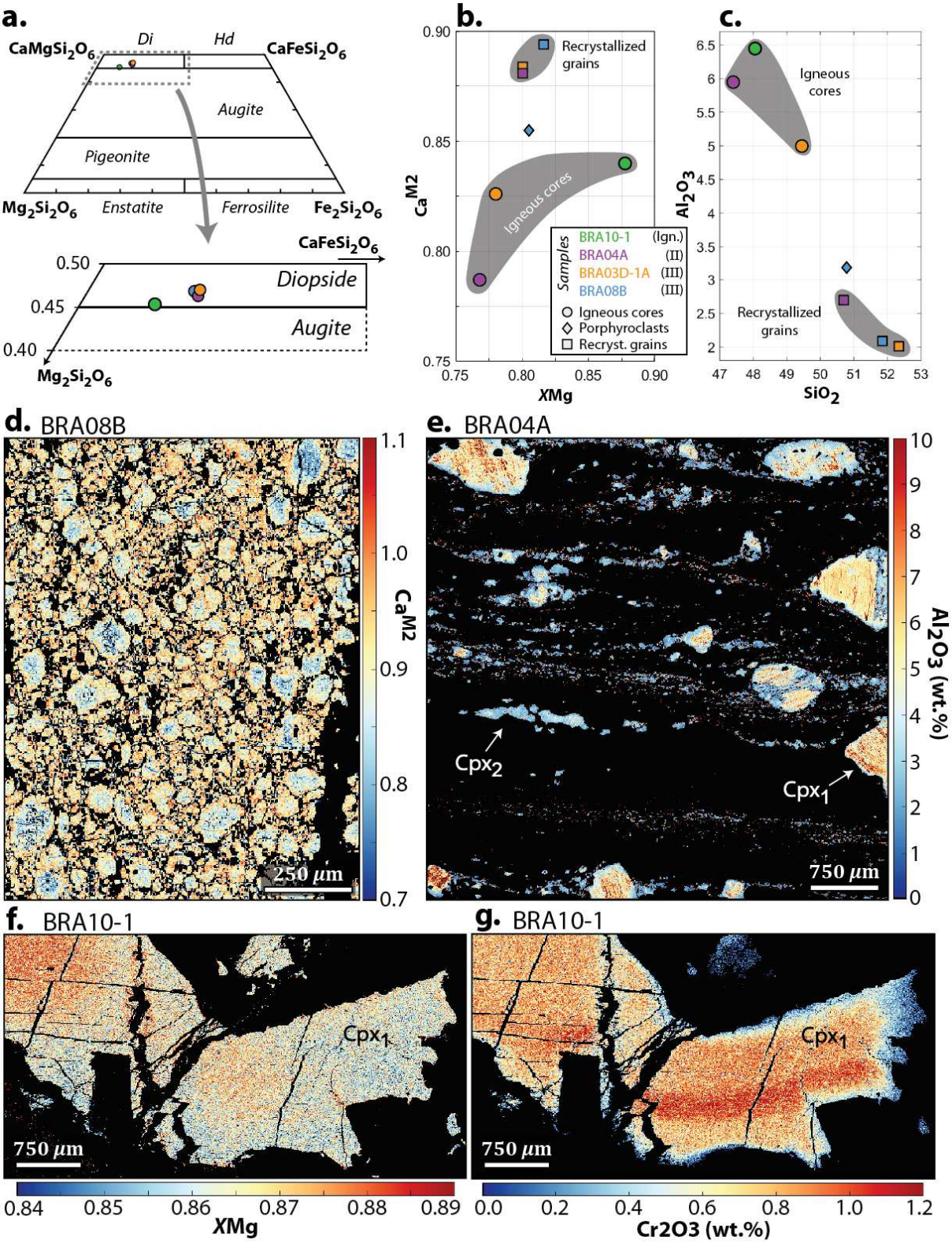
a.
CaMgSi2O6
Di
Hd
CaFeSi2O6
Augite
Pigeonite
Mg2Si2O6
Enstatite
Ferrosilite
Fe2Si2O6
CaFeSi2O6
0.50
0.45
0.40
Diopside
Augite
Mg2Si2O6
b.
Recrystallized grains
Igneous cores
Samples
BRA10-1 (Ign.)
BRA04A (II)
BRA03D-1A (III)
BRA08B (III)
Igneous cores
Porphyroclasts
Recryst. grains
CaM2
XMg
c.
Igneous cores
Recrystallized grains
Al2O3
SiO2
d. BRA08B
250 μm
CaM2
e. BRA04A
Cpx2
Cpx1
750 μm
Al2O3 (wt.%)
f. BRA10-1
Cpx1
750 μm
XMg
g. BRA10-1
Cpx1
750 μm
Cr2O3 (wt.%)

Figure 5.7

4.3.3. Amphibole composition

Only two of the five analyzed samples have significant amphibole modes, allowing their classification. Brown amphiboles measured in BRA03D-1A consists of magnesio-hornblendes (Figure 5.8a and Table 5.2), and brown amphiboles in BRA08B are magnesio-katophorites (Figure 5.8b). The amphibole Al_2O_3 and TiO_2 contents are similar to those measured in D_2 amphiboles for the ultramylonite BRA08B, and between D_2 and D_3 for BRA03D-1A, but with TiO_2 contents similar to D_1 (Menna, 2009; Figure 5.8c). Regarding Al_2O_3 and Na_2O, amphibole grains in BRA08B are clearly similar to the D_1 compositions and amphibole grains in BRA03D-1A are between D_2 and D_3 compositions (Menna, 2009), except for grains in Cpx_1 porphyroclasts pressure shadows (Figure 5.8c). A significantly lower *X*Mg ratio is measured in amphibole grains located in Cpx_1 porphyroclasts pressure shadows, and seems more pronounced at the rim of larger grains (Figure 5.8d). This occurs together with a slight increase of Ti (±Al) contents and a decrease of Si content.

Figure 5.8 *- Amphibole chemical compositions in studied samples. (a) Calcic amphibole composition in sample BRA03D-1A. The dashed-pattern areas indicate amphibole composition in Cpx_1 pressure shadows. (b) Sodic-calcic amphibole composition in sample BRA08B; diagrams in (a) and (b) are after Leake et al. (1997). The black squares correspond to the maximum clustering density of analyzed pixels, and the contouring to the measured range of compositions. (c) Amphibole compositions expressed by their Al_2O_3 content versus TiO_2 and Na_2O contents. Average compositions are plotted for the two samples (squares) and amphibole compositions from clinopyroxene tails (diamond) and within clinopyroxene recrystallized aggregates (circle) are distinguished for BRA03D-1A. The contouring of amphibole compositions associated with the different deformation events are from Menna (2009). (d) Quantitative compositional map of amphiboles XMg ratio in sample BRA03D-1A. The grey color corresponds to clinopyroxene grains. apfu: atoms per formula units. Indices 1 and 2 indicate, respectively, porphyroclasts and recrystallized grains.*

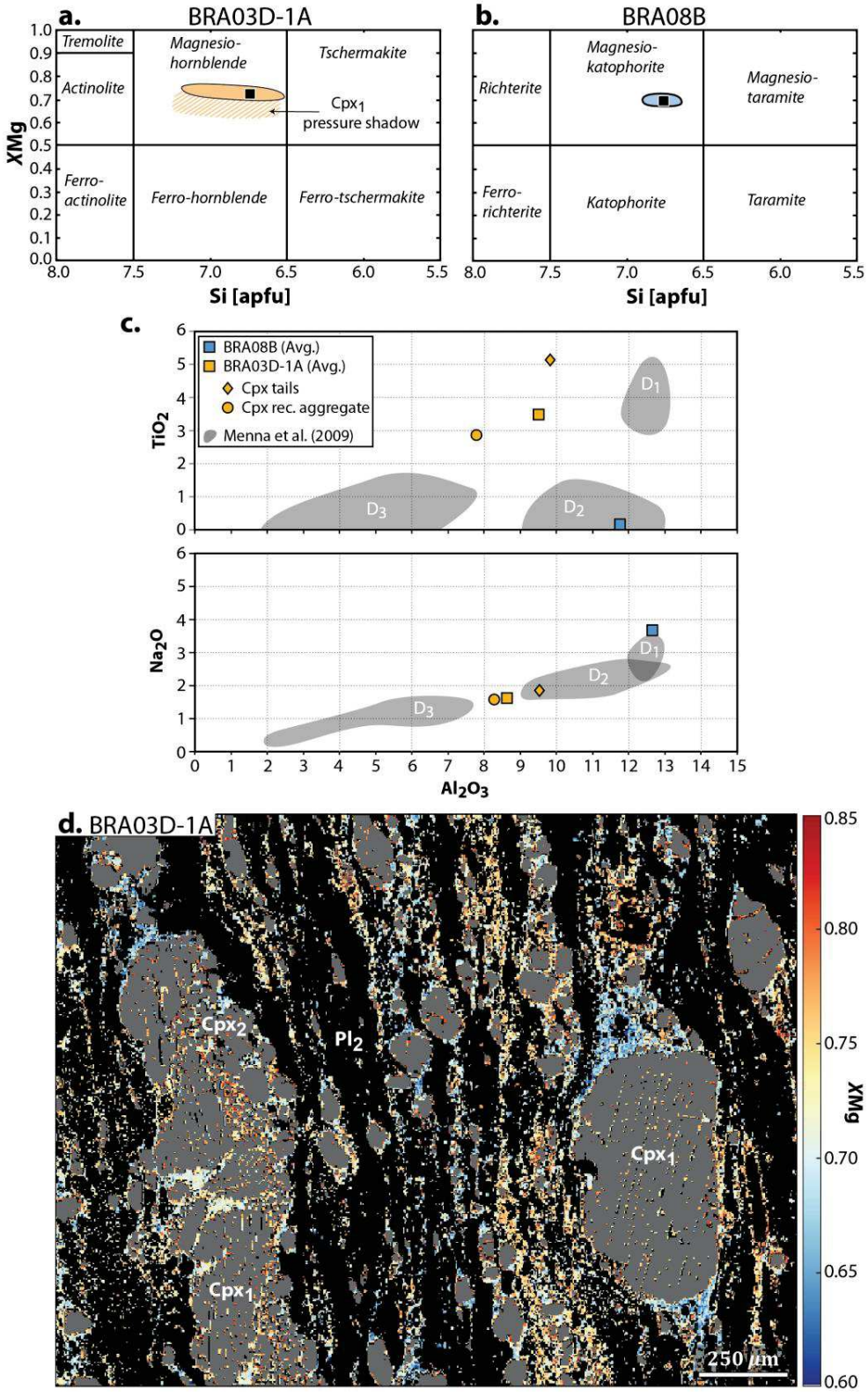
a.
BRA03D-1A
Tremolite
Actinolite
Magnesio-hornblende
Tschermakite
Cpx1 pressure shadow
Ferro-actinolite
Ferro-hornblende
Ferro-tschermakite
XMg
Si [apfu]
b.
BRA08B
Richterite
Magnesio-katophorite
Magnesio-taramite
Ferro-richterite
Katophorite
Taramite
Si [apfu]
c.
BRA08B (Avg.)
BRA03D-1A (Avg.)
Cpx tails
Cpx rec. aggregate
Menna et al. (2009)
D1
D2
D3
TiO2
Na2O
Al2O3
d. BRA03D-1A
Cpx2
Pl2
Cpx1
Cpx1
250 μm
XMg

Figure 5.8

4.3.4. Chlorite composition

The composition of chlorites analyzed in the HGF and LGF are different (Table 5.2). In the HGF, chlorite grains have relatively homogeneous *X*Fe values (*X*Fe = $Fe_{tot.}/(Fe_{tot.}+Mg)$) varying from 0.27 to 0.30, and Si apfu content of 3.0 to 3.3 (Figure 5.9a). Their compositions are in the range of the pycnochlorite endmember for BRA03D-1 and BRA04A, and in the range of diabantite for BRA08B (Figure 5.9a). In contrast, chlorite grains in the LGF are pennines with a more mafic composition, *X*Fe = 0.14, and a Si content of 3.2 (Figure 5.9a).

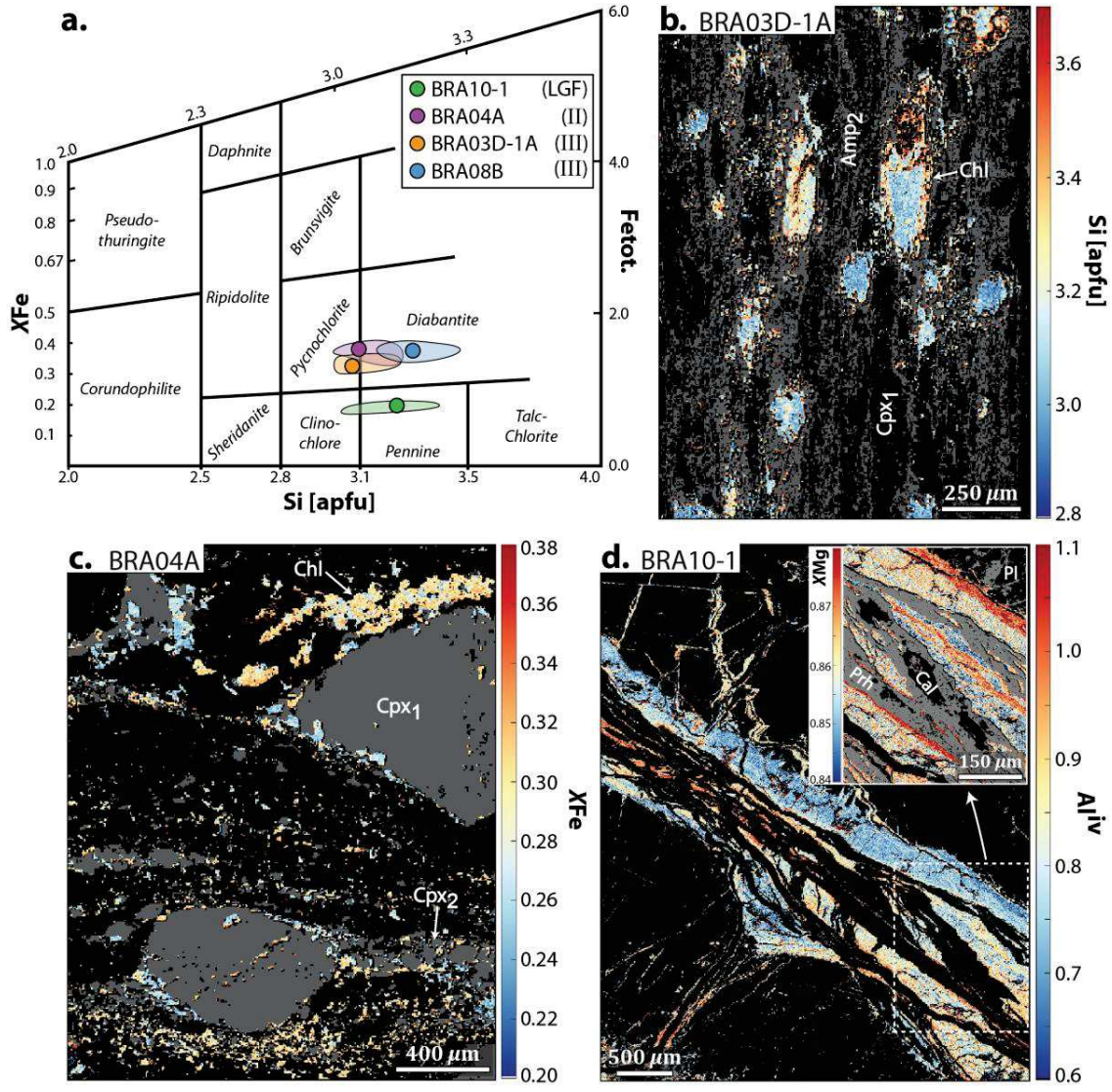

Figure 5.9 *- Chlorite chemical compositions in studied samples. (a) Composition of analyzed chlorites (diagram after Hey, 1954; see Figure 5.8 caption for plotting details). LGF: low-grade fault; I, II and III are fabric types (see text). (b) to (d): Quantitative chemical maps of chlorite Si*

content in samples BRA03D-1A, XFe in BRA04D, and Al^{iv} and XMg in BRA10-1. The grey color in (b) corresponds to amphibole grains, to clinopyroxene grains in (c), and to prehnite in (d). Indices 1 and 2 indicate, respectively, porphyroclasts and recrystallized grains.

Chlorite grains that pseudomorph Cpx_1 grains or Cpx_2 aggregates often display core-to-rim increasing Si content and decreasing Al and Fe content (Figure 5.9b). When in close association with Cpx_1 grains, chlorite grains display lower *X*Fe ratios and Al contents (Figure 5.9c). Finally, the composition of chlorite grains in the LGF indicates increasing Al content toward the core of the fault, and their *X*Mg ratio generally decreases at the contact of Prh from 0.88 to 0.84 (Figure 5.9d).

***Table 5.2** - Representative mineral compositions of the studied samples in high-grade foliations (HGF) and low-grade faults (LGF). Indices indicate porphyroclasts (1) and recrystallized grains (2). n.a.: not analyzed.*

Weight %	***Pl_2*** *BRA04A*	***Pl_2*** *BRA03D-1A*	***Cpx_1*** *BRA04A*	***Cpx_2*** *BRA04A*	***Amp_2*** *BRA03D-1A*	***Chl*** *BRA04A*	***Chl*** *LGF*	***Prh*** *LGF*
SiO_2	54.42	55.59	47.40	51.72	47.18	31.76	34.41	43.76
Al_2O_3	28.29	28.40	5.69	2.25	8.79	16.99	16.11	24.58
TiO_2	0.03	0.01	1.51	0.59	1.11	0.02	0.02	0.03
FeO	0.21	0.17	7.94	7.04	8.82	16.31	8.26	0.29
MgO	n.a.	n.a.	14.24	14.79	16.53	22.12	26.82	0.12
MnO	n.a.	n.a.	0.28	0.26	0.16	0.21	0.12	0.01
CaO	10.35	10.13	19.25	21.59	12.14	0.23	0.31	26.41
Na_2O	5.80	5.79	0.57	0.47	1.88	0.20	0.57	0.09
K_2O	0.04	0.03	0.01	0.01	0.21	0.01	0.02	n.a.
Cr_2O_3	n.a.	n.a.	n.a.	0.05	0.02	0.08	n.a.	n.a.
Total	99.14	100.13	96.90	98.76	96.88	87.96	86.77	95.29

4.4. Mineral thermometry

Deformation temperatures were estimated by mineral thermometry using the Holland & Blundy (1994) thermometer for plagioclase-amphibole pairs (at 150 MPa) in the two ultramylonites BRA03D-1A and BRA08B. Average temperatures calculated for amphibole grains are 688 ± 40°C in BRAO8B and 669 ± 40°C in BRA03D-1A. We performed a detailed analysis of the relation between the textural locations of amphibole grains and calculated temperatures in sample BRA03D-1A (Figure 5.10). Temperatures calculated for average Pl_2 and Amp_2 compositions in each micro-domain are higher in Cpx_1 pressure shadows and Cpx_2 recrystallized aggregates (~770°C ± 40°C; Figure 5.10b).

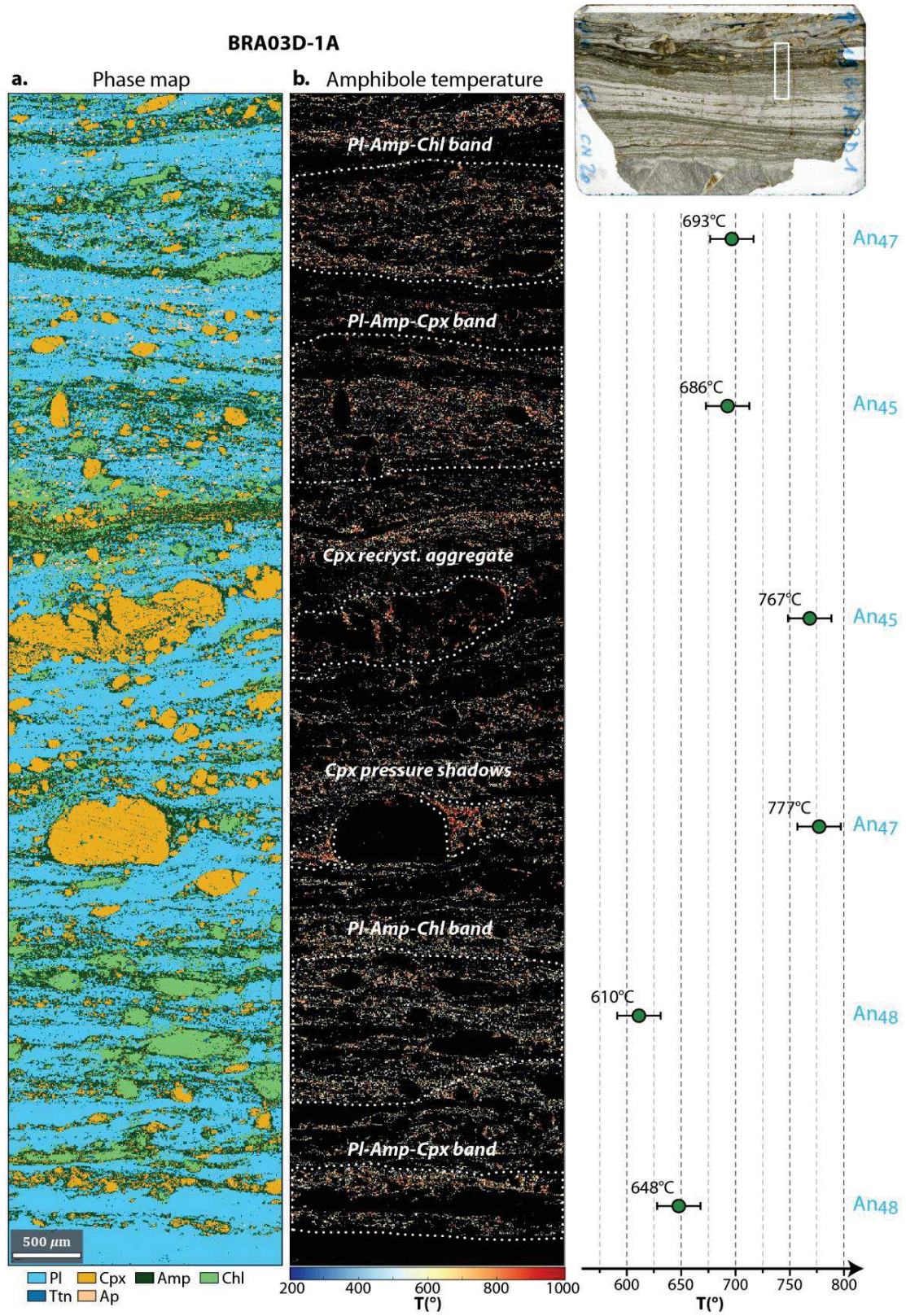
BRA03D-1A
a. Phase map
b. Amphibole temperature
Pl-Amp-Chl band
Pl-Amp-Cpx band
Cpx recryst. aggregate
Cpx pressure shadows
Pl-Amp-Chl band
Pl-Amp-Cpx band
500 μm
Pl
Cpx
Amp
Chl
Ttn
Ap
200
400
600
800
1000
T(°)
693°C
An47
686°C
An45
767°C
An45
777°C
An47
610°C
An48
648°C
An48
600
650
700
750
800
T(°)

Figure 5.10

Figure 5.10 *- Relations between calculated temperatures and the textural occurrence of amphibole grains in the ultramylonite BRA03D-1A. (a) EPMA phase map. (b) Amphibole temperature map with contouring of analyzed domains for temperature determination. The Temperatures are calculated for average plagioclase (An) and amphibole compositions in the domain. The upper right inset gives the location of the analyzed area in the thin section, at the interface between the mylonitic domain corresponding to samples BRA03D-2 (top), and a plagioclase-rich domain (bottom).*

No significant differences in temperature are observed between neighboring Cpx-Pl-Green Amp domains and Chl-Pl-Green Amp domains. However, a difference of 40° to 80°C is found between temperatures calculated in the upper part (~690°C ± 40°C) and the lower part (610-650 ± 40°C) of the analyzed area (Figure 5.10b).

4.5. EBSD analysis

4.5.1. Low-Grade Fault

Plagioclase and clinopyroxene grains rimming the LGF in the coarse-grained isotropic gabbro BRA10-1 display intragranular deformation, both in large igneous Pl_1-Cpx_1 grains and recrystallized Pl_2 grains (Figure 5.11a). Furthermore, misorientations in Pl_1 and Pl_2 grains are in the same order of magnitude. The Pl_2 CPO display clustering of (001) poles to the planes clustering to the N-S of the pole (Figure 5.12). About half of the grains have their (010) planes parallel to the LGF together with their [100] axes orthogonal to the plane of analysis. The other half shows (010) planes parallel to the plane of analysis and [100] axes sub-parallel to the trace of the LGF. The few Cpx_1 grains display similar orientations, particularly with the (100) plane parallel to the East-West direction of the pole figure (Figure 5.12).

4.5.2. Fabric I

In the porphyroclastic gabbro BRA03D-2, almost all grains display intragranular deformation (Figure 5.11b). Intragranular misorientations measured in Cpx_1 porphyroclasts point to important deformation, frequently associated with crystal bending around an axis orthogonal to lamellae orientations (Figure 5.11b). By contrast, the smallest recrystallized Cpx_2 are generally weakly deformed. Misorientations in igneous Pl_1 porphyroclasts are indicative of strong intragranular deformation. Deformation within recrystallized Pl_2 grains, often weaker, is frequent (Figure 5.11b). The plagioclase CPO strength is medium with a J index value of 1.63 and M index value of 0.04. Amphibole and clinopyroxene grains show weak to random CPO with J index values of 1.35 and 1.17, and M index values of 0.02 and 0.01, respectively (Figure 5.12). Recrystallization of plagioclase grains is associated with the development of a CPO characterized by the clustering of [100] axes close to the lineation, and (010) planes parallel to the foliation (Figure 5.12).

Amphibole fine grains exhibit an alignment of [001] axes parallel to the lineation, and (100) planes parallel to the foliation. The CPO pattern in Cpx is random.

4.5.3. Fabric II

In the protomylonitic gabbro BRA04B and mylonitic gabbro BRA04A, misorientation maps indicate internal deformation in grains (Figure 5.11c and d). In the two domains, the larger Pl_2 grains (~100-200 µm) show important deformation while smallest Pl_2 (~30-60 µm) display no or weak internal deformation. Cpx_1 porphyroclasts are severely deformed in sample BRA04B and weakly to moderately deformed in BRA04A, again with a lattice bending around an axis perpendicular to lamellae (Figure 5.11c). Smallest Cpx_2 are generally weakly deformed although a fraction exhibits medium to strong misorientation. In the mylonite BRA04A, fine-grained Cpx_2 are arranged in thin elongated bands and are associated with null measured intragranular misorientations (in black Figure 5.11d). In sample BRA04B, the calculated texture index J points to medium to strong CPO in plagioclase, clinopyroxene, and amphibole with values ranging from 1.62 to 1.94 (Figure 5.12). On the other hand, M index values indicate a medium fabric in plagioclase with a value at 0.05, and random to weak fabrics in clinopyroxene and amphibole with values at 0.01 and 0.02. In the mylonite BRA04A, plagioclase grains are associated to medium fabric strength with a J index value of 1.49 and M index value of 0.03. Clinopyroxene and amphibole have very weak to random fabrics with J index values at 1.13 and 1.22, respectively, and M index value at 0.01. In terms of orientation, plagioclase grains in the two samples (BRA04A and BRA04B) display close CPO patterns, with the preferred alignment of [100] axes parallel to the lineation (Figure 5.12). In BRA04B, both (010) and (001) planes exhibit a girdle distribution with a weak maximum parallel to the foliation, and this is true only for (010) planes in BRA04A. Amphibole CPO show the alignment of [001] axes with the lineation, which is accompanied in BRA04A by (100) planes preferentially aligned parallel to the foliation.

Figure 5.11 *- Deformation in plagioclase and clinopyroxene grains from the Low-Grade Fault (LGF) and porphyroclastic (Fabric I) to mylonitic (Fabric II) samples. (a) to (d): maps of misorientation relative to grain mean orientation in plagioclase (dark blue-light blue-yellow) and clinopyroxene (black-brown-yellow) grains on top of band contrast maps (grey shades). Sample names and phase modes are indicated on top of each map.*

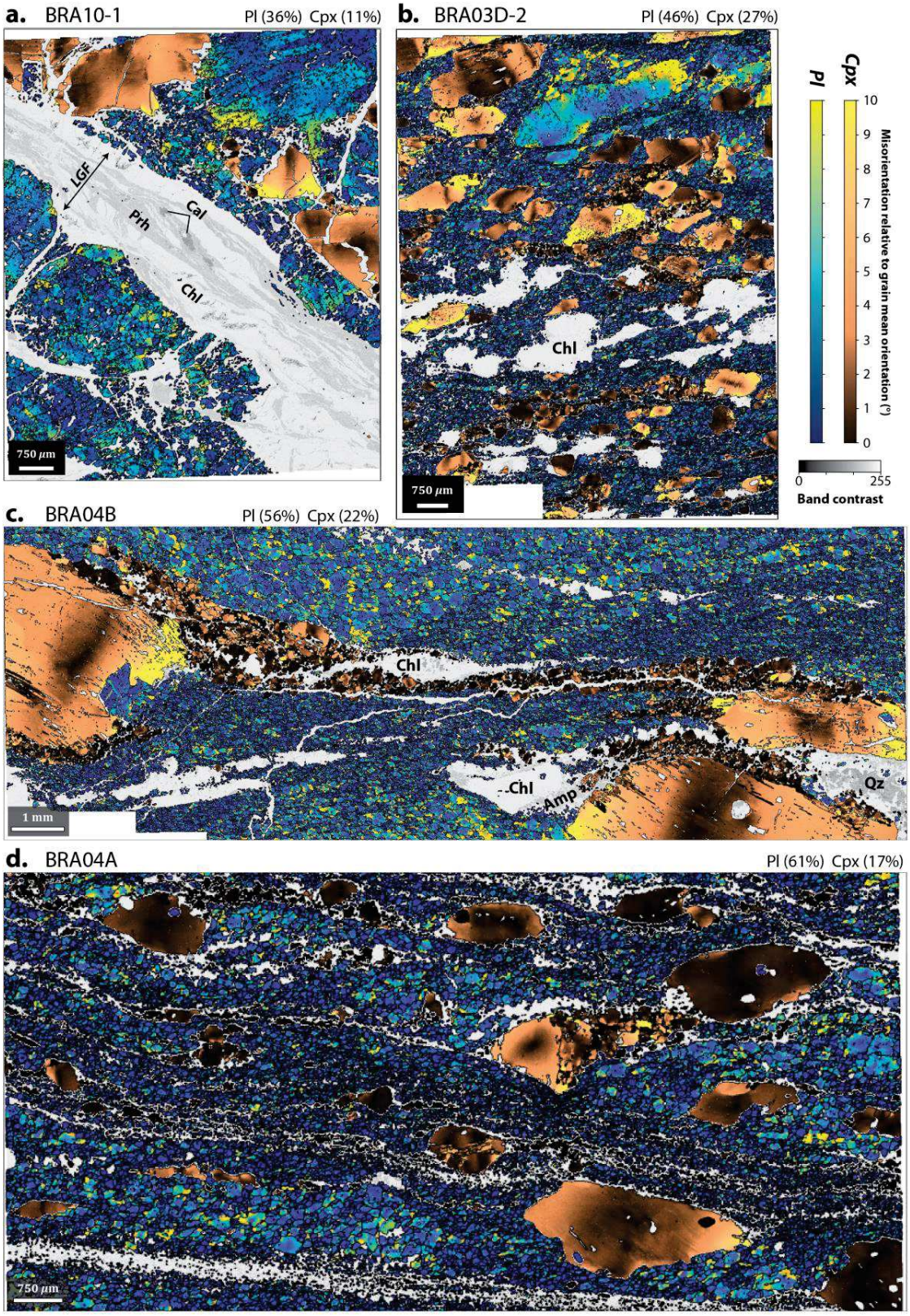
a. BRA10-1
Pl (36%) Cpx (11%)
LGF
Prh
Cal
Chl
750 µm
b. BRA03D-2
Pl (46%) Cpx (27%)
Chl
750 µm
Pl
Cpx
10
9
8
7
6
5
4
3
2
1
0
Misorientation relative to grain mean orientation (°)
0
255
Band contrast
c. BRA04B
Pl (56%) Cpx (22%)
Chl
Chl
Amp
Qz
1 mm
d. BRA04A
Pl (61%) Cpx (17%)
750 µm

Figure 5.11

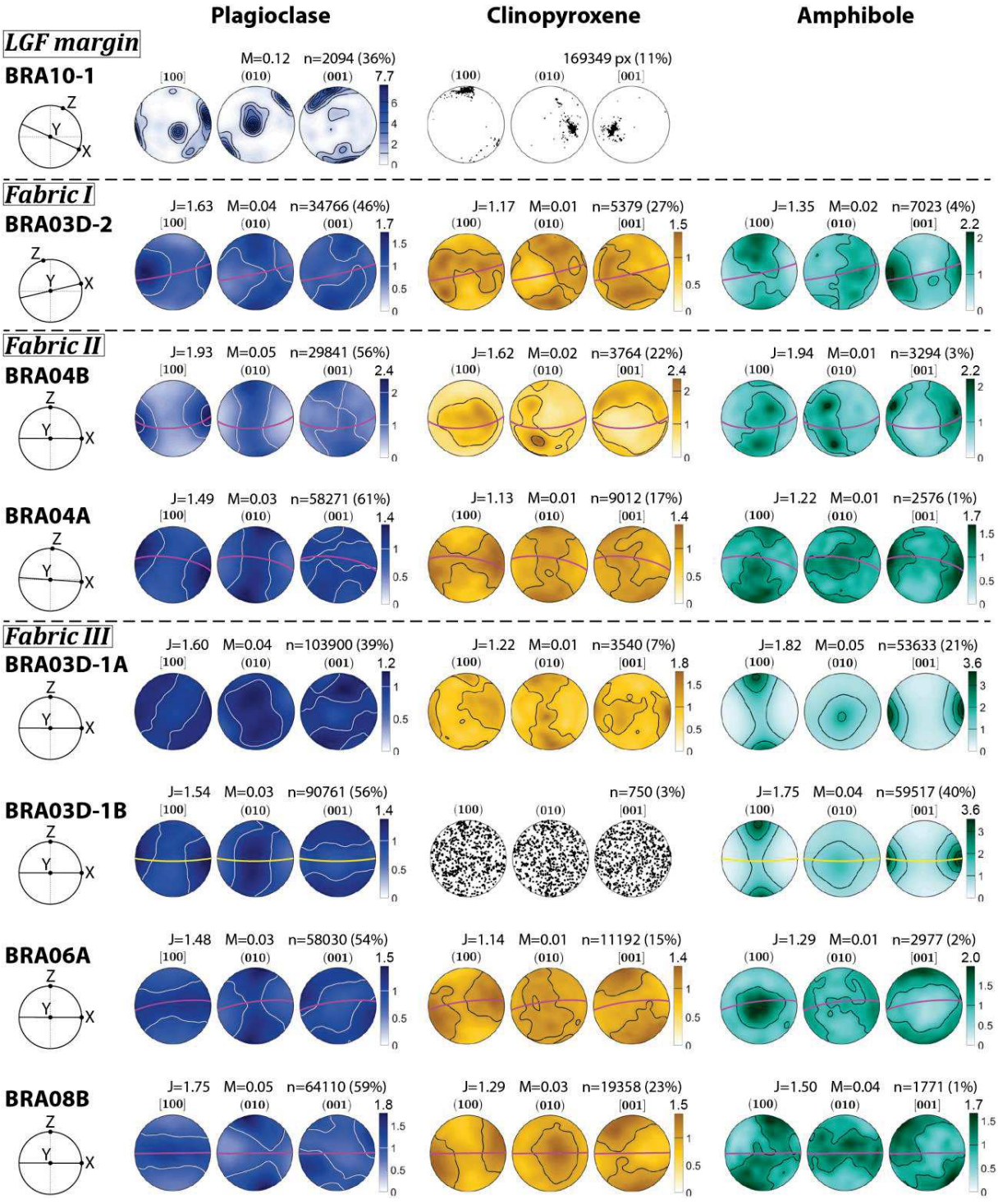

Figure 5.12 *- Pole figures in plagioclase (left, blue), clinopyroxene (middle, brown), and amphibole (right, green) grains in the studied samples (average grain orientation data, lower hemisphere, equal-area projection). Note that for sample BRA10-1, pixel data in clinopyroxene are represented instead of average grain orientation because the number of considered grains is*

biased by the fact that they are altered and fractured. Contour intervals are multiples of the uniform distribution, and the minimum density is set to zero for comparison between analyzed domains. Pole figures are calculated for phases with more than 1000 grains. The trace of the (010) plane in plagioclase (defined by the principal eigen-vector of the orientation tensor) is represented by the pink great circles, and the yellow ones correspond to the (001) plane. Kinematic directions of the deformation in samples (X, Y, and Z) are represented in the left stereo net. Above pole figures are indicated the J index (J), the M index (M), the number of analyzed grains (n), and the mode (%) of the analyzed phase. The maximum density in pole figures is indicated above the color bar.

Finally, the clinopyroxene CPO in BRA04B is characterized by the alignment of (100) planes nearly parallel to the plane of analysis, and [001] axes lying in this plane with no significant preferred orientation. In the mylonite BRA04A, clinopyroxene CPO exhibit girdle distributions with weak maximum at the periphery of pole figures (Figure 5.12). These maxima suggest the alignment of [100] axes parallel to the lineation and of (010) and (001) planes parallel to the lineation.

4.5.4. Fabric III

Plagioclase grains in the four studied ultramylonitic gabbros are mainly very fine grains (15-25 µm) with limited internal deformation, although locally some grains exhibit medium to high misorientation (Figure 5.13a, 5.13b and Table 5.1). In sample BRA08B, two plagiolcase-rich bands consist of Pl_2 with larger grains sizes (~150 µm) and medium to strong internal deformation (Figure 5.13a and Table 5.1). Overall, clinopyroxene grains display medium to strong intragranular misorientations in the largest grains, and null or weak misorientations in fine grains (Figure 5.13c and d). Only Cpx porphyroclasts in sample BRA06A lack significant internal deformation (Figure S5.3). Amphibole is principally present in samples BRA03D-1A and -1B (up to 21% to 40%), and displays medium internal misorientations in large grains (250-300 µm; Table 5.1), contrasting with the lack of, or weak misorientations measured in fine grains (~15 µm; Figure 5.13e and Table 5.1). Amphibole grains present within veins orthogonal to the foliation generally lack internal deformation as well.

A clear difference in CPO patterns of all phases is observed between the two samples BRA03D-1A and -1B, and the two other BRA06A and BRA08B (Figure 5.12). In BRA03D-1A and -1B, plagioclase grains have their [100] axes slightly oblique with, or parallel to the lineation, respectively. In BRA03D-1B, the (001) planes are dominantly parallel to the foliation, but no clear preferred orientation of (001) planes is identified in BRA03D-1A. The CPO of clinopyroxene grains in BRA03D-1A exhibit a weak preferred alignment of [001] axes parallel to the lineation, and (010) planes form a girdle orthogonal to the foliation (Figure 5.12). The number of grains in the other sample is too low to be significant. Finally, CPO of amphibole are

identical in the two samples, with the preferred alignment of the [001] axes parallel to the lineation, and of (100) planes parallel to the foliation. Texture indices point to medium to strong intensities of plagioclase and amphibole CPO, respectively (Figure 5.12). The J index varies from 1.54 to 1.82, and the M index from 0.03 to 0.05. In Cpx grains the fabric is nearly random.

The two other samples BRA06A and BRA08B exhibit girdles of plagioclase [100] axes parallel to the foliation plane. Both (010) and (001) planes are parallel to sub-parallel to the foliation in BRA06A, and only (010) in BRA08B. A detailed analysis of plagioclase-rich bands with variable grain sizes indicates a change of CPO patterns from medium-grained bands to fine-grained bands (Figure 5.13a). The fine-grained bands (Figure 5.13a-(1)) show a CPO similar to that calculated with all grains in the analyzed domain (Figure 5.12). Plagioclase grains from the middle medium-grained band (Figure 5.13a-(2)) exhibit a girdle of (010) planes with a weak maxima orthogonal to the foliation and (001) planes are oblique to the foliation. The medium-grained band in the bottom (Figure 5.13a-(3)) show [100] axes close to the lineation. The (010) planes form a girdle orthogonal to the foliation and (001) planes exhibit a weak maxima oblique to it. Note that this weak maxima for (001) planes is parallel to the one in the other medium-grained band (Figure 5.13a-(2) and (3)). The distribution of [100] changes from mainly point maxima in medium-grained bands to a girdle distribution in the fine-grained band. The clinopyroxene CPO in BRA06A and BRA08B are characterized by (001) planes parallel to the foliation and [100] planes aligned with the lineation (Figure 5.12). In the two samples, the CPO display maximum slightly oblique to the foliation and lineation (Figure 5.12). Amphibole CPO in BRA06A exhibits a strong arrangement of (100) planes parallel to the plane of analysis and scattering of [001] axes all around the pole figure periphery. The weak maxima of [001] axes is orthogonal to the foliation, such as (010) planes.

Figure 5.13 *- Representative deformation characteristics in plagioclase, clinopyroxene, and amphibole grains from the studied ultramylonitic gabbros (Fabric III). (a) to (e): subset domains from maps of misorientations relative to grain mean orientation in plagioclase (dark blue – light blue – yellow), clinopyroxene (black – brown – yellow), and amphibole (dark green – light green – yellow). Pole figures calculated for the three plagioclase-rich bands shown in (a) are given. Pole figure parameters are detailed in the caption of Figure 5.12.*

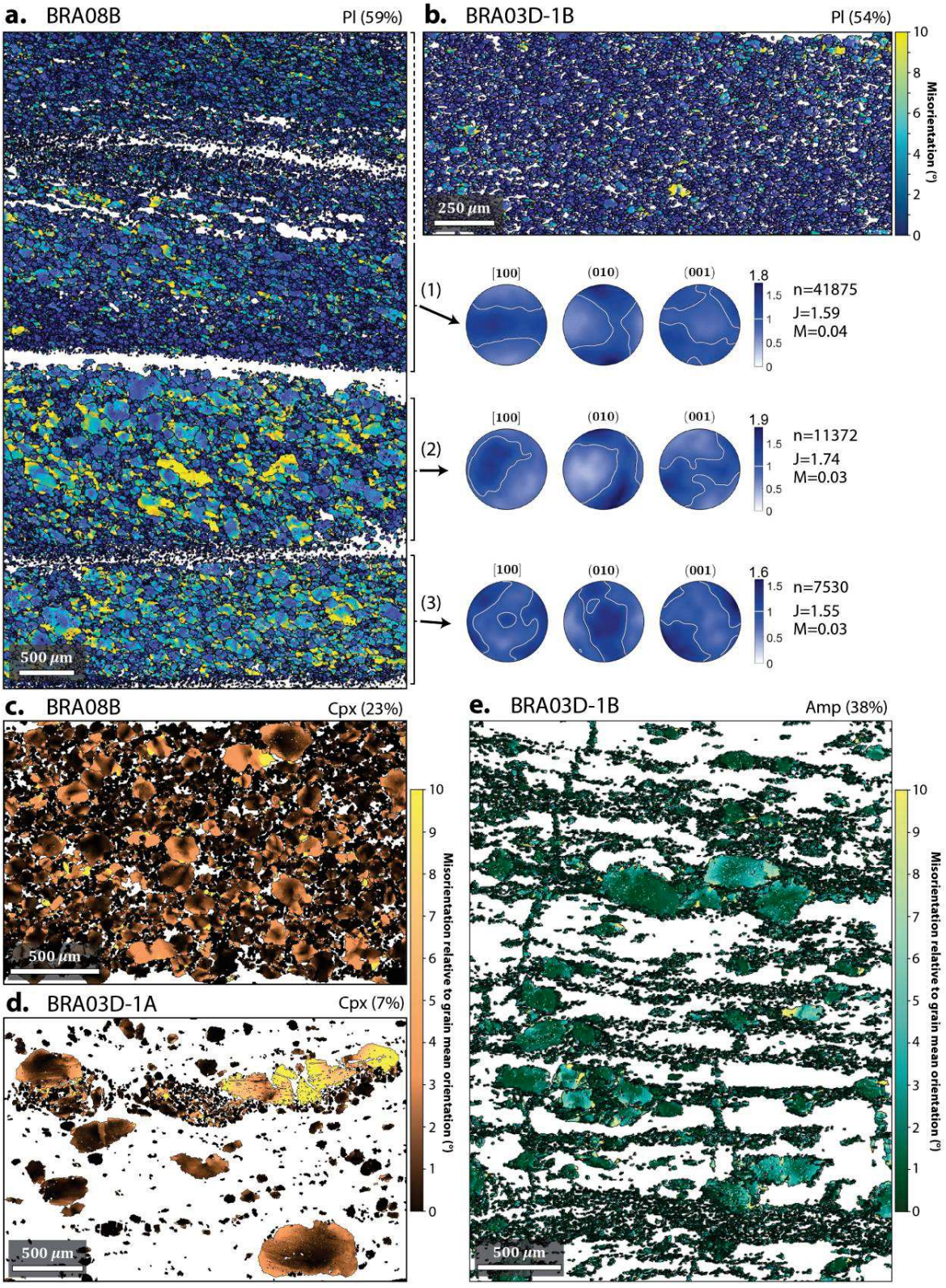
a. BRA08B
Pl (59%)
500 µm
b. BRA03D-1B
Pl (54%)
250 µm
Misorientation (°)
(1)
(2)
(3)
[100]
(010)
(001)
n=41875
J=1.59
M=0.04
n=11372
J=1.74
M=0.03
n=7530
J=1.55
M=0.03
c. BRA08B
Cpx (23%)
500 µm
d. BRA03D-1A
Cpx (7%)
500 µm
e. BRA03D-1B
Amp (38%)
500 µm
Misorientation relative to grain mean orientation (°)

Figure 5.13

In BRA08B, the CPO pattern of amphibole is again slightly oblique to kinematic axes, with (100) planes sub-parallel to the foliation and [001] axes at ~30° to the lineation. Calculated CPO strength are weak to medium overall, and higher for all phases in BRA08B than in BRA06A (Figure 5.12). The J index ranges from 1.14 in clinopyroxene to 1.48 in plagioclase from BRA06A, with M index from 0.01 to 0.03. BRA08B texture index J ranges from 1.29 in clinopyroxene to 1.75 in plagioclase (medium-strong CPO in plagioclase), and M index from 0.03 to 0.05.

5. Discussion

5.1. High-Grade Foliations

5.1.1. Temperatures of deformation events

Mineral thermometry yielded average temperatures of ~670-690°C in the two ultramylonites BRA08B and BRA03D-1A, which corresponds to deformation temperatures of the D_2 event (e.g., Menna, 2009). The detailed analysis performed in BRA03D-1A reveals higher calculated temperatures, up to ~770°C, in preserved domains into Cpx_2 recrystallized aggregates and in Cpx_1 pressure shadows. In contrast, lower temperatures are found in the upper part (~650°C) and the lower part (~590°C) of the analyzed area (Figure 5.10). This area is located at the interface between the porphyroclastic domain corresponding to sample BRA03D-2, and the core of the ultramylonite analyzed in sample BRA03D-1B (inset in Figure 5.10b and Figure S5.1). Although the calculated temperatures for the two ultramylonites suggest a D_2 origin, amphibole compositions point to a retrogressed D_1 origin. In BRA03D-1A, measured TiO_2 contents are similar to those in amphibole associated with D_1. In BRA08B, even if almost no TiO_2 is measured, both Al_2O_3 and Na_2O contents correspond to those of the D_1 event (Figure 5.8c). The presence of chlorite replacing clinopyroxene grains, and locally amphibole grains, indicates that retrograde alteration occurred under greenschist facies conditions, or in a continuum from granulite (D_1) to greenschist (D_3) as proposed by Menna (2009). This could explain the D_2-like calculated temperatures in the two ultramylonites. This retrograde alteration probably associated with fluid circulation, also permits the nucleation of albite grains in the andesine plagioclase matrix within all the studied deformed samples (Figure 5.6a and c). Recrystallized Cpx_2 grains also exhibit compositions similar to syn-D_1 Cpx_2, with Al_2O_3 content < 3 wt% and CaO content > 20 wt% (Figure 5.7b, 5.7c, and Table 5.2).

5.1.2. Structural orientations and spatial distribution

The structural analysis performed in the massif reveals a low amount of D_1-related structures (HGF) within a mostly undeformed gabbro framework, as already reported by Molli (1994, 1995) and Menna (2009). Measurements of HGF orientations indicate two principal structural trends with a NW-SE group and N-S group, often characterized by steep dips (70-80°), except in the

western area where dips are shallower (40-50°; Figure 5.4). These groups of orientations are similar to those reported for both magmatic foliation/layering and HGF in previous studies (Molli, 1994, 1995; Menna, 2009).

In the frame of an Oceanic Core Complex (OCC) system, as suggested by Menna (2009), the HGF formed in gabbros would correspond to deformation occurring at the spreading centre. The deformation event during which these HGF formed in the gabbro is proposed to occur at 850-950°C (D_1; Tribuzio et al., 2000; Montanini et al., 2008), probably coeval to the formation of mylonites in the serpentinized peridotites bordering the gabbro complex (e.g., Molli, 1995). The close orientation of D_1 structures (HGF), magmatic foliations and layering, was proposed to result either (1) from the continuous deformation of the gabbro pluton as the melt fraction progressively decreases from magmatic to high-grade granulitic conditions, or (2) from distinct event with similar stress fields (Menna, 2009). Several OCC have been studied in details over the past decades at present-day slow-spreading ridges. Drilling and seafloor sampling in these gabbro massifs revealed very similar high grade shear zones formed during the exhumation of plutons (e.g., Dick et al., 1991, 2000, 2019; Escartín et al., 2003; Ildefonse et al., 2006, 2007; Harigane et al., 2008). From these investigations, I propose to group exhumed gabbro plutons in OCC in two main types:

- An “early capture”-type of OCC, where the gabbro pluton exhibits extensive deformation with occurrence of thick crystal-plastic shear zones (several tens to hundreds of meters) and widespread deformation over the pluton. This is what is documented at the Atlantis Bank (Southwest Indian Ridge), and these deformations are shown to occur in a continuum from hypersolidus conditions to granulitic and retrograde metamorphic facies conditions. The onset of deformation associated with the detachment fault of the OCC while the gabbro pluton is still crystallizing is proposed to produce the widespread plastic deformation observed (e.g., Figure 15c in Escartín et al., 2003; Dick et al., 2019).
- A “late capture”-type OCC, where gabbro plutons are found with scarce and dispersed high grade shear zones, generally metric to decametric in size. This would correspond to examples such as the Atlantis Massif or the 15°45N OCC (Mid-Atlantic Ridge). In this case the crystallization of the pluton is proposed to have been nearly achieved before the onset of deformation related to exhumation through the detachment fault (e.g., Fig. 15a in Escartín et al., 2003; Kelemen et al., 2004; Blackman et al., 2006; Ildefonse et al., 2006). For this reason, the detachment fault may root into the brittle lithosphere rather than deeper in the ductile lithosphere. Fracturing of the oceanic crust related to ridge spreading would permit the penetration of seawater, leading to the partial serpentinization of peridotites surrounding the pluton. The significant weakening associated with serpentinization then produces important rheological heterogeneities between the strong gabbro pluton and weaker hydrated peridotites, favoring strain localization at the edges of

the pluton. Thus, the exhumation of the gabbro pluton is dominantly achieved by extensional tectonics in the surrounding serpentinized peridotites (Ildefonse et al., 2007; Blackman et al., 2011).

The sparse spatial distribution and limited thickness and extent of HGF zones in the Bracco complex are more compatible with a “late capture”-type OCC. In this model, the frequent occurrence of magmatic foliation and layering in "undeformed" gabbros could result from far-field spreading forces (Figure 5.14). The first stages of HGF formation could be coeval.

In the neighboring Scogna-Rocchetta Vara ophiolite (~10 km west to the Bracco in the Internal Ligurides), similar observations are made regarding high-grade structures. Ductile deformation is proposed to occur under granulitic conditions at ~850°C, then followed by amphibolite facies deformations at ~710°C (Sanfilippo & Tribuzio, 2011). These authors proposed that the gabbro pluton composing this ophiolite was accreted by sill intrusion near the ductile-brittle transition. High-grade deformation in the Scogna-Rocchetta Vara and Bracco ophiolites could occur at this stage. Then, the pluton would move up in the brittle crust and be captured by the detachment fault. The following episodes of deformation would then correspond to fluid circulation within shear zones under amphibolitic conditions (D_2 event in the Bracco; Figure 5.14b), and semi-brittle greenschist facies conditions (D_3 event; Figure 5.14c) associated to detachment faulting.

The general observation of reverse shear sense in HGF documented in the Bracco complex (Molli, 1994, 1995, 1996; Menna, 2009) was propose to correspond to an original extensional shear after reconstruction on the basis of magmatic layering orientation (e.g., Molli, 1995). Although from ophiolites structural analyses some authors proposed the use of, among other criteria, the magmatic layering to reconstruct the paleo-horizontal (e.g., Nicolas & Violette, 1982), this should be done with much care in slow-spread oceanic crust ophiolites. Indeed, investigations in recent OCC lying at the ocean floor revealed planar and wavy, curved, and irregular magmatic layering in exhumed gabbro plutons, with dip variations up to 50° (e.g., Kelemen et al., 2004; Dick et al., 2019; Ferrando et al., 2021).

Figure 5.14 *- Schematic model of a “late-capture OCC” applied to the Bracco-Gabbro complex (adapted from Sanfilippo & Tribuzio, 2011). For simplicity, the sketch focusses on the gabbro pluton corresponding to the Bracco at each stage. (a) Magmatic stage corresponding to the accretion of the pluton at the ductile-brittle transition. This stage is associated to the development of magmatic structures (layering and foliation) and to the high-grade shear zones. (b) The gabbro pluton is progressively lifted up into serpentinites by conjugate normal faulting at its edges. Deformation in the pluton is related to the capture by the detachment fault associated to fluid circulation. (c) Final stage and exhumation of the pluton through detachment faulting.*

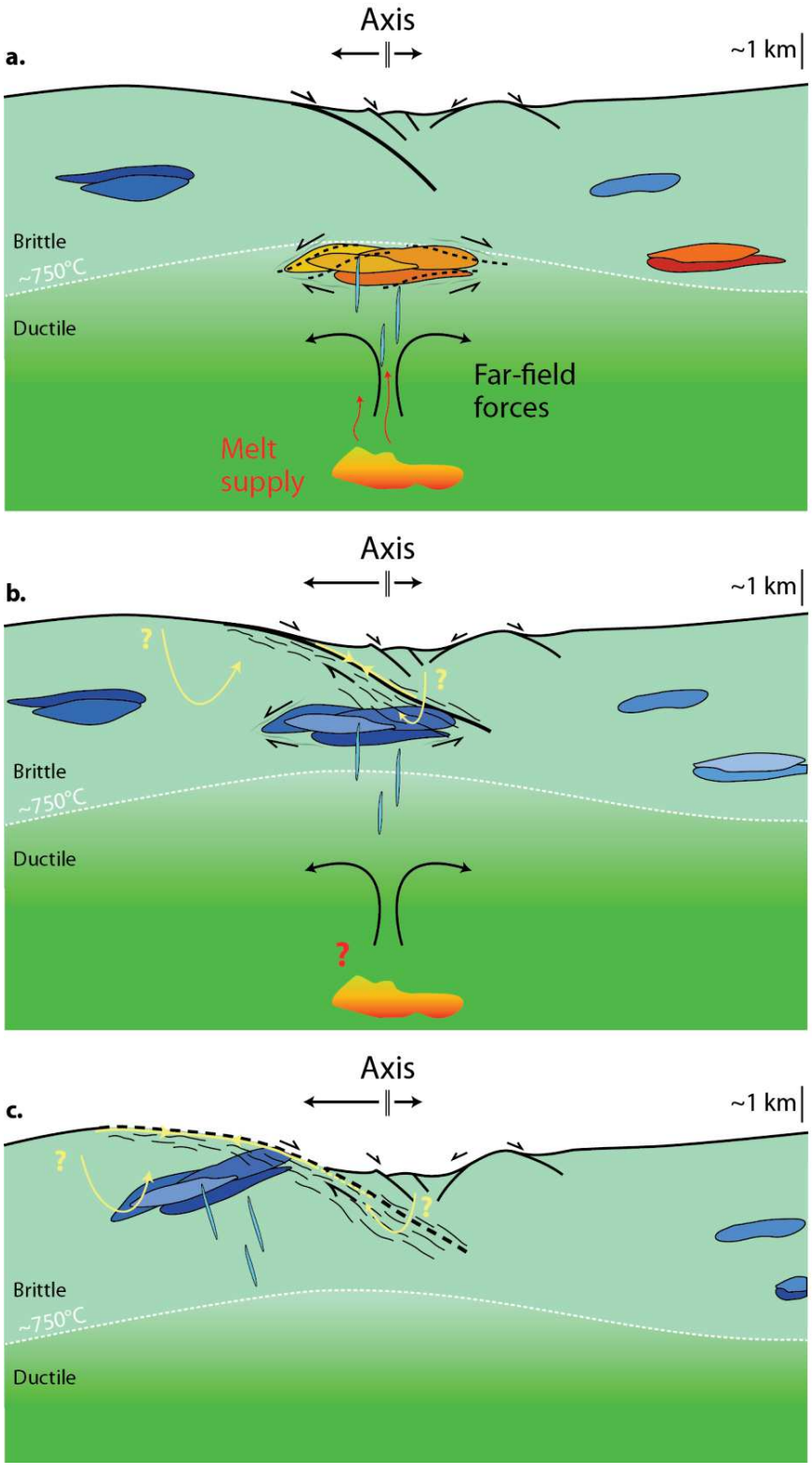

- Sill intrusion at the ductile-brittle transition.
- Crystallization in progress and development of magmatic layering and foliation.
- Ductile shear in the pluton resulting from far-field forces (Granulitic conditions: > 850°C).

: Gabbro sills

: Basalt dikes

: High-grade shear zones

: Faults

: Peridotites : Serpentinites

- Crystallization nearly achieved.
- Capture of the pluton by detachment faulting (Amphibolite to greenschist conditions: < 750°C).
- Fluid circulation throughshear zones & associated to the detachment.

: Brittle to semi-brittle deformation

: Fluid circulation

- Exhumation associated to detachment faulting (greenschist to sub-greenschist conditions: < 500°C).
- The exhumation is associated to the passive rotation of the crystallized pluton into weaker serpentinites.

Figure 5.14

However, in these OCC both reverse and normal shear senses have been described (e.g., Blackman et al., 2006; Dick et al., 2019). At the Atlantis Bank (Southwest Indian Ridge, Dick et al., 2019), normal shear senses are dominant in the upper portion of the gabbro pluton (maximum in the upper 450 m), while reverse shear senses are dominant deeper.

5.1.3. Deformation mechanisms and crystallographic preferred orientations

Extensive misorientations are measured in Pl_1 and Cpx_1 porphyroclasts (and large Amp_2 grains when present). Recrystallization is strong in these phases, indicating that crystal plasticity severely affected the studied samples (Figures 5.11 and 5.13). In clinopyroxene grains and to a lesser extent in plagioclase grains (almost completely recrystallized), observations of core and mantle structures are widespread. In addition, the presence of domains with high misorientations at the edges of porphyroclasts is common and dominant amounts of low angle misorientations (< 10°) are measured in grains (Figures 5.11 and 5.13, and Figure S5.4). Together these observations suggest that recrystallization occurred essentially by subgrain rotation (e.g., Poirier & Guillopé, 1979). Deformation and recrystallization are associated with the development of weak to medium intensity CPO, rarely strong, in plagioclase, clinopyroxene, and amphibole grains, generally consistent with the structural reference frame (foliation and lineation; Figure 5.12). The observation of a CPO in recrystallized minerals is characteristic of deformation in the dislocation creep regime, and indicative of the activated slip systems (e.g, Tullis & Yund, 1987; Wenk & Christie, 1991).

Overall, plagioclase CPO is characterized by the alignment of [100] axes parallel to the lineation with (010) planes parallel to the foliation (Figure 5.12). This CPO suggests the activity of the [100](010) slip system, which is common in plagioclase deformed at high temperature grains in oceanic gabbros (e.g., Mehl & Hirth, 2008; Satsukawa et al., 2013; Allard et al., 2021). In the two ultramylonites BRA06A and BRA08B, [100] axes form a girdle within the foliation plane, but are no longer parallel to the lineation (Figure 5.12). This occurs together with amphibole CPO where the [001] axes are also not observed parallel to the lineation. Also, in samples BRA08B the analysis of plagioclase-bands with different grain sizes reveals variable CPO patterns (Figure 13a). The CPO of the fine-grained domain dominates the CPO calculated for all the analyzed domains as it contains ~70% of the analyzed grains (Figures 12 and 13a). The lower of the medium-grained bands (Figure 5.13a-(3)) would be more compatible with the [100](001) slip system (e.g., Montardi & Mainprice, 1987; Mehl & Hirth, 2008; Michibayashi et al., 2014; Allard et al., 2021), and the other has a CPO in-between the two previous ones. In sample BRA03D-1B the (001) planes are found parallel to the foliation instead of (010) planes, and together with (010) in BRA04B, suggesting the activity of the [100](001) slip system. From intragranular misorientation rotation axes, it is observed that subgrain boundaries arrange essentially along the [100] axis (Figure S5.5). For samples where plagioclase grains have their (010) planes parallel to

the foliation, this suggest the activity of the [001](010) slip system by assuming that these misorientations are related to edge dislocations (e.g., Kruse et al., 2001).

The most common CPO observed in clinopyroxene grains is characterized by [100] axes parallel to the lineation, and (001) planes parallel to the foliation (Figure 5.12). This suggests glide on [100](001) twin system in the mylonite BRA04A and the ultramylonites BRA06A and BRA08B (e.g., Raleigh & Talbot, 1967; Kirby & Christie, 1977; Kollé & Blacic, 1982; Mauler et al., 2000). In the ultramylonite BRA03D-1A, clinopyroxene CPO patterns suggest the activity of the [001](010) slip system (Figure 5.12; Zhou & He, 2015).

A majority of amphibole grains in the analyzed samples exhibit [001] axes parallel to the lineation and (100) planes parallel to the foliation. The textural occurrences of amphibole grains are mostly indicative of replacement of former Cpx grains, which suggests that the CPO results from oriented growth and rigid grain rotation rather than recrystallization (e.g., Berger & Stünitz, 1996; Getsinger & Hirth, 2014). In the ultramylonite BRA03D-1B, amphibole occurs as large grains that appear to be pseudomorphs of an important fraction of clinopyroxene grains (Figure 5.13e). In addition, these large grains exhibit medium to strong misorientations and core and mantle-like structures with long tails forming bands parallel to the foliation. Despite this suggestive texture, it is proposed that this better result from the retrograde replacement of clinopyroxene rather than from recrystallization.

From the very fine grain sizes, equant grain shapes, and plagioclase and clinopyroxene grains mixing in ultramylonites (Fabric III), Molli (1994) proposed that grain size sensitive flow has occurred. The transition from dominant dislocation creep to dominant grain size sensitive creep could have occurred between Fabric II and Fabric III according to the author. These textural characteristics, together with weak measured CPO (or lack of CPO) are often interpreted as evidences of granular flow in rocks (e.g., Fitz Gerald & Stünitz, 1993; Paterson, 1995; Mehl & Hirth, 2008). Calculated crystallographic fabric intensities in plagioclase grains, the dominant phase in the studied rocks, are weak to medium which is a common observation in oceanic gabbros (e.g., Satsukawa et al., 2013; Allard et al., 2021). Both CPO patterns and texture indices in plagioclase grains show similarities between Fabric II and Fabric III samples (Figure 12), and no chemical changes in plagioclase and clinopyroxene grains are observed (Figures 5.6 and 5.7), as already pointed out by Molli (1994). This would rather suggest that dislocation creep continued being the main deformation mechanism during the formation of ultramylonites (Fabric III). However, in the two ultramylonites BRA06A and BRA08B, a transition from point maxima to girdle is observed in [100] axes pole figures. This indicates the scattering of grain orientations in the foliation plane. Ultimately, in the ultramylonite BRA08B this transition is observed from the medium-grained plagioclase-rich bands to the fine-grained band. This grain orientation scattering could be either the result from granular flow during strain localization or more likely from the progressive recrystallization by subgrain rotation. The latter is consistent with the

important intragranular deformations observed even in fine-grained in ultramylonites (e.g., Allard et al., 2021). An exception to this is BRA03D-1B where the high proportion of amphibole grains points to important fluid circulation.

5.1.4. Grain sizes and paleostresses

The measured recrystallized grain sizes presented in Table 5.1 for the different studied samples are used for paleostress estimations. These calculations were performed using the Twiss (1977) equation for recrystallized grain size paleopiezometer, with the same method as Mehl & Hirth (2008) also used in chapter III (see section 3.5, and chapter III). Calculated paleostresses range from ~70 MPa to ~110 MPa in the Fabric I and II samples, and from ~120 MPa to ~170 MPa in Fabric III ultramylonites (Figure 5.15). As expected from the measured grain sizes, paleostresses calculated in the four ultramylonites are higher than in less deformed samples. Also, the protomylonitic gabbro BRA04B (Fabric II) indicate lower stresses than the porphyroclastic gabbro BRA03D-2 (Fabric I), which is believed to result from a larger original grain size according to Cpx_1 sizes in BRA04B (Table 5.1 and Figure S5.1).

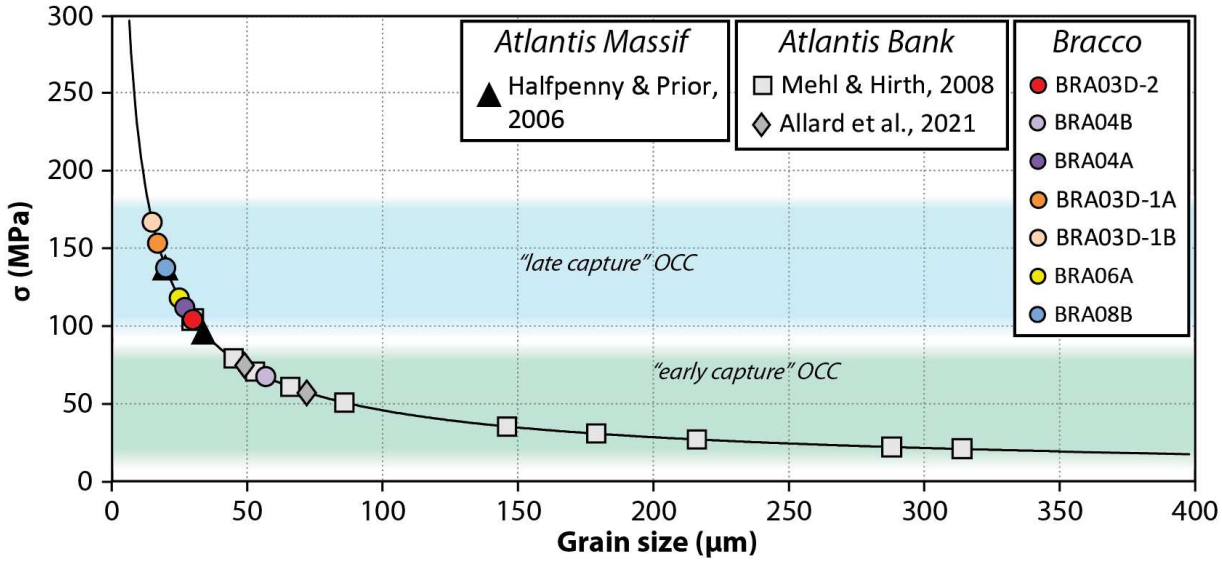

Figure 5.15 *- Paleostress calculated from recrystallized plagioclase grain sizes in the Bracco-Gabbro Complex (this study) and comparison with other OCC data from the literature. The black curve corresponds to the Twiss (1977) paleopiezometer equation (see Methods), and green and blue bands to the proposed range of differential stresses associated with strain localization in the two different types of OCC.*

The comparison to data from present-day OCC yields interesting results. Paleostress estimates for the Atlantis Massif mylonites/ultramylonites indicate values (95-137 MPa) similar to those obtained here for Bracco complex HGF. In contrast, those calculated for the Atlantis Bank

gabbros (Mehl & Hirth, 2008; Allard et al., 2021) are lower, ranging from 21 MPa to ~80 MPa (only one sample is estimated at ~104 MPa; Figure 5.15). These data suggest that high-temperature mylonites and ultramylonites form under higher stresses, by a factor of two on average, in "late capture"-type OCC than in "early capture" ones (Figure 5.15). This would be consistent with the observation of significantly less high-temperature deformation features in "late capture"-type OCC (e.g., Ildefonse et al., 2007), often narrower than in the other type of OCC, implying a more focused strain localization.

5.2. Low-Grade Faults

The mineral assemblage observed in the LGF (Chl-Prh-Cal ± Pmp) indicates the low-temperature nature of these structures. The presence of Prh, and to a lesser extent Pmp, suggests temperatures < 300°C for their formation (e.g., Schiffman & Liou, 1983; Liou et al., 1985; Frey et al., 1991). Although they are found cutting straight into isotropic gabbros, textural observations within LGF point to their (partly) ductile behavior (e.g., undulose extinction in constituting minerals and sigmoidal shape of some calcite grains; Figure 5.5a and b). The analysis of calcite grains indicates the presence of two different families of twins: thick twins, almost ubiquitous in grains, and thin twins. These thin twins frequently form an oblique set to thick twins, sometimes a parallel set (Figure 5.16).

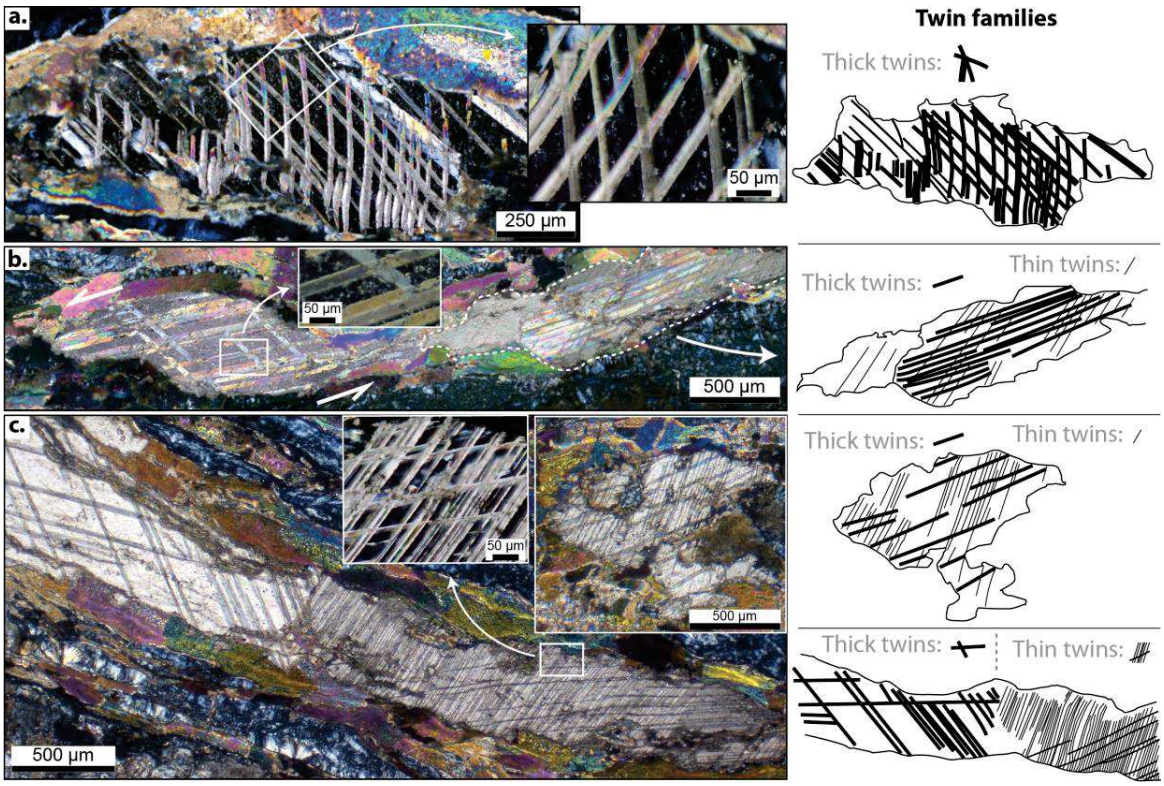

Figure 5.16 *- Calcite twins observed in the studied LGF. (a) Sets of thick twins (Type I; e.g., Ferrill et al., 2004). (b) Dominant sets of thick twins cut by a set of oblique thin twins (Type II;*

Ferrill et al., 2004), and details microphotograph of thick twins. (c) Calcite grain with a subgrain containing two sets of thick twins and the other with two sets of thin twins, and details microphotograph of thin twins. On the right side are sketches of twin families in grains.

No recrystallization is observed in calcite grains. During deformation, the plastic strain in calcite grains can be accommodated by: (1) dynamic recrystallization at temperatures > 250°C (sometimes 300°C, depending on grain size), (2) the formation of thick twins at temperatures > 200°C, and (3) the formation of thin twins < 170°C (Ferrill et al., 2004). Decreasing temperatures during deformation below 250°C would then result in the absence of recrystallization in grains, the presence of thick twins, and predominant amounts of thin twins (Figure 5.16; e.g., Ferrill et al., 2004). Observations performed in calcite grains suggest that the LGF formed and synchronously deformed in the 200-250°C temperature range, and continue to deform below 170°C. The continuation of deformation at temperatures < 200°C, and especially < 170°C, may have been rather limited according to the frequent observation of grains lacking thin twins, and to the lower stability bound of prehnite at ~150°C (e.g., Frey et al., 1991).

Important information arising from structural field measurement is the widespread observation of LGF over the BGC. Their orientations are principally grouped into two NW-SE and NE-SW families (Figure 5.4). The two families are observed together in the western and southern area that broadly corresponds to the western domain of the massif. Only the NE-SW set of LGF is encountered in the central area of the BGC, and solely the NW-SE set in the northern area. The dominant NW-SE family has an orientation and dip similar to the dominant HGF family, and the magmatic layering/foliation (e.g., Menna, 2009). It is important to note that the trend of structures associated to tectonic nappe emplacement in the Ligurian Alps is also NW-SE (Figure 5.1a).
Metamorphic veins with similar mineral filling are described at the Atlantis Massif and at the East Pacific Rise (Hess Deep), as the latest type of veins potentially related to unloading (e.g., Mével & Stamoudi, 1996; Expedition 304/305 Scientists, 2006). Frost et al. (2008) identified resembling veins in troctolites resulting from hydrous fluid circulation in fractures in IODP Hole U1309D at the Atlantis Massif. However, the formation of prehnite and chlorite in these veins require the former presence of olivine in the assemblage as they form during serpentinization (e.g., Mével & Stamoudi, 1996; Frost et al., 2008).
The veins described here in the LGF are observed cutting into gabbros essentially, instead of olivine-bearing lithologies. Furthermore, the widespread occurrence of the LFG in the Bracco complex gabbros contrasts with the few occurrences of similar veins in present-day OCC. From their distribution and orientations, together with prehnite-pumpellyite facies conditions (similar to the Alpine orogeny; Cortesogno et al., 1987; Marroni & Pandolfi, 1996), we suggests that the LGF formed during the orogenic phase rather than during the earlier oceanic stage.

6. Conclusion

The Bracco-Gabbro Complex exhibits many structural and compositional characteristics similar to modern slow-spreading oceanic ridges as also recognized in other Northern Apennines ophiolites. The gabbro pluton exposed in the Bracco preserves high-grade shear zones that developed at the ridge axis under granulitic conditions. Plagioclase and clinopyroxene grains within these shear zones extensively recrystallized under the dislocation creep regime, producing medium to weak CPO. The strength of CPO is observed to remain weak although the deformation intensity increases in samples. These CPO suggest the dominant activation of the [100](010) slip system in plagioclase grains, and [100](001) twin system in clinopyroxene grains. The tectonic evolution of the pluton at the ridge is proposed to correspond to a “late capture”-type OCC as recognized in Mid-Atlantic Ridge OCC. This implies that the granulitic shear zones may not be directly related to the detachment fault. Estimated differential stresses indicate higher values in these structures when formed in a “late-capture OCC” instead of in an “early-capture OCC”.

REFERENCES

Allard, M., Ildefonse, B., Oliot, E., Barou, F. (2021). Plastic deformation of plagioclase in oceanic gabbro accreted at a slow-spreading ridge (Hole U1473A, Atlantis Bank, Southwest Indian Ridge). Journal of Geophysical Research: Solid Earth, 126, e2021JB021964. https://doi.org/10.1029/2021JB021964

Abbate, E., Bortolotti, V., Principi, G., 1980. Apennine ophiolites: a peculiar oceanic crust. In: Rocci, G. (Ed.), Special Issue on Tethyan Ophiolites, Western Area. 59–96.

Allmendinger, R.W., Cardozo, N., Fisher, D.M., 2011. Structural geology algorithms: Vectors and tensors, Cambridge University Press. ed.

Barrett, T.J., Spooner, E.T.C., 1977. Ophiolitic breccias associated with allochthonous oceanic crustal rocks in the East Ligurian Apennines, Italy - a comparison with observations from rifted oceanic ridges. Earth and Planetary Science Letters 35, 79–91. https://doi.org/10.1016/0012-821X(77)90031-0

Baumgartner, R.J., Zaccarini, F., Garuti, G., Thalhammer, O.A.R., 2013. Mineralogical and geochemical investigation of layered chromitites from the Bracco–Gabbro complex, Ligurian ophiolite, Italy. Contributions to Mineralogy and Petrology 165, 477–493. https://doi.org/10.1007/s00410-012-0818-5

Beccaluva, L., Macciotta, G., Piccardo, G.B., Zeda, O., 1984. Petrology of lherzolitic rocks from the Northern Apennine ophiolites. Lithos 17, 299–316. https://doi.org/10.1016/0024-4937(84)90027-6

Berger, A., Stünitz, H., 1996. Deformation mechanisms and reaction of hornblende: examples from the Bergell tonalite (Central Alps). Tectonophysics 257, 149–174. https://doi.org/10.1016/0040-1951(95)00125-5

Blackman, D.K., Ildefonse, B., John, B.E., Ohara, Y., Miller, D.J., Abe, N., Abratis, M., Andal, E.S., Andreani, M., Awaji, S., Beard, J.S., Brunelli, D., Charney, A.B., Christie, D.M., Collins, J., Delacour, A.G., Delius, H., Drouin, M., Einaudi, F., Escartín, J., Frost, B.R., Früh-Green, G., Fryer, P.B., Gee, J.S., Godard, M., Grimes, C.B., Halfpenny, A., Hansen, H.-E., Harris, A.C., Tamura, A., Hayman, N.W., Hellebrand, E., Hirose, T., Hirth, J.G., Ishimaru, S., Johnson, K.T.M., Karner, G.D., Linek, M., MacLeod, C.J., Maeda, J., Mason, O.U., McCaig, A.M., Michibayashi, K., Morris, A., Nakagawa, T., Nozaka, T., Rosner, M., Searle, R.C., Suhr, G., Tominaga, M., von der Handt, A., Yamasaki, T., Zhao, X., 2011. Drilling constraints on lithospheric accretion and evolution at Atlantis Massif, Mid-Atlantic Ridge 30°N. Journal of Geophysical Research 116, B07103. https://doi.org/10.1029/2010JB007931

Blackman, D.K., Ildefonse, B., John, B.E., Ohara, Y., Miller, D.J., MacLeod, C.J., The Expedition 304/305 Scientists (Eds.), 2006. Proceedings of the IODP, 304/305, Proceedings of the IODP. Integrated Ocean Drilling Program. https://doi.org/10.2204/iodp.proc.304305.2006

Bortolotti, V., Principi, G., Treves, B., 2001. Ophiolites, Ligurides and the tectonic evolution from spreading to convergence of a Mesozoic Western Tethys segment. In: Vai, G.B., Martini, I.P. (Eds.), Anatomy of an Orogen: The Apennines and Adjacent Mediterranean Basins. Springer Netherlands, Dordrecht, 151–164. https://doi.org/10.1007/978-94-015-9829-3_11

Bunge, H.J., 1982. Texture Analysis in Materials Science: Mathematical Methods. Butterworths.

Cannat, M., 1993. Emplacement of mantle rocks in the seafloor at mid-ocean ridges. Journal of Geophysical Research: Solid Earth 98, 4163–4172. https://doi.org/10.1029/92JB02221

Cortesogno, L., Galbiati, B., Principi, G., 1987. Note alla '"Carta geologica delle ofioliti del Bracco"' e ricostruzione della paleogeografia Giurassico, Cretacica. Edizioni ETS.

Decandia, F.A., Elter, P., 1972. La" zona" ofiolitifera del Bracco nel settore compreso fra Levanto e la Val Gravena (Apennino ligure). Società Geologica Italiana Bulletin 11, 37–64.

Decrausaz, T., Müntener, O., Manzotti, P., Lafay, R., Spandler, C., 2021. Fossil oceanic core complexes in the Alps. New field, geochemical and isotopic constraints from the Tethyan Aiguilles Rouges Ophiolite (Val d'Hérens, Western Alps, Switzerland). Swiss Journal of Geosciences 114, 3. https://doi.org/10.1186/s00015-020-00380-4

Dick, H.J.B., Lin, J., Schouten, H., 2003. An ultraslow-spreading class of ocean ridge. Nature 426, 405–412. https://doi.org/10.1038/nature02128

Dick, H.J.B., MacLeod, C.J., Blum, P., Abe, N., Blackman, D.K., Bowles, J.A., Cheadle, M.J., Cho, K., Ciążela, J., Deans, J.R., Edgcomb, V.P., Ferrando, C., France, L., Ghosh, B., Ildefonse, B., John, B., Kendrick, M.A., Koepke, J., Leong, J.A.M., Liu, C., Ma, Q., Morishita, T., Morris, A., Natland, J.H., Nozaka, T., Pluemper, O., Sanfilippo, A., Sylvan, J.B., Tivey, M.A., Tribuzio, R., Viegas, G., 2019. Dynamic Accretion Beneath a Slow-Spreading Ridge Segment: IODP Hole 1473A and the Atlantis Bank Oceanic Core Complex. Journal of Geophysical Research 124, 12631–12659. https://doi.org/10.1029/2018JB016858

Dick, H.J.B., Meyer, P.S., Bloomer, S., Kirby, S., Stakes, D., Mawer, C., 1991. Proceedings of the Ocean Drilling Program, 118 Scientific Results, Proceedings of the Ocean Drilling Program. Ocean Drilling Program. https://doi.org/10.2973/odp.proc.sr.118.1991

Dick, H.J.B., Natland, J.H., Alt, J.C., Bach, W., Bideau, D., Gee, J.S., Haggas, S., Hertogen, J.G.H., Hirth, G., Holm, P.M., Ildefonse, B., Iturrino, G.J., John, B.E., Kelley, D.S., Kikawa, E., Kingdon, A., LeRoux, P.J., Maeda, J., Meyer, P.S., Miller, D.J., Naslund, H.R., Niu, Y.-L., Robinson, P.T., Snow, J., Stephen, R.A., Trimby, P.W., Worm, H.-U., Yoshinobu, A., 2000. A long in situ section of the lower ocean crust: results of ODP Leg 176 drilling at the Southwest Indian Ridge. Earth and Planetary Science Letters 179, 31–51. https://doi.org/10.1016/S0012-821X(00)00102-3

Escartín, J., Canales, J.P., 2011. Detachments in Oceanic Lithosphere: Deformation, Magmatism, Fluid Flow, and Ecosystems. Eos, Transactions American Geophysical Union 92, 31–31. https://doi.org/10.1029/2011EO040003

Escartín, J., Mével, C., MacLeod, C.J., McCaig, A.M., 2003. Constraints on deformation conditions and the origin of oceanic detachments: The Mid-Atlantic Ridge core complex at 15°45′N. Geochemistry, Geophysics, Geosystems 4. https://doi.org/10.1029/2002GC000472

Expedition 304/305 Scientists, 2006. Proceedings of the IODP, 304/305, Proceedings of the IODP. Integrated Ocean Drilling Program. https://doi.org/10.2204/

Ferrando, C., France, L., Basch, V., Sanfilippo, A., Tribuzio, R., Boulanger, M., 2021. Grain Size Variations Record Segregation of Residual Melts in Slow-Spreading Oceanic Crust (Atlantis Bank, 57°E Southwest Indian Ridge). Journal of Geophysical Research: Solid Earth 126. https://doi.org/10.1029/2020JB020997

Ferrill, D.A., Morris, A.P., Evans, M.A., Burkhard, M., Groshong, R.H., Onasch, C.M., 2004. Calcite twin morphology: a low-temperature deformation geothermometer. Journal of Structural Geology 26, 1521–1529. https://doi.org/10.1016/j.jsg.2003.11.028

Fitz Gerald, J.D., Stünitz, H., 1993. Deformation of granitoids at low metamorphic grade. I: Reactions and grain size reduction. 29.

Frey, M., De Capitani, C.D., Liou, J.G., 1991. A new petrogenetic grid for low-grade metabasites. Journal of Metamorphic Geology 9, 497–509. https://doi.org/10.1111/j.1525-1314.1991.tb00542.x

Frost, B.R., Beard, J.S., McCaig, A., Condliffe, E., 2008. The Formation of Micro-Rodingites from IODP Hole U1309D: Key To Understanding the Process of Serpentinization. Journal of Petrology 49, 1579–1588. https://doi.org/10.1093/petrology/egn038

Getsinger, A.J., Hirth, G., 2014. Amphibole fabric formation during diffusion creep and the rheology of shear zones. Geology 42, 535–538. https://doi.org/10.1130/G35327.1

Harigane, Y., Michibayashi, K., Ohara, Y., 2008. Shearing within lower crust during progressive retrogression: Structural analysis of gabbroic rocks from the Godzilla Mullion, an oceanic core complex in the Parece Vela backarc basin. Tectonophysics 457, 183–196. https://doi.org/10.1016/j.tecto.2008.06.009

Hey, M.H., 1954. A new review of the chlorites. Mineralogical Magazine and Journal of the Mineralogical Society 30, 277–292. https://doi.org/10.1180/minmag.1954.030.224.01

Holland, T.J.B., Blundy, J., 1994. Non-ideal interactions in calcic amphiboles and their bearing on amphibole-plagioclase thermometry. Contributions to Mineralogy and Petrology 116, 433–447. https://doi.org/10.1007/BF00310910

Ildefonse, B., Blackman, D.K., John, B.E., Ohara, Y., Miller, D.J., MacLeod, C.J., Integrated Ocean Drilling Program Expeditions 304/305 Science Party, 2007. Oceanic core complexes and crustal accretion at slow-spreading ridges. Geology 35, 623. https://doi.org/10.1130/G23531A.1

Ildefonse, B., Blackman, D.K., John, B.E., Ohara, Y., Miller, D.J., MacLeod, C.J., the IODP Expeditions 304-305 Scientists, 2006. IODP Expeditions 304 & 305 Characterize the Lithology, Structure, and Alteration of an Oceanic Core Complex. Scientific Drilling 3, 4–11. https://doi.org/10.5194/sd-3-4-2006

Kelemen, P.B., Kikawa, E., Miller, D.J., 2004. Site 1275. Proceedings of the Ocean Drilling Program, Initial Reports, 209: College Station, TX (Ocean Drilling Program), 167. https://doi.org/doi:10.2973/odp.proc.ir.209.2004

Kirby, S.H., Christie, J.M., 1977. Mechanical Twinning in Diopside Ca(Mg,Fe)Siz06: Structural Mechanism and Associated Crystal Defects. Physics and Chemistry of Mineral 1, 137–163. https://doi.org/10.1007/BF00307315

Kollé, J.J., Blacic, J.D., 1982. Deformation of single-crystal clinopyroxenes: 1. Mechanical twinning in diopside and hedenbergite. Journal of Geophysical Research 87, 4019. https://doi.org/10.1029/JB087iB05p04019

Kruse, R., Stünitz, H., Kunze, K., 2001. Dynamic recrystallization processes in plagioclase porphyroclasts. Journal of Structural Geology 23, 1781–1802. https://doi.org/10.1016/S0191-8141(01)00030-X

Lagabrielle, Y., 2009. Mantle exhumation and lithospheric spreading: An historical perspective from investigations in the Oceans and in the Alps-Apennines ophiolites. Italian Journal of Geosciences 279–293. https://doi.org/10.3301/IJG.2009.128.2.279

Lagabrielle, Y., Cannat, M., 1990. Alpine Jurassic ophiolites resemble the modern central Atlantic basement. Geology 18, 319–322. https://doi.org/10.1130/0091-7613(1990)018<0319:AJORTM>2.3.CO;2

Lagabrielle, Y., Vitale Brovarone, A., Ildefonse, B., 2015. Fossil oceanic core complexes recognized in the blueschist metaophiolites of Western Alps and Corsica. Earth-Science Reviews 141, 1–26. https://doi.org/10.1016/j.earscirev.2014.11.004

Lanari, P., Riel, N., Guillot, S., Vidal, O., Schwartz, S., Pêcher, A., Hattori, K.H., 2013. Deciphering high-pressure metamorphism in collisional context using microprobe mapping methods: Application to the Stak eclogitic massif (northwest Himalaya). Geology 41, 111–114. https://doi.org/10.1130 / g33523.1

Lanari, P., Vho, A., Bovay, T., Airaghi, L., Centrella, S., 2019. Quantitative compositional mapping of mineral phases by electron probe micro-analyser. Geological Society, London, Special Publications 478, 39–63. https://doi.org/10.1144/SP478.4

Lanari, P., Vidal, O., De Andrade, V., Dubacq, B., Lewin, E., Grosch, E.G., Schwartz, S., 2014. XMapTools: A MATLAB®-based program for electron microprobe X-ray image processing and geothermobarometry. Computers & Geosciences 62, 227–240. https://doi.org/10.1016/j.cageo.2013.08.010

Leake, B.E., Woolley, A.R., Arps, A.R., Birch, W.D., Gilbert, M.C., Grice, J.D., Hawthorne, F.C., Kato, A., Kisch, H.J., Krivovichev, V.G., Linthout, K., Laird, J., Mandarino, J.A., Maresch, W.V., Nickel, E.H., Rock, N.M.S., Schumacher, J.C., Smith, D.C., Stephenson, N.C.N., Ungaretti, L., Whittaker, E.J.W., Youzhi, G., 1997. Nomenclature of amphiboles Report of the Subcommittee on Amphiboles of the International Mineralogical Association Commission on New Minerals and Mineral Names. The Canadian Mineralogist 35, 219–246.

Lemoine, M., Tricart, P., Boillot, G., 1987. Ultramafic and gabbroic ocean floor of the Ligurian Tethys (Alps, Corsica, Apennines): In search of a genetic model. Geology 15, 622–625. https://doi-org.insu.bib.cnrs.fr/10.1130/0091-7613(1987)15<622:UAGOFO>2.0.CO;2

Liou, J.G., Maruyama, S., Cho, M., 1985. Phase equilibria and mineral parageneses of metabasites in low-grade metamorphism. Mineralogical Magazine 49, 321–333. https://doi.org/10.1180/minmag.1985.049.352.03

Mainprice, D., Bachmann, F., Hielscher, R., Schaeben, H., 2015. Descriptive tools for the analysis of texture projects with large datasets using MTEX : strength, symmetry and components. Geological Society, London, Special Publications 409, 251–271. https://doi.org/10.1144/SP409.8

Manatschal, G., Sauter, D., Karpoff, A.M., Masini, E., Mohn, G., Lagabrielle, Y., 2011. The Chenaillet Ophiolite in the French/Italian Alps: An ancient analogue for an Oceanic Core Complex? Lithos 124, 169–184. https://doi.org/10.1016/j.lithos.2010.10.017

Marroni, M., Molli, G., Montanini, A., Tribuzio, R., 1998. The association of continental crust rocks with ophiolites in the Northern Apennines (Italy): implications for the continent-ocean transition in the Western Tethys. Tectonophysics 292, 43–66. https://doi.org/10.1016/S0040-1951(98)00060-2

Marroni, M., Pandolfi, L., 2001. Debris flow and slide deposits at the top of the Internal Liguride ophiolitic sequence, Northern Apennines, Italy: A record of frontal tectonic erosion in a fossil accretionary wedge. The Island Arc 10, 9–21. https://doi.org/10.1046/j.1440-1738.2001.00289.x

Marroni, M., Pandolfi, L., 1996. The deformation history of an accreted ophiolite sequence: the Internal Liguride units (Northern apennines, Italy). Geodinamica Acta 9, 13–29. https://doi.org/10.1080/09853111.1996.11417260

Mauler, A., Bystricky, M., Kunze, K., Mackwell, S., 2000. Microstructures and lattice preferred orientations in experimentally deformed clinopyroxene aggregates. Journal of Structural Geology 22, 1633–1648. https://doi.org/10.1016/S0191-8141(00)00073-0

Mehl, L., Hirth, G., 2008. Plagioclase preferred orientation in layered mylonites: Evaluation of flow laws for the lower crust. Journal of Geophysical Research 113, B05202. https://doi.org/10.1029/2007JB005075

Menna, F., 2009. From magmatic to metamorphic deformations in a jurassic ophiolitic complex: the bracco gabbroic massif, eastern liguria (italy). Ofioliti 34, 109–130. https://doi.org/10.4454/ofioliti.v34i2.382

Mével, C., Stamoudi, C., 1996. Hydrothermal Alteration Of The Upper-Mantle Section At Hess Deep. In: Mével, C., Gillis, K.M., Allan, J.F., Meyer, P.S. (Eds.), Proceedings of the Ocean Drilling Program, 147 Scientific Results, Proceedings of the Ocean Drilling Program. Ocean Drilling Program. https://doi.org/10.2973/odp.proc.sr.147.1996

Michibayashi, K., Harigane, Y., Ohara, Y., Muto, J., Okamoto, A., 2014. Rheological properties of the detachment shear zone of an oceanic core complex inferred by plagioclase flow law: Godzilla Megamullion, Parece Vela back-arc basin, Philippine Sea. Earth and Planetary Science Letters 408, 16–23. https://doi.org/10.1016/j.epsl.2014.10.005

Molli, G., 1996. Pre-orogenic tectonic framework of the northern Apennine ophiolites. Eclogae Geologicae Helvetiae 89, 163–180. https://doi.org/10.5169/seals-167898

Molli, G., 1995. Pre-orogenie High Temperature Shear Zones in an Ophiolite Complex (Bracco Massif, Northern Apennines, Italy). In: Vissers, R.L.M., Nicolas, A. (Eds.), Mantle and Lower Crust Exposed in Oceanic Ridges and in Ophiolites, Springer, Dordrecht. Https://Doi.Org/10.1007/978-94-015-8585-9_6. 147–161.

Molli, G., 1994. Microstructural features of high temperature shear zones in gabbros of the Northern Apennine Ophiolites. Journal of Structural Geology 16, 1535–1541. https://doi.org/10.1016/0191-8141(94)90031-0

Montanini, A., Tribuzio, R., Vernia, L., 2008. Petrogenesis of basalts and gabbros from an ancient continent–ocean transition (External Liguride ophiolites, Northern Italy). Lithos 101, 453–479. https://doi.org/10.1016/j.lithos.2007.09.007

Montardi, Y.A., Mainprice, D., 1987. A transmission electron microscopie study of the natural plastic defonnation of calcic plagioclases (An 68-70). Bulletin de Minéralogie 110, 1–14.

Morimoto, N., 1988. Nomenclature of Pyroxenes. Mineralogy and Petrology 39, 55–76. https://doi.org/10.1007/BF01226262

Nicolas, A., Violette, J.F., 1982. Mantle flow at oceanic spreading centers: Models derived from ophiolites. Tectonophysics 81, 319–339. https://doi.org/10.1016/0040-1951(82)90136-6

Paterson, M.S., 1995. A theory for granular flow accommodated by material transfer via an intergranular fluid. Tectonophysics 245, 135–151. https://doi.org/10.1016/0040-1951(94)00231-W

Piccardo, G.B., Guarnieri, L., 2010. Alpine peridotites from the Ligurian Tethys: an updated critical review. International Geology Review 52, 1138–1159. https://doi.org/10.1080/00206810903557829

Poirier, J.-P., Guillopé, M., 1979. Deformation induced recrystallization of minerals. Bulletin de Minéralogie 102, 67–74. https://doi.org/10.3406/bulmi.1979.7256

Raleigh, C.B., Talbot, J.L., 1967. Mechanical twinning in naturally and experimentally deformed diopside. American Journal of Science 265, 151–165. https://doi.org/10.2475/ajs.265.2.151

Rampone, E., Borghini, G., Basch, V., 2020. Melt migration and melt-rock reaction in the Alpine-Apennine peridotites: Insights on mantle dynamics in extending lithosphere. Geoscience Frontiers 11, 151–166. https://doi.org/10.1016/j.gsf.2018.11.001

Rampone, E., Hofmann, A.W., Piccardo, G.B., Vannucci, R., Bottazzi, P., Ottolini, L., 1996. Trace element and isotope geochemistry of depleted peridotites from an N-MORB type ophiolite (Internal Liguride, N. Italy). Contributions to Mineralogy and Petrology 123, 61–76. https://doi.org/10.1007/s004100050143

Rampone, E., Piccardo, G.B., Vannucci, R., Bottazzi, P., 1997. Chemistry and origin of trapped melts in ophiolitic peridotites. Geochimica et Cosmochimica Acta 61, 4557–4569. https://doi.org/10.1016/S0016-7037(97)00260-3

Sanfilippo, A., Tribuzio, R., 2011. Melt transport and deformation history in a nonvolcanic ophiolitic section, northern Apennines, Italy: Implications for crustal accretion at slow spreading settings. Geochemistry, Geophysics, Geosystems 12, n/a-n/a. https://doi.org/10.1029/2010GC003429

Satsukawa, T., Ildefonse, B., Mainprice, D., Morales, L.F.G., Michibayashi, K., Barou, F., 2013. A database of plagioclase crystal preferred orientations (CPO) and microstructures – implications for CPO origin, strength, symmetry and seismic anisotropy in gabbroic rocks. Solid Earth 4, 511–542. https://doi.org/10.5194/se-4-511-2013

Schiffman, P., Liou, J.G., 1983. Synthesis of Fe-pumpellyite and its stability relations with epidote. Journal of Metamorphic Geology 1, 91–101. https://doi.org/10.1111/j.1525-1314.1983.tb00266.x

Schwarzenbach, E.M., Vogel, M., Früh-Green, G.L., Boschi, C., 2021. Serpentinization, Carbonation, and Metasomatism of Ultramafic Sequences in the Northern Apennine Ophiolite (NW Italy). Journal of Geophysical Research: Solid Earth 126. https://doi.org/10.1029/2020JB020619

Skemer, P., Katayama, I., Jiang, Z., Karato, S., 2005. The misorientation index: Development of a new method for calculating the strength of lattice-preferred orientation. Tectonophysics 411, 157–167. https://doi.org/10.1016/j.tecto.2005.08.023

Tribuzio, R., Garzetti, F., Corfu, F., Tiepolo, M., Renna, M.R., 2016. U–Pb zircon geochronology of the Ligurian ophiolites (Northern Apennine, Italy): Implications for continental breakup to slow seafloor spreading. Tectonophysics 666, 220–243. https://doi.org/10.1016/j.tecto.2015.10.024

Tribuzio, R., Tiepolo, M., Vannucci, R., 2000. Evolution of gabbroic rocks of the Northern Apennine ophiolites (Italy): Comparison with the lower oceanic crust from modern slow-spreading ridges. Special Paper 349: Ophiolites and Oceanic Crust: New Insights from Field Studies and the Ocean Drilling Program. Geological Society of America, 129–138. https://doi.org/10.1130/0-8137-2349-3.129

Tullis, J., Yund, R.A., 1987. Transition from cataclastic flow to dislocation creep of feldspar: Mechanisms and microstructures. 5.

Twiss, R.J., 1977. Theory and applicability of a recrystallized grain size paleopiezometer. In: Wyss M. (Eds) Stress in the Earth. Contributions to Current Research in Geophysics (CCRG). Birkhäuser, Basel. https://doi.org/10.1007/978-3-0348-5745-1_13

Wenk, H.-R., Christie, J.M., 1991. Comments on the interpretation of deformation textures in rocks. Journal of Structural Geology 13, 1091–1110. https://doi.org/10.1016/0191-8141(91)90071-P

Whitney, D.L., Evans, B.W., 2010. Abbreviations for names of rock-forming minerals. American Mineralogist 95, 185–187. https://doi.org/10.2138/am.2010.3371

Zhou, Y., He, C., 2015. Microstructures and deformation mechanisms of experimentally deformed gabbro. Earthquake Science 28, 119–127. https://doi.org/10.1007/s11589-015-0115-2

ANNEXES

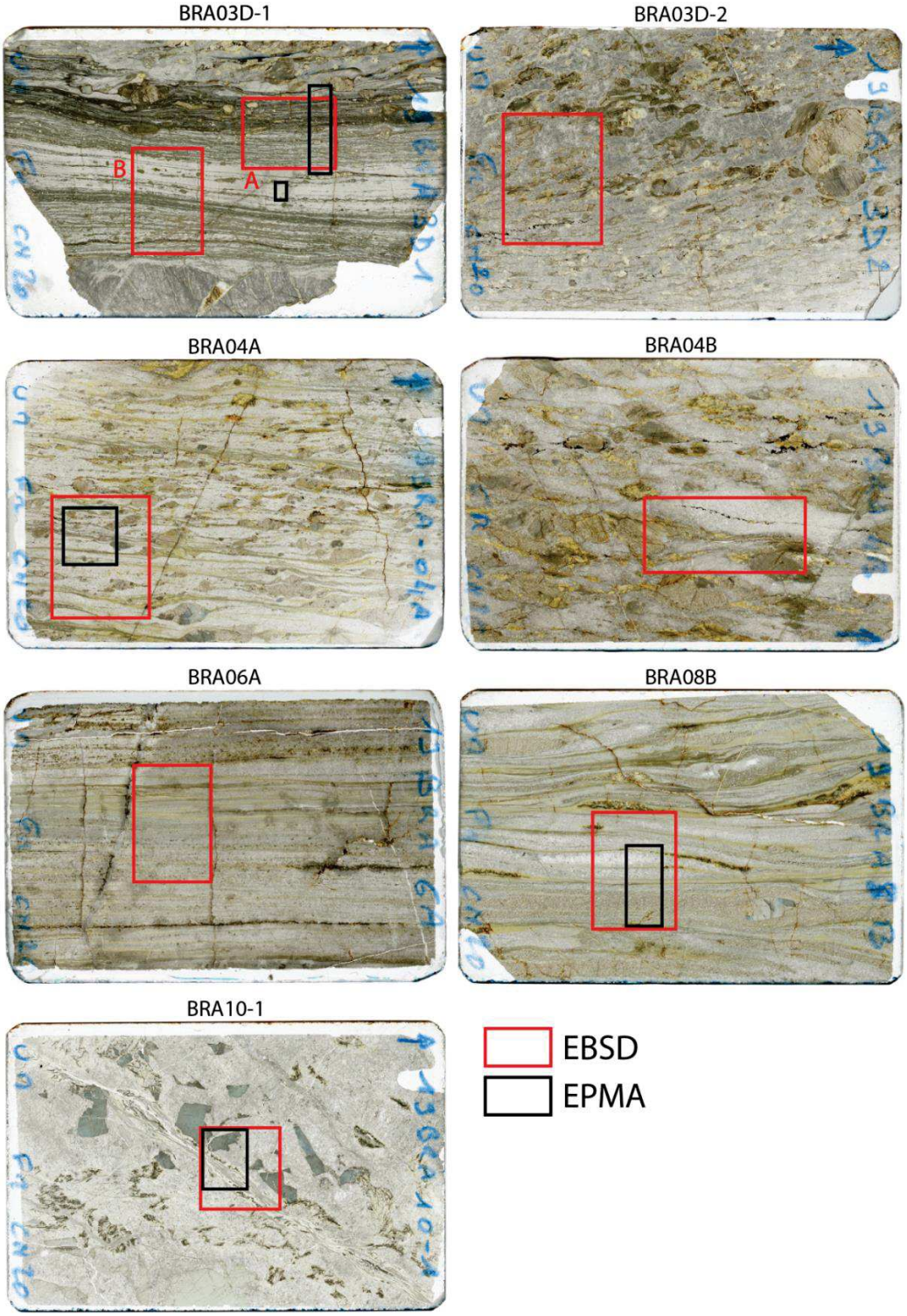

Figure S5.1 *- Thin section microphotographs and location of quantitative maps (EBSD and EPMA.*

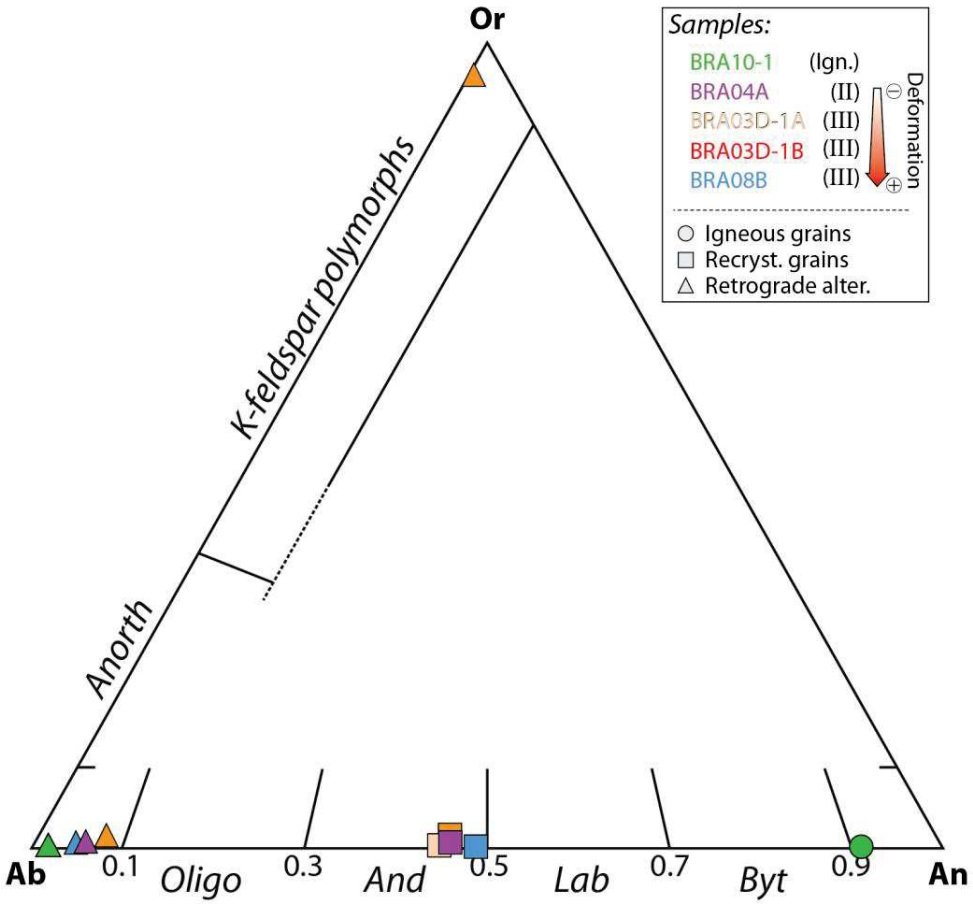

Figure S5.2 *- Plagioclase composition represented in the ternary albite-orthose-anorthite diagram.*

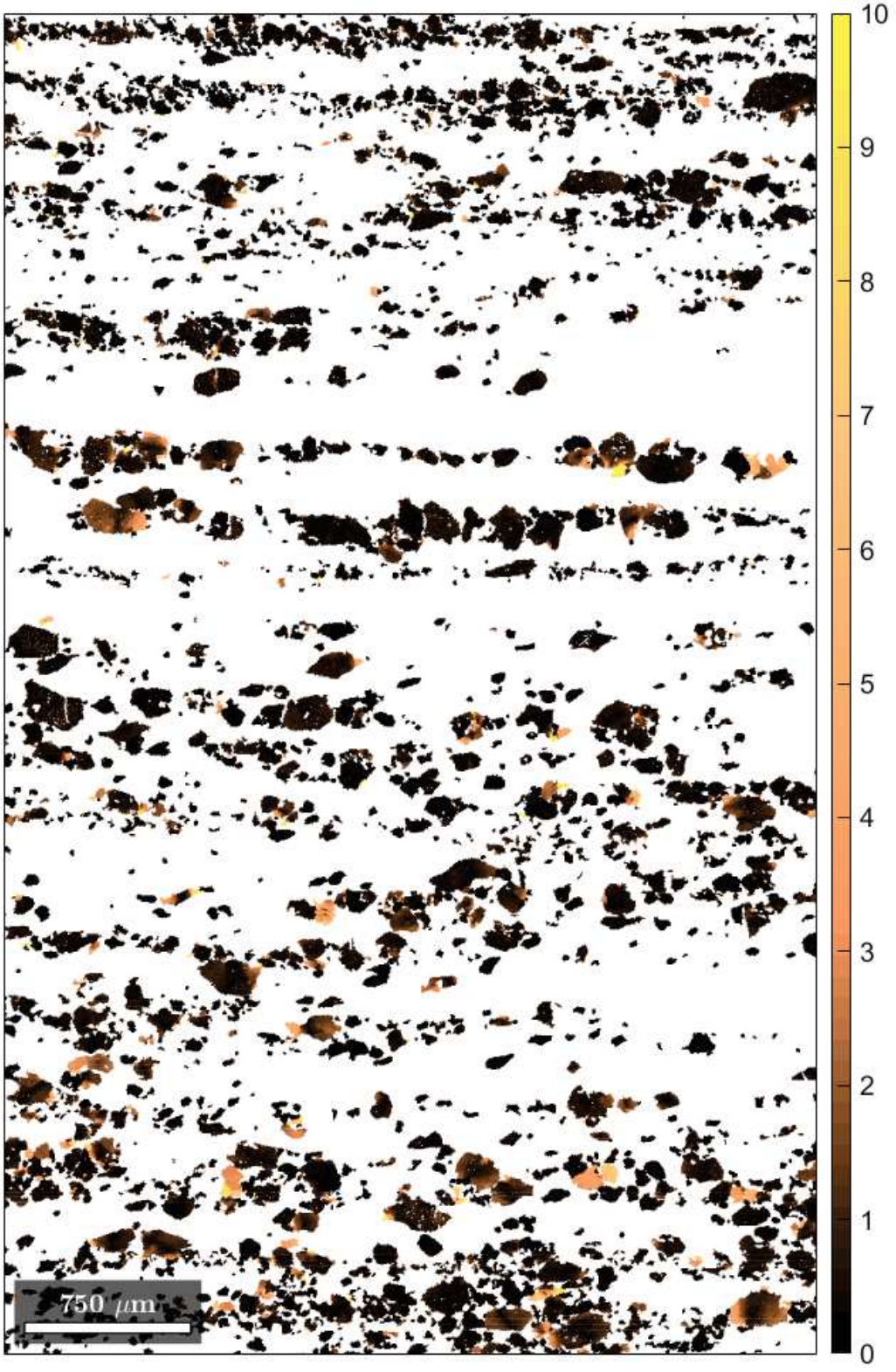

Figure S5.3 *- Misorientation relative to grain mean orientation in clinopyroxene grains from the ultramylonite BRA06A. Note the generally weak intragranular deformation of grains.*

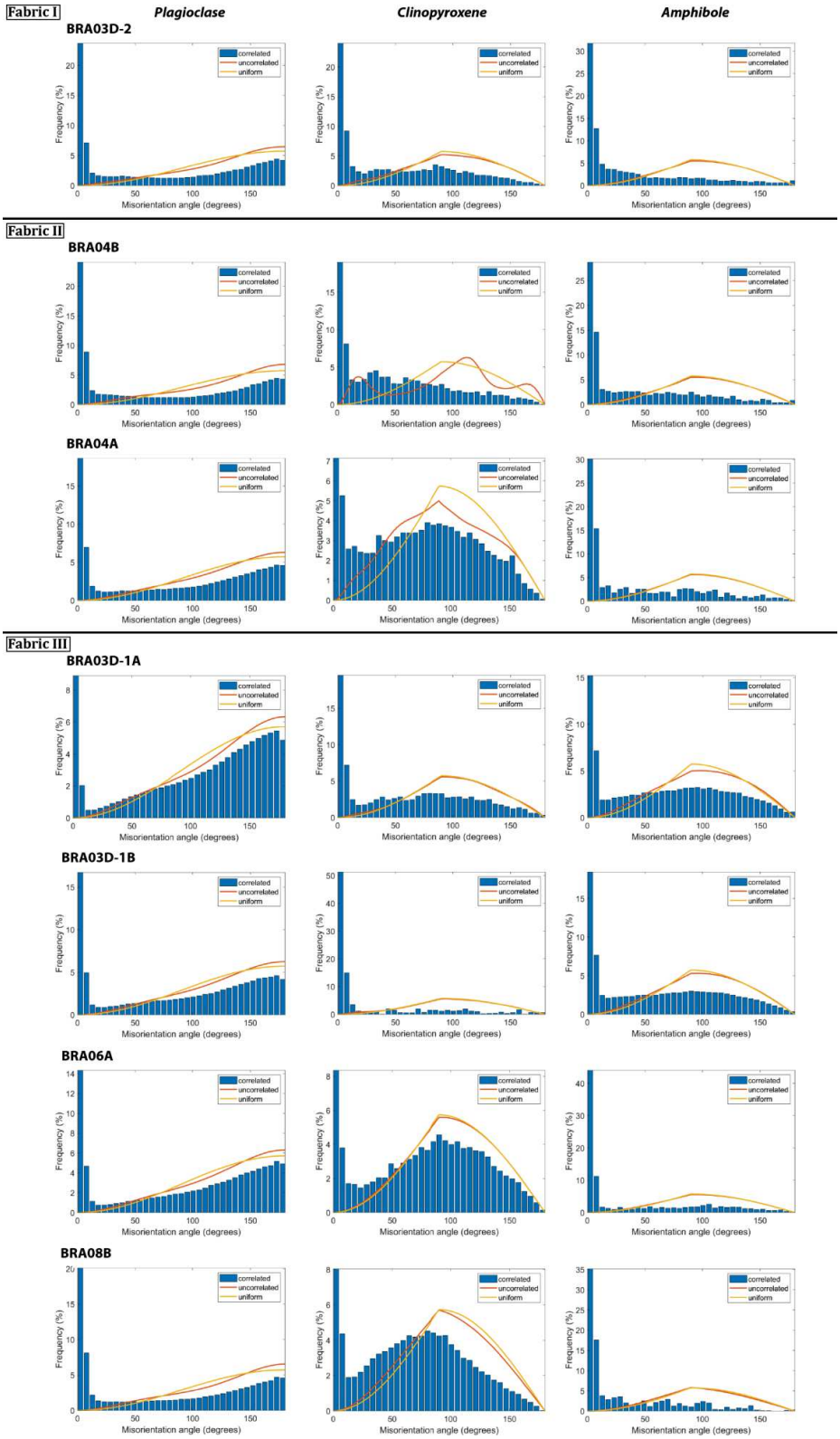

Figure S5.4 *- Misorientation angle distribution histogram measured in plagioclase, clinopyroxene, and amphibole grains. Note that twin boundaries are not considered here.*

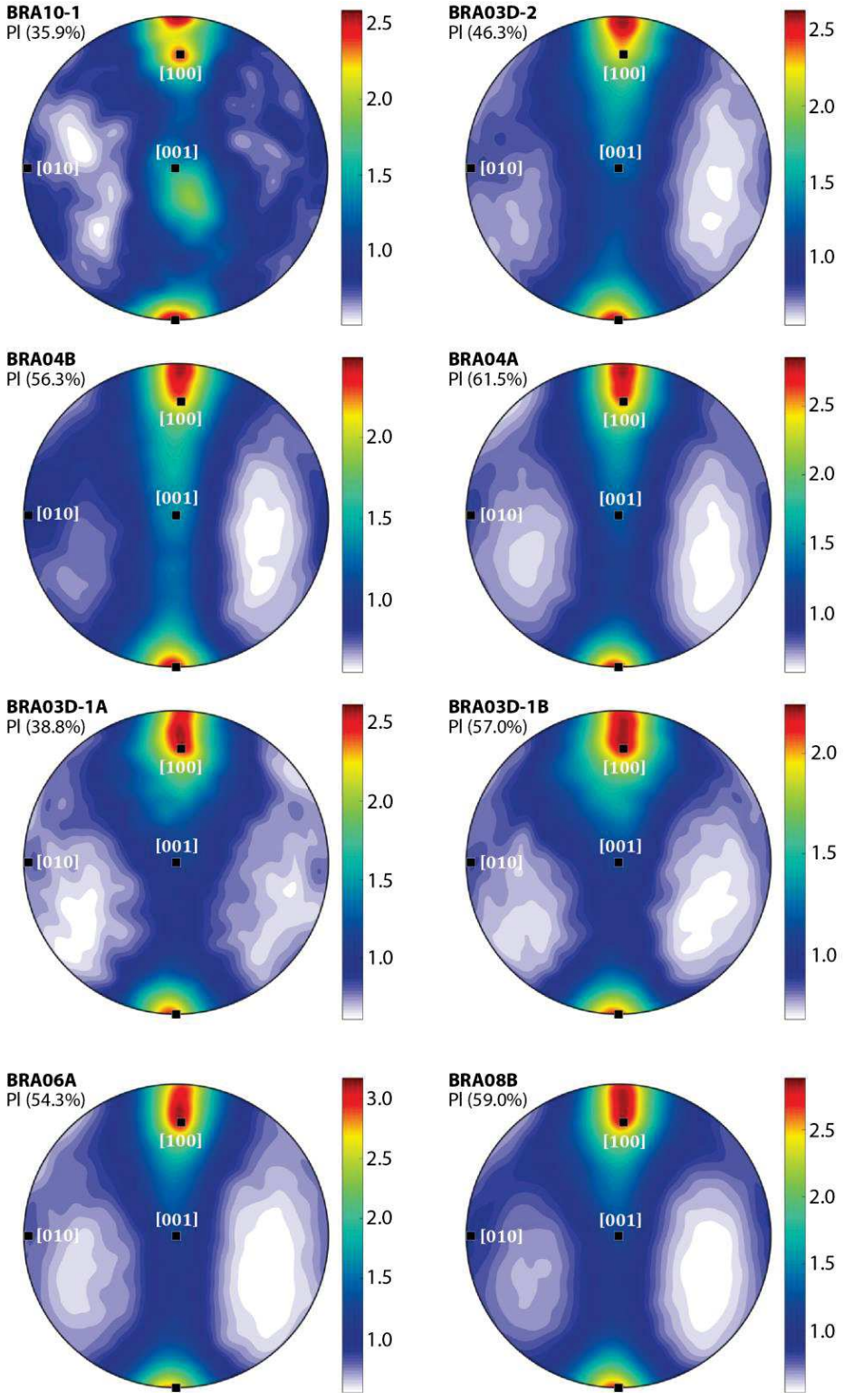

Figure S5.5 *- Inverse pole figures of misorientation rotation axes distribution in plagioclase grains. The rotation axes plotted correspond to low angle misorientations (< 10°; i.e., misorientations measured at subgrain boundaries).*

Table S5.1 *- Quantitative maps parameters. n.a.: not analyzed.*

	BRA03D-1A	**BRA03D-1B**	**BRA03D-2**	**BRA04A**	**BRA04B**	**BRA06A**	**BRA08B**	**BRA10-1**
EBSD								
Step size	3.5 µm	4.0 µm	5.8 µm	5.0 µm	7.0 µm	4.8 µm	4.0 µm	7.0 µm
Field width	2345 px	1625 px	1587 px	1909 px	2435 px	1621 px	1911 px	1177 px
Field height	1848 px	2720 px	2038 px	2252 px	1126 px	2662 px	2498 px	1413 px
Indexation rate	64.4 %	81.0 %	65.1 %	76.4 %	78.9 %	67.0 %	80.3 %	50.4 %
EPMA								
Step size	4 µm	2 µm	*n.a.*	5 µm	*n.a.*	*n.a.*	5 µm	7 µm
Field width	400 px	250 px	*n.a.*	1000 px	*n.a.*	*n.a.*	600 px	800 px
Field height	2000 px	500 px	*n.a.*	1000 px	*n.a.*	*n.a.*	1400 px	1000 px

CHAPTER VI

SYNTHESIS AND CONCLUDING REMARKS

About half of the present-day active mid-ocean ridges exhibit slow-spreading rates, and ~20% of the actual seafloor was accreted at slow-spreading ridges (e.g., Expedition 335 Scientists, 2012, Fig. F1 & F2; Dunn, 2015). At these spreading rates, the magmatic activity is heterogeneously distributed beneath the ridge axis (e.g., Lin et al., 1990), and deformation plays a significant role in the progressive tectono-magmatic construction of the crust. It generally results in heterogeneous crustal architecture, by contrast to the layered structure of the crust formed at fast-spreading ridges (e.g., Mével, 2003; Ildefonse, 2014). The development of detachment faults, which are long-lived low-angle normal faults, as a result of locally asymmetric extension (e.g., Escartín et al., 2008) leads to the exhumation of the deep oceanic crust and upper mantle (e.g., Cannat, 1993). This is known as an oceanic core complex (OCC; e.g., Escartín & Canales, 2011). Studying lower oceanic gabbros that are sampled in OCC provides a unique opportunity for investigating the tectono-magmatic processes occurring in the oceanic lithosphere at slow-spreading ridges.

My thesis aimed to characterize in detail the ductile deformation processes involved in magmatic accretion and subsequent exhumation of gabbroic lithologies through detachment faulting at slow-spreading oceanic ridges. It focusses principally on gabbros exposed and drilled at the Atlantis Bank at the ultraslow-spreading Southwest Indian Ridge. In addition, I draw comparisons with the Bracco-Gabbro Complex, a Northern Apennine ophiolite. Petrographic, microstructural and electron backscattered diffraction (EBSD) analyses reveal the ubiquitous occurrence of plastic deformation mechanisms in the investigated structures from the two gabbro plutons, and the major role of plagioclase in the accommodation of these deformation through intracrystalline slip (dislocation creep) and, to a minor extent, diffusion. Petro-structural analyses, EBSD analyses, electron probe micro-analyses (EPMA), and thermodynamic modeling permit to demonstrate that the onset of plastic deformation occurs under hypersolidus conditions and continues to lower grade metamorphic conditions at the Atlantis Bank. From these analyses, a tectono-magmatic model for OCC development at the ultraslow-spreading Southwest Indian Ridges is proposed. The petro-structural characterization of high-grade structures sampled in the Bracco-gabbro Complex, through EBSD and EPMA analyses, points to the onset of deformation under granulitic conditions into highly localized shear zones. I provide here a summary of the results and interpretations presented in the manuscript and draw general comprehensive conclusions.

Deformation in gabbroic rocks from the Atlantis Bank

The Atlantis Bank was drilled in three different holes, located on its summit (Pettigrew et al., 1999; Dick et al., 2000, 2019), and IODP Hole U1473A, the last drilled, is investigated in this manuscript. Previous studies of Hole U1473A documented widespread crystal plastic deformation in gabbroic lithologies, particularly in the upper ~500 mbsf of the hole. This deformation led to the development of porphyroclastic to protomylonitic microstructures with predominant reverse shear senses, locally evolving into ultramylonitic shear zones (e.g., Dick et al., 2019). Deformation occurred in a continuum from hypersolidus conditions while

gabbroic sill intrusion was still active, to granulitic and lower grade metamorphic conditions during the development of the OCC (Figure 4.18). The four main successive stages of deformation previously recognized in the literature (Mehl & Hirth, 2008; Miranda & John, 2010; Miranda et al., 2016; Gardner et al., 2020; Taufner et al., 2021) are re-evaluated and complemented herein by petro-structural analyses and thermodynamic modeling providing pressure and temperature estimates. The deformation stages are, from high- to low-grade conditions:

- (1) > 1050 °C – 200-300 MPa (6-10 km depth): Hypersolidus solid-state deformation resulting from far-field, spreading-related forces at the ridge axis. It induces the crystal-plastic deformation and dynamic recrystallization of plagioclase, olivine, and clinopyroxene;
- (2) 1000-1050 °C – 200-300 MPa (6-10 km depth): Mainly solid-state crystal-plastic deformation producing the commonly observed porphyroclastic to protomylonitic microstructures. At this stage melt is locally present, percolating through thin channels, inducing melt-rock reactions and promoting strain localization. It leads to a shift from dominant dislocation creep to melt-assisted grain boundary sliding. From this stage, deformation is related to the capture of gabbros by the detachment fault, and to the associated exhumation;
- (3) 800-860 °C – 130-150 MPa (4-5 km depth): Solid-state mylonitization associated to strain localization and intracrystalline hardening;
- (4) 700 °C – 100 MPa (2-3 km depth): Solid-state – semi-brittle strain localization associated to hydrothermal fluid circulation (seawater) and replacement of clinopyroxene by green amphibole. The deformation in these shear zones occurs through fluid-assisted grain boundary sliding. Temperature conditions at this stage can vary depending on the amount of circulating fluids.

These episodes represent the general deformation history recorded within Hole U1473A but are not systematically observed in all deformed intervals. Overall, the plastic deformation of plagioclase grains produces weak to medium crystallographic fabrics, which are progressively acquired as recrystallization increases in the rock. Dynamic recrystallization is mainly achieved through subgrain rotation, and dislocation creep occurs with the dominant activation of the [100](010) slip system in plagioclase, which induces a Crystallographic Preferred Orientation (CPO). The weakening of plagioclase CPO in ultramylonites where dislocation creep is observed to be dominant is explained by the progressive scattering of grains orientations through subgrain rotation. In addition to dynamic recrystallization, changes in slip system activity with decreasing deformation temperature are documented. Four different slip systems are identified through intragranular misorientation analysis: [001](010), [100](001), and two from the ⟨100⟩(001) family. In fine-grained mylonites/ultramylonites subjected to melt and/or fluid circulation, grain boundary sliding mechanism is inferred to produce the observed CPO weakening. Finally, average recrystallized grain sizes are higher in

the upper part of Hole U1473A (> 500 mbsf), where the deformation is pervasive, than in the lower part of the hole (500-800 mbsf) where the deformation is more localized. In this lower part, a switch from grain boundary migration recrystallization to subgrain rotation recrystallization seems related to variations in differential stresses during deformation rather than from temperature variations.

Deformation in gabbroic rocks from the Bracco-Gabbro Complex

The gabbros outcropping within the Bracco complex pertain to the internal Ligurides ophiolites and are characterized by sparse occurrences of high-grade deformation into an isotropic to locally foliated gabbro pluton. Structural, microstructural, and petrological studies performed in these gabbros revealed the occurrence of three main deformation episodes related to the original oceanic setting. Each episode is associated with different metamorphic grades from granulitic (D_1 at 850-950 °C) to greenschist conditions (D_2 at 550-500 °C, and D_3 < 500 °C), and proposed to correspond to a continuous evolution during exhumation into an oceanic core complex (e.g., Molli, 1994, 1996; Menna et al., 2007; Menna, 2009). The petro-structural analyses presented herein are consistent with the previous studies and provide further constraints on the active deformation mechanisms. Deformation in high-grade structures occurred by dislocation creep, dominantly through the activation of the [100](010) slip system in plagioclase grains, and of the [100](001) twin system in clinopyroxene grains. The extensive dynamic recrystallization observed in these structures occurred by subgrain rotation. It resulted in very fine-grained shear zones associated with high differential stresses (120-170 MPa). These observations suggest that the gabbro pluton exposed in the Bracco complex was captured and exhumed by the detachment fault after it nearly entirely crystallized. Thus, it corresponds to a "late-capture OCC" in contrast to the Atlantis Bank that is an "early-capture OCC". Applying the late-capture OCC model to the Bracco ophiolite implies that high-grade deformation occurred before detachment faulting (e.g., Escartín et al., 2003). Ultimately, the episode of formation of low-grade prehnite- and chlorite-bearing structures (prehnite-pumpellyite facies, ~200-250 °C) observed throughout the complex is inferred to be associated with the Alpine orogeny rather than with the later stages of exhumation at the ridge.

Concluding remarks

High-grade granulitic deformed zones are major features in gabbros accreted at slow-spreading ridges and can be highly heterogeneously organized within a pluton. Owing to its dominant proportion in gabbros (half of the rock volume) and to the fact that it acts as the weaker mineral under high-grade conditions (e.g., Kronenberg & Shelton, 1980), plagioclase behavior during deformation strongly controls the rheology of the lower slow-spread oceanic crust. It is shown that intracrystalline slip associated with subgrain rotation recrystallization is dominant in this mineral in the two gabbro plutons studied. It occurs essentially by activation

of the [100](010) slip system that produces the observed CPO, while the [001](010) slip system restricts to subgrain boundaries.

In the context of slow-spreading ridges, overall weak to medium intensities plagioclase CPO are progressively acquired during the deformation. These CPO patterns are generally characterized by the preferred alignment of [100] axes parallel to the lineation and of (010) planes parallel to the foliation. This CPO is similar to that measured in undeformed igneous gabbros (e.g., Satsukawa et al., 2013; Boulanger et al., 2021), which results from magmatic flow (e.g., Benn & Allard, 1989; Ji et al., 2014). However, the development of a significant magmatic fabric is rarely documented in slow-spread gabbros, which are more generally isotropic (e.g., Dick et al., 2019). As the progressive recrystallization of plagioclase grains is shown to be mostly host-controlled, starting from an isotropic state, this could provide an explanation for the systematically weak fabric intensities observed. This contrasts with the general observation of medium to strong intensities in plagioclase fabrics associated to deformation at fast-spreading ridges, where magmatic fabrics are common and extensively developed in gabbros (e.g., Mock et al., 2021).

The spatial distribution of high-grade structures, their thickness, and the associated calculated differential stresses are significantly different in the Atlantis Bank and the Bracco-Gabbro Complex (e.g., Menna, 2009; Dick et al., 2019). Contrasted original tectonic settings and evolutions are inferred to account for these differences. The Atlantis Bank corresponds to a detachment faulting that roots deep enough to capture a gabbroic pluton that is still a crystallizing magma body (i.e., with melt present; e.g., Dick et al., 2019). This corresponds to the "melt-assisted" model in Escartín et al. (2003). I propose that the Bracco-gabbro Complex was formed by a detachment faulting that captured the pluton after it was (almost) fully crystallized. It would correspond either to the "shallow detachment" or the "amagmatic extension" cases in Escartín et al. (2003). By considering the detachment fault capture from the perspective of the gabbro pluton, I propose the term “late-capture” to describe a capture occurring as the pluton is almost fully crystallized. In contrast, the term “early-capture” would refer to a capture during the magmatic construction of the pluton, when important fractions of melt are still present. An important implication for the Bracco complex is that the high-grade deformation is probably not related to detachment faulting in the case of a late-capture, in contrast to the early-capture model were they are related to both far-field forces and detachment faulting (e.g., Escartín et al., 2003).
However, the temperature conditions of deformation in the Bracco-Gabbro Complex (e.g., Tribuzio et al., 2000; Montanini et al., 2008) and the Atlantis Bank, are very close, resulting in similar deformation mechanisms for plagioclase grains. Hence, a change by a factor of two in differential stresses does not significantly impact the mechanical behavior of plagioclase during deformation.

Coupled EBSD analyses and thermodynamic modeling in some of the studied samples provide insights on the link between the temperature of the deformation and the activated slip

systems in plagioclase. Detailed misorientation analyses suggest similar activated slip systems in plagioclase grains from samples (porphyroclastic and protomylonitic olivine gabbros) deformed at temperatures higher than 850 °C. These slip systems are [100](010), [100](001), [001](010), together with a possible conjugated activity of ⟨100⟩(001). In contrast, other slip systems, in addition to the previous ones, are inferred from misorientations in plagioclase grains from two ultramylonites for which calculated deformation temperatures are below 850 °C (down to 700 °C). They are [201](010), most likely, and [101](010). One of these two ultramylonites is found cutting through the protomylonitic domain described above. Further investigations are required to constrain further the precise ranges of activity of the principal and secondary slip systems active in plagioclase grains during natural deformation.

REFERENCES

Benn, K., Allard, B., 1989. Preferred Mineral Orientations Related to Magmatic Flow in Ophiolite Layered Gabbros. Journal of Petrology 30, 925–946. https://doi.org/10.1093/petrology/30.4.925

Boulanger, M., France, L., Ferrando, C., Ildefonse, B., Ghosh, B., Sanfilippo, A., Liu, C. -Z., Morishita, T., Koepke, J., Bruguier, O., 2021. Magma-Mush Interactions in the Lower Oceanic Crust: Insights From Atlantis Bank Layered Series (Southwest Indian Ridge). Journal of Geophysical Research: Solid Earth 126. https://doi.org/10.1029/2021JB022331

Cannat, M., 1993. Emplacement of mantle rocks in the seafloor at mid-ocean ridges. Journal of Geophysical Research: Solid Earth 98, 4163–4172. https://doi.org/10.1029/92JB02221

Dick, H.J.B., MacLeod, C.J., Blum, P., Abe, N., Blackman, D.K., Bowles, J.A., Cheadle, M.J., Cho, K., Ciążela, J., Deans, J.R., Edgcomb, V.P., Ferrando, C., France, L., Ghosh, B., Ildefonse, B., John, B., Kendrick, M.A., Koepke, J., Leong, J.A.M., Liu, C., Ma, Q., Morishita, T., Morris, A., Natland, J.H., Nozaka, T., Pluemper, O., Sanfilippo, A., Sylvan, J.B., Tivey, M.A., Tribuzio, R., Viegas, G., 2019. Dynamic Accretion Beneath a Slow-Spreading Ridge Segment: IODP Hole 1473A and the Atlantis Bank Oceanic Core Complex. Journal of Geophysical Research 124, 12631–12659. https://doi.org/10.1029/2018JB016858

Dick, H.J.B., Natland, J.H., Alt, J.C., Bach, W., Bideau, D., Gee, J.S., Haggas, S., Hertogen, J.G.H., Hirth, G., Holm, P.M., Ildefonse, B., Iturrino, G.J., John, B.E., Kelley, D.S., Kikawa, E., Kingdon, A., LeRoux, P.J., Maeda, J., Meyer, P.S., Miller, D.J., Naslund, H.R., Niu, Y.-L., Robinson, P.T., Snow, J., Stephen, R.A., Trimby, P.W., Worm, H.-U., Yoshinobu, A., 2000. A long in situ section of the lower ocean crust: results of ODP Leg 176 drilling at the Southwest Indian Ridge. Earth and Planetary Science Letters 179, 31–51. https://doi.org/10.1016/S0012-821X(00)00102-3

Dunn, R.A., 2015. Crust and Lithospheric Structure - Seismic Structure of Mid-Ocean Ridges. Treatise on Geophysics. Elsevier, 419–451. https://doi.org/10.1016/B978-0-444-53802-4.00011-7

Escartín, J., Canales, J.P., 2011. Detachments in Oceanic Lithosphere: Deformation, Magmatism, Fluid Flow, and Ecosystems. Eos, Transactions American Geophysical Union 92, 31–31. https://doi.org/10.1029/2011EO040003

Escartín, J., Mével, C., MacLeod, C.J., McCaig, A.M., 2003. Constraints on deformation conditions and the origin of oceanic detachments: The Mid-Atlantic Ridge core complex at 15°45′N. Geochemistry, Geophysics, Geosystems 4. https://doi.org/10.1029/2002GC000472

Escartín, J., Smith, D.K., Cann, J.R., Schouten, H., Langmuir, C.H., Escrig, S., 2008. Central role of detachment faults in accretion of slow-spreading oceanic lithosphere. Nature 455, 790–794. https://doi.org/10.1038/nature07333

Expedition 335 Scientists, 2012. Deep drilling of intact ocean crust: harnessing past lessons to inform future endeavors. In: Teagle, D.A.H., Ildefonse, B., Blum, P., and the Expedition 335 Scientists, Proc. IODP, 335: Tokyo (Integrated Ocean Drilling Program Management International, Inc.). https://doi.org/10.2204/iodp.proc.335.104.2012

Gardner, R.L., Piazolo, S., Daczko, N.R., Trimby, P., 2020. Microstructures reveal multistage melt present strain localisation in mid-ocean gabbros. Lithos 366–367, 105572. https://doi.org/10.1016/j.lithos.2020.105572

Ildefonse, B., 2014. Crustal Accretion. Earth Sciences Series. Encyclopedia of Marine Geosciences, Springer 1–7. https://doi.org/10.1007/SpringerReference_350453

Ji, S., Tongbin, S., Salisbury, M.H., Sun, S., Michibayashi, K., Zhao, W., Long, C., Liang, F., Satsukawa, T., 2014. Plagioclase preferred orientation and induced seismic anisotropy in mafic igneous rocks. Journal of Geophysical Research: Solid Earth 119, 8064–8088. https://doi.org/10.1002/2014JB011352

Kronenberg, A.K., Shelton, G.L., 1980. Deformation microstructures in experimentally deformed Maryland diabase. Journal of Structural Geology 2, 341–353. https://doi.org/10.1016/0191-8141(80)90022-X

Lin, J., Purdy, G.M., Schouten, H., Sempere, J.-C., Zervas, C., 1990. Evidence from gravity data for focusedmagmatic accretionalong the Mid-Atlantic Ridge. Nature 344, 627–632. https://doi.org/10.1038/344627a0

Mehl, L., Hirth, G., 2008. Plagioclase preferred orientation in layered mylonites: Evaluation of flow laws for the lower crust. Journal of Geophysical Research 113, B05202. https://doi.org/10.1029/2007JB005075

Menna, F., 2009. From magmatic to metamorphic deformations in a jurassic ophiolitic complex: the bracco gabbroic massif, eastern liguria (italy). Ofioliti 34, 109–130. https://doi.org/10.4454/ofioliti.v34i2.382

Menna, F., Principi, G., Treves, B., Podetti, S., Garfagnoli, F., Corti, S., 2007. The pre-orogenic tectonic history of the Bracco gabbroic massif: review and news. Periodico Di Mineralogia 81–100. https://doi.org/10.2451/2007PM0010

Mével, C., 2003. Serpentinization of abyssal peridotites at mid-ocean ridges. Comptes Rendus Geoscience 335, 825–852. https://doi.org/10.1016/j.crte.2003.08.006

Miranda, E.A., Hirth, G., John, B.E., 2016. Microstructural evidence for the transition from dislocation creep to dislocation-accommodated grain boundary sliding in naturally deformed plagioclase. Journal of Structural Geology 92, 30–45. https://doi.org/10.1016/j.jsg.2016.09.002

Miranda, E.A., John, B.E., 2010. Strain localization along the Atlantis Bank oceanic detachment fault system, Southwest Indian Ridge. Geochemistry, Geophysics, Geosystems 11, 34. https://doi.org/10.1029/2009GC002646

Mock, D., Ildefonse, B., Müller, T., Koepke, J., 2021. A Reference Section Through Fast-Spread Lower Oceanic Crust, Wadi Gideah, Samail Ophiolite (Sultanate of Oman): Insights From Crystallographic Preferred Orientations. Journal of Geophysical Research: Solid Earth 126. https://doi.org/10.1029/2021JB021864

Molli, G., 1996. Pre-orogenic tectonic framework of the northern Apennine ophiolites. Eclogae Geologicae Helvetiae 89, 163–180. https://doi.org/10.5169/seals-167898

Molli, G., 1994. Microstructural features of high temperature shear zones in gabbros of the Northern Apennine Ophiolites. Journal of Structural Geology 16, 1535–1541. https://doi.org/10.1016/0191-8141(94)90031-0

Montanini, A., Tribuzio, R., Vernia, L., 2008. Petrogenesis of basalts and gabbros from an ancient continent–ocean transition (External Liguride ophiolites, Northern Italy). Lithos 101, 453–479. https://doi.org/10.1016/j.lithos.2007.09.007

Pettigrew, T., Casey, J., Miller, D., Araki, E., Boissonnas, R., Busby, R., Einaudi, F., Gerdom, M., Guo, Z., Hopkins, H., 1999. Leg 179 summary. ODP, Texas A and M Univ., USA.

Satsukawa, T., Ildefonse, B., Mainprice, D., Morales, L.F.G., Michibayashi, K., Barou, F., 2013. A database of plagioclase crystal preferred orientations (CPO) and microstructures – implications for CPO origin, strength, symmetry and seismic anisotropy in gabbroic rocks. Solid Earth 4, 511–542. https://doi.org/10.5194/se-4-511-2013

Taufner, R., Viegas, G., Faleiros, F.M., Castellan, P., Silva, R., 2021. Deformation mechanisms of granulite-facies mafic shear zones from hole U1473A, Atlantis Bank, Southwest Indian Ridge (IODP Expedition 360). Journal of Structural Geology 149, 104380. https://doi.org/10.1016/j.jsg.2021.104380

Tribuzio, R., Tiepolo, M., Vannucci, R., 2000. Evolution of gabbroic rocks of the Northern Apennine ophiolites (Italy): Comparison with the lower oceanic crust from modern slow-spreading ridges. Special Paper 349: Ophiolites and Oceanic Crust: New Insights from Field Studies and the Ocean Drilling Program. Geological Society of America, 129–138. https://doi.org/10.1130/0-8137-2349-3.129

General annexes

The following supporting information provide a summary of the main results from EBSD analyses in the samples studied in chapter IV (SG.1) and chapter V (SG.2).

360-U1473A-9R-5W (76.77 mbsf) - Domain A

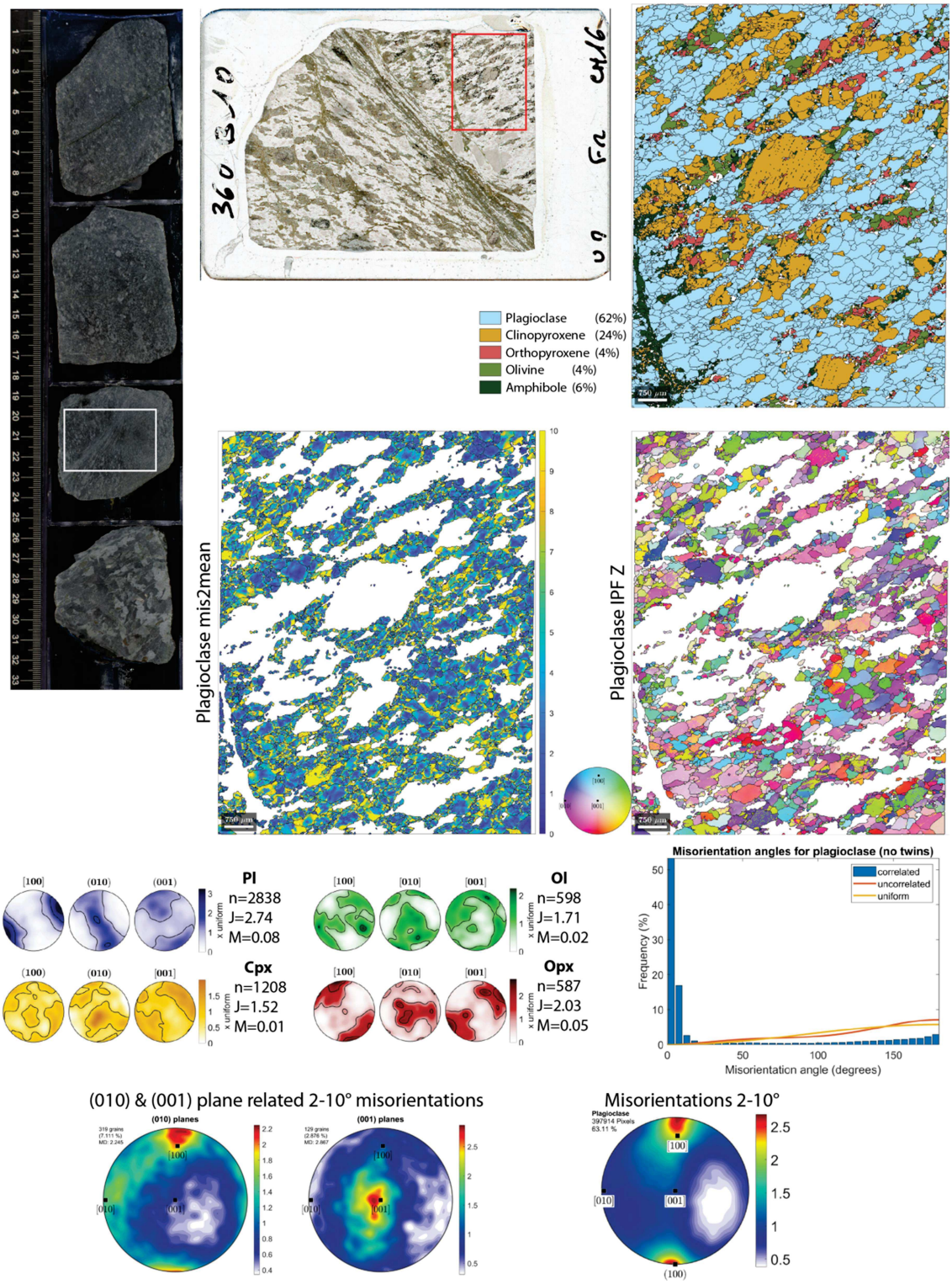

SG.1 *- Hole U1473A samples (Atlantis Bank, Southwest Indian Ridge). The two last numbers of sample names in these figures (e.g., "-**9**R-**5**W") correspond to the first number of the names used in chapter IV (e.g., sample "**9_5**_19").*

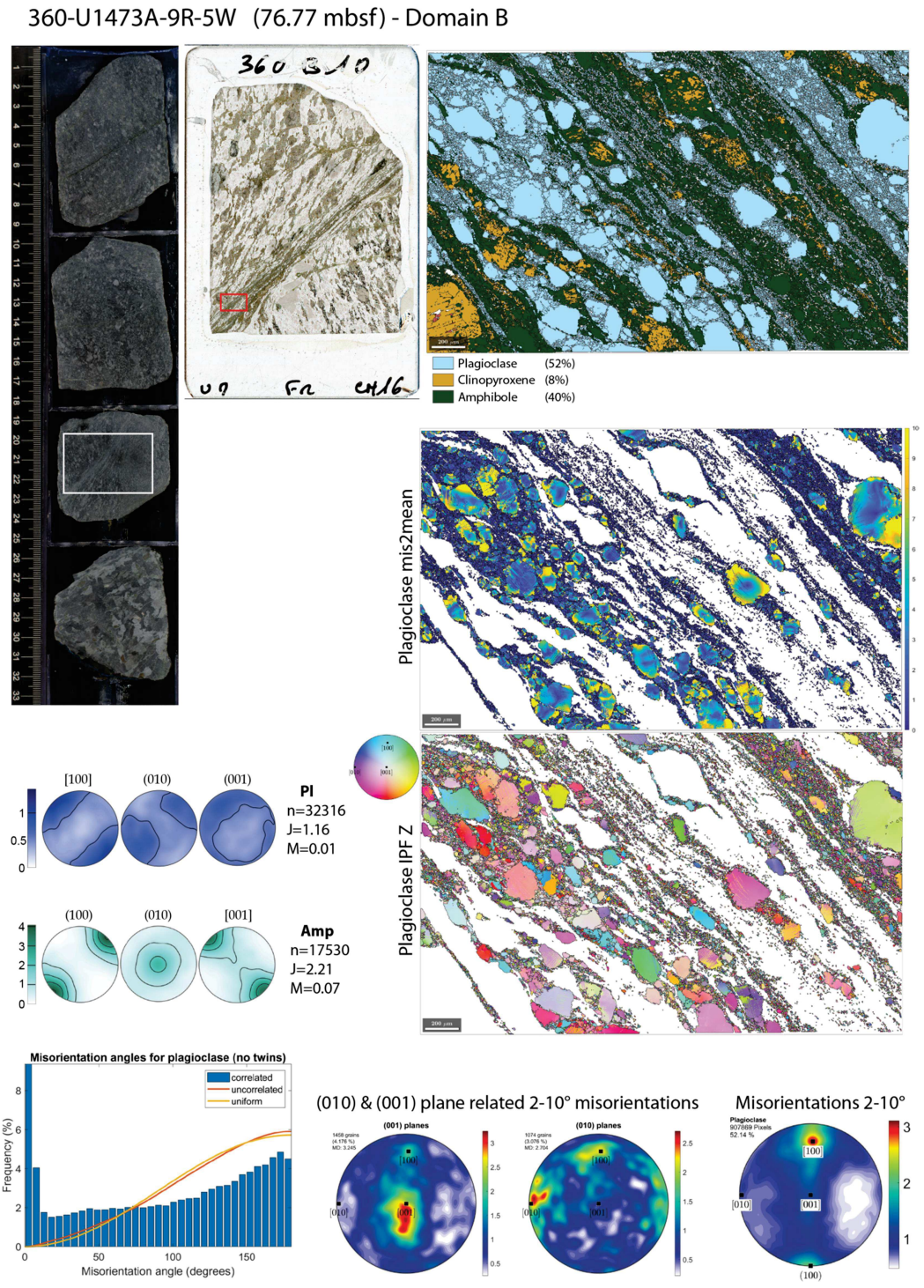

SG.1 (continued)

360-U1473A-88R-5W (775.14 mbsf)

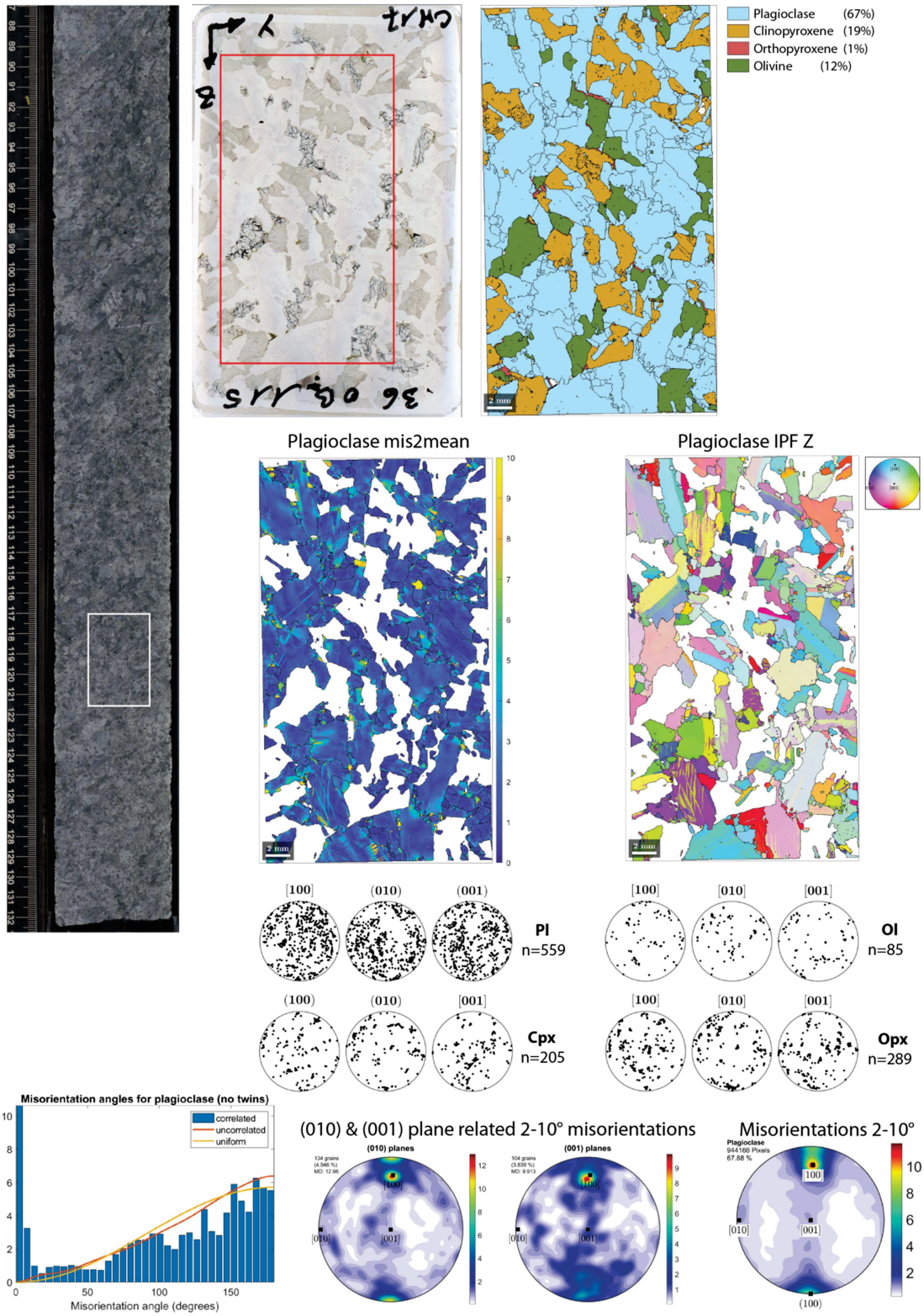

SG.1 (continued)

360-U1473A-58R-5W (252.06 mbsf) - Domain C

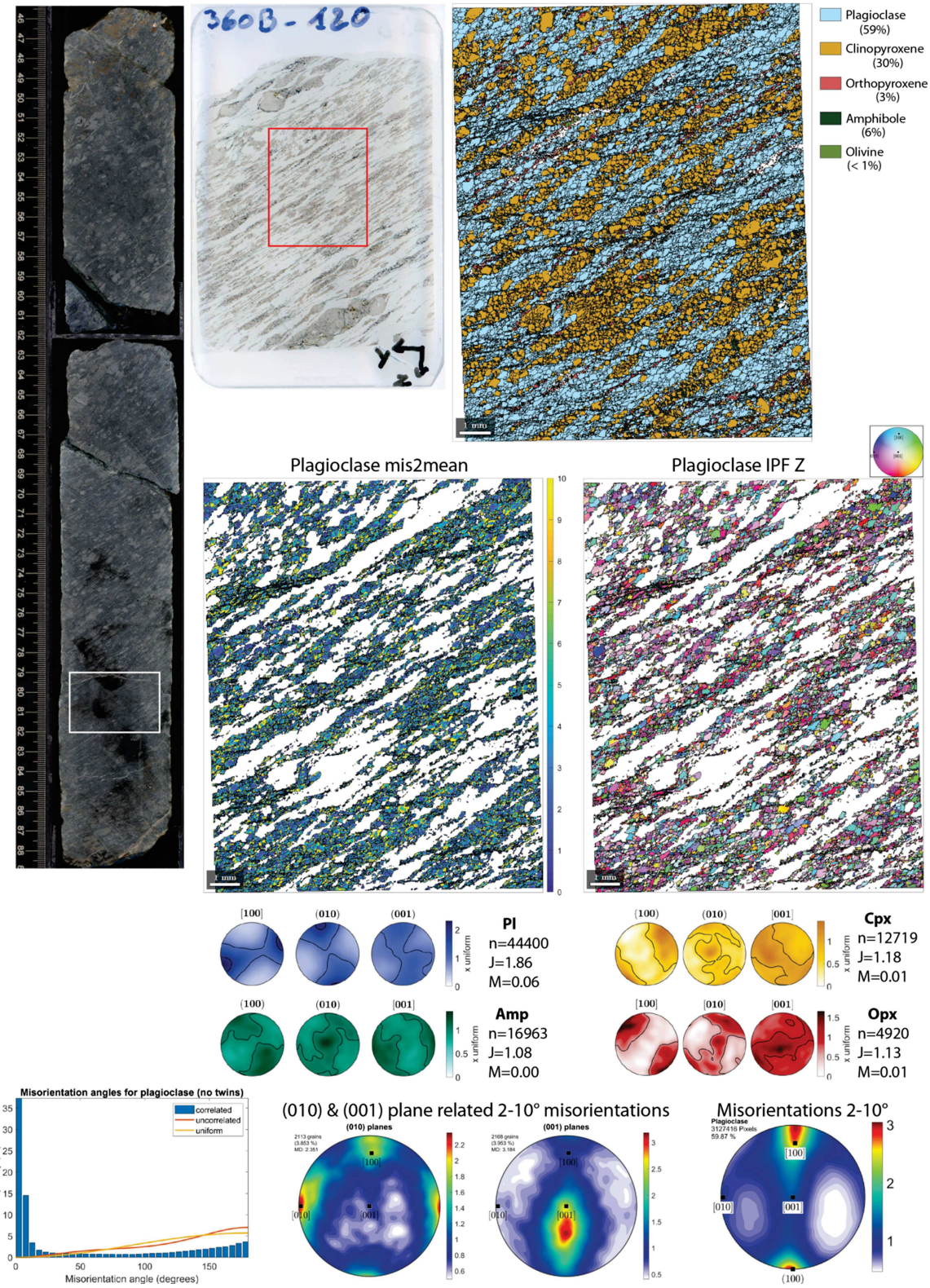

SG.1 (continued)

360-U1473A-69R-5W (631.10 mbsf) - Domain A

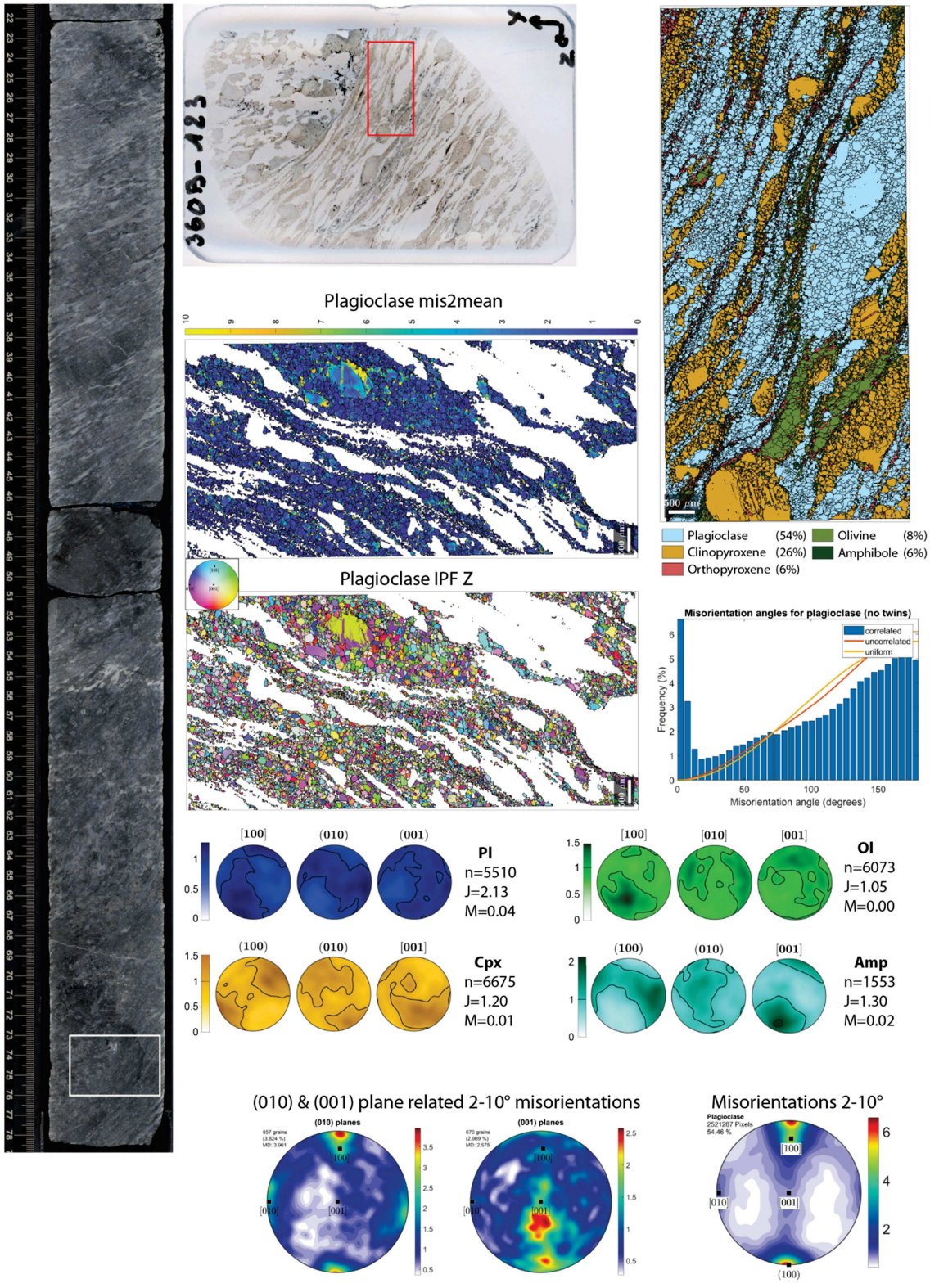

SG.1 (continued)

360-U1473A-69R-5W (631.10 mbsf) - Domain B

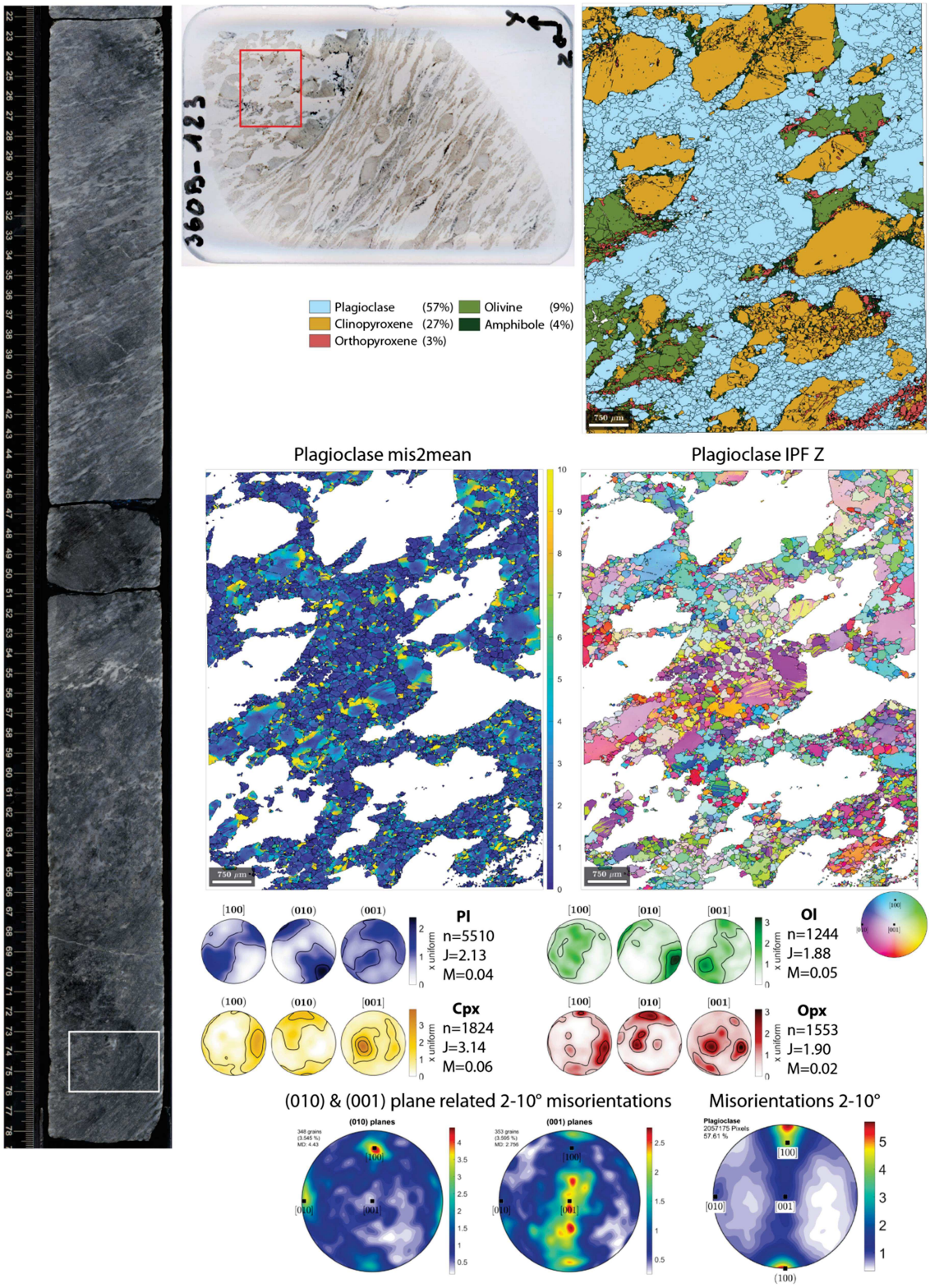

SG.1 (continued)

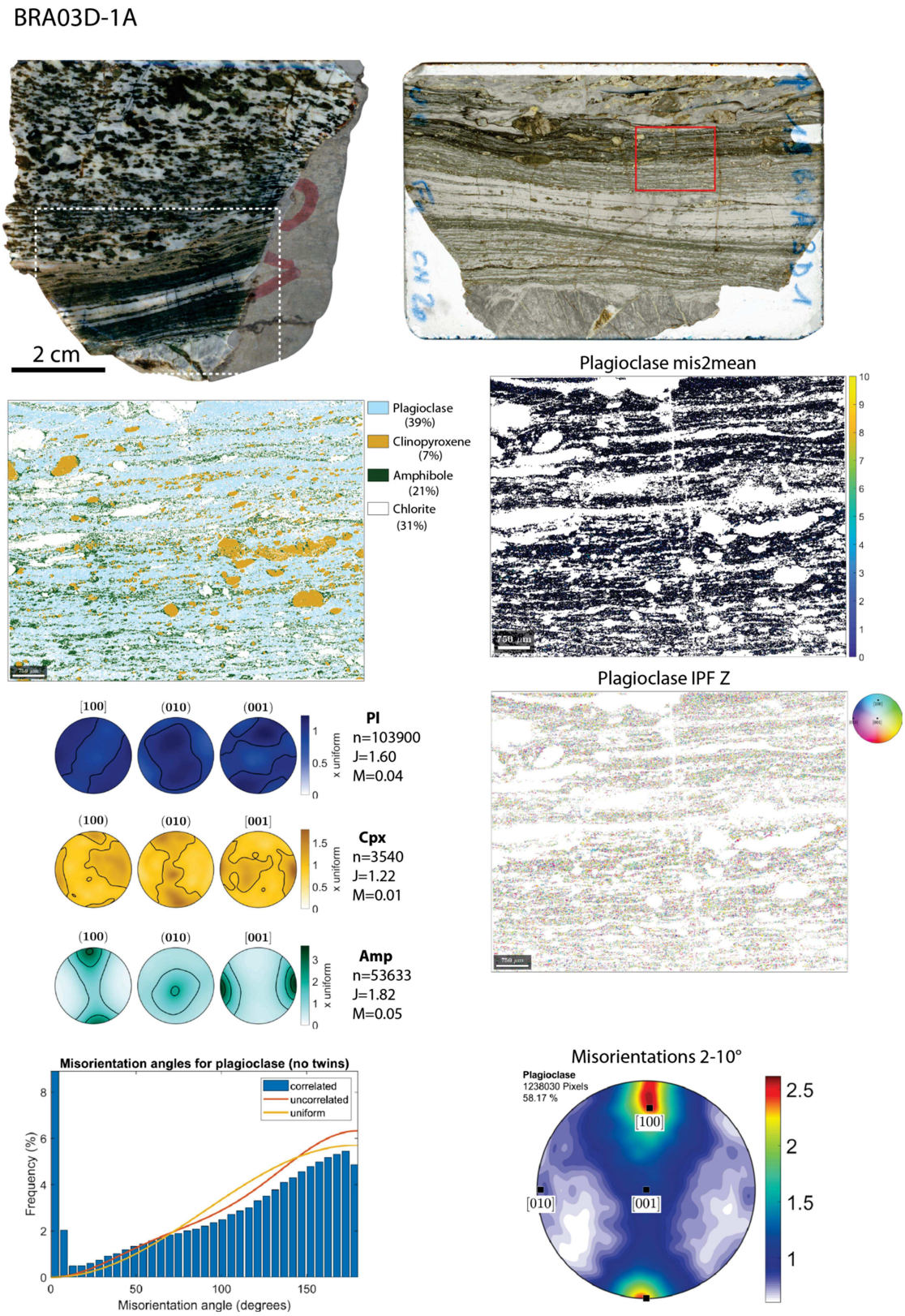

SG.2 *- Bracco-Gabbro Complex samples (Internal Ligurides, Northern Apennines)*

BRA03D-1A

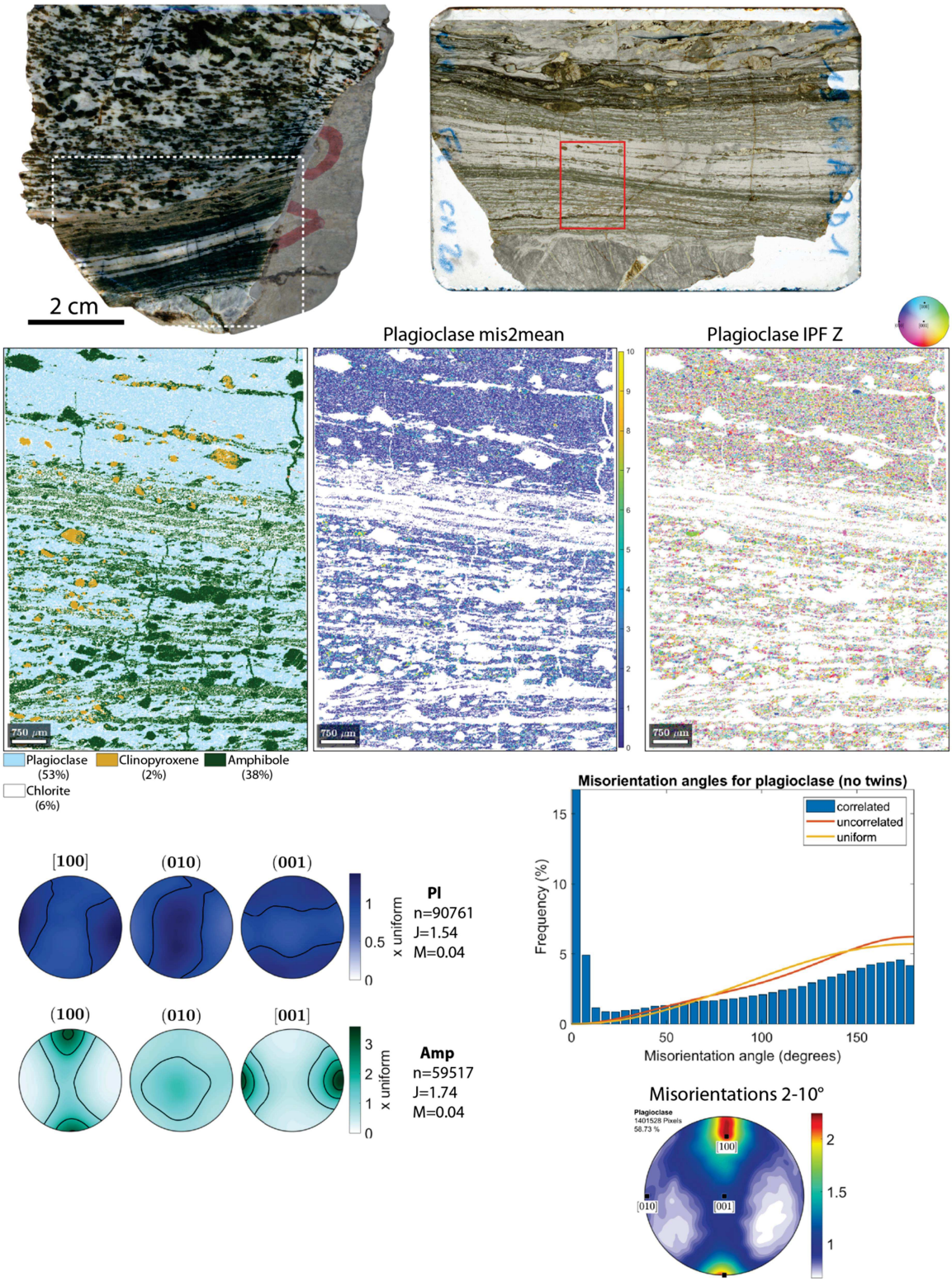

SG.2 (continued)

BRA03D-1A

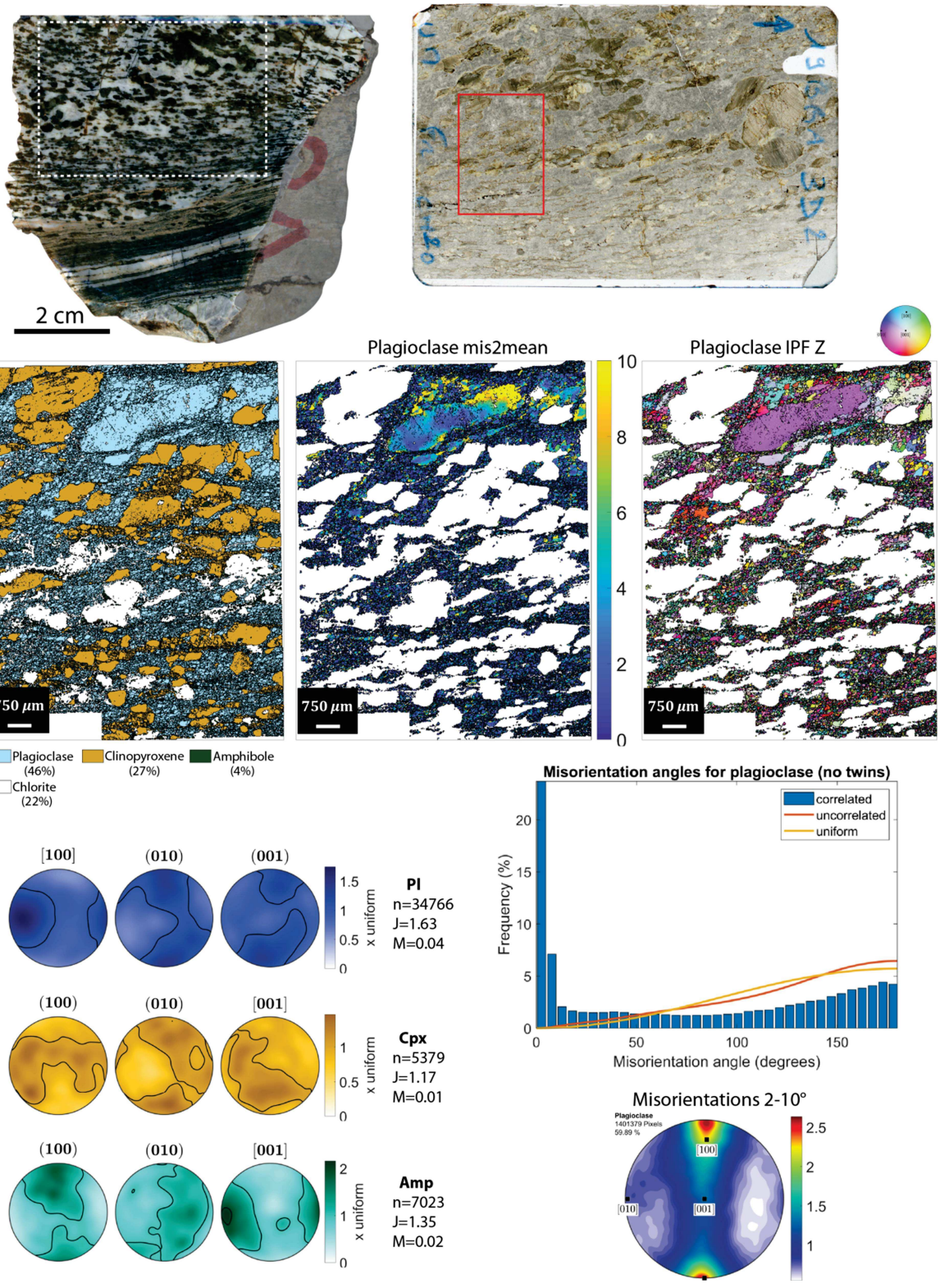

SG.2 (continued)

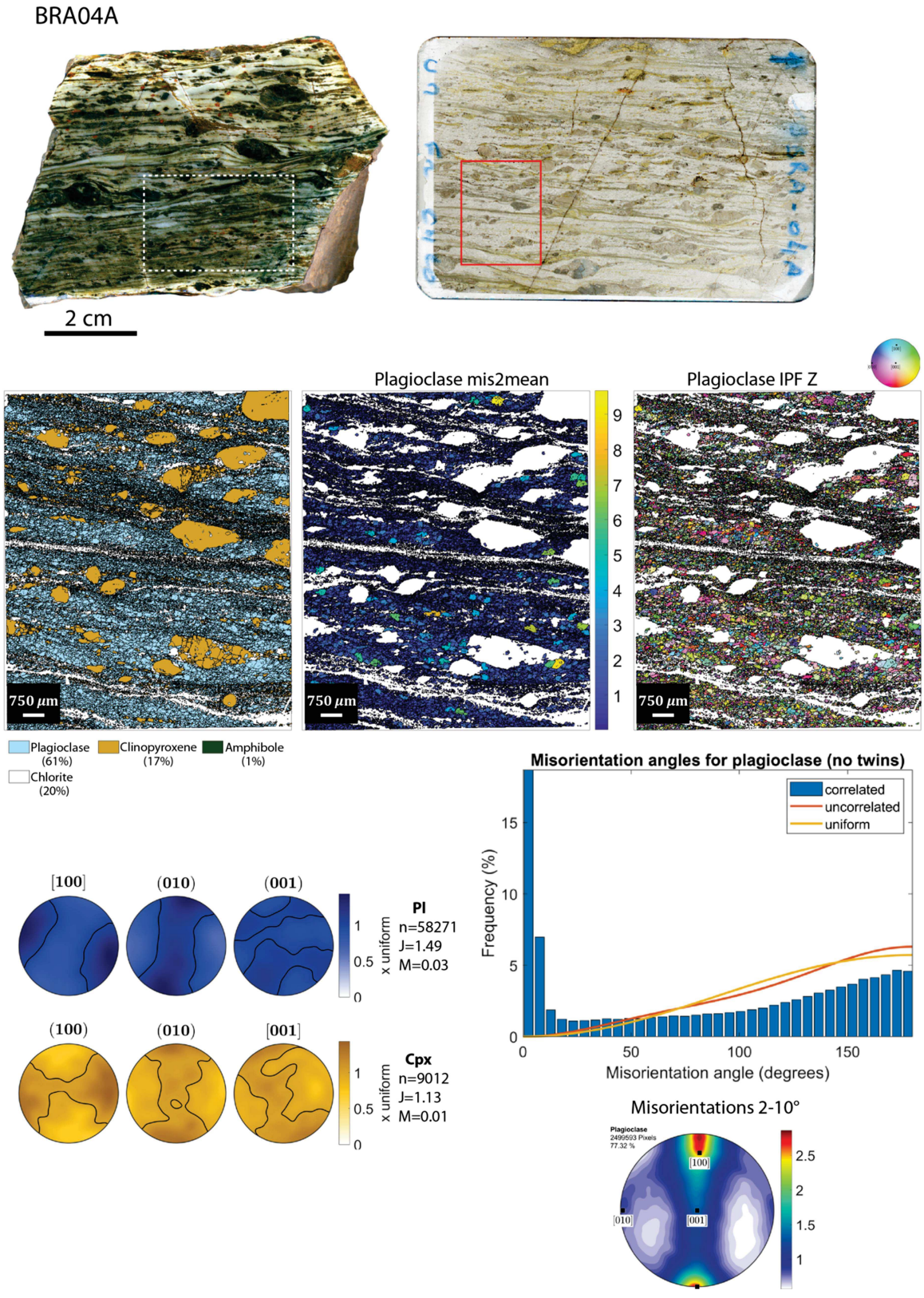

SG.2 (continued)

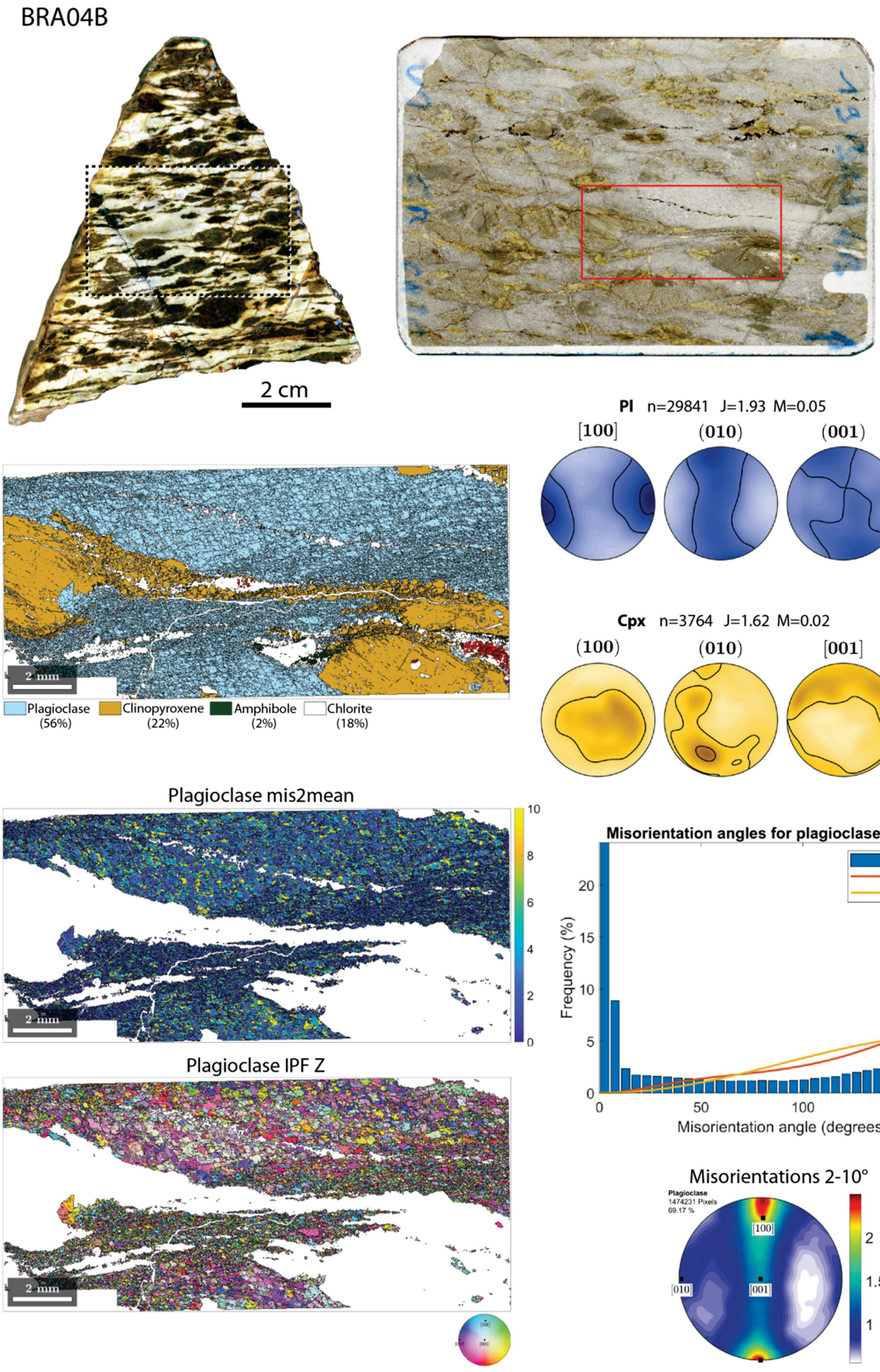

SG.2 (continued)

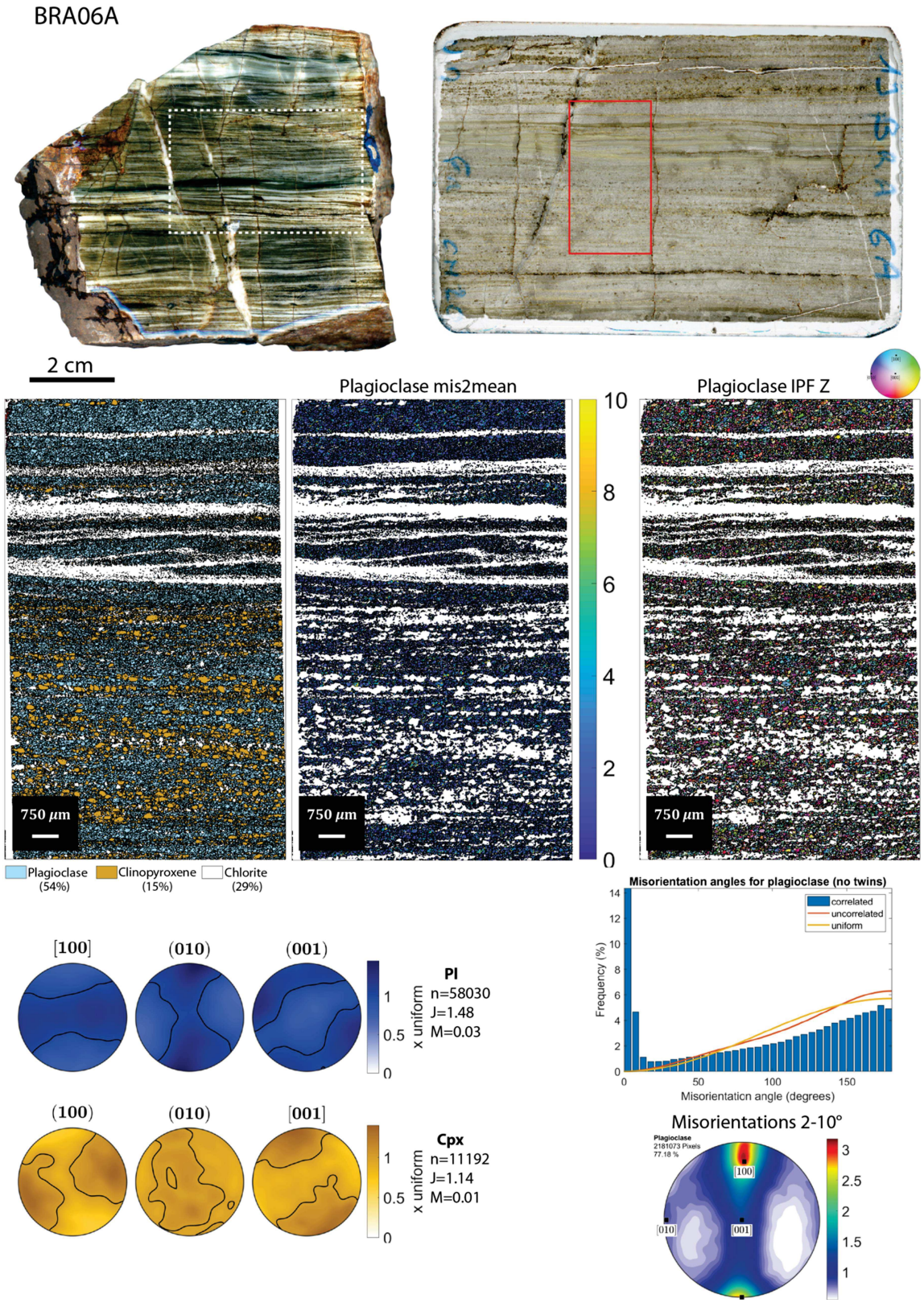

SG.2 (continued)

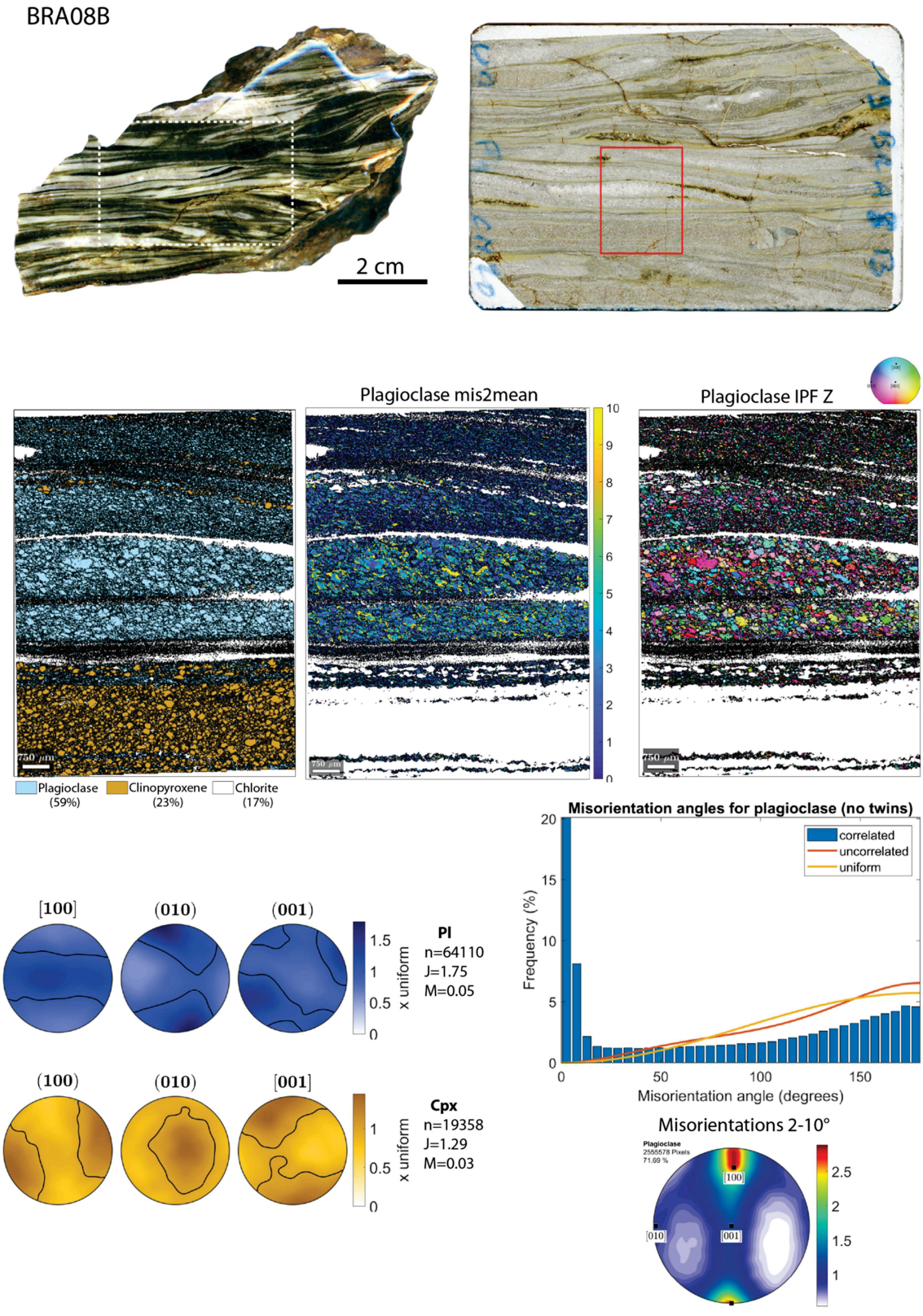

SG.2 (continued)

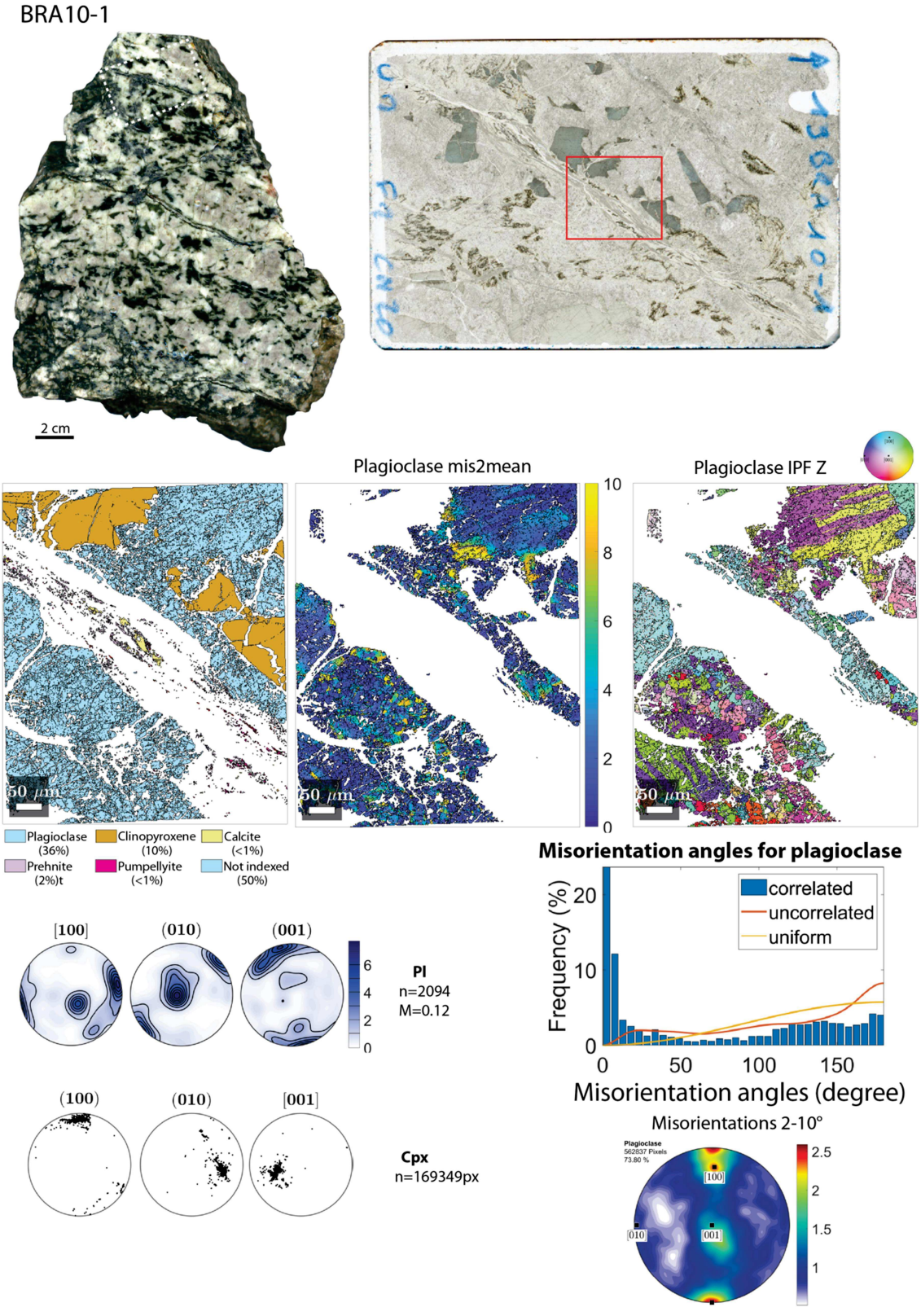

SG.2 (continued)